The University Of Sheffield.

Access To Thesis.

- A bound copy of every thesis which is accepted as worthy for a higher degree, must be deposited in the University of Sheffield Library, where it will be made available for borrowing or consultation in accordance with University Regulations.
- All students registering from 2008–09 onwards are also required to submit an electronic copy of their final, approved thesis. Students who registered prior to 2008–09 may also submit electronically, but this is not required.

Author: Stuart Robert John Walker Dept: Department of Mechanical Engineering

Thesis Title: Hydrodynamic interactions of a tidal stream turbine and support structure Registration No: 100132665

For completion by all students:

Submit in print form only (for deposit in the University Library): ☐

Submit in print form and also upload to the *White Rose eTheses Online* server: In full ☑

Edited eThesis ☐

Please indicate if there are any embargo restrictions on this thesis. Please note that if no boxes are ticked, you will have consented to your thesis being made available without any restrictions.

Embargo details: (complete only if requesting an embargo to either your print and/or eThesis)	Embargo required?		Length of embargo (in years)
Print Thesis	Yes ☐	No ☐	
eThesis	Yes ☐	No ☐	

Supervisor: I, the supervisor, agree to the named thesis being made available under the conditions specified above.

Name: Dr. Robert Howell Dept: Department of Mechanical Engineering

Signed:  Date: 15th December 2014

Student: I, the author, agree to the named thesis being made available under the conditions specified above.

I give permission to the University of Sheffield to reproduce the print thesis in whole or in part in order to supply single copies for the purpose of research or private study for a non-commercial purpose.

I confirm that this thesis is my own work, and where materials owned by a third party have been used copyright clearance has been obtained. I am aware of the University's *Guidance on the Use of Unfair Means* (www.sheffield.ac.uk/lets/design/unfair)

I confirm that all copies of the thesis submitted to the University (including electronic copies on CD/DVD) are identical in content.

Name: Stuart Robert John Walker Dept: Department of Mechanical Engineering

Signed: 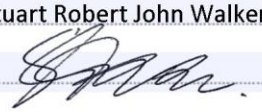 Date: 15th December 2014

For completion by students also submitting an electronic thesis (eThesis):

I, the author, agree that the University of Sheffield's eThesis repository (currently WREO) will make my eThesis available over the internet via an entirely non-exclusive agreement and that, without changing content, WREO may convert my thesis to any medium or format for the purpose of future preservation and accessibility.

I, the author, agree that the metadata relating to the eThesis will normally appear on both the University's eThesis server and the British Library's EThOS service, even if the thesis is subject to an embargo. I agree that a copy of the eThesis may be supplied to the British Library.

I confirm that the upload is identical to the final, examined and awarded version of the thesis as submitted in print to the University for deposit in the Library (unless edited as indicated above).

Name: Stuart Robert John Walker Dept: Department of Mechanical Engineering

Signed: 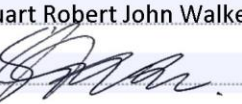 Date: 15th December 2014

THIS SHEET MUST BE BOUND IN THE FRONT OF THE PRINTED THESIS BEFORE IT IS SUBMITTED

Hydrodynamic interactions of a tidal stream turbine and support structure

A dissertation submitted for the degree of Doctor of Philosophy

Stuart Robert John Walker

Department of Mechanical Engineering

The University of Sheffield

December 2014

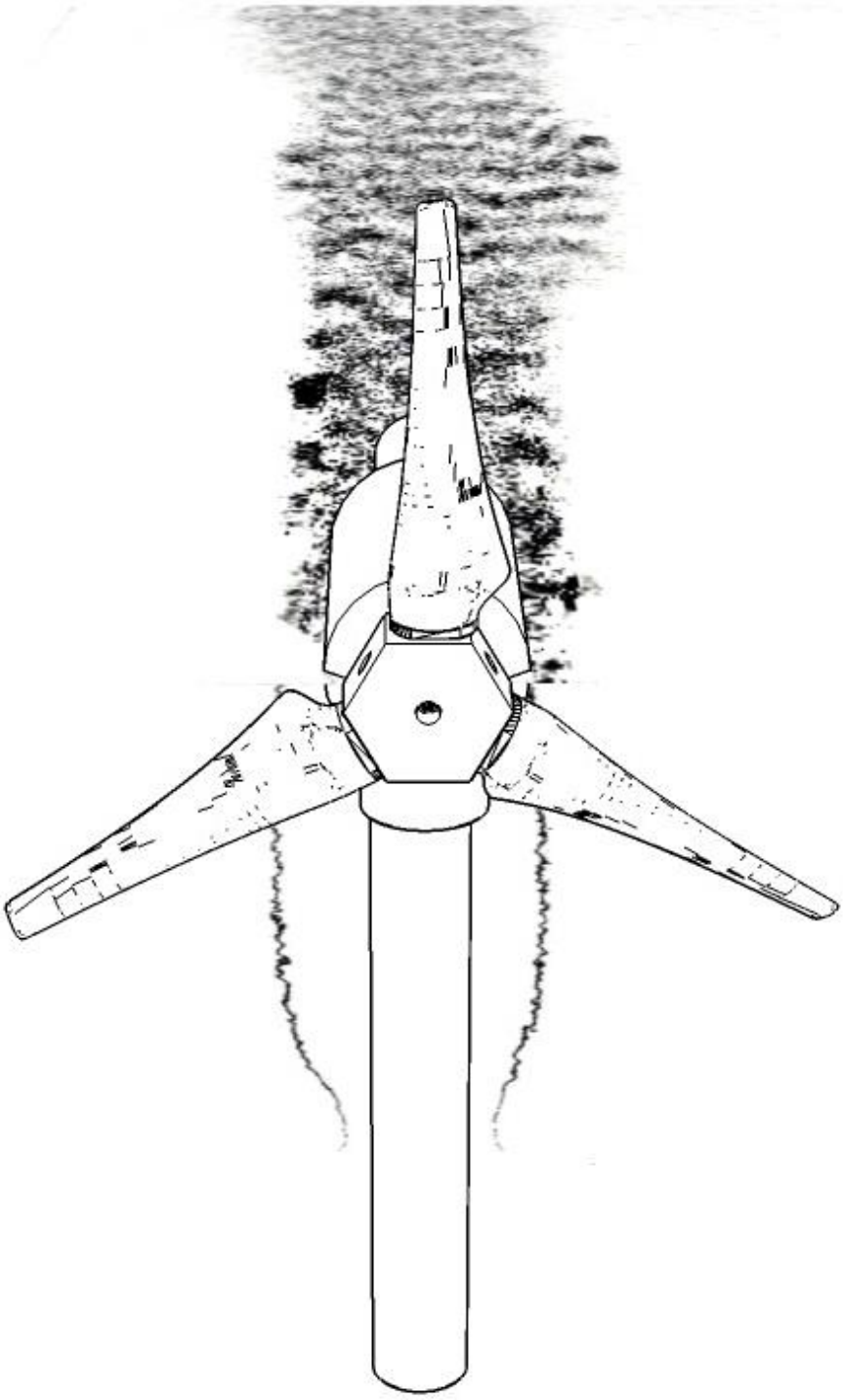

Summary

Amid growing concern over climate change and the resultant need to reduce CO_2 emissions, as well as an ever-increasing global population with a rising demand for electricity, renewable energy sources have an important role to play in future electricity generation. One such source is tidal stream energy, which offers the potential for predictable electricity generation by harnessing the energy of the tide using arrays of underwater turbines.

This research explores the impact of hydrodynamic interactions between the blades of a tidal stream turbine and its support structure on turbine performance, as well as the hydrodynamic interaction of multiple turbines. Experiments were carried out using scale model turbines installed in experimental water channels, and a motorised drive system and encoder was used to record turbine performance.

Due to turbulence in the region upstream of the support structure, separation distance between the turbine blades and support structure was found to significantly influence performance. An optimal separation distance between the blades and support structure was found to allow maximum performance. The turbulent wake of an upstream turbine was also found to have a notable impact on downstream turbine performance, leading to a reduction in power output. This effect is governed by upstream and offset separation distance and support structure diameter. Particle Image Velocimetry was used to record downstream turbine velocity wakes, which were found be a complex amalgamation of turbine and support structure elements.

The testing of a turbine installed on four complex support structures produced large differences in power outputs, further highlighting the influence of support structure design on turbine performance, and confirming its importance to the design of tidal stream turbine arrays.

Declaration

The work described in this dissertation is submitted in partial fulfilment of the requirements of the degree of Doctor of Philosophy, and was carried out between October 2010 and November 2014. I hereby declare that the work described is entirely my own, and that no portion has been submitted as of any part of another degree at this or any other university. Where the work of others has been used this been cited within the requirements of academic regulation and ethical conduct.

This thesis contains approximately 88,000 words and 222 figures.

Stuart Walker

Acknowledgements

I must first thank my main supervisor, Rob Howell, for his help and support throughout the duration of this work, and for allowing me to work independently whilst being on hand to help when needed. Without the help and knowledge of Rob and my second supervisor Wernher Brevis I would never have reached this stage, so I am truly grateful to you both. I am also grateful to UK EPSRC and the E-Futures Doctoral Training Centre for supporting this project.

Thanks must also go to the academic and non-academic staff in the Department of Mechanical Engineering who have given help during the course of my research, particularly Stephen Beck and Rob Dwyer-Joyce, and to the technical staff who helped with the preparation of the lab. I have also benefited from the generosity of colleagues and friends and am particularly grateful to Manar Safar, Jon Sumanik-Leary and Cora Fung.

Alstom Renewable Power (formerly Tidal Generation Limited) provided technical information to assist with the design of turbine models, and I would like to thank Paul Vigars for his input and guidance.

Lasers were important to this project and I would like to thank Robert at Dantec for his help in maintaining our laser; Sergei Lukashuk at the University of Hull for lending me another when it could no longer be maintained; Simon Tait for supplying seeding particles; and William Thielicke for offering assistance with the processing of the results.

During 2014 I spent time at the University of Florence working on the final phase of this project, and would like to say *grazie mille* to Lorenzo and the team at UNIFI for their help and hospitality.

My family were surprisingly supportive when I left a proper job and returned to University, and have remained so over the duration of this project. Without them I would not have got this far, so I would like to thank them all.

Finally I must thank my wife Lorna, for her constant support and unwavering confidence in me, and for winning most of the bread over the past four years.

For big dogs and little dogs.

Nomenclature

Abbreviations which are not given a specific definition at the time of use are defined below.

Channel Flow

A_C	Channel cross-sectional area (m²)
A	Blade swept area (m²)
A_D	Actuator disk area (m²)
D_H	Hydraulic diameter (m)
h	Water height (m)
P_A	Available power in water (W)
Q	Volumetric flow rate (m^3/s)
$\bar{u}$	Mean fluid velocity (m/s)
u_0	Free stream fluid velocity (m/s)
u_x	Fluid velocity at position x (m/s)
U	Bulk flow velocity (m/s)
v	Kinematic viscosity (m²/s)
μ	Dynamic viscosity (Ns/m²)
ρ	Density (kg/m³)
z	Height above base of water channel (m)
δ	Boundary layer thickness (mm)

Turbine performance

B	Blockage ratio
BF	Blockage Factor
C_T	Thrust Coefficient
C_p	Power Coefficient
D	Blade diameter (m)
d	Support structure diameter (m)

P_B Blade power (W)

P_{app} Motor applied power (W)

R Blade radius (m)

T_B Blade torque (Nm)

u_{def} Velocity deficit (%)

α Angle of attack (°)

λ Tip speed ratio

ω Rotational speed (rad/s)

Turbulence

k Turbulent kinetic energy (m^2/s^2)

t_L Integral scale turnover time (s)

t_η Kolmogorov microscale turnover time (s)

u_* RMS velocity

u' Velocity fluctuation from mean (m/s)

ε turbulence dissipation rate (m^2/s^3)

I Turbulent intensity (%)

η Kolmogorov microscale (mm)

$\vec{\omega}$ vorticity (1/s)

$\varphi_n(x)$ POD eingnfunctions

$\alpha_n(t)$ POD time functions

λ_n POD eigenvalues

Dimensionless numbers

Re Reynolds Number

Fr Froude Number

St Strouhal Number

Stk Stokes Number

Water channel planes and directions

With reference to the water channels used in this study, the following directional conventions are used:

The streamwise direction is defined as the direction along the length of the water channel, from the inlet to the outlet. The downstream direction is defined as the direction of travel of the channel flow from the inlet to the outlet (the positive streamwise direction), and the upstream direction as against the direction of flow (negative streamwise direction). Streamwise direction and velocity are given by x and u, respectively.

The cross-stream direction defines the horizontal direction across the channel width, perpendicular to the streamwise direction. When facing towards the oncoming flow, the positive cross-stream direction is to the right, and the negative to the left. Cross-stream direction and velocity are given by y and v, respectively.

Contents

1

Introduction

1.1 – The need for clean energy

1.1.1 – Climate change

The existence of anthropogenic climate change is now agreed on by the vast majority of scientists. A huge wealth of scientific data exists supporting the hypothesis that human activity, particularly the burning of fossil fuels, has led to dramatic changes in the world's climate, particularly since the industrial revolution [1].

Climate change is a blanket term used to describe the effects of human activities on the natural global climate on earth. Under the umbrella of climate change, the most well-known effect is "global warming". This is actually a misleading term, since the effects of climate change do not always manifest themselves as temperature increases, but is a term which has become common public parlance for the effects of anthropogenic climate change.

Greenhouse gases and Carbon Dioxide (CO_2)

The greenhouse effect is an essential component for life on earth. Within the composition of the thin layer of air surrounding earth are greenhouse gases such as Carbon dioxide, methane and water vapour, as well as others in low concentrations. These gases act to reflect, absorb and trap solar radiation incident on our planet, providing a thermal blanket which maintains the temperature of earth at a level which can sustain life. Without this effect (known as the greenhouse effect), the average global temperature would be around -1°C, making the existence of life unlikely. The principal of the greenhouse effect is illustrated in Figure 1-1.

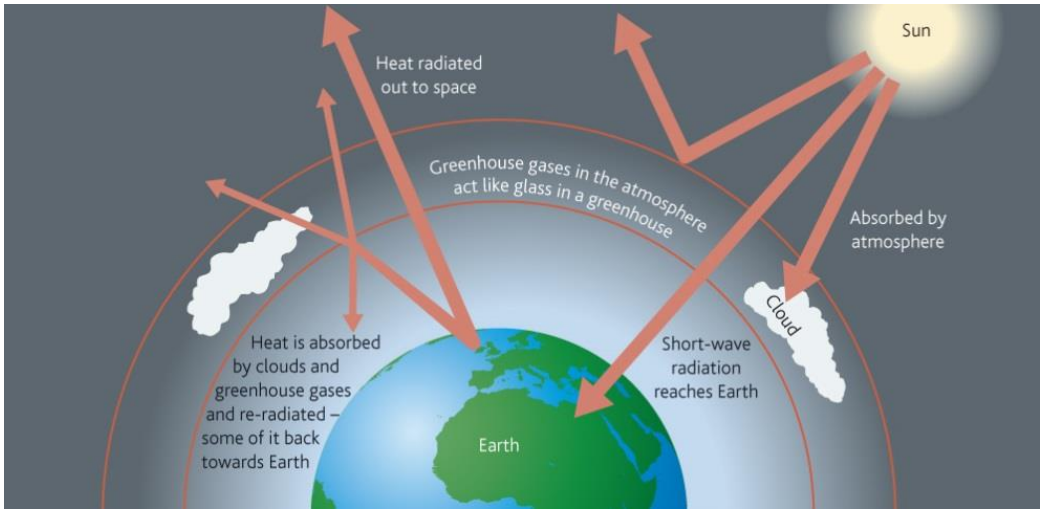

Figure 1-1 – The greenhouse effect[2].

Carbon dioxide is the best known greenhouse gas, but it is not the most powerful in terms of insulating effect. It is, however, highly abundant, meaning that its overall greenhouse effect is the greatest of all greenhouse gases. The potential of a greenhouse gases to trap heat and contribute to global warming is commonly measured using Global Warming Potential (GWP). This simple measure is a calculation of the heat-absorbing potential of a gas relative to that of CO_2.

Other greenhouse gases [3] are detailed below:

- Methane has a GWP of 21, but is much less abundant (pre-industrial levels were around 700ppb (parts per billion), and current levels are around 1700ppb). Methane also remains in the atmosphere for a much shorter period than CO_2, approximately nine years as opposed to approximately 100 for CO_2. There is increasing concern that the huge amounts of methane trapped in permafrost could be released due to global melting, and would make a significant contribution to global warming.
- Nitrous Oxide has a GWP of 310, meaning it is over 300 times more powerful as a greenhouse gas than CO_2. Pre-industrial concentration levels were around 270ppb, and 2005 levels were around 319ppb. Increases in nitrous oxide levels are primarily caused by microbe activity in soil, which is increased under warm and wet conditions, and through deforestation and chemically-intensive farming methods. Increases in these activities are also causing increased levels of nitrous oxide emission.
- "F-gases" is a blanket term for Hydroflourocarbons (HFCs), Perfluorocarbons (PFCs) and Sulphur hexafluoride (SF6). These are industrial gases, such as those used in refrigeration. These man-made products were not present in pre-industrial conditions, and are thousands of times more powerful than CO_2. However, they are only present in very small concentrations (parts per trillion).

Human activity has altered the concentration of greenhouse gases in earth's atmosphere, thus altering their effect on the incident solar radiation. Since the 1950s, records have been kept of the level of CO_2 in the atmosphere through the use of live monitoring stations. Ice core drilling has also been used to study historical data, by extracting air bubbles trapped in ice sheets frozen over hundreds of thousands of years. Studying these sources in conjunction with global temperature data indicates that the increased levels of atmospheric CO_2 correlate directly with changes in the global climate. Increased levels of greenhouse gases in the atmosphere mean that more solar radiation is trapped, thus meaning that the greenhouse effect is increased. The correlation between atmospheric CO_2 and global temperature is illustrated in data from the Antarctic Ice core analysis [4], as shown in Figure 1-2.

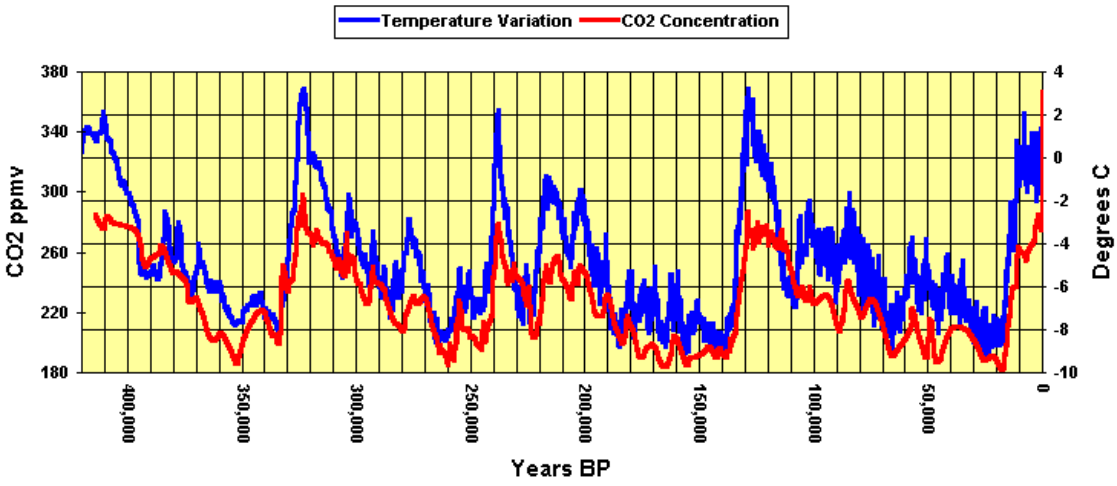

Figure 1-2 – Antarctic Ice Core data: CO_2 concentration and temperature variation over 420,000 years to 2005.

As this data illustrates, CO_2 concentration and temperature variation occurred naturally long before human life existed. Figure 1-2 illustrates temperature variation over four glacial cycles. However, variation in CO_2 levels until around 70 years ago remained between 180 and 300ppm. Since this time, a dramatic increase has been seen. CO_2 levels exceeded 400ppm during May 2014 and are currently increasing by around 2ppm per annum. Over the duration of this PhD project, atmospheric CO_2 has risen from 387ppm to 402ppm.

The effects of climate change

Though climate change is often thought of as a future problem which will occur if greenhouse gas emissions are not reduced, the effects of climate change are now beginning to be observed around the world. Since pre-industrial levels, a global temperature increase of 0.7°C has been observed, and even this modest increase has produced observable effects in nature, for example the bleaching of Coral Reefs in the Great Barrier Reef and the well-publicised retreat of glaciers around the world [5].

Figure 1-3 - The Evolution of the Rhone glacier from 1850 until today [5].

The United Nations Development Programme's Human Development Report [6] identified that 262 million people were directly affected by "climate disasters" per annum between 2000 and 2004, with 98% of these people living in the developing world. In such countries, approximately one in nineteen individuals has been directly influenced by climate change. In OECD countries, the figure is around 1 in 1500. The primary countries identified as the most at risk are in sub-Saharan Africa, south Asia, the Middle East and Pacific Island states. In such countries, flooding is one of the primary risks to life. Increased global temperatures will lead to the melting of ice sheets and glaciers, causing an increase in sea levels. A temperature rise of 2°C would lead to the disappearance of rainforests, huge levels of glacial melting and sea level changes, and the displacement of millions of people living in affected areas. A temperature rise of 3°C would be catastrophic, and would result in the displacement of an estimated 330 million people, including over 70 million people in Bangladesh alone. Glacial melting would be dramatic, resulting in sea level rises making some Pacific and Caribbean islands uninhabitable. Animal and plant species would be unable to adapt or evolve quickly enough to survive these effects, and an estimated 30% of species would be extinct.

The role of electricity generation

Electricity generation is the largest single source of greenhouse gas emissions, and contributes 26% of the global total [7]. For comparison, the next largest global sources are industry (19%), forestry (17%) and agriculture (14%).

However, electricity generation is a greenhouse gas source which can potentially be reduced. Renewable energy sources, as will be discussed in detail in Section 1.2.3, are able to dramatically reduce the greenhouse gas emissions necessary to produce a unit of electricity, and as technology advances are able to do so at a cost comparable to traditional energy sources.

Even with current energy sources, however, it is possible to dramatically reduce the greenhouse gas emissions of the world's electricity generation by simply reducing the amount of electricity required. This is known as "demand reduction", and can be achieved in a number of ways: Through the use of more efficient equipment; by reducing the need for electricity use (for example by improving home insulation to reduce heating demand); or by ensuring that equipment is used at the most suitable time, so that generated electricity is not wasted. Demand reduction at a domestic level is often driven by the associated cost savings, but can be led by governmental policy, an example of which was the EU directive switch from incandescent to "energy-saving" light bulbs, which is predicted to save 39TWh of electricity across the EU by 2020 [8]. However, demand reduction is only able to partly solve the problem of greenhouse gas emissions, and the decarbonisation of electricity generation is also required in order to limit the effects of climate change.

1.2 –Electricity generation

Electricity is generated by a wide range of sources in varying degrees across the world, but the burning of fossil fuels makes up by far the largest portion of global electricity generation. In total, all fossil fuel-based sources of electricity generation made up around 84% of global energy generation in 2011 [9], as illustrated in Figure 1-4 (energy generation is given in million tonnes of oil equivalent (Mtoe), a unit which describes the equivalent weight of oil which would be required to generate the same amount of electricity). For conversion, 1Mtoe is equal to 11,630 GWh.

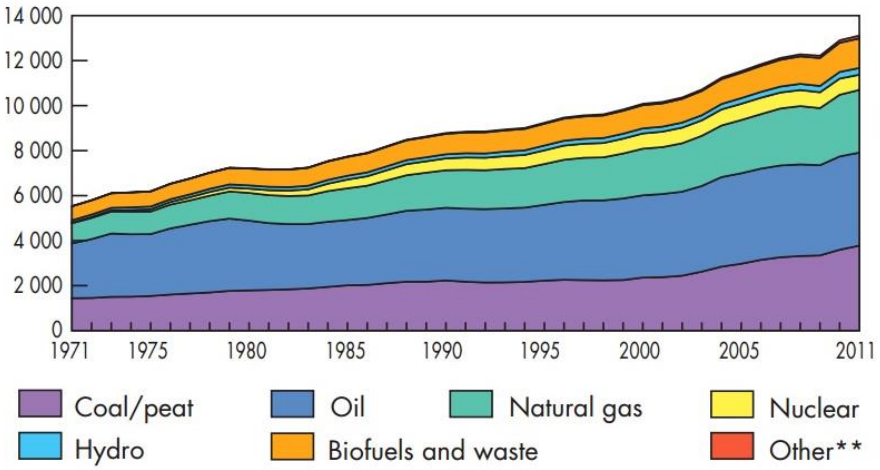

Figure 1-4 – World electricity generation sources (Mtoe)by volume: 1971 and 2011 [9].

The primary reason for this dominance of fossil fuel generation is the relative ease and low cost of generating large volumes of electricity. As countries develop and electrification begins, renewable energy sources are often the first source of power, particularly in rural areas [10], but as mass electrification begins these sources of electricity generation are likely to be too expensive to implement at a sufficiently large scale, and fossil fuel power stations are the most viable option. Nuclear power does offer the potential to generate sufficiently large volumes of electricity, but the implementation of this technology is challenging and costly. Reliability of supply is another major advantage of fossil-fuel generated power, since output from such power stations can relatively easily be adjusted to track changes in demand, which is not possible through the use of renewable energy and is difficult in the case of nuclear power, for example.

Around the world there are notable exceptions to this dominance of fossil fuels, such as France (10% fossil fuels) and Norway (4% fossil fuels). In France, electricity generation is dominated by nuclear power, which makes up around 76% of total generation capacity. The percentage of renewable energy is also high in France, with 14% of total generation capacity supplied primarily by hydroelectric power, including the La Rance tidal barrage, which is discussed in more detail in Section 1.4.1. Despite per capita electricity demand above the European average, the use of nuclear and renewable generation means France's CO_2 emissions are below the European average (6.1t per capita vs 8.6t per capita).

Norwegian power is dominated by renewable, and specifically hydroelectric, generation. This type of power generation makes up around 98% of annual demand (2008 figures), the remainder of which is supplied by a combination of wind and fossil fuel generation, both internally and imported.

In both countries, the import and export of electricity is an important part of the power network. France is the world's largest exporter of electricity due to its large nuclear capacity, and the aforementioned difficulty in adjusting the output of this method of generation. Norway imports up to 10% of annual electricity use in order to take up demand in times of low hydroelectric generation. Similarly, the country is also able to export power to neighbours at times when generation exceeds national demand.

Approximate life cycle CO_2 emissions (embodied CO_2 from manufacture, installation, and lifetime operation of a generation source compared to lifetime electrical generation) per unit of generated electricity by source are given in the table below [11] and highlight the potential for low per capita CO_2 emissions possible by avoiding the use of fossil fuel-based power generation. The figures given are European averages, as of 2008.

Electricity generation source	*CO_2 emissions (g/kWh)*
Nuclear	5
Wind	6
Hydroelectric	10
Solar PV	80
Combined cycle Gas	450
Oil	900
Coal	1,000

Table 1-1 – Life cycle CO_2 emissions (g/kWh) by source.

However, other environmental and social effects associated with electricity source must be considered in addition to CO_2 emissions. Such issues are particularly pertinent in the case of nuclear generation, with the storage of nuclear waste being a highly challenging and evocative issue. Furthermore, the potential dangers associated with nuclear power generation were highlighted recently by the meltdown of three nuclear reactors at the Japanese Fukushima nuclear power plant on 11th March 2011. The incident has resulted in the Japanese government changing the direction of its energy strategy towards an increased renewable energy supply, and has further fuelled the debate over the safety of nuclear power. Though nuclear power is highlighted by some [12] as the only viable future electricity generation method, particularly if nuclear fusion becomes possible, the associated cost, waste and safety issues mean the technology cannot be adopted universally, and alternatives must be sought.

1.2.1 – The current UK energy mix

The UK generates around three-quarters of its energy from fossil fuel sources[13], with the largest portion being generated by gas-fired power stations (around 40%). The UK has 76 gas-fired power stations, 36 of which are of the CCGT (Combined Cycle Gas Turbine) type, which have a CO_2 factor of around 450g/kWh. The remainder are the mostly the older single-cycle type with emissions of up to 800gCO_2/kWh. Coal-fired generation provides the second largest portion of energy generation at 31%, and the greatest contribution to CO_2 emissions. The UK's largest power station and largest source of CO_2 emissions is the Drax coal-fired power station in North Yorkshire, which alone produces around 6% of the total electricity [14]. Oil-fired power stations make up the remaining 1.5% of the fossil fuel total, which is around 73% of electricity generation.

The remaining 27% of the UK's electricity is generated by nine nuclear power stations (contributing 17% of the total); a contribution of around 1% from imported energy; 5% from renewable energy and 5% from other sources, which includes energy from waste facilities and on-demand generation such as the Dinorwig pumped storage facility, which is used to generate a short term contribution to the UK grid at very short notice, to cover peaks in demand. The renewable energy contribution is made up almost entirely of wind and hydroelectric power, making up 3% and 2% respectively. UK levels of electricity generation by source are given below (2012 figures [13]).

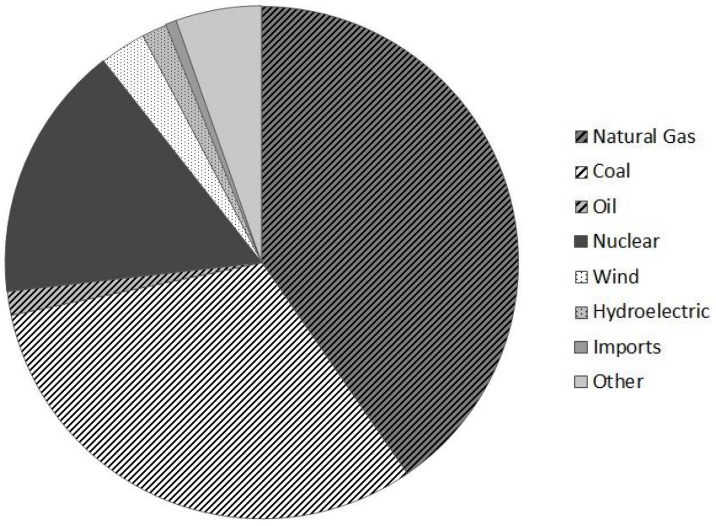

Figure 1-5 – UK electricity generation by source.

Base load

Energy demand, when considered over time at a national level, is commonly divided into three categories. These categories are known as base load, intermediate or cycling load, and peak load. At all times, the total demand is the sum of the three categories. Electrical demand for a typical hypothetical UK day and week are given in Figure 1-6 and Figure 1-7, illustrating the three categories in each case.

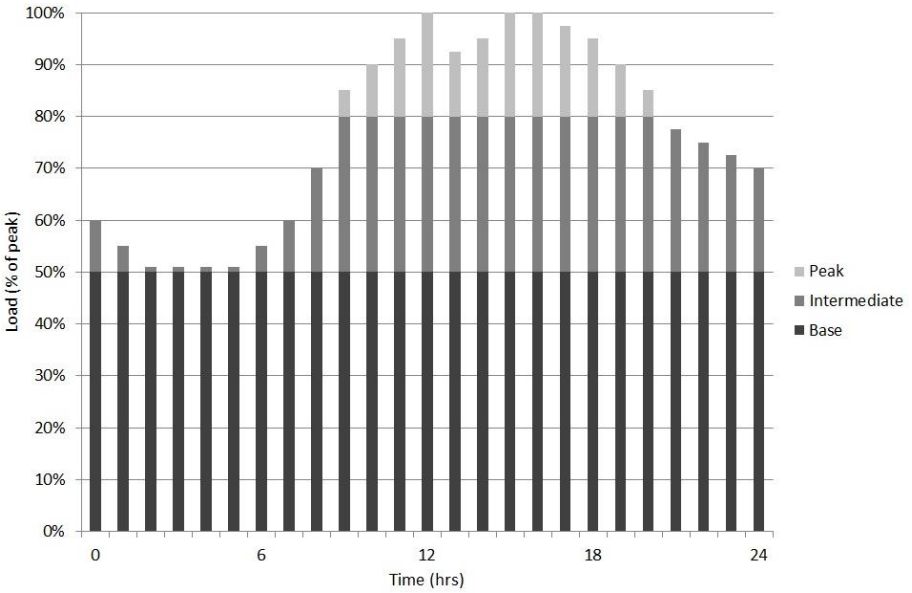

Figure 1-6 – Sample UK electrical demand over one day.

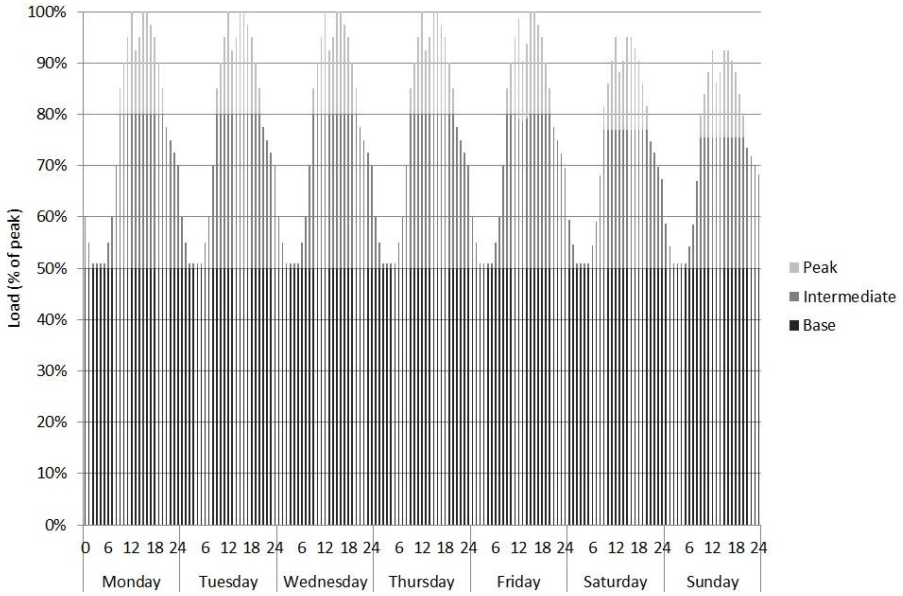

Figure 1-7 – Sample UK electrical demand over one week.

Each type of load is met most effectively by different types of electrical generation. Peak load can only be met by systems which are able to respond quickly to changes in demand by increasing or reducing their output to match requirements. The most suitable energy sources for this type of demand are currently gas-fired power stations, the most advanced of which are able to increase

power output by 35MW within one minute [15]. Intermediate demand must also be met by power stations capable of adjusting their output, though the frequency and speed of output changes are lower than in the peak load case. In the UK, intermediate load is primarily met by gas-fired power stations, in addition to cheaper coal-fired and oil-fired sources. Base load in the UK is supplied by Nuclear power and fossil fuels.

As illustrated in the previous section, Renewable energy provides a contribution of around 5% to the UK grid, but due to the intermittency of renewable energy supply this contribution cannot be relied upon. Grid capacity must be designed for a worst-case scenario, meaning that it must be possible to meet peak demand without any contribution from renewable energy. Consequently, the integration of renewable energy into the UK grid has not to date allowed a reduction in non-renewable power generating capacity. This inability to supply base load is often highlighted as a major disadvantage of renewable energy, and is indeed a major barrier to the prediction of a 100% renewable future. However, not all renewable energy sources suffer from the unpredictability of technologies such as wind and solar power, and the use of such technologies, in combination with energy storage systems in the future may allow base load to be supplied by intermittent power generation.

1.2.2 – Energy security

The reduction of CO_2 emissions is not the only reason why the UK and other countries around the world are pursuing the development of renewable energy. Another important reason is energy security. As was mentioned in Section 1.2.1, the UK imports a small proportion of its electricity through direct interconnects with other countries. The HVDC Cross-channel interconnect allows the import of electricity from the French grid, and the BritNed interconnect links the UK and Dutch national grids. Links are also in place to Northern Ireland (HVDC Moyle link) and the Republic Ireland (East-West Interconnector). The UK imports only around 1% of annual electricity through these systems, meaning that energy use could continue at its current level even without any direct grid connections to the UK. However, in addition to this direct importing of electricity, the UK also imports fuel for power stations, which is then used to generate electricity. The UK imports around 57% of the fuel used in fossil fuel and nuclear power stations [16], making security of fuel supply an important issue.

The UK imports uranium for nuclear power stations from Australia, Canada and South America; coal from the USA, Poland and Russia, and large amounts of liquefied natural gas from the Middle East. The security of our energy supply is a politically sensitive issue, particularly with imports from potentially unstable countries. History gives many examples of the use of fuel supply as a political tool, for example the recent conflict between the Ukraine and Russia which resulted in Russia limiting the supply of gas to Ukraine. Given that around 15% of natural gas used in western European power stations is of Russian origin and piped via Ukraine, this and other similar disputes have implications for a large number of countries. A summary of sources of fuel for the UK's power stations is given in Figure 1-8 [16].

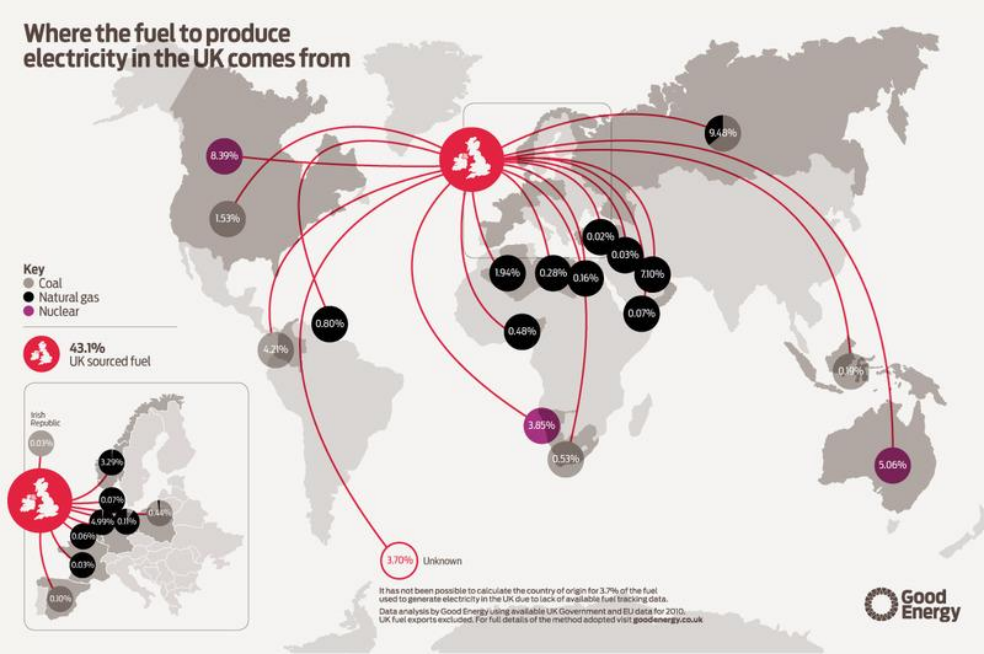

Figure 1-8 – Sources of fuel for electricity generation in the UK (from [16]).

As a consequence of the danger of political instability and supply restrictions on imported fuel, generating electricity with fuel from within a country's own borders has significant advantages. In the UK, the primary options for doing so include maximising the extraction of the remaining North Sea oil, developing renewable energy sources, or pursuing hard-to-access fossil fuel reserves using controversial techniques such as "Fracking". Though there are an estimated 12-25 billion barrels of oil remaining in the North Sea [17], any increase in extraction and use of domestic oil is currently limited by cost due to the difficulty of extraction. Onshore fossil fuel extraction has been met with huge public opposition and appears to offer limited potential returns, which appears to leave renewable energy as the UK's best option to reduce its reliance on imported energy fuel. Even this may not be without political challenges, as was highlighted during the recent Scottish independence referendum. Scotland is said to have at least 25% of the European wind energy resource, and during the referendum it was unclear whether an independent Scotland would have led to a rise in the price of wind-generated electricity for the rest of the UK [18]. However, despite its challenges there are enormous advantages to the adoption of renewable energy, and though the degree of adoption is unknown, such technologies are almost guaranteed to increase their share of UK and world electricity generation over the coming years

1.2.3 – Renewable energy

Under the heading of renewable energy there are a huge number of technologies. Despite differences in appearance, these technologies all fall into one of four broad categories, based on the original source of their energy:

Solar

Solar energy describes any technology which captures energy from the sun. This includes solar photovoltaic technologies which generate electricity directly, and solar thermal systems which use solar power to generate heat, as well as indirect solar technologies. Indirect solar technologies

include wind power (which is generated from the interaction of hot and cold air), wave power (wind far out at sea causes waves), and hydroelectric power (since the evaporation of water and melting of snow and ice are both caused by solar power).

Bioenergy

Bioenergy involves the use of any organic matter to generate power, for example the growth and burning of Biomass. This is a slightly controversial category as it can be argued that bioenergy is not entirely renewable, since resources are required to grow the crops which are eventually used, and the resource is finite. Since biomass is generated by the photosynthesis of sunlight it is also arguable that this is a further form of solar power. There are also issues relating to the use of land to grow biomass in preference to food, which can lead to food shortages in some parts of the world. This category also encompasses Hydrogen as a fuel.

Geothermal

Geothermal energy describes the use of the heat of the earth's core as an energy source. In parts of the world such as Iceland, highly active hot springs are found relatively close to the earth's surface. Energy can be extracted from these sources as heat, which can then be used directly or to generate electricity.

Gravitational

The final category of renewable energies is gravitational energy. This is the smallest category and contains only tidal power, which is generated from the relative gravitational movement of the earth, sun and moon. The tides and tidal energy are discussed at length in Sections 1.3 and 1.4 respectively.

The UK does not currently generate electricity from geothermal energy resources on a large scale, though parts of the UK do have stable underground temperatures which may be suitable for such extraction [19], and ground source heat pumps are successfully used for thermal energy extraction in domestic and commercial settings. Due to limited space the UK is not considered a particularly good location for large-scale bioenergy exploitation. However, its climate makes it suitable for some types of solar-derived energy; the north of the UK has a particularly good wind energy resource, with the south having reasonable direct solar energy potential. The UK is also particularly blessed with excellent marine energy resources, having around 50% of the total European resource of tidal power, again largely concentrated around Scotland.

1.2.4 – Future projections

Renewable energy currently supplies 5% of UK electricity, but this figure is forecast to increase dramatically over the coming years and decades. The UK has embarked on an ambitious but necessary program to reduce its CO_2 emissions. As stated in the 2008 Climate Change Act, the UK has a target to reduce emissions by at least 80% from 1990 levels by 2050. This target is anticipated to be partly achieved through demand reduction and the use of more efficient equipment as has been discussed, but a significant part of this reduction is anticipated to be delivered by integrating renewable energy into the UK's electricity generation mix. There are a number of different forecasts

for how this may be achieved, the detail of which is beyond the scope of this project, but an example from a 2013 report by the UK Energy Research Centre (UKERC) is given in Figure 1-9.

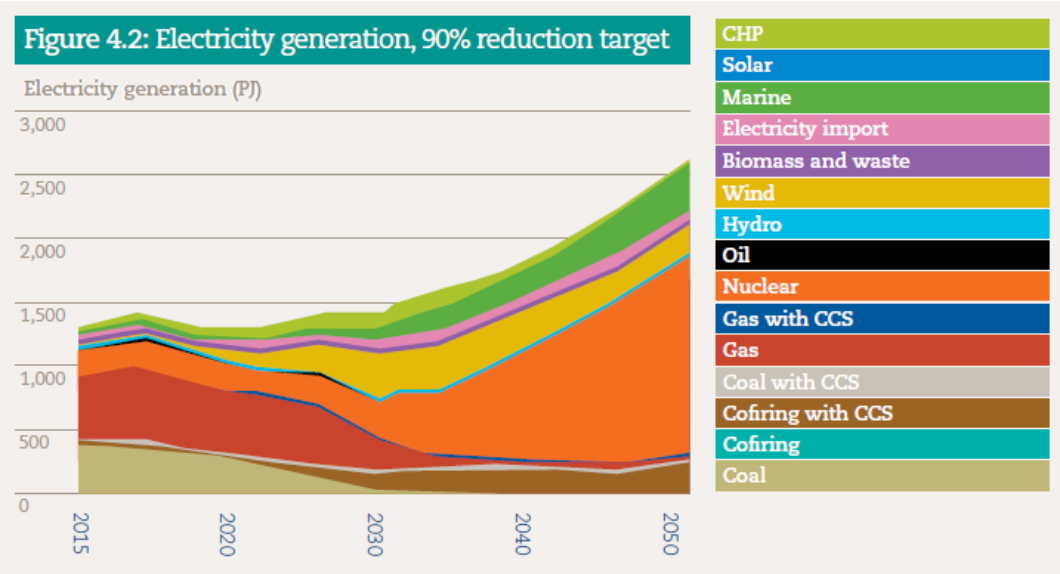

Figure 1-9 – UK Future energy projection, 90% CO_2 reduction strategy (from [20]).

Due to the level of predicted increase in Nuclear power, this particular forecast requires a lower level of growth in renewable energy than many other forecasts, but the level of increase in Marine and Wind energy is still significant. Current estimates of the UK's tidal power potential, as discussed further in Section 2.1, suggest a potentially extractable resource of around 95TWh/yr and the potential to supply 20% of our electricity requirement by 2050.

To gain an understanding of the required scale of this increase in renewable energy use, consider the UK's current level of wind power generation, with reference to Figure 1-9. Onshore and offshore wind turbines are now a common sight, but the current contribution of wind power generation is almost indistinguishable in the figure. The forecast shows an increase from the current 2% level to 25% by 2030, and 10% by 2050. This suggests a thirteen-fold increase in wind power capacity by 2030. The forecast increase in marine generation is even more significant, with current levels well below 1% and a 2050 prediction of 20% requiring an eighty-fold increase in capacity.

Public opinion

The implementation of renewable energy relies on economies of scale, so requires buy-in from the UK industrial and domestic markets. The adoption of renewable energy in an industrial context can be driven more easily by government, through regulation or subsidy, but domestic adoption requires public opinion to be in favour of the technology. In order to encourage this adoption, numerous government schemes have been implemented to incentivise the use of energy from renewable sources. Schemes such as the Feed-in Tariff and Renewable Obligation Certificate (ROC) scheme have raised public awareness of the need to decarbonise electricity generation and have led to increased uptake of domestic renewable energy technologies, but have had a limited effect on emissions to date. Public opinion of renewable energy has been set back by difficulties in the implementation of these schemes, and in some cases the schemes have led to the installation of inappropriate technologies due to a lack of full understanding of appropriate technology, leading to

further damage to public opinion. One such example is the installation of small wind turbines on buildings within the highly turbulent airflow of an urban setting, with many such turbines being reported to generate much lower outputs than forecast.

Figure 1-10 – Inappropriately-located wind turbines damage public opinion and may never repay the energy used in their manufacture.

However, public support for renewable energy on the whole is high (around 80% of respondents to a DECC survey said they supported UK electricity being generated by renewable sources [21]), and domestic renewable electricity suppliers such as Ecotricity and Good Energy have seen their customer numbers steadily increase since their establishment in 1996 and 2002 respectively.

1.3 – The ocean and tide

Mankind's relationship with the ocean began at the very beginning of civilised life, and it is believed that the sea has been used for transport and fishing for at least 40,000 years. The power of the ocean has fascinated humans since these times, and before the movement of the sea was understood it was a frightening source of unpredictable power. Storms were said to be caused by the anger of gods and the movement of the tide was believed in some Eastern cultures to be the breathing of the Earth.

Man's understanding of the tide changed dramatically over the centuries. By 3 BC, thinkers like Aristotle noted the link between the movement of the oceans and that of the earth and moon [22]. Through this link, understanding of tidal movement developed alongside that of cosmology. Though Aristotle correctly identified the fundamental source of tidal ebb and flow, his subsequent hypothesising proved inaccurate, since it was based on an earth-centred universe.

It was Nicolaus Copernicus who proposed the heliocentric (sun-centred) model of the universe and in doing so paved the way for a full understanding of tide. However, though Copernicus first described this theory in around 1510, it was not until the mid-seventeenth century that his ideas were fully accepted. In 1687 Isaac Newton produced his pivotal work *Philosophiæ Naturalis Principia Mathematica* [23], in which he described the concept of force, then used this concept to illustrate the gravitational effect of the moon and sun on the earth and its oceans within the heliocentric universe, thus for the first time fully explaining the ebb and flow of the tide.

As Newton observed, tidal movement is governed by the relative movement of the sun, moon, and earth. The motion of the moon around the earth exerts a gravitational pull on the water in the oceans on our planet, causing it to take the shape of a prolate spheroid (rugby-ball shape). As the earth rotates within this shape, an observer at a static position on earth would witness a changing depth of water over time. The sun causes a similar effect, though despite its larger mass, the sun's large distance from earth results in a smaller tidal effect than that of the moon. The overall tidal pattern is made up of a number of components, each with a slightly different time period. Each of these components causes sinusoidal changes in the water level over a slightly different time period, and the sum of these constituents produces the overall tidal pattern. Consequently, the tidal height pattern with respect to time varies slightly from day to day. Each constituent of the tidal cycle is described by its amplitude (the change in water level due to the influence of the constituent) and time period (the time between consecutive tidal maxima). Time periods are classified as either diurnal, meaning that a full cycle occurs approximately once during a 24 hour period, or semi-diurnal, meaning approximately two cycles occur within a 24 hour period. The two largest contributors to overall tidal range are the semi-diurnal constituents M_2 and S_2, which represent the principal gravitational contributions from the moon and sun respectively. A third semi-diurnal constituent, N_2, also has a significant contribution to the overall result. This is an additional lunar constituent, due to the elliptical orbit of the moon. Of the diurnal contributions, the most energetic are O_1, P_1 and K_1. These titles represent the principal lunar, solar and luni-solar constituents, respectively. The variation of these principal constituents over a 24 hour period for a sample UK location are illustrated in Figure 1-11, and the composite tidal pattern is given in Figure 1-12.

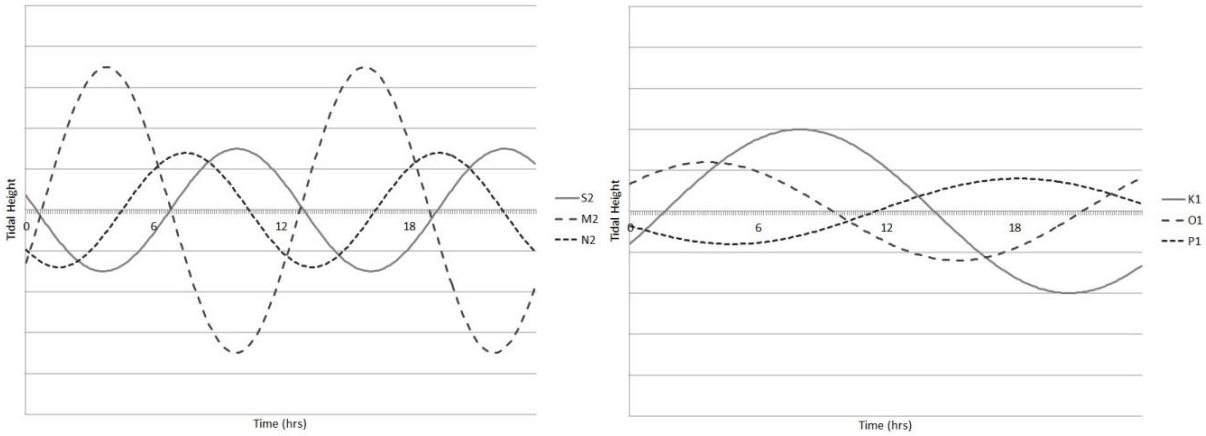

Figure 1-11- Principal semi-diurnal (l) and diurnal (r) constituents of composite tidal curve for a sample location over a 24 hour period.

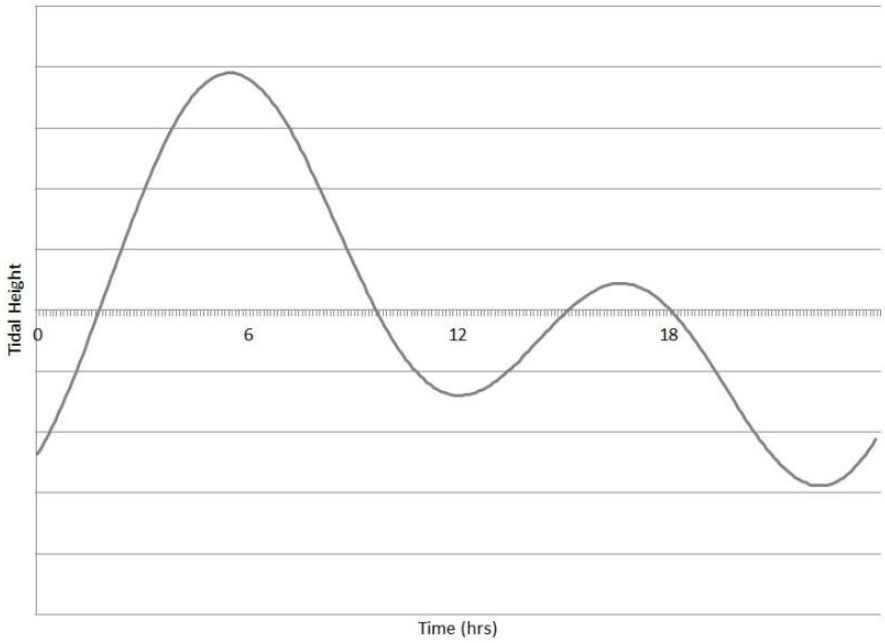

Figure 1-12 - Composite tidal curve for a sample location over a 24 hour period.

In addition to the gravitational causes of tide, the tidal velocity and range observed at a given shoreline is also influenced by the three-dimensional shape of the seabed, known as topography. The topography of the seabed can have a funnelling effect, for example, between islands or through channels. This provides a reduction in channel volume, and thus produces an increase in velocity, yielding the high tidal speeds often observed in such narrow channels. Due to this high tidal velocity in these areas, such locations often offer great potential for the harnessing of tidal energy. An example of such a location, the Pentland Firth between the Scottish mainland and the Orkney Islands, is given in Figure 1-13. The effect of the island channel and topography can be seen to cause acceleration in the tidal flow through the channel.

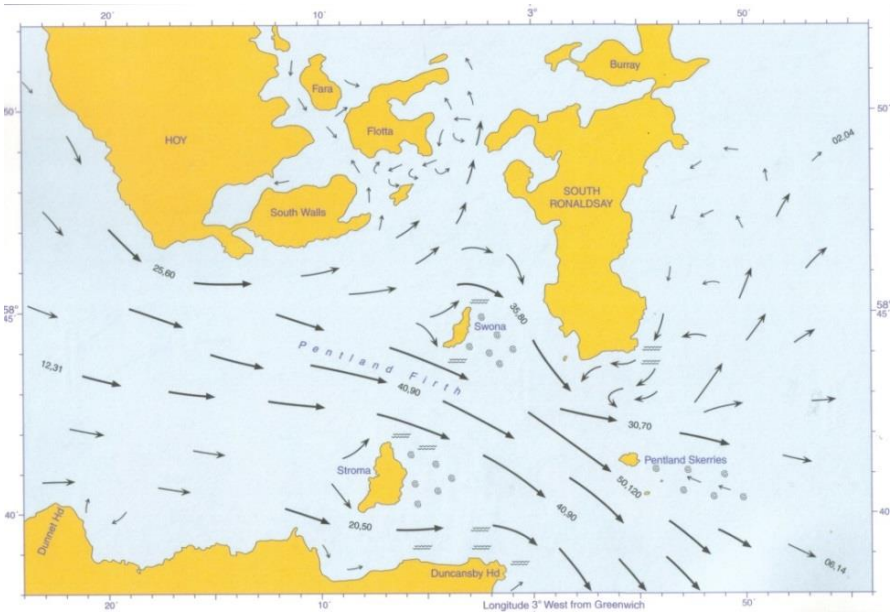

Figure 1-13 – Extract from Orkney Tidal Atlas illustrating the acceleration of tidal flow through the Pentland Firth [24].

1.4 – Marine energy

"Marine energy" is a blanket term used by the energy industry to describe energy extracted from the ocean, either from the ebb and flow of tides, or the movement of waves. It is worth noting at this stage the significant difference between the two. As has been discussed previously, tidal energy is extracted from the movement of the tides, which is caused by the relative gravitational movement of the earth, sun and moon. The energy contained within ocean waves is in fact solar energy. Waves are generated by wind far out at sea, which is itself caused by temperature difference in air, due to the heating of air by the sun. This source means that ocean waves are unpredictable, as therefore is the power extracted from them. There is also a third source of marine energy, known as OTEC (Ocean Thermal Energy Conversion). This technology uses the temperature difference and therefore the thermal gradient between the ocean surface and the deep ocean as a power source. In areas with a sufficiently high temperature difference between the surface and deep ocean, energy can be generated by using the thermal gradient to drive a turbine and generate electricity.

As discussed in Section 1.1, the need for low carbon energy is becoming ever more important, and tidal power has a role in this future. As with all sources of renewable energy, tidal energy has advantages and disadvantages, but does offer a significant advantage over other sources of renewable energy, in that it is entirely predictable. This offers a potential solution to the replacement of fossil-fuel provided base load electricity, which cannot reliably be achieved using other renewable energy sources due to their intermittency. Despite this, the technology is currently in its infancy, and is said to be around 20 – 30 years behind that of established renewable technologies such as solar and wind power [25]. Due to this, UK tidal power levels are currently very low. Tidal energy (generated from tidal stream and tidal barrage systems) currently supplies around 1% of the UK's renewable-generated electricity, equating to one twentieth of one percent of overall UK electricity generation.

This work is concerned with the development of electricity from the movement of tidal ebb and flow, not from the movement of waves or ocean thermal gradients. Specifically, this work relates to the development of the form of tidal energy known as "Tidal Stream" energy, rather than other methods of extracting energy from the tides, such as barrages or tidal lagoons. A brief description of the concept of tidal stream energy, as well as other forms of tidal energy, is discussed in the following section.

1.4.1 – Tidal barrages

The concept of a barrage is to allow the tidal flow to move water into a controlled area (known as a pond or reservoir), then to restrict the water outflow and use the gravitational potential energy stored therein to generate power by forcing the water to exit through some form of energy extraction device. The design of barrage systems varies widely, and the generation device can be used on both the tidal ebb and flow cycles, but the concept of using the gravitational potential of the water to generate energy remains constant. This concept has been in use for many centuries, with the earliest tidal barrages being used to drive wheels for the milling of flour, or to operate machinery such as bellows or saws. Tidal mills dating from more than 1000 years ago have been found in Ireland, the English Channel and the London area [22].

More recently, large tidal barrages have been constructed around the world. These modern barrages differ from the original mills in their scale, and in their use of turbines to generate electricity rather than the direct use of the power. Two notable projects are the La Rance barrage at St. Malo, France, as illustrated in Figure 1-14, and the Sihwa Lake Tidal Power Station in Gyeonggi Province, South Korea. The former uses 24 10MW turbines giving a capacity of 240MW and was the world's largest tidal barrage from its opening in 1966 until the 2011 opening of the Sihwa Lake project, which uses 10 turbines to give a capacity of 254MW.

Figure 1-14 - La Rance Tidal Barrage, France [26].

In the UK, there have been numerous proposals for similar barrages, particularly in the Severn estuary between Wales and England. Barrage designs have been proposed in this area since as early as 1849, ranging from 800MW to the 8.6GW of the final proposed design, which was finally rejected by the UK government on economic grounds in 2011 [27].

There are numerous theoretical advantages of barrages as a method of capturing tidal power as well as economic advantages (for example, a barrage may include the construction of a bridge, reducing the travel time between two areas and thus increasing the economic potential of previously difficult-to-access areas), but the technology also has disadvantages. Primarily, the construction of a barrage is a huge and challenging civil engineering project with a large cost attached. The construction of the La Rance barrage cost the equivalent of around €580 million [28]. In comparison, Whitelee Wind Farm in Scotland [29] has more than twice the theoretical capacity of the barrage (539MW), and a construction cost of around £300 million. This gives an approximate cost per rated MW of £1.92 million for a tidal barrage, and £550,000 for the wind farm. Tidal stream energy has a current approximate cost of around £2 million/MW, but this is predicted to fall to around £400,000 by 2020, through improvements in device efficiency and economies of scale [30].

1.4.2 – Tidal lagoons

The concept of a Tidal lagoon is similar to that of a tidal barrage, in that turbines are used to extract power from the controlled rise and fall of the tide within a fixed region. In the tidal lagoon concept, the region is generally a man-made area. The most high-profile tidal lagoon proposal is that developed by Tidal Lagoon Swansea Bay, an organisation planning to install the world's first man made tidal lagoon project in Swansea Bay. The proposed lagoon is made up of a wall constructed by

dredging and rock placement, able to contain 11km^2 of water. The project has attracted high-profile investment from sources such as the renewable energy supplier Good Energy, who invested £500,000 and will purchase 10% of the electricity generated by the project, once fully operational [31]. The developers aim to have 320MW of installed capacity in place and grid-connected by 2018. The proposed layout of the lagoon is shown in Figure 1-15, indicating the location of the proposed 26 low head "bulb" turbines installed in housing (to the lower left of the image).

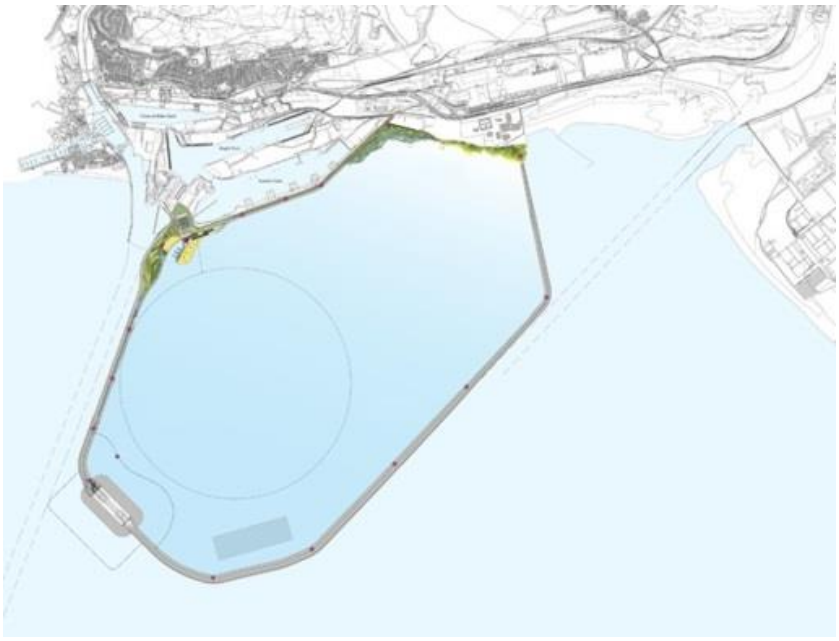

Figure 1-15 – Proposed layout of Swansea Bay Tidal lagoon [32].

Tidal Lagoon Swansea Bay also commissioned a report on the economics of tidal lagoons [33]. The report estimated a total capital cost to construct the lagoon of £913m, yielding a construction cost per rated MW of £2.85m/MW. However, the report also concluded that once operating, the technology has the potential to deliver electricity at a cost of around £100/MWh, which is comparable with current costs for onshore wind and nuclear generation [34].

1.4.3 – Tidal stream energy

Tidal stream energy involves the use of a turbine or other device to extract energy from tidal ebb and flow, and differs from a tidal barrage in the proportion of the flow cross section which is directed through the energy generating device. In a tidal barrage concept the entire flow is redirected to flow through turbines, whereas in the tidal stream concept bleed flow is allowed, meaning that some flow will pass around the energy generation equipment.

The concept of tidal stream power is similar in concept to that of wind power, in the sense that a device is placed in a moving flow with the aim of extracting energy from the kinetic energy of the flow. The concept has thus been in existence for many years, since hydroelectric power is first believed to have been used by the Greeks around 2000 years ago. The development of tidal stream power as a source of large scale electricity generation was first considered in around the early 1980s, when it was proposed as a source of power for illuminated marker buoys [35]. In 2000, the marine energy industry began in earnest when the first wave energy device was connected to the UK grid.

This is significant in the development of tidal stream energy because government funding for the development of tidal stream technology has generally been undertaken as part of schemes to develop marine energy as a whole (i.e. tidal stream and wave energy). A timeline of significant events from this point to the present day is given in Figure 1-16.

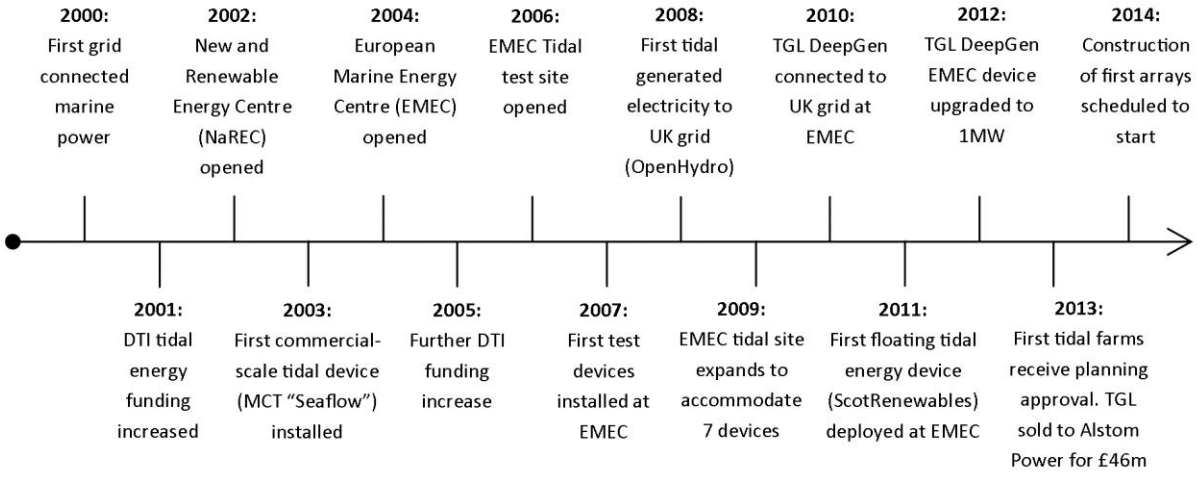

Figure 1-16 – Tidal energy development timeline (2000 – 2014).

As described in Figure 1-16, Marine Current Turbines were one of the earliest manufacturers to develop and test a tidal stream turbine. The company was founded in 1999, and began by developing the "SeaFlow" 300kW device, which was installed off the coast of Lynmouth in 2003. Following subsequent development, in 2008 the company installed the "SeaGen S" device in Strangford Lough, Northern Ireland. In December of that year the device became the first tidal turbine to achieve its rated power. The installation of the device at Strangford Lough is reported to have cost around £8 million, giving an installation cost of £6.7 million per MW. As discussed in Section 1.4.1, this figure has fallen for subsequent tidal turbine installations, and is predicted to fall further to around £400,000 by 2020 [30].

In 2003, the European Marine Energy Centre (EMEC) was established, based at Stromness on the Orkney Islands, 25 miles off the northern coast of Scotland. The centre is a hub of testing and development for both wave and tidal stream energy technology, and is widely acknowledged as an indicator of the UK's expertise in the marine energy field, which is regarded as amongst the world's best. The following section discusses the current state of the development of the most advanced tidal stream devices, the vast majority of which have undergone some testing or development at EMEC.

Since the first installation of the SeaGen device, a number of other companies have successfully deployed devices. However, most of these installations have taken place at EMEC, and the UK's installed capacity is currently around 9MW. However, as will be discussed in Section 1.6, planning approval has recently been granted for two large arrays of tidal turbines in UK waters, which will significantly increase this installed capacity over the next decade.

1.5 – The tidal turbine

Turbines designed for the extraction of energy from tidal streams are known by many names: Tidal turbine; Tidal Energy Convertor (TEC); Hydrokinetic turbine or Marine Energy Device are commonly-used examples. This study focuses on the use of horizontal axis rotating devices for the extraction of energy from the tide, either mounted on the seabed or suspended within the water column, so will use the term Tidal turbine. Other types of device, such as vertical axis turbines and oscillating hydrofoil devices are discussed in Section 2.5.2.

Though there are currently a wide range of tidal turbine designs proposed by manufacturers and developers, it is possible to consider a typical horizontal axis tidal turbine, which appears to represent the likely form of future devices. Devices of this type which have been developed to date have typically had a rated power of 1MW, weigh in the region of 200t, and are around 30m tall from the seabed to blade tip. Such a device is illustrated and its major parts briefly described below.

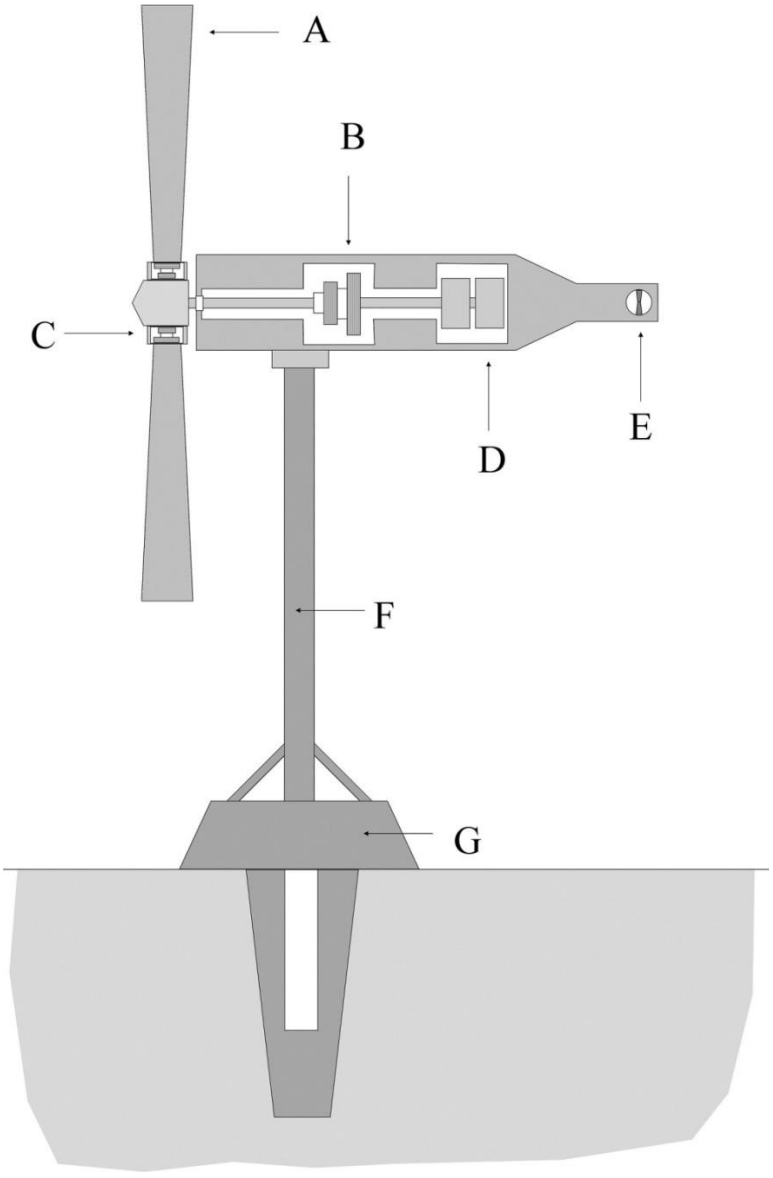

Figure 1-17 – Schematic diagram of a typical tidal stream turbine.

A: Blades

Tidal turbine blades are generally manufactured from composite materials. Most commercial turbine designs use three blades, though twin blade designs are also common. Individual blade lengths of most current tidal turbine designs are of the order of 10m.

B: Main gearbox

The turbine gearbox is used to increase the rotational speed of the blades (typically around 15rpm) to a speed suitable for energy conversion using a generator.

C: Nacelle and pitch control gearboxes

The turbine nacelle connects the blades to the drive shaft, and in turbines where blade pitch control is employed the inbuilt gearboxes and control systems are used to rotate the blades about their axis to adjust angle of attack.

D: Generator and power electronics

A generator attached to the main gearbox output converts the turbine rotation to electrical energy. Power electronics are used to control the voltage and current of power supplied through cables to the shore.

E: Yaw thruster

In order to operate in both tidal ebb and flow, the turbine unit rotates on top of its support structure. This is achieved through the use of an electrical yaw thruster unit, which rotates the turbine about its pivot on top of the support structure.

F: Support structure

The turbine support structure connects the turbine to the seabed, where it is mounted using a gravity base or piled foundation system. In the case of a floating device design, the buoyant body of the device can be thought of as the equivalent of the support structure. Designs of this type use cables mounted onto gravity base or piled foundations to hold the device in place. In the case of devices with traditional support structures, power transfer cables tend to be routed inside the support structure.

G: Base mounting

Devices using a traditional support structure of the broad type illustrated in Figure 1-17 are mounted to the seabed using either a gravity base or piled foundation system. In the former case, large blocks (commonly of concrete) are used to anchor the device support structure in place and prevent the device moving in the tidal flow. In the latter case, piled foundations are driven into the seabed, onto which the support structure is mounted. Monopile and multi-pile foundations are proposed.

The example given above is a very basic representation of the main features of a tidal turbine, but the devices are highly complex and comprise multiple sub-systems. The design and engineering of a tidal turbine is highly challenging, since in addition to the complexities of a large energy-generating structure the device must also be designed to withstand an extended lifetime in a harsh subsea environment. In addition to the challenges of device design and array layout, work is also ongoing in areas such as biofouling [36], deployment and recovery, and cabling.

1.6 – Tidal stream turbine arrays

In order for tidal stream energy extraction to become a viable contributor to the UK's energy landscape, many multiples of the device type described in Section 1.5 must be installed. As in the case of wind turbines, it is proposed that tidal turbines will be installed in large multi-device arrays. The interaction of devices within such arrays is the primary focus of this work, since research in this area to date has been limited. The spacing of devices within an array must be designed in balance between the available area for the array and the separation distance between devices in the cross-stream and streamwise directions.

In 2013, planning permission and Crown Estate leases were granted for two tidal energy arrays in UK waters. These are the first multiple turbine arrays to be planned, and are likely to be the first to be installed. Both sites lie in channels between the Scottish mainland and islands.

The first project to be granted permission was the MeyGen project, situated in the Pentland Firth between the Scottish mainland and Stoma, a small outlying island in the south of the Orkney Islands (see Figure 1-13). The project plans to install an array of 398MW rated capacity by the early 2020s, and is beginning with the installation of four 1.5MW Atlantis turbines, which are expected to be operational by 2016. The MeyGen website [37] states that *"As the first large-scale tidal project of its type in the world to successfully reach a funding agreement, the MeyGen project will be a catalyst for the global tidal power market, signalling the transition of the industry from demonstration projects to commercial arrays."* Details of the array spacing to be used in this projects is not publically available, though idealised layout plans suggest a spacing strategy of approximately three rotor diameters between devices in the cross-stream direction and seven rotor diameters between devices in the streamwise direction.

The ScottishPower Renewables Sound of Islay project is located between the islands of Jura and Islay, the most southerly of the Inner Hebrides. Islay is located approximately 20km west of the mainland, and 40km north of Ireland, with Jura located to its north-east. This project consists of ten 1MW turbines, with devices designed by Alstom and Hammerfest Strom being used. The project was initially planned for installation during 2013 but appears to be delayed. The planned array layout for this project is illustrated in Figure 1-18, and indicates streamwise device separation distances of between 300m and 600m, or approximately 15 to 30 rotor diameters. Cross-stream separation distances cannot be ascertained from the data provided, though the channel width is of the order of 1km.

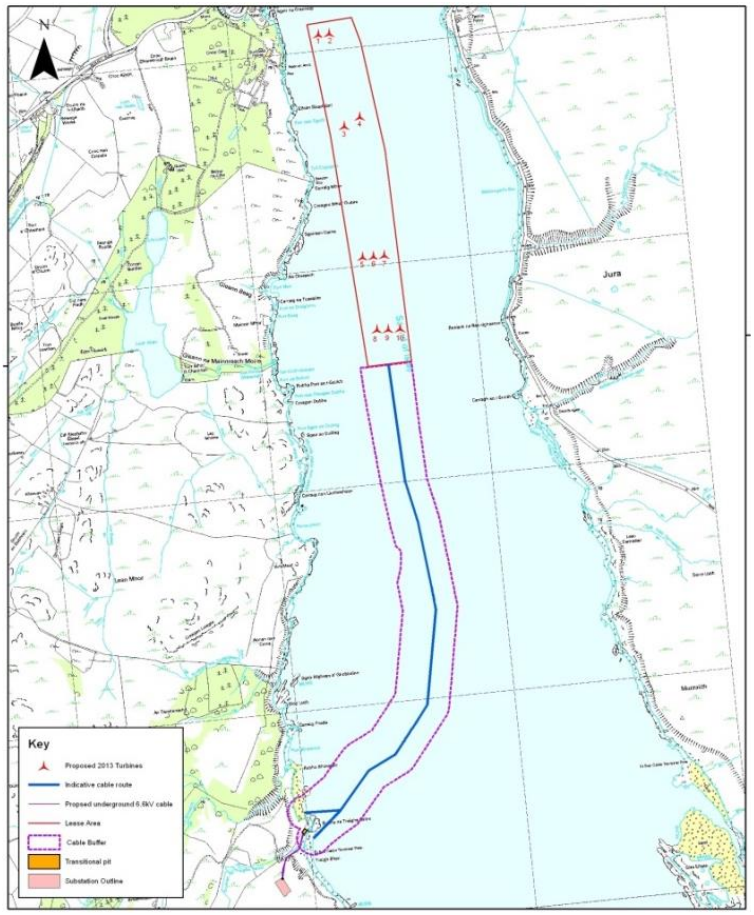

Figure 1-18 – ScottishPower Renewables Sound of Islay array: Proposed layout [38].

Since these two projects represent the first tidal array installations in the world, it is perhaps inevitable that some challenges will be faced, and that valuable lessons will be learnt. The design of tidal turbine array layout is the subject of some academic work (including the current project), as well as commercial work by the developers of these and other forthcoming arrays, but remains the major area in which the industry must develop in order to become a viable contributor to the UK's electricity supply. Existing work in the development of array layout and planning is discussed in Section 2.5.2.

1.7 – Project aims

The focus of this work is the advancement of the understanding of hydrodynamic interactions between a tidal stream turbine and support structure, as well as the downstream interaction of multiple devices. As will be discussed, the interaction of the flow around the tidal turbine blades and the support structure is complex and must be understood in order to allow the technology to successfully advance to the installation of large arrays of devices, which is the next step towards a viable industry with significant electricity-generating potential.

This thesis describes work towards this aim through an experimental project conducted at the University of Sheffield (and later at the University of Florence) using scale models of tidal stream turbines.

The remainder of this thesis is divided into seven chapters. A brief description of each is given below:

- Chapter 2 describes a comprehensive literature review, studying the state of the art in the field of tidal stream power both as a commercial industry and as an area of academic research. The development of tidal stream turbine devices and proposed device arrays is discussed, followed by a review of the available body of work on the hydrodynamics of such devices. Experimental and computational methods used to conduct such work are also assessed in order to inform the design of experiments used in the present study.

- Chapters 3 and 4 describe these methods in detail, with the former focussing on the equipment used and the latter on the processing of subsequently-generated data. Chapter 3 describes the model turbines used in this study, and the water channel within which experiments were conducted. The measurement methods used to record both flow and turbine performance data are also described in this chapter, before a discussion of the processing and analysis of the recorded data, which is given in Chapter 4.

- Chapters 5 and 6 describe the major results of the study, focussing respectively on those of single turbine experiments and experiments using two turbines. These experiments were conducted in four distinct phases, the results of three of which are given in Chapter 5, and the remaining one in Chapter 6. Recorded turbine performance data and flow results are given throughout both chapters.

- Chapter 7 introduces a further phase of experiments, conducted at the University of Florence, which involved the testing of larger scale models of complex support structure designs. Full details of this work and initial results are given.

- Chapter 8 describes the conclusions of the experiments and the overarching results obtained in each phase of experimentation. A discussion of the application of these results, as well as the contribution of this study to the existing body of work on tidal turbine hydrodynamics is also included. Finally, details of opportunities for further work resulting from this study are identified.

2

Literature Review

2.1 – Introduction

This literature review will present the current state of the art in the field of tidal energy, in order to develop the research aims of this project, prior to the presentation of the work. This review covers four broad areas, and includes a detailed and specific review of the state of the art in each area. The primary areas identified as relevant to the research are: Tidal Turbines in operation; Computational modelling relating to tidal turbines; Physical modelling of tidal turbines; and Flow Measurement, with a particular focus on Particle Imaging Velocimetry.

Prior to this focussed research, a more general investigation of the position of tidal energy in the UK's future energy outlook was conducted. A good starting point in any renewable energy project is David MacKay's seminal book *Sustainable Energy – without the Hot Air* [34]. MacKay is positive about the technology, and in his chapter on tidal energy estimates that 11kWh per person per day could be economically extracted from UK waters. This equates to around 10% of his estimate of the average energy use per person per day in the UK. He also highlights a key advantage of the technology (as discussed in Chapter 1) in the predictability of its output.

A 2006 Carbon Trust report on the UK's energy strategy [30, 39] estimated a UK extractable tidal stream resource of 18TWh/yr, and highlighted the importance of the UK as a global centre for tidal stream energy, with half of the extractable European tidal resource and 10-15% of the world's tidal stream resource estimated to be in UK territorial waters. A subsequent 2011 report by the Carbon Trust and Crown Estate [40] raised the estimated extractable UK tidal stream resource to between 16.4TWh/yr and 38.4TWh/yr, and this figure was again raised by Crown Estate Reports [41] to 75TWh/yr and 95TWh/yr in 2012. Despite their differing predictions of total resource, these estimates generally agree that tidal stream power has the potential to deliver around 20% of the UK's electricity needs.

It appears that the UK government is broadly supportive of tidal stream energy, a consideration which is critical to its potential development as a viable future energy source. The mechanism for funding the development of tidal stream energy in the UK has primarily been the Renewable Obligation Certificate (ROC) scheme. The ROC scheme works by forcing electricity suppliers to purchase a portion of their electricity portfolio from renewable sources. ROCs are attached to units of electricity generated by renewable sources, thereby earning the purchaser ROCs when the electricity is purchased. Different renewable energy sources are allocated a different number of ROCs per MWh of electricity generated, meaning that an energy supplier is able to earn more ROCs per MWh of electricity purchased if it is purchased from sources with high ROC value. For example, current ROC values for Energy from Waste with CHP, Offshore Wind and Photovoltaic Solar (up to 10kW) are 1, 2 and 4 per MWh respectively [42]. Until 1st April 2013, Tidal stream power had a ROC allocation of 2 ROCs/MWh, but since this date the allocation has been raised to 5 ROCs/MWh for projects of up to 30MW size (remaining at 2 ROCs/MWh for projects above this size). Between 2014 and April 2017, the ROC support mechanism will gradually be replaced by the Contract for Difference (CfD) mechanism. The CfD mechanism pays generators of renewable electricity based on the difference between the electricity sale price (the "reference price") and a pre-set price (known as a "strike price"), allowing renewable electricity to be sold at a competitive price, while generators receive a fixed price per unit. If electricity is sold at the strike price, the payment is zero, and if electricity is sold at above the strike price, the generator is obliged to make a payment of the

difference between the strike and reference prices. The strike price effectively determines the level of financial support given to a technology, and the expected £305/MWh strike price for tidal stream power is approximately equal to the current level of support given through the ROC mechanism [43]. This strike price is forecast to remain until 2019, and has generally been seen as an indication of positive government support for tidal stream energy in the UK. Consequently, a number of high profile acquisitions of small tidal stream device developers by large energy engineering companies have occurred recently, such as the 2013 purchase of Tidal Generation Limited by Alstom Renewable Power [44].

2.2 – Flow and turbulence

2.2.1 – Reynolds number

The Reynolds number is a dimensionless quantity which describes the ratio of inertial to viscous forces acting within a fluid flow. The ratio gives the relative importance of these two types of forces on the overall motion of the flow, and it is this relationship which governs the turbulence within the flow, with flows dominated by viscous forces exhibiting smooth and ordered laminar flow conditions, whilst those dominated by inertial forces exhibit turbulent characteristics. This ratio is described by the Reynolds number, *Re.* This number is named after Osborne Reynolds, who in 1883 was the first to describe the number and its application [45]. *Re* is given as follows:

$$Re = \frac{\rho u \mathrm{L}}{\mu}$$

The quantity *L* is a characteristic length, selected depending on the application to which the equation is applied. In the case of a channel or pipe flow, this characteristic length is represented by a hydraulic diameter, D_H. Thus the equation above can be re-written as follows:

$$Re = \frac{\rho u D_H}{\mu} = \frac{u D_H}{\nu} = \frac{Q D_H}{\nu A}$$

In the case of an open channel flow, the hydraulic diameter is defined as four times the cross-sectional area of the channel divided by the wetted perimeter length:

$$D_H = \frac{4A}{P}$$

The value of *Re* of a flow case gives the relationship between the laminar-based viscous forces and the turbulent inertial forces, thus allowing a calculation of the type of flow to be expected. In the case of a Newtonian fluid (one whose viscosity remains constant with shear rate) such as water [46], *Re* can be used to identify the point at which fluid flow undergoes a change from laminar to transition flow, and from transition to turbulent flow. Fluid flows with *Re* < 2300 exhibit laminar characteristics, then enter the transition region between *Re* = 2300 and *Re* = 4000, at which point flow becomes fully turbulent, remaining so with increasing *Re*.

2.2.2 – Froude number

A fundamental fluid flow property of particular relevance to tidal flows is the Froude number, *Fr*. This number is, like the Reynolds number, a ratio of forces. However, whereas *Re* describes the ratio of viscous to inertial forces, the Froude number describes the ratio of inertial to gravitational forces. *Fr* is named after William Froude, though it was first investigated by Jean-Baptiste Bélanger in 1828 [47]. Bélanger noted that the ratio of water velocity to square root of acceleration due to gravity multiplied by water depth had an effect on the appearance of the flow around an emerged cylinder. When the value was greater than 1, the flow would appear rapid and disturbed, but when the value was less than 1 flow would appear smooth. The parameter eventually developed from this work and now known as the Froude number is as follows:

$$Fr = \frac{u}{\sqrt{gh}}$$

The flow states as observed by Bélanger are also now more succinctly defined. For $Fr < 1$ the flow is said to be in the subcritical region. At $Fr \approx 1$ a "critical" transition region exists, and at $Fr > 1$ the flow is said to be supercritical. This value defines the waves observed around an object placed in a flow, as illustrated in Figure 2-1. In the subcritical region, flow is dominated by gravitational forces, meaning that surface waves are generated around an object and can be observed both upstream and downstream. As *Fr* increases and reaches criticality, the surface waves are no longer observed upstream, and now form a 45° angle with the direction of downstream flow. As the flow velocity increases beyond critical, the wave angle decreases further. Subcritical and supercritical flow patterns are illustrated in Figure 2-1.

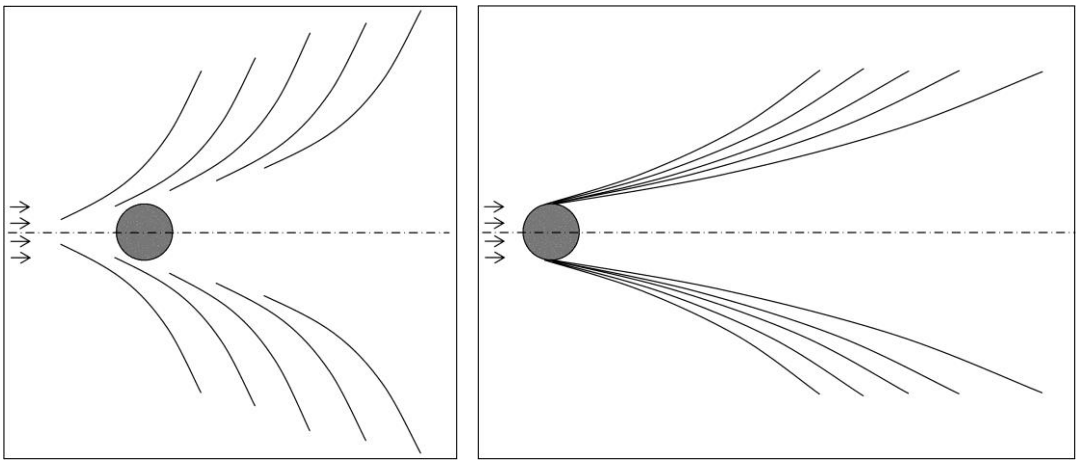

Figure 2-1 – Wave effects around an object in flow at subcritical (l) and supercritical (r) values of Froude number.

2.2.3 – Turbulence

The majority of fluid flows in nature exhibit one of two characteristics: either smooth, orderly flows in which fluid layer interaction is minimal, known as laminar flow, or rough-appearing disrupted flow in which energetic eddies can be seen, known as turbulent flow. As flow velocity increases, flow conditions tend to move from laminar, through a transitional region in which laminar and turbulent

characteristics are seen simultaneously, to fully turbulent flow. Laminar, transitional and turbulent flow are illustrated in Figure 2-2, as visualised using smoke.

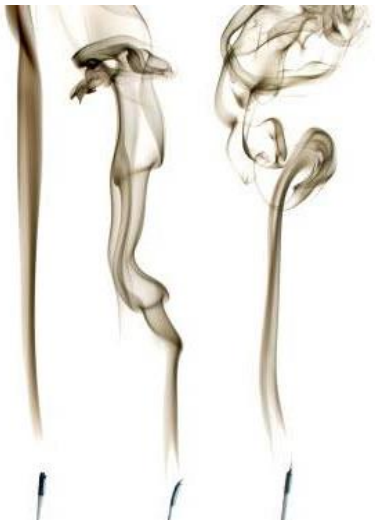

Figure 2-2 – Examples of (l-r) laminar, transitional and turbulent flow, illustrated by smoke visualisation [48].

Turbulence has a large influence on all fluid flow problems, including those involved in this study. The specific details of turbulence in tidal turbine installations and in the scale testing carried out during this study are discussed in Section 3.2.1., but it is worth noting that in both cases, all flow conditions considered in this work are expected to be fully turbulent. Reynolds numbers for scale channel flow of the order of 10^5 and for real tidal installations of the order of 10^8 have been calculated.

Kolmogorov's turbulent spectrum

Within a turbulent regime, energy is transferred throughout the flow by energetic flow structures. Energy is initially stored in large, highly energetic eddies, which break down into smaller and less energetic eddies, dissipating their energy to produce a greater number of less energetic structures. These smaller eddies themselves break down into smaller, less energetic structures, and so the process continues until the eddies reach the smallest size and least energetic structures which can be sustained by the flow. This breakdown of flow structures was described in 1941 by Kolmogorov [49, 50] as an energy cascade. The size of the smallest sustainable eddies in a flow is consequently known as the Kolmogorov Microscale, and its size is governed by the flow conditions in question, specifically by the rate of turbulent dissipation and the viscosity of the fluid. When eddies reach this size they have very little individual energy and can therefore no longer be sustained in the flow, so when they break down their energy is dissipated as heat.

The breakdown and eventual dissipation of turbulent energy can be shown visually on a flow spectrum of turbulent energy, which can be plotted for any turbulent flow. Such a flow spectrum illustrates three distinct regions, each containing flow structures of different energy levels. Those with the largest energy are contained in the first region, known as the Large Eddy Containing (LEC) region. Flow structures in the LEC region break down into smaller, less energetic structures, which lie in the inertial region. Finally, these structures break down further and the energy is dissipated into

yet smaller structures. These structures lie in the dissipation region. The energy cascade and the relative energy contained in eddies of each region, as illustrated by Kolmogorov, is shown in Figure 2-3.

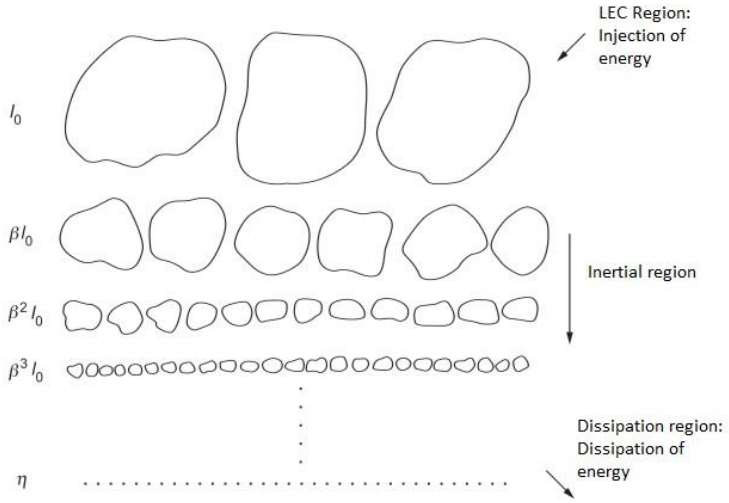

Figure 2-3 – Energy cascade as described by Kolmogorov [49].

The energy cascade can also be illustrated on a log-log plot of turbulent energy and frequency, as illustrated in Figure 2-4. When plotted in such a way, energy dissipation within the inertial region is characterised by a slope of -5/3, thus allowing the three regions to be identified graphically.

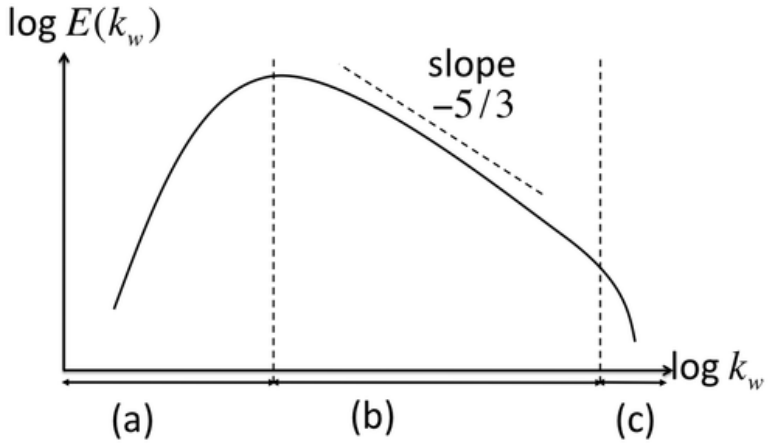

Figure 2-4 - Energy Spectrum diagram showing LEC (a), Inertial (b) and Dissipation(c) regions.

Within each region of the energy spectrum, the energy contained in the turbulent fluctuation of a flow is governed to a differing degree by geometric or viscous effects. The energy spectrum can therefore be used to identify the major factors governing the turbulent energy within a flow, and thus to ensure that scale modelling takes place in a representative environment, as will be explained in Section 3.3.

2.2.4 – Blockage

When an experimental water channel or similar device is used to represent the installation of a tidal turbine in a real oceanic environment, there is an inherent difference in the relative size of the turbine and the environment it is installed in. As has been discussed previously (for example the ScottishPower Renewables Sound of Islay installation discussed in Section 1.6 and Figure 1-18), a real tidal installation might involve one or two turbines installed in a channel with a width of the order of 1km, and water depth in the region of 50m. Though the precise value will depend on the bathymetry of the site, a rough calculation suggests that this installation might have a cross-sectional flow area of around 50,000m². A tidal stream turbine of 18m blade diameter has a blade swept area of 254.5m². The ratio between these areas is known as a simple blockage ratio (*B*) and is commonly expressed as a percentage [51]. In this real example, *B* = 0.5%.

When simulating real tidal stream turbine installations using scale models installed in water channels, as in this study, such blockage ratios are effectively impossible to achieve since the resulting turbine models would be too small to be accurately manufactured or effectively instrumented. Furthermore, as explained in Section 2.5.2, turbine rotational speed increases with reducing diameter, meaning that such models would rotate at very high speed, resulting in further practical difficulties as well as unrealistic effects such as the early onset of cavitation (see Section 2.5.2). At achievable scales of turbine models, blockage ratios in experimental work involving wind and tidal turbines of around *B* = 10% are common [52-54]. Due to the relative closeness of wall boundaries to the turbine, flow passes through the turbine region faster than would be the case in an unbounded situation, meaning that turbine power output can be greater than it would be in an unbounded case. Consequently, the difference in blockage between a real case and scale model testing must be acknowledged and measured, in order that its effects on results generated can be understood.

Furthermore, it has been suggested that simple blockage ratio does not fully describe the effects due to blockage in a channel when turbine models are used, and that a momentum-based calculation may be more effective in understanding the true effect of a rotating device in a channel. Chen and Liou [55] propose such a calculation and introduce the concept of a blockage factor (*BF*) for the correction of calculated turbine power coefficients. The blockage effect was found to depend on much more than the ratio of turbine to tunnel areas as in simple blockage; turbine rotational speed, pitch angle and blade number were also found to be important. The work was conducted in relation to scale wind turbines in a wind tunnel but retains relevance to tidal turbines in water channels. *BF* was defined as the cube of the ratio of calculated wind tunnel conditions (subscript T) to free stream conditions (subscript F), as follows:

$$BF = \left(\frac{U_T}{U_F}\right)^3$$

This concept was also adopted by Bahaj *et al* when studying the power and thrust of marine current turbine models in a towing tank [56]. Simple blockage ratios of *B*=17% were calculated. By assuming a wake expansion with uniform flow at any downstream cross-section, and assuming that turbines operating in free stream and tunnel conditions will have the same operating characteristics and angle of attack if they have the same thrust, flow speed and rotational speed, the relationship

between free stream and tunnel flow velocities can be calculated. The calculation is based on the measured velocity in the turbine wake, rotor area and tunnel cross-sectional area (full details of the calculation method are given in the appendix of the referenced work).

This method subsequently allows the calculation of U_T and U_F, and thus correction factors for turbine power coefficient (C_P), as above, thrust coefficient (C_T), and Tip Speed Ratio (λ, see Section 2.5.1). These corrections are as follows:

$$C_{PF} = C_{PT}\left(\frac{U_T}{U_F}\right)^3$$

$$C_{TF} = C_{TT}\left(\frac{U_T}{U_F}\right)^2$$

$$\lambda_F = \lambda_T\left(\frac{U_T}{U_F}\right)$$

By considering this method in addition to the simple blockage ratio, the effect of blockage on calculated turbine output can be quantified. The application of this method is discussed in Section 3.5.2.

2.3 – Flow measurement

In order to understand the influence of a tidal turbine on the flow conditions in its surrounding area, the link between the measurement of turbine performance and flow conditions is imperative. Turbine performance measurement is studied in Section 2.8.2, and this section deals with the measurement of flow conditions. Due to its importance in this thesis, Particle Image Velocimetry is described in a separate section (Section 2.4).

Due to the relative lack of studies on the flow analysis of turbines in water channels, an initial study of work in the wind industry was conducted. Vermeer, Sørensen and Crespo studied the computational and physical modelling of turbines in wind tunnels [57], and listed a number of flow visualisation techniques, some of which could also be applied to the monitoring of turbines in water flow.

- Smoke (either from flow inlet or part of model)
- Blade flags or thread
- Mechanical flow meters
- Hot wire anemometry
- Acoustic Doppler Velocimetry (ADV)
- Laser Doppler Velocimetry (LDV)
- Particle Image Velocimetry (PIV)

The use of smoke is clearly not a feasible option for the study of flow in water, but is analogous to the use of dye injection, which is a commonly-used method in the study of flow around submerged objects in water channels, an area on which there is a significant volume of literature.

Following a review of literature in which these methods had been used [58], it was concluded that flags and dye injection were useful qualitative techniques which allow the general pattern of a flow to be observed. However, since these methods do not allow the direct measurement of qualitative flow data it was concluded that they would only be suitable for initial investigations in the present study, and that a more comprehensive method of flow data measurement would be required for subsequent stages. Hot wire and hot film anemometry are commonly used in the study of wind turbines and air flows [59], but these techniques can present difficulties when used in water flows [60] and generally only offer the ability to measure flow in one dimension. Consequently, it was also decided that these techniques would not be suitable for the acquisition of the bulk of data required in this study, and that another method would be required.

Acoustic and Laser Doppler Velocimetry (ADV and LDV respectively) are commonly-used techniques in the measurement of flow in water, both in laboratory and field cases (the latter particularly in the case of ADV) settings [61]. Both employ the principal of Doppler shift, which describes the expansion or contraction of a wave field as an emitting object travels away from or towards the receiving location. This expansion or contraction shifts the original wave frequency, meaning that if the original and resulting frequencies are known, the velocity of the movement can be calculated. ADV employs this technique by emitting acoustic waves from a measurement probe suspended in the water, whereas LDV uses converging laser beams from outside the flow to generate a fringe pattern, leading to a pulsed reflection from a particle as it passes through the fringe, from which velocity can be calculated.

ADV has advantages over other flow measurement techniques in its simplicity and robustness, though it does have a significant disadvantage. Due to the fact that the probe must be suspended in the water in order to emit and receive sonic waves correctly, the technique is intrusive, meaning that its presence in the flow causes an inherent disturbance to the flow being measured. LDV does not suffer from this problem, and is highlighted by Vermeer *et al* [57] as a particularly useful flow measurement technique. Indeed, the technique has been applied in a number of recent studies using scale model tidal turbines [52, 62].

Similarly, PIV is also non-intrusive, and due to the fact that recordings are taken at a 2-dimensional field rather than at a single point, this method is able to generate a large amount of data much more quickly than LDV, as well as allowing the imaging of an entire flow field at a single instantaneous in time [63]. This ability to produce an instantaneous image of the entire flow field means that PIV is often described as an “instantaneous flow field” method, which is highly advantageous in the study of turbulent flows.

A study of the relative merits of five flow measurement techniques in marine energy applications was carried out by Lyon *et al* [60]. In addition to ADV, LDV, PIV and hot wire anemometry as discussed previously, this work also considered the use of Acoustic Doppler Current Profiler (ADCP) equipment, a technique commonly employed for the real scale analysis of tidal flows, but not regularly used at laboratory scale. ADCP operates on a similar principal to that of ADV, though in the former case the resolution is larger and the sample rate generally lower, with typical a sample frequency of 1Hz and sample volume of 10 to 10^4 cm^3. This system is therefore useful in the study of real-scale tidal flows, and can be mounted to the bottom of a boat and systematically moved across a site in order to generate a full 3D picture of the flow pattern through such a site. ADCP devices can

alternatively be fixed to the seabed and operated over extended periods of time, allowing the measurement of the tidal movement through an area over multiple tidal cycles.

On the subject of laboratory analysis, the study concluded that despite its relative expense in comparison to hot wire or ADV techniques, PIV offered the advantage of greater spatial resolution and comparable temporal resolution than these methods. Of the other methods considered, only LDV offered similar resolutions, but as previously discussed, the method is unable to capture an instantaneous flow field at a single point in time. This ability is offered only by PIV.

Due primarily to this ability, it was felt that PIV offered the most suitable measurement technique for use in this study, and would be employed in the majority of cases. However, ADV and LDV were also used at various stages during this work, and their use is described in detail in Chapter 3. Due to its importance to the present study, a separate review of PIV literature was subsequently carried out, as described in the following section.

2.4 – Particle Image Velocimetry

Particle Image Velocimetry (PIV) is a non-intrusive flow measurement technique. The technique has evolved over time and its development has been formed by the advent of new technology, but the principal as a method of visualising the flow of a fluid by capturing imagery of particles suspended in the flow has remained constant. The first use of a method of this type is generally credited to the German engineer Ludwig Prandtl in the early 20th century. Prandtl was also one of the first engineers to use a device resembling a modern water channel to conduct fluid mechanics experiments. Prandtl is illustrated with one such device in Figure 2-5.

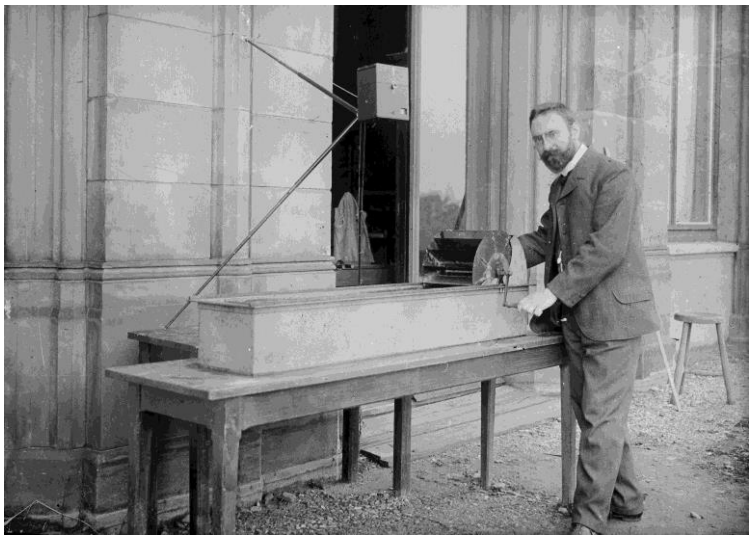

Figure 2-5 - Ludwig Prandtl and a water test channel (1904).

The size of channel upon which the method is applied has grown since Prandtl's early experiments, and PIV systems are now commonly used on water channels of over 300m in length such as the GWK channel at the University of Hannover [64].

PIV as it is recognised today evolved from a similar method known as Laser Speckle Velocimetry, which was used to measure flow velocity in laboratory experiments in the 1970s [65]. This method

used a much higher seeding density than is common in the case of PIV, and at the time also required the processing of images from analogue cameras. The computational restrictions at the time also meant that it was not possible to record two independent images to make up an image pair, and it was common to record both images to a single frame. This was then processed using auto-correlation rather than the currently favoured cross-correlation, which avoids problems associated with auto-correlation such as the understanding of particle direction.

The advent of CCD (charge-coupled device) digital cameras during the 1980s allowed the technique to take a step forward, as the computational power required for image processing was dramatically reduced [66]. Computational power had also improved and during the 1990s PIV became a feasible laboratory technique for flow imaging. During this time the method began to replace LDV as the most common such technique in research laboratories around the world, as it still remains today.

2.4.1 - Fundamentals of the method

The most common method of using the technique involves the illumination of a 2D section of flow using a light sheet, the light from which is reflected by seeding particles suspended in the flow and captured using a camera system perpendicular to the light sheet. By recording pairs of images with a known temporal separation, the position of the same particle in each of the two images is known, thus allowing particle velocity to be ascertained. Variations on the basic technique include the use of additional cameras to create a 3D image, or the use of additional optics to allow visualisation of very small scale fluid flows, known as Micro PIV.

2.4.2 - Illumination and image capture

Image capture is clearly a critical part of the PIV process, being the stage at which the images which are subsequently used to generate velocity fields are actually captured. In order to capture images successfully, the flow must be suitably illuminated during image capture, meaning that seeding particles and illumination must both be correctly established.

Illumination and optics

PIV Illumination is normally achieved through the use of a laser, commonly an Nd:YAG laser (that is, a laser using a neodymium-doped yttrium aluminium garnet crystal as the lasing medium). Nd:YAG lasers emit laser light at a wavelength of 1064nm and its harmonic wavelengths of 532nm, 266nm, and so on, but most PIV laser units incorporate a band pass filter to ensure that only light at 532nm is emitted by the unit. This band pass system is applied for safety reasons, since this wavelength produces a visible green light. In order to allow a small time gap between two subsequent laser pulses, it is common in PIV measurement to use a double cavity laser. In this case, two lasers are incorporated into a single unit and share the optics and control system.

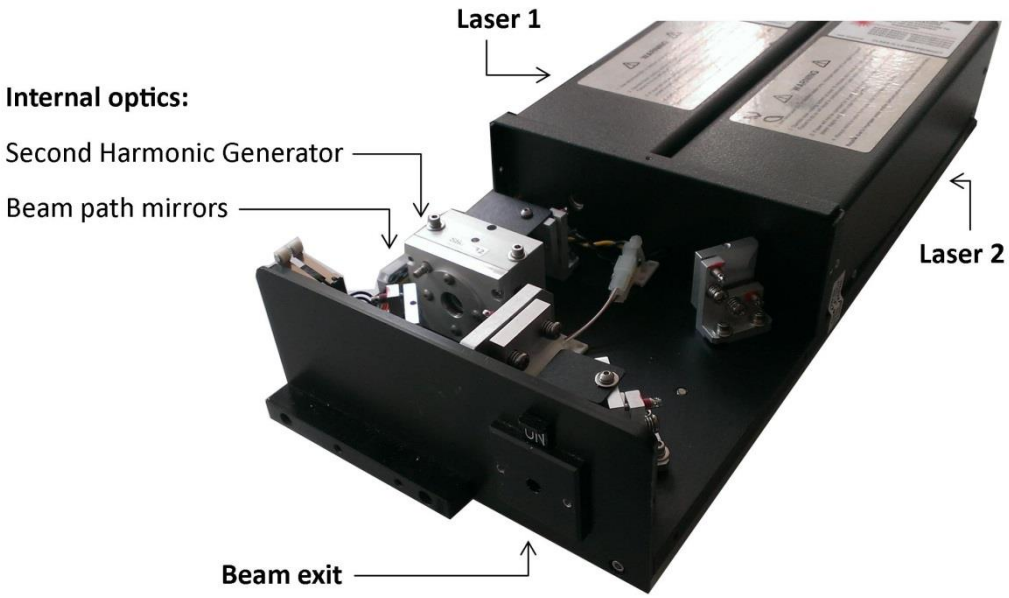

Figure 2-6 – Double cavity laser.

In order to generate a laser sheet of sufficient size to illuminate the required area of flow, a lens is used to produce a thin sheet of light with the required spread. Depending on the case in question, the laser sheet angle and therefore the width of the sheet at the measurement location can be modified by using a different external lens. The width of the laser sheet is also dependent on the separation distance between the laser and the measurement location, meaning that the illuminated area can be enlarged by moving the laser further from the measurement location. However, doing so will result in reduced laser intensity at the measurement location.

The thin laser sheet required for 2D PIV is generated by a combination of spherical and cylindrical lenses. The cylindrical lens is used to broaden the laser sheet in the y-direction with increasing x-direction distance, whereas the spherical lens works to flatten the laser beam into a thin sheet. [67]

Laser sheet thickness is crucial to the success of PIV illumination. Ideally, the laser sheet thickness should be sufficient only to contain a single particle in the z-direction, rather than multiple particles which overlap when viewed from above. The actual minimum possible thickness of a laser sheet is of the order of its wavelength, though generating a sheet as thin as this is often challenging and sheets of greater thickness can still yield results with sufficient accuracy [68].

Flow seeding

Though PIV and LDV are non-intrusive techniques, it is valuable to note that these techniques are also indirect methods of flow visualisation. This means that flow velocity is not calculated directly from the flow particles, but from tracer or seeding particles suspended in the flow. Provided that these particles faithfully represent the motion of the flow, this indirect measurement does not affect the accuracy of the method, but this fact does emphasize the importance of flow seeding.

In the case of PIV, seeding particles designed to reflect the laser light are added to the fluid. Such particles are designed to remain suspended in the flow and to faithfully represent its movement,

meaning that they must be of a suitable mass. If a particle is too heavy it will sink to the bottom of the flow, whereas an overly light particle will not properly follow the flow and may rise to the top surface or become trapped in eddy currents. Advantageous features of a seeding particle, in addition to mass, are its ability to scatter light of the wavelength to be used, a diameter which is small enough to allow the particle not to alter the fluid flow, and a shape as close to a perfect sphere as possible.

The ability of a particle to follow the flow around an obstacle of diameter d_c is described by the Stokes number, *Stk*, which describes the ratio of a particle's characteristic time to the characteristic time of the flow:

$$Stk = \frac{\tau\, u_0}{d_c}$$

τ describes the relaxation time of the particle, and is itself calculated from the particle diameter (d_d) and density (ρ_d), and the fluid density:

$$\tau = \frac{\rho_d\, d_d^2}{18\mu}$$

The seeding particles chosen for use in the PIV studies in this project, and subsequent Stokes number calculations, are given in Section 3.4.4.

Timing

The timing and triggering of laser and camera systems is critical to the image capture phase of a PIV study. The temporal spacing between images in each pair allows the required in-plane movement distance to be achieved, and the time between image pairs gives the temporal resolution of the resulting data. Timing settings applied to this study are again given in Section 3.4.4.

2.4.3 - Pre-processing

Following image capture, the pre-processing phase of PIV analysis involves the preparation of images for the correlation procedure. In order to optimise the correlation procedure, filtering can be applied to the image pairs at this stage. A number of filters commonly applied to PIV image data are described in the following section.

Background subtraction

This method involves the capture of a background image, taken under the same conditions as the experimental images, but in the absence of seeding. This image can then be subtracted from subsequently captured PIV images in order to give uniform background intensity.

High pass filter

Similarly to background subtraction, high pass filtering of PIV data can remove background variation whilst leaving the particle intensity unmodified. This is achieved by first generating a version of the image with the high intensity areas removed, by applying a low pass filter of an appropriate level to

the image. The low passed image is then subtracted from the original image in a procedure similar to that of background subtraction, producing an image of only the particle reflections which can be subsequently processed or used in correlation procedures.

Low pass filter

Low pass filtering is sometimes useful to remove high frequency noise or erroneous results from an image, in cases where the particle reflections are not the highest intensity pixels in the image. In this case, the filter intensity level must be carefully set in order to ensure that particle reflections are not affected.

Image binarisation

Image binarisation is the conversion of a grayscale image, which contains 256 levels of intensity, to a binary two-colour image. This conversion reduces the computational size of images and provides faster processing, but can lead to errors. Errors are caused by pixels with intensities around the mean value, which are either characterised as particle reflections or are reduced to background intensity. Due to the likelihood of these errors, image binarisation should be carried out following the application of other pre-processing methods which are likely to clarify the nature of particles with intensity around the mean value. A sample image illustrating the potential for the loss of information through binarisation is given in Figure 2-7, in which it can be seen that bright pixels observed in the greyscale image to the left are lost when the image is converted to binary. These reflections may not necessarily represent particle reflections, but their loss at this stage does not allow this to be confirmed.

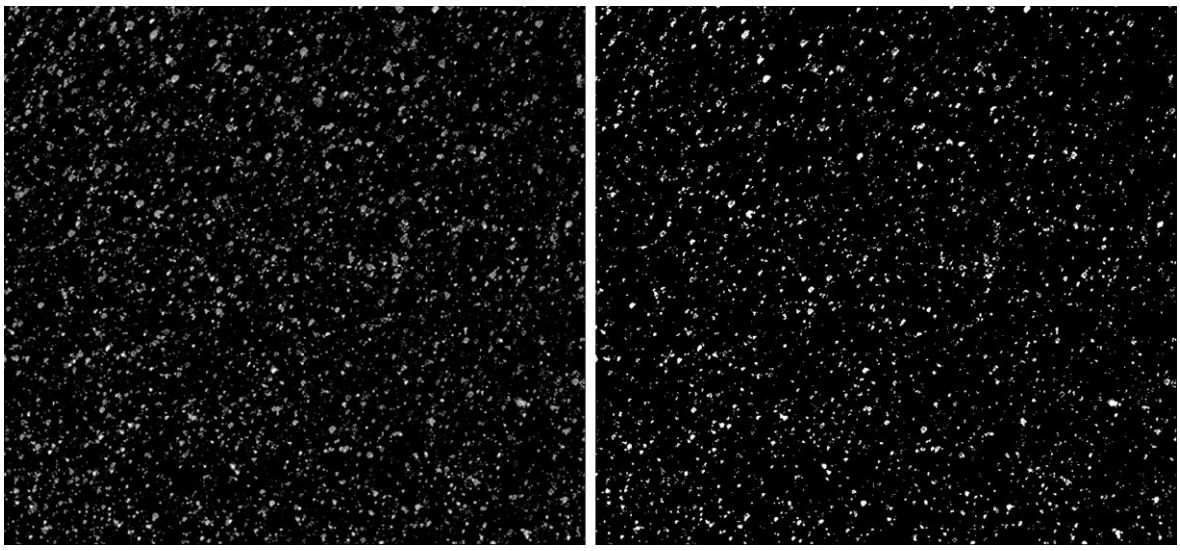

Figure 2-7 – Sample PIV image in 256 colours (l) and binarised (r).

Adaptive Histogram Equalisation

The most common histogram equalisation technique in PIV is CLAHE (Contrast-limited adaptive histogram equalization), which was originally developed for medical imaging purposes [69]. CLAHE describes the contrast-limited adaption of the original adaptive histogram equalisation (AHE) filter, which is itself a development of a more basic histogram equalisation (HE) filter [70], also known a

histogram stretching. Histogram equalisation involves the modification of an image's histogram of pixel intensities. Images which suffer from low contrast have pixels spread over a narrow range of intensity values, meaning that the difference between maximum and minimum pixel intensity is small, and thus making the contrast low and the image difficult to see. By modifying the image so that the lowest intensity values are effectively white or 0% of the available intensity and the maximum are effectively black or 100% of the available intensity, the image contrast can be improved.

Whilst the adaptive histogram method can improve the contrast of an image, it does have some disadvantages. Since the histogram adjustment is constant across the entire image, the change in contrast is indiscriminate, meaning that areas of low importance may have a large influence on the modification of the image and thus the contrast of a more important area of the image may actually be reduced. This issue can be addressed by the use of Adaptive Histogram Equalisation (AHE). AHE applies the same principal as HE, but whereas HE generates a single histogram to represent the intensity distribution of the entire image, AHE generates multiple histograms for multiple areas of the image. The number of histograms is governed by the size of the sample region, which is a region of a defined size, for which a separate histogram is created. The region size is defined as a parameter of the method, with a smaller size giving a smaller region of calculation and a larger number of histograms for an image of a given size.

A drawback of the AHE method occurs when the sample region is largely homogenous, i.e. the pixels in the region are mostly of the same or similar intensity. This case produces a histogram with a large peak, since a high proportion of pixels are of (or close to) the mean intensity. By equalising this histogram peak over the full range of intensity values, the region becomes less homogenous. In terms of processing an image signal, this can have the effect of amplifying noise. It is for this reason that the final development of the histogram equalisation method is useful, and is most commonly applied in the pre-processing of PIV images. By applying Contrast-Limited Adaptive Histogram Equalisation (CLAHE), the noise amplification effect is avoided by limiting the amplification which can be applied to a single pixel to a predefined level. This level, known as the clip limit, is calculated based on the cumulative distribution function of pixel intensities within the sample region. A sample image and its distribution histogram in unprocessed, processed using HE, and processed using CLAHE forms is illustrated in Figure 2-8.

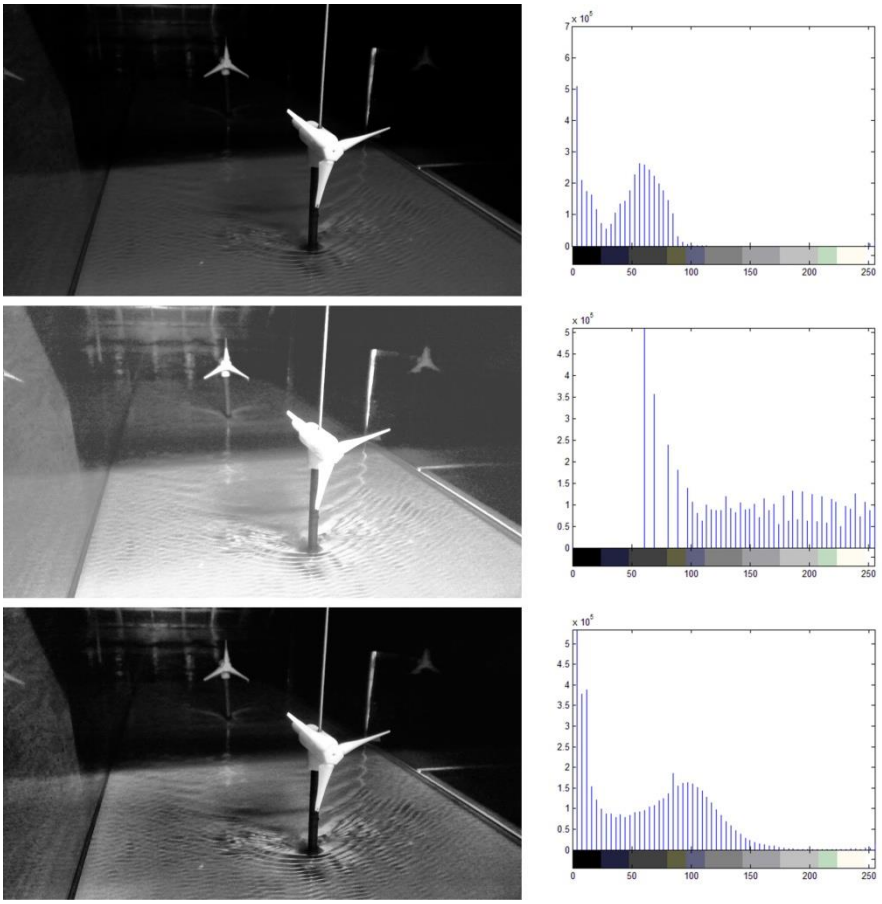

Figure 2-8 – Sample image and their intensity histograms (Top: unprocessed, Middle: HE, Bottom: CLAHE (clip limit = 0.01))

Intensity capping

Bright spots in PIV images are most commonly caused by the presence of multiple particles at the same point, and are particularly apparent if they occur within a highly-illuminated region of the flow such as the centre of a laser sheet. These spots have intensities much greater than that of the mean intensity of the image, and greater than that of other particles within the image. When correlation is carried out, bright spots are likely to dominate the resulting correlation peak, and hence velocity field. If the bright spot pixels do not represent the mean flow, this will result in an erroneous velocity field which does not represent the actual motion of the field.

In order to avoid this undesirable effect, bright spots can be removed from the image using a procedure known as intensity capping, as proposed by Shavit *et al* in 2007 [71]. Intensity capping is a relatively simple procedure which removes the bright spots from an image by replacing any pixel intensity which is greater than a pre-defined value with the intensity of that value. The value is defined relative to the median intensity of the image, I_0 and a multiple *n* of the standard deviation of the intensity, δ_1, as follows:

$$I_0 + n\,\delta_1$$

The value of *n* is chosen by the user. Examples given by Bastiaans in his book on the subject [72] suggest that a value of 2 may often give good results, but testing should be conducted on the data

set on which the capping procedure is to be applied in order to ensure that only spurious bright spots are removed.

Clipping

Clipping is a pre-processing procedure designed to improve the performance of the subsequent correlation procedure by ensuring that all non-illuminated pixels in the image are of zero intensity. Due to variation of illumination within an image, some background particles may not have zero intensity, which can lead to errors during correlation. Clipping is a simple procedure which overwrites the intensity of any pixel with intensity below a pre-set level to zero, thus ensuring that only genuine particle reflections are used in the correlation process.

2.4.4 – Image correlation

The correlation phase of PIV analysis is a critical one, being the stage during which image pairs showing the position of seeding particles are transformed into velocity fields. The process involves the discretisation of each image into a series of interrogation windows, each of which is analysed individually before combining the results. The analysis is carried out by correlation, specifically either auto-correlation or cross-correlation. The former is used when single image PIV is employed, that is to say that two flow field illuminations have been recorded in a single image. Though it has advantages, this technique can produce difficulties in the analysis of the PIV images, in areas such as directional uncertainty [72]. Cross-correlation is employed when, as in the case of this study, image pairs have been recorded. The correlation procedure then compares the position of pixels in the two images in order to ascertain the velocity and direction of the movement of each illuminated particle. Under the umbrella of cross-correlation, there are two correlation methods which are commonly used in PIV, namely the DCC (Direct Cross-correlation) method and the FFT-CC (Fast Fourier Transform Cross-correlation) algorithm [73]. Both processes aim to compare a portion (of size K x L) of an image pair and to ascertain the relative i and j positions of an individual particle over the time gap between the first and second images (I and I' respectively), as described:

$$R(x,y) = \sum_{i=-K}^{K} \sum_{j=-L}^{L} I(i,j)I'(i+x, j+y)$$

When using DCC, the initial image I is shifted linearly about its original position and the results statistically compared to I'. The shifted position which produces the results which most closely match those of I' is then used as a direct estimate of I', and the process moves on to the next image portion. Since multiple shift positions are tested for each image portion, DCC is a lengthy process, requiring N^4 processes to evaluate a square interrogation area of size N. It also suffers from other disadvantages, such as the fact that due to its linear approach, the method is unable to correlate non-linear particle movement [66]. This problem can be solved by reducing the interrogation window size to such a degree that the particle movement is linear, but this clearly requires a large number of interrogation windows to be analysed, and has a resultant effect on the computational requirements of the method.

The time and computational power required to successfully conduct DCC, particularly in the early development of PIV, was a limiting factor to the accuracy of the technique. Hence an alternative

method was sought. The resulting method is FFT-CC and has remained the dominant correlation method, even since the advent of more modern computers which theoretically allow the use of DCC. Using Fast Fourier Transforms reduces the number of processes required to evaluate a square interrogation area of size N from N^4 processes (using DCC) to $N^2 \ln N$. This is a significant improvement, meaning for example that the number of processes required for a single 64x64 interrogation window correlated using FFT-CC is around 1000 times less than the number of processes which would be required to correlate the same window using DCC (17,034 processes using FFT-CC, versus 16,777,216 using DCC).

Although FFT-CC is by far the most commonly used of the two methods, and has been applied in the vast majority of PIV studies of turbines [53, 74], there is nonetheless some debate as to the accuracy of the FFT-CC method in comparison to DCC. Oliver Pust [73] conducted a comparative study using numerous versions of both methods to analyse the same set of data. Results from this study illustrate that the FFT-CC is able to predict the results of direct CC with variation of less than 1%. Given the number of experiments proposed in this study, it was concluded that the increased computational efficiency of the FFT-CC method made it the more viable choice of algorithm for use in this study. A comparison from [73] illustrating results from the same data set analysed using direct CC and FFT-CC methods is shown in Figure 2-9.

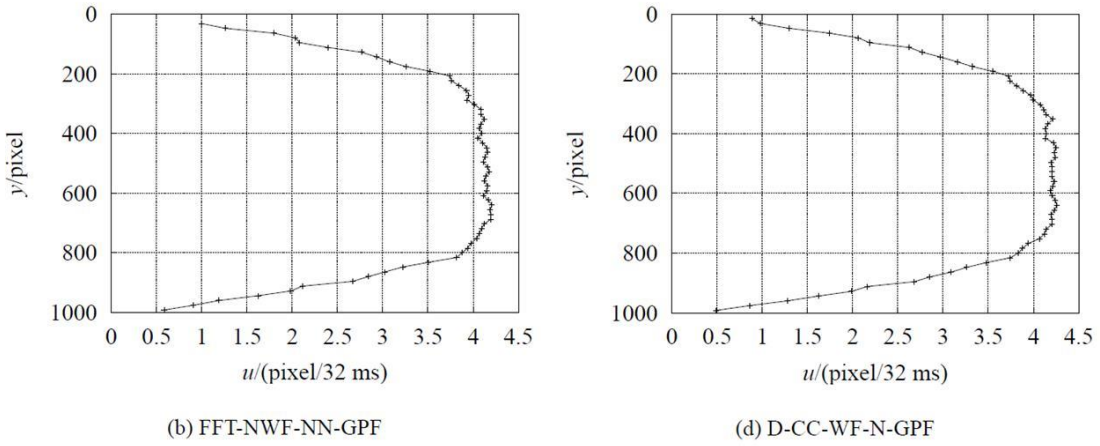

Figure 2-9 – Comparison of processed PIV velocity results from a study of a horizontal cross-section of a water channel using FFT-CC (l) and direct CC (r) PIV processing algorithms [73].

Correlation is carried out by the software over small sections of the image at a time. Prior to correlation, each image pair is divided into a number of such areas, known as interrogation windows. It is common for multiple passes of correlation to be undertaken, each with a smaller area than the previous. The size of the chosen interrogation window is another area of some debate in the literature. It has historically been assumed that smaller interrogation areas will yield greater accuracy in results, but recent research [75] suggests that reducing the area below a certain level does not yield any further increase in accuracy, and may even lead to less accurate results. This is because at very small interrogation window sizes the number of out-of-plane particle movements will be high (i.e. a high proportion of the particles present in the first image of a pair will not be present in the second), thus increasing the likelihood of erroneous correlations, as particles only present in the first image are paired with others only present in the second. Notwithstanding this

possibility, each additional pass certainly adds significantly to the overall time required to conduct the correlation procedure, with diminishing returns in the increase in result accuracy as the interrogation area size is reduced.

Sub-pixel velocity estimation

In order to increase the resolution of velocity calculations, it is possible to estimate the position of particles below pixel level, using a process known as sub-pixel estimation. This process requires the particle to be recorded at a size larger than one pixel, since the particle must extend over at least two pixels to apply the method. The procedure assumes that the intensity of a particle follows a Gaussian distribution and is therefore, by fitting a Gaussian distribution curve to the pixel intensity image, able to pinpoint the position of the particle centre based on the relative intensity in the surrounding area. Sub-pixel estimation as used in this study is described in Section 4.3.3.

2.4.5 – Calibration and post-processing

Post-processing describes procedures carried out to improve the PIV output data after the correlation process by identifying and removing any erroneous results. Three main methods are described in this section, namely vector validation, standard deviation filtering, and median filtering. Specific details of the application of these methods to the data generated in this study are given in Section 4.3.5.

Vector validation

Vector validation is a preliminary post-processing procedure whereby vectors whose magnitude lies outside a predefined range are excluded. This is achieved simply by defining limits to the magnitude of velocity in the streamwise and cross-stream directions, and using software to apply these limits across a data set. Following the removal of vectors whose magnitude lies outside this range, the question of replacement arises. If these vectors are not replaced they are likely to behave as vectors of zero magnitude in any subsequent analysis, which may distort results. Consequently it is often preferable to replace vectors found to lie outside of the acceptable range with a value generated by interpolating the magnitude of nearby vectors [76]. This technique is implemented in the PIVLab software used in this study. Specifically, PIVLab employs a boundary value interpolation, which was found to outperform other interpolation techniques (when compared to the 3x3 mean method and a range of 2D methods, boundary value interpolation was found to estimate the value of removed pixels around 8% more accurately than other methods, as illustrated in Figure 2-10).

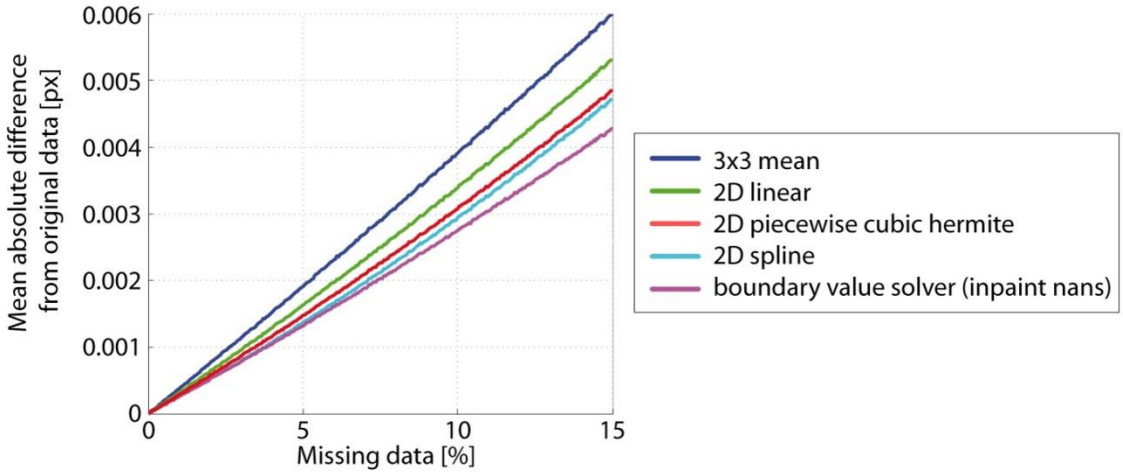

Figure 2-10 - Comparison of boundary layer interpolation methods (from [75]).

Median filter

Two common methods of filtering large samples of numerical data are standard deviation filtering and median filtering. Both are often used in the post-processing of PIV data, and are described in this section.

Median filtering is used in many image processing applications, and is often applied in the post-processing of PIV data [77]. This filter can be applied to any data set arranged in a matrix format, and works by replacing each matrix element with the median of its surrounding elements. The median of a data set is the value at which when arranged in ascending numerical value, half the data lies above and half below. A simple median filter operation is illustrated in Figure 2-11. The left matrix is the original, and in the right matrix the central element (79) has been replaced with the median of its surrounding elements.

42	49	55
41	79	50
34	36	39

42	49	55
41	41.5	50
34	36	39

Figure 2-11 – Matrix before (l) and after (r) median filtering of the central element.

When using median filtering, a threshold is often defined. If the difference between the value of the element being analysed and the median value which would be used to replace it is below this threshold amount, the element is not replaced. This allows the user to allow differences between an element and its surrounding elements, whilst still replacing elements whose values are significantly different to their neighbours.

Standard deviation filter

Standard deviation filtering is applied by calculating the mean and standard deviation of particle velocity of a data sample, and defining a threshold value. The product of this threshold and the

standard deviation defines the range within which results are retained; any results falling outside this range are discarded. The threshold value is therefore commonly set just above the maximum expected flow rate within the area in question, meaning that any vector with a velocity greater than this can be either removed entirely from the data set, or can be replaced by a vector generated by interpolation of those in the surrounding area. Standard deviation filtering was applied throughout this study, and is detailed in Section 4.3.5.

2.4.6 – Errors in PIV

There are a number of potential sources of errors throughout the PIV process, all of which can lead to low accuracy or erroneous results. Errors can be caused at all stages of the PIV process, as described in the previous sections.

Illumination

Raffel's comprehensive guide to PIV [66] highlights a number of potential sources of errors during the pre-image stage, beginning with incorrect illumination. Areas of a PIV image which are badly illuminated exhibit low contrast between genuine particle reflections and background, meaning that image correlation is difficult. These errors can be avoided relatively easily by ensuring that all areas of images from which results are required are correctly illuminated, and by using suitable optics to ensure that the illumination source is spread over the area of interest. In many cases, it is sensible to illuminate an area wider than that which will subsequently be analysed, and then to restrict the field of analysis by applying a region of interest during later calculations.

Particle displacement

Similarly, there is potential for a number of errors during the image recording stage. The choice of time step is critical in order to ensure suitable levels of particle movement between images. If the chosen time step is too short, particles will only be seen to move a few pixels between images in a pair. This causes velocity estimation errors, since an increase in particle position of one pixel between frames represents a large change in the overall velocity. Furthermore, any noise present in the signal is likely to have a significant effect if the particle movement is small. If the time step between two frames is too large, particles seen in the first image of a pair may have left the image by the second image, meaning that their movement cannot be correlated. This is known as out-of-plane particle loss, and is a significant source of error if the chosen timestep is too large. Potential errors due to the selection of a timestep which is too small or too large are illustrated in the following figures. In all cases, the position of particles in the first frame is shown (in black) in the left hand image. In the right hand image, a superimposition of the first and second frame is shown (frame 1 particles in black, frame 2 particles in grey). Particles not present in the first frame will also enter the second frame, but these are omitted from these figures for clarity.

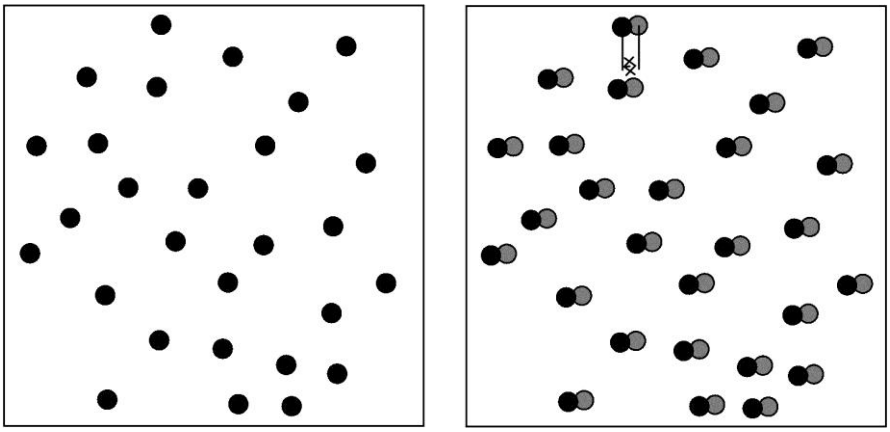

Figure 2-12 – A sample image pair illustrating an insufficiently long timestep, meaning in-plane particle movement between frames is very small.

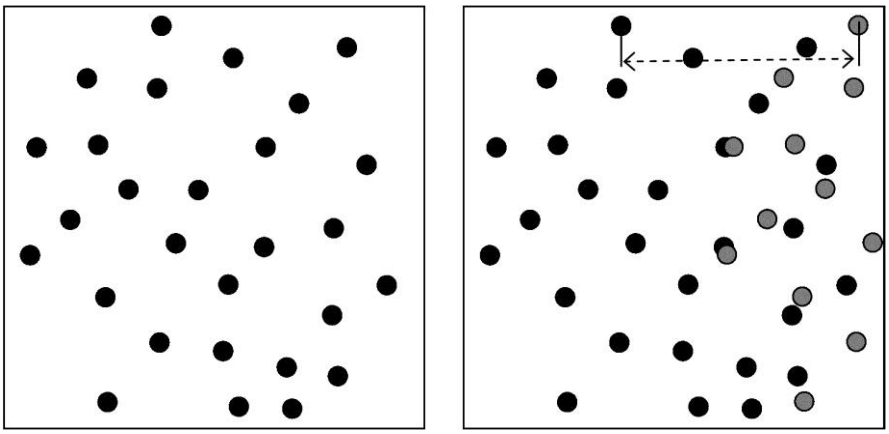

Figure 2-13 - A sample image pair illustrating an overly long timestep, meaning out-of-plane particle loss is high.

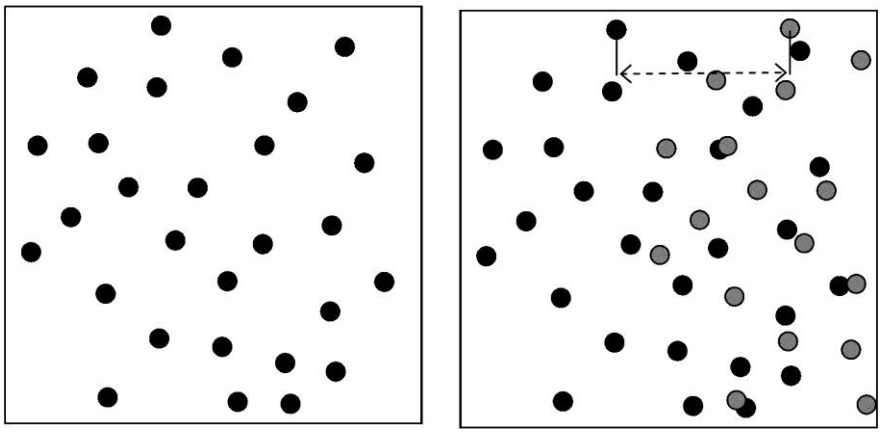

Figure 2-14 – A sample image pair illustrating an optimal timestep, balancing in-plane particle movement and minimal out-of-plane loss.

In order to minimise out-of-plane loss whilst ensuring a measurable movement of particles between image pair frames, the size of the final interrogation window used during the correlation procedure must be taken into consideration. Particle displacement of around half of the size of the interrogation window in the direction of flow is recommended [75]. For example, in the case of an

interrogation window of 16px width and 16px height, a particle displacement between frames in an image pair of around 8 pixels is suggested.

Pre-processing filters

The use of pre-processing filters can lead to errors, since the over-enthusiastic application of such filters can lead to the loss of data from the original sample. As discussed in Section 2.8.3, a range of filters can be applied, including high-pass and low-pass filters, image binarisation, and contrast-limited adaptive histogram equalisation. Though all methods of filtering can result in data loss, the pre-processing phase is particularly prone to the introduction of error through the use of image binarisation. Data loss through image binarisation occurs when there are areas in the original (256 colour) image with brightness close to the image mean value. When the image binarisation process is undertaken, these areas may be categorized only as either background or as particle reflections. The potential for errors occurs in that a reflection which is a particle may be, if its brightness is slightly below the image mean value, converted to a background particle by the binarisation process and lost. Similarly, a reflection which is not necessarily a legitimate particle, but has a brightness slightly above that of the image mean, would be categorised as a legitimate reflection, and hence an erroneous reflection would be taken forward to the correlation process. The potential for errors in the image binarisation process can be minimised through the use of other filters prior to its application, and through the minimisation of noise in the PIV images during the capture phase.

Peak locking

A common error in correlation phase of PIV experimentation is known as “peak locking” [78]. This phenomenon most commonly occurs through the use of inappropriate sub-pixel estimation methods, and results in the bias of results towards integer or half-integer values of pixel displacement. The effect can be observed by plotting a histogram of particle displacement across an image, as illustrated in Figure 2-15.

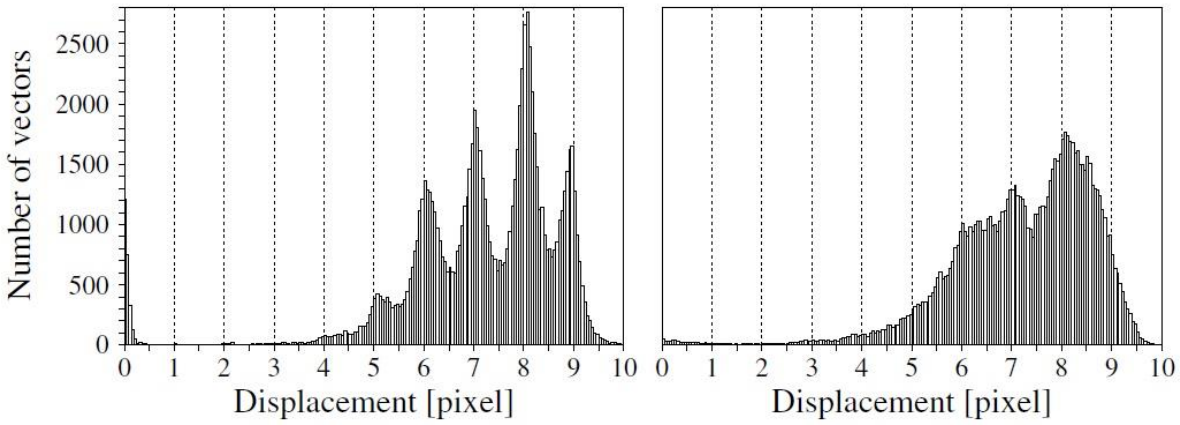

Figure 2-15 – Displacement vs frequency histograms for sample data illustrating the presence of peak-locking (l) and the same data without peak-locking (r). From [66].

Histograms equivalent to those illustrated above (such as those illustrated in Figure 4-9, Figure 4-10 and Figure 4-11) were generated for experiments carried out as part of this study in order to check

for the presence of the peak-locking effect. The effect was not observed, suggesting that the Gaussian 2x3-point estimator method used for sub-pixel estimation in this study was appropriate.

Total error in PIV results is made up of bias error ($\mathcal{E}_b$) and random error ($\mathcal{E}_r$) [66]. Bias error describes the difference between the result of the mean of a large collection of results and the actual mean flow, and is sometimes defined as "trueness". Random error is used to describe the precision of the results (i.e. the similarity of repeated results). High bias error and low random error would describe a set of results with an incorrect velocity prediction, but little variation between the predictions in each case. Results with a low bias error and high random error would exhibit a correct mean prediction of the velocity, but would have a larger spread of values than the real case.

PIV literature offers a number of estimations of the overall error likely in PIV experimentation. For example, Adrian [79] suggests overall errors of 1% are common in digital PIV experiments, and PIVLab's own developers [80] conducted an extensive study of the accuracy of the software using a number of sample experiments, concluding that bias errors of 0.005px and random errors of 0.02px pixel displacement could be expected for a mean particle displacement of 6px. This corresponds to an error of 0.42%.

Adrian [81] also offers a method to calculate the estimated maximum error in PIV calculations. The method takes into account the flow velocity (u_{max}), size of interrogation window (d_τ), timestep (Δt), and the accuracy of the calculation of the particle movement (c), calculated from mean values of correlation peak intensity.

$$\varepsilon = \frac{c\, d_\tau\, u_{max}}{\Delta t\, u_{max}}$$

This calculation was found to give an estimate of $\mathcal{E}_b$ = 0.8px between frames, corresponding to 0.018m/s or a maximum particle velocity error of 6%. As a calculation of maximum error, the actual error in most cases is expected to be well below this value.

2.5 – Tidal stream turbines in operation

As has been discussed in Chapter 1 and Section 2.1, tidal stream energy has been highlighted by many as a viable future source of renewable energy [30], particularly in the UK. However, the industry is in its infancy, and to date there are relatively few devices at a commercial stage of development, and even fewer actually supplying electricity to the UK grid. This literature review section aimed to find out which device designs are the most developed, and to ascertain whether a clear market leading design or style of device has yet emerged.

2.5.1 – Fundamental principles

Initially, the fundamental principles which govern the operation of a tidal turbine were studied. These relate to the conditions discussed in Section 2.2, but specifically relate to tidal turbine device operation.

Available power

The fundamental theory behind both wind and tidal stream turbines is the extraction of power from a moving fluid. The availability of power in a stream of water or air is clearly critical to the potential for wind or tidal stream power as an energy source. The available power P_A in a stream of fluid of cross-sectional area A, velocity u and fluid density ρ is given by:

$$P_A = \frac{1}{2}\,\rho\,A\,u^3$$

However, not all of this power can be extracted from the flow. In the 1920s, Albert Betz discovered that a limit exists to the amount of power which can be extracted from a moving flow by a turbine, and that this limit is 16/27, or 59.3% [82]. Consequently, the maximum power able to be extracted from a flow by a turbine is 59.3% of P, above. Tidal energy devices, like wind turbines, aim to get as close as possible to this level of power extraction, though results from the wind industry suggest that reaching the Betz limit is challenging. The extraction of most commercial wind turbines is in the region of 75 – 80% of the Betz limit [83]. Despite this, many attempts have been made to design a turbine which can overcome this limit. Since it applies only to an open disk flow, the Betz limit can theoretically be overcome by using a diffuser system in which fluid motion perpendicular to the direction of flow is restricted. By using such a system, the limit is no longer applied and higher power extraction rates can theoretically be achieved. This has led to the suggestion of "ducting" being applied to both wind [84] and tidal turbines. However, due to the additional complexity, cost and structural loading applied to the support structure, ducted wind turbines have remained a niche design and none are believed to have exceeded the limit. Numerous ducted tidal turbine designs have been proposed, as will be discussed shortly. Furthermore, it has been suggested that tidal turbine power extraction is not entirely governed by the Betz limit, since the limit only applies to kinetic energy. Since a free surface drop can occur over a tidal turbine, meaning that energy is also extracted from potential energy to which the Betz limit does not apply, it is theoretically possible to reach and exceed the limit [85].

Power coefficient

The ratio of the power generated by a turbine in a given flow case (P_T) to the available power (P_A) is given by the power coefficient, C_p. The maximum power in a flow case is calculated over the turbine swept area using the equation given above, thus giving C_p as follows:

$$C_p = \frac{P_T}{P_A}$$

As discussed previously, the available power is limited by the Betz limit, so a theoretical C_p limit of 0.593 exists in the case of standard horizontal-axis devices.

Tip Speed Ratio

Tip Speed Ratio (TSR, λ) describes the ratio of the tangential rotational speed of a turbine device to the flow speed in which it operates. The ratio is given as follows:

$$\lambda = \frac{\omega R}{u}$$

When turbine performance over a range of TSR values is known, TSR is commonly plotted against power coefficient to generate $C_P - \lambda$ plots, which are commonly used to illustrate the performance of a device. A hypothetical $C_P - \lambda$ is given in Figure 2-16. This plot illustrates that the peak power output of the device occurs at a λ value of 3.5. In the case of a tidal stream turbine, which may have a rotor diameter of around 20m, and may be installed in on a site with a peak tidal flow of 2.5m/s [86], this would correspond to a turbine rotational speed of 0.875 rad/s (around 8 revolutions per minute). At this position, the example curve below gives C_p = 0.45. The power available in a 20m diameter cross-section of flow at 2.5m/s is approximately 2.45MW, suggesting that the turbine could produce 1.1MW. Due to the cubic relationship between power and flow velocity given above, the power produced by a turbine drops dramatically in reduced water flow speeds, as can be seen by the steep fall in C_p values to either side of the peak in Figure 2-16.

C_P is used alongside blade torque measurements in this thesis to illustrate the power generated by turbine models relative to the power available in a given flow case. However, due to the volume of experiments undertaken in order to test as many support structure and layout configurations as possible, only two flow cases, and consequently two λ values were used. As discussed in Section 5.1.2, experimental λ values as close as possible to real case values were selected, however it should be noted that the application of λ values across a number of experiments may lead to some experimental results being recorded closer to optimal λ than others, which must be borne in mind when subsequently comparing results.

C_P – λ plots were not generated for the main phases of this work, but subsequent work using different models (detailed in Chapter 7) did include testing at multiple tip speed ratios and the calculation of $C_P - \lambda$ plots.

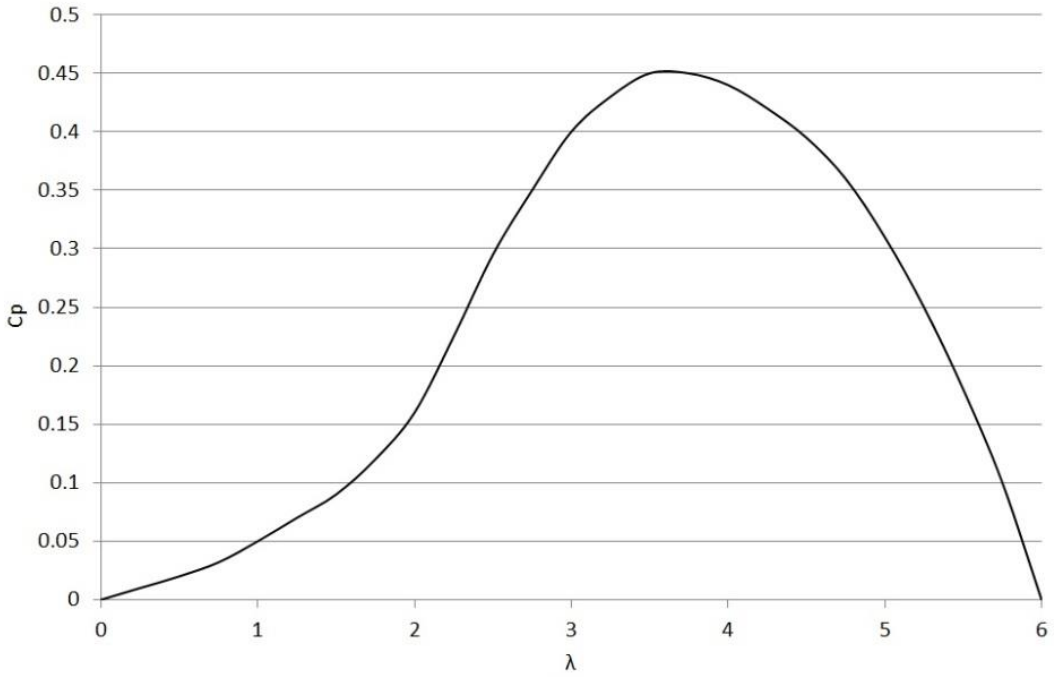

Figure 2-16 – Sample $C_P - \lambda$ plot.

Flow conditions – Water boundary layer & Turbulence

The flow conditions in which a tidal turbine operates are complex. Expected values of *Re* are in the order of $3x10^8$ during peak flow conditions, meaning that the operating environment in these cases is a turbulent one. However, due to the nature of tidal movement, during slack water periods (the period of low flow velocity at the turning of the tide) flow velocity will drop to zero. Consequently the tidal turbine will experience the full range of laminar, transitional and turbulent flow conditions. However, the fluid velocity at which laminar and transition conditions dominate are less than 0.1 m/s. Velocities this low will only occur for a short time at the point of the tide turning, and minimum flow velocities for electricity generation from tidal turbines are of the order of 1m/s, so although all tidal turbines will experience laminar, transitional and turbulent flow conditions, turbulent conditions will always dominate while the turbine is actually generating power.

The velocity profile and turbulent characteristics of tidal environments have been studied by many in the field of marine hydrology [87, 88], both through the use of monitoring techniques such as Acoustic Doppler Current Profiling (ADCP), and through computational modelling. The measurement of turbulent characteristics is discussed at length in Section 2.9.

Velocity profiles in tidal regions have been measured at potential tidal energy sites in the UK, including the Solent by Dyer [88] and Wales and the Severn by O'Doherty *et al* [89]. The former used mechanical flow meters mounted at eight vertical positions to record velocity profiles, and the latter a ship-mounted ADCP system. Both studies also compared measured profiles to power law-generated data. The power law is commonly used to estimate wind speeds at a given height, and is written as follows:

$$u = u_1 \left(\frac{z}{z_1}\right)^{\frac{1}{p}}$$

Where u and u_1 represent velocity at height z and z_1 respectively. The value of p defines the profile of the generated curve, and a value of 7 is commonly used in the wind industry [90]. Velocity profiles in tidal flows are less well understood but it has been suggested that the same profile law may apply [91]. A comparison of the data from [88] and [89] above to the 7^{th} power law is given in Figure 2-17.

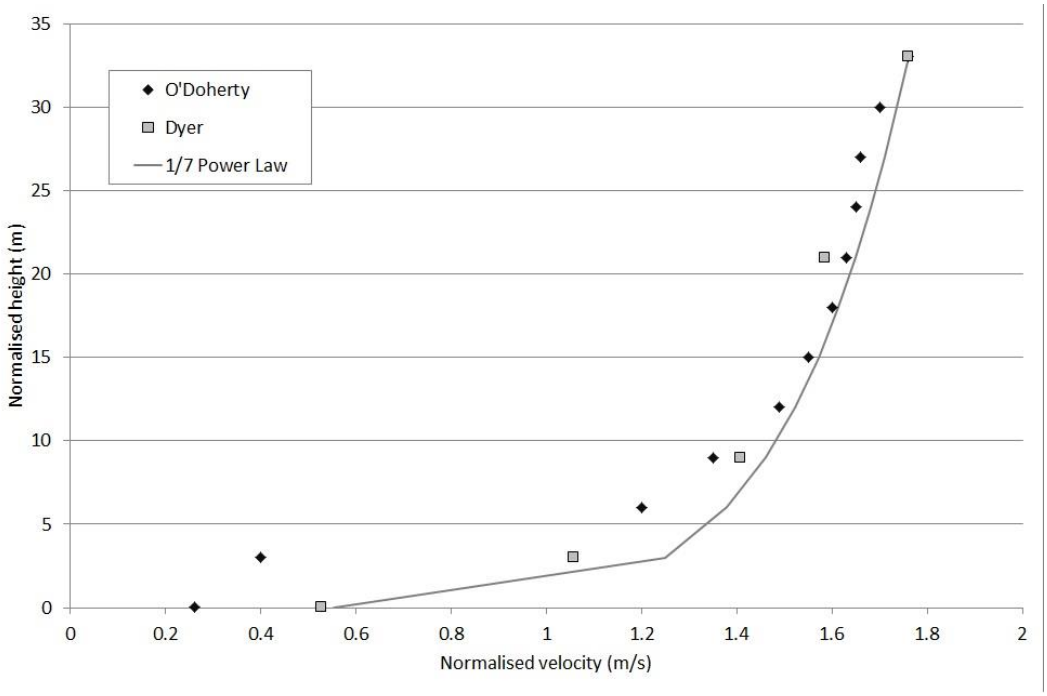

Figure 2-17 - Comparison of tidal flow velocity profile data from Dyer [88]and O'Doherty et al *[89] to 7th power law prediction.*

The results of these studies illustrate that the 7th power law gives a reasonable approximation of the velocity profile in a tidal region, as supported by [90]. It should however be noted that this law is likely to under-predict turbulent energy, as illustrated by Okorie *et al* [92]. As can be observed in the recorded velocity data illustrated in Figure 2-41, the actual variation in velocity is much greater than that recorded by averaging or by applying the power law. Consequently, velocity fluctuation and therefore turbulent intensity calculated from 7th power law velocity data is likely to give lower values than that calculated from recorded velocity. Okorie [92] observed 3.5 times greater values of turbulent intensity in measured ADCP data than that predicted by power law predictions.

Vortex Shedding

Vortex shedding has been the cause of numerous disasters, since it is the underlying principal which causes the generation of large oscillatory forces on objects such as bridges or towers subject to wind loading. A famous example of the effect is the collapse of the Tacoma Narrows Bridge in 1940. Vortex shedding is also seen on a very large scale around islands subject to high velocity winds, as illustrated in Figure 2-18.

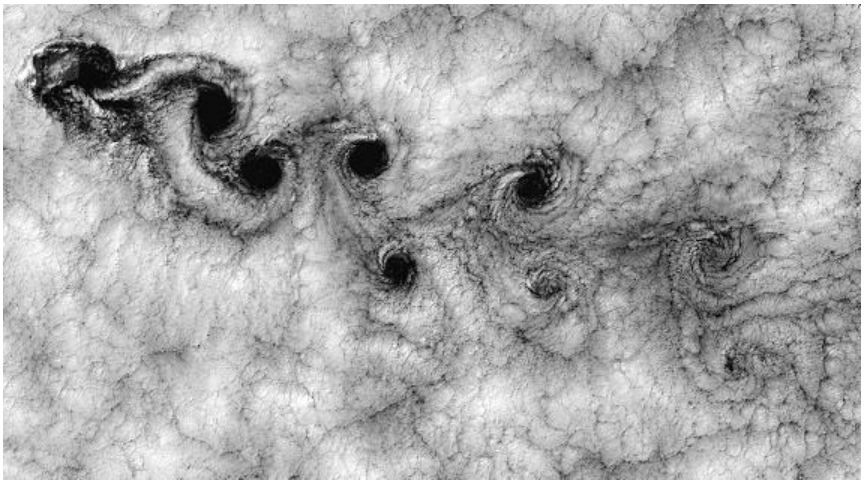

Figure 2-18 – Vortex shedding around the Juan Fernández Islands (NASA)

Vortex shedding was first documented by Theodore von Kármán [93], though it was previously studied by others (Mallock [94] and Bernad [95]). Vortex shedding describes the observed effect of eddy regions formed behind a solid object in a flow, which are seen to grow behind the object before propagating downstream to be replaced by another eddy. The eddies are initially formed by instability in the incoming flow, which triggers the generation of a low pressure region at one side of the object and generates the first vortex. This in turn causes the flow around the object to be distorted, and thus generates the next vortex. In a constant flow, eddies are then formed in a regular sequence by one side of the object and then the other, generating a pattern of vortices moving downstream behind the object, as illustrated in Figure 2-18 and Figure 2-19. In Figure 2-19, point A can be observed to move downstream on the edge of the vortex region. Point S in images (e) and (f) indicates the formation of a new vortex, when the streamline seen attached to the cylinder in (d) separates from the object and forms a new eddy.

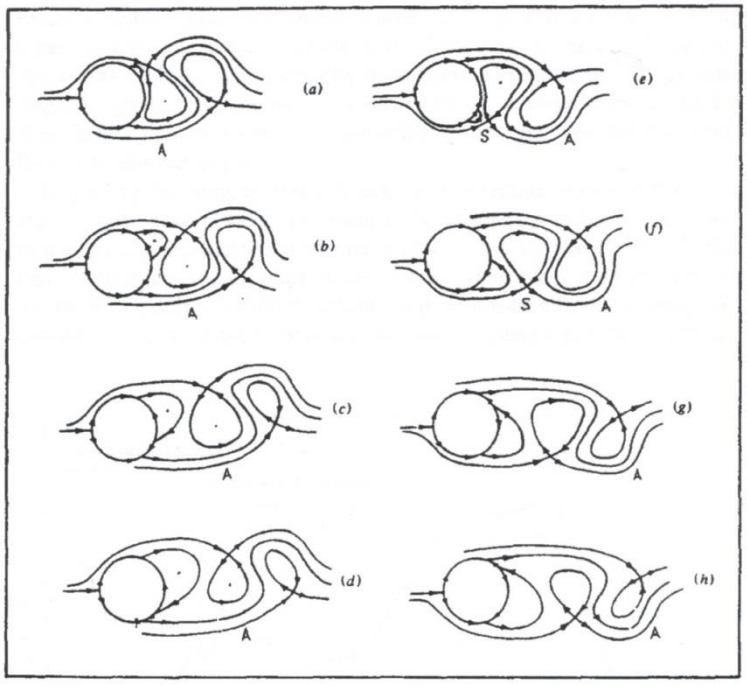

Figure 2-19 – Streamline image of von Karman vortex street generation (from[96])

The conditions under which shedding occurs are governed by the properties of the fluid and the object, and can be described by a range of *Re* values under which vortex shedding is observed. *Re* values between 10^2 and 10^5 are required in order for shedding to occur. The frequency of shedding can be calculated using another value, the Strouhal number, *St*. This value is a ratio of two sets of inertial forces; those due to the unsteadiness in the flow and those due to the flow velocity. The Strouhal number is described by the following equation:

$$St = \frac{\omega l}{\mathrm{v}}$$

St can be calculated from its relationship with *Re*, which is known from analytical results [96], which allows the prediction of vortex shedding frequency ω for a flow of known velocity past an object of known diameter.

Vorticity

Vorticity ($\vec{\omega}$) is a calculated property of a velocity field which describes its tendency to rotate, and for a velocity field u is calculated as the curl (∇) of the field, as follows:

$$\vec{\omega} = \nabla \vec{u}$$

The concept of vorticity can be understood by imagining a small two-dimensional portion of fluid within a flow, and considering its motion in terms of velocity and shear effects. If the portion of fluid is subject to the same shear effects throughout its area, then vorticity is zero, whereas if different shear effects can be observed across the area of the portion, then vorticity exists. In Figure 2-20 below, three examples of flow patterns are illustrated, indicating no relative velocity across the imagined element in case 1, and positive relative velocity and thus vorticity in cases 2 and 3.

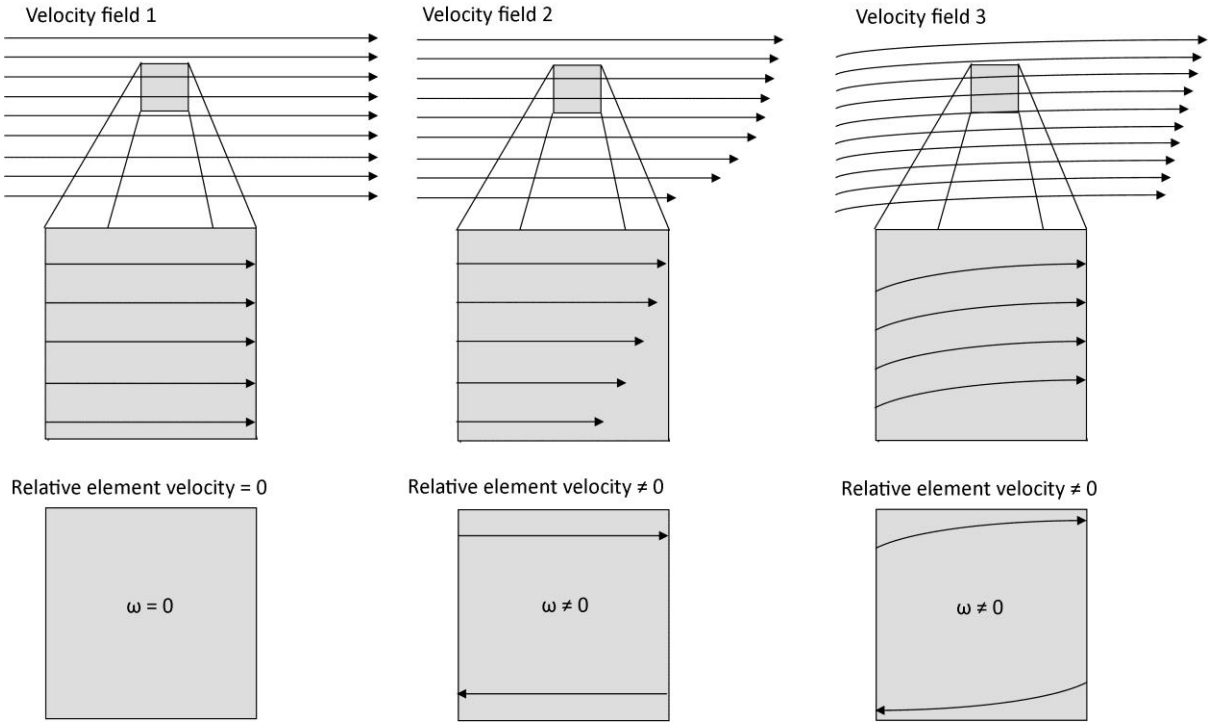

Figure 2-20 – Three sample velocity fields and corresponding vorticity.

Vorticity is expressed in units of 1/s. The visualisation of vorticity allows fluid elements with high levels of rotation to be highlighted, for example eddies generated by structures in a flow. This is useful as these eddies may not be highlighted in simple velocity fields, but may be important energetic structures which help explain the properties of a flow.

Vortex identification using the Q-criterion

It has become common in recent work [97] to use criterion methods in addition to vorticity to illustrate the location of vortices in a flow, due to the potential difficulties in differentiating between a vortex caused by swirling motion and one generated by pure shear when considering only vorticity. One such criterion is the *Q*-criterion, as hypothesised by Hunt *et al* [98]. For the purposes of data generated during this study, *Q*-criterion is of limited use due to the 2D nature of the recorded flow data, however its use in the literature described later in this section merits its inclusion. A fuller description of the *Q*-criterion, along with other criterion, can be found in the thesis of Holmén [99].

The use of the criterion involves the calculation of the second invariant of the curl (∇u) of the velocity u across the flow field, the value of which is defined as Q. This value is positive in the case where the vorticity magnitude is greater than the magnitude of strain on a fluid element. If, for a given point, $Q > 0$ and the pressure is lower than the ambient pressure, then the criterion is said to be satisfied. A plot can then be generated of points in the 3D flow field with positive values of Q, in order to view the vortices identified by the method.

2.5.2 – Devices

Lift and drag forces

Any aerofoil device in a moving flow experiences both lift and drag forces. One factor which determines whether an aerofoil primarily experiences lift or drag is the angle of attack (AoA or α). α is defined as the angle created between the centreline of the aerofoil profile (known as the blade chord) and the direction of the incoming flow. In the context of a rotating turbine, the incoming flow velocity is known as the resultant velocity, and is made up of the velocities of the fluid flow and the turbine rotation, as illustrated in Figure 2-21.

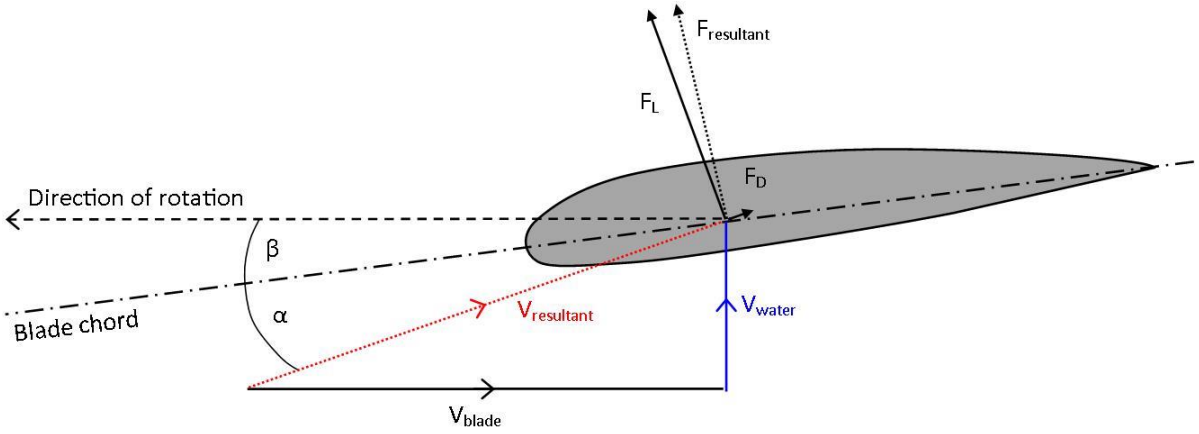

Figure 2-21 – Turbine blade velocity and force diagram (viewed from above, flow from bottom to top).

For a given rotation rate, the tip of a turbine blade has a greater speed than the root. Due to this, the value of α can be expected to be lower at the blade tip than at the root. In order to counteract this effect and ensure a constant angle of attack over the blade length, turbine blades are often twisted, thus reducing the pitch angle β towards the tip and resulting in a constant α value. Two aerofoil sections from a turbine blade are illustrated in Figure 2-22, showing the additional twist applied at the blade tip (right).

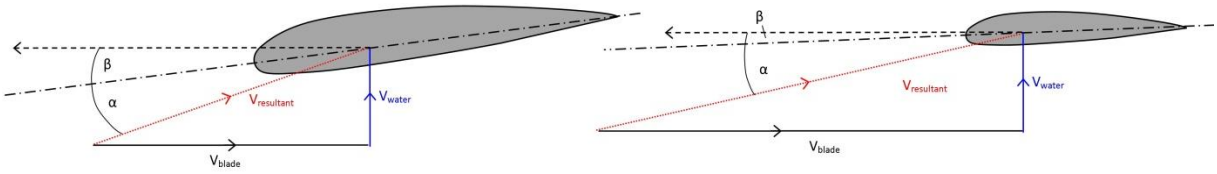

Figure 2-22 – Blade twist to give constant α: Root (l) and tip (r).

The horizontal axis turbine principle, in both its wind and tidal turbine designs, extracts power from the combination of lift and drag forces generated by the blade. The greatest drag forces are generated at low (α < -5°) and high (α > 20°) angles, though at all α angles above around -5°, lift forces outweigh drag forces A comparison of the forces experienced by an example aerofoil at AoA values between -10° and 30° shown in Figure 2-23.

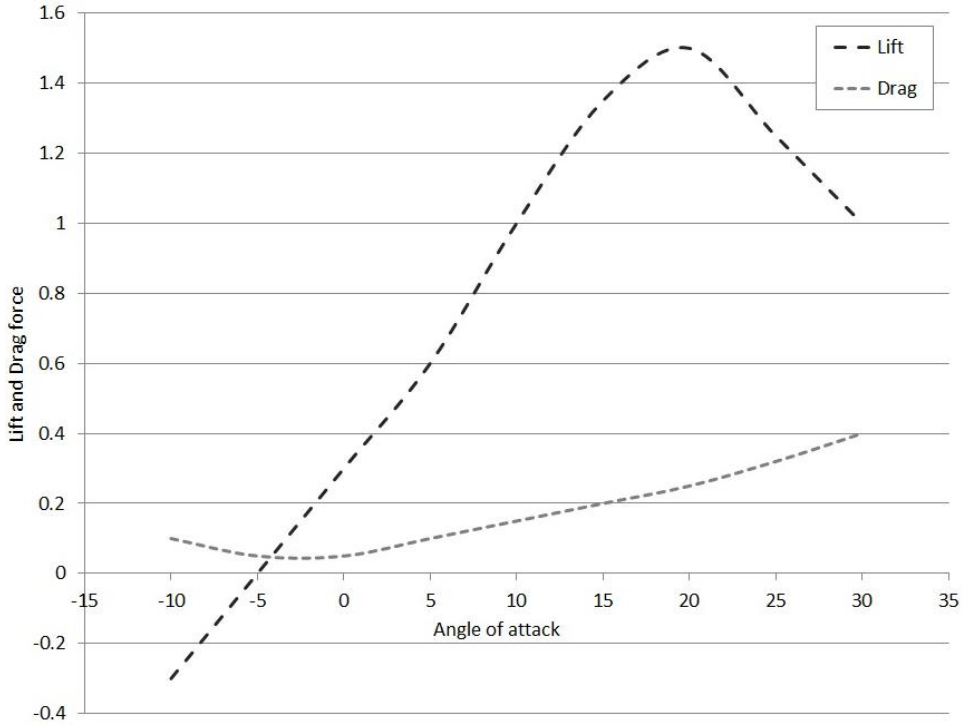

Figure 2-23 - Comparison of lift and drag forces for AoA between -10° and 30°.

Alternative designs of turbine utilise lift and drag forces to alternative effect. Vertical axis wind turbines are relatively common, and fall into two categories: Darreius type designs primarily use lift force to generate rotation, whereas Savonius types generate power primarily through the use of drag forces.

Vertical axis tidal turbine designs of both types have also been proposed [100, 101] (a range of proposed turbine designs will be discussed in detail shortly). However, this type of turbine has

limitations, and though Darreius-type vertical axis wind turbines (VAWTs) have found favour in certain environments, they are sometimes less efficient than horizontal axis devices given the same conditions. This is primarily due to the fact that not all of the blade area is able to face the oncoming wind at the same time. Sagrillo [102] found that Savonius type VAWTs have efficiencies of around 10%, whereas a Darreius design can achieve around 30%, compared to HAWT efficiencies of around 35%. The inefficiency of the Savonius type stems from its use of drag forces to generate power, which requires a large shaped blade design. Considering a traditional two-blade Savonius turbine, when one blade is not facing the oncoming wind it must be pushed against the flow, which requires the use of a portion of the energy generated by the second blade. Since the blades are large, this energy requirement is significant and the resulting output energy of the turbine is consequently diminished.

Both Savonius and Darreius type VAWTs have a high starting torque threshold, so are often unable to self-start, meaning that if wind speed falls below that at which the device can sustain rotation, it will stop. In order to avoid this problem and to allow turbines to operate in a range of conditions, VAWTs generally use a motor system to begin rotation as necessary. Modern devices achieve this easily and the lack of self-starting is not generally considered problematic, but it should be noted that the use of a motorised starting system does reduce the net output of a turbine, as well as increasing cost and complexity.

Device designs

As a consequence of the issues identified previously, it appears that the majority of relatively advanced tidal energy device designs are horizontal axis machines. In 2009, King and Tryfonas conducted a comprehensive review of the position of the industry at the time [25]. The work identified all tidal energy device designs available at the time, and provided comprehensive details of the development stage of all such devices, based on information from the manufacturers or designers. The study found over 20 device designs, which were categorised into five groups:

- Single open-rotor horizontal axis turbines (HATs)
- Ducted HATs
- Multiple open-rotor HATs
- Vertical axis turbines
- Transverse axis devices

At the time of publication, the authors identified only eight devices which appeared to have successfully developed prototype designs and undergone some level of scale model testing. Of these, two were single rotor HATs (developed by Andritz Hydro Hammerfest and Tidal Generation Ltd.), two were ducted HATs (OpenHydro and Atlantis Resources Corporation), two multiple open-rotor HATs (Marine Current Turbines and ScotRenewables) and two VATs (Blue Energy and GCK Technologies). There were no transverse axis devices reported to have reached this level of development. The eight devices identified are illustrated in Figure 2-24. The authors highlighted that at the time, development of tidal stream turbines was in its early stages, suggesting that the equivalent wind turbine industry position was even earlier than others had suggested, likening the 2009 tidal energy industry to the wind industry of the 1970s.

It should be noted that since the sale of Tidal Generation Ltd. to Alstom Power in 2013, this device will subsequently be referred to as being manufactured by Alstom Renewable Power.

Figure 2-24 – Eight tidal energy devices successfully developed to prototype stage, as identified in 2009 by [25] (Top l-r: Andritz Hydro Hammerfest, Alstom Renewable Power, Atlantis Resource Corp., OpenHydro. Bottom l-r: Marine Current Turbines, ScotRenewables, Blue Energy, GCK Technologies).

Marine Current Turbines (commonly known as MCT) was established in 1999, and was one of the earliest organisations to develop a tidal stream energy device. As illustrated on the development timeline shown in Chapter 1 (Figure 1-16), MCT installed the world's first offshore tidal stream device in 2003. Prior to this, in 2002, MCT employee Peter Fraenkel published *Power from marine currents* [103] in the Institute of Mechanical Engineering Journal of Power and Energy. The paper aimed to describe the research and development being undertaken across the tidal stream industry at the time. The paper identifies a number of broad advantages to tidal stream power, citing the predictability of tides as a major advantage over many other forms of renewable energy, but noting that the spring to neap cycle, as discussed in Section 1.3, must be carefully considered, since the output from a tidal energy device at neap tides will be significantly lower than at spring tides. Work presented at the World Renewable Energy Congress 2004 [104] highlights this, finding spring tides with up to 2.5 times greater mean flow velocity than neap tides at Cape Wrath (a location highlighted as a potential tidal turbine installation site the north-western tip of Scotland). This was calculated by the author of the work to give a potential tidal turbine output during the neap period of less than 10% of the potential spring tide aggregate outputs.

Fraenkel's work goes on to discuss types of machine, highlighting the same range of device types as King *et al* [25], and highlighting that lift-type machines offer greater energy potential than drag-type machines, due to the inefficiency of the latter. It should be noted that none of the devices highlighted by King and Tryfonas as having reached prototype stage are drag-type designs. The use of ducts in order to generate a venturi effect and avoid the limitations of the Betz limit is also discussed, but as highlighted in [103], this theory is difficult to justify in reality, since no devices are reported to be limited by this limit. As noted in the development of ducted wind turbines, the use of

ducting increases blade velocity [84]. In the case of a tidal turbine this increased velocity could lead to the onset of cavitation. Cavitation occurs when fluid pressure at a point within a flow falls below the vapour pressure of the fluid. This causes the formation of gas bubbles, and can occur due to high flow speed in a region where the fluid is in contact with a solid boundary. The pressure within the bubbles generated is insufficient to sustain them within the high pressure of the surrounding fluid and they rapidly collapse, causing a shockwave to be generated, which can cause damage to the surface of solid objects. Damage due to the shockwave generated when cavitation bubbles implode is a significant problem in areas such as marine propulsion [105], and has the potential to cause damage to the surface of a turbine blade. The increased fluid velocities generated in ducted turbine designs makes this issue much more likely to occur, and is a major reason why ducted tidal energy devices have not been pursued by the majority of developers. An image of cavitation occurring on a model tidal turbine blade is illustrated in Figure 2-25, [106].

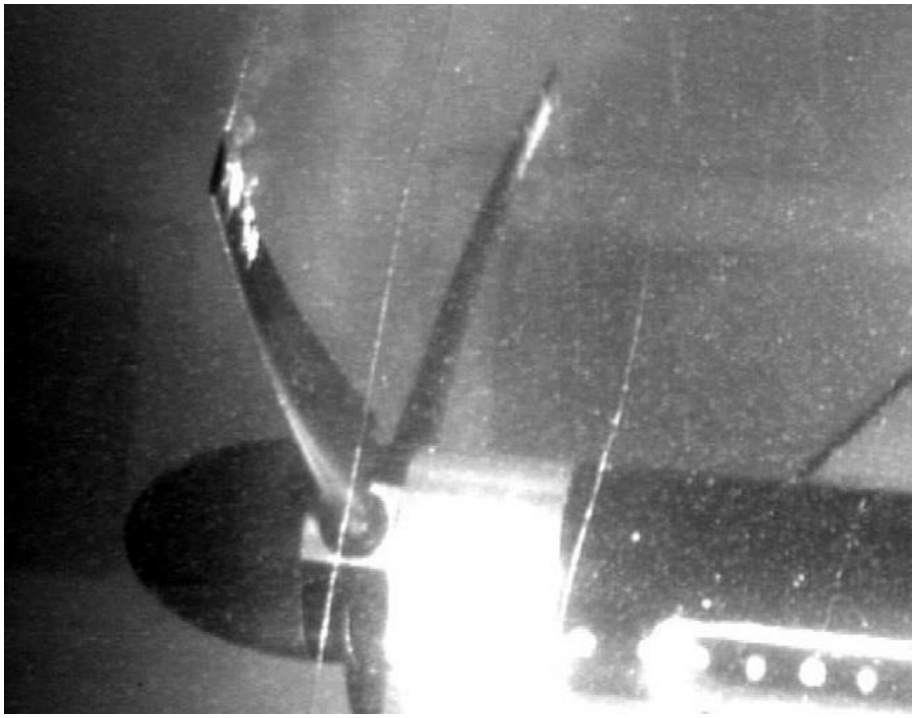

Figure 2-25 – Example of cavitation effect on a model tidal turbine blade (from [106]).

Having focussed on lift-type machines, Fraenkel discusses two main types, namely HATs and VATs. Specifically, these are defined as an axial horizontal axis turbine, broadly similar in appearance to a horizontal-axis wind turbine, and a Darrieus type vertical axis turbine, respectively. Again and in agreement with [107], numerous problems with VATs are identified, including lack of self-starting; difficulty of stopping in an emergency; and reliance on high quality blade surfaces. The work suggests that the HAT design is likely to represent the future shape of a tidal turbine. Further work carried out by [108] also highlights the same disadvantages of VAT designs.

Since King and Tryfonas' work in 2009, of the eight identified devices, development has continued in six cases. Development of the Blue Energy and GCK vertical axis devices stopped after initial prototype testing proved unsuccessful, though no information on the precise reasons is available. During the intervening years, development of the remaining devices has continued, with the testing of larger scale models and full-scale prototypes. The ducted device originally proposed by Atlantis

Resource Corporation was dropped in favour of a three-blade HAT known as the AK-100, which has subsequently been tested to full scale stage. To date, the remaining six devices have now all undergone full-scale testing and are described by their manufacturers as commercially ready. Below is a brief synopsis of the current commercial version of each device.

	Andritz Hydro Hammerfest [109]	*Alstom Renewable Power [110]*	*Atlantis Resource Corp. [111]*	*OpenHydro [112]*	*Marine Current Turbines [113]*	*Scot-renewables [114]*
Device name	HS1000	DeepGen	AK-1000	Open Centre	SeaGen	SR2000
Type	Single open rotor HAT	Single open rotor HAT	Single open rotor HAT	Ducted HAT	Twin open rotor HAT	Twin open rotor HAT
Blade diameter	21m	18m	18m	16m	2 x 17.5m	2 x 16m
Height	32.5m	28m	22.5m	22m	40m	Surface floating
Rated power	1MW	1MW	1MW	2MW	1.2MW	2MW
Rated Tidal speed	2.7 m/s	2.7 m/s	2.65 m/s	2.5 m/s	2.4 m/s	3 m/s
TSR @ rated	4.2	5.2	2.6	Unknown	4.8	Unknown
Support Structure	Angled post (piled foundations)	Vertical post (piled foundations)	Vertical post (piled foundations)	Support frame (piled foundations)	Vertical post (piled foundation)	Catenary moored (concrete anchors)
Comments	Candidate for 10 device installation in Sound of Islay array	Candidate for 10 device installation in Sound of Islay array	Six device installation proposed in Pentland Firth array	Four device installation proposed in Paimpol Brehat array	Installed in Strangford Lough, Ireland since 2008	250kW prototype in ongoing testing at EMEC

Table 2-1 – Summary of six leading tidal stream turbine designs

Blade layout, pitch and yaw control

As can be seen in Figure 2-24 (though the previously-discussed change to Atlantis Resource Corporations' device design should be noted), the devices manufactured by Hammerfest Strom, Alstom Tidal and Atlantis all use a single three-blade rotor. Marine Current Turbines and ScotRenewables both incorporate a pair of twin-blade rotors, and the OpenHydro device uses a unique large diameter multi-blade turbine.

The Hammerfest and Alstom devices use variable pitch rotors, meaning that the blades are able to rotate about their central axis in order to adjust angle of attack (AoA), and the body of the device is designed to rotate to face opposing tidal flows. This process of device rotation is known as yaw control, and is often powered by a small electric thruster mounted on the rear of the device body, as illustrated in Figure 1-17. A similar yaw control system is used by the Atlantis device, but the blade pitch appears to be fixed in this case.

The ScotRenewables SR2000 device rotates about its mounting position to face the oncoming tide, and uses fixed pitch rotors. The Marine Current Turbines device does not rotate to face the oncoming tide, but instead uses pitch control to adjust its blade angle to generate energy from the tidal ebb and flow. The OpenHydro Open Centre Turbine is a fixed device, and is not believed to incorporate any pitch or yaw control mechanism. Operation in tidal flow from opposing directions is achieved by the counter-rotation of the turbine.

Array installation

Each of the devices described above are designed with the eventual intention of installation in arrays of multiple devices. To date, no installations of multiple devices have been completed, though planning permission has been granted for two arrays in Scotland (Scottish Power Renewables plans a 10MW array in the Sound of Islay [38], and MeyGen an initially 9MW array in the Pentland Firth [37] and one in France (EdF's 8MW Paimpol-Brehat array [112]).

Array layout has been considered by many, including [103], [115] and [87]. Unlike wind turbine planning where, though a primary wind direction is known, devices must be able to operate in flow from any direction, the direction of flow in a tidal stream is known and fixed with little variation between ebb and flow directions (though variation does occur in some cases, due to differences in bathymetry caused by inlets and headlands, for example). Due to this, it has been proposed that tidal turbines can be spaced relatively close together in the cross-stream direction.

A range of separation distances between devices are proposed in literature, with estimates for required streamwise separation ranging from 2 rotor diameters into the hundreds of rotor diameters. Planned device spacing proposed for the MeyGen array is believed to be in the region of 7 rotor diameters in the streamwise direction and 3 rotor diameters cross-stream, whereas initial proposals for the layout of the ScottishPower Renewables Sound of Islay array suggest streamwise spacing of between 15 and 30rotor diameters.

Support structure

Due to focus on the development of the turbine itself, Tidal energy device support structures are an area in which only limited resources have been directed to date. The purpose of the support structure is to place the device in the area of flow it is designed to operate in, but the structure itself also has an impact on the device performance. The geometry and location of the support structure relative to the position of the device is expected to have an impact on the performance of the device, since the wake developed by the support structure will influence the velocity field around the turbine [52]. The performance of downstream devices is also expected to be heavily influenced by the wake behind an upstream device and support structure.

Of the six devices highlighted in the previous section, five use solid support structures fixed to the seabed. Only the ScotRenewables device does not use this method of fixing, instead using a moored floating body unit with turbines mounted below. Each method of fixing the turbine will have a different effect on the combined wake of the device and support structure. Four major methods of seabed mounting are highlighted in Figure 2-26.

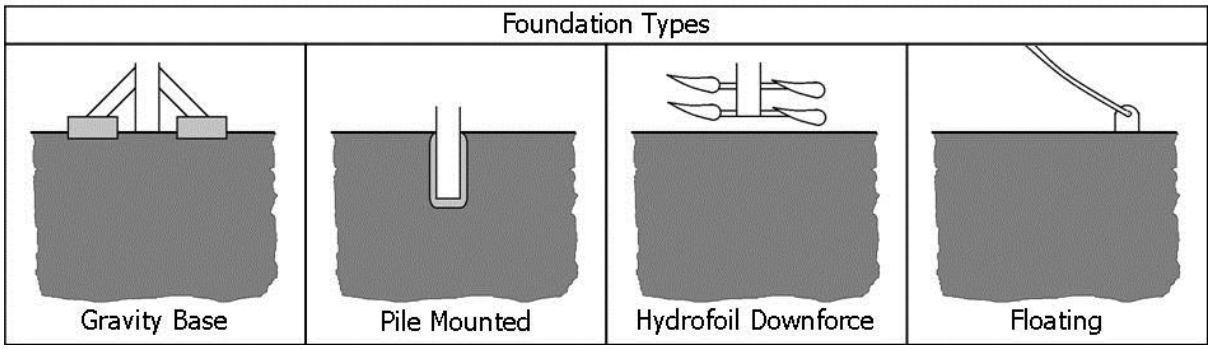

Figure 2-26 – Major foundation types proposed for use with tidal turbines (from [116]).

None of the six devices discussed propose the use of a hydrofoil downforce foundation system, indeed no currently-proposed tidal energy extraction concept proposes this design, though it has been proposed in the past, hence its inclusion.

The understanding of the wake impact of the support structure is one of the major aspects of this work, and is discussed at length in later chapters.

2.6 – Wind turbine literature

Tidal turbines share operating principles with wind turbines, so the similarities and differences between the two appeared to be an obvious starting point. It is important to note that there are some specific design requirements of tidal turbines which do not exist in the field of wind turbines. Highlighted examples [107] include the effect of waves on the water surface, leading to a continuously varying boundary layer profile [117], and the generation of a turbulent wake in the region behind a tidal turbine which can lead to the redistribution of sediment and the generation of a scour hole behind the device support structure. However, the two device types still share many similarities, and wind turbine literature is a useful starting point in the analysis of tidal turbines.

Wind turbine comparison

The differences between design drivers for wind and tidal turbines was studied by A. Winter in 2011 [107]. It has been suggested that the development of tidal stream turbine industry is around 10 - 15 years behind that of the wind turbine (though others have suggested a much longer time lag between the two, of up to 40 years [25]), so this work aimed to ascertain to what degree the volume of research undertaken in the development of wind turbines could be applied to advancement of tidal turbine technology, in order to advance the development curve more quickly than would otherwise be possible.

Winter's work concludes that although initially similar, there are numerous differences between the two situations. There are major differences between the fluid conditions in which the devices

operate such as density and viscosity, and operating conditions such as fluid velocity. Seawater at 20°C has a viscosity approximately sixty times more viscous than air at 20°C, and approximately 860 times greater density [118]. The fluid velocity in a likely installation of each device type is also different, since favourable sites for wind turbine installation generally exhibit wind speeds of around 12.5m/s, whereas potential tidal turbine installation sites have flow velocity in the region of 2.5m/s (data sources below). These differences mean that although tidal turbines and wind turbines appear similar, their operating conditions are very different, as illustrated in Table 2-2:

Typical fluid / case values:	*Viscosity (Ns/m^2)*	*Density (kg/m^3)*	*Velocity (m/s)*	*Reynolds Number*
Wind Turbine [118]	1.82×10^{-5}	1.19	12.5	4.1×10^{7}
Tidal Turbine [92]	1.077×10^{-3}	1024.8	2.5	2.5×10^{9}

Table 2-2 – Fluid properties in the operating conditions of wind and tidal turbines (Blade diameter characteristic length used for Reynolds number calculation: 50m wind; 18m tidal)

Vermeer *et al* [57] conducted a detailed study incorporating both computational and experimental modelling of the wakes generated by wind turbines. Despite the issues highlighted in [107], which pointed out that wind turbine research is not necessarily universally applicable to tidal turbines, the work does provide some relevant discussion on the modelling of wake structures. Firstly, a useful definition of near and far wakes, which could be applied to tidal turbines, is given as follows:

- Near wake – within one rotor diameter downstream of the blades
- Far wake – beyond one rotor diameter downstream of the blades

This definition of a near wake region extending around 1 device diameter downstream has also been adopted by those conducting computational and experimental modelling of tidal turbines, such as Bahaj and Myers [52]. This work is discussed in Section 2.8.

Vermeer *et al* [57] also studied the wakes behind wind turbines, and conclude that Reynolds-Averaged Navier Stokes (RANS) equation modelling is the most appropriate and accurate method for use the near stream wake area, however this method can be slow and computationally intensive. An alternative modelling system called UPMWAKE is also described, as was studied in more detail by Crespo *et al* [119]. The system is a mathematical model developed at the Universidad Politecnica de Madrid (UPM), designed to be integrated into computational models of wind turbine arrays in order to accurately represent the energy losses in downstream devices due to the effect of those upstream. The method may offer a more computationally-efficient procedure than the use of full RANS modelling, and [119] aimed to validate the UPM model using experimental data. Experimental results from 360mm diameter scale models (known as “TNO”) and full scale testing at the Nibe test centre (“MILLY”) were compared to results using both standard three-dimensional and simplified one-dimensional (“Linear”) versions the UPMWAKE method. The experimental and UPM comparison for a wind turbine with a Tip Speed Ratio of 8.5 is illustrated in Figure 2-27.

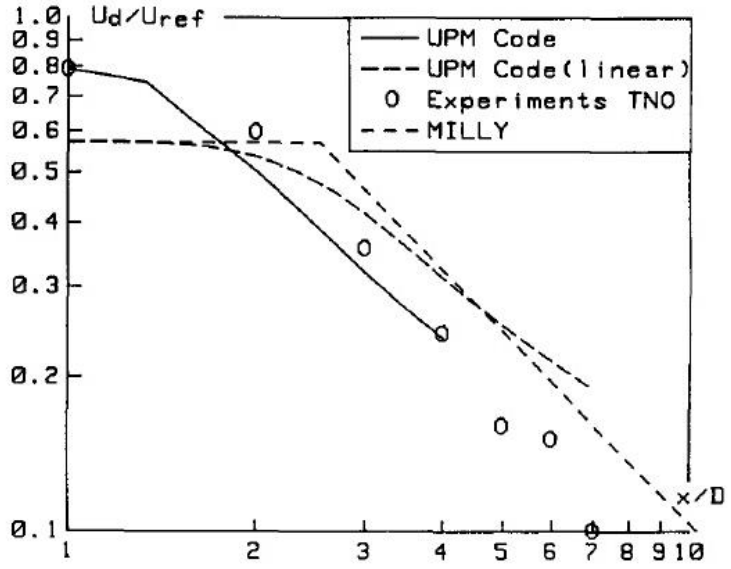

Figure 2-27 – Comparison of velocity deficit (Ud/Uref) vs. downstream position (x/D) for the UPM model and two experimental results at TSR=8.5 (from [119]).

The figure illustrates a reasonable correlation between the UPM method and experimental results, and also provides some useful information on the velocity deficit behind wind turbines. Experimental results in this case predict 90% recovery of reference velocity at between 7 and 10 rotor diameters downstream, whereas projections of the UPM model would suggest 90% recovery would not occur until well beyond this figure, possibly up to 20D downstream. The work of Crespo *et al* is therefore useful as a reminder that computational prediction of velocity recovery is not always accurate, and that a wide variation in experimental results of velocity recovery also exists. Though this work relates to wind energy, there is no reason not to expect it to hold true for tidal turbine data.

2.7 – Computational modelling of tidal turbines

This area of the literature review aimed to investigate existing work on the computational modelling of tidal turbines, focussing particularly on that involving the modelling of wake patterns. While it is not proposed to carry out any computational modelling during the present project, and the volume of computational literature relating to tidal turbines is limited, there exists a large volume of computational work on the flow around submerged cylinders, and results from such work can provide useful reference as well as potential validation of experimental results.

Computational Fluid Dynamics

The majority of computational work studied during this literature review involves the use of Computational Fluid Dynamics (CFD). CFD modelling can be conducted in one of three discrete methods, which vary in computational cost and solver accuracy, though various subscales of complexity exist within each method. The most computationally intensive method is Direct Numerical Simulation (DNS) calculation, in which the full equations of fluid motion are solved for every computational element, at all scales from the largest to the smallest eddies. This type of analysis has only recently become possible through the advent of high-powered multi core

processors, and remains the least common method. Conversely, the least computationally intensive method of CFD calculation is the Reynolds-averaged Navier Stokes (RANS) method, which reduces the number of equations to be solved at each timestep by time-averaging the conservation of mass, conservation of momentum and conservation of energy equations rather than solving them directly as in DNS. In between these methods lies Large Eddy Simulation, in which the DNS method is applied at large scales, and the RANS method at smaller scales. This is still a highly intensive method, but can now be achieved at University level.

CFD modelling: Tidal stream turbines

Of the limited number of computational modelling studies relating to tidal turbine wakes, one of the most relevant was carried out by Bryden *et al* [120]. After highlighting the advantages of tidal turbines over other renewable energy technologies the work identifies that "there has been no detailed study of optimal layouts for tidal turbine farms". CFD modelling was carried out using 3D-NS, an in-house software package using a Navier-Stokes solver and k-epsilon turbulence closure model. The tidal energy devices were assumed to be simple turbines of 20m diameter, in 120m water depth and 4m/s mean spring average tidal flow. Turbines were not modelled in full detail and were instead represented as static semi-permeable membranes incorporating pressure jumps (analogous to experimental actuator disks, which will be introduced in Section 2.8), described by the following equation:

$$\Delta P = C_t \frac{1}{2} \rho u^2$$

Following modelling of a single turbine in a flow field, a second turbine was added downstream. Firstly this was done at a distance of 5 turbine diameters (i.e. 100m) downstream, and secondly at 8 diameters (160m) downstream. It was found that the downstream turbine was able to produce approximately the same power output in each case, but in the initial (5 diameter separation) case the downstream turbine did experience a higher turbulent intensity. It was found that the first turbine achieved a velocity deficit of 0.31 compared to free stream conditions, and the second achieved approximately 0.24 in both cases. Results for an upstream turbine and downstream turbines in two locations as described above are given in Figure 2-28. It should be noted that results are for a downstream turbine at 5*D* or 8*D*, but do not illustrate a simultaneous case with turbines in both locations.

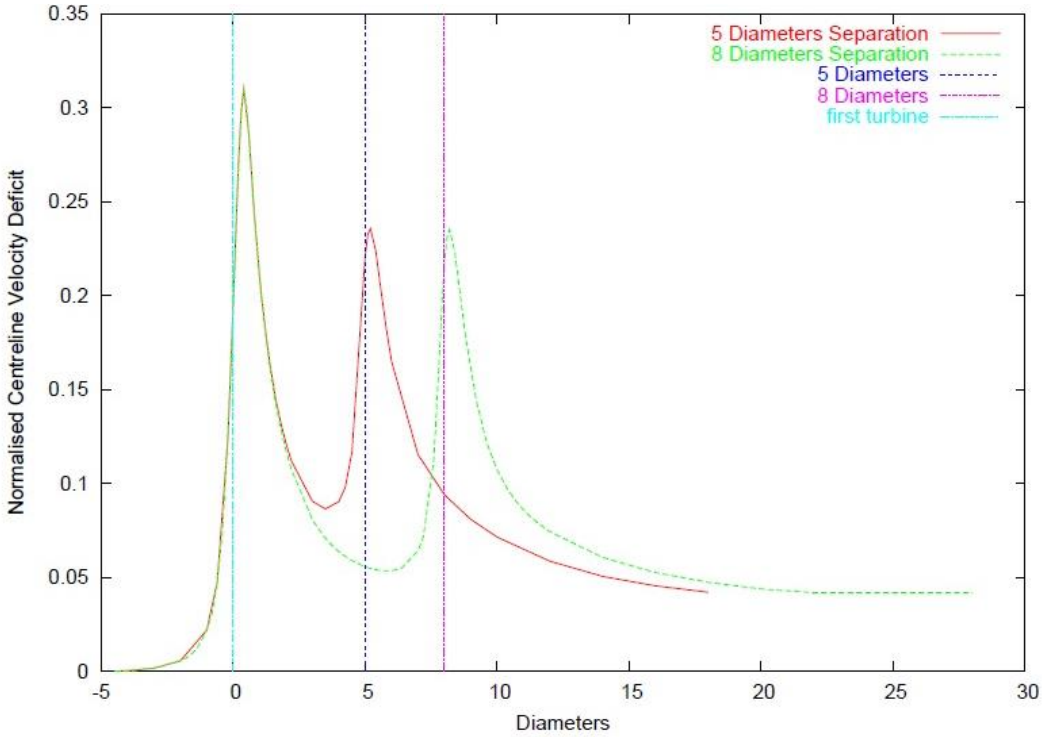

Figure 2-28 – Velocity deficit behind an upstream turbine and downstream turbines in two locations (from [120]).

These results can be compared to those illustrated in Figure 2-27, which showed 90% velocity recovery within 7 to 10*D* predicted by experimental models, and computationally-predicted results illustrating recovery within 20*D*. Data in this work illustrates that in the case of a tidal turbine, 90% velocity recovery is achieved by around 10*D*. Figure 2-28 illustrates that the presence of an upstream turbine does not appear to affect this figure, and recovery occurs at around the same position. However, it should be noted that these are computational results and were not explicitly validated during the study, hence the comparison of these results with experimental data in Section 2.6 is crucial.

Kang *et al* [121] carried out a numerical simulation using the LES method, based on the Gen4 turbine proposed by Verdant Power for the Roosevelt Island Tidal Energy project in New York City [122]. Two separate studies were conducted: The first considered only the turbine blades, and the second included the full turbine and support structure system.

In the first case, simulations of the 5m diameter turbine were conducted at real scale, within a domain of length 45m, width 40m and depth 40m, with the turbine blades positioned at the three-dimensional centre. The turbine rotational speed and flow speed were 3.61 rad/s and 2m/s respectively, giving a tip speed ratio of λ = 4.51. As discussed previously, the use of LES requires a turbulence closure model to be applied to the smaller flow scales. The Smagorinsky method [123] was applied in this case. Results were validated by comparison to flow data recorded using ADCP, as introduced in Section 2.3, at the proposed installation site. Flow velocity results from the modelled and recorded cases without the turbine in place were found to exhibit agreement within 4% for the final mesh iteration, which the authors deemed a satisfactory variation given the differences in ambient turbulence and site-specific conditions (which applied to the measured data but not the computational results) between the two cases.

In the second case, the turbine and support structure were installed in a computational domain of length 45m and width 40m, as before, but a height of only 9.15m was used. As before, a rotational speed of 3.61 rad/s, flow speed of 2m/s and TSR of 4.51 were used.

By comparing the results of the two simulations carried out by Kang *et al*, it can be noted that the downstream wake behind the case with only turbine blades recovers to free stream conditions more quickly than that with the support structure in place, for otherwise identical conditions. However, as noted by the authors, the pressure field around the blades is almost identical, suggesting that blade power is likely to be accurately predicted by the blade-only model. This hypothesis was confirmed by the measurement of power coefficients in both cases, which showed strong agreement of around 5% maximum difference. It is important to note at this stage, that the device in question is a "downstream" device, meaning that its support structure is located upstream of the blades. Images of near-region wake effects for the two cases are illustrated in Figure 2-29.

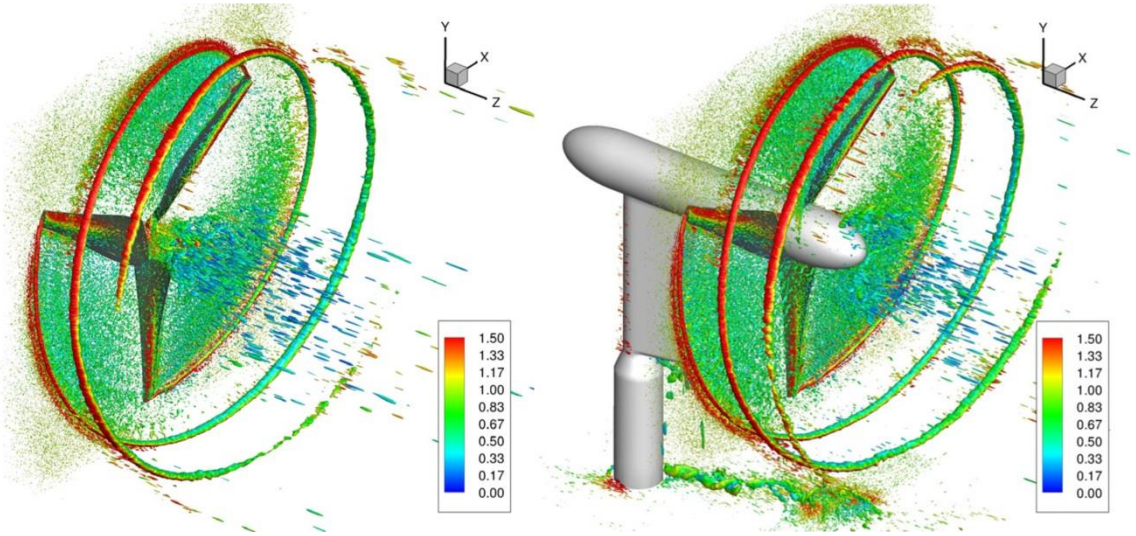

Figure 2-29 - Blade tip vortices generated by Verdant Power Gen4 turbine with blades only (l) and full turbine (r). Illustrated by Q-criterion and velocity magnitude nondimensionalised by u_∞ = 2m/s (from [121]).

Not shown in the above figures but nonetheless of great interest to the present work is the complex blade region wake found by Kang *et al*. The work revealed the predicted blade-tip vortex structures rotating in the direction of the blade rotation, but in the complete turbine case also revealed two additional structures generated by blade rotation. A counter-rotating (with respect to blade rotation) inner region of flow was observed inside the region bounded by the spiral blade-tip vortices. At the centre of this region was found a third region of approximately the diameter of the turbine hub, this time again rotating in the direction of blade rotation. The work hypothesised that the use of LES allowed these regions to be discovered for the first time.

Work carried out at the US National Wind Technology Center [124] studied the wake propagation and power production of an array of tidal turbines. This work again uses LES simulations, and differed from the previously-discussed work by conducting an initial simulation to generate an incoming turbulent flow profile prior to the main experiments (Kang *et al* assumed a non-turbulent inlet profile). The Smagorinsky model was again used to close the turbulent equations in the case of scales below those calculated directly.

Turbines of blade diameter 20m was used in this study, and were represented by actuator lines, as proposed by Sorensen and Shen [125]. The turbines were arranged in ten layout configurations within a domain of 240m length and 80m width. The turbines were arranged into two rows, with a non-staggered configuration requiring upstream and downstream rows of two turbines each, and a staggered configuration requiring an upstream row of two turbines and downstream row of three turbines. Various configurations of spacing and rotational direction were also studied, resulting in ten separate tests. A velocity plot from a non-staggered configuration with a free-stream velocity of 1.9m/s is illustrated in Figure 2-30. The separation between upstream and downstream devices is 5*D* (100m).

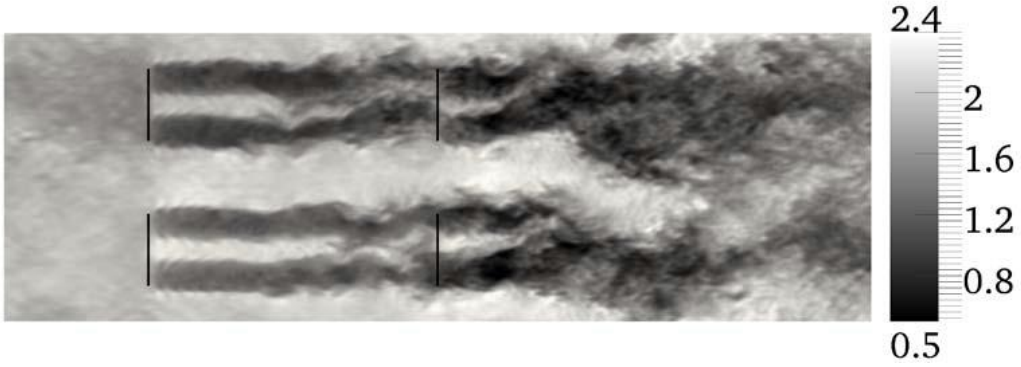

Figure 2-30 - Instantaneous streamwise velocity plot for two-row four turbine configuration (all turbines rotating clockwise) viewed from above. Black lines indicate turbine locations, scale in m/s, flow from left to right. From [124].

A particular conclusion of this work which has not been highlighted in previous studies is the asymmetry of the turbine wake in the cross-stream direction. In all ten configurations, the wake behind each device was found to propagate downstream asymmetrically. In conclusion, the authors attribute this effect to the incoming turbulent profile. Device performance in a range of array layouts was also considered, with the conclusions that staggering rows of devices improved downstream device performance by around 20%, and that rotating a downstream device in the opposite direction to an upstream device led to a slight (~1%) performance improvement compared to rotating both in the same direction. However, the authors do acknowledge that the results also indicate that the domain size was insufficient to represent the largest scale structures formed during the tests, and that further validation work is required.

Computational array modelling

As discussed in Section 1.6, Electricite de France (EdF) announced during July 2008 their intention to install the world's first tidal energy array at Paimpol-Brehat in Brittany, France during 2011 or 2012 [112]. Members of EdF's technical team published work [126] aiming to describe the methodology and software methods used to analyse the potential site. The work introduces EdF's own Telemac-2D software and explains how this, in combination with ADCP monitoring, was used to calculate the theoretical output from the site. The Telemac-2D software is part of the Telemac package, and works by solving finite element shallow water equations, as described in detail by Hervouet [127]. The primary aim of the work conducted using Telemac-2D was to calculate the potential resource at the proposed site, which given the required scale necessitated the use of a high level modelling

package. Telemac-2D is a very large-scale modelling package in comparison to those used in the work discussed earlier in this section and proposed in this thesis, and is incapable of modelling the individual wake effects behind a single turbine. The maximum (i.e. smallest) resolution used in this project was 50m.

The authors go on to describe a comparison of Telemac-2D with three other simplified methods of resource calculation, the results of which are reported to correlate with the Telemac-2D results reasonably well, being within 15% of Telemac-2D predictions. The use of these large-scale methods for resource calculation is acknowledged as ignoring the important effects of device wake generation, which it is noted will have an effect on device output. The work highlights a gap in knowledge of turbine-scale wake effects, even by developers working on current installations of tidal energy arrays. The work acknowledges this and states that information on wake effects would be useful, particularly as this would allow more detailed comparison with at-sea measurements. The array to be installed in Paimpol-Brehat will use device spacing of 10*D* in the streamwise direction and 2.5*D* in the cross-stream direction, as suggested in work conducted by consultants Black and Veatch in 2004. However, at present it has not been possible to acquire a copy of this work in order to understand the methodology used.

A recent study by Mycek *et al* [62] describes computational modelling carried out as part of a largely experimental study, which will be described further in Section 2.8. The computational aspect of this study used software which is currently under development, and uses the Lagrangian vortex particle method. This technique is an alternative to the RANS and LES CFD techniques discussed previously, and does not use a grid to subdivide the problem into computational elements as these methods do [128]. In the study by Mycek *et al*, vortices generated from the blade tips are used as the computational elements, and their downstream propagation in the Lagrangian frame is used to provide numerical data. The computational work described in this study is based on that of a previous study [129], which described the computational modelling of two three-blade turbines: An 800mm diameter clockwise-rotating turbine at *Re*=580,000 and a 700mm diameter anti-clockwise rotating turbine at 280,000. Simulations of these two turbines were again conducted using the vortex particle method, and results were found to be in agreement with previous experimental results (within 2.5% in most cases). However, the accuracy of computational results was found to depend heavily on the smoothing parameter ε, which is a parameter of the vortex particle method, and is directly proportional to inter-particle spacing, and thus the temporal separation between particle generations. Wake patterns behind the two turbines were calculated for a range of smoothing particle values, from ε=0.075 to ε=0.2, and it was found that for ε<0.15, results appeared to show good correlation with experimental results, with wake velocity deficit predicted within 7%. In both turbine cases, recovery to 80% of free stream velocity was observed at 10 device diameters downstream. However, in order to achieve these results, the computational time required was significant, with calculations at ε=0.075 requiring over 2 days of computation on 16 quad-core nodes.

Computational modelling: Cylinder wakes

As discussed in Section 2.2, a wide range of tidal turbine designs currently exist, with almost as many different designs of support structure. As has been noted, this static part of the turbine is likely to contribute to the wake behind a complete device unit, so must be carefully considered. There is a

large volume of experimental literature available on wake structures behind submerged cylinders due to the relevance of these studies to bridge piers and similar structures. This literature is considered during Section 2.8, and computational work in the same field is studied in this section since cylinders are, to a degree, analogous to tidal turbine support structures.

Kirkil [130] conducted a study of coherent structures in the flow field around a circular cylinder including both experimental work (see Section 2.8) and numerical modelling. The numerical part of the work was conducted using LES CFD, which was employed to study the development of a scour hole in the region behind a fixed cylinder in a hydraulic, and to study the flow structures in the cylinder near wake region at *Re*=16,000. A computational domain defined by cylinder diameter *D* was used, with a length of 15*D*, width of 16*D* and height of 1.12*D*. The cylinder was placed at 5*D* downstream of the domain inlet, in the centre of the domain width.

The resulting structures in the near wake region were found to be similar to those hypothesised in previous studies and observed by others [131, 132]. The structures identified are illustrated in Figure 2-31, and are known collectively as necklace vortices.

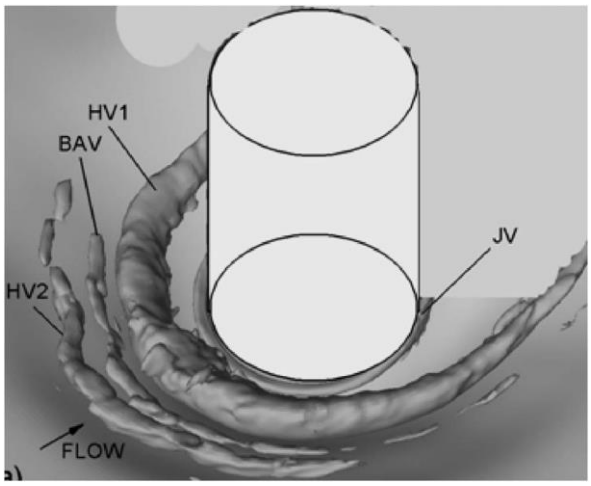

Figure 2-31 – Cylinder wake structures (mean flow): Primary Horseshoe vortex (HV1); Secondary Horseshoe vortex (HV2); Base attached vortex (BAV) and Junction vortex (JV) illustrated from mean flow by Q-criterion (from [130]).

Around the base of the cylinder, the most prominent necklace vortex is the primary horseshoe vortex, labelled HV1. This structure is relatively stable and was observed consistently throughout the study. Upstream of this structure was found a secondary horseshoe vortex, labelled HV2. This structure is much less stable than HV1 and was found to vary in its presence in instantaneous flow fields, though it did appear in the majority of cases and can clearly be observed in the mean flow. The third necklace vortex structure identified is labelled BAV and described as the bottom-attached vortex. This structure is again relatively stable and occurred in most instantaneous flow fields. This structure remains attached to the base of the domain, and when viewed from above lies between HV1 and HV2. The junction vortex (JV) occurs around the base of the cylinder, where it meets the domain base. This structure extends further around the cylinder in the downstream direction than the others, but does not completely surround the cylinder.

Further to these mostly stable structures, some less stable features were also observed. The length of the "legs" of HV1 were found to vary with time, and in some cases smaller intermittent flow structures appeared in the region between HV1 and HV2, sometimes interacting with the major structures. The necklace vortices identified by Kirkil have been observed in many other cases, both through computational simulation and experimental work. A further description of these structures as observed experimentally by Euler and Herget [133] is given in Section 2.8.

The downstream wake of a cylinder has also been studied extensively over many years. As has been discussed, von Karman [93] illustrated the shedding of alternate vortices in the region behind a cylinder for *Re* values between 10^2 and 10^5, and Strouhal [134] illustrated the calculation of the frequency of the shedding. Of interest to the present work, a recent study of vortex shedding of two in-line cylinders was conducted by Xu and Zhou [135]. This work studied two identical diameter (d) cylinders with a variable separation distance (L) under a range of *Re* values from *Re* = 800 to *Re* = 4.2×10^4. The work illustrated a strong relationship between the frequency of vortex shedding as described by *St* and *L/d*. Four distinct regions of behaviour were observed, each with its own shedding characteristics:

- Category 1 ($1<L/d<2$): Vortices shed from the upstream cylinder "roll up" behind the downstream cylinder
- Category 2 ($2<L/d<3$): Transition region from category 1 to reattachment of vortices from the upstream cylinder to the downstream cylinder
- Category 3 ($3<L/d<5$): Transition from category 2 to co-shedding
- Category 4 ($L/d>5$): Co-shedding

Co-shedding, as observed in cases of $L/d>5$, describes the effect of vortices being shed from the upstream and downstream cylinders at an identical frequency.

Nicole and Eames [136] conducted a detailed study of the wake effects of a range of arrays of cylinders. This work provides some useful results as the cylinders modelled are partly analogous to tidal turbines. Direct Numerical Simulation (DNS) CFD modelling was employed in this work. As discussed in the previous section, this method resolves the flow field at all scales by directly solving the equations of fluid motion at each scale, producing accurate results, but is much more computationally intensive than the more commonly used RANS approach which uses models to replicate turbulent effects at smaller flow scales. The work studied cylinders arranged in arrays of size between $n = 1$ and $n = 133$, in $Re = 2100$. The work illustrates that a closely packed array of cylinders (void fraction < 0.15) behave in a similar way to a large single cylinder, producing a single wake rather than individual device wakes as are observed at greater void fractions. The work also includes detailed discussion of the far field (greater than one multiple of the overall array diameter) wake effects behind such arrays, concluding that a widely spaced array will yield individual cylinder wakes, which will result in an overall wake of much greater length and turbulent intensity than a case with more tightly spaced cylinders resulting in a combined wake.

2.8 – Physical modelling of tidal turbines

This section of the review studied papers relating to the physical modelling of tidal turbines, which mainly involves the testing of scale models or representations such as porous disks. An important consideration in physical modelling is the method used to measure flow conditions, which is discussed in Section 2.8.2.

2.8.1 – Turbine modelling literature

The vast majority of modelling of tidal turbines has been carried out using computational methods as described in Section 2.7, but some physical modelling has been conducted. This work will focus on the use of physical models, in an attempt to enhance the level of knowledge in this area.

Cylinder models

As discussed in Section 2.7, work conducted on the wake structure behind cylinders in a fluid flow is a good starting point towards the study of a turbine wake. Work by Euler and Herget published in the journal Catena [133] describes the modelling of cylinders in a water channel at *Re* values ranging from 2030 to 8370. The work describes in detail the flow pattern predicted and measured around objects in a fluvial environment, including the scour and deposition effects caused by vortices from the object. Hemispheres and cylinders are both considered. The major flow structures predicted around a cylinder in moving fluid flow were identified as illustrated in Figure 2-32.

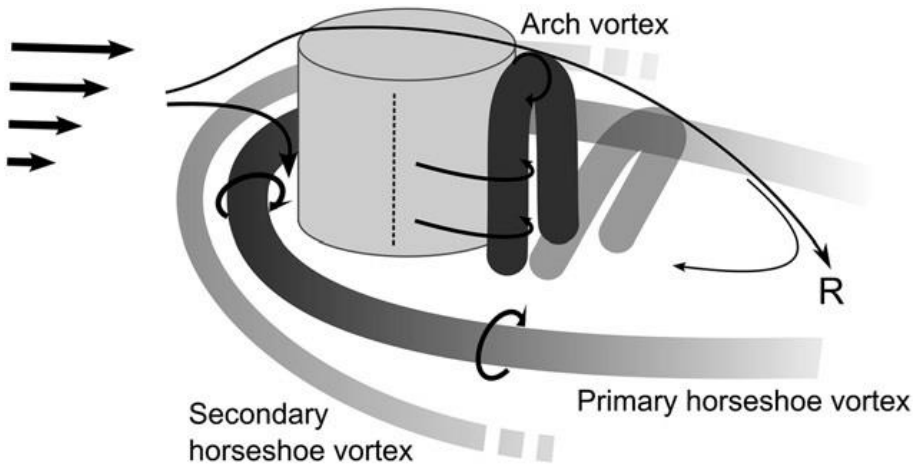

Figure 2-32 – Major flow structures predicted in the flow around a submerged cylinder (from [133]).

The primary and secondary horseshoe vortices discussed in Section 2.7 (as identified by Kirkil and others) are again illustrated in this work. In addition, an arch vortex behind the cylinder is predicted, as well as a recirculating vortex over the top of a submerged cylinder, in cases where the cylinder height was below that of the water level.

The experimental section of this work used velocity probes and ink visualisation for flow measurement. There are many relevant observations relating to the structure of the seabed surface

behind a submerged object, and how this varies with Reynolds number (object Reynolds number Re_o was used during this study, meaning the *Re* value calculated using the characteristic length of the object), for example noting that scour holes are only generated at Re_o values greater than 3000. Particularly of interest in this work is the observation and measurement of the major wake elements a submerged cylinder, as predicted in Figure 2-32. These predictions were tested experimentally, as illustrated in Figure 2-33, in which the generation of the predicted primary horseshoe vortex can clearly be seen. As has previously been observed, other vortex structures did appear to be present during further tests, but were notably less energetic than the primary horseshoe vortex, which appears to be the greatest contributor to the development of cylinder wakes, as well as to levels of scour and deposition.

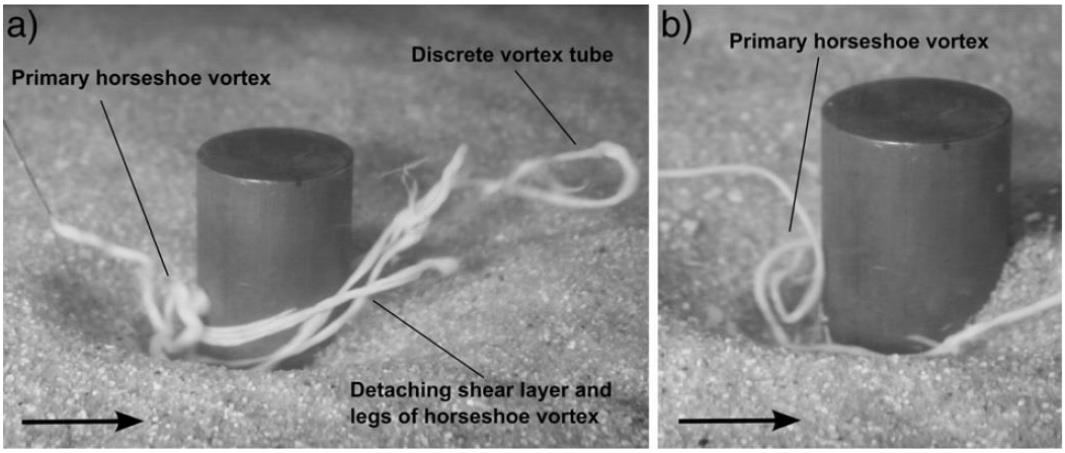

Figure 2-33 – Ink visualisation of primary horseshoe vortex around a submerged cylinder (cylinder diameter 30mm, height 20mm, Re = 5585) from [133].

Horseshoe vortices are also studied in detail by Simpson [137], Unger and Hager [138], and Kirkil [130]. The computational part of the latter has already been discussed, and in the experimental part of his work Kirkil highlights the complexity of the flow structures around the cylinder. HV1 and HV2 are observed experimentally as predicted, and also noted are smaller unsteady vortices which occur periodically in the region between HV1 and HV2. These vortices were found to appear in some cases and not in others. Two sample images, visualised using dye, are given in Figure 2-34.

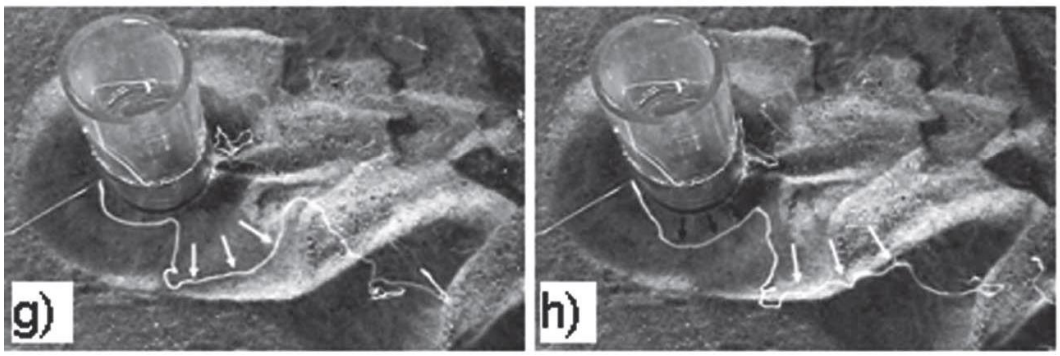

Figure 2-34 – Sample flow visualisation images (visualised using dye) illustrating HV1 [130].

Work described in this section illustrates the structure of the wake behind a cylinder, comprising a relatively stable clockwise-rotating primary horseshoe vortex (HV1) and inward-rotating arch vortex, a secondary horseshoe vortex (HV2) which was present in most cases though not entirely stable, and

additional less stable vortices observed intermittently between HV1 and HV2 as well as at the cylinder base. In summary, even without the additional complexity of a turbine, the wake behind a tidal turbine support structure is not trivial. A summary diagram of the wake structures identified in this section is given as part of the overall expected flow structure behind the turbine models tested in this study, as illustrated in Section 2.12.

Turbine models

In most cases, the physical tidal turbine models tested in water channels have not been fully representative scale turbine models, with studies instead favouring porous disk models. “Actuator disk” is the accepted term for a porous disk used to represent a turbine in a water channel or wind tunnel study [83], as well as a common term in computational modelling. Such models allow the general shape, pressure drop and porosity of a turbine to be represented without the complexity of constructing a scale model, and have a number of advantages over scale turbine models, such as cost and ease of manufacture (particularly at low size).

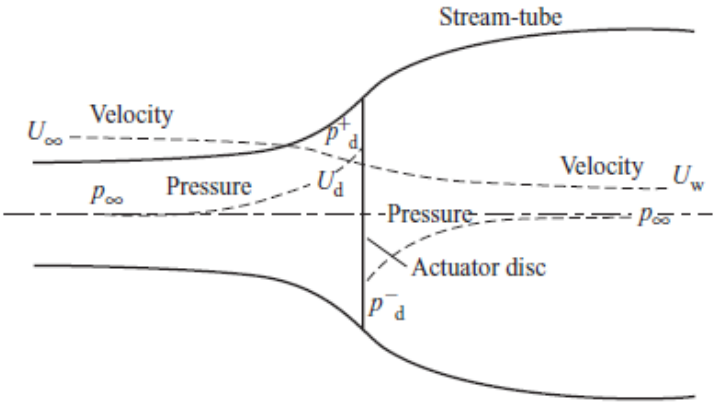

Figure 2-35 – The Actuator disk concept (from [83]).

However, it should be noted that the wake behind a tidal turbine is a complex one made up of a number of individual wake structures, and though the actuator disk is able to represent many of these, it cannot represent them all. The body of work completed to date using physical models has been studied, and is discussed in this section. Modelling using actuator disks and scale turbine models is discussed in this section, with the following section devoted to the study of the construction and instrumentation if scale turbine models.

Generating electricity from the oceans [106] by AbuBakr S. Bahaj is a comprehensive paper dealing with numerous aspects of wave and tidal energy devices, including the physical testing of tidal energy devices. The work is highly pertinent to the current project, since it discusses the impact of wake creation and device spacing on farm performance. An initial investigation into the modelling of turbine wakes was conducted, and a number of useful conclusions were drawn, specifically:

- Water surface and seabed constrict the vertical wake behind a device, so wind turbine models cannot be reliably used.
- This effect also extends the wake downstream, suggesting that tidal turbines will require larger downstream spacing than wind turbines.

- The support structure of the device has a noticeable influence on the wake.

Experiments were conducted using two water channels, a 21m x 2m x 1.5m tilting channel at the University of Southampton and a 18m x 2m x 4m channel in Boulogne sur Mer, France. Flow speeds of up to 2m/s were used, yielding maximum channel *Re* values in the region of $Re = 4x10^6$.

Further work by Bahaj and others [139] focuses on the physical modelling of a turbine, modelled as a porous actuator disk, in a flow representing real-scale shallow flow (less than 20m). It is noted that these shallow flows will lead to different wake characteristics than deeper flows, due to seabed proximity. This work is one of the first to consider the wake structure behind a tidal turbine, which the continuation and development of forms the basic aim of the work described herein. Experimental work was carried out on a tilting water channel of 21m length, with a 1.37m x 0.4m cross-sectional area. The actuator disk used to represent the turbine in the channel was constructed from stainless steel mesh, at 1:100 scale. Flow conditions were recorded using an Acoustic Doppler Velocimetry (ADV) device. The conclusions of the work suggest that a site with mid water depth (defined as 30 – 50m) will produce the shortest wake length, with devices installed in shallower or deeper sites producing longer wake structures. In scale experimental tests using turbine models, velocity deficit returned to zero at 20*D* downstream of the disk in the mid-depth case, but a deficit of between 10% and 12% remained in the deep and shallow cases.

Studies using scale model tidal turbines have been carried out, most notably by Chamorro *et al* at the University of Minnesota Saint Anthony Falls Laboratory. Two studies [53, 140] using scale turbine models have been published. The first study used a 3D PIV system to monitor the wake generated behind the blades of a small scale (0.126m diameter) tidal turbine. No instrumentation was attached to the model turbine as the study focussed on studying the wake generated behind the device. The turbine models were placed along the water channel centre line, at relative spacing of 0*D*, 7*D* (0.882m) and 14*D* (1.764m) downstream, in a flow with hub height mean velocity of 0.265m/s. The wake within one turbine diameter behind each device was observed in detail using the 3D PIV system, resulting in three major conclusions:

- There is minimal interaction between the wake generated by the blade hub and the blade tip vortices.

- The blade tip vortex is slowed by the slower-moving fluid in the lower part of the flow, such that a secondary tip vortex (generated in the upper area) may overtake it, leading to a highly complex turbulent wake.

- The presence of an upstream turbine causes a downstream one to exhibit a more highly turbulent wake with shorter length scales.

Figure 2-36 illustrates the wake behind each of the three turbines, highlighting the increasingly turbulent wake observed in each case due to the presence of one and two upstream devices.

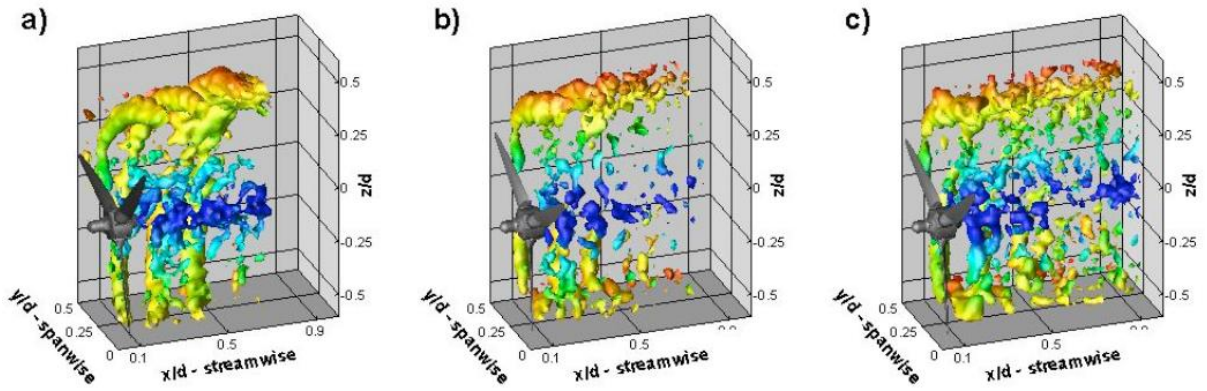

Figure 2-36 – Turbine blade wake structure recorded using 3D PIV behind three tidal turbine models: Without upstream device (l), with upstream device at 7D (centre), and with upstream devices at 7D and 14D (r), illustrated by Q-criterion (from [53]).

Although this work did not involve any study of the device support structure wake, the results are still highly relevant to the current project, and the complex transient nature of the blade area wake highlights that the actuator disk method cannot accurately represent the full details of the flow structure behind a tidal turbine.

Similar work [52] undertaken at the University of Southampton did consider the wake effect of a tidal energy device support structure as well as that of the turbine itself. A 1:20 scale three-blade turbine of 800mm diameter was fitted to a support structure in a top-mounted configuration, with the support structure fixed above the water channel and reaching down to the turbine. A flow velocity of 0.8m/s was used. Velocity data was recorded using ADV at 50Hz, with the unit located downstream of the device at a range of separation distances and vertical heights, in order to produce full 2D profiles (horizontal profiles were also recorded). Turbulence intensity was calculated from velocity data, as will be described in Section 2.9. Full wake recovery distance was not recorded, but a velocity deficit of 22% was measured at 10*D* downstream of the rotating turbine, which appears to agree with the results of similar studies. The support structure downstream wake velocity and turbulent intensity between 2.5*D* and 5*D* are given in Figure 2-37, though it should be noted that during support structure wake measurement tests, the turbine was not allowed to rotate. The model turbine used in this study is illustrated in Figure 2-40 (r).

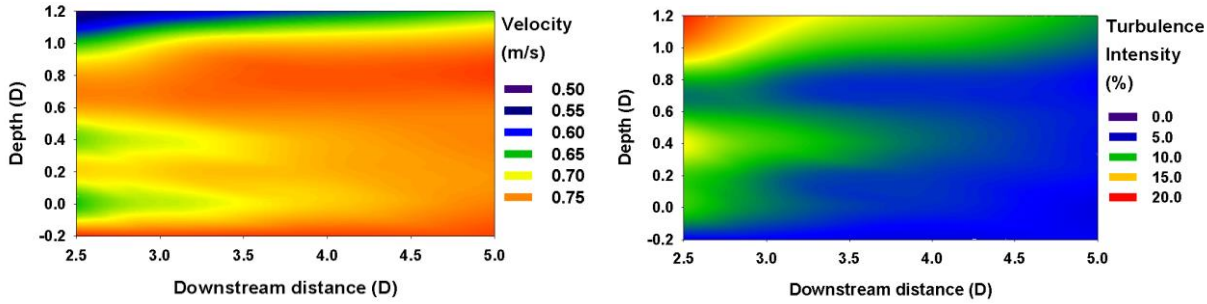

Figure 2-37 – Velocity and Turbulence Intensity plots downstream of a scale tidal turbine model top-mounted support structure (turbine static). From [52].

As has been discussed in Section 2.7, Mycek *et al* conducted an experimental study to consider the interaction of two tidal stream turbines [62]. The computational aspect of this work has been discussed in the previous section, but the study was primarily an experimental one. The two turbines tested were of 1:30 scale, giving a turbine rotor diameter of 0.7m, and were three-blade horizontal axis devices with top-down support structures. The turbines were mounted at a blade centre height of 1.1m below the free surface, in a water depth of 2m. Tests were conducted at $\lambda = 3$ and $\lambda = 4$ with an upstream ambient turbulent intensity of $I = 3\%$, at separation distances of 4, 6, 8 and 10 multiples of rotor diameter (i.e. 2.8m, 4.2m, 5.6m, and 7m). Turbine performance was measured in terms of downstream device C_P relative to C_P generated by a single device with no upstream device at $\lambda = 3$, defined as η, the result of which is illustrated in Figure 2-38.

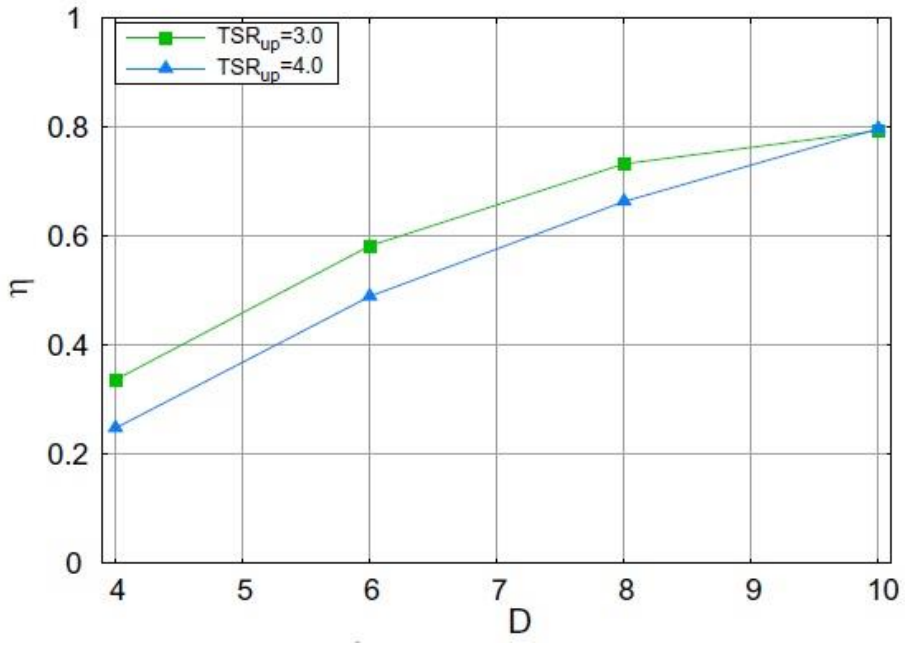

Figure 2-38 – η vs separation distance for a downstream turbine in λ *= 3 and* λ *= 4 [62].*

As illustrated above, even at a separation distance of 10*D*, only 80% of unrestricted turbine performance can be achieved, and at smaller separation distances as little as 25% may be expected. Mycek *et al* hypothesise that this reduction is largely related to the incoming turbulent intensity. The work found that with an incoming turbulent intensity $I = 3\%$, the turbulent intensity behind a single device was around 30% at 2*D*, decaying to 15% at 6*D*, and remaining above 10% at 10*D*. The incoming flow received by the second turbine is therefore of much greater turbulent intensity, and the resulting power generation ability of the turbine is reduced. However it was also noted that with increasing turbulent intensity, velocity recovery occurred more quickly.

In addition to the tests described above, this work offers a proposed definition of the important dimensions within a tidal stream turbine array, characterising them as follows:

- a_1 = distance between “even” rows
- a_2 = distance between “odd” rows
- a_3 = distance between one row and the next
- b_1 = distance between two adjacent turbines
- b_2 = distance between an odd and even turbine

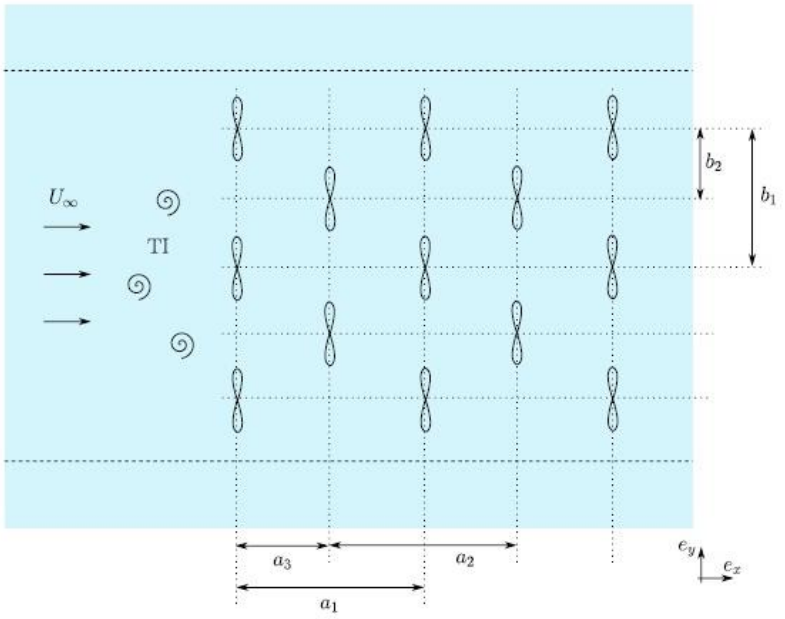

Figure 2-39 – Schematic diagram of a turbine array illustrating the location of critical distances (from [62]).

2.8.2 – Turbine models & instrumentation

Studies using scale turbine models fall into two broad categories: The first simply uses the turbine models to generate a representative turbine wake, allowing the analysis of the resulting flow but not any study of the performance of the turbine itself. This can be thought of as the passive use of a turbine model. The second category, which can be thought of as the active use of a turbine model, would involve the turbine being instrumented in some way, in order that its performance can be monitored. In order to conduct a successful study using a model turbine, it is necessary in both the active and passive case to control the turbine in order to ensure that it behaves as a correct representation of a real-scale turbine. Secondly, in the case of an active turbine model, it is necessary to establish a method of extracting data from the model.

The turbine models used by Chamorro *et al* [53], as discussed in the previous section, were three-blade devices with a rotor diameter of D = 0.126m and a hub height of 0.11m. These turbines had a swept area of 0.0124m², yielding a blockage ratio of B = 3.6% in the 0.5m x 0.7m cross-section (A_C = 0.35m²) water channel. These were passive turbine models and since only flow data was monitored during this study, no data acquisition system was required. The subsequent study by the same research group [140] employed much larger turbine models of D = 0.5m rotor diameter and hub height of 0.425m, in a water channel of A_C = 4.95m², and thus a blockage ratio of B = 4%. These active turbines incorporated a measurement system, and included a drive system made up of a stepper motor and indexer (Danaher Powermax II M21 NEMA 23 and Parker 6104, respectively) to allow the turbine to be driven with precise control of angular position. This system allowed the control of turbine position at a frequency > 400 Hz, meaning that variation in velocity over a single rotation could be monitored. The system also allowed the measurement of torque transferred to the turbine. A torque transducer was also installed in the turbine unit, allowing the measurement of the

total torque experienced by the turbine. From these two torque figures, the authors were able to ascertain the torque generated by the turbine itself, from the water flow.

The turbine model employed by Bahaj *et al* [52] did not use a drive motor system. Due to the relatively large diameter (D = 0.8m, B = 6.3%) of these turbines, this study was able to instead use a conventional generator system. The turbine was first connected to a planetary gearbox, housed within the turbine nacelle. The gearbox was used to increase the rotational speed in order to allow the successful operation of the permanent magnet generator, which was also housed within the nacelle.

There are a number of practical difficulties which must be overcome during the use of turbine models in a water channel. One such challenge is how to ensure that the data acquisition equipment is not damaged and is able to operate effectively and consistently underwater. In the case of the turbine designs used by Chamorro *et al* as discussed above [140], this was achieved through the use of a sealed turbine unit in combination with a vacuum air pump to ensure that water did not enter the turbine unit. This method was considered for use in the subsequent design of turbines for the author's project, but a power take-off system and external drive system was eventually chosen instead. A diagram of the models used by Chamorro *et al* and a photograph of those used by Bahaj *et al* are shown in Figure 2-40.

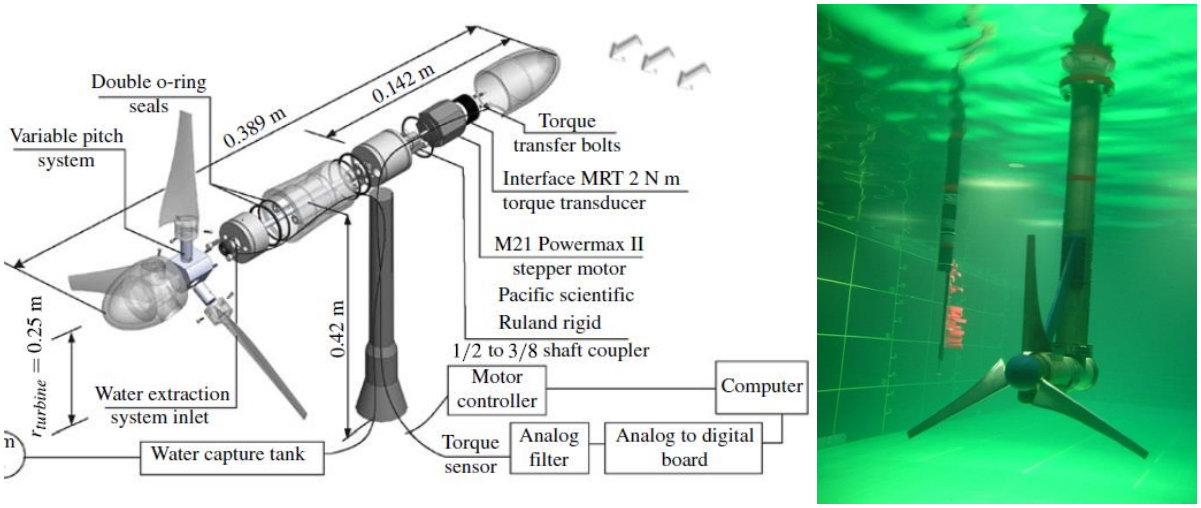

Figure 2-40 – Active turbine models (from [140] (l) and [52] (r)).

Similar experimental work using active turbines has been used during studies by O'Doherty *et al* [54] (D = 0.5m, A_C = 1.17m² section channel, B = 16.6%), Stallard *et al* [141] (D = 0.27m, A_C = 2.45m², B = 2.5% - 12.7% (multiple turbines used)), and others. Whilst sizes, designs and drive systems varied, all incorporated some method of blade torque output measurement.

2.9 – Analysis of turbulence

As has been discussed previously, the environment within which a tidal turbine operates is a turbulent one, with real scale Reynolds numbers in the region of 10^8. Consequently, much of the work considered in this literature review includes the calculation of turbulence, either computationally or from experimental measurements. Since the analysis of turbulence is likely to

form an important part of the present study, the approaches used by others to gather and analyse turbulence information from experimental work were considered at this stage.

Experimentally, turbulence cannot be measured directly, and must be calculated from velocity data. In the experimental work described in Sections, 2.6 and 2.8 (relating to Wind and Tidal turbines respectively), research is described detailing velocity data capture using anemometry, pressure sensors, mechanical flow meters, ADCP, acoustic and laser Doppler systems, and PIV.

Work on the flow around cylinders with a particular focus on turbulence was carried out by Eames *et al* [142]. This work used ADV equipment to record 400s data sets at 25Hz, giving 10,000 data points per test. From this data, time averaged ($\bar{u}$) and root mean square (RMS) velocity (u_*) data was calculated as follows, for *n* valid samples of velocity u_k*:*

$$\bar{u} = \frac{1}{n}\sum_{k=1}^{n} u_k$$

$$u_* = \sqrt{\frac{1}{n}\sum_{k=1}^{n}(u_k - \bar{u})^2}$$

Similar calculations were carried out in both the streamwise and cross-stream directions for u, v and w velocity data. RMS velocity is the square root of the sum of, at each point, the square of velocity fluctuation from the arithmetic mean of the whole series. This value thus describes the sum of the magnitude of variance from the mean of the series at each point. For a turbulent flow with even variation around the mean over the full time series, the RMS velocity allows the degree of this variation to be known, which the arithmetic mean does not. If one considers two velocity signals, varying around a given value with the same frequency but a greater amplitude in case 2 than case 1, the arithmetic mean would give an identical result in both cases, whereas the calculation of the RMS of the signals would reveal a greater total variation from the mean in case 2, illustrating a more energetic signal.

However, even u_*would not reveal the difference in variation between case 2 and a third case with constantly varying amplitude of the same mean fluctuation as case 2. In order to understand any change in the variation of individual velocity values from the mean with time (as in case 3 above), it is necessary to generate turbulence data for each data point in the sample. Such calculations were carried out by Thomson *et al* [143]. This work used ADCP and ADV measurement methods to study the velocity profiles and turbulent characteristics of flow conditions at two potential tidal energy sites in Washington State, USA. Turbulent Kinetic Energy (TKE or *k*) and Turbulence Intensity (*I*) were calculated from recorded velocity data as indicators of turbulence. TKE is a measure of the energy contained in the instantaneous variation of velocity around its mean value, defined as half of the mean of the squared velocity variation in each recorded direction. If an instantaneous velocity recording is relatively close to the mean, its variation (*(u_k – $\bar{u}$)* as above, or *u'*) will be relatively low, and therefore the turbulent kinetic energy at that point will also be low. If an instantaneous velocity value is far from the mean, a high variation and hence turbulent kinetic energy value will be

observed. Turbulent kinetic energy is calculated using velocity recordings in all available directions, hence for velocity variation in the *x*, *y*, and *z* directions of u_x' , u_y' and u_z' respectively, TKE is given as follows:

$$k = \frac{1}{2}\left[\overline{(u_x')^2} + \overline{(u_y')^2} + \overline{(u_z')^2}\right]$$

Turbulent intensity (*I*) gives an indication of the level of turbulence in a flow over a given recording period as a single value per direction, by calculating the ratio of velocity fluctuation to mean velocity. Root mean square values of velocity fluctuation at each measured point are taken in order to avoid positive and negative fluctuations cancelling each other out, and the sum divided by the mean velocity over the same recording period to give turbulent intensity, which is commonly expressed as a percentage. For *n* recordings of *u* direction velocity fluctuation *u'* turbulent intensity is given by:

$$I = \frac{\sqrt{\frac{(u_1')^2 + (u_2')^2 + (u_3')^2 + \cdots + (u_n')^2}{n}}}{\bar{u}}$$

Thomson *et al* also estimated turbulent energy dissipation rates for ADV and ADCP recorded data. Dissipation rate ε describes the rate at which turbulent energy is transferred from large scale turbulent structures, through smaller and smaller flow structures, until eventually reaching the smallest scale which can be sustained in the flow and finally dissipating the remaining energy as heat. This gradual decay and the associated energy spectrum is discussed in detail in Chapter 3. Longer dissipation rates are associated with greater turbulent intensity, since the initial turbulent energy in these cases is greater, and consequently the time required for structures to break down and dissipate is greater.

The work concluded that for one test site with a water depth of 22m and maximum hub height flow velocity of 1.8m/s, turbulent intensity at turbine hub height could be expected to be around 10%, with a variation between around 8% at the water surface and 15% at 4m above the seabed. The turbulent intensity and dissipation rate profiles recorded at this site are illustrated in Figure 2-41 [143].

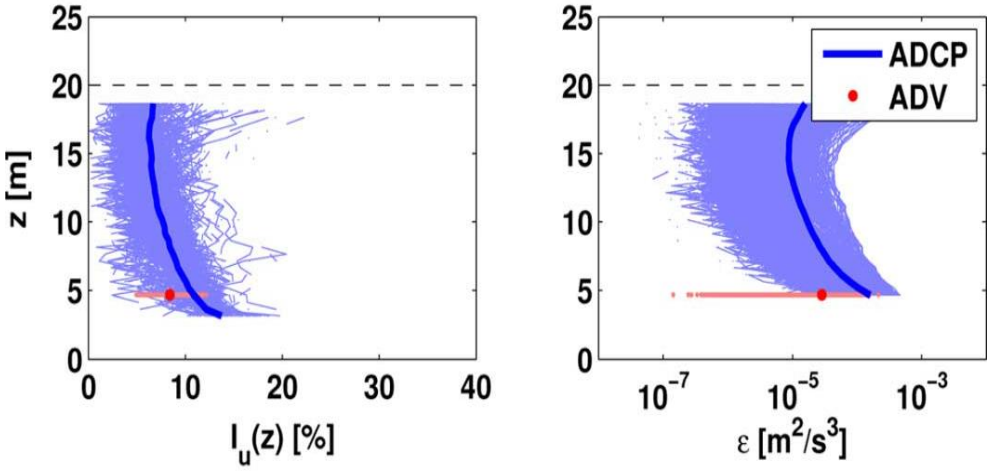

Figure 2-41 – Turbulent intensity (I) and turbulent dissipation rate (Ɛ) at a sample tidal energy site (from [143]),Thin blue: ADCP data, thick blue: ADCP average, red: ADV average.

By calculating k, I and $\mathcal{E}$ at each velocity point in a sample, in addition to $\bar{u}$ and u_* a much greater level of understanding of the turbulence in a flow can be gained.

Though not directly related to this section, it is interesting to note that these results highlight that for a traditional design of horizontal axis tidal turbine a variation in turbulent intensity can be expected over the swept region of the blades. Furthermore, the region of flow in which the turbine support structure would be mounted is expected to be the most highly turbulent region of the flow profile, meaning that any turbulence-inducing geometrical effects from physical structures in this region may be exacerbated by the highly turbulent incoming flow.

Statistical analysis of turbulence

The earliest studies considered relating to turbulence in this review are those of Kolmogorov (1941) [49, 50] and Taylor (1938) [144]. Both identify turbulence as a dynamic effect, and propose methods to present and analyse data in a statistical format. Kolmogorov's work on the energy cascade and the gradual breaking down of highly energetic turbulent structures in to lower order structures was a critical moment in the understanding of turbulence, and will be described in detail in Chapter 3. One outcome of this work was the understanding that turbulence can be studied in the frequency domain as well as in the time domain. This subsequently led to the application of the Principal Components Analysis (PCA) method to the study of turbulent flow. PCA was developed independently by Pearson [145] and Hotelling [146, 147] and described by the former as a method to "represent a system of points in plane, three, or higher dimensioned space by the "best-fitting" straight line or plane". The technique has different titles in different fields, being commonly known as the Karhunen–Loève decomposition in signal processing, the Hotelling transformation when applied in quality control, and the Proper Orthogonal Decomposition (POD) method when applied in mechanical engineering. The title POD has therefore been adopted for the remainder of this thesis.

The principal of the Proper Orthogonal Decomposition (POD) method in the context of fluid mechanics is the representation of a complex flow with variation in both time and space as a series of energy-containing modes, each with an attached frequency. Each mode describes a flow pattern which contributes to the overall pattern. The level of contribution to the overall pattern of an individual mode is given by its energy.

The method relies on the assumption of linear approximation, which assumes that a complex signal can be described by the superimposition of an infinite number of repeating signals, each with its own amplitude and frequency. This assumption is generally valid for flow which can be considered inviscid, but begins to break down for very small scale turbulent flows where viscosity governs the energy contained within the flow. In terms of the energy spectrum illustrated in Figure 2-4, the assumption of linear approximation is valid in the LEC (a) and inertial (b) regions, but loses validity in the dissipation region (c) [148]. Due to the limitations of the water channel, the present study aims to focus on these larger scale geometry-governed effects, so the POD method could be used.

The POD technique aims to represent a high-dimensional signal as efficiently as possible using fewer dimensions. For an original time series of N samples, the outcome of the POD calculation is a series of i modes, which represent the i most energetic elements of the flow pattern being studied, and corresponding coefficients, which describe the frequency of each mode. The POD process calculates and arranges these modes into descending order of energy contribution. By recombining the modes

it is possible to create an approximation of the signal of lower dimensional order than the original (if $i = N$, then the signal will be the same as the original), but it is often found that a relatively small number of modes can represent a high proportion of the energy in the original signal [149].

Adrian [150] applied the POD method to the study of turbulent velocity fields. The work aimed to propose a number of alternatives to the Reynolds decomposition method of studying turbulence, which the author described as "the de facto standard method of describing turbulent velocity fields". The alternatives suggested are Galilean decomposition and LES decomposition, incorporating POD. Galilean decomposition is a process similar to low-pass filtering, whereby the bulk translational velocity of the flow is removed from the velocity at each point, resulting in the highlighting of vortices, since the direction and speed of a vector within a vortex is different to the bulk flow. In most flows, a variation in bulk flow exists across the region of analysis, so a range of translational velocities are used, with each analysis yielding any vortices found to be moving at that translational velocity [151]. Adrian found that whilst the Galilean decomposition offered advantages over the Reynolds decomposition in the visualisation of vortices, it was found to be less effective than the inhomogeneous filtering version of the LES method. This is the POD method.

The POD calculation methodology as used in this study is detailed in Section 4.4.2, but a brief overview of the method is given in Figure 2-42 and Figure 2-43. The steps illustrated relate to the use of a data set of recorded images as the basis for the analysis, so include steps which would not be necessary if the base was already a matrix.

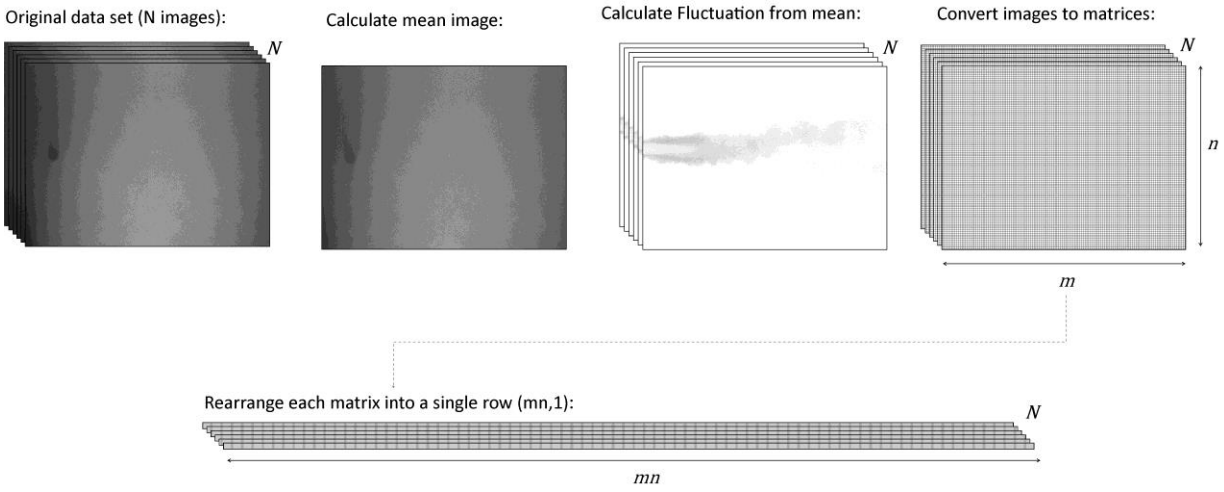

Figure 2-42 – Outline of POD process (Image processing phase)

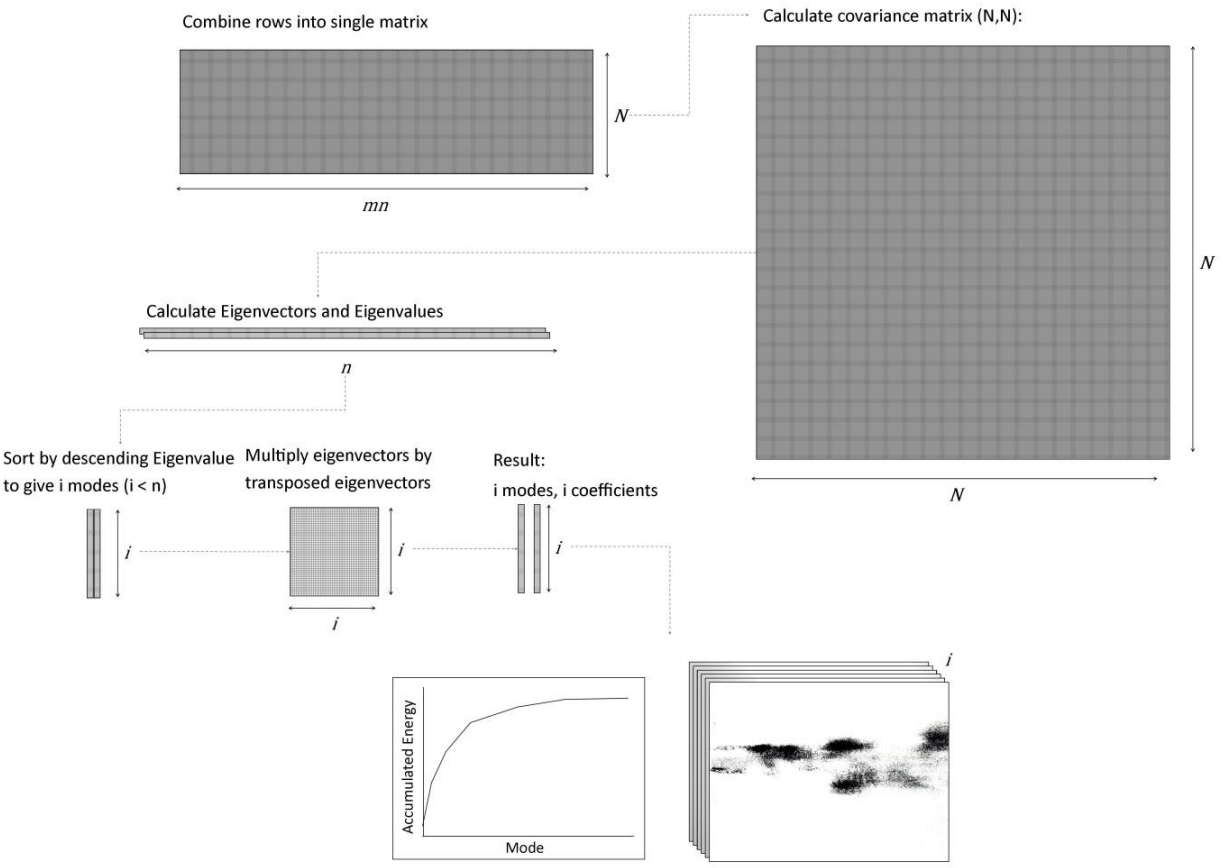

Figure 2-43 – Outline of POD process (Calculation phase)

The POD method was applied by Brevis and García-Villalba [152] to laboratory experiments on the wake developed behind a 125mm diameter cylinder installed in a shallow (18mm deep) flow in a water channel at *Re* = 16,200. Results were visualised using the injection of dye and recorded using a commercial video camera at 25Hz. The processing of results using POD was the focus of the work, with the experiment conducted being chosen as results of previous tests of the same case were available in the literature [153]. The work by Brevis and García-Villalba introduces the POD technique and explains the calculation methodology, before illustrating the calculated POD modes and coefficients, and demonstrating that the method offers excellent agreement with previous work conducted using LDV. The work concludes that the use of POD to analyse dye injection images offers a method of cheaply and quickly identifying the predominant sources of energy within a flow pattern, and goes on to suggest that although the method cannot compete with PIV or LDV in terms of detail, it offers a good starting point in a research scheme, and is perhaps able to highlight areas which can be further investigated using more precise methods.

2.10 – Summary

A literature review of the current state of the art in the field of tidal energy has been conducted and described in the previous section. Literature specific to the field was limited, but relevant information was also found in literature in other fields. Four major areas were investigated: Tidal Turbines in operation; Computational modelling relating to tidal turbines; Physical modelling of tidal turbines; and Flow Measurement, with a particular focus on Particle Imaging Velocimetry. In order to summarise the critical learning from the review, the following conclusions have been reached:

- There are many tidal turbine designs under development. Horizontal axis machines have advantages over vertical axis devices, and machines generating torque from lift forces are likely to be more efficient than drag-based devices. The ducting of tidal turbine devices has the potential to cause problems via cavitation, and is unlikely to allow efficiency levels beyond the Betz limit (59.3%) since current tidal turbine efficiencies are around 35%. The most promising device designs appear to be horizontal axis turbine designs being developed by Marine Current Turbines; Alstom; Andritz Hydro Hammerfest; OpenHydro, Atlantis Resource Corporation and ScotRenewables. A number of turbine arrays are now proposed and are expected to begin operating within the next 5 years.

- Literature on computational modelling of fluid flow around cylinders is extensive, though the wake structure is complex and some small structures are difficult to identify. The major wake structures highlighted are the clockwise-rotating primary and secondary horseshoe vortices produced, the size of which is governed by cylinder diameter. Between these relatively large structures a number of other smaller intermittent structures can be observed. A vertical arch vortex may also be present behind the cylinder.

- The wake behind a rotating turbine blade is also complex, and is heavily influenced by the degree of turbulence in the incoming velocity profile. Blade tip vortices are shed and form an expanding spiral region. Within this region, a region of fluid rotating in the opposite direction to the spiral vortex may be observed (described herein as the central region wake), and within this region a further region rotating with the turbine may also exist (described herein as the core region wake). The presence of an upstream device is likely to increase ambient turbulent intensity and thus reduce the coherence of the wake structures. Turbine wake recovery without an upstream device generally occurs in a downstream distance of the order of 20 multiples of rotor diameter, and within a shorter distance if turbulent intensity is greater in the presence of an upstream device.

- There has not, to date, been an analysis of the wake structures generated by a tidal stream turbine in as great a level of detail as those conducted for cylinder wakes or turbine blades, as described in Sections 2.7 and 2.8 respectively. Based on the current literature described in those sections, the predicted wake generated by a complete tidal stream turbine is given in Figure 2-44. However, the interaction of the cylinder and turbine wake components may lead to the observation of additional effects not present in either component. It should also be noted that the downstream length of the wake features illustrated are not necessarily to scale.

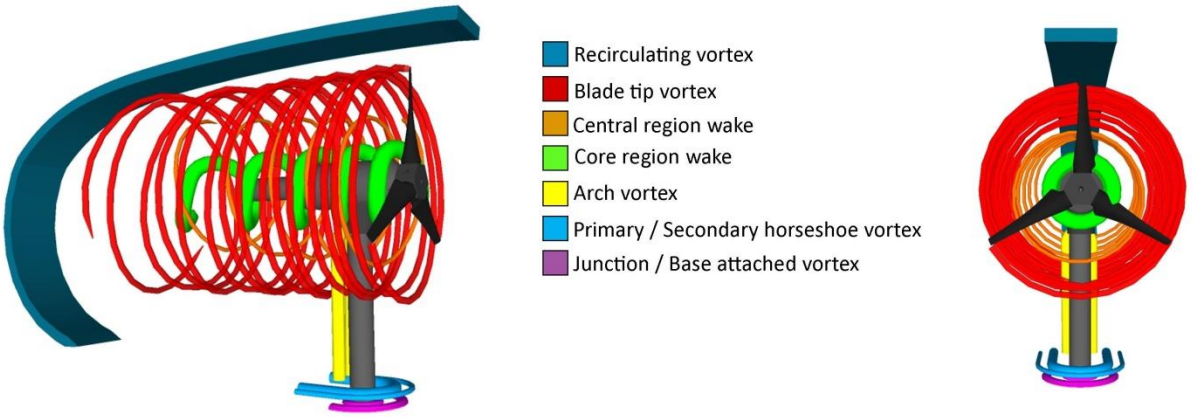

Figure 2-44 – Predicted turbine and support structure wake elements.

- Physical modelling of a turbine using an actuator disk can only replicate some of the structures seen in the wake, and cannot replicate any wake effects generated by the dynamic motion of the blades, meaning that swirl effects in the near wake, blade tip vortices and other wake effects which are specific to the moving parts of the turbine will be lost.

- Physical modelling of tidal turbines has been carried out using water channels in relatively few studies. A range of flow measurement and visualisation techniques are used, with Acoustic Doppler Velocimetry (ADV), Laser Doppler Velocimetry (LDV) and Particle Imaging Velocimetry (PIV) being the most successfully employed. The latter two methods have the advantage of being non-intrusive, and PIV offers the ability to record instantaneous velocity fields across a 2-dimensional section through a flow. PIV has been investigated in detail and will be used as the primary flow measurement method for the remainder of this work.

- Turbulence data can be studied in both the time and frequency domains. The latter allows statistical analysis of data over a recording period. Care must be taken if mean flow data is studied, as this can potentially result in the loss of highly energetic events in a data set.

- The measurement of blade torque from scale model turbines can be achieved through the use of a driven turbine and motor control system, or by the use of a conventional gearbox and generator system, given a suitably large system in order to generate the torque required. Blockage ratios of turbines used in previous studies range from 2% to over 17%, though the calculation of blockage factor is likely to give a fuller understanding of the level of influence of blockage, and the calculation of any required correction.

2.10.1 – Research aims

Following the literature review described in this chapter, a series of research questions and aims were formulated. Due to the apparent importance of the interaction of the blade and support structure wakes, its influence on the performance of a tidal array, and the relatively small volume of work in this area, efforts were focused for the remainder of this study on understanding the influence on turbine performance of this interaction, and of further investigation of the impact of the installation of an upstream device on the performance of a downstream one. Three resulting aims were therefore defined, as detailed below:

- To investigate the effect of changing the diameter of the support structure on the power output of a tidal turbine, and the resulting effect on the wakes generated by the turbine and support structure.

- To investigate the effect of changing the streamwise direction separation distance between the blades of a tidal turbine and its support structure on the output of a tidal turbine, as well as on the velocity wake generated by the turbine and support structure, under given flow conditions.

- To investigate the effect on the output and resultant velocity wake of a tidal turbine of placing another turbine upstream, and to investigate the impact of changing the separation distance between the two devices in both streamwise and cross-stream (offset) directions.

3

Experimental Apparatus

3.1 – Introduction

This chapter describes the equipment and systems used in the experimental part of this study. Initially, equipment such as the water channel is introduced and described in detail, along with discussion of the measurement techniques and equipment used to measure both water flow within the channel, and the response and performance of the model turbines installed therein. The suitability of the water channel for the experiments proposed is studied in detail, and a series of characterisation measurements conducted to assess this suitability are described. Fluid flow measurement techniques are introduced and their use described, and details of the development of the turbine models constructed for use in this study are given.

3.2 – Water channel

Circulating water channels are commonly used in the experimental study of fluid flow and the interaction of fluid and objects, where full-scale testing or study is impractical. The use of such a channel to replicate the flow characteristics around scale model turbines formed a large part of the experimental work undertaken in this study. The selection of turbine model scale and measurement equipment was partly determined by the water channel.

The channel located in the Sheffield University Sediment Transport Laboratory was used in experiments conducted during phases 1, 2, 3 and 4 of this study. The channel is 18m in length, with a width of 0.5m and a maximum water depth of 0.6m. An 11kW impeller pump is used to circulate water from a 9000 litre reservoir tank through the channel with a maximum flow rate of 40 l/s. Flow velocity and level through the channel working section are governed by a computer-controlled valve at the inlet to the main channel section and a manually adjustable tailgate respectively. Since the flow opening is defined as a percentage of maximum, the correlation between opening percentage and flow rate is given in Figure 3-1. In all experimental cases, as discussed in Section 5, flow rates of 30l/s and 40l/s were used, corresponding to opening percentages of 56% and 85% respectively, as highlighted in Figure 3-1.

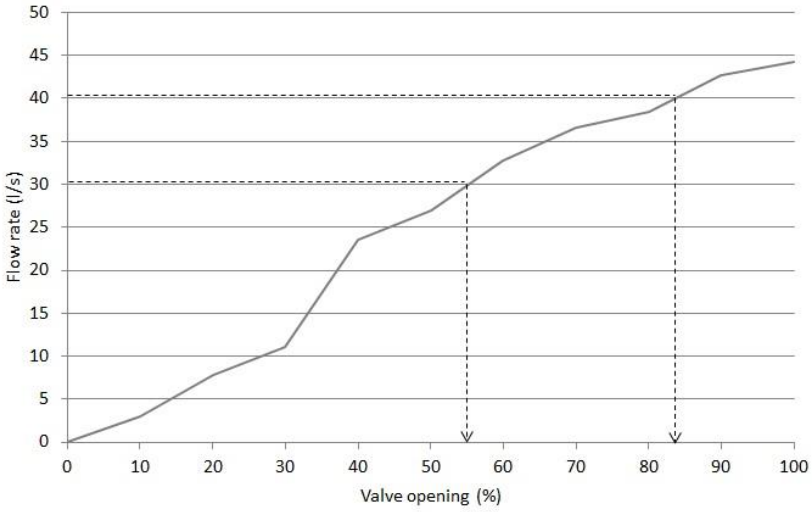

Figure 3-1 – Water channel valve opening percentage vs. flow rate.

A honeycomb flow straightening section of 40mm length and 3.5mm cell diameter and a tethered float placed on top of the water flow were installed at the channel inlet to smooth the flow.

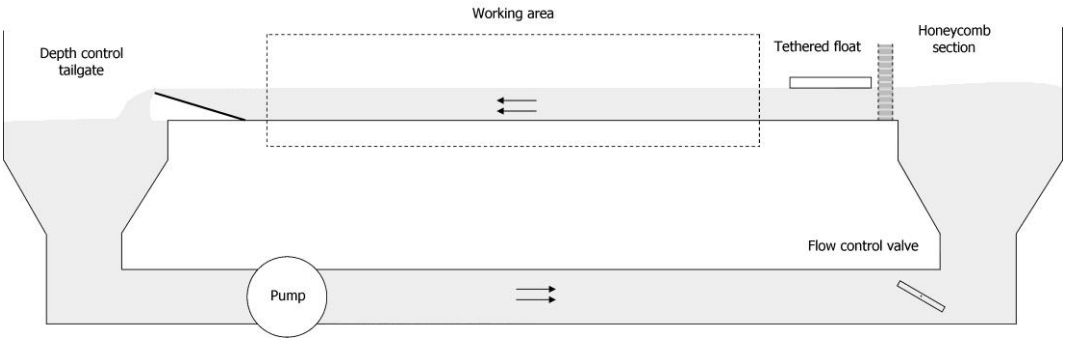

Figure 3-2 – Water channel layout schematic.

The channel side and base panels are manufactured of glass, allowing the use of both vertically and horizontally-mounted flow measurement systems. Rails are also installed along the top of the side panels, onto which trolleys containing measurement equipment such as cameras can be placed. Equipment can thus be precisely positioned along the length of the channel as required. The channel is shown in situ in Figure 3-3.

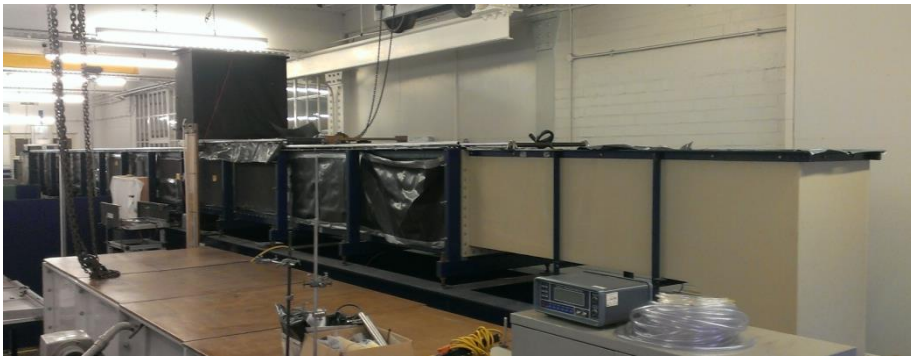

Figure 3-3 - 18m water channel in Sheffield University Sediment Transport Laboratory.

The water contained in the channel was replaced as necessary in order to maintain cleanliness and an appropriate level and size of seeding particles. Following the use of dye in the water, the channel and tank were emptied and cleaning carried out in order to ensure that no dye remained in the water. Similarly, following the use of 5µm seeding particles for LDV experiments, water was emptied before the introduction of 100µm seeding particles for PIV.

3.3 – Scaling & water channel suitability

A major issue encountered with any experimental facility like the channel used in this study is the matching of flow conditions to reality, the achievement of which is known as similitude. In order to achieve similitude, three criteria must be satisfied:

- Geometric similarity
- Kinematic similarity
- Dynamic similarity

Geometric similarity refers to the geometric accuracy of the scale model. Turbine models are discussed later in this chapter. Geometric similarity was achieved through the use of exact scale models of a commercial tidal turbine design. The geometry of a commercial turbine was supplied by Alstom Renewable Power. This geometry was scaled using the Autodesk Inventor 2012 Computer Aided Design package, ensuring that all dimensions and angles were scaled simultaneously. As detailed in Section 5.1.2, the final models were designed with a rotor diameter of 125mm, giving a scaling ratio to the current (at the time of manufacture) iteration of the Alstom Renewable Power turbine design [110] of 1:143.

Kinematic similarity describes the scaling of the flow pattern around an object, and is ensured by controlling the scaling of the flow field between the real and scale models. White [134] states that "*velocities at corresponding points on the model and prototype are in the same direction and differ by a constant scale factor, SF_k*". Though this condition is considered a separate criterion for similitude, it is generally met automatically if the conditions for geometric and dynamic similarity are achieved.

Dynamic similarity describes the forces acting on the object, in reality and at scale. The forces at similar points on each should vary by a constant scale factor for dynamic similarity to be achieved. The forces in question are described by dimensionless numbers, the selection of which depends on the type of flow. In the case of incompressible flow with a free surface, the most critical dimensionless numbers are Froude number, *Fr*, and Reynolds number, *Re*. In the case of flow through a channel, the importance of each of these two values is also variable, and is governed by the blockage ratio and speed of flow. For a relatively low speed, low blockage ratio case, the most critical value is *Re*. Conversely, in a high speed, high blockage case, *Fr* becomes the most critical value for similitude. As discussed later in this section, the models used in this study have a blockage ratio of around 7%, and mean flow rates used in the experimental section of this study are around 0.3m/s, meaning that the flow in this case can be defined as low speed, and the blockage ratio as low. Consequently, *Re* is the critical value for ensuring kinematic similarity. However, *Fr* is still a relevant consideration, and was calculated for both the real case and the scale model case (Fr_r and Fr_s respectively) as follows:

$$Fr = \frac{\mathrm{v}}{\sqrt{gh}}$$

The resultant values for real and scale Froude numbers were $Fr_r = 0.54$ and $Fr_s = 0.065$ respectively.

The final requirement of kinematic similarity, and therefore full satisfaction of the criteria for similitude, is Reynolds number. In the case of water flow through a channel, high *Re* values are only achievable through the use of full scale models or at very high flow rates, neither of which are possible in this case. It is therefore not possible to achieve *Re* similarity between real and scale models across the entire flow spectrum. However, by fully considering the most important characteristics of the flow, *Re* similarity in relevant areas of the flow spectrum can be achieved, meaning that similitude can be achieved for certain flow conditions. In order to achieve such flow matching, an understanding of the turbulent characteristics of the flow is first required. This is discussed and explained in the following section.

3.3.1 – Turbulence in water flow

As has been introduced in Chapter 2, the majority of fluid flows in nature are turbulent. In reality, practically all flows in ocean or river environments are fully turbulent, since the characteristic lengths of these flows tend to be relatively large, resulting in large Reynolds numbers. For example, an inter-island channel might have a width of 2km, and an average tidal flow rate of around 1.5m/s, which would yield a Reynolds number of the order $Re = 3x10^8$. Consequently, water flows in tidal turbine installation areas can be assumed to exhibit turbulent flow characteristics.

The energy cascade and spectrum introduced in Section 2.9 are useful when considering the scale representation of a flow and determining whether it is possible to achieve similitude. As discussed previously, the dissipation region contains the smallest and least energetic flow structures. Flow structures in this region are directly affected by the viscosity of the flow, but are independent of geometrical conditions [154]. Length scales in this range are a function of the Reynolds number, and hence cannot be accurately replicated using scale models at Reynolds numbers different to those of real-scale flows. Flows contained within the LEC region are the largest and most energetic flow features. Within this region, length scales are a function of geometry. These scales are independent of viscosity but their dynamics depend on the mechanism, within the inertial range, governing the transfer of energy through the energy cascade.

Reynolds similarity indicates that an adequate representation of the most important geometrical features and the existence of a fully developed turbulent flow condition is enough to properly simulate the dynamic of large scales in a laboratory environment. Since high Reynolds numbers cannot be achieved in the laboratory due to limitations in the channel size and water speeds, the accurate observation of small scale flow dynamics is not possible. The size and energy of the smaller structures is a direct function of the Reynolds number, and thus these dynamics cannot be properly described under restricted Reynolds conditions. However, the dynamics of large scales, which are independent of viscosity, can be properly represented if the energy is transferred through a proper, well developed, inertial range. Consequently, similitude can be achieved at a laboratory scale for the models used in this study, provided that detailed study of the smallest turbulent aspects of the flow is not required.

In order to ensure that the required fully developed inertial range was provided by the experimental apparatus, characterisation was conducted to map the development of the flow profile along the channel length.

3.3.2 – Water channel characterisation

Velocity and turbulence profiles at a number of points along the length of the channel were measured using Pitot tube and ADV measurements. Profiles were calculated by collecting flow velocity data at 29 vertical points using a sampling frequency of 25Hz and a sample length of 3500 data points, at streamwise positions 1, 3, 5, 7, 9, 11 and 13 metres downstream of the channel inlet. In each case, profiles were recorded at 25% and 50% of the channel width. These point velocity series were then analysed and the mean of each set recorded. For each position, velocity values at each vertical point were then combined to produce a velocity profile for that point. This process was repeated in order to give a series of profiles along the centreline and three-quarter width lines of the channel. Full details of ADV data collection and processing are given in Section 3.4.2.

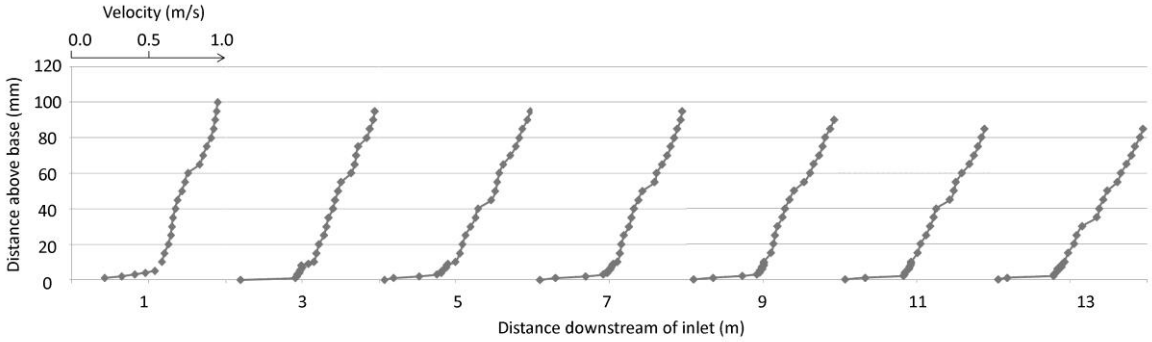

Figure 3-4 – Centreline velocity profiles as recorded during characterisation

The profiles in Figure 3-4 illustrate the development of the velocity profile as the measurement point is moved further from the water inlet. As discussed in Section 3.3.1, in order to meet the criteria for dynamic similarity of flows, the area to be used for measurement must exhibit a fully-developed turbulent boundary layer.

Skin friction is generated by the effect of shear when a portion of fluid experiences different velocities over a separation distance. In the case of a streamlined fluid flow (defined by a large length in the direction of flow relative to a small height) over a static boundary or wall, skin friction is generated in the region above the boundary as the fluid velocity is reduced to zero at the boundary, but remains moving above it. This generates a shear force in the fluid region above the boundary, since each layer of fluid is moving faster than the fluid below it. This shear force between the wall and the first moving layer of fluid is known as wall shear stress *(τ_w)*. From zero velocity at the wall, fluid velocity increases with increasing distance from the wall. The area between the wall and the height at which fluid velocity is first equal to 99% of free stream velocity u_0 is defined as the boundary layer. The height of this layer perpendicular to the wall is known as boundary layer thickness, δ, and is defined mathematically as the height at which:

$$u_\delta = 0.99\, u_0$$

In the case of flow in a channel, boundary layer thickness increases with distance from inlet. The transition from laminar to turbulent flow can be observed through changes in boundary layer thickness. The value of δ grows with distance downstream of the inlet, initially as a laminar flow. Further downstream, boundary layer thickness continues to grow, laminar flow begins to give way to turbulence, and a transitional region is observed. Further still downstream, the flow becomes fully turbulent and the boundary layer thickness continues to grow. During this phase a very small viscous sub-layer can be observed in the near wall region. Eventually, boundary layer growth ceases and a constant boundary layer thickness is maintained downstream. After this constant boundary layer thickness is reached and maintained, the boundary layer is said to be fully developed [46].

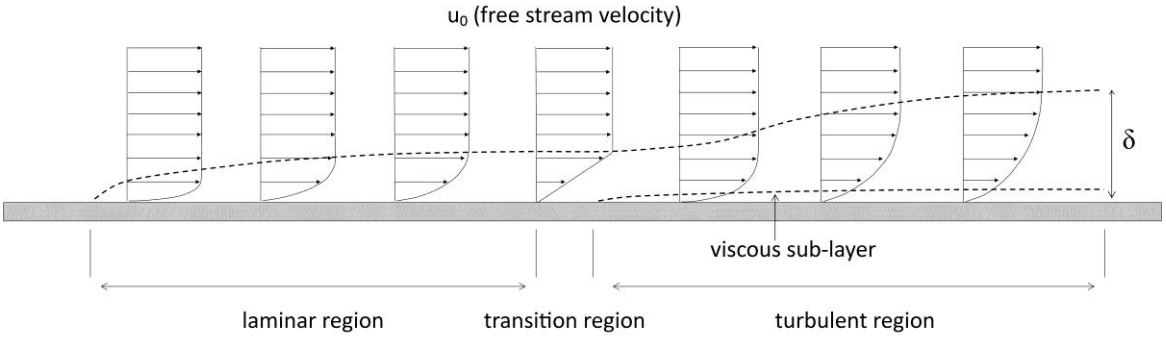

Figure 3-5 – Boundary layer development

Using the profiles illustrated in Figure 3-4, boundary layer thickness was calculated at each characterised point along the channel length, in order to identify the point at which a fully developed boundary layer was first observed.

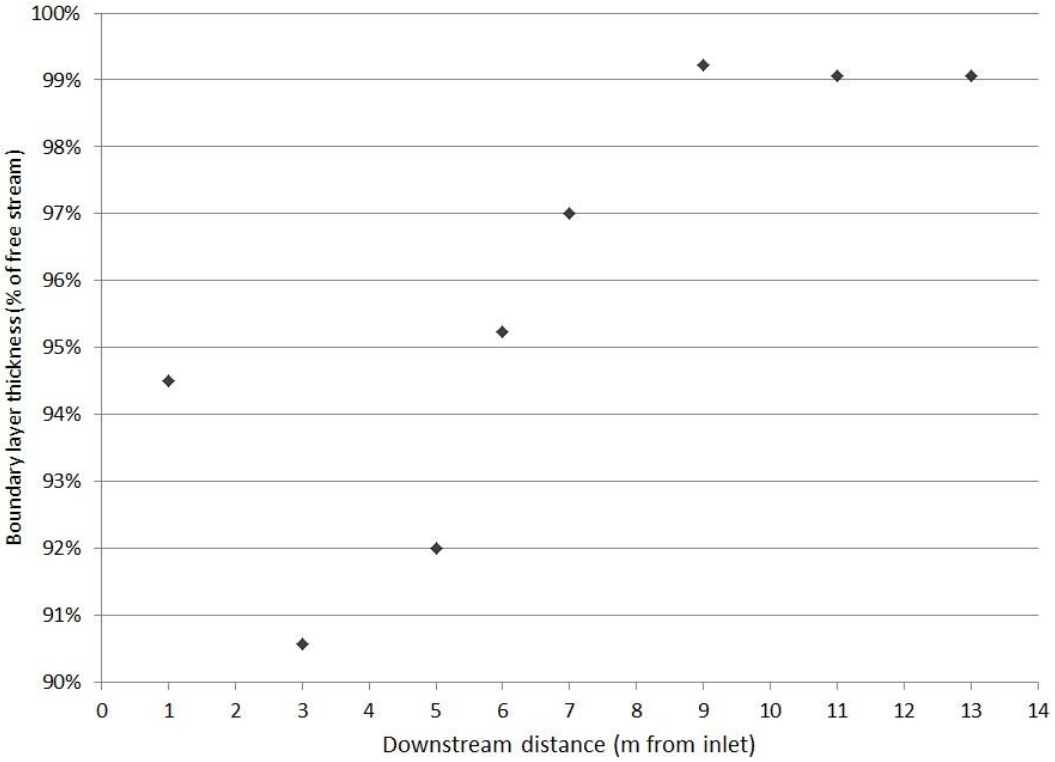

Figure 3-6 – Boundary layer growth along water channel length between inlet and 14m downstream (see note regarding 1m data point).

Figure 3-6 illustrates the development of the flow boundary layer, taken from characterisation data as described previously and as illustrated in Figure 3-4. The data point at 1m appears to be erroneous, since it is unlikely that a boundary layer thickness of 94.5% of flow height would be reached 1m downstream of the channel inlet. The cause of this error is likely to be the disturbance of the top surface of the flow, since this data recording point is less than 1m downstream of the tethered float illustrated in Figure 3-2, which causes a downstream disturbance in the top surface of the flow.

Excluding the 1m data point, Figure 3-6 appears to show the expected growth of a boundary layer and the presence of a constant boundary layer thickness in the region from 9m to 13m downstream of the channel inlet, indicating a fully developed profile within this region. Consequently, this area was used for all subsequent experimental work. Due to the layout of the water channel and the position of flow measurement equipment, the downstream part of the 9m to 13m region was not easily accessible for the installation of turbine models, so a position 9m downstream of the channel inlet was used as the installation point for all experiments using turbine models.

In order to fully understand the flow pattern in this area, additional velocity profiles were calculated at the 9m position over the height of the turbine models. Profiles were calculated at five horizontal positions: Channel centre; centre -125mm; centre –250mm; centre +125mm; centre +250mm. These positions were chosen to give profiles at single and double multiples of turbine rotor diameter (referred to as *1D* and *2D* respectively) to each side of the centre line.

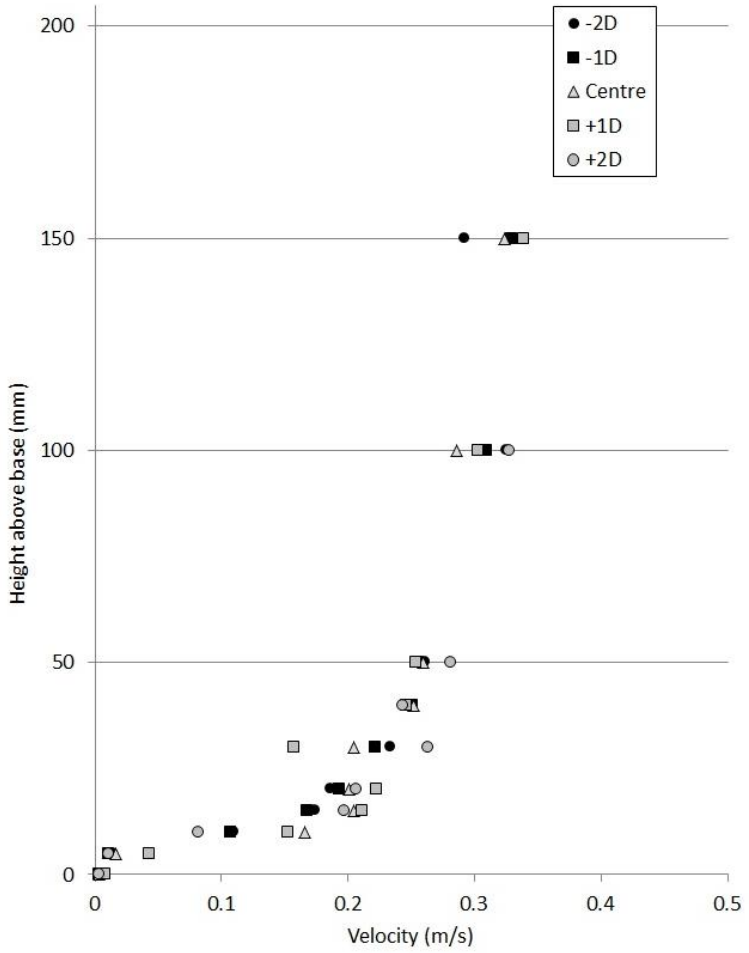

Figure 3-7 – Vertical velocity profiles at -2D, -1D, centre, +1D, +2D, at 9m downstream

Generally, these profiles were found to be similar at each position, suggesting that the side walls of the channel do not influence the velocity profile at distances up to 2*D* from the centreline. This characterisation was important in order to illustrate that any performance difference subsequently identified between turbines located at the channel centreline and the 1*D* or 2*D* positions were not caused by the impact of the channel side walls in an empty channel.

3.4 – Flow measurement

Four different techniques were used to measure flow velocity in the channel during the course of this study. Dye injection was used during preliminary testing, followed by the use of Acoustic Doppler Velocimetery (ADV) which was used primarily during the characterisation phase of the work. Laser Doppler Velocimetery (LDV) was employed during the testing of the surface smoothing plate, and Particle Imaging Velocimetery was used for the major part of the experimental work in this study. The equipment and techniques used in each case and the reasons for their use are described in this section, with the subsequent data processing techniques described in Chapter 4.

3.4.1 - Dye injection

Dye injection was the first flow measurement and visualisation technique employed during this project. The injection of coloured dye or other "tracer" fluids into a fluid flow is a very simple flow visualisation technique, but is useful to understand overriding flow patterns and to produce qualitative flow physics results. The visual element of this method made it particularly suitable for preliminary testing of the channel and initial turbine models since basic properties such as the support structure wake expansion distance could easily be observed. Dye injection was carried out using red food dye diluted with water, which was injected using a 2mm diameter angled tube installed 100mm upstream of the turbine or support structure. Simple analytical tests were carried out to ascertain the optimal concentration of the dye and water mix, and a volume of 30ml dye in 500ml water (i.e. 6%) was found to give clear results. Ratios with lower dye concentration than this were found to make it difficult to see the pattern of the dye, and those with greater concentration quickly led to pollution of the channel water, again making visualisation difficult. The dye injection system as used in this study is illustrated in Figure 3-8 and Figure 3-9. Figure 3-8 illustrates the constant head pumping system which was used to ensure a constant flow rate of dye over the course of each test. This is ensured by the use of a central reservoir from which the dye mixture was drawn, which is surrounded by a deeper reservoir, from which the central reservoir fills, thus ensuring a constant level of dye mixture in the central reservoir. The pump and power supply is also illustrated in this figure. A 12 volt peristaltic pump was used, with an adjustable flow regulation valve on the line between the pump and the injection tube. This control valve was used to deliver dye at the same velocity as the water channel flow in each test.

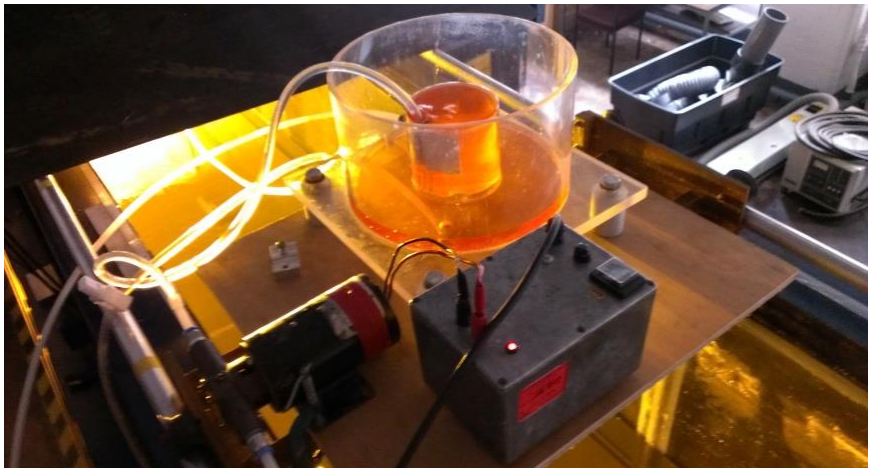

Figure 3-8 – Dye injection system pump and constant head reservoir

Figure 3-9 illustrates the flexible tube used to transfer dye from the pump to the injector tube, and the injector tube mounted in the water channel prior to testing.

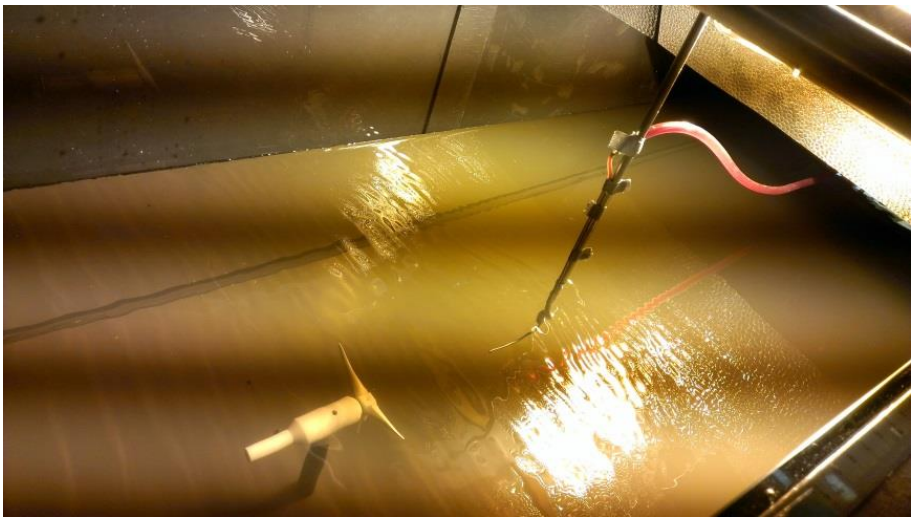

Figure 3-9 – Dye injection system injection tube

Observations of the pattern of dye behind the support structure were used to inform later decisions like the selection of PIV camera field of view, and results were also used during preliminary calculations of primary wake fluctuation modes using Proper Orthogonal Decomposition, which is discussed in detail in Section 4.4.2. Images recorded using this technique are shown, with full results, in Section 5.2.1.

3.4.2 - Acoustic Doppler Velocimetery

Acoustic Doppler Velocimetery (ADV) is a velocity flow measurement technique, commonly used in laboratory and field measurements of water flow. In the case of this study the technique was used primarily during the characterisation phase of the work. The specific device used was a Nortek Vectrino.

The underlying principal which allows ADV to be used as a flow measurement technique is that of Doppler shift, i.e. the effect of a moving object on the frequency of the sound waves it generates, whereby wavelength is shortened as the source moves towards from the receiver, and lengthened as it moves away. The ADV unit is made up of a body containing the control and signal conditioning electronics, a shaft and a head, which incorporates the signal transmitter and receiver. The head unit is made up of a central transmitter and three or four legs, which each house a signal receiver used to measure flow in a single direction, either streamwise, horizontal or vertical (in the case of a head with four legs, two are used in the vertical direction in order to improve accuracy). An acoustic signal of a fixed frequency is transmitted from the central transmitter, transmitted through the moving fluid flow and received by the receiver legs. The difference between the transmission frequency and the received frequency allows the calculation of the velocity of the fluid in each direction. The volume of fluid in which velocity is recorded is cylindrical in shape and of fixed diameter, though its height can be controlled. In the case of the equipment used in this study, the sample volume was 0.05m from the transmitter, and had a diameter of 6mm and a height of 5.5mm [155]. A schematic diagram of a typical ADV system is shown in Figure 3-10.

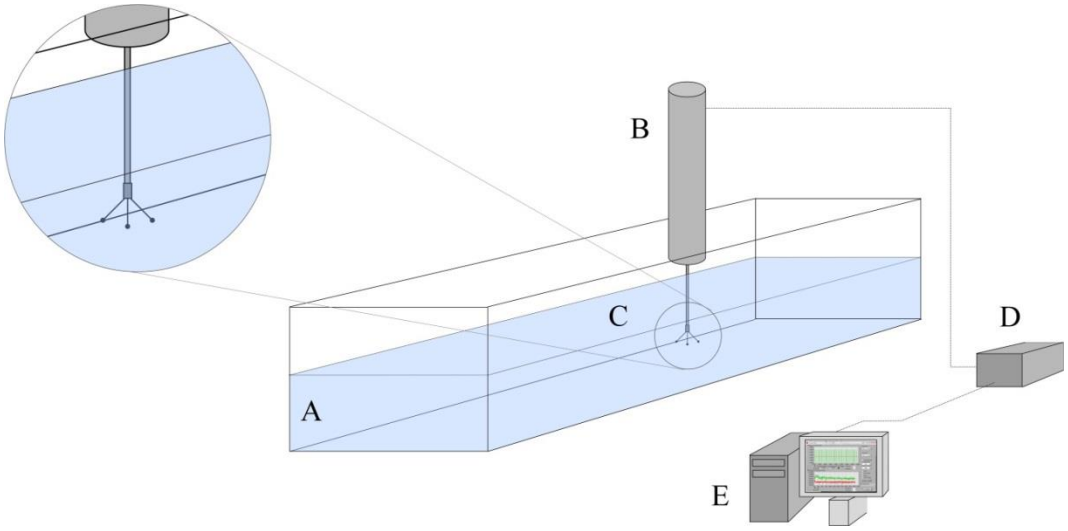

Figure 3-10 – Schematic diagram of a typical ADV system (A: Water channel (not to scale), B: ADV unit body, C: ADV transmitter and receiver unit, D: Power supply, E: Data computer).

ADV is a relatively simple and reliable technique for fluid flow measurement, but does have limitations. The technique requires the head to be positioned in the water flow for measurements to be taken, so measurements close to an object are likely to be influenced by the presence of the equipment. This requirement also means that ADV cannot be used to record flow very close to the water surface, as locating the sample volume just below the surface would require the head to be out of the water.

During the channel characterisation experiments conducted as part of this study, an ADV sample rate of 25Hz was used. This is the maximum sample rate achievable by the Vectrino device, and it was felt that as high a sample rate as possible should be used at this stage in order to capture the flow characteristics fully, since data could be resampled at a later stage if necessary. Since the width of the water channel used was 0.5m, the maximum diameter of flow structure possible within the flow was also 0.5m. At a mean bulk flow rate of 0.2m/s, which is the minimum rate used during subsequent experiments and characterisation, this suggests that the largest eddies which could exist in the channel would take 2.5s to complete one rotation. During characterisation, a sample length of 3500 samples was used in all cases, giving a data recording time of 140 seconds. This time period would allow the largest potential eddies in the flow to be captured 56 times. Similarly to the selection of a high capture frequency, this long sample time was chosen in the knowledge that it could subsequently be resampled or trimmed as necessary and would still contain multiple instances of such flow structures. During final experiments, as described in Section 5, 4500 data points were recorded over a time period of 180s, though due to the processing methodology applied in the software used, the actual number of results processed was the nearest power of 2 value below the actual number recorded, which was 4096. In all cases, a sample volume of 155.5mm^3 (height 5.5mm, diameter 6mm) was used.

The quality of ADV recording can be monitored using signal-to-noise ratio (SNR) and correlation. An SNR value is the ratio of the amplitude of coherent signal responses to that of background noise responses. A value of greater than 15dB is recommended by manufacturers, and is likely to yield results with an uncertainty of around 1% [155]. Correlation values indicate the similarity of two subsequent signals as a percentage, and values of 80% and above are recommended for reliable

results [61]. SNR values of 20dB and above were recorded on all four channels during channel characterisation, and correlation of around 94% on x and z channels, and around 91% in the y direction. A scatter plot illustrating the relationship between correlation and SNR with velocity over 4500 samples (180 seconds) recorded during characterisation is illustrated in Figure 3-11.

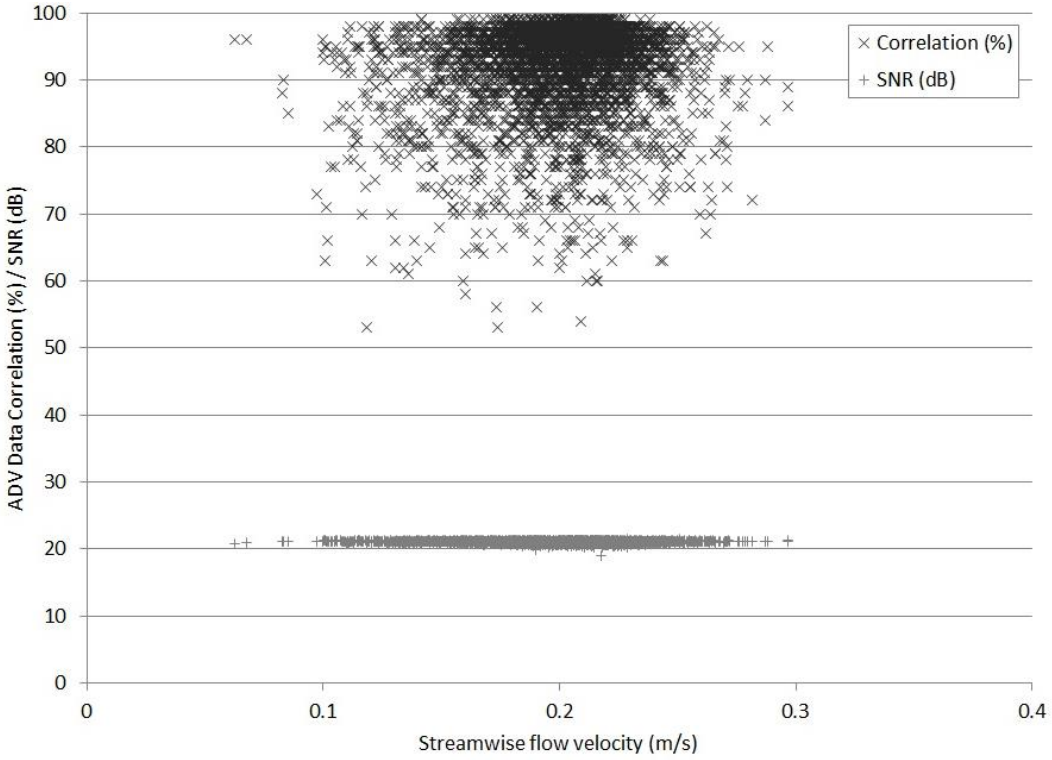

Figure 3-11 – ADV data correlation and SNR results for a sample test.

3.4.3 – Laser Doppler Velocimetery

The principal of Laser Doppler Velocimetery is similar to that of Acoustic Doppler Velocimetery, in that it takes advantage of the Doppler effect, and reflection of an emitted signal is used to ascertain the relative movement of the flow. The underlying principal of LDV flow measurement is the generation of a fringe pattern by focusing the light from two phase-shifted beams a single point. When a seeding particle suspended in the flow passes through the fringe pattern, it will alternately reflect and not reflect the light as it passes through light and dark areas. This signal is received by optics and converted to an electrical signal by a Photomultiplier Tube (PMT), from which the frequency of the signal, f_D, is calculated. Since the fringe spacing, δ_f, is known, this frequency is then used to calculate the velocity of the particle:

$$u = f_D \delta_f,$$

A single laser beam split into a phase-shifted pair is required for the measurement of flow in a single direction, meaning that two or three (in the case of two- or three-dimensional LDV respectively) pairs of beams of different wavelengths of laser light are used in order to measure flow velocity in multiple planes. The principal of the system is illustrated in Figure 3-12.

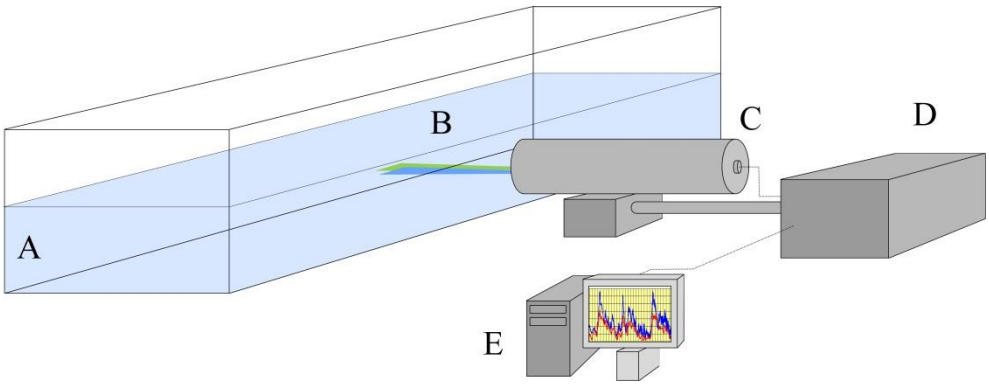

Figure 3-12- Schematic diagram of a typical LDV system (A: Water channel (not to scale), B: Laser beams, C: Laser head unit, D: Beam splitter, control unit and PMT, E: Data computer).

A two channel LDV system was used in this study. The system is made up of a TSI control unit and PMT, Melles Griot 43 Series Argon Ion Laser, TSI Aerometrics beam splitter and TSI remote laser head unit. The laser light generated by the laser unit is split by the beam splitter into two separate channels, giving pairs of green (wavelength 514.5 nm) and blue (wavelength 488 nm) beams. The beams were focused at the horizontal centre of the channel using a pin-hole calibration vane.

The flow was seeded with reflective particles. 20g of silver-coated hollow glass spheres of 5µm diameter were used. These particles have a density of 0.72g/cm^3 [156] giving a seeding density of 3 ppm.

During the surface smoothing plate tests described later in this section, the LDV system was used with a PMT voltage of 800 V and burst threshold value of 100 mV. PMT voltage controls the gain applied to the signal from the photodetector, with a higher voltage giving greater amplification of individual particle response signals. However, since this gain is applied to the signal as a whole care must be taken to avoid using excessively high values, as this will result in background noise signals also being multiplied and distorting the signal. The burst threshold is the value of signal strength at which a signal is recognised by the PMT unit as a viable response, rather than noise. These values were selected iteratively in order to maximise the performance of the data recording, which was monitored using data rate and burst efficiency statistics. Data rate describes the number of signals received by the PMT each second which are above burst threshold strength, and burst efficiency is a measure of the number of these signals to the number of emitted triggers. Guidance for monitoring acceptable levels of both measurements was sought from equipment manufacturers [156]. Finally, a band pass filter was set between 0.03 MHz and 0.3 MHz in order to avoid any erroneous signals outside this range. The range was validated by plotting a frequency histogram during the analysis. The clearly visible bell-shaped curve which was observed confirms that this filter range does not remove any valid data. Data rates of between 180 and 300 Hz and burst efficiencies of around 67% were observed during the surface smoothing plate tests.

3.4.4 – Particle Imaging Velocimetry

In order to achieve acceptable results, the measurement technique chosen for the major experimental part of this study was critical. Requirements of the system to be used included minimal disturbance of the flow, the ability to generate a full velocity field at an instantaneous point in time, and suitable resolution to capture the expected size and turnover time of flow structures generated.

Particle Imaging Velocimetery (PIV) was therefore chosen for this part of the study due to a number of reasons. PIV is non-intrusive (i.e. it keeps disturbances to the flow to a minimum in order to measure it), which is a huge advantage compared to ADV techniques which require a probe to penetrate the water surface. Due this, the use of an acoustic system in this project would undoubtedly distort the flow field in the measurement location, which it was felt was unacceptable. The LDV system described previously is a non-invasive flow measurement technique, but this method is limited to a single point measurement. In order to construct a velocity profile over a horizontal or vertical line a traverse system is required, meaning that measurements at subsequent points are not actually recorded simultaneously. This means that the velocity profile produced does not give a single snapshot of flow conditions at a point, so will not represent transient features such as vortex shedding correctly.

In order to overcome these disadvantages, PIV was employed. PIV is a non-invasive optical flow measurement technique, which allows the capture of multiple instantaneous velocity field images, which through a calibration and processing can be converted to give a time series of velocity fields. The comparison of images with small temporal separation allows the flow over time to be reconstructed numerically, meaning that further data can subsequently be calculated from the velocity field.

Systems can be two- or three-dimensional, with results from the former giving flow fields at a pre-set plane, and the latter giving results over a full three-dimensional region. For the purposes of this study, two-dimensional PIV (2D PIV) was used. 2D PIV uses a laser sheet of small thickness to illuminate a flat plane within a flow field. Seeding particles designed to reflect the laser light are suspended throughout the flow, and cameras placed perpendicular to the laser sheet are used to record images at pre-set time intervals. Laser power, wavelength, frequency, and camera image size, shutter frequency and resolution are all dependant on the flow in question. The size of seeding particles used and the density of seeding in the flow are also highly dependent on the fluid and flow conditions in question. A schematic of a typical 2D PIV system is shown in Figure 3-13.

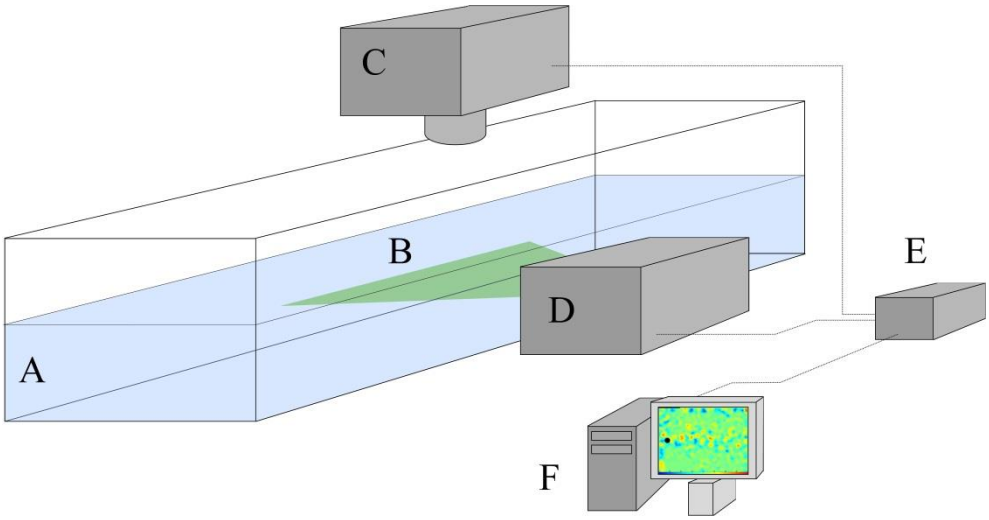

Figure 3-13 – Schematic diagram of a typical 2D PIV system (A: Water channel (not to scale), B: Laser sheet, C: Camera unit, D: Double laser unit, E: Control unit, F: Data computer).

PIV system

The 2D PIV system used in this study is mounted on the University of Sheffield Sediment Transport Laboratory water channel, as described earlier in this section. The laser used in this system is a New Wave Research Minilase III pulsed Nd:YAG laser, mounted horizontally alongside the channel. The laser has a maximum power output of 50mJ and produces green light at a wavelength of 532 nm. As discussed in Section 2.4.2, a combination of spherical and cylindrical lenses was used to generate a horizontal laser sheet. The expansion angle of the laser sheet from the laser head centreline was 13.6°. With the laser head positioned 1.5m from the cross-stream centre of the channel, this produced a laser sheet length of 377mm length at the centreline. The laser sheet thickness at the channel centreline was 2mm. During processing, masking was used to select a Region of Interest (ROI), in order to ensure that only velocity vectors captured in areas with sufficient illumination were used for analysis.

In the University of Sheffield Sediment Transport Laboratory, cameras are mounted on a moveable trolley on rails above the channel, allowing the camera position to be adjustment as necessary. The system incorporates two identical cameras, the simultaneous use of which allows a larger area to be photographed. The majority of experiments described herein did not require this larger field of view, and hence a single camera was used. The cameras used are Dantec Dynamics FlowSense E0 2 megapixel cameras, mounted above the channel, perpendicular to the plane of the laser sheet. Nikon PC-E tilt and shift lenses were fitted to allow fine adjustment of the camera view. The cameras were connected to the PIV control system by National Instruments PCIe-1427 frame grabber units. The PIV system as used is shown in Figure 3-14.

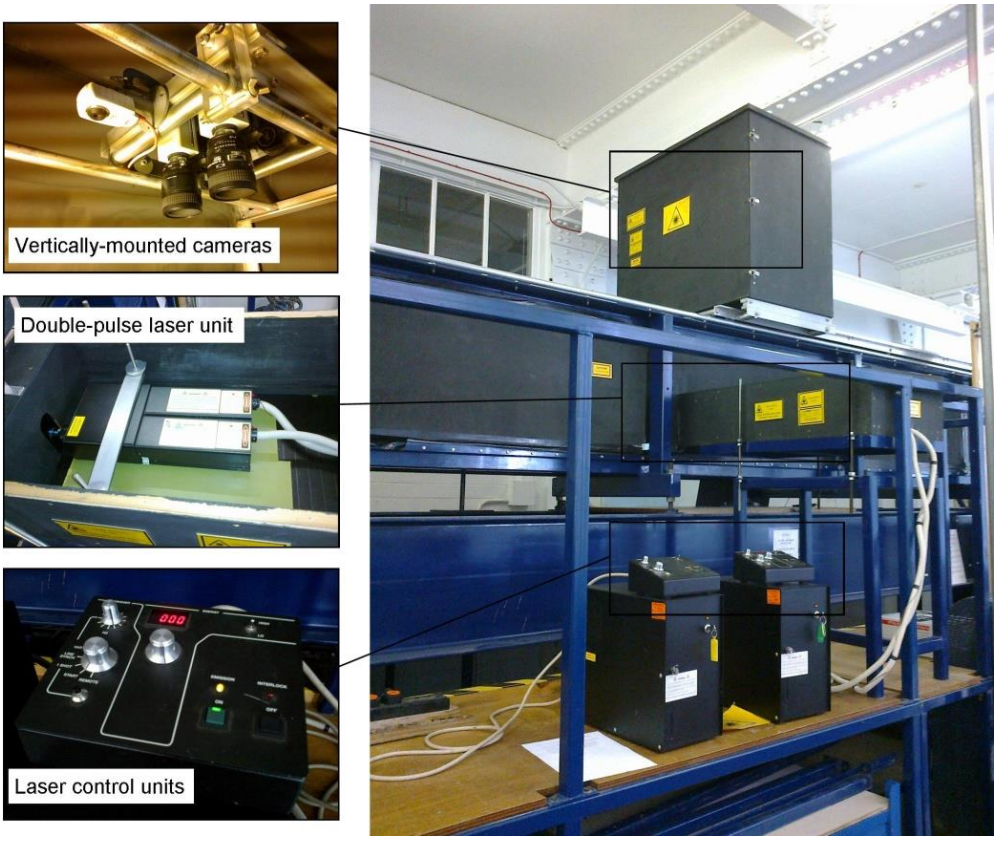

Figure 3-14 – PIV system cameras and laser.

Seeding

As discussed in Section 2.4, the choice of appropriate seeding particles is critical to the success of PIV studies. Seeding particles used in water flow experiments range in size, and a number of different materials are used. Key requirements are the ability of the particle to remain suspended in the fluid in order to accurately represent the bulk flow, and reflectivity of the particles under the laser light used. The former is achieved through the selection of an appropriate particle mass for the flow rate of the fluid, since a heavy particle will fall to the bottom of a slow-moving flow. Reflectivity of particles is greatly enhanced by using a spherical particle. For this study, Talisman 30 particles were used. Though originally designed as a powder coating particle, these particles are commonly used as a PIV seeding particle due to their spherical shape and high reflectivity. The particles have a mean diameter of 100µm [157] and a density of 0.4 g/cm³. In order to confirm the suitability of these particles, the Stokes number *Stk* was calculated, as described in Section 2.4.2. When *Stk* < 1, particles are said to closely follow the flow, with *Stk* < 0.1 yielding tracing errors of less than 1% [66] For the worst case scenario in this project (that is, the case with a maximum value of $\tau\, u_{0,}$ and minimum value of d_c), Stk was calculated to be 0.011.

During experiments, seeding was delivered using a seeding tank and mixer to inject a stream of high-density seeded water at the channel inlet for the duration of each experiment. The system is shown in Figure 3-15.

Figure 3-15 – Seeding mixing tank and injection system.

This system allowed a consistently high seeding density to be guaranteed for each experiment. Seeding densities were analysed by processing captured PIV images and were found to be around 12 particles per 32px x 32px interrogation window, which is in agreement with established recommendations, which state that an average of at least ten particles per interrogation window is required for successful PIV processing [158, 159].

Timing settings

During final experimentation, the camera system was operated in double frame mode, meaning that a pair of images is recorded each time the camera is activated. The double frame technique allows

image pairs to be recorded more rapidly than when a single frame method is used. The method involves two laser pulses and two camera frames. The first laser pulse is activated towards the end of the first camera shutter opening, and a second laser pulse towards the beginning of the second camera shutter activation. This results in two images with a temporal separation governed by the ability of the laser unit to produce two pulses in close succession. The Minilase III is a double pulse laser, meaning that it has two laser units sharing a single set of optics. This system allows the time between the two laser pulses to be reduced in comparison to a single pulse laser by firing the two laser units alternately. Using this double pulse double frame method, the system is capable of capturing image pairs with very small temporal separation.

Optimal PIV image capture spacing is critical to the generation of useful PIV images, and was tested extensively in order to choose the most suitable settings for this work. Variables to be optimised are the total number of images recorded, the temporal spacing between image pairs (as governed by the spacing between laser pulses), and the image size and pixel depth specification.

For the main data collection experiments, 400 12 bit image pairs at 1600 x 1200 pixels were recorded. A trigger rate of 15 Hz was used, and a laser pulse spacing of 10,000µs (0.01s). This resulted in the capture of 15 image pairs per second, with a time gap of 10,000µs between the two images in each pair. The movement of seeding particles during this time period is the basis of the PIV calculation of flow velocity. Using these settings, particle displacement between image pairs of between 10 and 12px was observed in all experiments. This is slightly above recommended levels of between 8 and 10 (see Section 2.8.6), but was selected as the best balance between particle displacement and overall length and frequency of data capture.

A timing diagram of the system is shown in the image below.

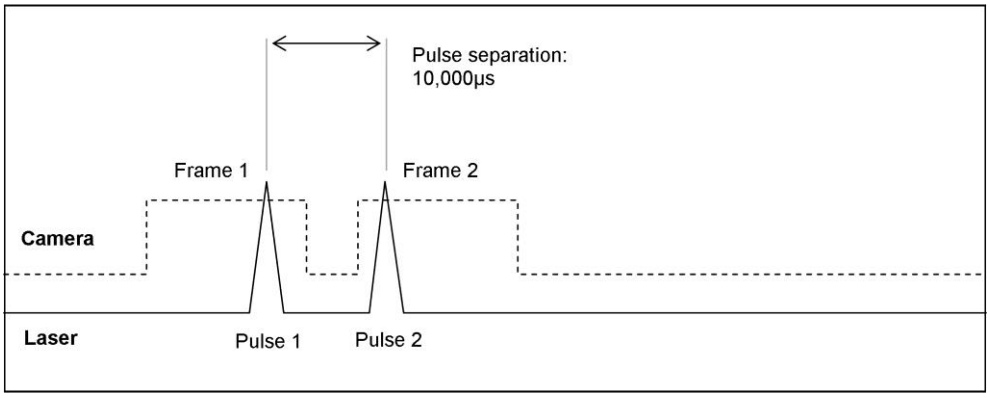

Figure 3-16 – PIV image capture timing diagram.

This timing was found to give a mean particle movement distance between the two images in a pair of around 16px. The displacement of particles between image pairs is an important consideration. If particle displacement between frames is too large, particle pairs are lost since a particle present in the first frame is not present in the second, and its velocity can therefore not be calculated.

Phase locking

In some experimental projects involving turbine rotation or similar situations, PIV data capture can be “phase locked” to the rotation of the turbine, in order that each PIV image pair is captured while

the turbine is in the same rotational position. This method allows mean flow images to be generated with relatively little noise, since the majority of the image remains constant over the series of image pairs. However, by phase locking image capture to the point at which a blade passes the support structure, for example, PIV images will not be captured during the intermediate period between blades passing the support structure, meaning that flow structures generated in this time period would not be captured.

For this reason, and due to practical difficulties in achieving phase locking in the case of multiple turbine studies, PIV results in this project were not phase locked.

3.4.5 – Surface smoothing plate

During preliminary PIV measurements, it was found that ripples on the top surface of the water generated by the motor drive shaft led to distortion in the images recorded by PIV cameras. The ripples generated radiating areas of interspersed high and low water height (above and below the mean water level). This distortion resulted in PIV particle movement being overestimated in areas of the flow with raised water levels above them, and underestimated in areas with water height below the mean. In order to avoid these ripples it was proposed to suspend a transparent plastic plate on the surface of the water in the measurement area, in order to smooth the top surface of the flow and remove the measurement error. Such a plate was designed and constructed, and is shown in Figure 3-17.

Figure 3-17 – Transparent surface smoothing plate in situ.

Prior to commencement of experiments, tests were carried out with and without the surface smoothing plate in order to understand its influence on the flow, to ensure that its use would not modify the flow regime in the measurement location. These tests were conducted using a Laser Doppler Velocimetery (LDV) system mounted on a vertical traverse. The system was used to measure a vertical velocity profile at the centreline of the channel, at 9m downstream of the channel

inlet. Velocity data was recorded at 20 vertical positions between 20mm and 286mm height, in a water depth of 300mm and *Re* value of 5.4 x10^5.

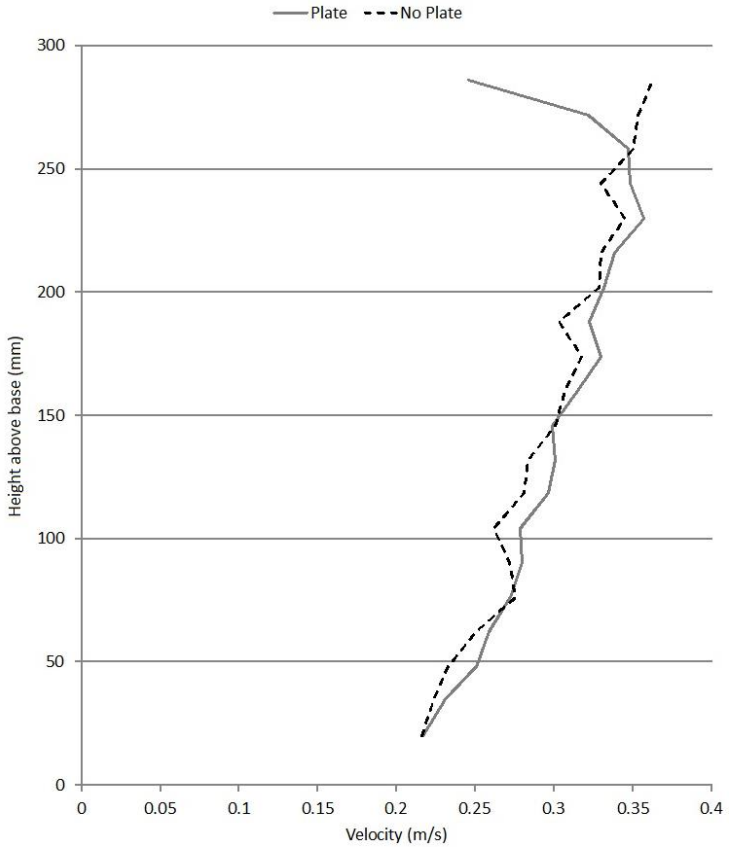

Figure 3-18 – Comparison of flow velocity with and without surface smoothing plate.

As illustrated in Figure 3-18 above, the influence of the smoothing plate on the flow velocity appears to only be significant at the top surface of the flow. Excluding the top two recording positions (272mm and 286mm), the mean percentage difference between the flow velocities in the two cases is 3%. Since the velocity profile shape remains similar, and the turbine location area is well below the top area where the difference is seen, this was deemed an acceptable difference.

3.5 – Turbine models

3.5.1 – Introduction

This study used instrumented and non-instrumented turbine models. These models allowed the measurement of turbine power and torque data, which in conjunction with flow data captured using the methods described previously, allowed a complete data set to be constructed, which was necessary in order to investigate the research aims identified in Section 2.10.1. By combining flow and turbulence data with turbine performance data for the same experimental case, the relationship between the two can be fully understood. In order to generate useful turbine performance data, numerous initial models were constructed and tested before an optimal solution was reached.

3.5.2 – Blockage

When testing models in a wind tunnel, water channel or similar experimental equipment, blockage is an important consideration. The principal of blockage has been discussed in Section 2.2.4, and the low blockage ratios expected at real tidal installation sites (0.1% and 0.5% [38, 86]) has been highlighted. As discussed in Section 2.2.4, blockage ratios of this order are unachievable in scale model testing, so guidance on acceptable blockage conditions was sought from previous experimental studies.

Numerous studies using model tidal turbines have been conducted by the University of Minnesota's St. Anthony Falls Laboratory [53, 140, 160] and the Sustainable Energy Research Group at The University of Southampton [139, 161, 162], yielding blockage ratios between B = 5% and B = 17%. Work by these institutions illustrates that at these blockage ratios, the walls of a channel do not significantly influence the flow around turbine models. These values were therefore used as a guide in defining acceptable limits for simple blockage ratio in this study. Blockage ratio was also assessed experimentally during the testing of actuator disk models, as described in Section 5.2.1.

In addition to simple blockage, blockage factor (*BF*) as proposed by Liou [55] was also considered. This method allows the calculation of correction factors which can be used to correct calculated values of power coefficient C_p and tip speed ratio λ to account for blockage, based on the ratio of free stream and blockage-affected flow speed (U_F and U_T respectively). The method was applied to actuator disk results as described in Section 5.2.1, where U_F = 0.3 and U_T = *0.306*, giving a proposed maximum C_p correction factor of 1.19 and a maximum λ correction factor of 1.06.

3.5.3 – Actuator disks

Prior to the use of any scale turbine models, initial testing was carried out using actuator disks. The primary purpose of this testing was to confirm the suitability of the proposed blockage ratio limit by comparing the free stream velocity of an empty channel to the free stream velocity observed around an obstruction with a similar blockage ratio to that proposed for later models.

As discussed in Section 2, actuator disks are commonly used in the modelling of wind and water turbines as they provide a simple method to represent the velocity deficit and wake caused by a turbine, though since they are static they do not include any wake structures due to blade rotation. Three porous stainless steel wire mesh disks of diameter D = 105mm were used, with porosity 0.34, 0.39 and 0.45 (i.e. open areas of 34%, 39% and 45% of the disk area) and a blockage ratio of 5.8% in all cases. The disks were installed on the cantilever thrust measurement arm and positioned in the centre of the channel, 9m downstream of the channel inlet, with the disk centre located at a height of 100mm above the channel base. Above the level of the water surface the arm was connected to two ball bearings held in a mounting clamp, which allowed the arm to pivot. Above the bearings, a shorter arm extended was connected to a load cell, which measured the force applied to it by the arm. Flow velocity was measured using the ADV system described previously, positioned at separation distances from the disk of 3D, 5D, 10D, 15D and 20D downstream and 3D upstream, with thrust measurements recorded simultaneously. The thrust measurement system used incorporated a cantilever arm and a load cell, as shown in Figure 3-19.

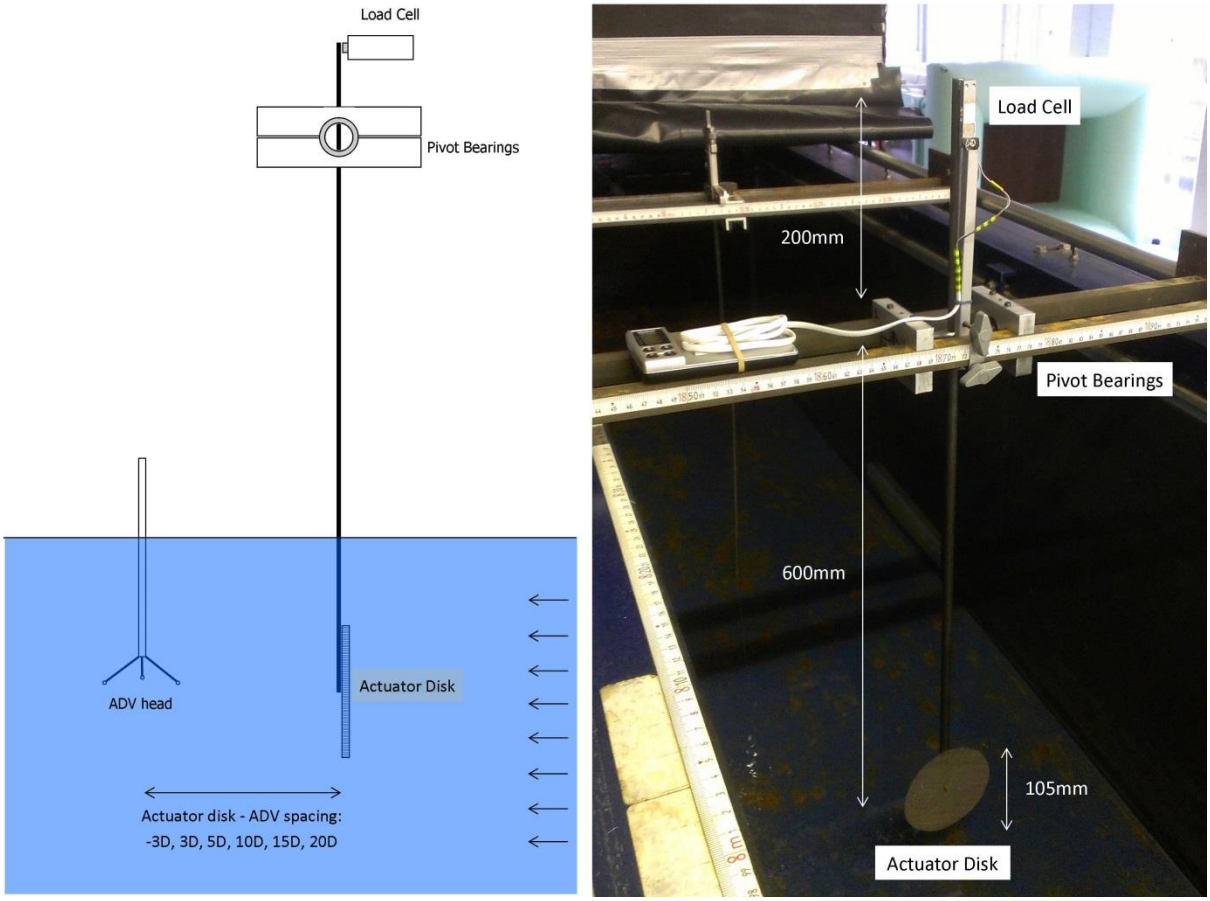

Figure 3-19 – Schematic diagram and photograph of actuator disk and thrust measurement apparatus.

The load cell used in this system recorded the load applied to the cantilever arm by the thrust on the actuator disk for each experiment. The load cell used was taken from a digital weighing scale (Model Smartweigh SWS1000), and had a resolution of 0.1g and a maximum load of 1000g. Measurements in grams were initially taken, then calibrated to give disk thrust. This was then multiplied by the ratio of the cantilever arm length above and below the pivot to give the thrust experienced by the disk itself. The cantilever arm was manufactured from 6mm diameter steel rod in order to ensure that no bending of the arm would occur under the thrust applied to the disks. Load readings were in the region of 60g, giving a potential error of 0.17% based on the 0.1g resolution.

For each of the three disks, a separate set of experiments was carried out. Initially, the ADV unit was placed at six streamwise positions, in line with centre of the disk. Firstly, a position 3*D* upstream was used to measure free stream flow conditions without the interference of the disk, following which positions at 3*D*, 5*D*, 10*D*, 15*D* and 20*D* downstream were used. Following these centre line measurements, the positions were then repeated at 0.5*D,* 1*D* and 1.5*D* horizontal spacing in both directions from the channel centre line. A schematic diagram of the positions used is illustrated in Figure 5-10 (Section 5.2.1). Full results of actuator disk experiments can also be found in Section 5.2.1.

3.5.4 – Initial turbine models

Prior to the construction of the final turbine models used in this study, prototype model turbines were constructed in order to test the proposed design. In order to minimise cost and time requirements, these models were constructed from mild steel, and simple “paddle” blade geometry was used. The central shaft of the turbines was supported on two 8mm internal diameter roller bearings, with the central hub mounted onto the shaft and held in place with a grub screw. However, the alignment of the shaft through two sets of fixed bearings proved difficult, and it was decided that subsequent turbine models would use a less rigid method of fixing the central shaft in place.

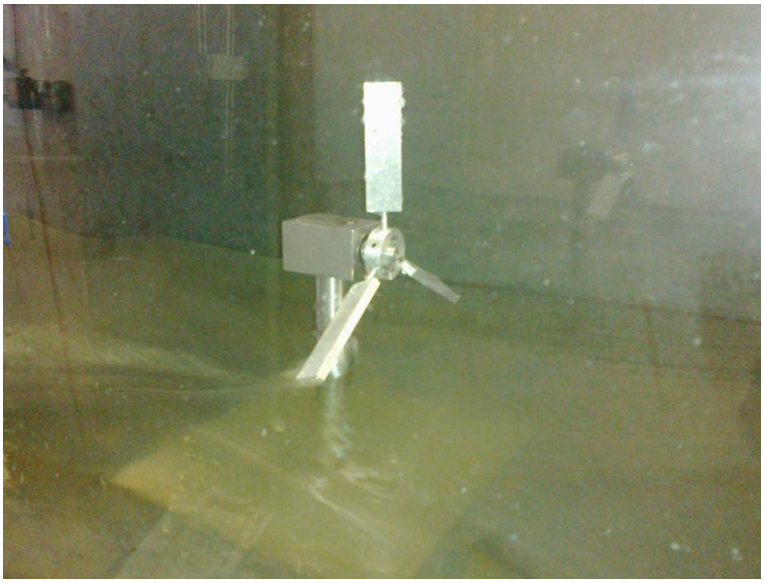

Figure 3-20 – Initial turbine model.

Initial turbine models also highlighted that the mounting base of the turbine was a critical part of the design. The initial turbine model used a relatively small base plate of 5mm height, with an upstream distance of 150mm. It was noted during preliminary testing that the front edge of this plate caused turbulence at high flow rates, and it was therefore decided that subsequent models would be mounted on a large false base plate in order to ensure that a fully developed boundary layer would exist at the location point of the turbines.

3.5.5 – Final turbine models

Turbines were mounted on a false base installed in the water channel in order to allow accurate positioning of the models. The support structure posts were fitted with threaded shafts, and were screwed into threaded holes in the false base, allowing turbine position and spacing to be adjusted as required for the planned experiments. The geometry of the false bases used is illustrated in Figure 3-21 and the turbine models and the false base are shown in Figure 3-22.

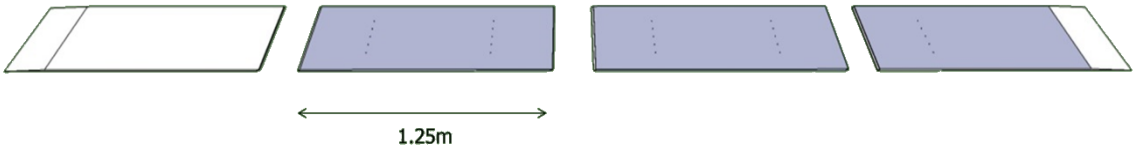

Figure 3-21 – CAD image of false base panels used for turbine mounting.

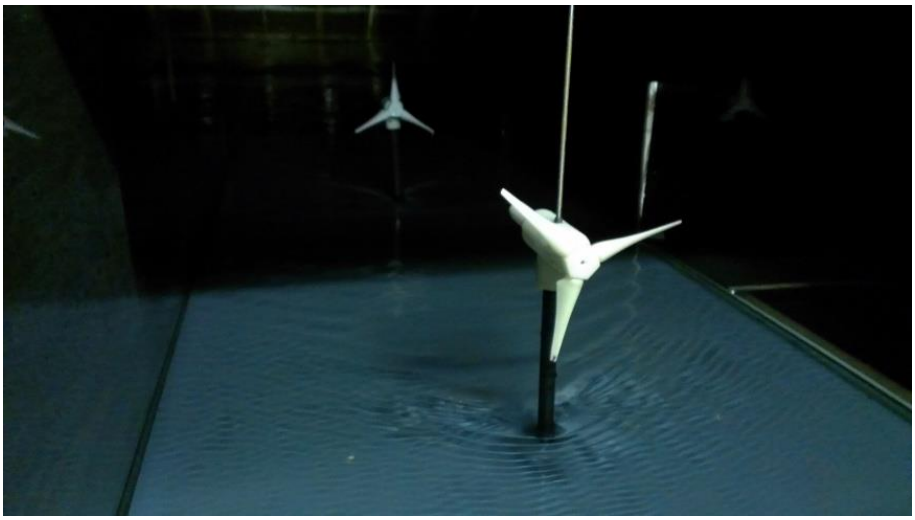

Figure 3-22 – Final turbine models mounted on false base.

The false base was designed to take up the full horizontal width of the channel. A total of five panels were installed, with a 2m section upstream of the first turbine in order to ensure that the step at the edge of the first panel did not influence the flow profile in the measurement area. Similarly, panels were installed downstream of the final turbine installation position in order that the flow behind a second turbine was not influenced by the end of the false base section. The flow profile was measured during characterisation with and without the base panels in position in order to confirm that the position of either end of the panels did not influence the flow profile in the measurement area. A chamfer was also applied to the front and back of the first and last panels to help ensure this. The panels were 10mm deep and were manufactured from PVC sheet.

The models used for the final study were based on the design of a commercial tidal turbine, using data and geometry supplied by Alstom Renewable Power. The turbine models were designed at 1:143 real scale, giving a turbine body length of 119mm and diameter of 24mm, a blade diameter of 125mm and a blade hub height of 135mm. The model turbine body, blades and hub were manufactured by Selective Laser Sintering (SLS). SLS is a rapid prototyping method in which parts are manufactured by using a CO_2 laser and mirror system to melt nylon powder. Parts are manufactured in layers of 0.1mm, which fuse together during the process to give the resulting complete part. The turbine body was manufactured in two parts in order to allow the installation of a bevel gear system and bearings inside the unit, to allow the connection of the blades and the turbine drive motor and speed measurement encoder, which were mounted vertically above the channel. The turbine blades were mounted onto the hub unit, which was then fitted to a 3mm diameter stainless steel shaft. Small flat sections were added to the root of the blade to allow the setting of blade angle, and blades were attached at a fixed angle of attack (AoA or α). As discussed in Section 2.5.2, tidal turbine blades are generally twisted, so blade pitch angle β was reduced with length to give a fixed α value

over the blade length. As discussed in Section 2.5.2, α defines the angle between the blade chord and the resultant flow velocity experienced by the blade due to the incoming flow and the rotation of the turbine. A value of α = 6° was used, as illustrated in Figure 3-23. This value is in line with that used by commercial developers [109, 113]. At the time of writing, the real device upon which the models were based incorporates a pitch control system to allow adjustment of AoA during generation, but it is commonly suggested that tidal energy device designs as a whole must undergo a technology simplification phase in the near future in order to reduce cost and increase lifespan, and that pitch control may be removed from devices in favour of simpler fixed pitch blades. Consequently, it was not felt that the additional complexity of varied blade AoA was necessary in this study.

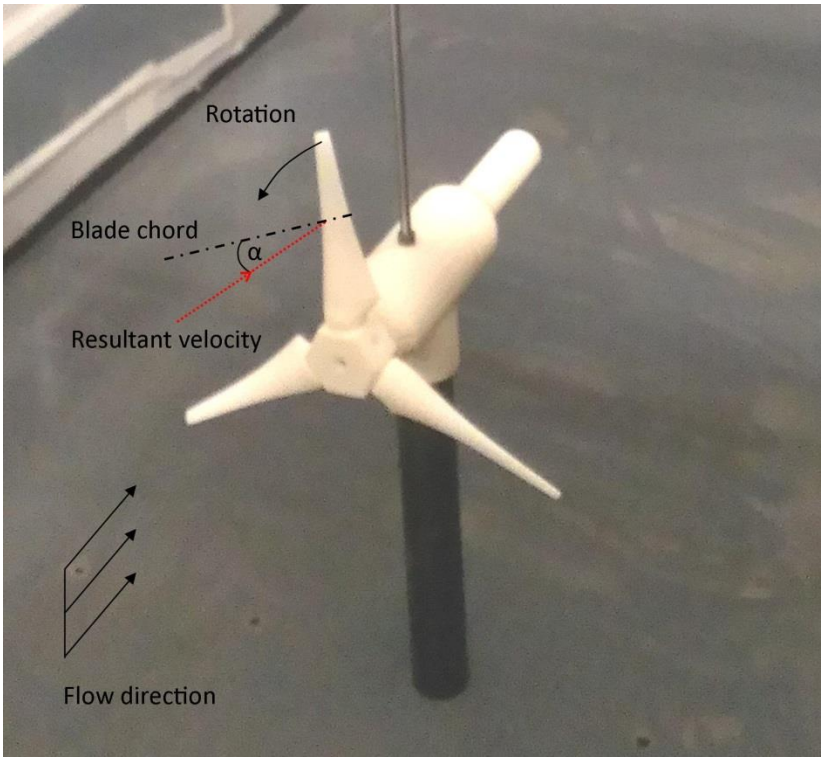

Figure 3-23 – Photograph illustrating 6° angle of attack used in turbine model tests.

Polymer plain bearings were fitted to the turbine body to support the shaft, and the horizontal bevel gear was mounted on the shaft by a stainless steel mounting collar. A vertical shaft ran through another plain bearing on the top of the turbine body and was connected by a flexible coupling to the turbine drive motor, mounted on a moveable trolley above the channel. This method of power take-off and external measurement was used in preference to the internal measurement system employed in other studies [140] as it allowed the turbine body to be constructed at the same scale as the blade unit, which would not have been possible with internal instrumentation. The body of the turbine was designed to allow the planned experiments to take place, so was constructed to allow the support structure to be mounted to the body at one of five different positions, so to adjust the distance between the support structure and the turbine blades. The final design of the turbine models used in this study had a simple blockage ratio of B = 7%.

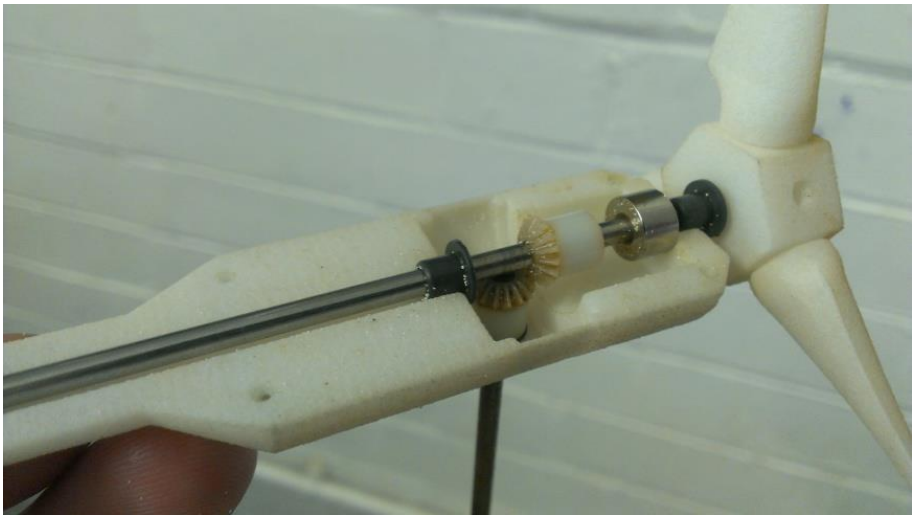

Figure 3-24 – Top section of turbine body with bevel gear system.

The support shafts were manufactured from Nylon 66 Polyamide rod, an engineering polymer with a high hardness, allowing it to be very accurately machined [163]. The material is manufactured by extrusion and then annealed to give it a smooth surface. The rods used for support structure were then machined at the top and bottom to allow mounting to the turbine body and false base. Nine diameters of turbine support structure were tested (6, 8, 11, 14, 16, 18, 20, 22 and 25mm diameter), each with a height between the false base and turbine body of 110mm.

3.6 – Turbine performance measurement

The accurate measurement of turbine performance formed a critical part of this study. In order to provide sufficient data for the correlation of turbine performance and flow characteristics, it was critical to gather data on turbine power and torque output under a wide range of experimental conditions. In order to achieve this, the turbine models used for the main part of this work were driven by a Como Drills 12v drive motor (part number RE-385) [164] via an electronic current sensing module (Allegro MicroSystems, Inc.: part number ACS712) [165], and the drive system coupled to an infra-red rotary encoder (Hobby Components: part number HCMODU0025) to measure speed. The turbine rotation direction was anti-clockwise (when looking towards the turbine from a downstream position, as in Figure 3-22) in all cases. A Rapid Electronics variable power supply unit (part number 85-1902) was used to drive the motor at a constant voltage in each test, in order to operate the turbine at a known rotational speed, as measured during no-load tests. In all cases, the mechanical losses in the drive system were greater than turbine generated power, meaning that (when connected to the drive system) the turbine would not rotate without the assistance of the motor.

The motor drive system was used to calculate the turbine-generated power. During each test, motor voltage was noted and subsequently multiplied by measured current to provide the instantaneous power supplied to the drive motor. Rotational speed was also recorded using the encoder, meaning that the torque applied to the turbine could also be calculated. The current measurement module and encoder were connected to a desktop computer using a 12-bit LabJack U12 USB DAQ (Data AcQuisition) unit. The layout of the turbine data acquisition system is shown in Figure 3-25. Further details of the acquisition and processing of data from the encoder and current sensing module are given in Section 4.5.

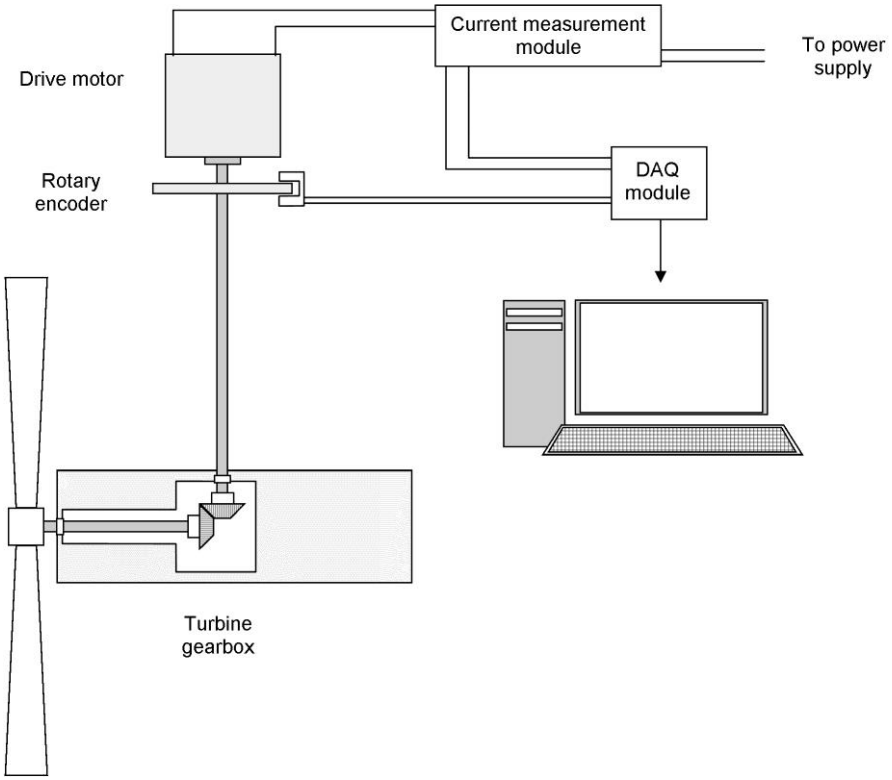

Figure 3-25 – Sketch of turbine drive and data acquisition system layout.

The method applied to ascertain the power generated by the turbine can be thought of as the calculation of the contribution of the turbine-generated power to the overall power required to rotate the turbine at a known speed, with the remaining power supplied by the drive motor. Though the power generated by the turbine was insufficient to overcome the losses in the drive system, any power generated by the turbine was found to reduce (in the flow cases studied) the motor power required to rotate the system at a given speed.

In order to measure this turbine-generated power, the power supplied to the motor must be known, alongside the rotational speed of the turbine, and any losses which must also overcome.

In the majority of experiments, power supplied to the motor was controlled by adjusting the supply current in order to give the rotational speed required (in the majority of cases, 9 rad/s for case 1 tests, and 10 rad/s for case 2 tests, corresponding to approximately 86 and 95 revolutions per minute) as measured by the rotary encoder. This produced respective values of Tip Speed Ratio of λ = 3.5 and λ = 3.1 for the two flow rate cases used, as discussed further in Section 5.1.2. The power supplied to the turbine by the drive motor was calculated from the voltage applied by the power supply and the current measured by the current module. The voltage value remained constant throughout each test, so was recorded manually, whereas due to minor fluctuations over the duration of experiments, the current recording module was used in preference to manually recording the applied current. The resulting value of power supplied to the motor is the power required, in addition to any power generated by the turbine itself, to rotate the turbine at a known speed. This value was known as P_{appB}. The power supply module and drive system are illustrated in Figure 3-26.

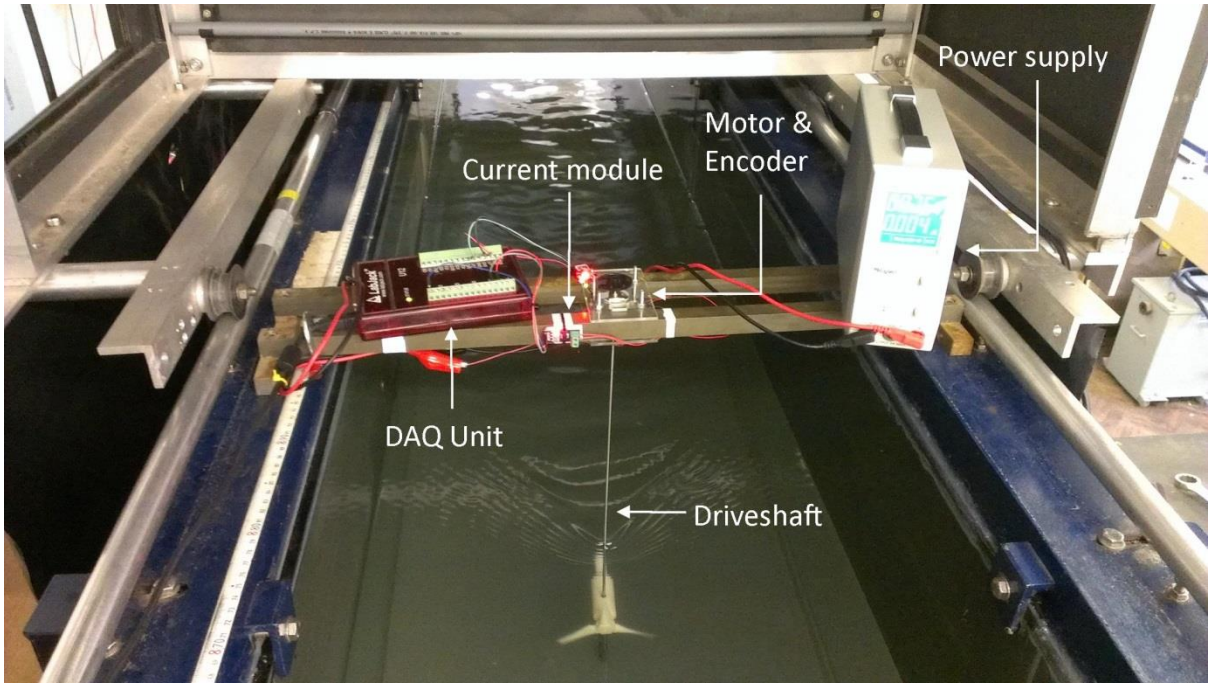

Figure 3-26 – Labelled experimental setup illustrating power supply unit, drive system and current and speed measurement.

In order to isolate the power generated by the turbine itself, the same recordings we re-calculated for an otherwise identical case using a turbine without blades. This time, the power supplied to the drive motor (P_{appNB}) was not assisted by any turbine-generated power, so provided that the turbine in the previous case made a positive contribution to the overall power, the applied power in the case without blades would be greater. Having measured these two power values, it was then possible to deduce the contribution of the turbine blades to the rotation in the first case by finding the difference between values of motor power in the cases with and without blades (P_{appB} and P_{appNB} respectively), thus giving the power generated by the turbine blades as follows:

Blade Power

$$P_B = P_{appNB} - P_{appB}$$

Though not previously applied to tidal turbine models, the method is similar to that used by Edwards [166], who used a “spin down” method to ascertain the blade torque of a vertical axis wind turbine.

The deduction of P_{appB} and P_{appNB} in order to calculate the overall turbine-generated power also removes the influence of any power losses within the motor and drive system, since these losses would be almost identical in the two cases and would therefore cancel out. The only potential difference in the power losses between the two cases would come from additional loading on the bearings within the turbine model due to the presence of the blades. In order to ascertain the influence of these loads on the power calculation, additional tests were performed to measure the minimum power required to drive the turbine with and without the blades in place, under otherwise identical conditions. These tests were carried out with the turbine and drive system installed in the water channel, but without water in the channel. Such measurements were taken by driving the turbine at a relatively high speed, then reducing the applied power until the minimum power required to sustain rotation was found, thus ensuring the measurement of dynamic loading. In the cases tested, the variation in minimum power to achieve rotation of the turbine with and without

blades was found to be 0.002% of P_B. Since this value is below the threshold of accuracy of the measurement equipment, it was thus deemed negligible and system power loads were henceforth assumed to be identical in the two cases. From the calculated value of P_B, blade generated torque can also be calculated, as follows:

Blade Torque $$T_B = P_B \omega$$

Potential sources of error produced by this method of measurement and calculation are considered below.

3.6.1 Blade power measurement errors

The measurement of turbine blade generated power using the method described above yields a potential source of experimental error. The rotational speed of the turbine and the resulting drive power depend on the frictional loading on the turbine, drive shaft, and mounting system. These loads will be increased by the presence of additional sources of friction in the system, the most likely occurrence of which is due to any vertical misalignment of the driveshaft. During the installation of turbine models (a process which was conducted as few times as possible in order to reduce the introduction of such errors) care was taken to ensure that the turbine drive shaft was as close to perfect vertical alignment as possible, and thus that additional frictional loads on the drive motor were as low as possible. This was achieved using a spirit level during installation to measure the angle of streamwise and cross-stream lean of the driveshaft, and by careful movement of the motor mounting until the spirit level indicated that the driveshaft was vertical. Following this installation, the turbine was not removed or the position of the motor or driveshaft adjusted between cases with and without blades in each experiment, so any additional friction which did exist in each case would be present in both cases, and would thus be removed by the calculation of P_B from P_{appB} and P_{appNB}. However, it was important to minimise this error as much as possible, since if any additional loading was not constant (i.e. due to a misalignment an additional load may be applied to the motor over only part of the rotation), this may not be removed during the subsequent calculation.

Turbine driveshaft misalignment error calculation

The potential for error due to misalignment of the turbine driveshaft was estimated based on the maximum misalignment possible while the spirit level indicated that the shaft was vertical. It was measured that when the 300mm spirit level was misaligned by 1mm between top and bottom, the level indicator showed that it was vertical, however when misaligned by 2mm the level indicator showed a misalignment. Hence a conservative value of maximum misalignment of 2mm was assumed. In order to quantify this in terms of power applied to the turbine, a test was conducted whereby the motor position was moved 2mm in the streamwise direction from a position used for previous experiments (and therefore believed to be correctly aligned). The power required to rotate the turbine with blades in place at 9 rad/s was measured in both cases, and was found to yield a difference of 5mW. This error, if measured in only either the with blades or without blades case (if measured in both the with and without blades cases, the error would cancel out and would not be carried forward to the power coefficient or torque calculations), would result in the blade generated power recorded being 5mW greater or lower than the actual value. Assuming that this maximum error was recorded in the case with the lowest value of blade generated power in subsequent

experiments (around 22mW); this would yield a worst case error of 23%. In the case of the mean generated blade power recorded during phase 3 tests (55mW), the potential error due to the maximum estimated misalignment of 2mm would be 9%.

Further potential errors relevant to each phase of results are described in the appropriate sections within Chapters 5 and 6, as well as an overview of potential experimental errors given in Section 4.6.

4

Data Analysis

4.1 – Introduction

This section describes the processing of data acquired via a range of methods, including fluid flow data acquired using Laser Doppler Velocimetry (LDV) and Particle Image Velocimetry (PIV) techniques, as well as turbine torque and speed data.

The bulk of fluid flow data recorded during this project was acquired using PIV, and hence a detailed description of the control systems and data processing applied to this data is provided. The fundamentals of PIV as a technique are discussed in Chapter 2, and the equipment used in the application of the technique to this project is discussed in Section 3.4.4.

4.2 – PIV system control

A Dantec Dynamics 2D PIV system was used in this project, as described in Section 3.4.4. A schematic diagram of a system of this type is illustrated in that section. The system was controlled by a desktop computer (Intel® Xeon® CPU E5-2630 0, 2.30GHz) via a Dantec 80N77 Timer Unit, connected via a National Instruments PCI-6602 PCI Interface. Image acquisition was controlled by a National Instruments PCIe-1427 frame grabber. A schematic diagram of the control system employed is illustrated in Figure 4-1.

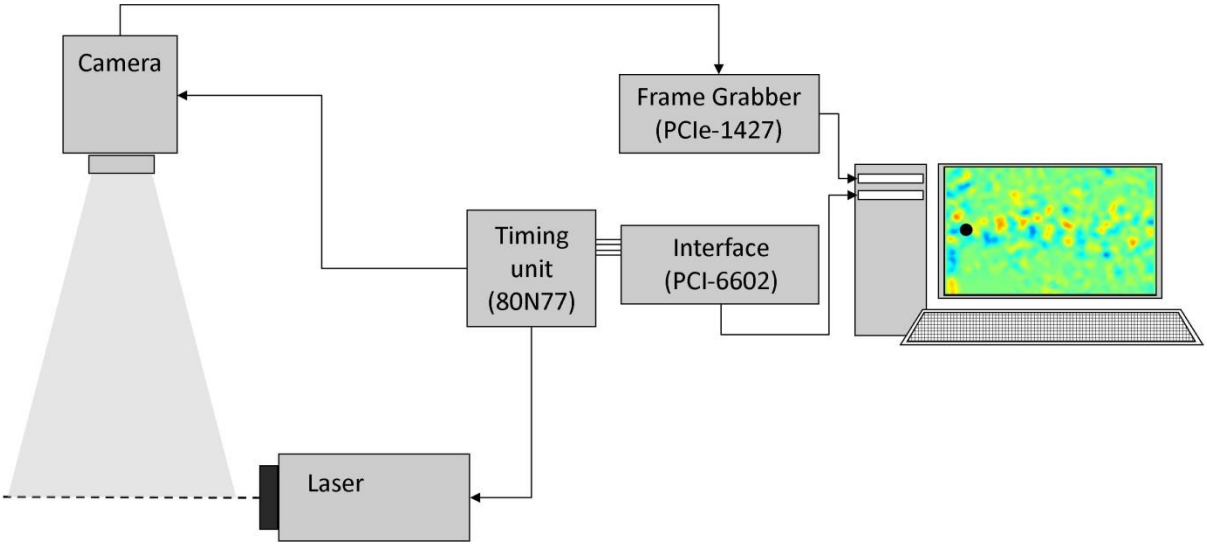

Figure 4-1 – Schematic block diagram of PIV system used in this study.

4.2.1 – Timing settings

The same timing settings were applied to the majority of experiments. As has been described in Section 3, the New Wave Minilase III laser was operated in double pulse mode, giving 400 12 bit image pairs at 1600x1200 pixels, recorded using a Dantec Dynamics FlowSense E0 2MP camera.

Trigger Rate & Pulse Spacing

A trigger rate of 15 Hz and a laser pulse spacing of 10,000μs were used, giving 15 image pairs per second, with a time gap of 10,000μs between the two images in each pair. After testing both lower and higher trigger rates and shorter and longer pulse spacing times, the chosen values were found to

give the best balance of particle displacement between images (around 12px) and the length of the overall data set captured. Capturing 400 images at these settings gave a total recording period of 26.6 seconds, which was sufficiently long to capture multiple turnover periods of the largest eddies expected in the flow. The turnover time of the largest eddy able to be sustained in a channel flow can be calculated from the bulk flow velocity of the flow and the maximum cross-sectional dimension of the channel, as follows [167]:

$$t_L = \frac{L}{U}$$

Hence, for a channel of 0.5m width, with a bulk flow velocity of approximately 0.3m/s, the maximum eddy turnover time expected is around t_L = 1.7s. By capturing images over this 26.6 second time period, multiple instances of these eddies can be observed. However, a balance must be sought: A relatively long time period allows the capture of multiple instances of the largest eddies, but a high frequency of image capture is required in order to capture the smallest eddies. As discussed in Chapter 3, energy dissipates through smaller and smaller eddies, until eventually reaching the smallest sustainable eddy size. The smallest eddies in a flow are the Kolmogorov Microscales. Energy from these microscales is then dissipated as heat when they collapse.

The size of the Kolmogorov microscale (η) in a flow can be calculated from the kinematic viscosity ν and energy dissipation rate ε of a given case, as given by:

$$\eta = \left(\frac{\nu^3}{\varepsilon}\right)^{\frac{1}{4}}$$

In order to calculate η we therefore require an estimated value of turbulent energy dissipation rate. This can be estimated using two assumptions: Firstly, that the kinetic energy dissipation rate is the same as the kinetic energy supply rate, and secondly that the kinetic energy supply rate is proportional to the inverse of the largest eddy turnover time (t_L as described above). Thus the turbulent kinetic energy can be estimated as the kinetic energy in the flow (the square of the flow velocity: U^2) multiplied by the inverse of the largest eddy turnover time (U/L). Thus:

$$\varepsilon = \frac{U^3}{L}$$

The Kolmogorov microscale turnover time can be calculated from the turbulent kinetic energy and the kinematic viscosity of the flow thus:

$$t_\eta = \left(\frac{\nu}{\varepsilon}\right)^{\frac{1}{2}}$$

Using these equations, the Kolmogorov microscale length for the channel in question was estimated to be around 0.065mm, and the turnover time 0.12s. This gives a turnover frequency of around 8Hz, meaning that the use of a 15Hz trigger rate should allow the capture of the full spectrum of turbulent eddies observed in the flow. As was discussed extensively in Chapter 3 however, it should be noted that due to the scale of the models in question, the smaller flow structures observed within the dissipation region may not be a true representation of reality. Nonetheless, it is sensible to

ensure that the recording equipment used in this study is able to capture the full spectrum of flow structures predicted.

Exposure

Camera exposure was set through an iterative process of image capture and analysis at a range of exposure time settings. By studying results generated using each exposure time setting for a sample experiment, it was possible to determine the optimal value for further experiments. Exposure time is an important consideration when setting up a PIV experiment. If the exposure time is too short, particles with a lower brightness will not be captured, leading to an incomplete capture of the flow field. If exposure time is too long, particles will move during the exposure and will be recorded as a streak rather than a static particle. Images illustrating these effects are shown in Figure 4-2.

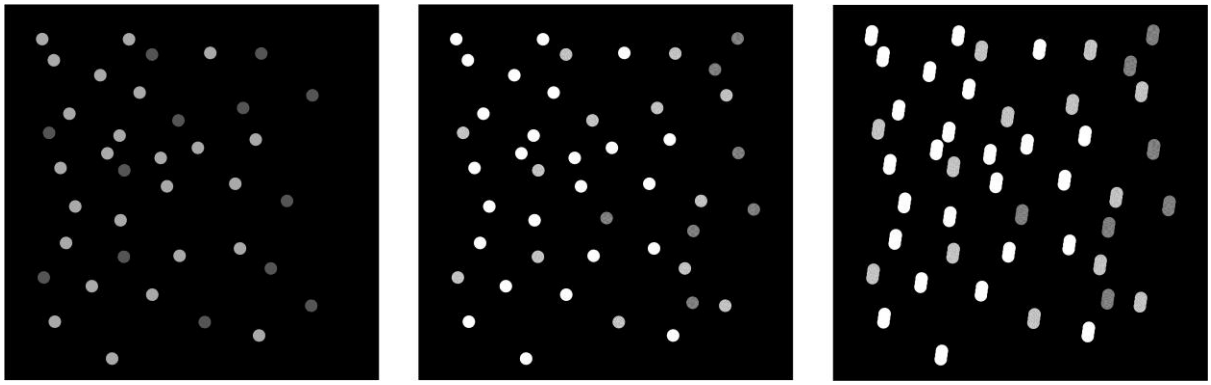

Figure 4-2 – Example image illustrating loss of data due to short exposure time (l), acceptable exposure time (centre) and streaking of particles due to long exposure time (r).

Exposure time for experiments was selected by calculating the particle movement which could be expected during a single exposure, in order to avoid streaking problems as illustrated in Figure 4-2.

The seeding particles used during PIV experiments had a diameter of 100µm. Based on flow velocity and exposure time settings it is possible to calculate the aspect ratio of the particle which will be produced in the imaged result. For flow velocities of 0.2 and 0.3m/s (the maximum bulk flow velocity which will be used in subsequent experimental work) and exposure times of 100, 200, 300, 400 and 500µs, the resulting aspect ratios are given in Table 4-1.

Imaged particle width (µm)	*Flow velocity (m/s)*	*Exposure time (µs)*	*Imaged particle length (µm)*	*Aspect ratio (length/width)*
100	0.2	100	20	1
100	0.2	200	40	1
100	0.2	300	60	1
100	0.2	400	80	1
100	0.2	500	100	1
100	0.2	600	120	1.2
100	0.3	100	30	1
100	0.3	200	60	1
100	0.3	300	90	1
100	0.3	400	120	1.2
100	0.3	500	150	1.5
100	0.3	600	180	1.8

Table 4-1 – Aspect ratio of resulting PIV seeding particle images for exposure times from 100 µs to 500µs under two flow velocity conditions.

Based on this data, an exposure time of 500µs was selected for use in further experimental work. This figure was chosen in order to give the maximum exposure time possible whilst minimising the potential for any streaking effects.

4.3 – PIV data processing

Following the capture of PIV image pairs, a key stage in the process is the processing of the images in order to generate usable data. As explained in the description of the fundamental PIV process in Section 2.4.1., this is a multi-stage process. All PIV processing undertaken after the capture of images was carried out using the PIVLab software package (version 1.32) for MatLab developed by William Thielicke [75, 80]. This software is a non-commercial package and was chosen due to its computational efficiency and the transparency and adjustability of its processing methodology, as opposed to a commercial "Black box" package which does not allow the user to see all settings applied to the data processing. All post-image capture processes were undertaken using PIVLab, including masking, pre-processing and filtering, correlation and calibration. Each of these processes is described in detail in the following section.

4.3.1 – Masking and ROI

In order to minimise computational time and avoid wasting resources by processing areas of a PIV image which are not relevant, a region of interest (ROI) can be set using PIVLab. Only data within the ROI is then used in subsequent data processing. In this project, the camera position and field-of-view remained constant throughout the experimentation, and ROI was used to adjust the data included in each analysis. ROI was used to exclude the regions very close to the edge of the image, since these regions were not as well illuminated by the laser sheet as the remainder of the image. The PIV cameras and lasers were set up to maximise the captured area, following which ROI was used to focus analysis on the relevant area in each experimental case. This was felt to be a more sensible

method of image capture than simply focusing the cameras on the required area, since by imaging a larger area it would be possible to later select the relevant area after studying results.

Masking allows a region within the ROI area to be selected, and the results contained within this area excluded from the final image output. Unlike in the case of ROI, vectors are still calculated within a masked region, but are later excluded from results. The masking function was used to exclude the turbine support post or turbine unit from data calculation. A sample pre-processed image with ROI and masked region is illustrated in Figure 4-3.

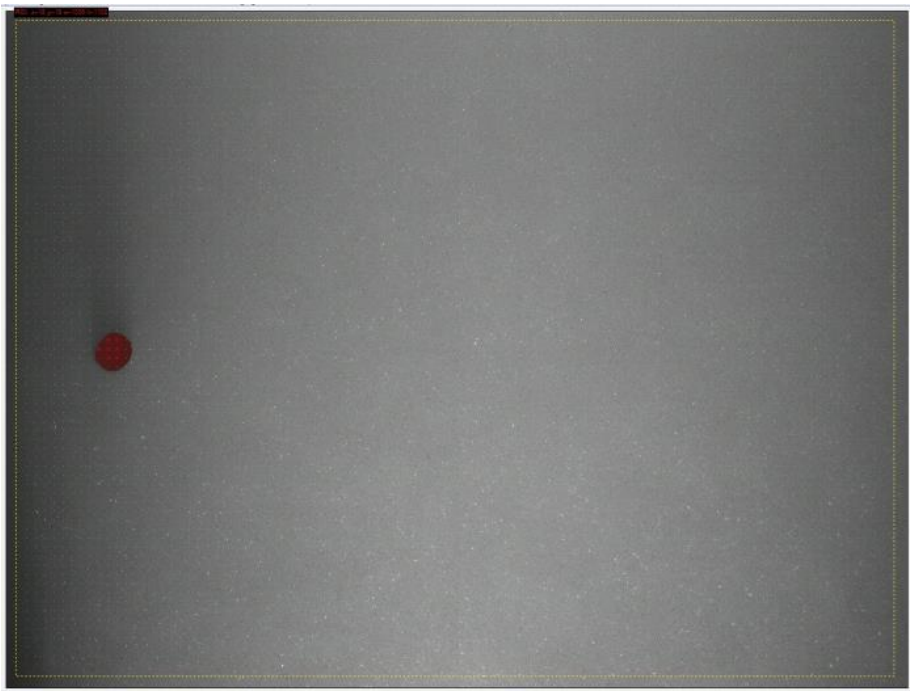

Figure 4-3 – Sample raw PIV image showing masked support structure and selected ROI.

4.3.2 – Pre-processing

As discussed in Section 2.4.1, filtering and other pre-processing methods can be applied to raw PIV images prior to image correlation, and can help to improve the quality of processed results by removing erroneous data or outlying results. In this study, pre-processing was carried out using the PIVLab software package, as was later used for image correlation.

Four pre-processing techniques (clipping; intensity capping; highpass filtering; and CLAHE) were applied during the course of this project, though not all processes were applied to all data sets. Details of these and other pre-processing techniques have been discussed in detail in Section 2, so only their application will be described in this section.

Image binarisation was not used, since as explained previously this method has the potential to remove useful data by reducing the intensity of pixels with intensity levels around the mean to background intensity. The method can reduce the computational size of the data, but since a similar outcome can be achieved by using other techniques, with less risk of data loss, binarisation was rejected.

Clipping and intensity capping were used to ensure that illuminated seeding particles appeared as clearly as possible in images. Clipping was applied to raw pixel images, meaning that any pixel with an intensity value below the predefined threshold value would be given an intensity of zero. A sample PIV image illustrating the effect of clipping at three different values of intensity threshold is shown in Figure 4-4.

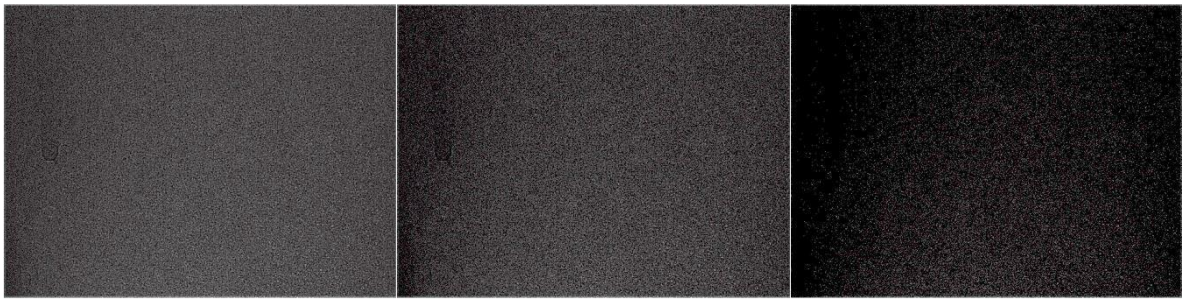

Figure 4-4 – Sample PIV image with clipping applied using threshold of (I-r) 5, 50 and 100 (CLAHE also applied).

As the figure above illustrates, overly high clipping threshold values lead to the removal of valid seeding particle reflection pixels. Consequently, it is imperative to choose a suitable value for the data in question. After testing a number of threshold values on images captured during all experimental stages of the work, a clipping intensity value of 10 was chosen and applied to all PIV data processing. This value was chosen as greater values were noted to result in the loss of a small number of pixels which appeared to represent valid data. Using a value of 10 excluded some data on the edge of the images which was inadequately illuminated to be considered valid, but did not significantly affect the data in the main portion of the image, which was adequately illuminated. A sample image illustrating the pre-clipping intensity levels across a PIV image is given in Figure 4-5.

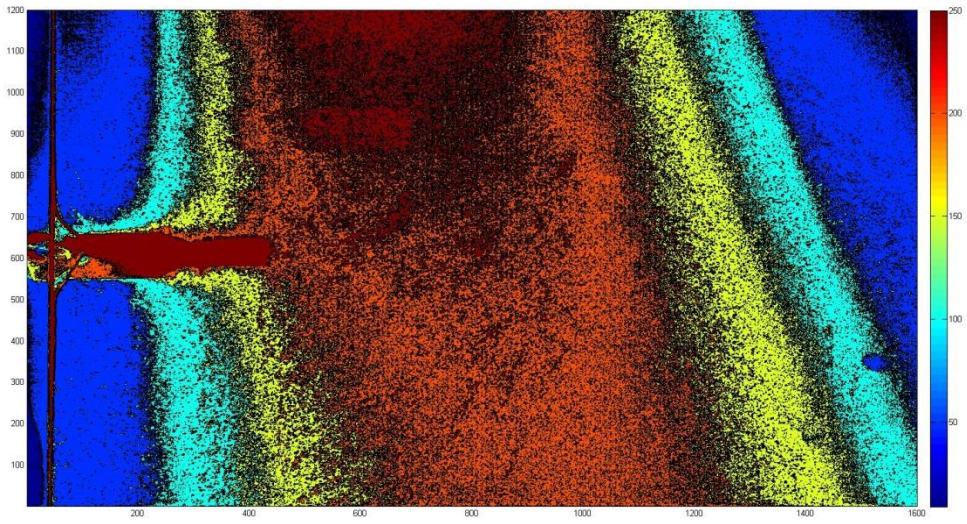

Figure 4-5 – Sample PIV image illustrating pre-clipping pixel intensity levels.

In order to ensure that bright spots in the image did not cause other particles to be ignored in the correlation phase, intensity capping was also applied. As described in Section 2, intensity capping

reduces the intensity of bright spots to a fixed value defined relative to the median intensity of the image, I_0 and a multiple *n* of the standard deviation of the intensity, δ_1, as follows:

$$I_0 + n\,\delta_1$$

Values of around *n=2* are proposed in the literature [71] and suggested by the designers of the PIVLab software [80]. In order to ascertain the most suitable value for use on the data described herein, pixel intensity histograms were produced from sample PIV images, as illustrated in Figure 4-5. These results were found to illustrate that the variation in pixel intensity from the mean of genuine particle reflections and all other data (excluding erroneous high-intensity pixels, which it is the aim of the intensity capping method to reduce to normal levels) lay within around 2 multiples of standard deviation As expected, high-intensity data was found to have much greater variation from the mean. Consequently, a value of *n=2* was applied to the data, since this would reduce the intensity of these erroneous particles whilst not affecting that of the genuine data.

Histogram equalisation was carried out using the CLAHE (Contrast-limited adaptive histogram equalization) filter [69] in order to improve the contrast of the PIV images prior to the correlation procedure. A number of sample window sizes were tested in order to determine the most suitable. Recommendations in the literature [66] proposed sample region sizes of 7x7px or 15x15px. Testing confirmed that these two window sizes yielded improvements in contrast compared to the initial image due to the widening of the contrast range across the images. However, it was found that in some cases the 15x15px window method led to similar errors as those highlighted in Section 2.4.3 with reference to the original Histogram Equalisation method, since the image contrast was equalised over a large area and hence the effect of noise or erroneously high-intensity particles was amplified. This effect can be observed in Figure 4-6b. The use of the 7x7px window required a greater processing time than the 15x15px window, though this time was of the order of minutes and therefore negligible in comparison to that required for the PIV correlation procedure, but was found to yield the required improvements in the image contrast range without the error amplification effects observed with the 15x15px sample window. Hence a sample window size of 7x7px was applied to all further CLAHE filter operations.

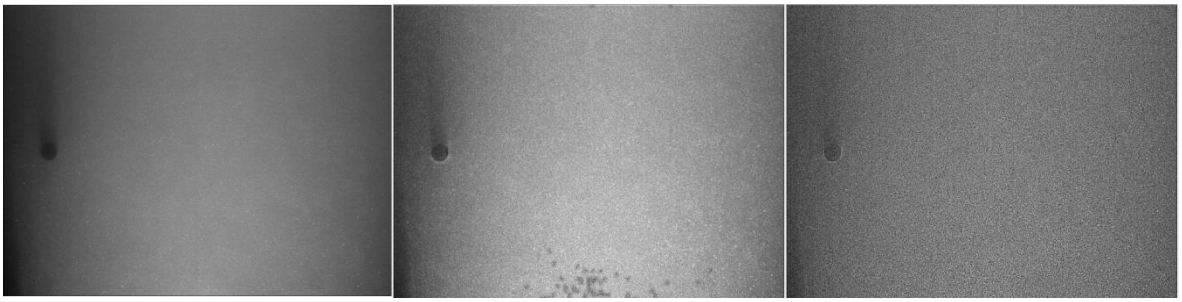

Figure 4-6a,b,c – Left to right: Unprocessed image, image with CLAHE filter applied (15x15px sample window), image with CLAHE filter applied (7x7px sample window).

4.3.3 – Correlation

As has been discussed in Chapter 2, the correlation method applied in this study was cross-correlation. This method was possible as image pairs were captured, as opposed to single double-exposed images, which necessitate the use of autocorrelation. The Fast Fourier Transform cross-

correlation (FFT-CC) method was applied in preference to the Direct Cross-correlation (DCC) method due to its much greater computational efficiency. Though the FFT-CC method does in fact produce an approximation of the resulting particle movement instead of calculating its actual movement as in the DCC method, the accuracy of the FFT-CC was found to be within 1% of DCC (as discussed in Section 2.4.4 and [73]).

Interrogation window size was chosen based on recommendations in the literature, and on the available processing time. A three-pass approach was ultimately chosen to give the best balance between resolution of results and processing time, with an initial interrogation window size of 64x64px, a second pass of 32x32px and a final pass of 16x16px. This yielded a processing time for a set of 400 image pairs of size 1600x1200px of the order of six hours, using a quad-core 3.4GHz desktop PC.

Sub-pixel estimation was carried out using the Gaussian 2x3-point estimator. This describes the fact that the pixels used to estimate the position of the particle intensity peak are, in each of the horizontal and vertical cases, the three directly adjacent particles. PIVLab does offer an alternative method of peak calculation in the 2D Gaussian method. However, this method has greater computational requirements and does not, when used in conjunction with the FFT-CC correlation method, offer any improvement in result accuracy [75]. The use of the Gaussian 2x3-point estimator method was tested in order to confirm that peak-locking was not observed in the resulting pixel displacement histograms.

4.3.4 – Calibration

Due to the curvature of the camera lenses used, the movement of a particle a given distance in a region relatively distant from the centre of the camera field of view will appear to be greater than the same case occurring in the region directly below the camera. Consequently, in order to ensure the correct calculation of velocity from PIV images, it is necessary to conduct a calibration process. This was achieved through the use of a calibrated image placed in the water channel, suspended at the required height. Calibration images were recorded at the two heights at which PIV images were captured (66mm and 135mm above the false base, corresponding to the mid-height of the support structure and the horizontal centreline of the blades), allowing the appropriate calibration image to be used during calculations for each case. The calibration image used is made up of a matrix of dots, as illustrated at the left of Figure 4-7. The dot size and spacing is used by the software to calibrate the relative distortion of a distance between the region directly below the camera and in more distant regions. The image also uses a pattern of smaller dots passing through the centre of the image in the streamwise and cross-stream directions, and a larger dot in the centre. The combination of these dot sizes allows the software to calibrate u- and v- directions.

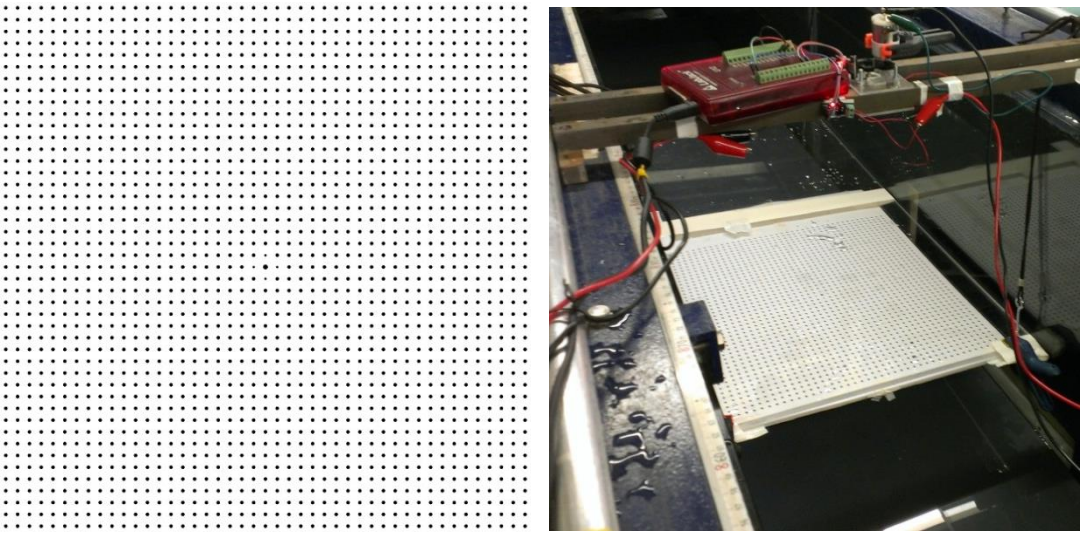

Figure 4-7 – Calibration image (l) and the printed image in situ in the water channel (prior to filling) (r).

During calibration processes, the image was illuminated using natural light and a halogen lamp instead of the PIV laser system. Due to the relatively low light levels, a greater image exposure time was used. In order to allow the image to be captured underwater, the image was commercially printed and encapsulated in plastic. This image was then fixed to a rigid board in order to ensure it did not flex during the calibration process and suspended at the heights described above, before the water channel was filled to the height used during experimental tests, and calibration images were captured.

4.3.5 – Post-processing & data validation

The post-processing of PIV data and the exclusion of vectors in subsequent calculations is described in Section 2.4.5. Following the correlation of PIV data and the production of velocity fields, data was studied in order to ensure that only valid vectors were used in the analysis of results.

Errors in PIV data are primarily caused by poorly illuminated areas, which can lead to erroneous high or low velocity vectors. As discussed in Section 2.4.5., a common method for excluding such errors is to apply filters to the velocity data after correlation. Using PIVLab software, two filters were applied to data in this study. Firstly, velocity limits were used to exclude data which fell outside a certain range, defined using a scatterplot of velocity data in order to view any obviously erroneous results. A sample result is illustrated in Figure 4-8, illustrating a small number of very high velocity vectors. In this illustration, a sample image of a scatterplot of velocity vectors for a single frame is given, though a combined image for the entire PIV capture sequence was used during data processing. Velocity limits were set in this case prior to the use of a calibration image, hence the horizontal and vertical scales of the scatterplot are given in velocity units of pixels/frame.

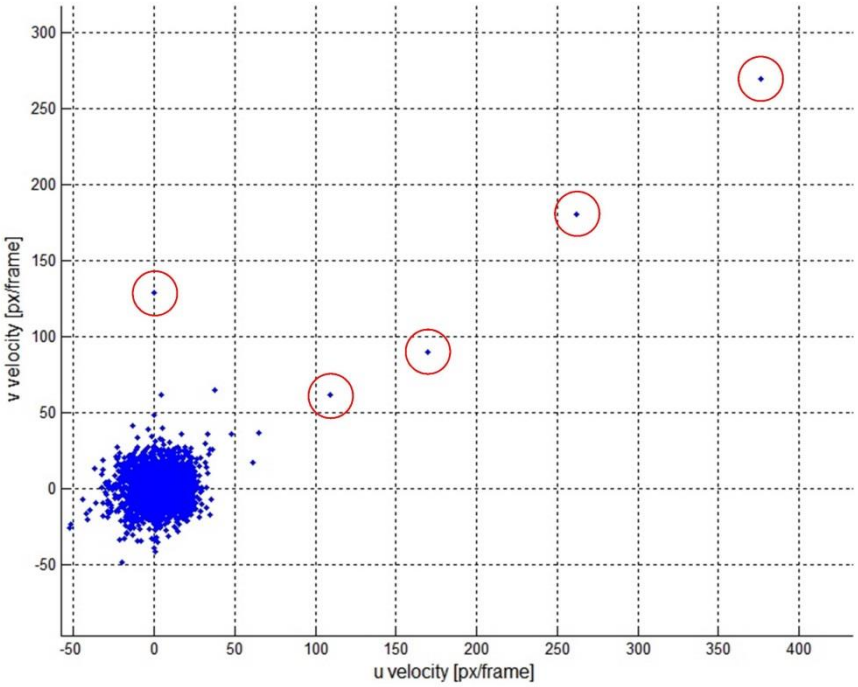

Figure 4-8 – Sample velocity scatterplot for single frame (points subsequently removed by velocity limit filter are highlighted).

Velocity range limits were used to exclude highly erroneous data such as the points highlighted at (105,60), (165,90), (260,175), (375,270) and (0,130) in Figure 4-8. In order to further filter the data, a numerical filter was applied. PIVLab includes two such filters. Firstly, a standard deviation filter can be applied, to exclude data lying outside of a given multiple of standard deviation in u and v directions. Secondly, the software also includes a local median filter, which is used to remove erroneous vectors by replacing each pixel with the median of its surrounding pixels. The application of filters to PIV data has been discussed in Section 2. Median filtering was not applied to PIV data during this study, but the standard deviation filter was used. As discussed previously, standard deviation filtering is defined by a threshold value, which is multiplied by the standard deviation of a data set. The resulting value is the limit of permitted variation from the mean, applied both above and below the mean to give the total allowable range. Outside this range, vectors are discarded and were replaced by the software with interpolated data from surrounding vectors. Sample plots illustrating the spread of data and the proportion of replaced vectors for standard deviation multiple limits of 1, 3 and 7 are illustrated in the following figures. Vectors which have been replaced by interpolated data are shown in orange, whilst original vectors are shown in green. The vertical line observed in PIV images in Figure 4-9 - Figure 4-11 indicates the location of the edge of the surface smoothing plate, which was used to ensure the accuracy of PIV image. The plate has been discussed in Section 3.4.5, and the presence of this edge in PIV result images is discussed in Section 4.6.

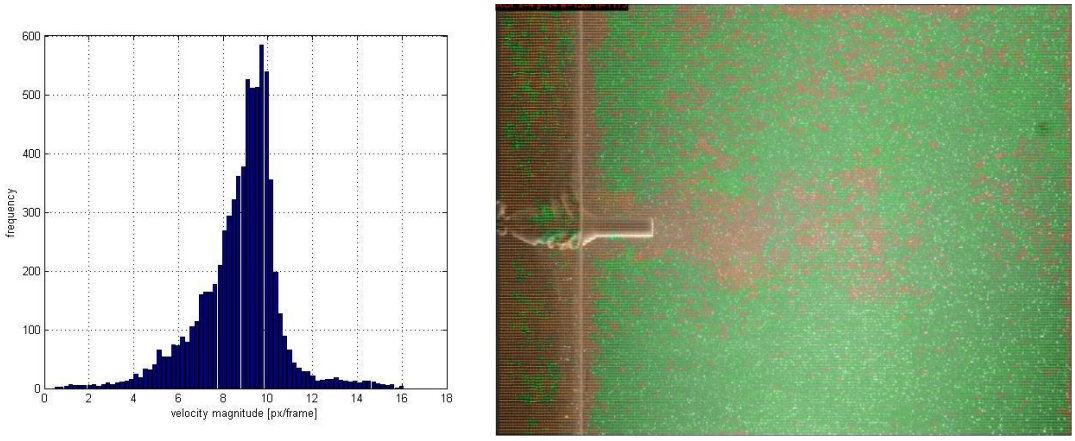

Figure 4-9 – Histogram of velocity (l) and vector plot (r) with n=1 standard deviation filter applied and removed vectors interpolated.

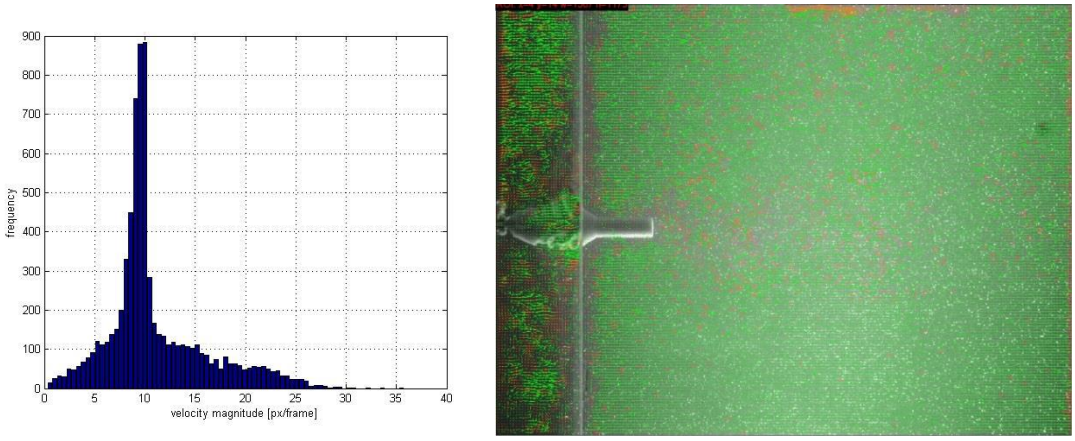

Figure 4-10 – Histogram of velocity (l) and vector plot (r) with n=3 standard deviation filter applied and removed vectors interpolated.

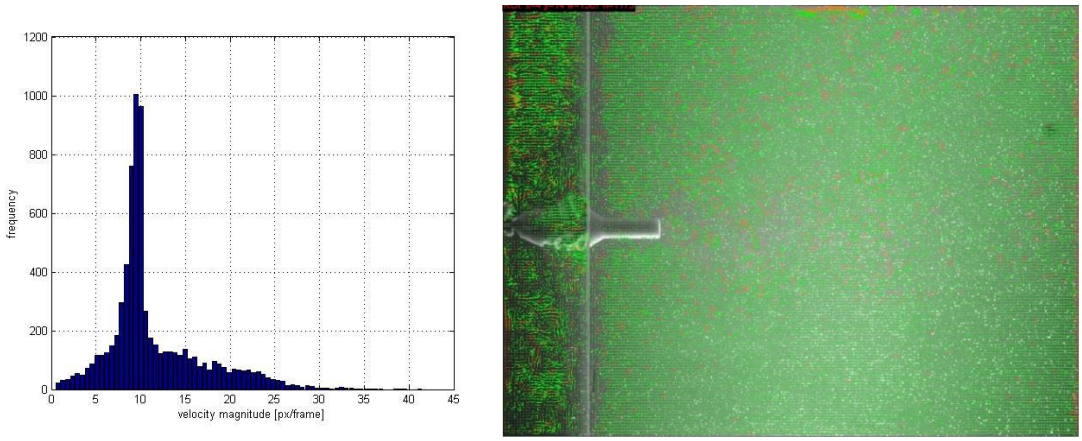

Figure 4-11 – Histogram of velocity (l) and vector plot (r) with n=7 standard deviation filter applied and removed vectors interpolated.

In order to ensure that important flow characteristics are not lost by the replacement of genuine result data, it is generally recommended [66] to keep the number of vector replacements as low as possible; hence suggesting that it is sensible to use as large a filtering threshold value as possible. As illustrated in Figure 4-9, using a low multiple of standard deviation as a filter causes the removal of a

large number of vectors. This is undesirable since vectors within this range are likely to be valid in most cases, so their removal and replacement distorts the flow field. Plots like those shown above were generated for standard deviation multiples between 1 and 10, and a value of 7 (as illustrated in Figure 4-11) was chosen for use in further experimental cases. This led to the replacement of between 3% and 9% of vectors per image pair. At greater standard deviation multiples than 7 a significant increase in the number of clearly erroneous high-velocity vectors was seen, and at lower values the amount of vectors rejected and replaced was higher than that recommended in the literature [80]. A test of the level of vector replacement in PIVLab is able to be conducted by calculating a mean flow vector image after processing. This image illustrates green vectors when less than 50% of frames have been replaced, and orange vectors when more than 50% of vectors have been replaced. In the case used for this example with a scatterplot region of (-50,-50) to (50,50) px/frame and standard deviation multiple of 7 selected, this mean flow image is illustrated in Figure 4-12.

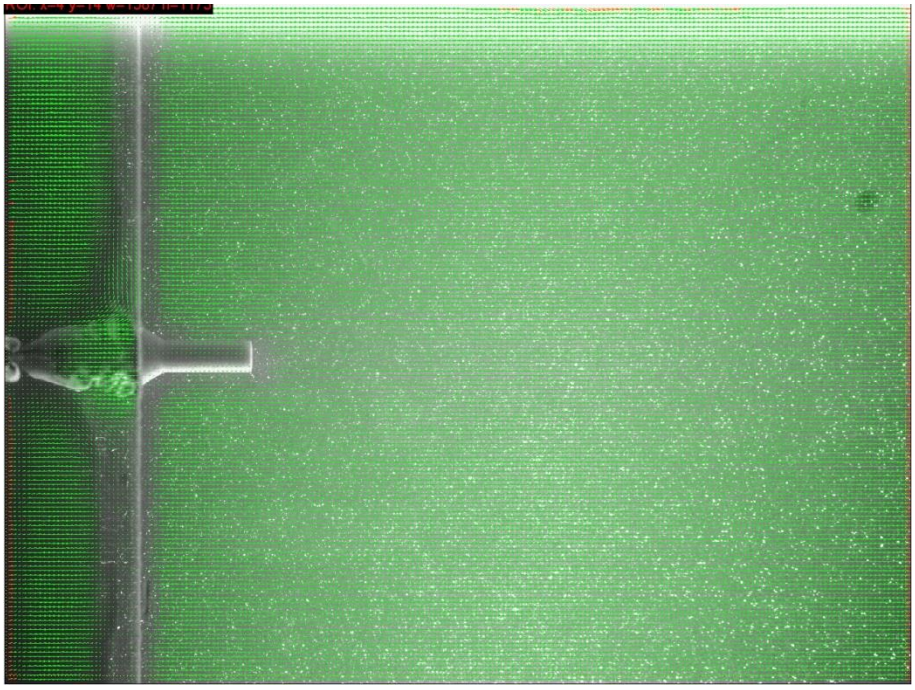

Figure 4-12 – Resulting mean flow image for example case above (Figure 4-8 & Figure 4-11).

As illustrated, the only vectors replaced in more than 50% of frames were at the wall region, which is to be excluded from future results due to ROI selection. This appears to validate the variables selected, which were thus applied to future experiments. In all cases, a scatterplot region was selected separately to exclude the most extreme outlying points (typically up to 20 points), and a standard deviation multiple of 7 was used.

4.4 – Analysis of flow data

Experimental flow data was captured during experiments carried out in phases 1, 2, 3, 4a and 4b. During phase 1, data was collected using a pitot tube and digital manometer, followed by dye injection imagery and finally ADV measurement. During phases 2, 3, 4a and 4b, the primary method of data collection was PIV. This section describes the analysis of the captured data in order to produce velocity and turbulence results.

4.4.1 – Time-domain analysis of turbulence

Analysis of turbulence has previously been mentioned in Section 2.9 and Section 3.3.1. In the former section, the concept of mean velocity $\bar{u}$ was introduced. Using $\bar{u}$, the turbulent variation of each data sample can be calculated. The simplest variation is known as the turbulent fluctuation, and is given for a point velocity u using the following equation (known as the Reynolds decomposition, and valid for an incompressible flow and a homogenous fluid):

$$u' = u - \bar{u}$$

Section 2.9 also introduced another turbulent variation, RMS velocity (u_*), which is given for n point velocity samples as:

$$u_* = \sqrt{\frac{1}{n}\sum_{k=1}^{n}(u_k - \bar{u})^2}$$

A further value used to describe turbulence within a sample is Reynolds stress τ, which is calculated by taking the mean value of the fluctuation of the flow in two perpendicular directions and the density of the fluid at each sample point. In a 3D flow, Reynolds shear stress can be calculated on three planes (τ_{xy}, τ_{yz}, τ_{xz}). On the horizontal plane, Reynolds stress is calculated as follows:

$$\tau_{xy} = \overline{\rho\, u_x' \, u_y'}$$

Though both τ and u_* can be used to illustrate the overall level of turbulence over a sample, Reynolds stress differs from the RMS value in that it includes fluctuation in two directions. However, neither value fully reveals the turbulent characteristics of a flow, since the result in each case is a single value for the entire sample length. Temporal variations in the fluctuation from the mean are therefore not illustrated by these values. In order to reveal this higher order variation, turbulent variables calculated for each sample are required.

By calculating turbulent kinetic energy, again as discussed in Section 2.9, the energy of the turbulent fluctuations in the flow at a given sample is calculable. Turbulent kinetic energy (k) is given as:

$$k = \frac{1}{2}\left[\overline{(u_x')^2} + \overline{(u_y')^2} + \overline{(u_z')^2}\right]$$

Where x, y, and z represent the streamwise, cross-stream and vertical directions respectively. In the case of 2D PIV data, as used during this work, velocity in the vertical direction is not measured, so k is calculated from the x and y velocity fluctuations only, and defined as k_{xy}, as given below:

$$k_{xy} = \frac{1}{2}\left[\overline{(u_x')^2} + \overline{(u_y')^2}\right]$$

In order to understand any potential variation in turbulence with time, PIV data was analysed using a MatLab script to calculate values of k_{xy} for each sample within the data sets recorded during this work. In the first instance, k_{xy} was calculated along the centreline of each PIV result, giving a graph of the variation in turbulent kinetic energy directly behind the turbine installation location. An example illustrating a sample centreline position k_{xy} plot is given in Figure 4-13.

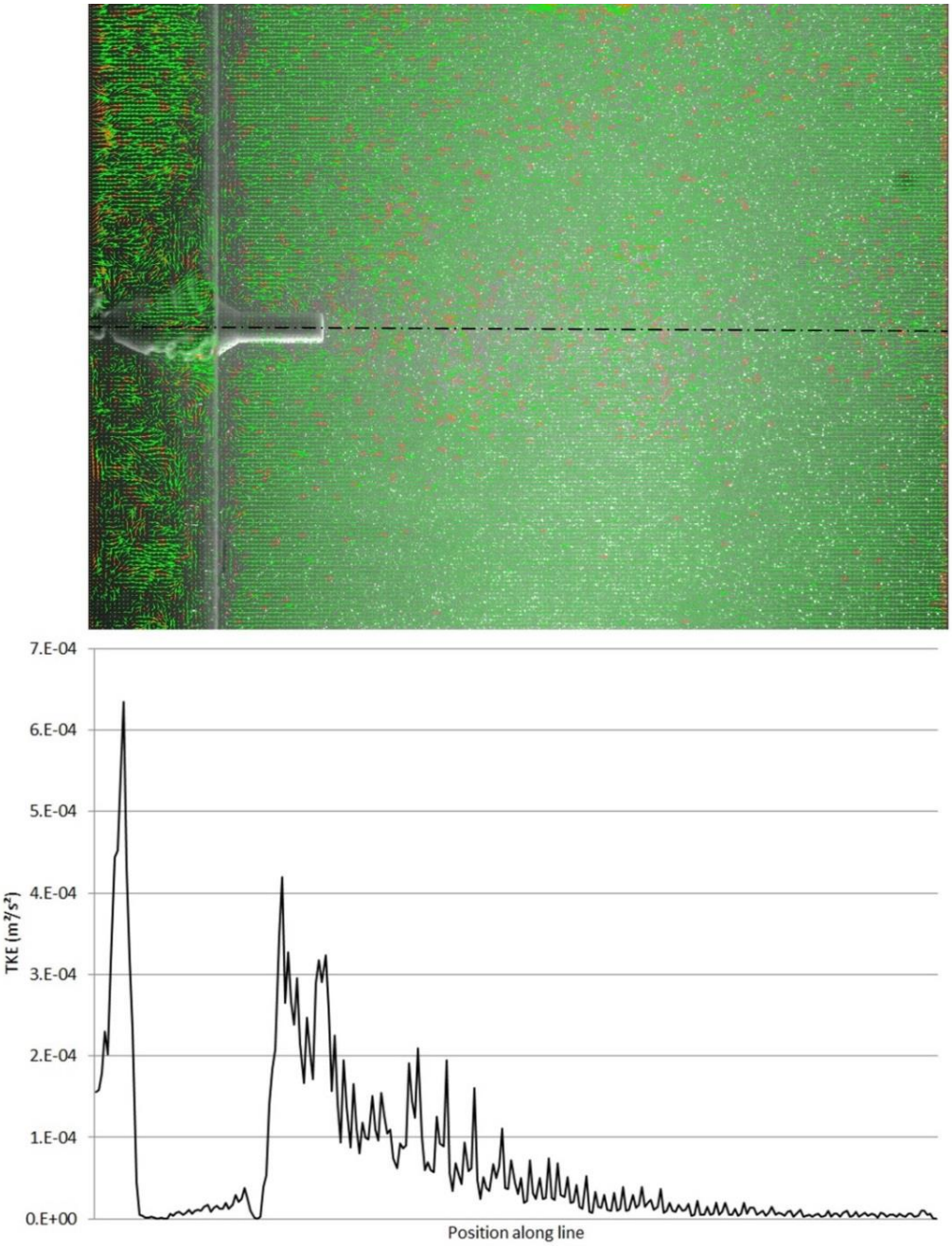

Figure 4-13 – Sample horizontal plane TKE plot at support structure mid height (flow case 2).

However, as one can imagine, the calculation of such a plot for each sample produces a large volume of data (400 samples were recorded during each experiment), and when multiplied by the number of overall experiments conducted (91 separate experiments were carried out in total), the volume of data generated makes it difficult to conduct a meaningful analysis of each image. Animations were generated for each experiment in order to allow any changes in k_{xy} to be observed with time, but although changes could be seen this method provided no way of recording them accurately. Furthermore, this collection of over 36,000 plots only contained data for variation in turbulence directly in front of and behind the turbine installation location, and did not illustrate any of the recorded data in the remainder of the image. A more effective method of visualising a greater volume of data was required.

Consequently, in addition to generating k_{xy} data, methods of reducing the volume of data whilst still allowing higher order analysis were sought. This led to the use of frequency-domain turbulent analysis and the POD method.

4.4.2 – Frequency-domain analysis of turbulence

The concept of the turbulent energy cascade as proposed by Kolmogorov has been discussed in Section 3.3.1. The transformation of time domain data into the frequency domain allows the presentation of a large amount of data in a single plot. By calculating k and transforming the data to the frequency domain, it was possible to plot energy against frequency and thus to observe the most energetic turbulent regions in each experiment using a graph of energy vs frequency, as illustrated in Figure 2-4. By transforming the data into the frequency domain, the POD method can also be used to study the energetic structures within the results of each experiment.

Proper Orthogonal Decomposition

The concept and broad method of the Proper Orthogonal Decomposition (POD) have been discussed briefly in Section 2.9. The actual implementation of the method in this study is described in the following section. Prior to the use of the method, the shallow flow criteria proposed by Jirka [168] was assessed in order to confirm that the flows under consideration in this study are suitable for the application of the method. The criteria states that a flow must be fundamentally shallow in order for the POD method to be used, meaning that the horizontal dimensions in the flow domain must greatly exceed those in the vertical. Given that the length of the water channel used in this study is much greater than the flow height, and is in a similar ratio to that of previous studies employing the POD method, this criterion was deemed to be met.

The first stage of the POD method involves the arrangement of the data into a format for the calculation to begin. In this work, the data studied using the POD was recorded using a digital camera during dye injection studies, so was initially stored as RGB colour images. The data was transformed into 8-bit greyscale images prior to the application of the method. This was achieved using a MatLab script based on the *rgb2gray* function. The resulting images were then converted to matrices, with each pixel in the image being converted to an element in the matrix. Each pixel in the grayscale image had an intensity between 0 and 255, so the resulting matrix was made up of elements with these values. The resulting matrices were of the same element size as the initial images (*m*,*n*). This ensemble of velocity fields is given for *N* samples by:

$$V = V(x, t_z)$$

Where *x* represents vectors and *t* time. As illustrated in the graphical representation of the method given in Figure 2-42, these matrices were rearranged to give a long string of intensity values for each image, of length *mn* and height 1. These strings allow the entire data set to then be combined into a single matrix of length *mn* and a height corresponding to the number of time samples in the data set (*N*). The process described above was carried out using MatLab, resulting in a single large matrix for each data set. The POD process was then conducted on this matrix as follows.

Calculation of eigenfunctions

The function of the POD calculation is to find the collection of eigenfunctions $\varphi_n(x)$ and time functions $\alpha_n(t)$ which represent the least square best fit to the ensemble $V(x,t)$. For an integer value of N, this can be described as the minimisation of:

$$\left\| V(x,t) - \sum_{n=1}^{N} \alpha_n(t)\varphi_n(x) \right\|_x^2$$

This is found by solving the eigenvalue problem for φ_n to give eigenvalues (λ_n) and the two-point correlation tensor (R):

$$\int R\varphi_n \, dx = \lambda_n \varphi_n$$

R is defined as:

$$R(x,x') = \langle V(x,t)V(x',t) \rangle$$

The resulting best fit collection of eigenfunctions, i.e. the POD modes, $\varphi_n(x)$ can thus be determined from R, by rearranging the eigenvalues into descending order ($\lambda_1 \geq \lambda_2 \geq \lambda_3 \geq \lambda_4 \geq \ldots$) and finding the corresponding modes.

Calculation of POD modes and coefficients

From these values, the POD coefficients are determined by projecting the original velocity data onto the modes, to give $\alpha_n(t)$ for each $\varphi_n(x)$. The result of the process is a collection of POD modes (φ_1, φ_2, φ_3, …), POD coefficients (α_1, α_2, α_3, …) and POD eigenvalues (λ_1, λ_2, λ_3, …). The energy contained in each mode as a proportion of the total energy of the flow can be calculated using the eigenvalues:

$$E = \frac{\lambda_i}{\sum_{i=1}^{N} \lambda}$$

As discussed in Section 2.9, a significant proportion of the energy is often found in a small number of modes. The original flow pattern can be fully recreated by calculating $i = N$ modes, or can be represented with lower dimensionality using $i < N$ modes.

The calculations described above were conducted using MatLab scripts based on those used by Meyer [169] and Brevis and García-Villalba [152]. The scripts used are given in full in Appendix 1.

4.4.3 – Vorticity

In addition to the velocity and turbulence values calculated in time and frequency domains described in previous sections, flow results were also studied by the calculation of vorticity. As has been discussed in Section 2.5.1, vorticity gives an illustration of the tendency of a fluid flow to rotate and is therefore a useful indicator of the energetic regions of a flow field. As has also been discussed, Q-criterion was not applied due to the two-dimensionality of PIV results. Vorticity was calculated for PIV data using the inbuilt calculator in PIVLab. As in the case of TKE, vorticity was calculated using streamwise and cross-stream velocity data only, meaning that only horizontal plane vorticity is reported in this study.

4.5 – Analysis of turbine performance data

The equipment used to capture the recorded experimental data from installed turbines has been described in Section 3.5. In summary, the turbine blades were driven using a small electric motor, with power supplied by an adjustable power supply. Voltage and current were both recorded, the former being recorded manually during each test, and the latter through the use of a current recording module. Turbine speed was monitored using an optical encoder installed on the driveshaft. The current measurement module and optical encoder signals were both recorded using a LabJack U12 DAQ system. Data from the current measurement module and encoder were recorded simultaneously, using two separate inputs to the DAQ system. The system was connected to a desktop computer by USB, and the signal recorded directly to the computer's hard drive. The software used (LJscope, supplied by LabJack and designed to operate with the U12 system) allows control of the volume of data and sample time in each recording. In all experiments conducted during phases 2, 3, 4a and 4b as described herein, data was recorded at a frequency of 512Hz, over a duration of 4 seconds, producing 2048 data points for each of the two signals.

A high sample rate was chosen in order to ensure that any variation in the current module signal would be recorded. The time duration chosen allowed the turbine to complete at least five full rotations during the slowest flow cases used in subsequent experimental phases, allowing any variation in recorded current (and thus, potentially, in calculated power coefficient) with rotational position to be observed multiple times during each test. The high sample rate was also necessary in order to ensure accurate measurement of the turbine rotational speed, since knowing the precise time at which the encoder signal changed from high to low was critical to the subsequent speed calculation. This data, when recorded at 512Hz, allowed the turbine rotational speed to be calculated with an error of 0.4% (calculated based on an error of 1/512s in two consecutive recordings, leading to an overall error of 2/512s). The user interface of the LJscope software is illustrated in Figure 4-14. The red signal is the variation with time of the current module signal voltage, as explained below, and the green signal is the variation in encoder voltage.

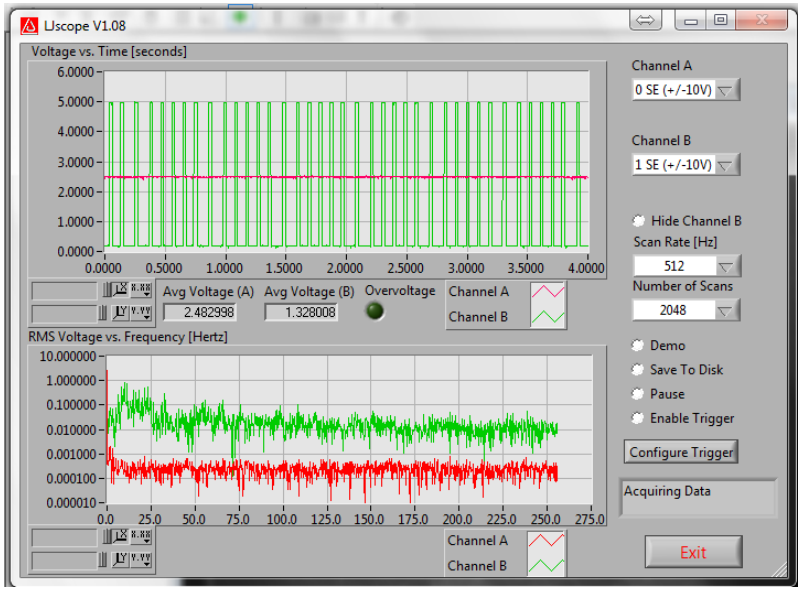

Figure 4-14 – Sample output window (LJscope software) showing live encoder position and current measurement output during a preliminary test.

At the end of each experiment, the LJscope software was set to save a file containing the data recorded, using a three-column format to record time in seconds, encoder signal in volts, and current module signal in volts. In order to process these results into the required data, the following procedures were carried out.

Encoder signal calculation

As illustrated in Figure 4-14, the encoder signal is a simple high/low signal, with the module supplying a high voltage when a hole on the encoder disk aligns with the optical measurement position, and a low voltage signal when a solid portion of the disk aligns with the measurement position. The encoder disk used in these experiments was a six hole design, meaning that the encoder signal would be high six times during a single turbine rotation. The encoder disk was aligned such that every second high signal would indicate a blade passing in front of the support structure. In order to calculate turbine rotational speed from the data described above, the data was processed using MatLab. A script was written which, for each sample of encoder voltage, would compare the voltage to the voltage at the previous time. If an increase or decrease with an absolute value of greater than 2 volts was observed, the signal would be counted as a rising or falling edge and a 1 would be recorded at the time position in a secondary matrix. If an edge was not detected the secondary matrix would contain a zero at that time position. By using this new matrix of edges, the centre of each high signal could be detected, from which the time step between subsequent centres could be recorded, therefore giving the time taken for the blades to complete 1/6 of a rotation. From this, any variation in rotational velocity over a complete revolution could be ascertained, and the rotational speed could be calculated.

Current measurement module signal calculation

The current measurement module used in this work was the Allegro ACS712 module, a Hall effect linear current sensor [165]. The module was installed in series with the motor power supply, and works by generating a voltage signal based on the current passing through its sensing circuit. The voltage signal varies with the sensed current, at a rate of 185mV per Amp, from a base signal of 2.5V at zero current. The output increase with current is linear, as illustrated in Figure 4-15, allowing a simple calculation to ascertain the current supplied to the motor from the voltage output of the unit.

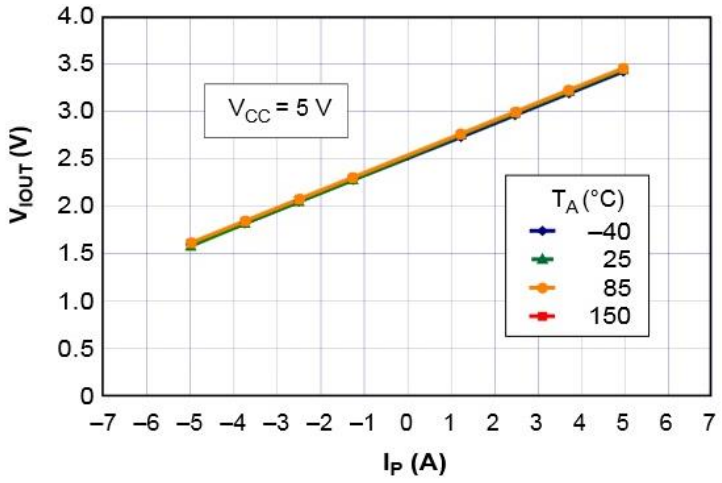

Figure 4-15 – ACS712 current sensing module output voltage vs sensed current (from [165]).

Again, a MatLab script was written to capture the data acquired by the DAQ module and translate the current sensing module signal voltage into measured current values. The device has a quoted minimum accuracy of +/-5mV/A, meaning that for a sensed current of 1A, the signal output voltage could, in the worst case, lie anywhere between 180mV and 190mV. This suggests a potential error of 0.55%. Calculated for the supply currents used in this study, which ranged from around 20mA to 70mA, this gives a variation in output signal voltage of between 0.111mV and +/- 0.385mV. Total maximum device error, including potential errors due to signal noise and zero output variation, is given by the manufacturers as 1.5% [165].

4.5.1 – Power calculation

As discussed in Section 3.5, turbine power and blade torque output were calculated through the calculation of motor applied power in the case of each experiment with and without turbine blades in place. The difference between the required power to drive the turbine at the required rotational speed in the given flow conditions with the blades and the power required to do so without the blades yields the power generated by the blades themselves. The subtraction of these two values also allows other power sinks within the drive and measurement systems to be accounted for, since these are present in both cases and thus cancel out when the blade generated power is calculated.

From this value of blade generated power, blade generated torque is calculated by multiplying the power generated by the rotational speed of the turbine as measured using the optical encoder system described in Section 3.5 and the data recording methods described in earlier in this section. The calculation of power coefficient (C_p) involves dividing the power generated by the turbine by the theoretical power available in the swept area of the turbine blades. Potential errors in these results could occur due to misalignment of the turbine driveshaft, as has been discussed in Section 3.5.1. This potential error was calculated to cause a maximum possible variation in power results of 23%, and a mean case value of 9%. However, actual error is expected to be lower than this, since even the mean case value calculation is based on a worst case misalignment of the turbine driveshaft. The likelihood of errors in the calculation method described in the previous section are assumed to be negligible due to the simplicity of the calculation, and the high sample rate chosen in order to ensure accurate measurement of the encoder signal.

4.6 – Experimental errors (Phases 2, 3 & 4)

Potential sources of error in all subsequent phases of work involving the use of instrumented turbine models and PIV measurement equipment (phases 2, 3 and 4) fall into two categories: Those relating to the measurement of turbine power and torque, and those relating to the measurement of flow conditions. In the case of turbine measurement, the major sources of potential errors are the measurement of motor applied power, and the calculation of turbine blade torque and C_p from this data. In the case of flow condition measurement, the major source of error is the PIV equipment and measurement process, and the associated data processing and calculation.

In all cases, turbine power was calculated from the power applied to the motor in order to drive the turbine in otherwise identical cases with and without the turbine blades in place. As calculated in Section 3.5.1, the maximum error in turbine blade torque measurements is estimated to be 23%,

with a mean level of error estimated at 9%, assuming the maximum 2mm misalignment of the turbine driveshaft.

Actual error can be estimated by comparing the results of identical experiments carried out during different phases of this work. Identical experiments were carried out during each phase, but in order to minimise the potential introduction of alignment errors as discussed in Section 3.5.1, these experiments were all conducted with the same alignment conditions (i.e. without removing and re-installing the turbine into the water channel), meaning they cannot be used comparatively to quantify potential errors. Identical experiments were carried out in two independent cases: 11mm, 16mm and 20mm diameter support structure turbines were all tested under flow case 2 conditions (λ=3.1) whilst installed in the central turbine position at 9m downstream of the channel inlet, without an upstream turbine, separately during phases 3 and 4a. Blade torque results for these tests are illustrated in Table 4-2.

	Blade torque (Nm)	
Support structure diameter (mm)	*Phase 3*	*Phase 4a*
11	0.573	0.565
16	0.529	0.534
20	0.517	0.515

Table 4-2 – Comparison of independently measured results of identical cases recorded during separate experimental phases.

Calculated variation between experimental results for the 11mm, 16mm and 20mm diameter support structure cases is 1.4%, 0.9%, and 0.4% respectively. This low value of variation between experiments suggests that misalignment of the drive shaft and the additional error which would result does not appear to be present in these results.

Potential measurement errors in PIV have been discussed extensively in Section 2.4.6. The estimated maximum error in the PIV experiments conducted in this study was calculated to be $\mathcal{E}$ = 6%. A summary of the estimated errors for the experiments carried out in this work are given in Table 4-3.

Category	*Error source and calculated value*	
Turbine performance	Drive system	9.0%
	Speed measurement	0.4%
	Current measurement	1.5%
Flow measurement	PIV calculation	6.0%

Table 4-3 – Calculated errors in Phases 2, 3 and 4 experiments.

The total estimated maximum error in turbine blade torque calculation is therefore around 11%, and the total estimated maximum error in flow measurement using PIV is 6%, though actual errors are likely to be lower than these values. The interaction of these errors occurs when turbine

performance is calculated relative to the prevailing flow conditions. At this stage, the theoretical maximum total error in an experiment during phase 2, 3 or 4 of this work is 17%.

Surface plate distortion

Though not a numerical error, it should be noted in all PIV images that the surface smoothing plate (as described in Section 3.4.5) was found to distort recorded PIV images. The presence of the plate leads to an apparent reduction in velocity in the area below the plate, due to the bottom surface of the plate which rests on the water surface slowing the flow in this area. This effect can be seen in the region upstream of the region of interest highlighted in the images shown in Figure 5-31, for example. In order to avoid this effect having any influence on results, data recorded in this region has not been used in further calculations, but the region has been included in the illustrated images found in Sections 5.2.3, 5.2.4 and 6.2.1 since removing it would not allow the position of the turbine or support structure to be indicated.

Mean flow images

Mean flow images generated from series of instantaneous PIV image frames are used in subsequent sections of this work to illustrate velocity wakes downstream of a turbine. This is a useful technique as it allows the illustration of a time series of data in a single image, thus allowing such data to be presented in a document such as this. However, the use of time-averaging must be treated with caution since, as discussed in Section 4.4.1, the use of such methods can result in the extremes of a data series being lost. In order to avoid this, instantaneous wakes are often presented alongside mean flow images.

In order to aid the reader in the understanding of explanations given in this thesis, a series of wake image animations have also been produced from PIV data, and are available online. A full list of the cases for which results are provided is given in Appendix 2, as well as the URL of the collection.

5

Results – Single Turbine

5.1 – Introduction

5.1.1 - Flow rate, Velocity and Tip Speed Ratio

Throughout the experimental results described in this chapter, blockage ratio (*B*), tip speed ratio (λ), Reynolds number (*Re*) and Froude number (*Fr*) are frequently referred to. These variables are defined in Section 2.2.

5.1.2 – Definition of experimental flow case conditions

In order to ensure accurate experimental replication of the flow regime around a real tidal turbine, it was important to establish correct flow conditions in the water channel experiments. Multiple interdependent variables required optimisation, and nearly all of the variables identified were governed to some degree by other variables. The primary values identified are illustrated in Table 5-1, along with details of those upon which they are governed by.

#	*Variable*	*Governed by*
1	Turbine model scale	2, 9
2	Water depth	
3	Blockage ratio	1, 2
4	Flow velocity at turbine height	2, 10
5	Turbine rotational speed	1, 4
6	Reynolds number, *Re*	1, 4
7	Froude number, *Fr*	2, 4
8	Tip Speed Ratio, λ	4, 5
9	Turbine construction constraints	
10	Flow rate	

Table 5-1 - Experimental setup variables.

Using the dependence data from the table above, the variables were re-arranged into a flowchart, as illustrated in Figure 5-1.

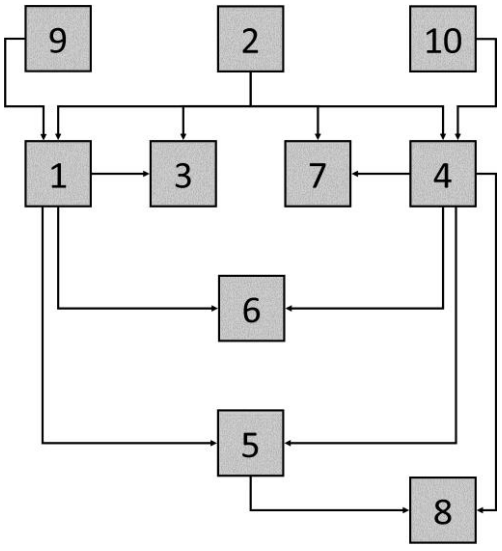

Figure 5-1 – Experimental setup variables interdependency flowchart.

The conclusion of this chart appears to be that the initial variable upon which all others are directly or indirectly based is the depth of water in the water channel (variable 2). The restrictions on the turbine design based on its construction methods (variable 9), and the limitations in flow rate capability of the water channel (variable 10) are also important initial values. In order to conduct an optimisation procedure, the target numerical value for each variable was identified. In some cases such a value did not exist, since the turbine model scale and rotational speed do not require optimisation themselves, but their dependants (*Re* and λ) do. Similarly, any value of flow velocity at turbine height is acceptable; since it is the values it governs which must be optimised. The variables are again listed below, with the target numerical values identified. In cases with limited scope for control, the maximum and minimum values are also listed.

#	Variable	Target	Minimum	Maximum
1	Turbine model scale (rotor diameter)	-	100mm [a]	-
2	Water depth	-	-	500mm [b]
3	Blockage ratio	4% [c]	-	8% [c]
4	Flow velocity at turbine height	-	-	-
5	Turbine rotational speed	-	-	-
6	Reynolds number, *Re*	4.8×10^8 [d]	-	-
7	Froude number, *Fr*	0.06 [d]	-	-
8	Tip Speed Ratio, λ	5.6 [d]	-	-
9	Turbine construction constraints	-	-	-
10	Flow rate	-	-	45 l/s [b]

Table 5-2 - Experimental setup variables optimisation target values.

[a] – Limited by size of internal gear components for turbine models

[b] – Limited by maximum capability of the water channel

[c] – Values from previous experimental modelling (see Section 3.5.2)

[d] – Values from real tidal installation site (18m rotor diameter, 2km wide 50m deep channel, 2.5m/s tidal speed)

Following this process, an optimisation procedure was carried out to deduce the values of water depth and flow rate which would yield ideal values of the four output variables (*B*, *Re*, *Fr* and λ), within the constraints of allowable flow rate and turbine scale. This process was carried out by calculating the output variable values for water depths of 200mm, 300mm, 400mm, and 500mm, with flow rates of 10l/s, 20l/s, 30l/s, and 40l/s in each case. Each result was calculated as a percentage variation from the target value for each of the output variables. Turbine height and rotor diameter were calculated based on real data on turbine height and rotor diameter relative to water depth, in order to ensure that the scale turbine models were located at the same position within the water column as a real turbine. A known installation [110] has a turbine base to tip height of 28m and rotor diameter of 18m in a water flow of 50m depth, so this ratio was used, yielding size ratios of 0.56 and 0.36 respectively for turbine height to water depth and rotor diameter to water depth. These ratios immediately ruled out the use of a water channel flow depth of 200mm, since this produced a rotor diameter of 72mm, which is below the 100mm minimum value. Similarly, calculations revealed that in order to maintain this ratio of turbine size to water depth in a 500mm

deep flow, a turbine of diameter 180mm would be required. This led to a swept area blockage ratio of 10.2%, above the defined maximum of 8%, so the use of a 500mm water depth was also ruled out. Flow depths of 400mm produced a rotor diameter of 144mm and a blockage ratio of 8%. Although this blockage ratio was equal to the defined maximum, this case was considered further. Results of the optimisation process are illustrated in the following figures.

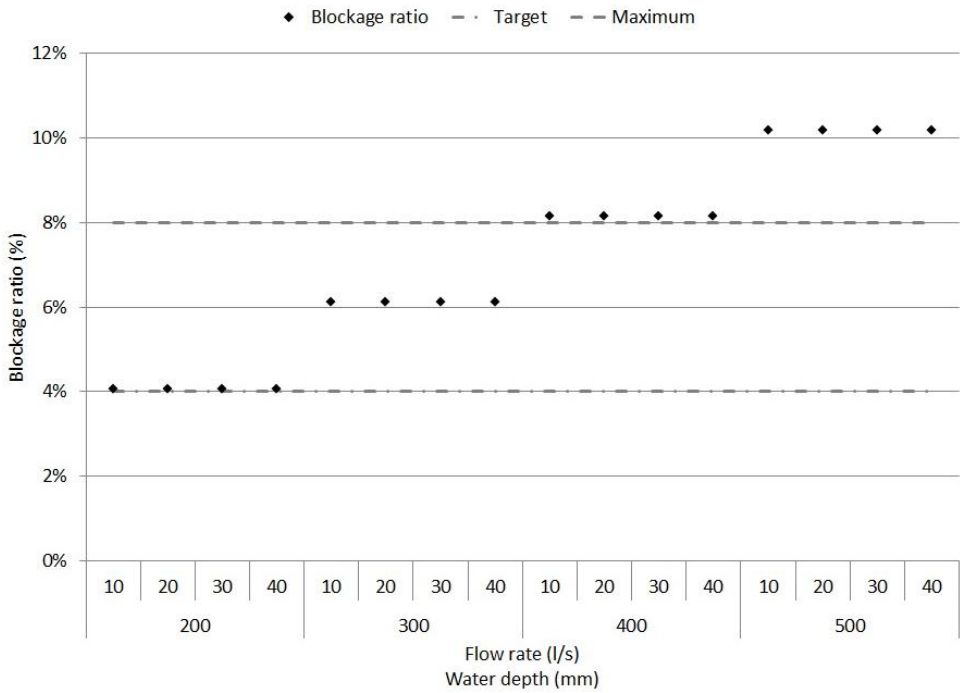

Figure 5-2 – Flow condition optimisation: Water depth and flow rate vs. blockage ratio (B).

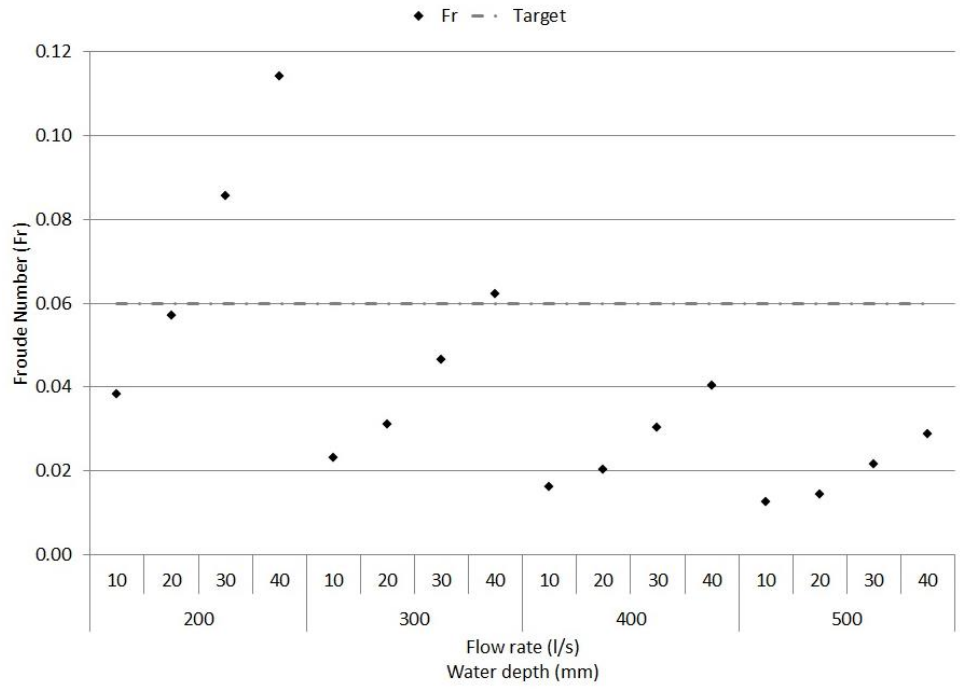

Figure 5-3 – Flow condition optimisation: Water depth and flow rate vs. Froude number (Fr).

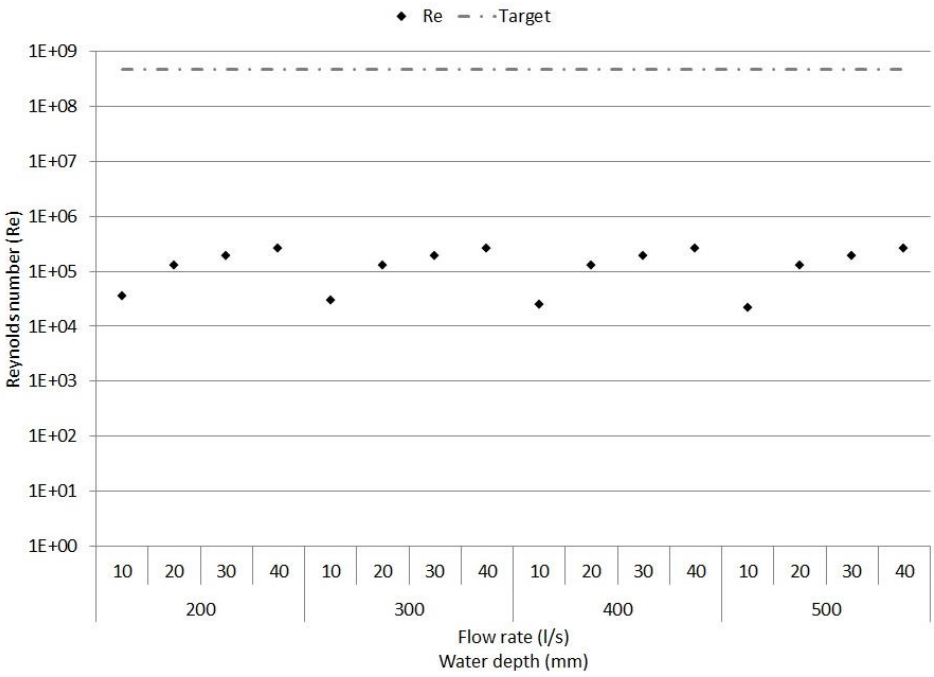

Figure 5-4 – Flow condition optimisation: Water depth and flow rate vs. Reynolds number (Re).

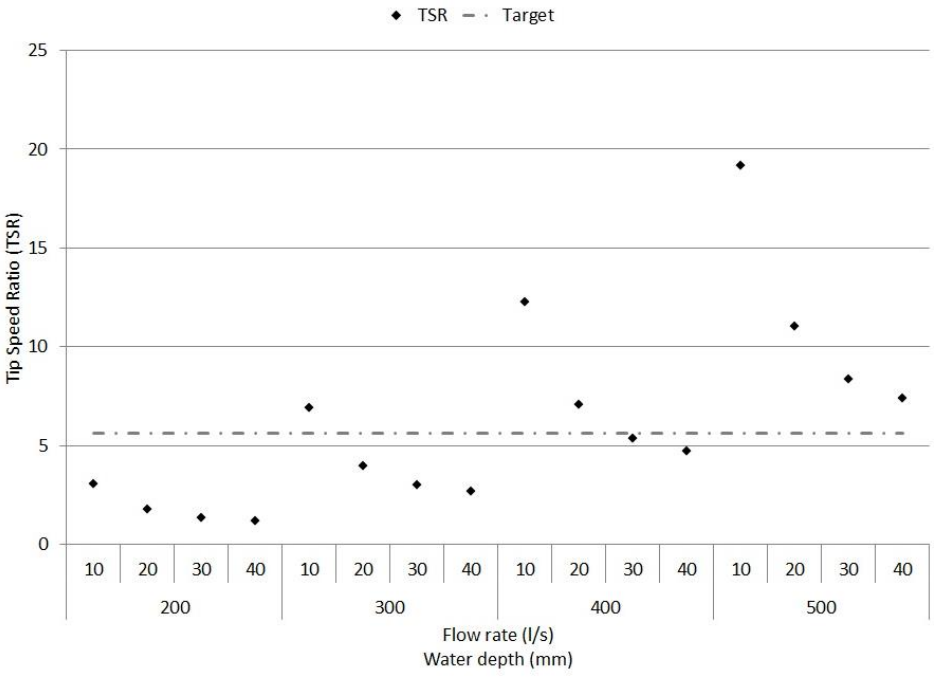

Figure 5-5 – Flow condition optimisation: Water depth and flow rate vs. Tip Speed Ratio (λ).

As discussed above, due to the need for the turbine to be positioned within the correct part of the flow, Figure 5-2 illustrates that the requirement for a correct ratio of turbine size to water depth means that water depths of 500mm lead to a turbine rotor diameter which causes an unacceptably high blockage ratio of 10.2%. Water depths of 400mm produce a blockage ratio of around 8%, which is defined as acceptable based on previous studies. Water depths of 300mm and 200mm produce lower blockage ratios of around 6% and 4% respectively, with the latter being the closest to the target ratio of 4%.

Froude number values within 5% of target values are achieved by a water depth of 200mm and flow rate of 20l/s, and a water depth of 300mm with a flow rate of 40l/s. Water depths of 400mm and 500mm yield lower Froude number values.

Reynolds number values in all cases are significantly lower than those calculated for the real tidal installation case. However, as has been extensively discussed in Chapter 3, due to the location of the effects studied by this work within the inertial region of the turbulent energy spectrum, the absolute replication of Reynolds number values is not necessary to ensure accurate scale modelling of these effects. In all cases, *Re* values calculated using channel dimensions are of the order of $3x10^5$, with a fully turbulent boundary layer profile as confirmed during the characterisation process described in Section 3.3.2. Consequently, wake effects generated by relatively large scale geometric features will be faithfully replicated despite the difference in Reynolds number values when compared to reality. It is acknowledged that small scale turbulent eddies which lie in the dissipation region of a real scale tidal flow may not be correctly replicated in the experimental conditions used in this study. However, as has been discussed in Section 2.8, numerous previous experimental studies at similar *Re* values have produced results comparable to real scale turbines when studying effects in the LEC and inertial regions.

The range of TSR values for both 300mm and 400mm water depths cross the target value, with the closest values being at 10l/s flow rate in the 300mm depth case, and 30l/s in the 400mm depth case. The 500mm case, already ruled out due to its high blockage ratio, produces tip speed ratios ranging from 19.1 in the 10l/s case to 7.4 in the 40l/s case, all of which are above the target value. 200mm flow depth yields values below the target TSR, ranging from 3.0 to 1.2 for the same cases. Due to these low values, the 200mm depth case was also ruled out at this stage, and a comparison of the two remaining depth cases carried out to determine the most appropriate cases to use for subsequent experimental work. In order to compare the closeness of the two cases to the target output values, Table 5-3 was produced. Values were compared by percentage variation from the target values of Blockage ratio, *Fr* and λ, and then combined to give a mean variation across the three values for each depth and flow case. *Re* was not included in this analysis since all *Re* values lie in the acceptable region to allow scaling, and the variation in *Re* between cases is small. Furthermore, due to the large numerical values associated with Reynolds number, calculation of mean variation would be dominated by its inclusion in this calculation, and percentage variation due to the other three values would be hidden in the overall mean.

		% variation from target value							
		300mm depth				400mm depth			
Variable	*Target value*	*10l/s*	*20l/s*	*30l/s*	*40l/s*	*10l/s*	*20l/s*	*30l/s*	*40l/s*
Blockage ratio, *B*	4%	53%				104%			
Froude number, *Fr*	0.06	62%	48%	22%	4%	73%	66%	50%	33%
Tip Speed Ratio, λ	5.6	23%	29%	46%	53%	119%	26%	5%	16%
Mean variation		*46%*	*43%*	*40%*	*37%*	*99%*	*65%*	*53%*	*51%*

Table 5-3 – Summary of variation of B, Fr and λ for 300mm and 400mm depth cases, at 10, 20, 30 and 40l/s flow rates in each case.

Following this analysis, the two cases with the lowest mean variation were selected for use in subsequent experimental work. Ideally a greater number of cases would have been used, but due to the number of experimental phases proposed and the limited time resources available, this was not possible. A final summary of the two cases selected in comparison to ideal values is given below.

Variable	*Target value*	*Case 1*	*Case 2*
Turbine model scale (rotor diameter)	-	108mm	
Flow rate	-	30l/s	40l/s
Water depth	-	300mm	
Blockage ratio, *B*	4%	6%	
Reynolds number, *Re*	4.8×10^8	2×10^5	3×10^5
Froude number, *Fr*	0.06	0.046	0.062
Tip Speed Ratio, λ	5.6	3.0	2.65

Table 5-4 – Summary of two cases selected for use in further experimental work.

During the design of the turbine models, it became apparent that in order to maintain scale ratio it would be necessary to increase the diameter of the blades to 125mm. This value was chosen as the minimum value at which the internal components of the turbine could be included in a correctly-scaled turbine body. An alternative would have been to maintain blade diameter at 108mm whilst increasing the body diameter of the turbine, but it was felt that the loss of a correct scaling ratio between the blade diameter and body size would have a significant impact on the turbine power output, since a greater portion of the blade swept area would be influenced by the body. With 125mm blade diameter, TSR values of case 1 and case 2 became 3.5 and 3.1 respectively, and blockage ratio increased slightly to 7%. The ratio of turbine height to water depth also increased slightly, but this difference is minimal due to the fact that the overall height of the turbine is only increased by half of the diameter increase (i.e. 8.5mm). This variation is equivalent to an increase of 1.2m in a real turbine case, which is well within the potential range of water depth variation due to waves.

Turbine rotational speed (ω)

As described above, TSR calculations require turbine rotational speed for a given flow speed to be known. These values were recorded during the characterisation phase of work, and were obtained by allowing a turbine model to rotate in a water flow. The turbine was tested without the gearbox or measurement equipment used in subsequent experiments in place, and its rotational speed was measured using video recording at 25Hz. Processing this video on a computer allowed the rotational speed of the turbine under each flow case to be calculated. Turbine rotational speeds in flow of 300mm depth for flow rates from 10 l/s to 40 l/s are illustrated in Figure 5-6.

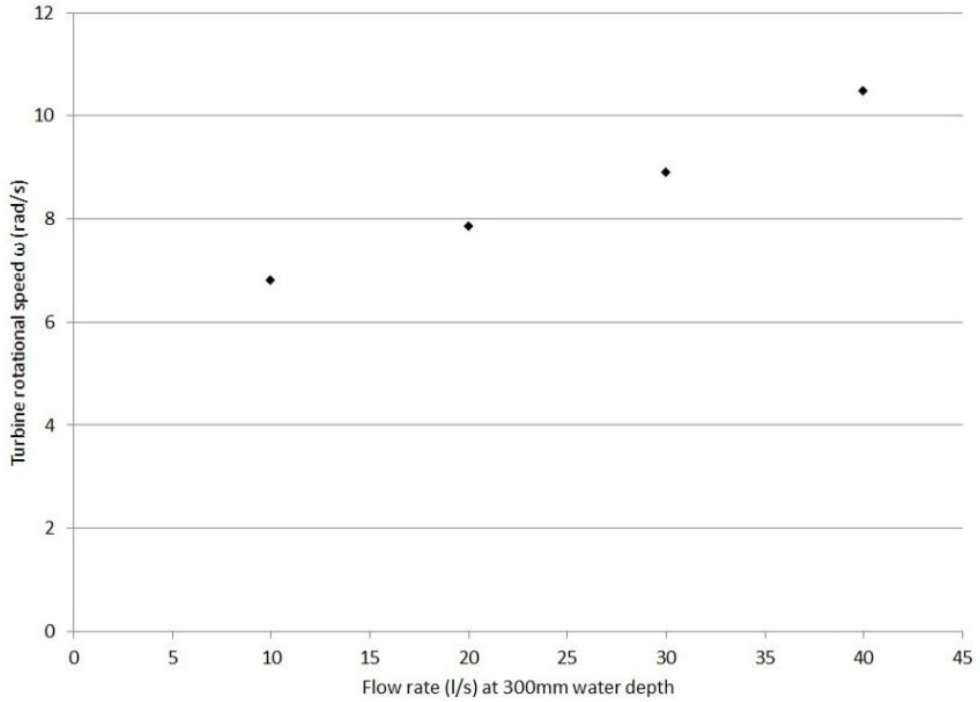

Figure 5-6 – Turbine rotational speed vs. water channel flow rate.

The values illustrated above were calculated for turbines without the bevel gear system which was used to measure torque attached. Once the system was attached, the additional friction meant that the turbine models were unable to drive themselves, or were only able to rotate very slowly, under experimental conditions. Consequently, as discussed in Section 3.4.5, the turbine models were driven by a small electric motor during testing. Drive speeds were set equal to those measured without the gear system in place, as illustrated in Figure 5-6. The use of rotational speeds as measured in uninhibited turbine case for subsequent tests ensured that the measurement equipment did not lead to artificially low rotational speeds, which could produce incorrect wake effects.

Blade angle of attack

As has been discussed previously (Section 2.5.2), a fixed pitch, twisted blade design was used throughout the experimental work described herein. This is a feature of some current tidal turbine designs, and the replacement of pitch controlled blades with fixed pitch designs has been highlighted as a cost-saving measure likely to be applied to other designs in the future. As discussed in Section 3.5.5, an angle of attack of $\alpha = 6°$ was used in all experimental cases.

5.2 – Experimental Phases

At the culmination of the literature review (Chapter 2), the following three aims were developed for the experimental phase:

- To investigate the effect of changing the diameter of the support structure on the power output of a tidal turbine, and the resulting effect on the wakes generated by the turbine and support structure.

- To investigate the effect of changing the streamwise direction separation distance between the blades of a tidal turbine and its support structure on the output of a tidal turbine, as well as on the velocity wake generated by the turbine and support structure, under given flow conditions.

- To investigate the effect on the output and resultant velocity wake of a tidal turbine of placing another turbine upstream, and to investigate the impact of changing the separation distance between the two devices in both streamwise and cross-stream (offset) directions.

A total of 128 experiments were conducted during the major experimental part of this work, divided into four major phases. A fifth phase involving the testing of additional complex support structure designs was also carried out, and is described in Chapter 7. Each phase aimed to provide data useful in the analysis of the aims described above. Phase 1 experiments provided a background understanding and allowed the confirmation of test conditions and experimental methods, whilst phases 2, 3 and 4 address each of the research aims in turn. The four phases are given below:

- Phase 1: Initial wake experiments
- Phase 2: Impact of blade position on turbine power output
- Phase 3: Impact of support structure diameter on turbine output
- Phase 4: Impact of upstream turbine on downstream turbine performance (discussed in Chapter 6)

This chapter describes the results of experiments carried out on a single turbine and support structure, as performed during phases 1, 2 and 3. Results from multiple turbine tests (phase 4) are described in Chapter 6.

5.2.1 – Phase 1: Initial wake experiments

Empty water channel experiments

The aim of this phase was to experimentally replicate the wake observed behind a tidal turbine support structure. However, prior to this, experiments were conducted without turbines in place, in order to measure boundary layer profiles for the turbine installation location. Using a flow depth of 300mm, boundary layer profiles were measured at 9m downstream from the water channel inlet, using case 2 flow conditions. Profiles were recorded initially using a pitot tube and digital manometer (Furness Controls FCO510) system, then subsequently using the Acoustic Doppler Velocimetry system detailed in Chapter 3. The profile generated using the ADV equipment is illustrated in Figure 5-7a. Turbulent intensity was also calculated from ADV data, and is illustrated in Figure 5-7b.

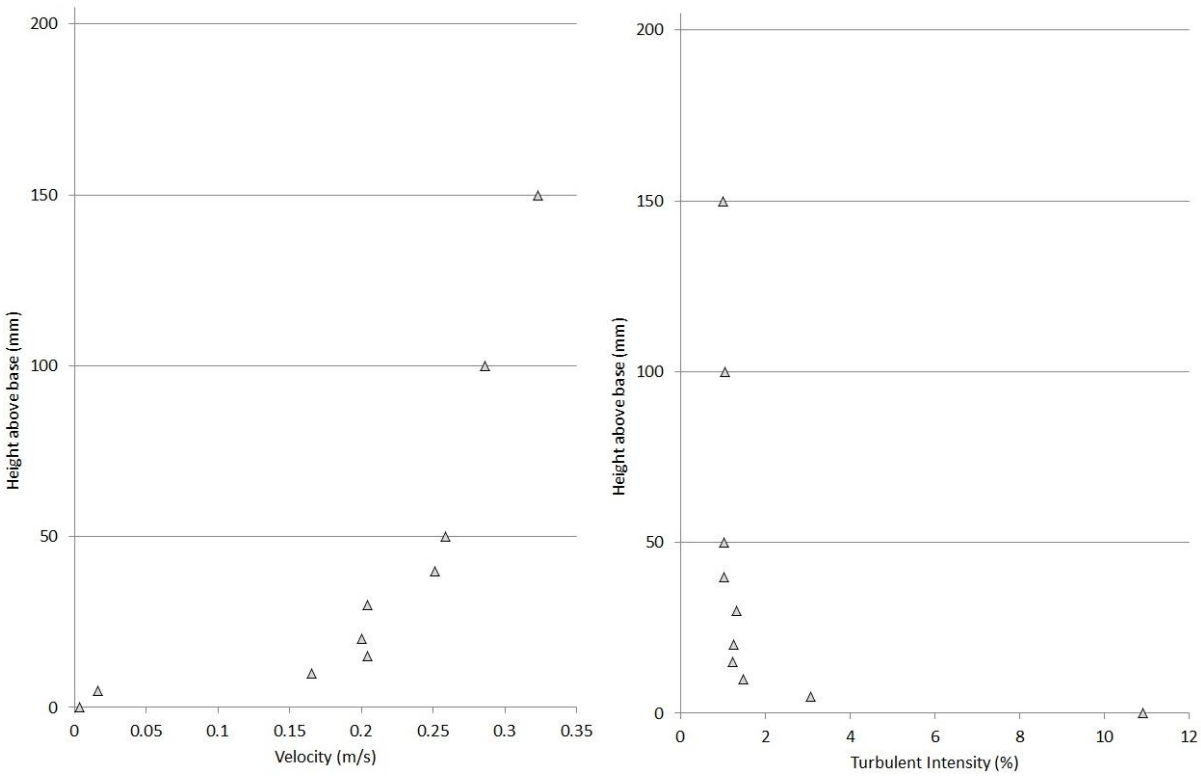

Figure 5-7 a&b – Velocity (l) and turbulent intensity (r) profiles at channel centreline (9m downstream, flow case 2).

Actuator disk experiments

Prior to the first experiments using the full turbine models described in Section 5.1, a series of experiments were carried out using actuator disks, as introduced in Section 3.5.3.

A series of experiments using actuator disks were conducted, under flow conditions described in case 1 above (30l/s flow rate, 300mm water depth. Re = 2x10^5, Fr = 0.046). Stainless steel mesh disks of 34%, 39% and 45% porosity were used. The disks used were of 105mm diameter, each yielding a blockage ratio of 5.8%. Sample disks are shown below.

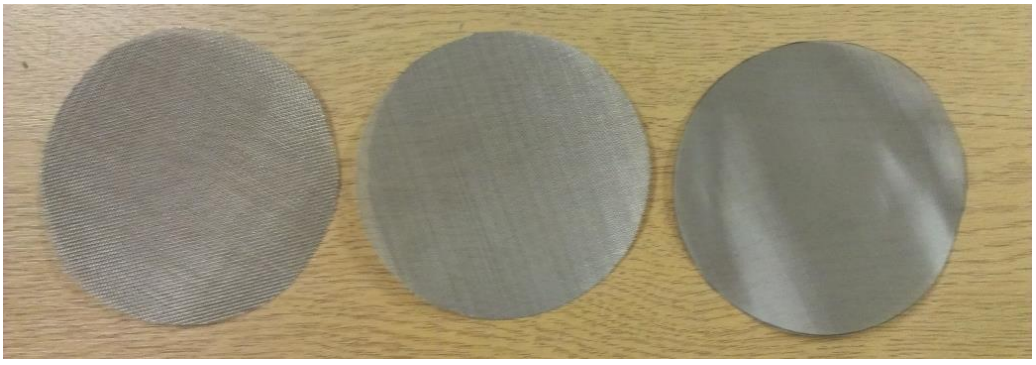

Figure 5-8 – Actuator disks of (l-r) 34%, 39% and 45% porosity.

During experiments, actuator disks were mounted on a cantilever thrust measurement rig in order to measure the thrust experienced by the disk during each experiment. The thrust measurement rig

comprised a 6mm diameter arm, with the actuator disk mounted onto the lower part. The rig is shown in Figure 5-9.

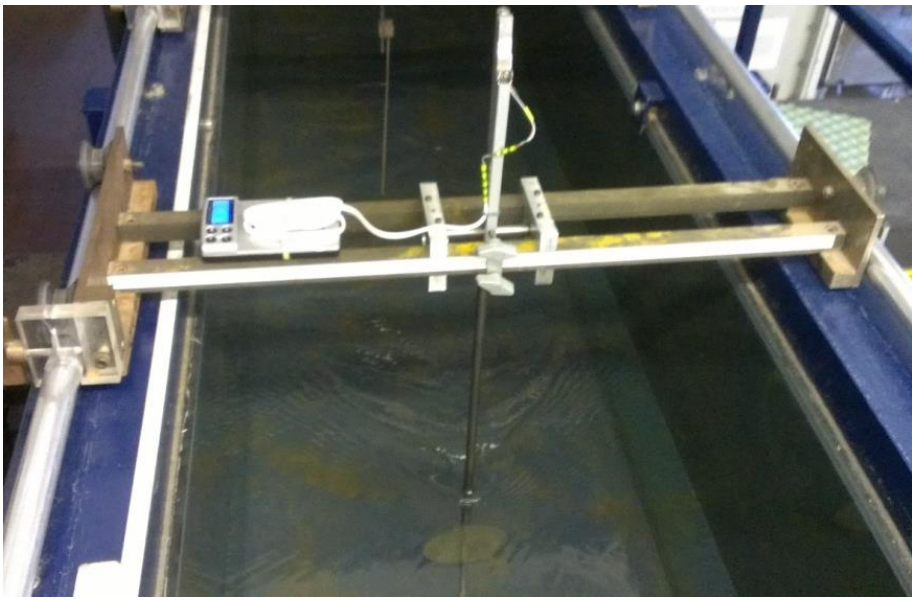

Figure 5-9 – Actuator disk thrust measurement rig in situ.

In addition to thrust measurement, flow velocity was measured at five downstream positions behind the disk, as well as at one upstream position (diameter multiples of -3*D*, 3*D*, 5*D*, 10*D*, 15*D* and 20*D* from disk position). At each streamwise position, velocity was recorded at four horizontal positions (diameter multiples from the channel centreline of 0*D* (directly downstream of the actuator disk), 0.5*D*, 1*D*, and 1.5*D*). In the case of the 34% and 39% porosity disks, all measurements were recorded at the vertical height of the centre of the actuator disk (i.e. 0*D* vertical height relative to actuator disk centre). In the case of the 45% porosity disk, two vertical positions were used; 0*D* and 0.5*D* (i.e. at the height of the top edge of the disk). Measurement locations are illustrated in Figure 5-10.

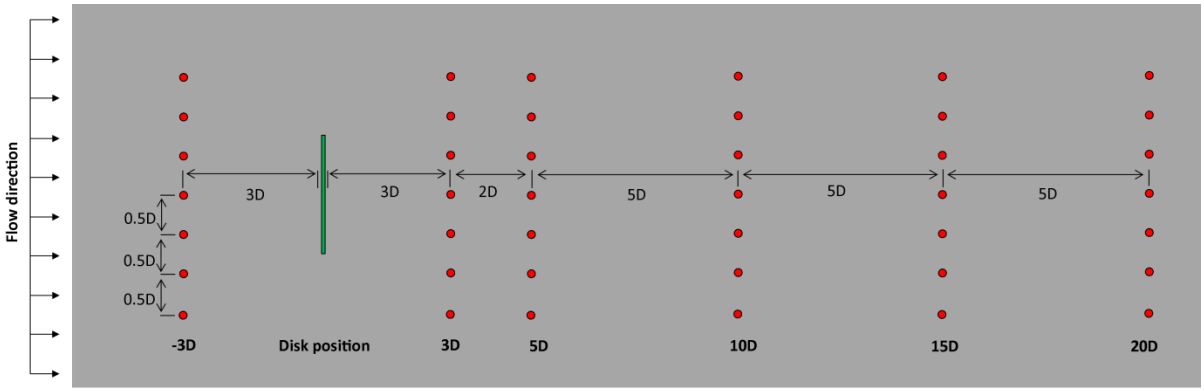

Figure 5-10 - Graphical representation of actuator disk experiments carried out during phase 1 (ADV measurement positions shown in red, actuator disk shown in green).

Velocity measurements were conducted using a Nortek Vectrino ADV unit, as detailed in Section 3.4.2. Flow velocity was measured at the points given above (five downstream and one upstream), for each of the three disks. Streamwise centreline flow velocity deficit was calculated for each case, as illustrated in Figure 5-11. Velocity deficit at downstream position x was calculated as follows:

$$u_{def} = \frac{(u_0 - u_x)}{u_0}$$

By recording thrust and velocity data for each experiment, velocity deficit results were able to be normalised by thrust coefficient, in order to allow a direct comparison of velocity deficit over the three porosities. Thrust coefficient was calculated thus:

$$C_T = \frac{T}{0.5\rho u_0^2 A_D}$$

Using free stream velocity measurements (u_0) recorded without a disk in place, the following values of C_T were calculated:

Disk porosity (%)	*Thrust coefficient*
34	0.83
39	0.80
45	0.77

Table 5-5 – Thrust coefficient values for actuator disks of 34, 39 and 45% porosity.

Velocity deficit vs. downstream position for centreline streamwise velocity measurements for each of the three C_T cases is illustrated in Figure 5-11.

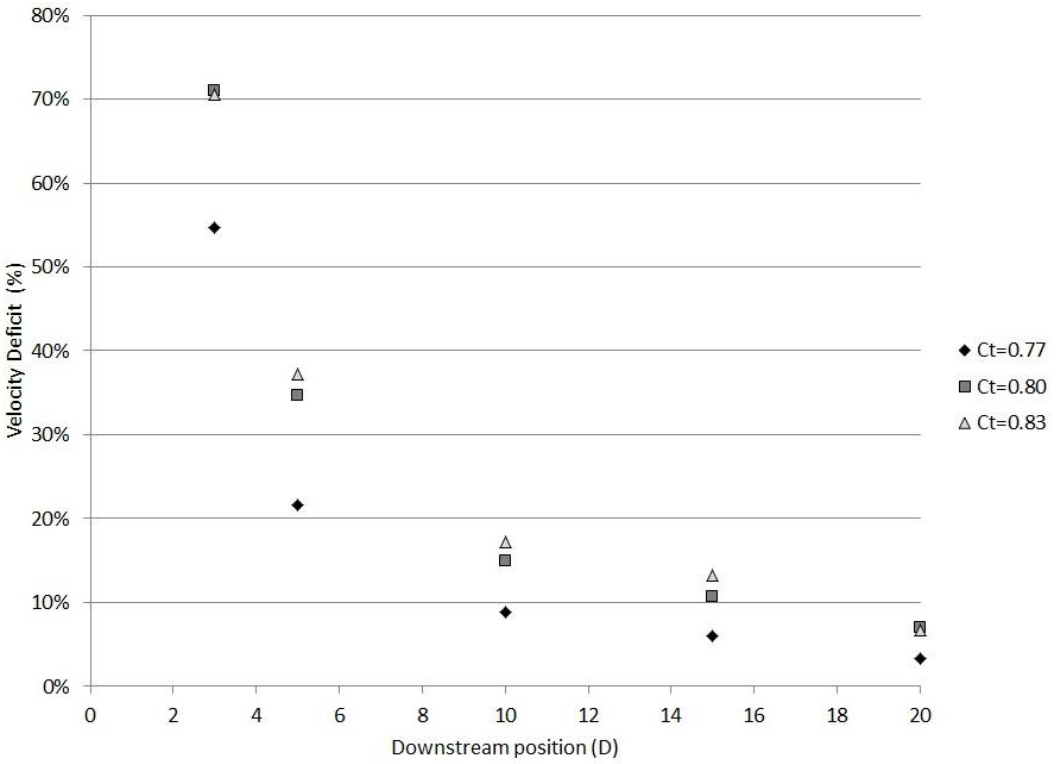

Figure 5-11 – Centreline streamwise velocity deficit for thrust coefficient C_T = 0.77, 0.80 and 0.83, in case 1 flow conditions.

As shown in the figure, flow velocity is reduced to between 25% and 50% of its original value within 3 rotor diameters distance of the turbine location, before gradually returning towards free stream

conditions as observed at -3*D*. Greater values of C_T (i.e. lower disk porosity, greater disk solid area) yielded greater velocity deficit and longer recovery times as one would expect. However, this effect decreases with separation, and at 20 rotor diameters downstream of the actuator disk, the observed difference in velocity deficit between the C_T = 0.77 and C_T = 0.83 cases was 3%. It is also notable that full velocity recovery is not observed until beyond 20*D* downstream of the actuator disk.

Velocity deficit data was also recorded for three additional cross-stream positions (0.5*D*, 1*D* and 1.5*D* from the streamwise centreline) at the water channel centreline, for each of the three C_T conditions and five downstream positions (3*D*, 5 *D*, 10 *D*, 15 *D* and 20*D*). These results are illustrated in Figure 5-12, Figure 5-13 and Figure 5-14.

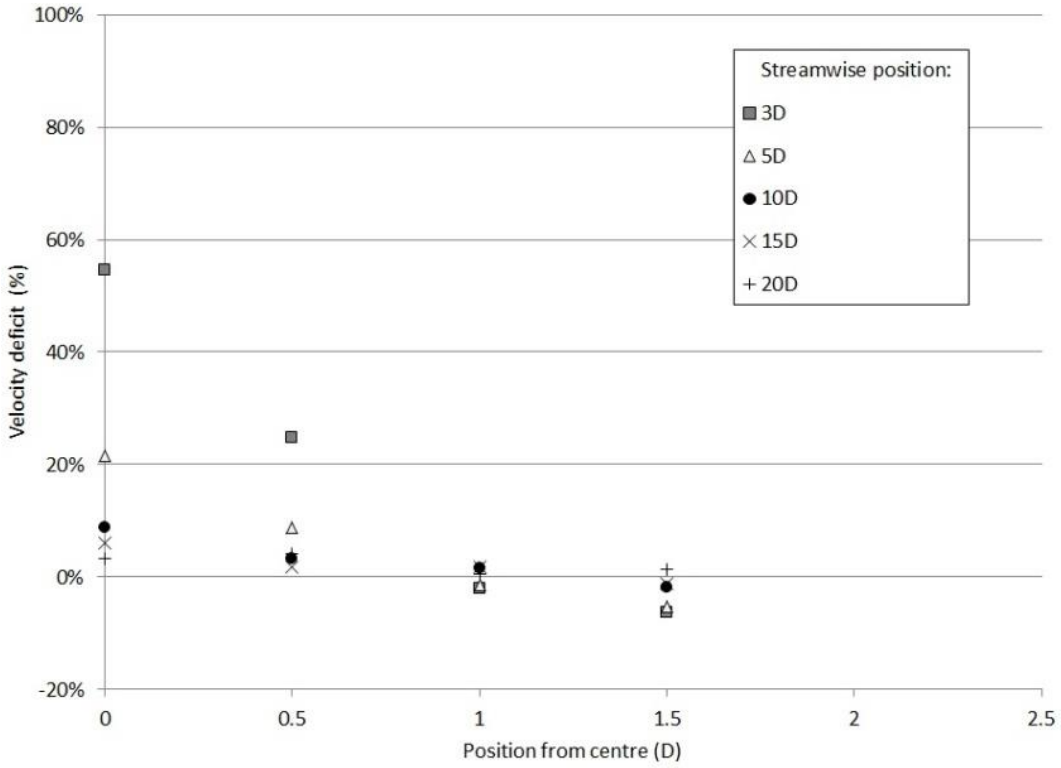

Figure 5-12 – Cross-stream position vs. velocity deficit at 3, 5, 10, 15 and 20D downstream (Porosity = 45%, C_T = 0.77).

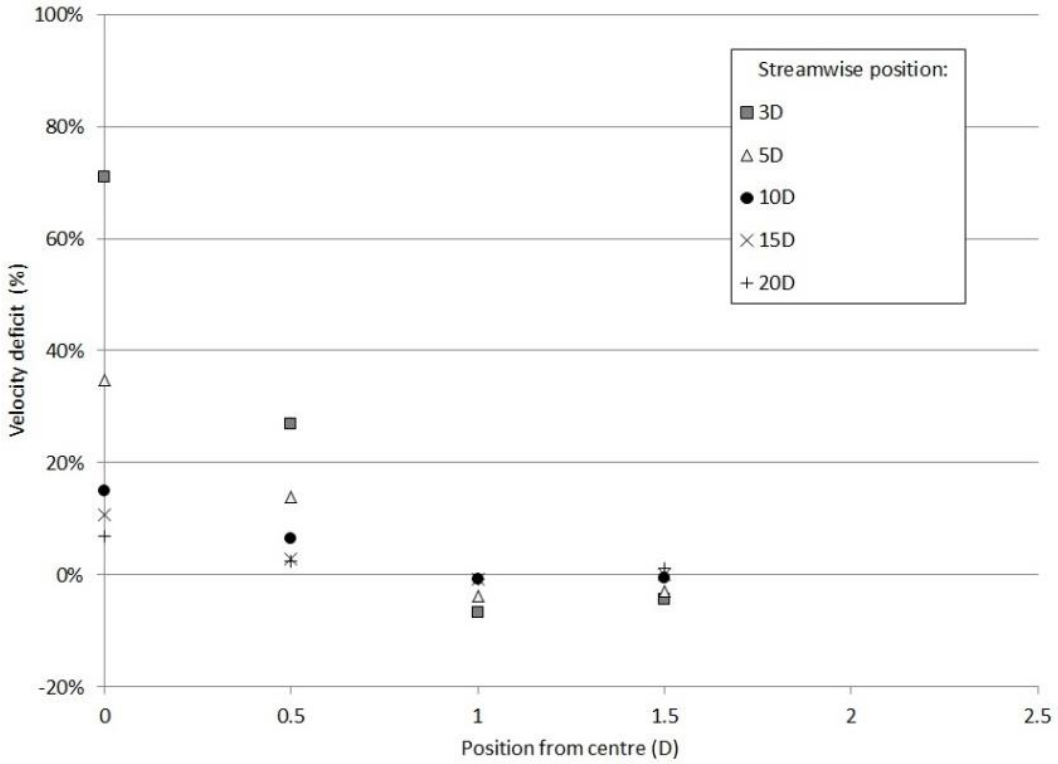

Figure 5-13 – Cross-stream position vs. velocity deficit at 3, 5, 10, 15 and 20D downstream (Porosity = 39%, C_T = 0.80).

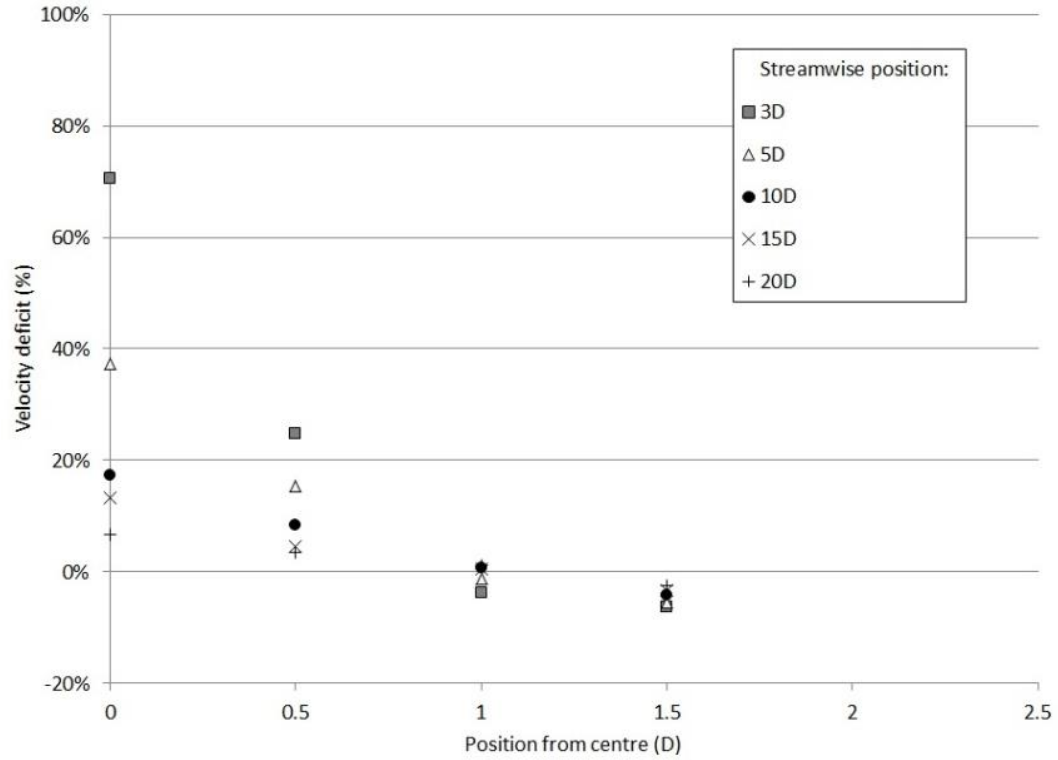

Figure 5-14 – Cross-stream position vs. velocity deficit at 3, 5, 10, 15 and 20D downstream (Porosity = 34%, C_T = 0.83).

In all cases, negative deficit is observed for horizontal positions further than 1*D* each side of the disk, indicating that velocity in this region is greater than that observed at the channel centreline without a disk in place. This is to be expected due to the requirement of conservation of mass, and the consequential acceleration of bypass flow as the flow through the disk is slowed. The wake region can be defined as the region within which velocity deficit greater than zero is observed. Using this definition, the edge of the wake is observed at a horizontal distance of around 1*D* from the actuator disk centre in each of the three C_T cases above. The precise horizontal diameter position at which the 0% deficit line lies is given for downstream distances in the cases above in Table 5-6.

	Horizontal 0% deficit point (D from disk centre)		
Downstream position	*C_T = 0.77*	*C_T = 0.80*	*C_T = 0.83*
3D	0.90	0.85	0.95
5D	0.95	0.85	0.90
10D	1.05	0.90	1.25
15D	1.05	>1.50	1.25
20D	1.15	>1.50	1.10

Table 5-6 – Horizontal wake velocity recovery distance for five rotor diameters at C_T = 0.77, 0.80, and 0.83.

Using the results described in Table 5-6, a diagram of the wake pattern (as defined as the area within which velocity deficit greater than zero is observed) for each of the three tested cases was generated. Figures illustrating the downstream wake velocity decay in horizontal and vertical directions for the channel centreline and horizontal positions of 0.5*D*, 1*D* and 1.5*D* to one side of the water channel are shown in adjacent figures in each case.

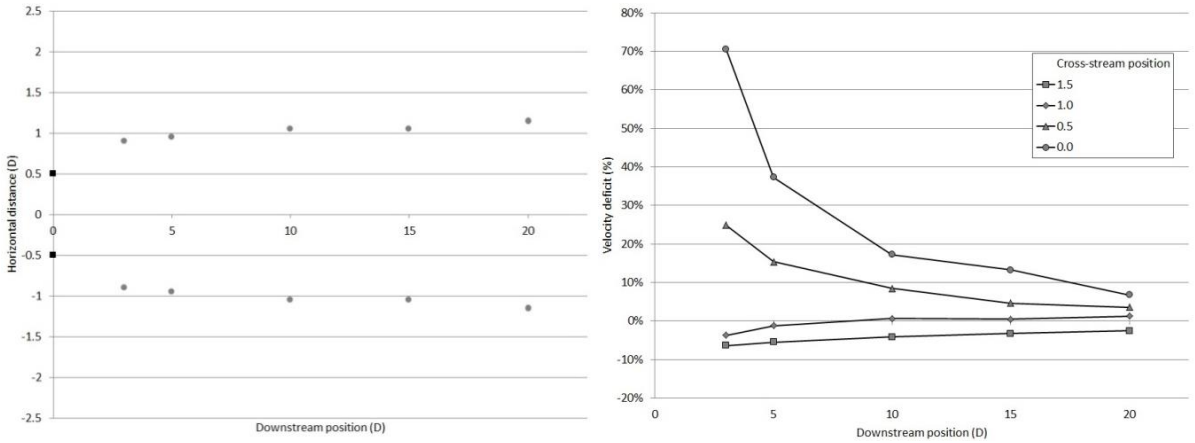

Figure 5-15a&b – Wake region measured using actuator disk at C_T=0.77 (Porosity = 45%).

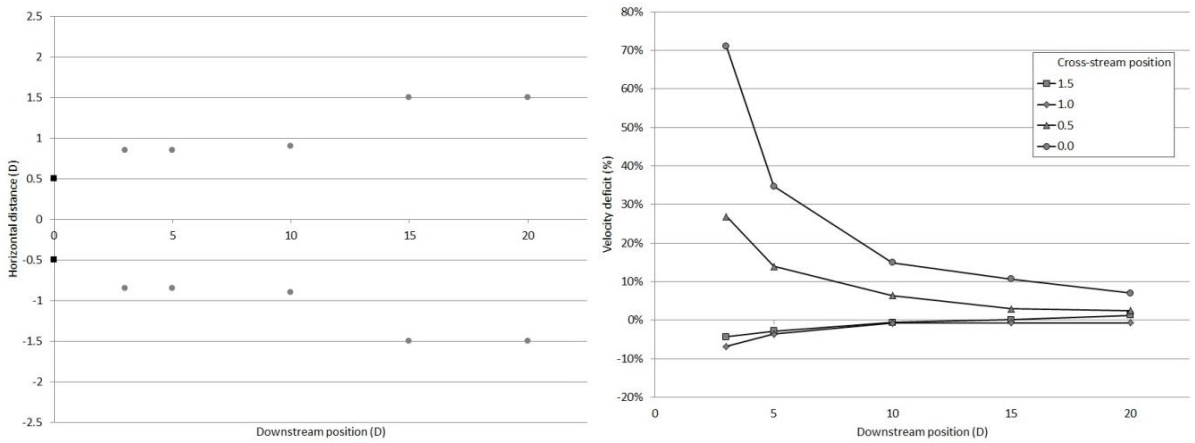

Figure 5-16a&b – Wake region measured using actuator disk at C_T =0.80 (Porosity = 39%).

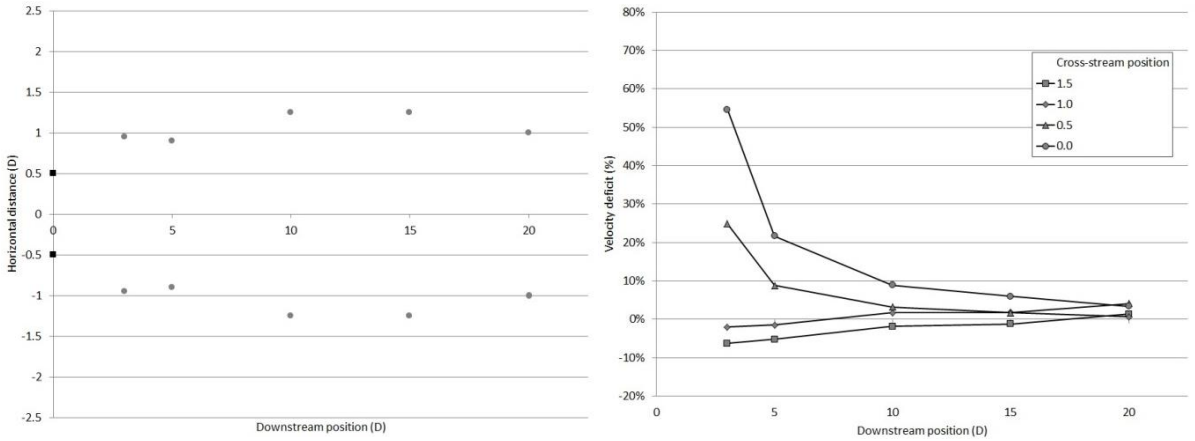

Figure 5-17a&b – Wake region measured using actuator disk at C_T =0.83(Porosity =34%).

The primary aim of actuator disk experiments was to ascertain the size of the expected streamwise and cross-stream wake region. Although wake length is a function of the turbulence and viscosity of the flow, and significant differences are therefore expected between actuator disk wakes and those observed during experiments using turbine models, the use of this method has nonetheless produced useful information.

As is illustrated in the figures above, the wake behind an actuator disk appears to extend downstream for more than 20 disk diameters under the conditions described, with horizontal influence of up to around 1.5*D* to each side of the centre line. These results are comparable with those of previous similar studies [52], and suggest that at the blockage ratio used (B = 5.8%) appears to allow an unconstrained wake to develop. Blockage has been discussed extensively in Sections 2.2.4 and 3.5.2, and blockage factor corrections of 1.19 for C_p and 1.06 for λ were calculated using the method described in Section 3.5.2. However, given that numerous comparable studies with simple blockage ratios of below 10% were not found to have applied any blockage correction to results, this correction was not universally applied to the results in this study. The effect of blockage is however discussed in the conclusions given in Chapter 8.

Dye injection experiments

Subsequent experiments were carried out using the support structure models installed on the false base described in Section 3.5, in a central position at 9m downstream from the water channel inlet, both with and without turbine models installed.

Dye injection was used to gain a visual understanding of the wake behind the support structure and turbine models. A mixture of red food dye and water was injected from an angled tube of 2mm internal diameter located 100mm upstream of the turbine, which was mounted at 9m downstream from the channel inlet. As described in Section 3.4.1, tests were carried out to determine a suitable ratio of dye to water ratio, and a concentration of 6% dye was subsequently selected. Dye was injected using the system and equipment described in Section 3.4.1, which incorporated a constant head tank to ensure a constant delivery rate of dye throughout the tests. Dye mixture flow rate was adjusted to deliver at the same flow velocity as the water channel. Case 1 and case 2 flow conditions were used, as well as some testing with a valve opening percentage of 15%, corresponding to a flow rate of 5.4 l/s (lower than both case 1 and case 2). Support structure diameters of 11mm, 16mm and 20mm were used. Results were observed for understanding, and recorded using both a standard digital video camera (Kodak Easyshare) and the PIV camera system, which was set to an increased exposure rate of 100ms in order to capture the relatively dimly-lit conditions in these experiments. 2000 images were recorded during each test, at a frame rate of 20Hz.

The dye injection tests confirmed the generation of vortices (as predicted in Section 2.10) behind the support structure. Vortex shedding was observed when case 1 or case 2 flow conditions were used, but not when the lower flow rate was used. As discussed in Chapter 2, these effects are generally observed at Reynolds number values between around $Re = 10^2$ and $Re = 10^5$, for Re values calculated using the cylinder diameter characteristic length. At the 5.4 l/s flow rate, Reynolds number values for the three cylinder diameters were 394, 573 and 717 respectively. For case 1, values were 2254, 3279, and 4099, and in case 2 flow conditions were 3381, 4919 and 6148 respectively. Images of vortex shedding observed in the wake of the 16mm diameter support structure in flow case 2 are given in the figures below.

Figure 5-18 – Vortex shedding behind 16mm diameter support structure (Re = 4919).

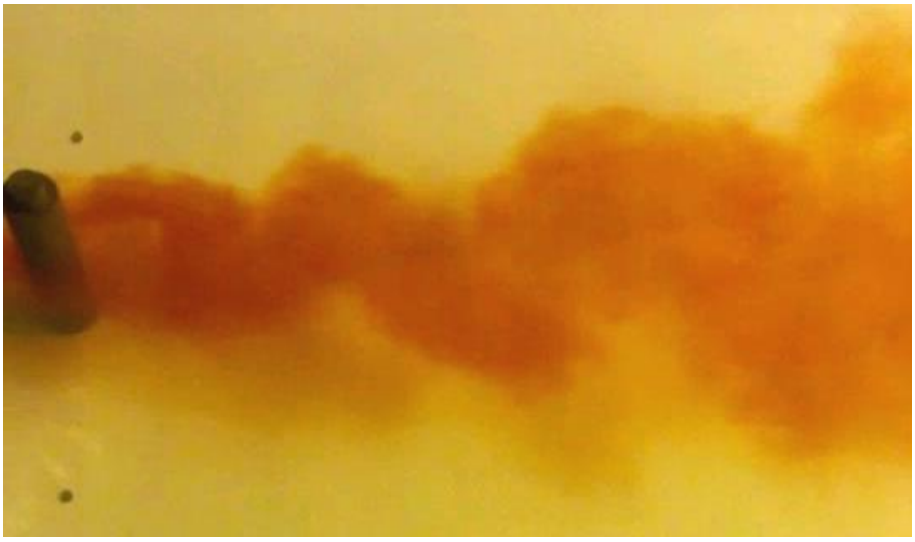

Figure 5-19 – Vortex shedding detail behind 16mm diameter support structure (Re = 4919).

Dye injection experiments were also conducted with a turbine installed on the support structure. These tests were undertaken in flow case 1 conditions. The turbine was allowed to rotate freely, and was not attached to the drive or torque measurement systems. The rotational speed of the turbine was calculated from recorded digital video to be 80 revolutions per minute (8.4 rad/s), giving a TSR value of 2.65. The wake observed in the turbine case was much less defined than in the support structure only case; video recordings of the tests do indicate the generation of some vortex structures, but the pattern of generation and shedding is not regular as in the support structure only case, suggesting that the wake structure is a combination of wakes generated by different parts of the turbine and support structure. It was noted that under the same case 1 flow conditions and with the same concentration of dye, the length of support structure wake which could be observed before the dye concentration was too low to see was around 2m (equivalent to 16D), whereas with the turbine in place this was around 1.5m (12D). Though this is a qualitative observation, it may suggest that the composite turbine wake does not persist as far downstream as the wake from the support structure alone. A sample image of the observed wake behind a turbine and support structure is shown in Figure 5-20.

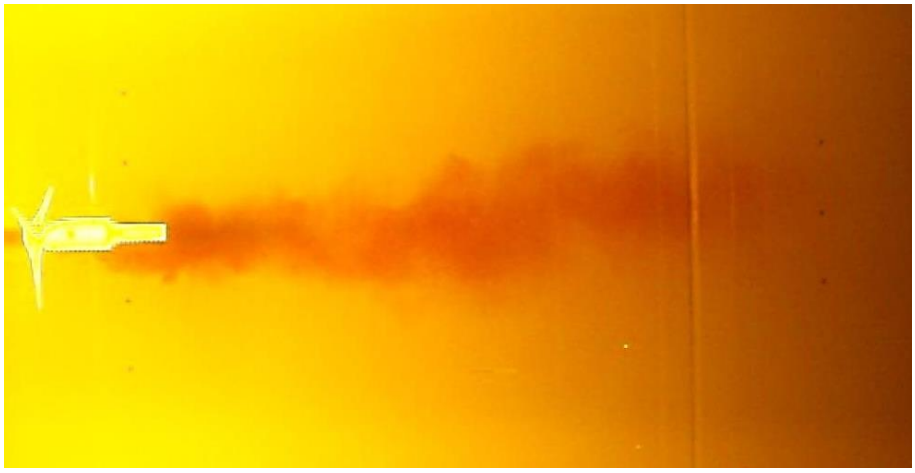

Figure 5-20 – Sample of observed wake behind turbine and 16mm diameter support structure (Re = 4919, TSR = 2.15).

POD analysis of dye injection experiments

As has been discussed previously, the Proper Orthogonal Decomposition (POD) is a statistical technique which allows the calculation of the major sources of energy in a flow pattern, and the simplified representation of the flow pattern as a composite of a number of these energy sources. This technique was used to find the major sources of energy within the wake of a tidal turbine model. The 125mm rotor diameter turbine described previously was installed on a 16mm diameter support structure post and installed in the water channel at 9m downstream of the inlet. Flow condition case 1 was applied, and dye was injected as described in the previous section. The camera and image recording system installed for subsequent PIV experiments was used to record images, though the PIV laser system was not used in this case, and the camera image exposure time was increased to 100ms to account for lower light levels. The aim of these tests was to identify the major energetic structures in the wake of a model tidal turbine, and to identify the sources of these wake structures. Sample images used in this analysis are illustrated in Figure 5-21.

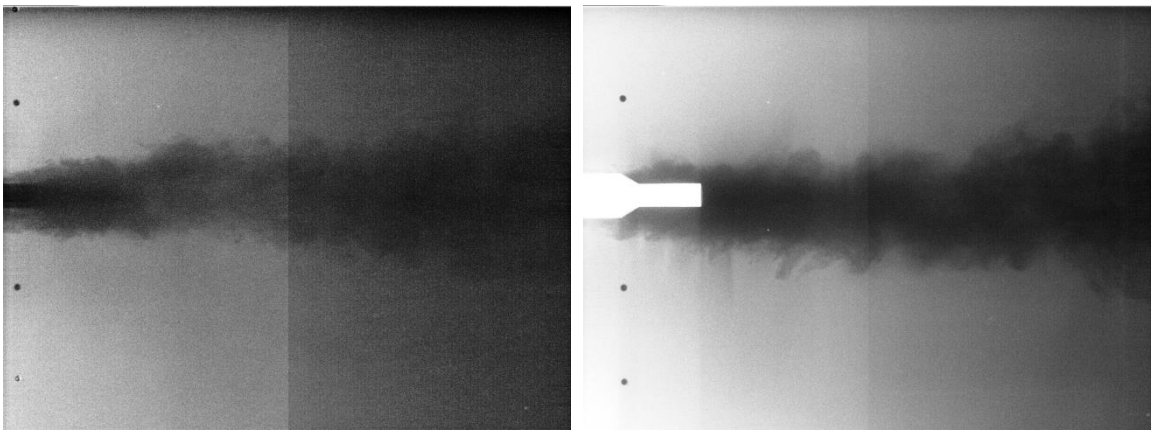

Figure 5-21 – Sample dye injection images used in POD processing: Support structure only (l) and support structure with turbine (r).

Results of the POD analysis are illustrated below. The method highlights the generation of vortex shedding behind the support structure post, with vortices of a range of scales observed in results both with and without the turbine in place. In the latter case however, the energy structures identified are highly disrupted and appear “chopped” by the turbine blades. This is particularly the case in later modes, and appears to lead to the extension of the wake more widely in the cross-stream direction, as well as reducing the size of the energetic structures moving downstream and thus leading to the slightly shortened wake hypothesised in the previous section. It should be noted that the images shown in the figures below do not represent a time series, so the wake structures illustrated in (for example) mode 3 do not directly represent the downstream movement and breakdown of those seen in mode 2. Instead, mode 2 illustrates the second, and mode 3 the third, most energetic set of wake structures observed over the recording period. However, due to drop in energy levels as the wake structures decay, the images do illustrate the decay of large wake elements into smaller and smaller structures. The percentage of the overall energy contained within each mode is detailed for each case. In the images below, energy is illustrated from high to low by black to white areas respectively. In both cases, the primary and most energetic mode is the background flow, which contains around 13.5% of the total energy of the flow in both cases. As

would be expected, the almost universal grey colour of these two images indicates that the background flow is not highly energetic, but is much more homogenous than subsequent modes.

Support structure only:

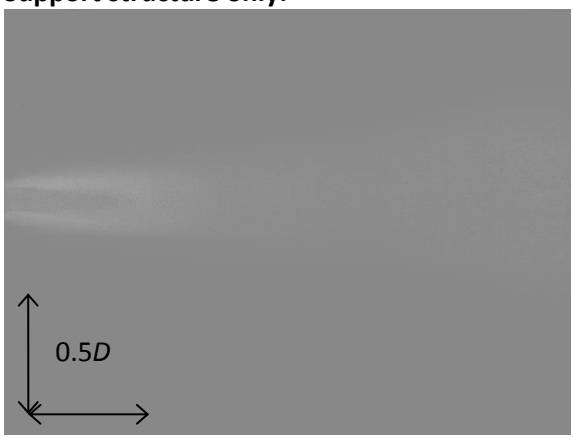

Mode 1 (background): 13.5%

Mode 2: 11.5%

Mode 3: 10.8%

Support structure and Turbine:

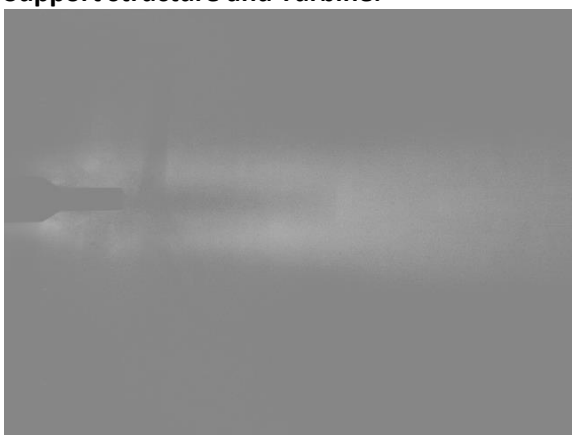

Mode 1 (background): 13.4%

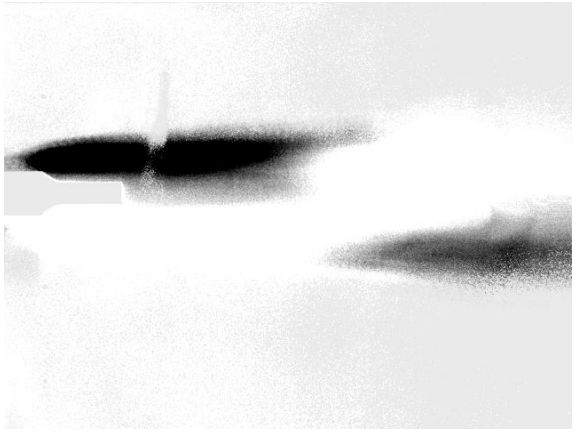

Mode 2: 12.4%

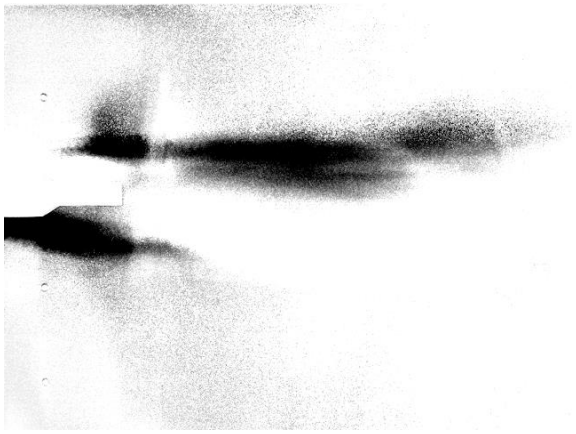

Mode 3: 12.5%

Figure 5-22 – First ten wake modes as calculated by POD analysis for support structure only (l) and support structure with turbine (r).

(Part 1)

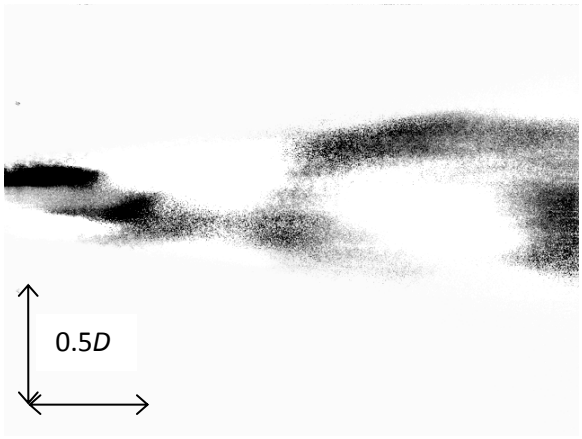

Mode 4:10.2%

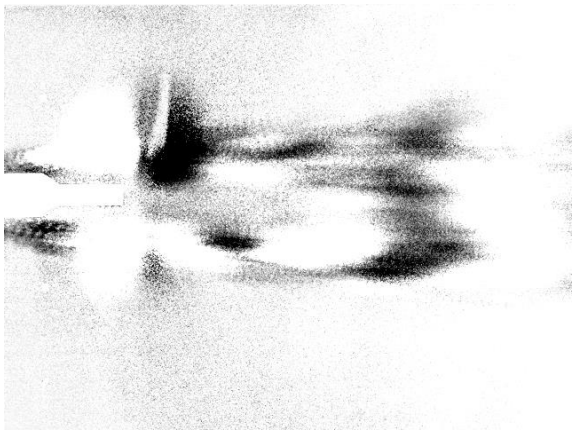

Mode 4: 10.4%

Mode 5: 10.0%

Mode 5: 9.8%

Mode 6: 9.8%

Mode 6: 9.2%

Figure 5-23 - First ten wake modes as calculated by POD analysis for support structure only (l) and support structure with turbine (r).

(Part 2)

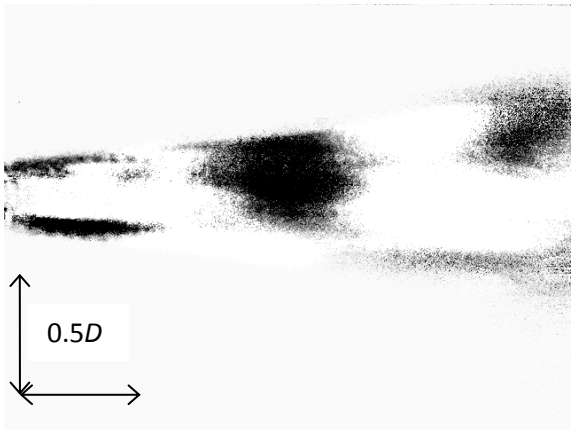

Mode 7: 9.4%

Mode 7: 8.8%

Mode 8: 8.8%

Mode 8: 8.4%

Mode 9: 8.2%

Mode 9: 8.2%

Figure 5-24 - First ten wake modes as calculated by POD analysis for support structure only (l) and support structure with turbine (r).

(Part 3)

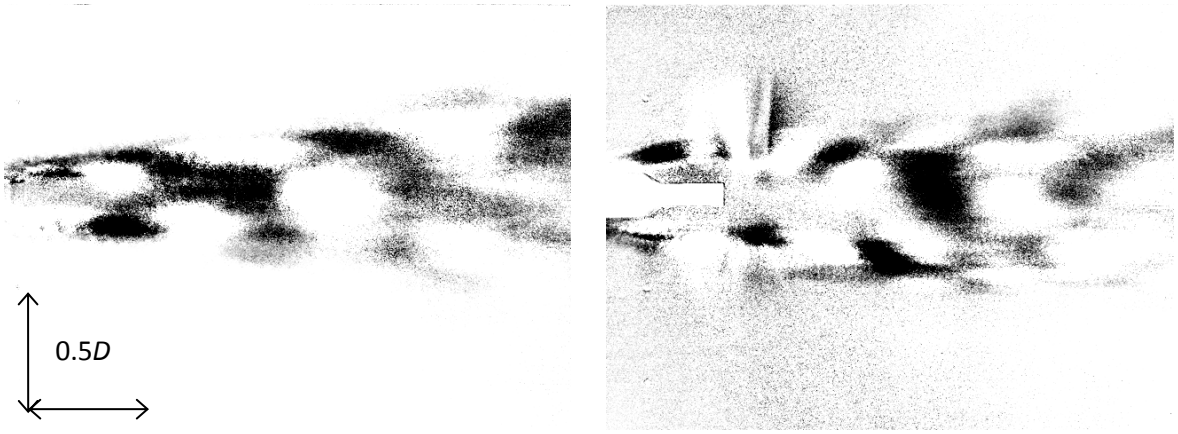

Mode 10: 7.9%

Mode 10: 7.4%

Figure 5-25 - First ten wake modes as calculated by POD analysis for support structure only (l) and support structure with turbine (r).

(Part 4)

A further POD process was carried out to produce images of wake structures with less energy than those imaged above. This was achieved by subtracting the mean of the velocity fluctuation from each image and conducting the POD process again. The results of this process for the support structure case are given below, illustrating the smaller and smaller structures contained within the wake. The background flow is not included in this case, since this is a continuation of the previous series, indeed it can be seen that mode 2 of this second POD phase appears to be the same as the final mode of the previous calculations. As before, highly energetic areas appear darker.

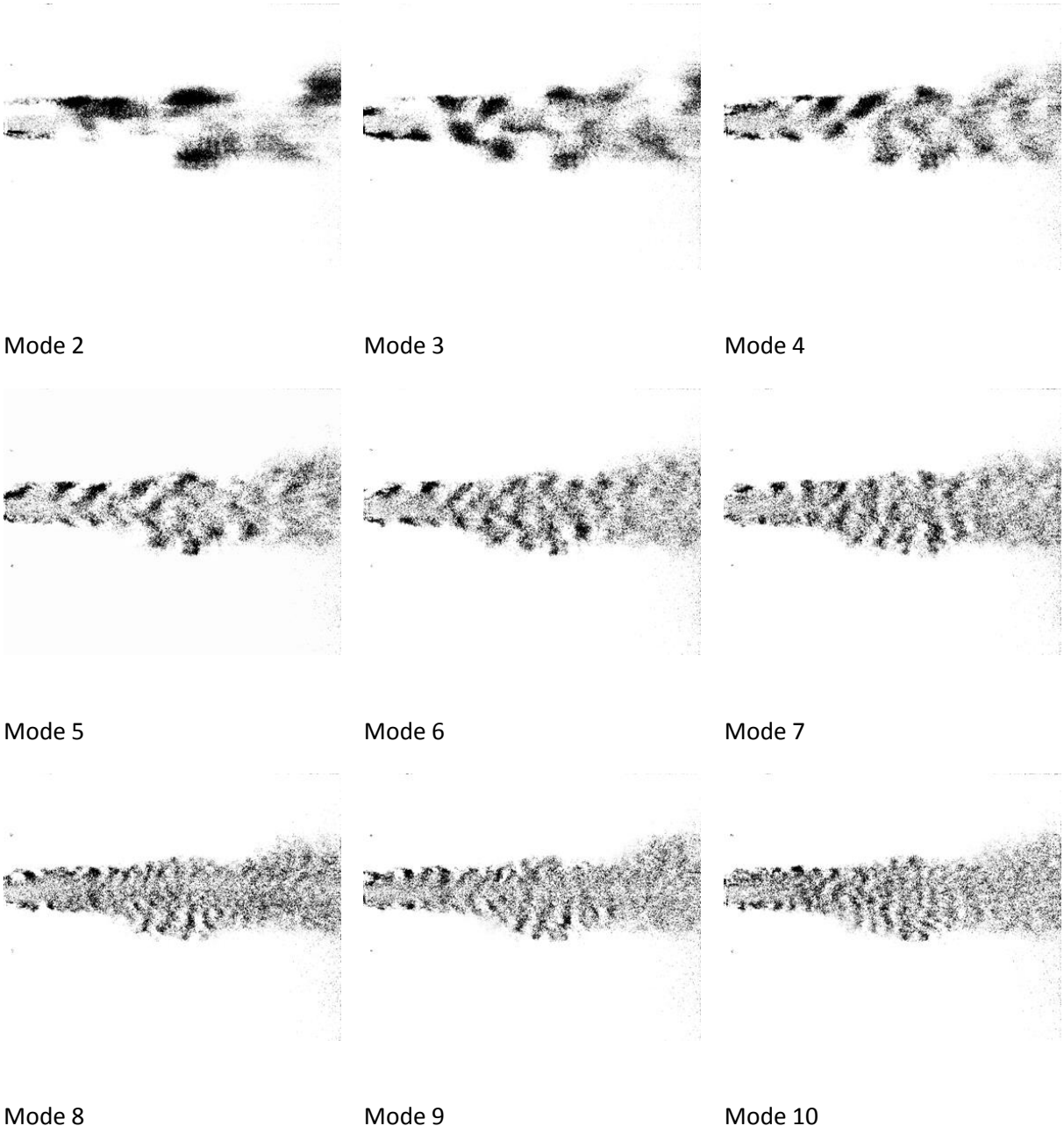

Figure 5-26 – Further POD wake modes for support structure without turbine.

The use of the POD method allows a flow structure which has been simplified to its modes to also be reconstructed using the modes, producing a simplified flow pattern containing all the primary energy sources of the original. Simplified images of the reconstructed wakes behind support structure only and the support structure with turbine in position are illustrated in Figure 5-27 and Figure 5-28.

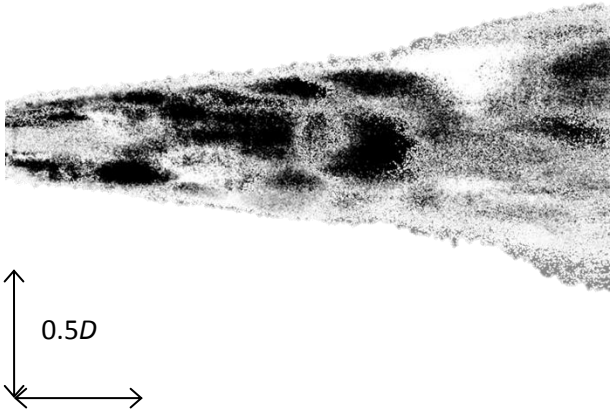

Figure 5-27 - POD reconstruction of wake behind support structure.

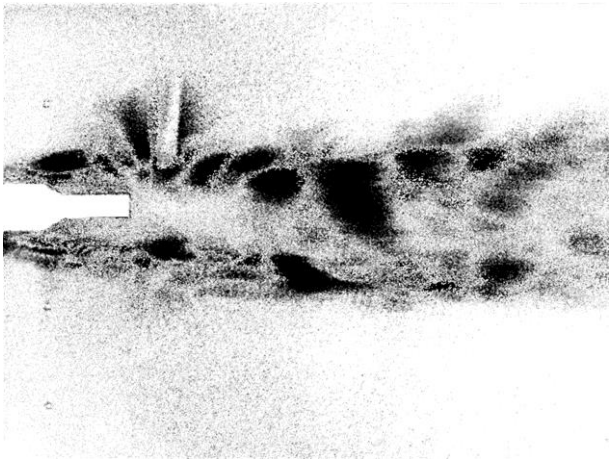

Figure 5-28 - POD reconstruction of wake behind support structure with turbine.

As can be observed in these figures, it appears that the wake of the support structure alone is initially narrow and quickly expands downstream. The wake of the support structure with turbine is initially wider than that without the turbine, but does not undergo such an expansion. It is also notable that the wake of the device without a turbine includes larger energetic structures than in the turbine case, in which it appears that the largest structures are divided into smaller structures by the rotation of the blades. This goes some way to explaining the shorter length of the wake with a turbine in place.

POD results with the turbine in place also appear to show a narrower wake than that predicted by actuator disks, again highlighting that the dynamic wake structures of the turbine appear to restrict the cross-stream size of the composite wake.

Subsequent sections of this chapter will discuss results from further experimental phases, particularly the comparison of torque output with flow condition data, which was recorded primarily using PIV in order to give detailed numerical flow field results.

Summary results – Phase 1

- Actuator disks of three values of porosity (34, 39, 45%) and C_T (0.83, 0.80, 0.77 respectively) demonstrated different wake characteristics. Velocity deficit was greater for lower porosity disks, and at 10*D* ranged from 9% to 18%. Wakes were found to extend beyond 20*D*, with deficit at this position ranging from 4% to 7%. Cross-stream wakes appeared to extend up to 1.5*D* each side of the streamwise centreline.
- Dye injection revealed that the wake of a support structure without a turbine is initially narrow, and undergoes a rapid cross-stream expansion. The wake of a support structure with turbine in the same flow case was initially wider, but the cross-stream expansion was less pronounced. In qualitative observation the combined turbine and support structure wake also exhibited more rapid recovery than the support structure alone (requiring 12*D* and 16*D*).
- POD analysis of dye injection images highlights the blade tip vortices as the most energetic structure in the combined wake, containing around 25% of total wake energy.

5.2.2 – Phase 2: Impact of blade position on turbine performance

The aim of this phase was to study the effect on turbine power output of adjusting the streamwise separation distance between the turbine blades and the support structure. Three separation distances were studied, defined by the distance in the streamwise direction between the swept path of the blade centre and the centre of the turbine support structure. Separation distances of 20mm (referred to as front), 40mm (centre) and 60mm (back) were used, corresponding to 0.16D, 0.32D and 0.48D respectively. Blade-support separation distance was adjusted by moving the mounting position of the turbine body on the support structure, as illustrated in Figure 5-29.

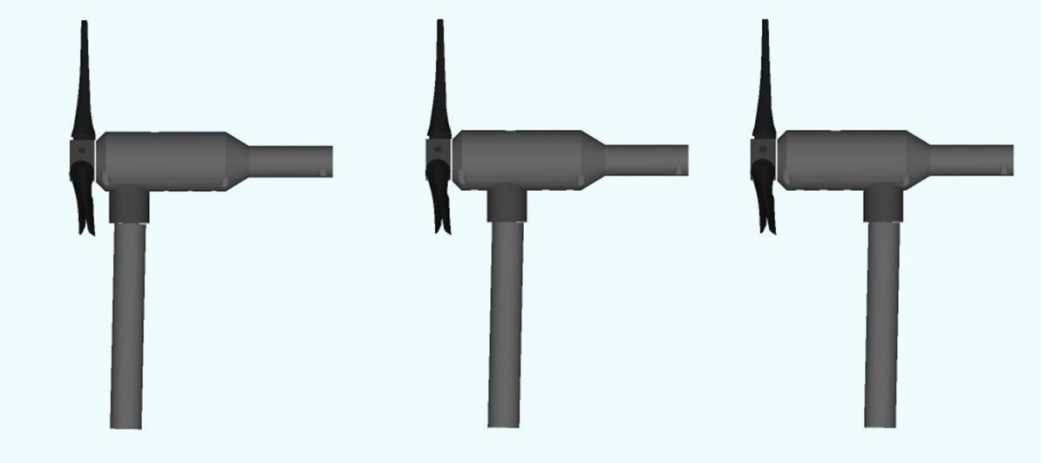

Figure 5-29 – Blade-support separation mounting positions as tested (l-r): Front (20mm); Centre (40mm); Back (60mm).

A total of eighteen experiments were carried out during this phase. Initially, a cylindrical support structure of 11mm diameter was installed on the false base at 9m downstream of the water channel inlet, in a central position, with an instrumented turbine model installed on top. In order to study any relative effect of the position of the blades relative to the support structure, the same experimental procedure was carried out thrice: initially with the turbine body mounted in the front position, then the centre position, and finally the back position. Case 2 flow conditions were used throughout (Water depth = 300mm, λ = 3.1, Re = $3x10^5$, Fr = 0.062, B = 7%), and turbine performance was monitored by measuring the required power to drive the turbine. Full details of the turbine performance measurement methodology are given in Section 3.6. The three experiments described above were then repeated using a support structure of 16mm diameter, then again using a support structure of 20mm diameter to give results for front, centre and back turbine mounting locations for each support structure diameter. Reynolds numbers in the region of the support structures, calculated using support structure diameter characteristic length, were Re = 3300, 4800 and 6000 for the 11mm, 16mm and 20mm diameter cases respectively.

The flow field around the turbine was also measured in each case, using PIV. Experiments were repeated to allow recording of PIV images at two heights: 135mm and 66mm above the water channel false base, giving the total of eighteen experiments in this phase.

PIV results

PIV was used to calculate velocity and turbulence characteristics around the structures tested during this phase. PIV data was recorded at two height planes during each test. Initially a plane height corresponding to the blade axis was used (135mm above the channel base), followed by a second plane at the vertical centre of the support structure (66mm above the channel base). The lower plane lies just below the edge of the blade swept region, which is between 72.5mm and 197.5mm above the channel base at the centre line. The two measurement planes are illustrated in Figure 5-30.

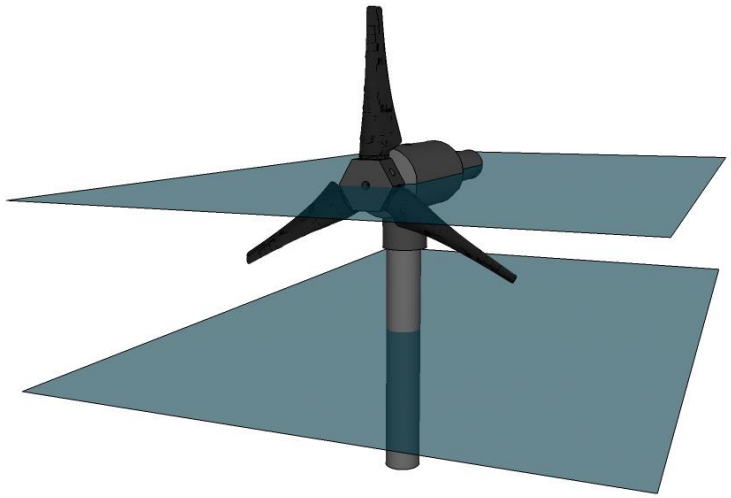

Figure 5-30 – CAD model turbine illustrating location of two PIV measurement planes (66mm and 135mm above channel base).

400 image pairs were recorded and correlated in each test at a frequency of 15Hz, giving a total sample time of 26.6s. Sample frames illustrating velocity in the region downstream of the turbine mounted on a 16mm diameter support structure in each of the three test configurations are given in the following figures. Sample frames are illustrated in preference to mean flow images, since due to the turbulent nature of the flow conditions observed mean flow images may be unable to illustrate the dynamic characteristics of the flow appropriately. The location of the turbine or support structure at the sample height in each case is shown, as is the region of interest from which data for further analysis was extracted (see Section 4.3.1).

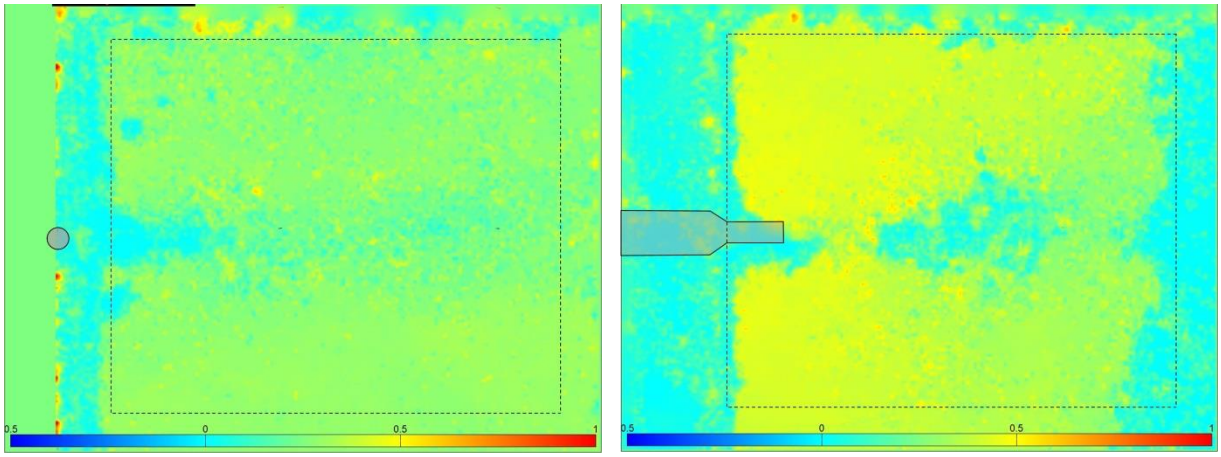

Figure 5-311&b – Sample streamwise direction velocity (m/s) frames recorded at 66mm (l) and 135mm (r) above channel base, front position, 16mm diameter support structure.

(Image scale: 0.362m x 0.272m in all cases)

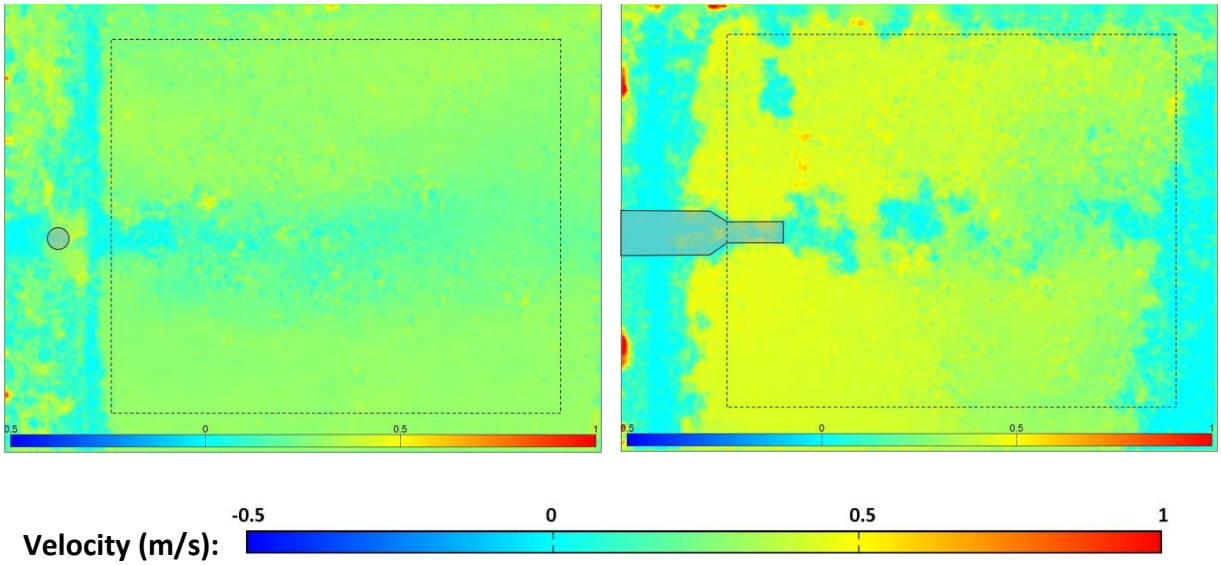

Figure 5-32a&b – Sample streamwise direction velocity (m/s) frames recorded at 66mm (l) and 135mm (r) above channel base, centre position, 16mm diameter support structure.

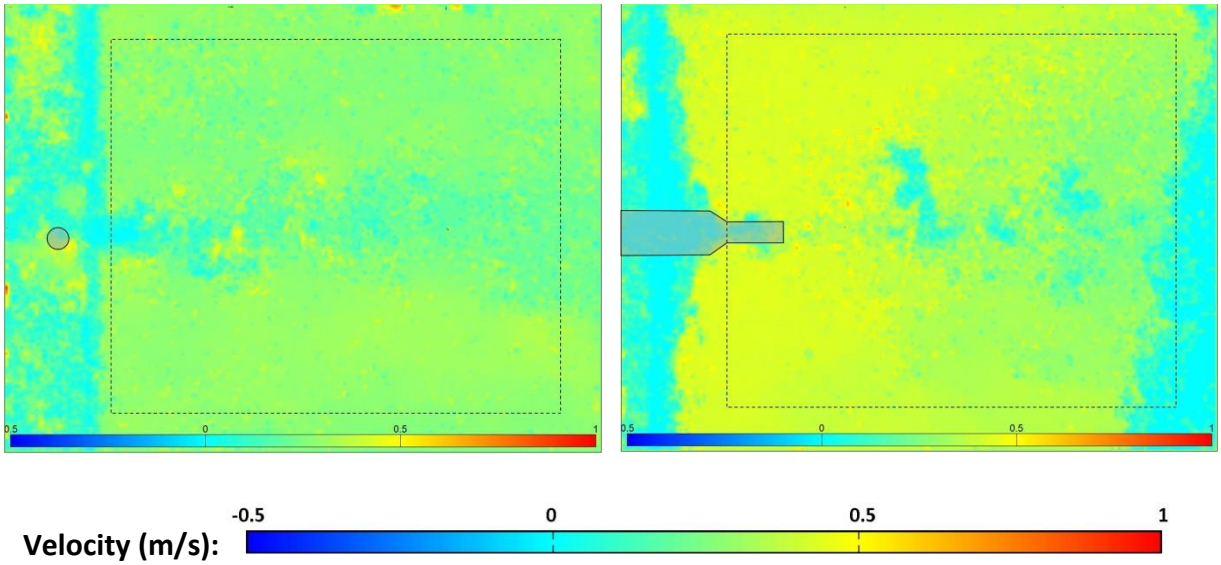

Figure 5-33a&b – Sample streamwise direction velocity (m/s) frames recorded at 66mm (l) and 135mm (r) above channel base, back position, 16mm diameter support structure.

These sample frames illustrate the greater velocity magnitude present at the higher measurement plane, as predicted from the velocity profiles calculated in Chapter 3. Bulk flow velocities in the downstream region of interest are around 0.25m/s at the 66mm plane, and 0.35m/s at the 135mm plane. The reduction in flow velocity downstream of the support structure or turbine can also be clearly seen, and the turbulent wake is illustrated by the pockets of high and low velocity flow generated behind the turbine and support structure.

These results were studied quantitatively in combination with blade torque data in order to understand the observed differences in torque output from the turbine when mounted in each of the three locations. These differences are described in the following section.

Performance data

Turbine performance was measured under flow case 2 (depth = 300mm, λ = 3.1, Re = 3x10^5, Fr = 0.062, B = 7%) in all cases. Results of the experiments conducted during this phase are given in Table 5-7. Results are presented as mean blade-generated torque over the 4 second turbine data recording period. In all cases experiments were repeated twice in order to reduce the potential for erroneous results. Mean blade torque was calculated for each of the two data sets, from which a further mean of the two results was then calculated, as given below. Variation between mean blade torque results was found to be within 5% for all tests undertaken during phase 2.

Mean blade torque and power coefficient (C_p) results for the experiments described above are given in Table 5-7, followed by a graphical representation of C_p data.

TSR λ	***Support structure diameter***	*Blade position (mm from support centre)*	*Mean blade torque (Nm)*	*Power coefficient (C_p)*
3.1	**11mm / 0.088*D***	Front (20)	0.40	0.24
		Centre (40)	0.43	0.26
		Back (60)	0.27	0.16
	16mm / 0.128*D*	Front (20)	0.42	0.25
		Centre (40)	0.45	0.27
		Back (60)	0.29	0.16
	20mm / 0.16*D*	Front (20)	0.42	0.26
		Centre (40)	0.47	0.28
		Back (60)	0.22	0.13

Table 5-7 – Mean blade torque results for phase 2 experiments in case 2 flow conditions.

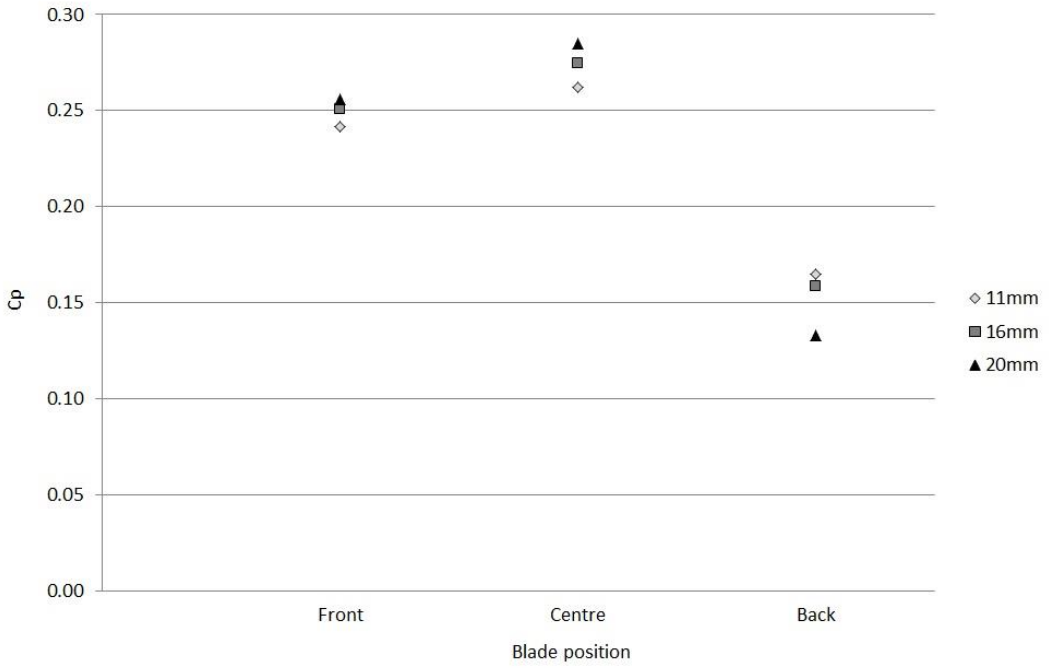

Figure 5-34 – Power coefficient recorded for turbines mounted in three streamwise positions, on three support structure diameters (Flow case 2).

Figure 5-34 illustrates the major finding of phase 2: In all support structure diameter cases, it was found that the turbine produced greater power output when installed in the centre (40mm / 0.32*D* separation) position than when installed in either the front (20mm / 0.16*D* separation) or back (60mm / 0.48*D* separation) positions. In all cases, the front position yielded the second greatest blade power result, with the back position producing the least blade power. The centrally-mounted turbine position generated at least 7.5% greater C_P than other positions, and a maximum of 53% greater. This is a significant result, and experimental data was therefore studied in order to understand the cause. PIV results with a new region of interest were generated in order to study the region in which the blades operate, upstream of the support structure. Data from this region is given in the following section, followed by a summary of phase 2 results. A combined discussion of phase 2 and phase 3 results is given in Section 5.3.

Area upstream of support structure

PIV data was used to analyse the area upstream of the support structure, for the series of experiments illustrated in Figure 5-34. Velocity results were recorded at the lower of the planes shown in Figure 5-30, 66mm above the channel base, allowing a full velocity profile to be captured at a height just below the turbine swept region. Again, 400 results were recorded at 15Hz, image results were processed using PIVLab, and centreline results were exported using MatLab. For each frame, streamwise and cross-stream velocity results were computed for the region upstream of the support structure.

Time-averaged results in each case are shown below, with the turbine unit in place. In all cases flow is from left to right, with the support structure front face located at the horizontal axis zero position to the right of the image. The position and size of the turbine body and blades is illustrated in each case, at the same scale as the horizontal axis. However, it should be noted that these results were recorded at the lower measurement height, 6.5mm below the swept region of the turbine blades. The blade swept region is situated upstream of the support structure (i.e. to the left of the vertical axis in the above figures) between 10mm and 14.5mm in the front case (Figure 5-35 and Figure 5-38), 30mm and 34.5mm in the centre case (Figure 5-36 and Figure 5-39), and 50mm and 54.5mm in the back case (Figure 5-37 and Figure 5-40).

All results are illustrated along the channel centreline, with streamwise velocity results for the front, centre, and back cases are given first, followed by cross-stream velocity results for the same cases (note that a different vertical axis scale is used in streamwise and cross-stream cases). Positive directions are downstream in the streamwise direction, and to the right in the cross-stream direction, as viewed when facing the oncoming flow.

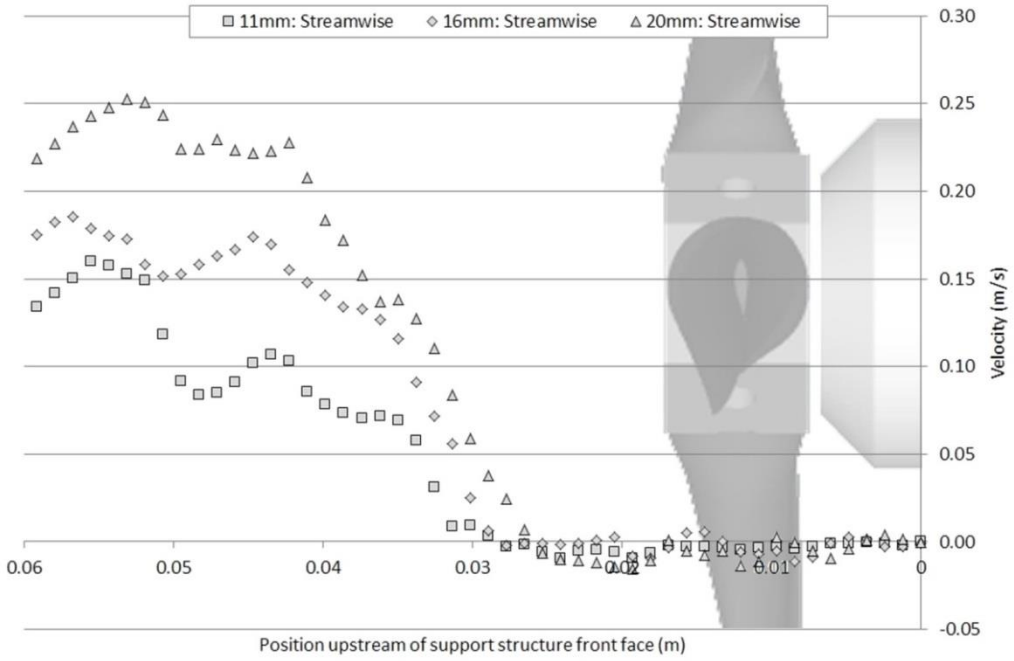

Figure 5-35 – Time-averaged streamwise velocity in upstream region of 11mm, 16mm and 20mm diameter support structure located in front position at 66mm above channel base (flow from left to right).

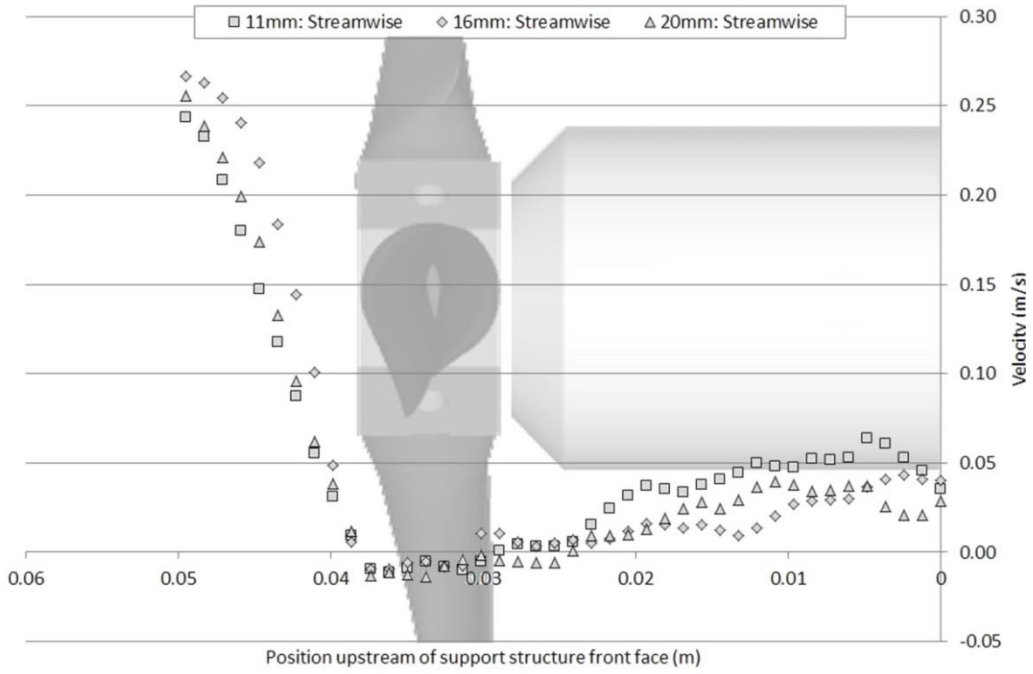

Figure 5-36 – Time-averaged streamwise velocity in upstream region of 11mm, 16mm and 20mm diameter support structure located in centre position at 66mm above channel base (flow from left to right).

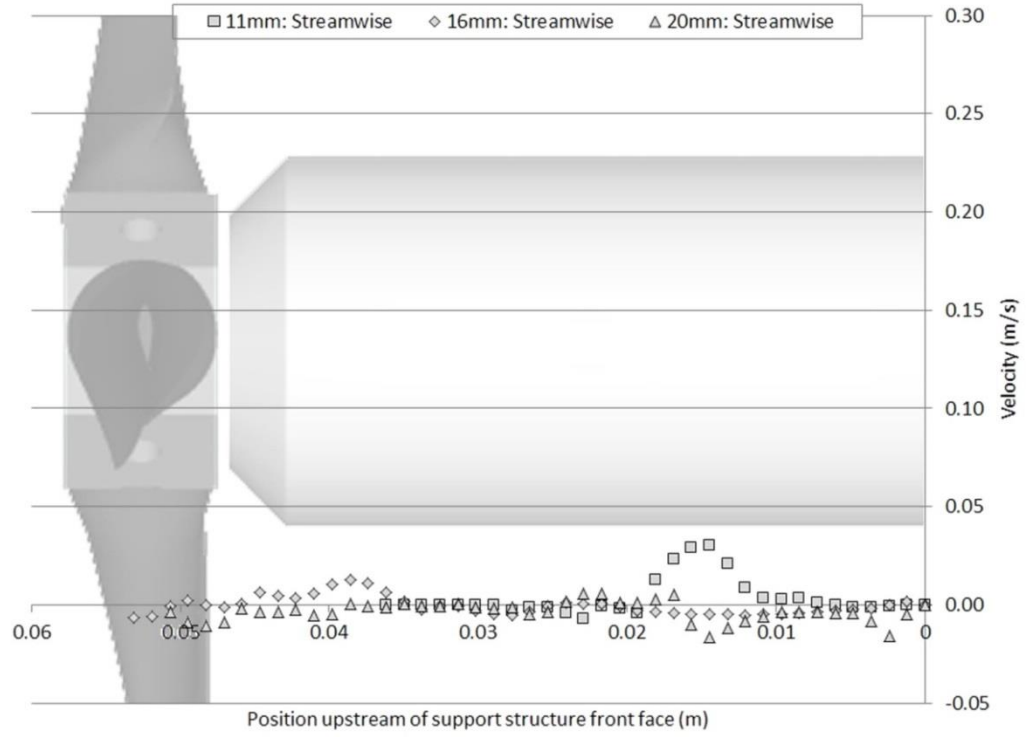

Figure 5-37 – Time-averaged streamwise velocity in upstream region of 11mm, 16mm and 20mm diameter support structure located in back position at 66mm above channel base (flow from left to right).

It can be seen that in all streamwise velocity cases, a low velocity region appears to exist just downstream of the location of the turbine blades, in the area directly below the blade swept area. In

all cases, velocity in this area falls to zero and then becomes slightly negative for a short distance. This velocity deficit region correlates with actuator disk velocity deficit observed in Phase 1 results, and appears to be due to the extraction of energy from the flow by the blades.

There is a notable difference in the position at which the velocity drop is observed between the front and centre cases. In the front cases, velocity is reduced to zero at around 15mm upstream of the blade swept region, whereas in the centre mounted case, velocity does not reduce to zero until around 5mm upstream of the blades. Velocity recovery also appears to begin earlier in the centre case, with recovery to around 15% of free stream conditions observed within 35mm (0.28*D*) of the blade swept region. In the back case, velocity appears to recover in the 20mm diameter support structure case, but then drops to zero again, and does not appear to recover within the 50mm (0.4*D*) region between the blades and the support structure front face.

Cross-stream velocity results for the same three cases are given in the following figures (note the different vertical scale to that used in streamwise results).

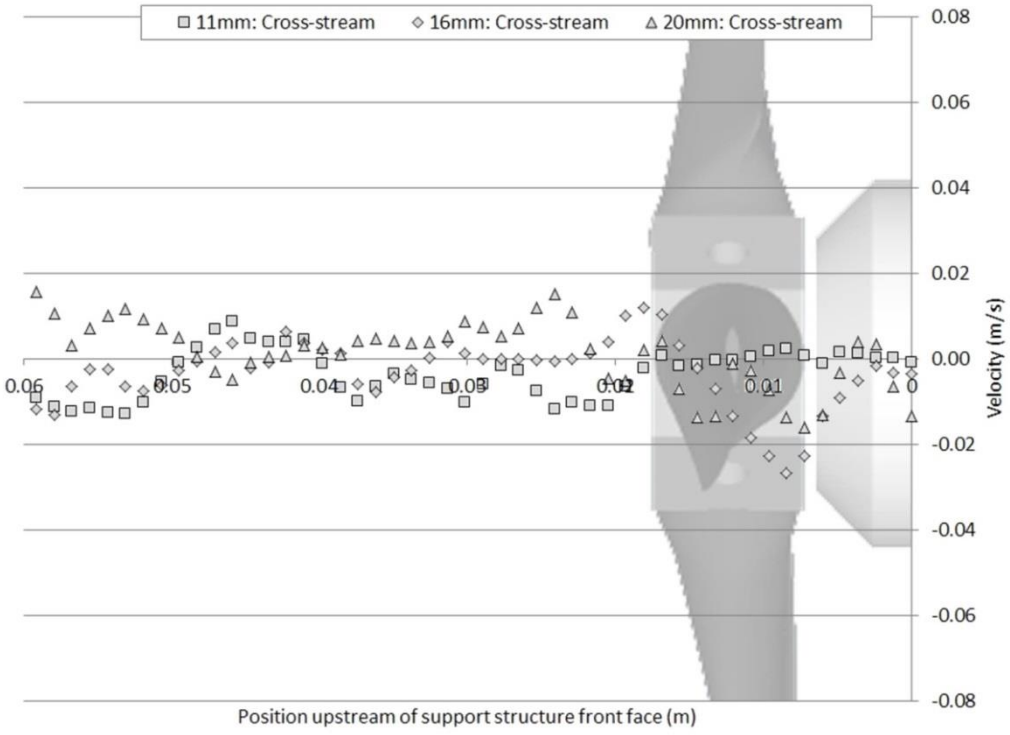

Figure 5-38– Time-averaged cross-stream velocity in upstream region of 11mm, 16mm and 20mm diameter support structure located in front position at 66mm above channel base (flow from left to right).

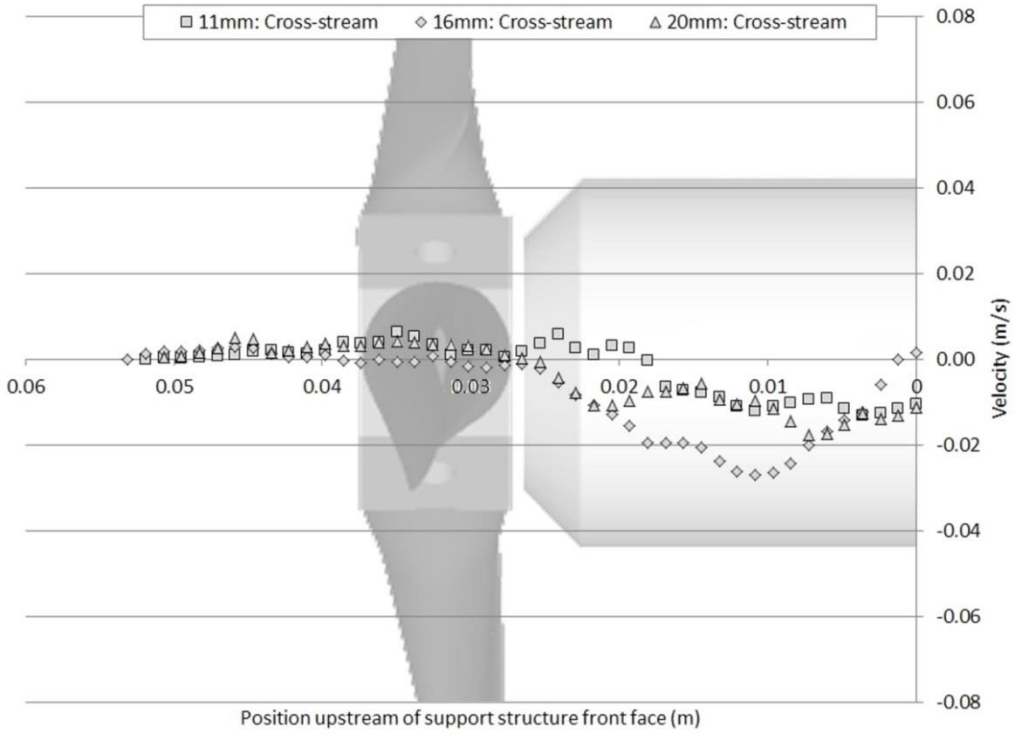

Figure 5-39– Time-averaged cross-stream velocity in upstream region of 11mm, 16mm and 20mm diameter support structure located in centre position at 66mm above channel base (flow from left to right).

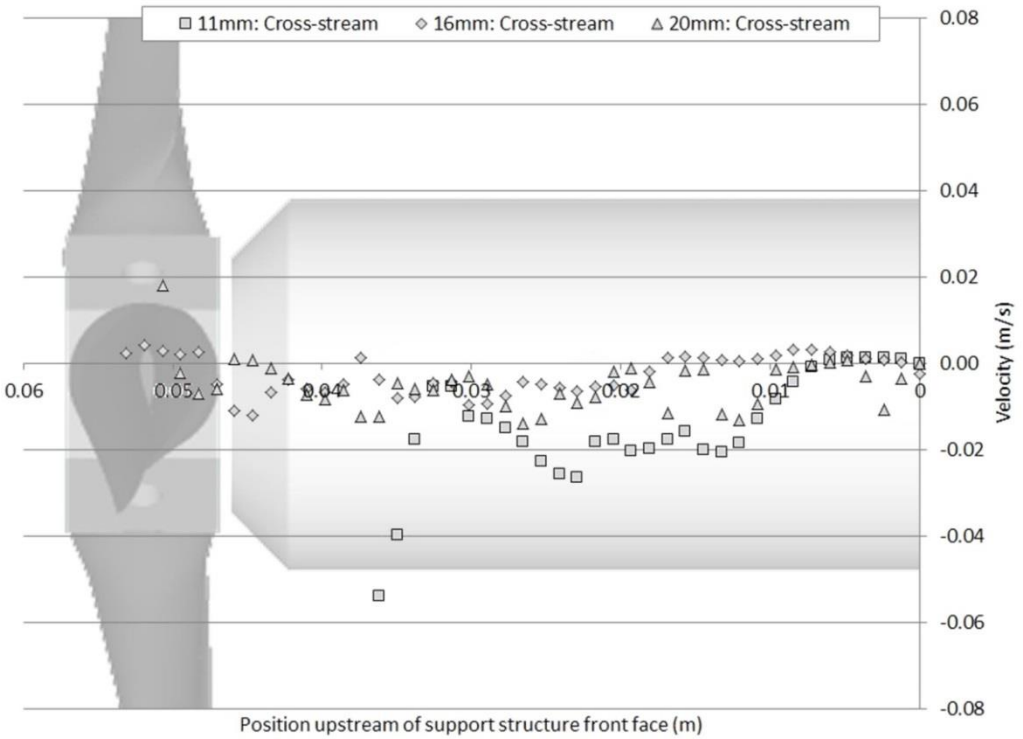

Figure 5-40– Time-averaged cross-stream velocity in upstream region of 11mm, 16mm and 20mm diameter support structure located in back position at 66mm above channel base (flow from left to right).

Cross-stream velocity exhibits less difference between the regions upstream and downstream of the blades than in the streamwise case, but the downstream flow appears to meander to the right before returning to the centre, as illustrated in the centre and back (Figure 5-39 and Figure 5-40 respectively) cases.

The reason for these effects may be related to the interaction of the blade and support structure wakes, which is expected to occur differently in the two cases, due to the differences in separation between the blades and support structure. This effect is discussed in detail in Section 5.3, and was initially investigated by calculating and studying turbulent kinetic energy as described in the following section.

Turbulent kinetic energy

Using PIV data calculated in the cases described above, the horizontal plane turbulent kinetic energy k_{xy} in each case was calculated. As introduced in Section 2.9, TKE is a measure of the energy contained in the instantaneous variation of velocity around its mean value in all recorded directions. In the case of PIV results, flow velocity in the streamwise (x) and cross-stream (y) directions was recorded, giving TKE as follows:

$$k_{xy} = \frac{1}{2}\left[\overline{(u_x')^2} + \overline{(u_y')^2}\right]$$

Where u_x' and u_y' represent velocity fluctuation from the mean value in the x and y directions, respectively. For each of the three support structure diameter cases, k_{xy} was calculated at three upstream positions along the channel centreline: 20mm, 40mm and 60mm upstream of the support structure centre at 135mm above the channel base, representing the location of the turbine blades when installed in the front, centre, and back positions. TKE values were calculated from PIV velocity data at each timestep, giving a 400-point time series at three positions for each support structure diameter. Support structures without turbines were used, since it was not possible to measure the TKE in these positions with the blades in place as the velocity in the blade region was too low to record reliably.

A sample of this data, illustrating a portion of the time series at front, centre and back locations for the 11mm diameter support structure case is shown in Figure 5-41. In order to aid the clarity of the graph, only 100 timesteps are shown, giving a total time period of 6.6s. Due to the range of the data at the back measurement location, the graph is provided at two scales to allow all data to be seen.

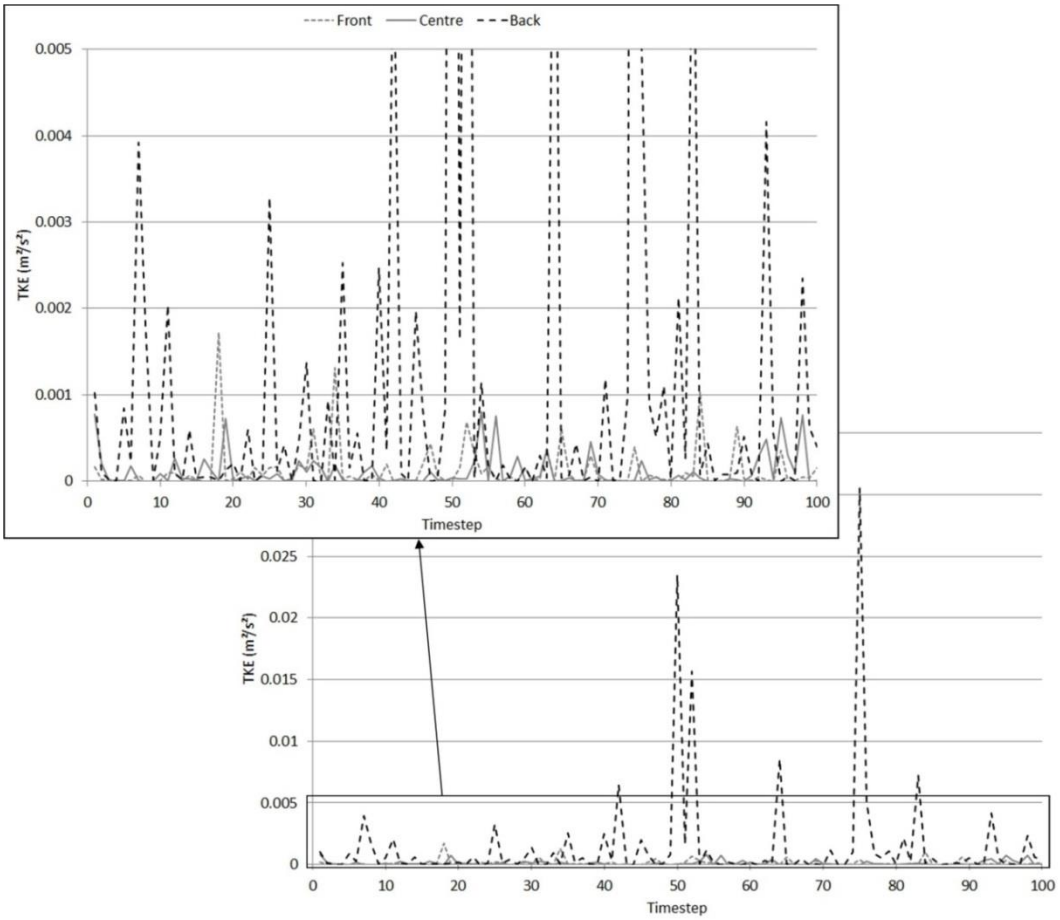

Figure 5-41 – Horizontal plane turbulent kinetic energy (TKE) per timestep at front, centre and back locations upstream of an 11mm diameter support structure.

The data shows the greater values of and greater variation in k_{xy} exhibited by the front and back cases in comparison to the centre case, which appears to correlate with the increased blade torque generated at the centre position. This data is given for all cases in Table 5-8, which gives the mean and variability (in terms of standard deviation) of TKE for each turbine mounting location, in each support structure diameter case.

		Blade / Support structure separation position		
k_{xy} (m^2/s^2)	***Support structure diameter (mm)***	*Front (20mm)*	*Centre (40mm)*	*Back (60mm)*
Mean	**11**	0.00021	0.00016	0.00070
	16	0.00012	0.00010	0.00060
	20	0.00012	0.00011	0.00077
Std. Dev	**11**	0.00036	0.00019	0.00154
	16	0.00048	0.00035	0.00256
	20	0.00025	0.00015	0.00727

Table 5-8 – Comparison of mean and standard deviation of horizontal plane turbulent kinetic energy for Front, Centre and Back turbine positions mounted on 11mm, 16mm, and 20mm support structures.

The values of mean and standard deviation shown in Table 5-8 illustrate the greater turbulent energy seen in the front and back-mounted turbine case, relative to that observed in the centrally-mounted case (though there is only a small difference between the front and centre cases). This appears to suggest a correlation between the location of the blades in a region of low turbulent kinetic energy and greater C_p. Plotting the correlation between turbulent kinetic energy and power coefficient for phase 2 data yields the results illustrated in Figure 5-42.

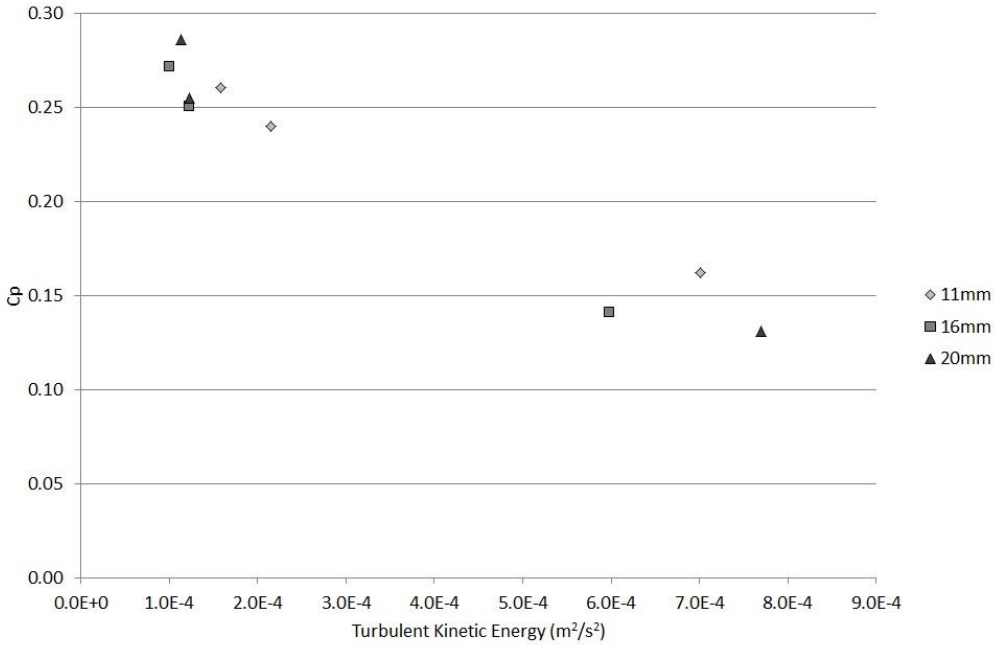

Figure 5-42 - Comparison of horizontal plane turbulent kinetic energy and blade torque for turbine mounted at three positions on 11mm, 16mm, and 20mm support structures.

The comparison of k_{xy} and C_p for the three turbine installation positions appears to support the trend of decreasing power generation with increasing TKE. The significant difference in both TKE and C_p between the three back cases and the collective front and centre cases is clearly visible in this data (the back cases are those located to the lower right of the figure). This data strongly suggests that the location of the turbine blades in a region of high TKE is the cause of the lower output when the turbine is mounted in the back position. The underlying reason for this variation in TKE with position is believed to be due to the separation distance between the front face of the support structure and the swept area of the blades. Further details of this theory are given as part of phase 3 analysis in the following section, and a full discussion of the effect is given in Section 5.3.

Summary results - Phase 2

- Across three support structure diameters tested at λ = 3.1, turbine C_p is greatest when the turbine is installed at the centre mounting position, second greatest at the front mounting position, and lowest at the back mounting position.

- High C_p appears to correlate with the location of the blades in a region of low horizontal plane turbulent kinetic energy, and low C_p with the location of the blades in a region of high horizontal plane turbulent kinetic energy.

5.2.3 – Phase 3: Impact of support structure diameter on turbine performance

The aim of this phase of work was to investigate any impact on the generated blade power caused by changing the diameter of the device support structure. In addition to the 11mm, 16mm and 20mm support structures used in phase 2, six additional diameters of cylindrical support structure were used, giving a total of nine structures with diameters of 6, 8, 11, 14, 16, 18, 20, 22 and 25mm.

In all cases, the turbine was mounted in the centre position, with a streamwise distance of 40mm (0.32D) from the centre of the support structure to the centre of the blade swept area. As in previous tests, the support structure was mounted to the base of the water channel at a distance of 9m downstream from the inlet, and a water depth of 300mm was used. The 11mm, 16mm and 20mm diameter cases were studied under flow cases 1 and 2, with the remaining diameter structures tested in flow case 2. Instrumented turbines were used in all experiments, allowing C_p to be calculated for each test. As in Phase 2 tests, rotational position and speed was also recorded. Flow conditions were recorded during tests of the 11mm, 16mm and 20mm diameter support structures, but were not recorded during all other tests due to the time consuming nature of the experiments.

Potential errors

Due to the difference in support structure diameters, each of the nine experimental cases tested led to a slightly different blockage ratio. The variation in blockage between the minimum (6mm) and maximum (25mm) diameters was calculated, and in terms of simple blockage produced a variation of 1.5%. This variation suggests that the widest support structure diameter would still yield a blockage ratio within the range deemed acceptable by previous tests, as discussed in Section 2.2.4. This variation is also within the limits of experimental error as defined in Section 4.6, so no further correction was undertaken.

As in previous experimental phases, encoder and current measurement module results were recorded simultaneously, and were repeated twice for each experimental case. The resulting torque and C_p calculations revealed a variation between pairs of repeated experiments of between 0.01% and 0.47%. The mean resulting value was used in all cases.

PIV results

Instantaneous frames illustrating velocity in the region downstream of the turbine and 11mm, 16mm and 20mm support structure are given in the following figures, under flow case 2 conditions. The centre (40mm spacing between support structure and blade swept region) position was used in all cases illustrated. The location of the turbine or support structure at the sample height in each case is shown, as is the region of interest from which data for further analysis was extracted (see note regarding surface smoothing plate in Section 4.6).

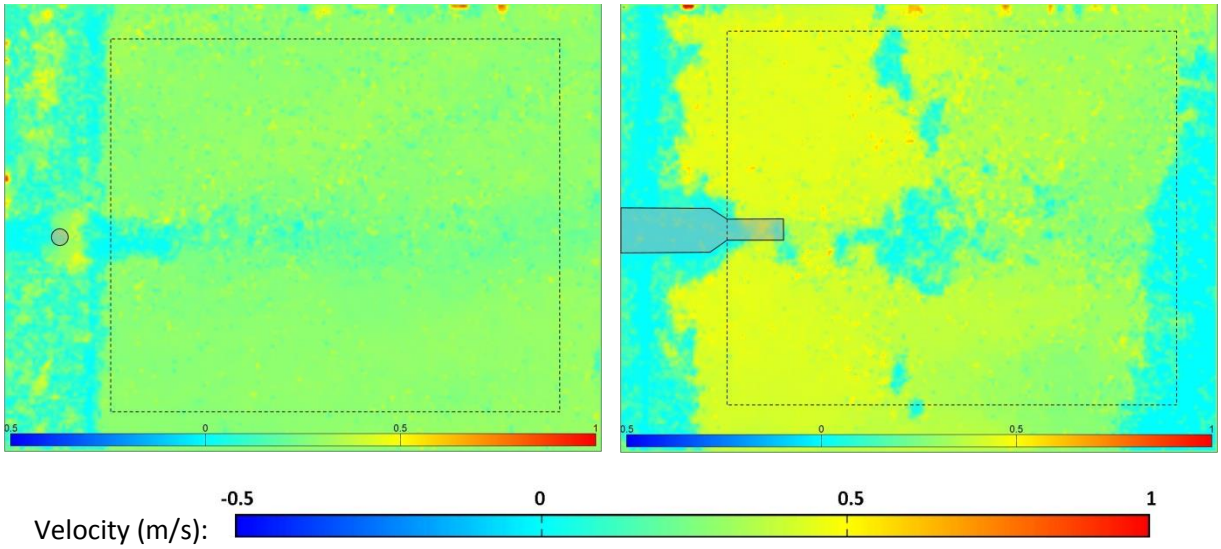

Figure 5-43a&b – Instantaneous streamwise velocity (m/s) frames recorded at 66mm (l) and 135mm (r) above channel base, turbine mounted 11mm diameter support structure.

(Image scale: 0.362m x 0.272m in all cases)

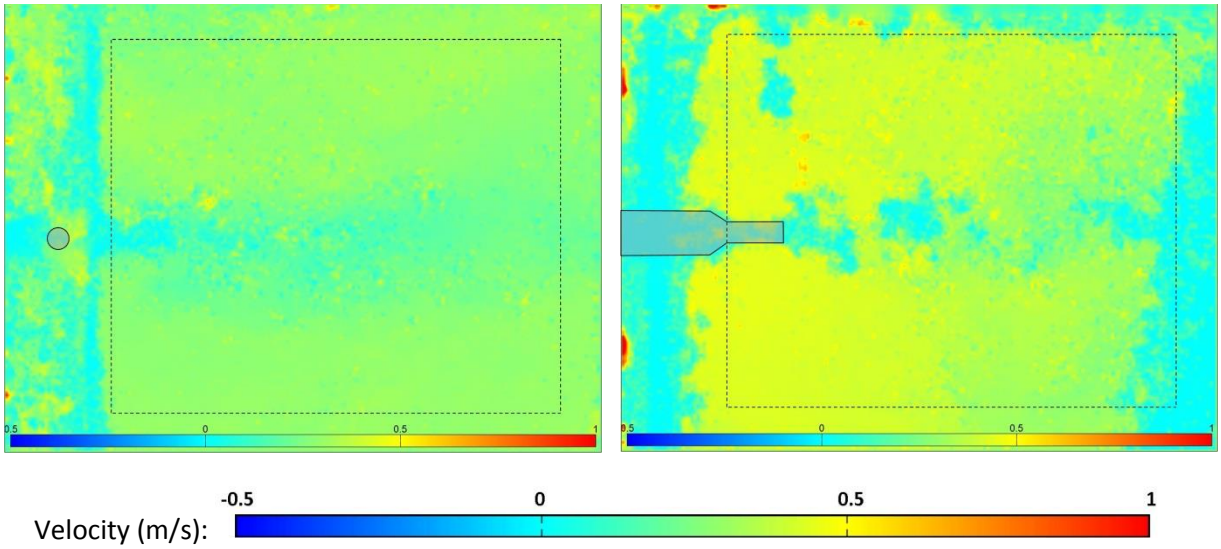

Figure 5-44a&b – Instantaneous streamwise velocity (m/s) frames recorded at 66mm (l) and 135mm (r) above channel base, turbine mounted on 16mm diameter support structure.

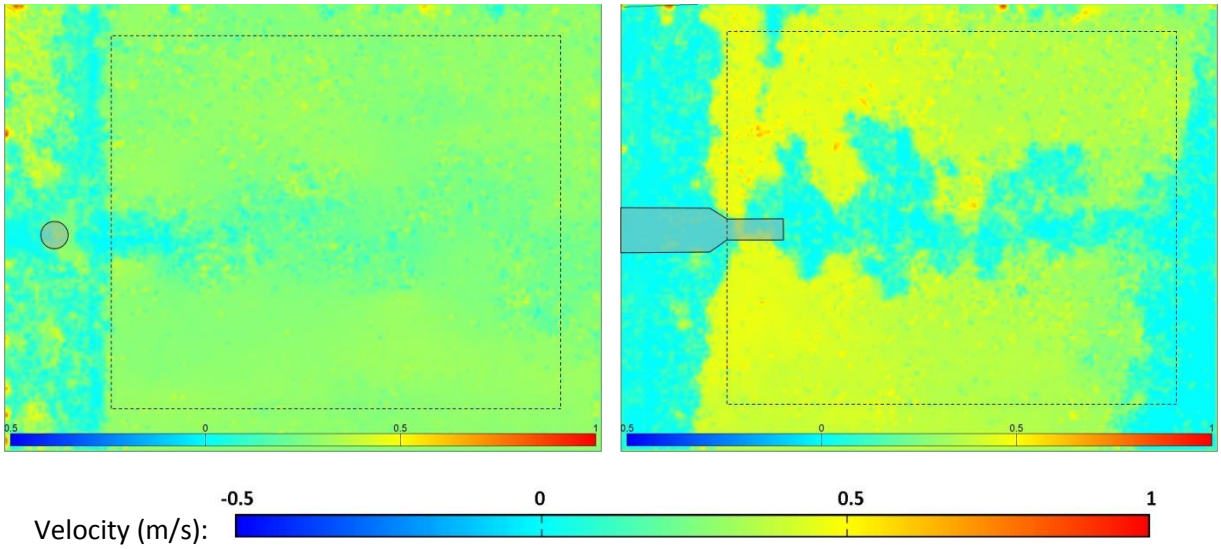

Figure 5-45a&b – Instantaneous streamwise velocity (m/s) frames recorded at 66mm (l) and 135mm (r) above channel base, turbine mounted on 20mm diameter support structure.

These frames are illustrated as an indication of the data captured, and illustrate two clear qualitative observations:

- In all cases, the mean velocity across the region of interest at the 135mm sample height is around 35% greater than that at the 66mm sample height.

- As support structure diameter is increased, the level of disturbance in the downstream wake is visibly greater, suggesting, as one would expect, that downstream turbulence increases with support structure diameter.

Turbulent kinetic energy

TKE data was plotted along the centreline of the images illustrated in Figure 5-43, Figure 5-44 and Figure 5-45 above, as well as the corresponding experiments conducted without the turbine in place. As has been described previously, horizontal plane TKE, k_{xy}, is used throughout this study. TKE comparisons at the 66mm and 135mm height planes were then plotted with and without the turbine in position, as illustrated in Figure 5-46 and Figure 5-47. In both cases, a diagram of the turbine is included to illustrate its position on the horizontal axis. The same scale is used in both cases to illustrate the difference in TKE values at the two locations.

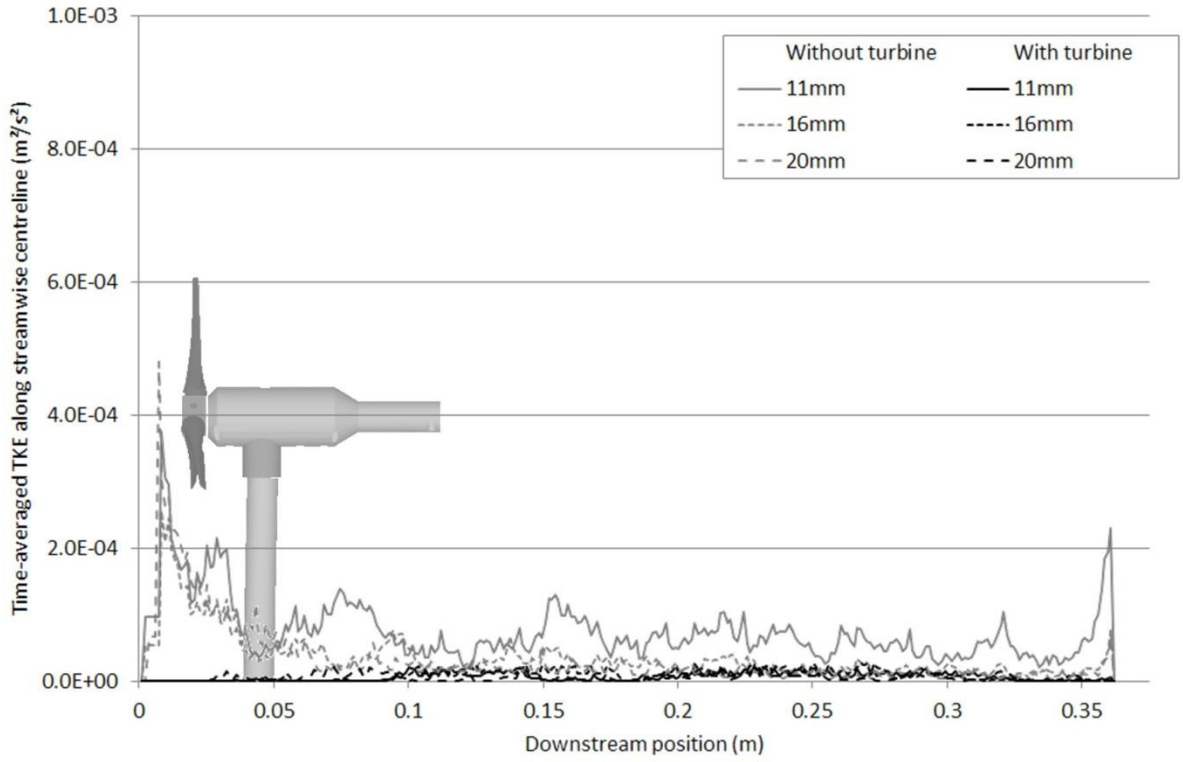

Figure 5-46 – Horizontal plane TKE plots for three support structure diameters, with and without turbines, in flow case 2. Recorded at 66mm above channel base.

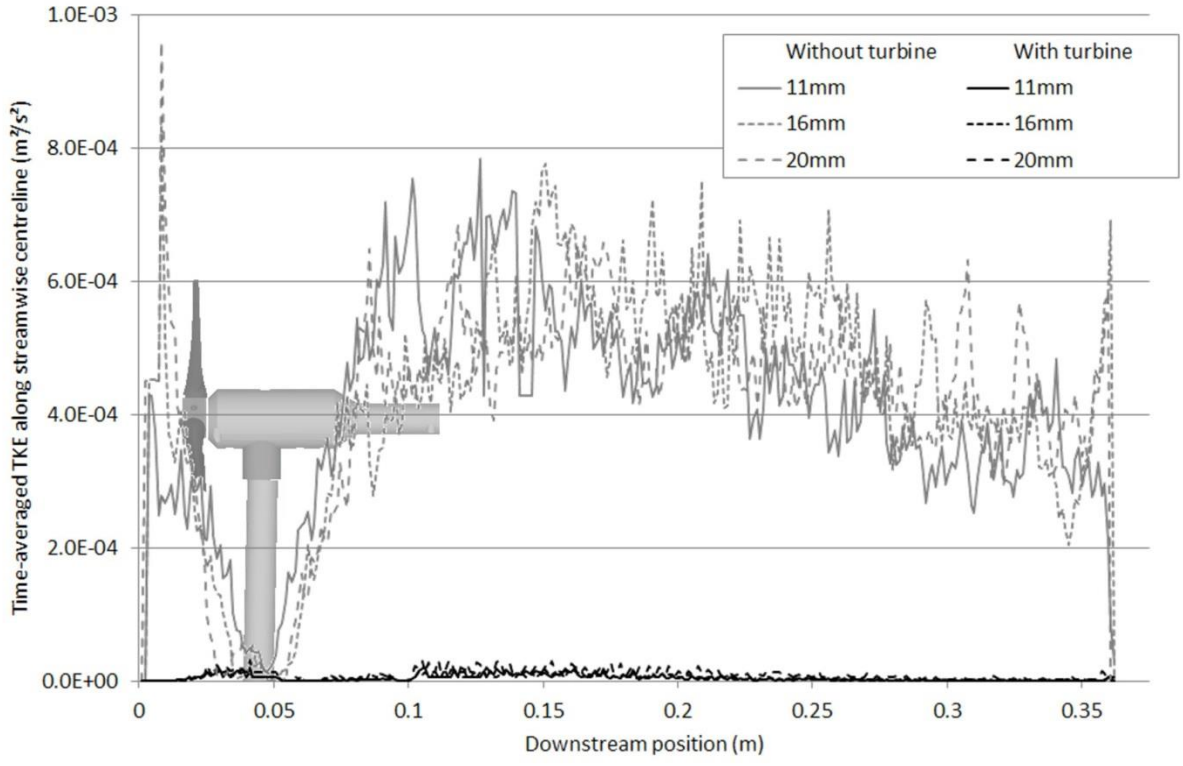

Figure 5-47 - Horizontal plane TKE plots for three support structure diameters, with and without turbines, in flow case 2. Recorded at 135mm above channel base.

As observed in these figures, TKE appears to be greater in cases without a turbine in place than the equivalent case with a turbine in place. This effect is seen particularly at the 135mm measurement plane, where mean downstream TKE is around 20 times greater without a turbine than with a turbine. At 66mm above the channel base, cases without a turbine have TKE around four times greater than with a turbine in place. At 135mm this effect is believed to be caused by the vertical location of the support structure relative to the measurement plane. Without a turbine in place, the top of the support structure is located at 120mm. The location of the measurement plane is 15mm above this height, and is therefore likely to capture the highly turbulent region around the top of the support structure. As was highlighted in Section 2.7 and illustrated in Figure 2-44, the wake downstream of a submerged cylinder has a number of elements, including a recirculating vortex which reaches over the top of the cylinder and circulates in a clockwise direction, as viewed from the side with flow from left to right. The mixing of this vortex, the arch vortex behind the cylinder and other cylinder wake elements with the bypass flow around the cylinder is expected to cause the high levels of turbulence observed without turbines in Figure 5-47. At the higher measurement plane wake turbulence appears to dissipate over the region recorded, with peak downstream values recorded at 1*D* downstream, and decay to approximately half this level occurring by 2.5*D* downstream. At the 66mm measurement plane decay appears to be slower, particularly without turbines in place, in which case mean TKE remains constant over the recorded downstream distance.

Relative to cases without a turbine in place, cases with a turbine exhibit much lower turbulent kinetic energy in the downstream region, which is believed to be caused by the extraction of energy from the flow by the turbine, resulting in lower velocity and a less energetic turbulent regime downstream of the turbine. As illustrated in Figure 5-43 - Figure 5-45, mean downstream velocities at turbine height in the region up to 2.5*D* downstream of the turbine are around 0.15 m/s, compared to 0.3m/s without a turbine in place. TKE results with turbines in place also appear to support the suggestion that greater support structure diameter leads to a more turbulent downstream region, though only a small variation between TKE levels is observed.

A final observation from these figures is the peak in TKE recorded in the region just upstream of the blades at both measurement planes. This is observed primarily in cases without turbines, suggesting that it is perhaps caused by an element of the support structure wake. As will be discussed later in this section, it is believed that support structure wake features generated in this upstream region contribute to the performance of the turbine.

Performance data

Time-averaged power coefficient results for a turbine mounted on each of the nine support structure diameters studied are illustrated in Figure 5-48. Data was recorded in flow case 2 conditions.

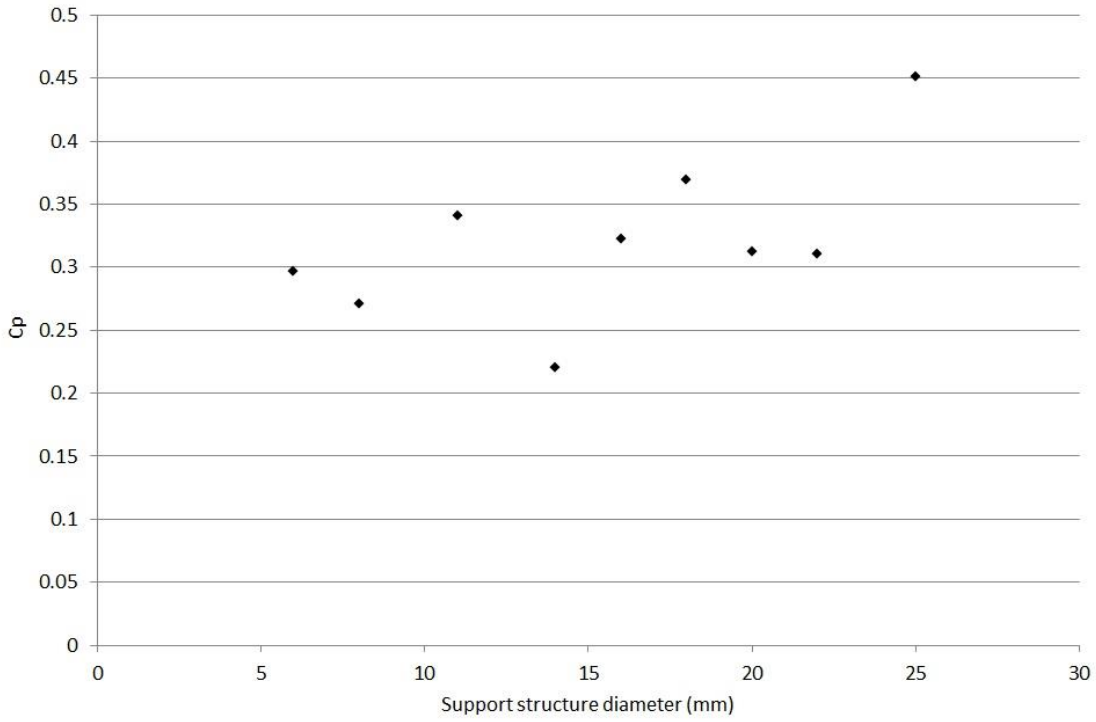

Figure 5-48 – Phase 3 turbine C_p for flow case 2 conditions on support structure diameters between 6mm and 25mm.

Phase 3 results, as illustrated in Figure 5-48, appear to indicate that as support structure diameter is increased, the power coefficient generated by a turbine mounted on the support structure tends to increase. As shown in the figure, this is not universally true, and there is notable variation. However, since the results do illustrate a broad tendency for increasing power generation with increasing support structure diameter, a number of potential explanations of this effect were considered. Given that the turbine unit, flow conditions and water channel specification remain constant between all experiments, the observed trend appears to be related to the variation in the diameter of the support structure. Three potential effects which could be caused by the support structure diameter variation and could result in the observed differences in power output were noted and investigated. The potential effects considered are detailed below, followed by an investigation into the likelihood of each to cause the variation of blade torque with support structure diameter observed in Figure 5-48.

- Variation in torque output throughout rotation:

As the turbine rotates, each blade will pass the support structure once during each rotation. As it does so, the flow field experienced by the blade will be different to that experienced during the remainder of its rotation. It is possible that this change may alter the power generating characteristics of the blade during the time it is in the region of influence of the support structure, and hence it is possible that the turbine output may rise or fall as each blade passes the support structure. In the case of a larger diameter support structure, the region of influence is expected to be larger, and hence this effect would occur over a longer time period, for a given rotational speed.

- Variation in frequency of vortex shedding due to support structure diameter:

As observed and described in Section 5.2.1, vortex shedding from the support structure does occur under the flow conditions tested, and the frequency of this shedding is dependent on the diameter of the structure, with smaller diameter support structures leading to higher frequency vortex shedding. It was considered possible that the lower frequency shedding generated by a larger structure may lead to a less turbulent environment in the blade swept region, which may result in an increase in generated blade torque, and hence explain the results observed in Figure 5-48.

- Increased separation distance from blades to post with reduced support structure diameter:

As has been studied in phase 2 and explained in Section 5.2.2, there appears to be an optimal performance region in front of the support structure, the placement of a turbine within which will increase its power coefficient relative to placement in front of or behind this area. As has been discussed in the previous section, this appears to be due to reduced turbulent intensity within this region relative to the regions upstream and downstream.

Power coefficient and flow data for each case was studied in order to investigate these effects and to determine to what degree, if at all, each of them may influence blade power output. The following sections describe the analyses carried out in each case.

Variation in torque output throughout rotation

As described above, it was suggested that as each turbine blade passes in front of the support structure the difference in flow conditions relative to the rest of the blade rotation could lead to a change in the torque generated by the blade over that portion of rotation. If this is the case, it follows that a greater diameter support structure will cause this effect to be observed over a greater portion of the rotation of the turbine, and hence will have a greater overall effect on the C_P of the turbine. If this effect caused an increase in blade generated torque, it may explain the results observed in Figure 5-48.

In order to ascertain whether this effect could be the cause of the observed variation in blade torque with support structure diameter, instantaneous values of blade torque were plotted against turbine rotational position, using data recorded by the turbine rotational speed encoder. The rotary encoder used in this case was a six-hole model, with holes aligned to produce a high output encoder signal as the centreline of each blade passed the support structure, and another high output half way between consecutive blades. By comparing blade torque to encoder position it was possible to observe the variation of turbine generated torque against rotational position. Illustrations of this comparison for the 6mm and 25mm (i.e. minimum and maximum) diameter support structures are given over the duration of a single turbine rotation in Figure 5-49 and Figure 5-50 respectively.

It should be noted that, in both Figure 5-49 and Figure 5-50, the recorded variation in blade torque is very small, and the observed variation around the mean value is at a level close to the minimum bit resolution of the current measurement module used to calculate the power supplied to the motor (as discussed in Section 3.6 a 12-bit data acquisition system was used). The module is able to detect changes in current of 0.25mA, and measures variation in current through an output signal at 185mV/A, yielding a minimum output resolution of 0.05mV. This variation, in the cases illustrated, corresponds to a change in blade torque of 0.002Nm. The actual recorded value can be seen to

increase and decrease with time by small multiples of this value, indicating that the recorded blade torque is close to the minimum resolution achievable by the instrument.

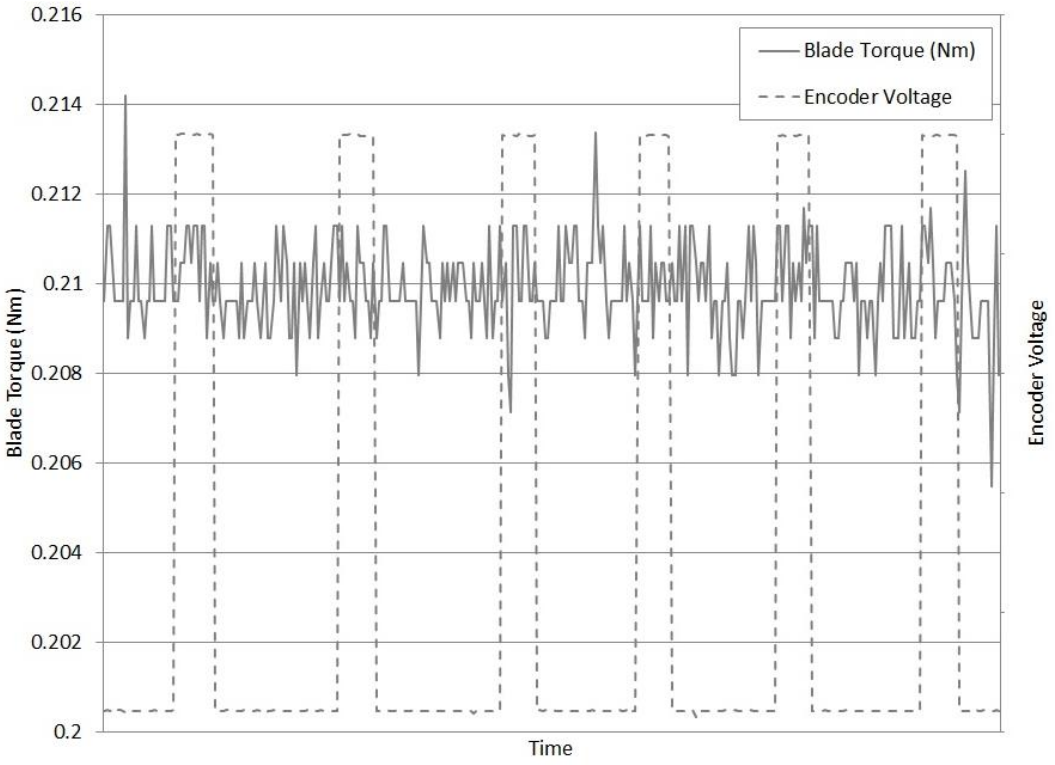

Figure 5-49 – Blade torque variation over single rotation (6mm support structure)

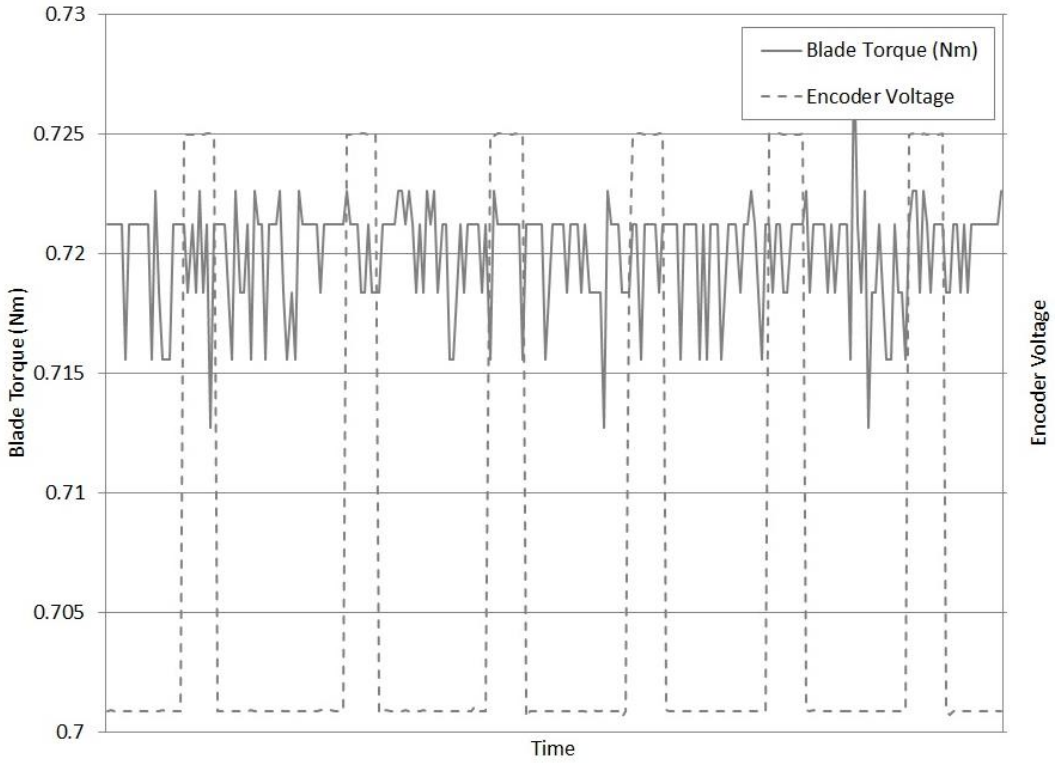

Figure 5-50 – Blade torque variation over single rotation (25mm support structure)

As shown in the above figures, though maximum variation from the mean value of blade torque of around 2% in the 6mm case and 1% in the 25mm case was observed, this variation does not appear to coincide with the point at which a blade passes the support structure, or to correlate with the encoder position.

This suggests that overall blade torque, and thus C_p, does not appear to be affected by the rotational position of the blades relative to the support structure. Similar variation was also observed in all intermediate support structure diameter cases. Standard deviation of blade torque variation was also calculated over the full sample length (2048 data points) for the cases illustrated above, as well as for all intermediate cases, and was found to be around 1% in all cases, as illustrated in Table 5-9. This relatively minor variation does not appear to suggest that blade generated torque varies significantly over the course of turbine rotation.

Support structure diameter (mm)	*Standard deviation of Blade Torque (%)*
6	1.046%
11	1.125%
14	1.045%
16	1.044%
18	1.108%
20	1.057%
22	0.875%
25	1.179%

Table 5-9 – Standard deviation of blade torque for support structure diameters as tested during phase 3 (flow case 2).

Due to the apparent lack of influence of the blade rotational position on blade torque and therefore C_p, it can be concluded that this effect is unlikely to be the cause of the observed increase in C_p due to increased support structure diameter.

Variation in frequency of vortex shedding due to support structure diameter

Another effect identified as a potential cause of the observed increase in power coefficient with increasing support structure diameter is the difference in vortex shedding frequency for each of the support structure diameters. Lower frequency vortex shedding in cases with larger diameter support structures was observed during phase 1 and phase 2 tests, as described in Section 5.2.1. It is suggested that this lower frequency shedding may lead to a less turbulent blade region, which may therefore lead to an increase in turbine C_P as observed in Figure 5-48.

In order to test this idea, PIV vorticity results for 11mm, 16mm and 20mm diameter support structures were analysed using PIVLab. Results of both case 1 and case 2 tests were studied, for cases both with and without blades in place.

Vorticity plots in three cases are illustrated below. As described previously, since the use of 2D PIV means that velocity was measured only in streamwise and cross-stream directions during this study, subsequently calculated values of turbulent kinetic energy and for a horizontal plane, and hence are

described as k_{xy}. Similarly, vorticity values were calculated from streamwise and cross-stream velocity, meaning that vorticity can only be calculated for the horizontal plane.

Values are illustrated as recorded at the support structure mid-height (66mm above the channel false base). PIV results recorded under flow case 2 for both the support structure alone and the support structure complete with turbine are given. Vorticity results for the region downstream of the support structure only are illustrated in Figure 5-51, Figure 5-52 and Figure 5-53 (11mm, 16mm and 20mm diameter support structures, respectively).

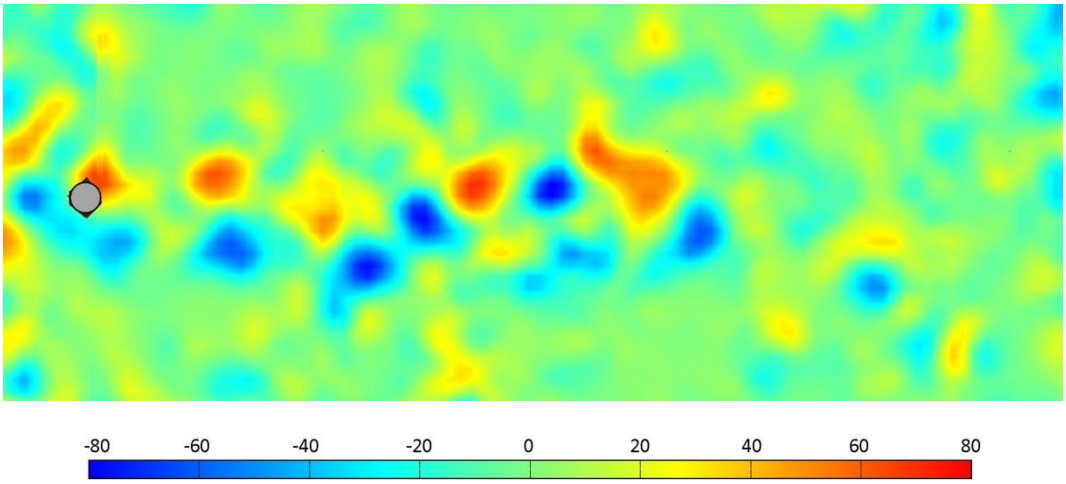

Figure 5-51 – Horizontal plane vorticity (1/s): 11mm diameter support structure (without turbine) in flow case 2 at 66mm above false base.

(Image scale: 0.36m x 0.14m in all cases)

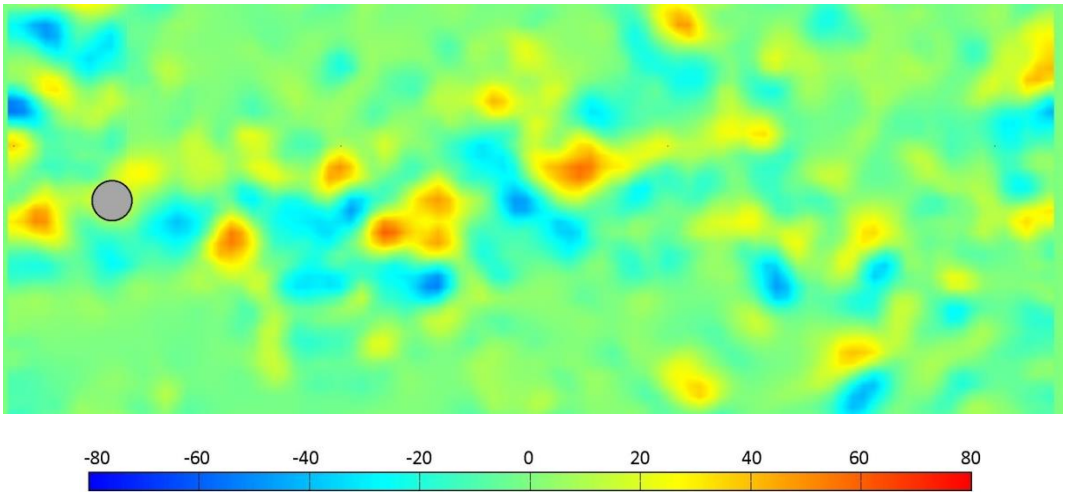

Figure 5-52 – Horizontal plane vorticity (1/s): 16mm diameter support structure (without turbine) in flow case 2 at 66mm above false base.

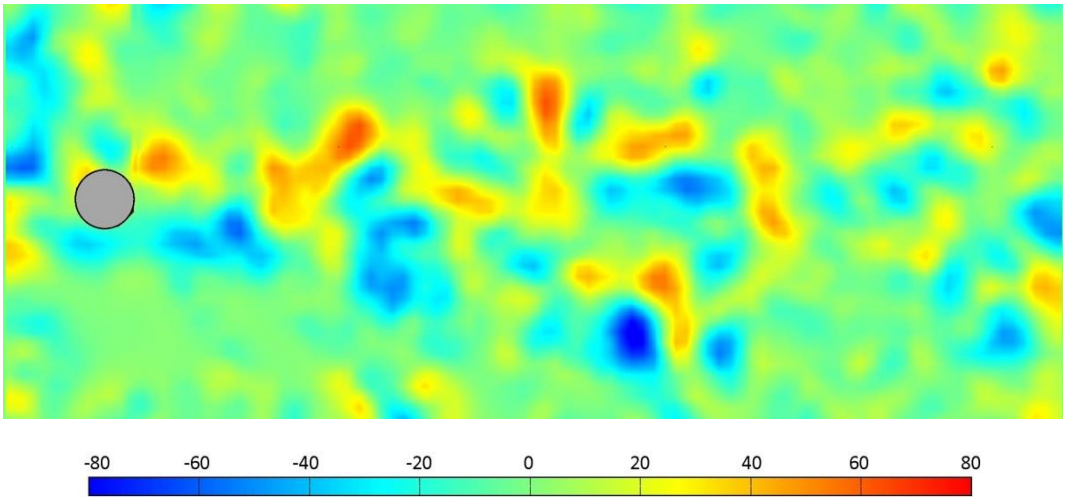

Figure 5-53 – Horizontal plane vorticity (1/s): 20mm diameter support structure (without turbine) in flow case 2 at 66mm above false base.

Vorticity plots for experiments with support structures complete with turbines are given in Figure 5-54, Figure 5-55, and Figure 5-56 (for 11mm, 16mm and 20mm diameter support structures, respectively). Vorticity colour scales are retained from the previous figures to allow direct comparison. The location of the turbine and support structure is shown, as is the region of interest from which data for further analysis was extracted (see note regarding surface smoothing plate in Section 4.6).

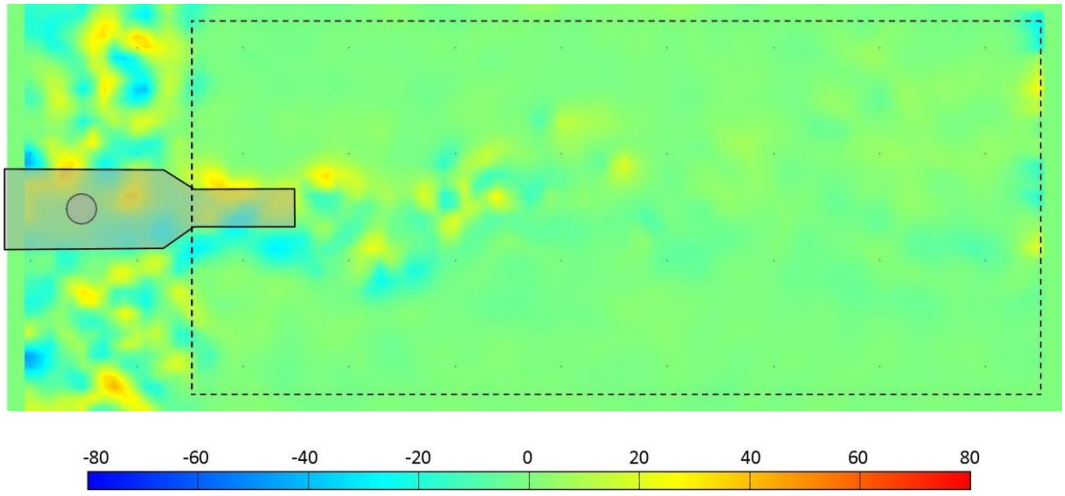

Figure 5-54 – Horizontal plane vorticity (1/s): 11mm diameter support structure (with turbine) in flow case 2 at 66mm above false base.

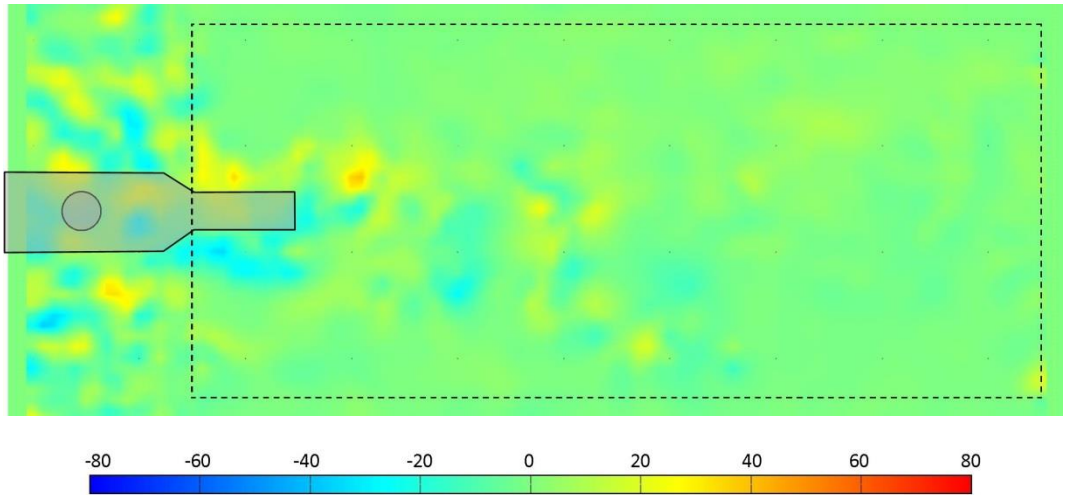

Figure 5-55 – Horizontal plane vorticity (1/s): 16mm diameter support structure (with turbine) in flow case 2 at 66mm above false base.

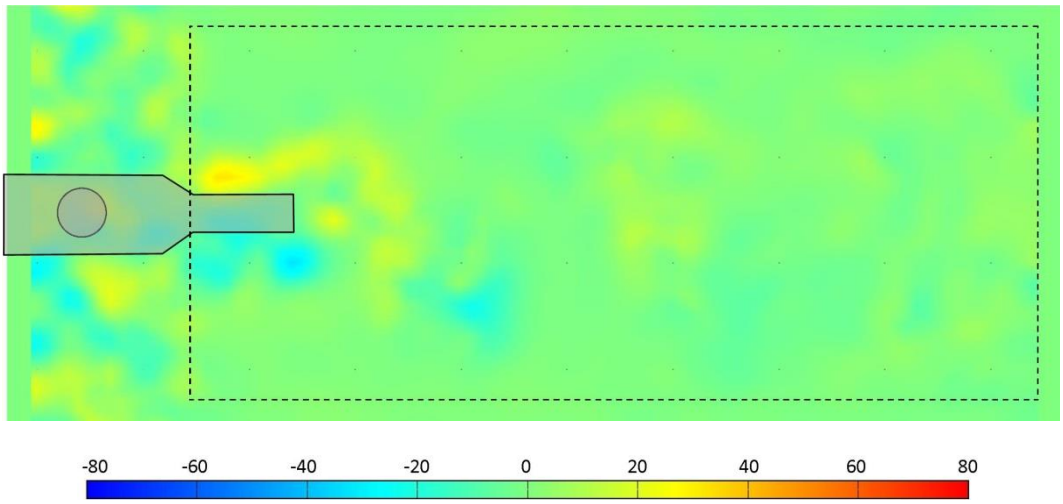

Figure 5-56 – Horizontal plane vorticity (1/s): 20mm diameter support structure (with turbine) in flow case 2 at 66mm above false base.

Results without turbines in place clearly illustrate vortex shedding, as observed during similar tests in Phase 1, as described in Section 5.2.1. As has been shown in previous results, cases with the turbine in place illustrate much lower velocity magnitude than support structure only cases due to the extraction of energy from the flow by the turbine. Similarly, vorticity was noted to be much lower with the turbine in place. As was highlighted during the analysis of dye injection POD analysis, turbulent eddies generated by the support structure appear to be subdivided by the rotational wake generated by the blades, resulting in smaller eddies propagating downstream than those observed in otherwise identical cases without turbines.

Mean vorticity in each case was calculated in order to quantify the overall vortical energy, to study the vorticity variation between support structure diameter cases, and to investigate whether an increase in vorticity was associated with the greater values of blade torque generated with increased support structure diameter.

Centreline vorticity was calculated using absolute values for each frame, which was then used to calculate the mean vorticity along the centreline in each case. These centreline results were then used to calculate the overall mean value of vorticity in each case as given in Table 5-10.

Mean centreline horizontal plane vorticity (1/s)	*11mm*	*16mm*	*20mm*
Without turbine	33.9	33.2	34.6
With turbine	15.1	17.5	20.3

Table 5-10 – Mean absolute time-averaged vorticity values for three support structure diameters with and without turbine in place (recorded at 66mm above channel base)

These results suggest that despite a lower frequency of shedding, vorticity is generally greater in cases with larger diameter support structures. At subcritical Froude numbers (as in the case of all experiments described herein) as discussed in Section 2.2.2, vorticity downstream of the support structure can also have an influence on the flow field upstream of the support structure. Since eddies shed behind a larger diameter structure are themselves larger, and the wake occupies a wider area behind the support structure, the overall vorticity in the region around a wider structure is greater than that of a narrower structure.

Vortex shedding and its potential effect on the blade torque output of a turbine was studied further by considering the relationship between shedding frequency and blade torque.

Since the frequency of vortex shedding is a function of the diameter of the support structure cylinder, this offers a potential explanation for the variation in blade torque output with support structure diameter. The frequency of vortex generation for a cylinder can be calculated using a dimensionless number known as the Strouhal number. Whereas the Reynolds number is a ratio of inertial to viscous forces, the Strouhal number is a ratio of two sets of inertial forces; those due to the unsteadiness in the flow and those due to the flow velocity. Vortex oscillations contribute to the flow unsteadiness, producing the following equation:

$$St = \frac{\omega l}{u}$$

Using this equation, the oscillation frequency ω of a flow around a cylinder can be calculated from the known velocity u and cylinder diameter l, provided that St is known. It is possible to ascertain the value of St from the Reynolds number of a flow. The relationship between Re and St can be plotted from experimental data [170] as shown in Figure 5-57.

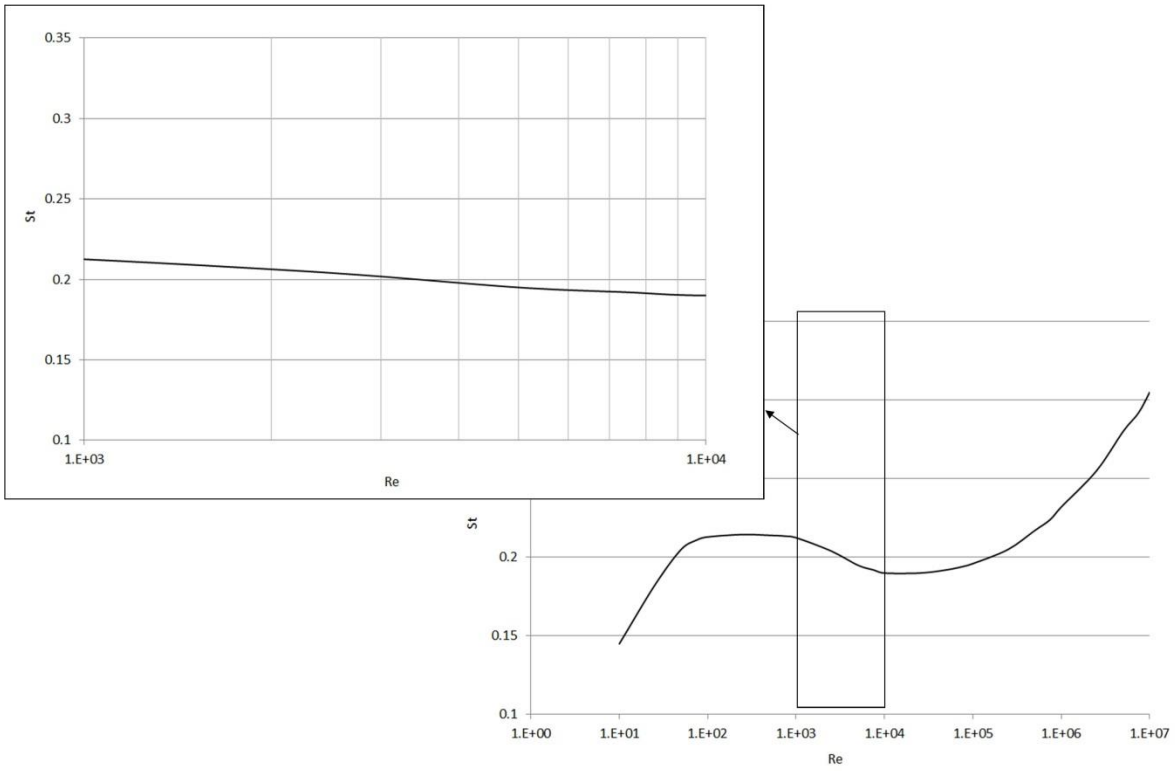

Figure 5-57 – Relationship between Re and St (enlarged $1x10^3$ < Re < $1x10^4$ region).

Reynolds number values for the experiments conducted as part of Phase 3 of this work lie between 1500 and 6250, yielding values of *St* between 0.212 and 0.185, as shown in the enlarged section of Figure 5-57. *St* values were calculated from this data, and were subsequently used to calculate the predicted frequency of vortex shedding for each support structure diameter. These values are illustrated in Table 5-11.

Diameter (mm)	*Re*	*St*	*Predicted Frequency (Hz)*
6	1500	0.212	10.60
8	2000	0.210	7.88
11	2750	0.205	5.59
14	3500	0.200	4.29
16	4000	0.195	3.66
18	4500	0.190	3.16
20	5000	0.190	2.85
22	5500	0.185	2.52
25	6250	0.185	2.22

Table 5-11 – Re and St values for Phase 3 experiments (flow case 2)

In order to confirm the validity of the calculated frequency of vortex shedding, Strouhal numbers were calculated from measured shedding frequency of three experiments (those with 11, 16 and 20mm diameter support posts), as conducted without turbines in place and described in detail in Section 5.2.1.

During dye injection tests of these support structures as part of Phase 1, a video camera (Model Kodak Easyshare) was installed over the water channel in order to record the wake development. Video was recorded at 25 frames per second, then copied to a computer and analysed using video editing (Serif MoviePlus X5) software. Using this package it was possible to review the vortex shedding in slow motion, and to measure the shedding frequency for each of the three support structure diameters. The resulting frequencies of vortex shedding were 5, 3.6, and 2.5Hz for the 11, 16 and 20mm support structure diameter cases respectively, giving variation of between 2% and 12% between experimentally measured results and those calculated as described in Table 5-11. The most likely source for this variation is the experimental measurement of the shedding frequency, since the exact moment of the detachment of each vortex was not always identifiable, and sometimes occurred between video frames. However, despite this variation, the similarity of these results was felt sufficient to provide some validation of the calculated shedding frequencies given in Table 5-11.

Calculated values of vortex shedding frequency as given in Table 5-11 were plotted against generated blade torque, in order to assess any impact of shedding frequency on the output of the turbine. This comparison, with labels of support structure diameter, is given in Figure 5-58.

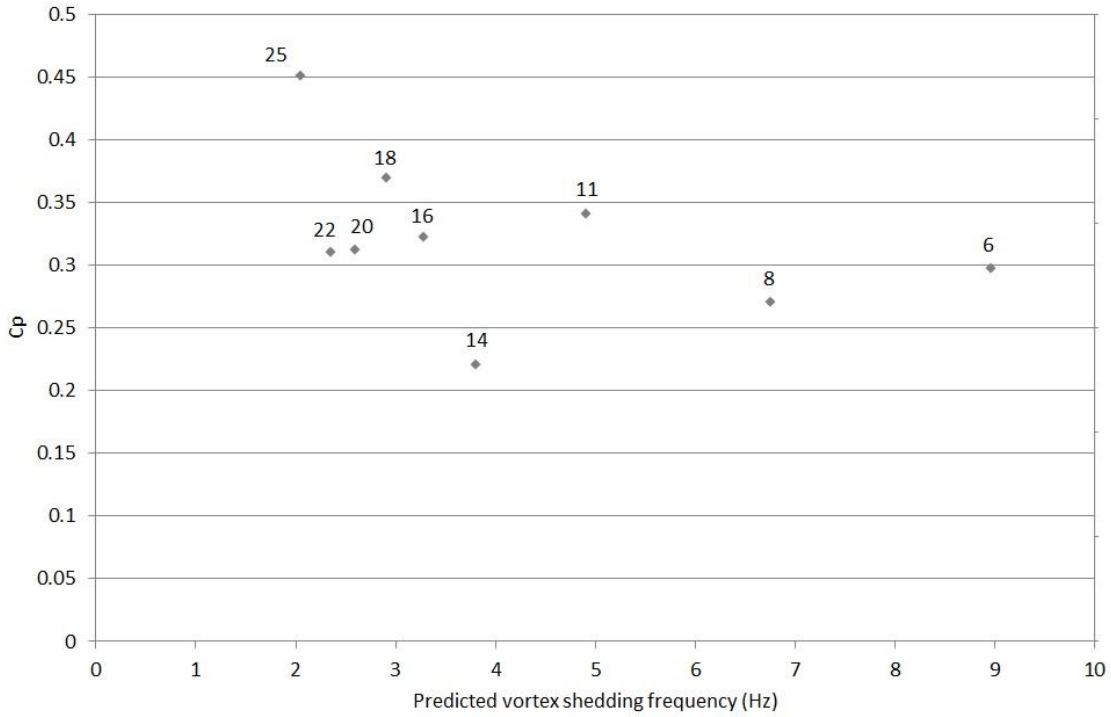

Figure 5-58 – Predicted vortex shedding frequency under flow case 2 conditions vs C_p *for nine support structure diameters.*

The results illustrated in Figure 5-58 show a weaker correlation between predicted vortex shedding frequency and blade torque than that observed between support structure diameter and blade torque in Figure 5-48. This suggests that although blade torque does vary with shedding frequency, this is an indirect effect due to the variation of shedding frequency with support structure diameter, rather than a direct effect in itself. Consequently, it does not appear that the variation in blade torque with support structure diameter is caused by changes in shedding frequency.

Increased separation distance from blades to support structure

Another effect which may explain the variation in blade power with support structure diameter is the separation distance between blades and support structure. This effect was observed in phase 2 data and is described in Section 5.2.2. All phase 3 tests were conducted using the central blade location position, meaning that the separation distance between the blade swept area and the centre of the support structure was 40mm. However, the separation distance between blade swept area and the front face of the support structure varies with diameter. For clarity, the definition of this separation distance is illustrated in Figure 5-59.

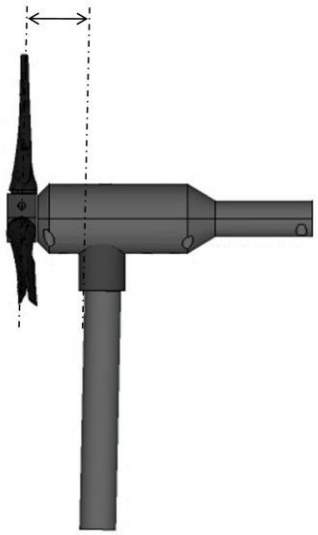

Figure 5-59 – Separation distance between blade swept area and front of support structure upstream face

The separation distance between the blade swept area and the upstream front surface of the support structure in each case tested during phase 3 is given in Table 5-12.

Support structure diameter (mm)	*Separation distance (mm)*
6	37
8	36
11	34.5
14	33
16	32
18	31
20	30
22	29
25	27.5

Table 5-12 – Separation distance between blade swept area and support structure upstream face for all phase 3 cases.

Separation distances as given in Table 5-12 were plotted against C_p in each case, in order to ascertain whether separation distance appears to affect turbine performance. Since separation distances in all cases are 40mm minus the radius of the support structure diameter, the data is a reflection of that illustrated in Figure 5-48. This graph is illustrated in Figure 5-60.

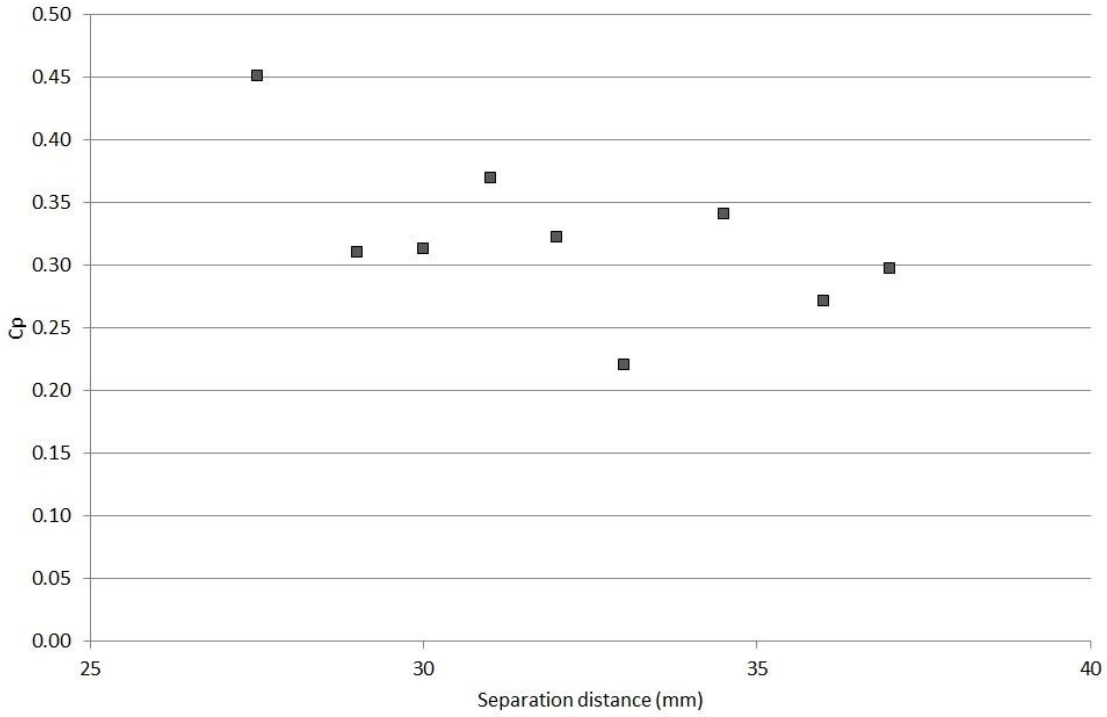

Figure 5-60 – Phase 3 C_p *vs separation distance between blade swept area and support structure upstream face.*

The data illustrated in Figure 5-60 does suggest a correlation between separation distance and C_p, with greater separation distance appearing to lead to lower values of C_p.

Analysis of Phase 2 results indicated the location of a region of relatively low turbulent kinetic energy around 40mm upstream of a 20mm diameter support structure (i.e. a separation distance of around 30mm), and region of relatively high turbulent kinetic energy around 60mm upstream of a 20mm diameter support structure (i.e. around 50mm separation distance), which was found to correlate with C_p. Greater values of C_p were observed in cases where the blades were located in the low TKE region, and vice versa. Phase 3 results illustrated in Figure 5-60 show a similar trend, suggesting that when located at the central position, a large diameter support structure, and therefore short separation distance, places the blades in the low TKE region observed during Phase 2, allowing greater power generation and C_p. Smaller diameter support structures, however, yield greater separation distance and place the blades in a region of higher TKE, leading to lower power generation and C_p. This effect is studied further in Section 5.3, along with the results of Phase 2 data.

5.3 – Discussion

It has been found in phases 2 and 3 that the separation distance between the area swept by the blades and the front upstream face of the support structure appears to have a significant effect on the performance of the turbine. It appears that locating the blades either too close or too far away

from the support structure reduces the power coefficient, relative to blades located in the central region. Within this central region, a weak trend for reducing C_p with increasing separation appears to exist. This section aims to quantify this effect, to locate the position of this optimal performance region, and to understand its causes. Combined results of separation distance vs C_p from phase 2 and phase 3 are illustrated together in Figure 5-61.

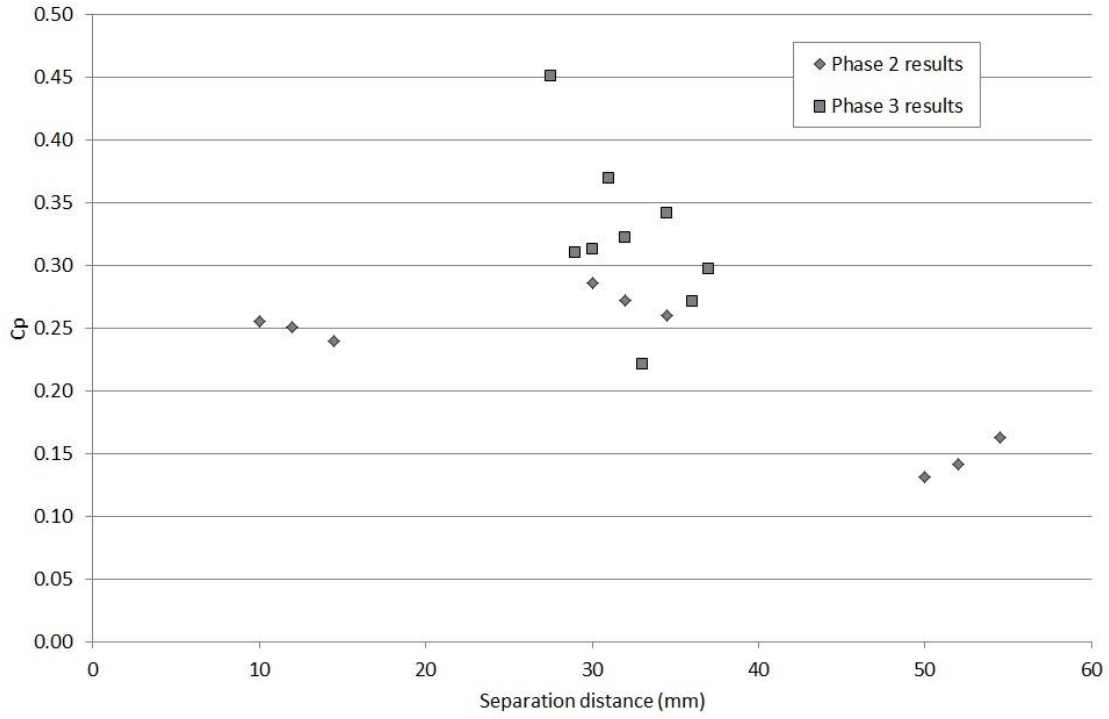

Figure 5-61 – Combined phase 2 and phase 3 results: C_p *vs separation distance between blade swept area and front face of support structure.*

As can be observed in this data, it appears that when separation distance is between 0mm and 25mm, C_p values were around 0.25, with variation across the region of 5%. Separation distances of greater than 25mm and less than 40mm demonstrated greater C_p values, with a mean across the region of 0.31. Greater variation in this region was observed than in the previous region, but 92% of data points had greater C_p than those in the previous region. Across this region, a weak trend for reducing C_p with increasing separation distance was also observed. This trend appears to continue when separation distance is greater than 40mm, with this region exhibiting the lowest C_p values of all, with a mean C_p of 0.14.

These regions led to the suggestion of a broadly bell-shaped trend of C_p variation with separation distance, within the studied range.

A link between reduced turbulent kinetic energy and increased power coefficient was suggested in Section 5.2.2. In order to test this theory, using data calculated from the phase 2 PIV results, horizontal plane turbulent kinetic energy (k_{xy}) can be added to the results illustrated in Figure 5-61. This result is illustrated in Figure 5-62. k_{xy} is illustrated as a band linking the recorded values, since there was a variation in the values of TKE at similar separation distances. The maximum difference in TKE for separation distances of 1mm apart was 0.09m²/s², so the band is illustrated at this width in order to illustrate the potential range of values.

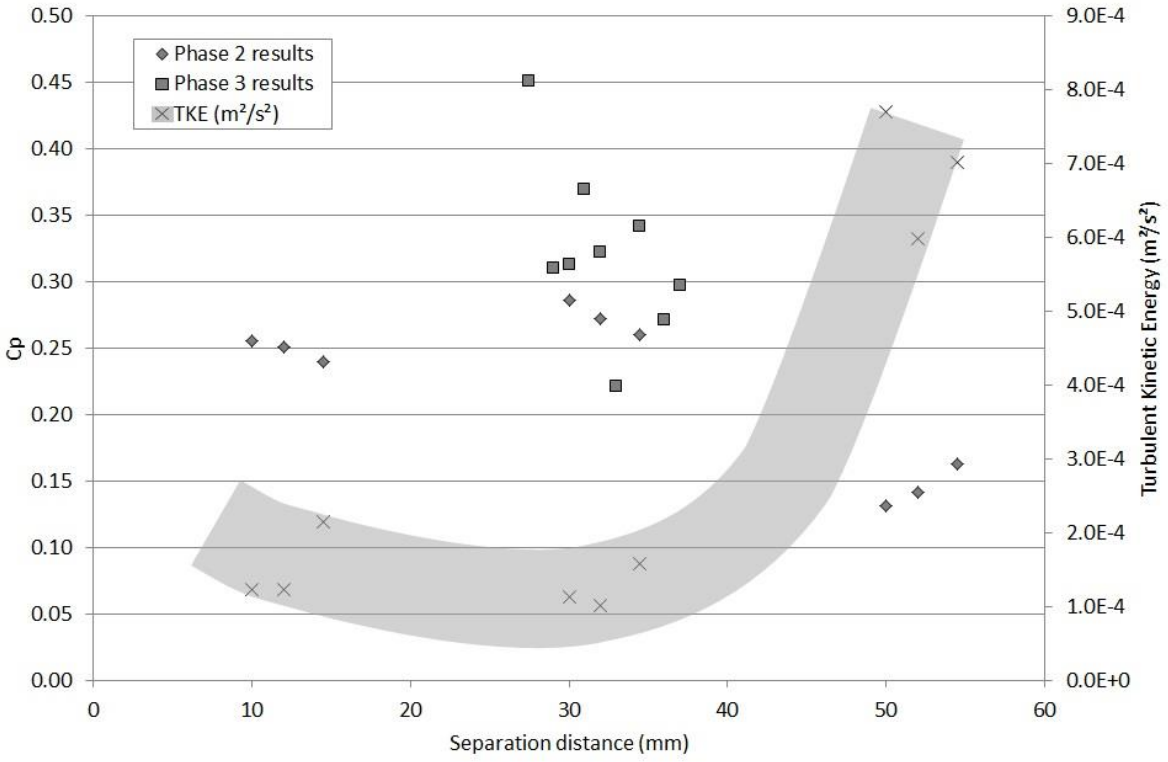

Figure 5-62 - C_p *vs separation distance between blade swept area and front face of support structure and turbulent kinetic energy.*

As has been highlighted, in the flow cases tested, blades placed in the region between 25mm and 40mm from the upstream face of the support structure generate greater blade torque than those placed outside this region. Blades located in this region generated around 20% greater than those placed closer to the support structure, in the 0mm to 25mm region, and around 53% greater than those placed further upstream (in the 40mm to 60mm region). This central region also experiences lower horizontal plane turbulent kinetic energy than the regions upstream or downstream. It is believed that this lower TKE is a cause of the increased power coefficient due to the strong correlation between the two which is observed in phase 2 and phase 3 data.

Detailed study of turbulence at blade level is beyond the scope of this study, since as highlighted in Section 3.3, values of *Re* achievable using the experimental equipment employed are not sufficiently high to allow the representation of flow structures in the dissipation region of the turbulent spectrum to be correctly represented. However, increased turbulent kinetic energy in the blade swept area is known to lead to the formation of turbulent eddies around the blades, increasing blade drag [171]. In the case of a real turbine, this will lead to a reduction in rotational speed and consequently a reduction in power generation. In the case of the turbine models used in this study increased blade drag will lead to an increase in the power required to maintain the required rotational speed, P_{appB}. Since P_{appNB} is unaffected, this increase will lead to a reduction in blade generated power P_B and thus a reduction in C_p.

5.3.1 – Support structure wake

As identified in Chapter 2, the expected wake downstream of a tidal stream turbine is made up of two constituents: The wake of the blades and turbine body, and the wake of the support structure. Both incorporate a number of elements which combine in a complex manner to form the resulting overall wake. As has been suggested in Section 5.2 and earlier in this section, the flow structures in the region upstream of the support structure are believed to have a significant impact on the observed performance of tidal turbine models in this study. Based on Figure 2-44, the wake structures observed in the support structure region are illustrated in Figure 5-63. Again it should be noted the downstream length of the primary and secondary horseshoe vortices are indicative.

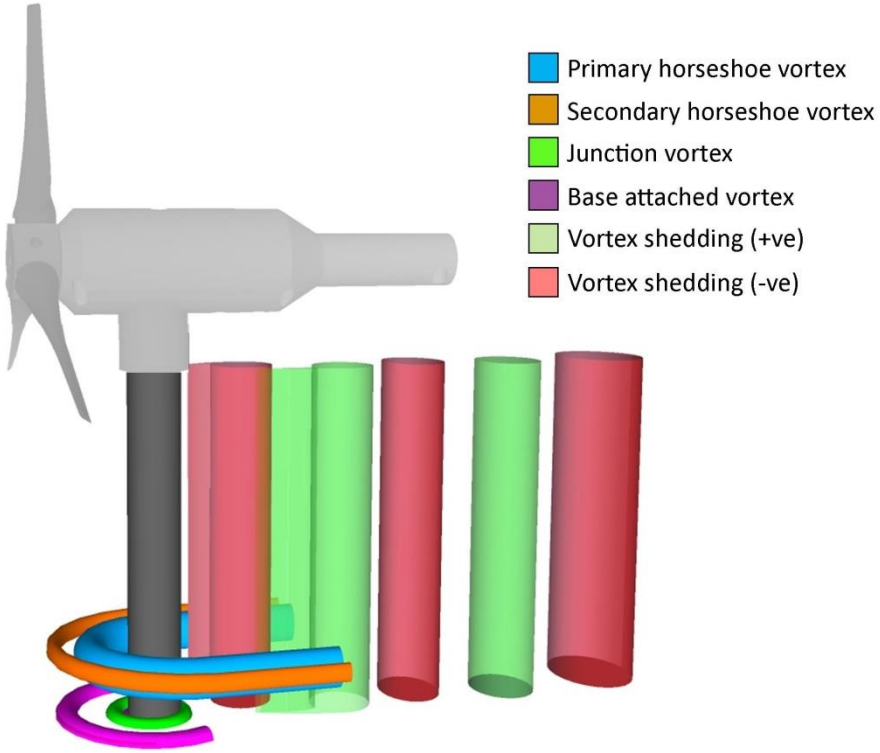

Figure 5-63 – Support structure wake elements.

As highlighted by low values of *Fr*, flow in this study is subcritical, meaning that the downstream wake has an influence on flow structures in the region upstream of the support structure. This suggests that the size of the upstream flow features illustrated in Figure 5-63 can change depending on support structure diameter. Given that the "Base attached" and "Junction" vortices (BAV and JV respectively) are generated due to the interaction of the support structure and the channel base, these wake structures are found only at the base of the support structure, and are not expected to influence the flow further up the support structure or in the blade location region. The primary and secondary horseshoe vortices (HV1 and HV2 respectively) are the most energetic of the support flow structure elements, with HV1 having greater energy and stability than HV2, which can be intermittent [131]. Again as discussed in Chapter 2, both HV1 and HV2 rotate in a clockwise direction, and their size is governed by that of the cylinder and the velocity and turbulent energy of the incoming flow. The influence of these structures with respect to height above the base also

appears to be dependent on the energy of the incoming flow, with a more energetic flow allowing the structures to extend to a greater height.

The presence of HV1 and HV2 structures in PIV data recorded during this study is suggested by the region of low horizontal plane turbulent kinetic energy observed upstream of the support structure, which is of the location and size which would be expected of these structures, as suggested by previous studies. Such regions of low k_{xy} observed upstream of the support structure are illustrated in Figure 5-46 and Figure 5-47, for example. Due to the measurement planes used in this study, JV and BAV were not observed. It is therefore not known whether these structures were present in the cases studied. However as discussed above, these structures have been identified in previous studies as low energy structures and are consequently not believed to impact turbine performance. The presence of the hypothesised arch vortex downstream of the support structure was not observed in results. Vortex shedding as illustrated in Figure 5-63was instead found to occur. Vortex shedding is also suggested in mean flow results such as Figure 5-43 and Figure 5-44, as well as POD results given in Section 5.2.1 (see mode 2 and 3 reconstruction in Section 6.3 (Figure 6-50)), where rotating regions were observed downstream of the support structure. However, due to the location of this downstream shedding, it appears that the upstream structures have a much greater effect on turbine performance.

Though the study of the precise mechanisms of these vortices is, unfortunately, beyond the scope of this work, it is believed that the HV1 and HV2 vortices result in a region of low turbulent kinetic energy in the region upstream of the support structure front face. Locating the blades in this region allows optimal turbine performance. At the scale of the turbine studied in this work, this optimal performance region extends from around 25mm to around 40mm upstream of the support structure, and TKE increases slightly with separation distance over this region. Two further regions are also identified, and are located downstream and upstream of the optimal performance region respectively:

- The area downstream of the optimal region (i.e. between the support structure and the optimal performance region) is believed to experience a mean TKE approximately 200% of that in the optimal performance region, resulting in a mean C_p approximately 70% of that of the optimal performance region.

- The region upstream of the optimal performance region (up to 60mm separation distance) experiences a mean level of TKE approximately 400% of that in the optimal performance region, resulting in a mean C_p of 40% of that than within the region.

A diagram of these three regions and their streamwise location relative to the turbine is illustrated in Figure 5-64, with the optimal performance region highlighted. C_p is given normalised by that in the optimal performance region, and a band is used to illustrate the range of the values used in this calculation.

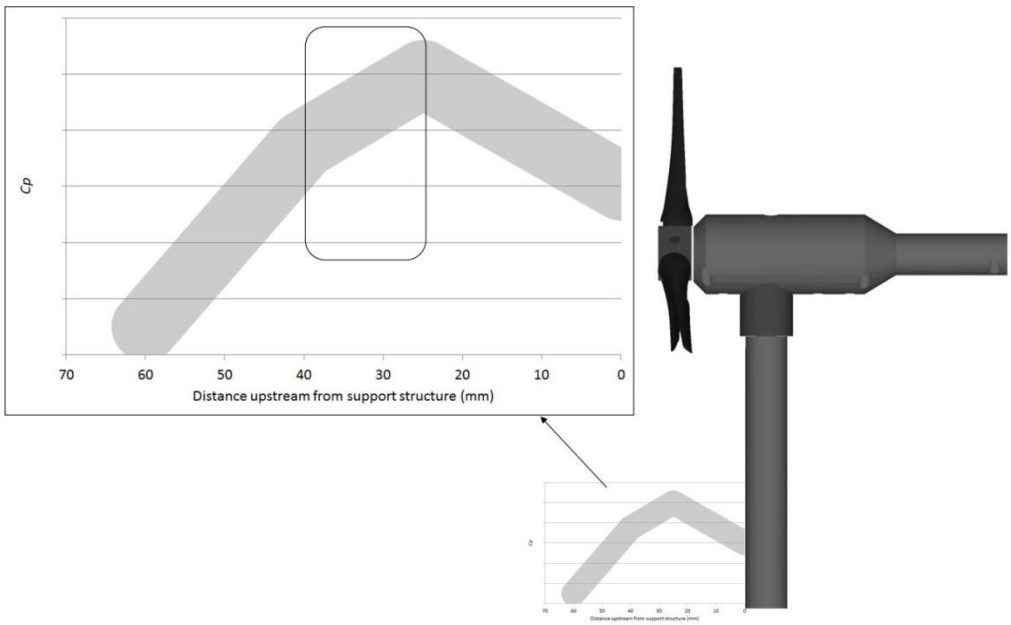

Figure 5-64 – Diagram illustrating the location of the suggested optimal performance region and surrounding regions.

It is believed that the size and location of this region is a function the turbulent kinetic energy of the incoming flow and the diameter of the support structure (*d*) rather than that of the blades (*D*). Based on results from phases 2 and 3, the location of the region appears to be approximately the same in the case of 11mm, 16mm and 20mm diameter support structures, suggesting that a definition based on the mean of these diameters could be used. Based on this mean value (15.6mm), the location of the optimal performance region can be said to lie between 1.5*d* and 2.5*d*. However, this value is a current best estimate based on the data available; and further study at a wider range of support structure diameters and different scales of turbine models would be required in order to fully verify both the hypothesis and the location of the optimal performance region. Due to this uncertainty, the region will continue to be defined by a distance of between 25mm and 40mm from the support structure front face.

Summary results – Phase 3

- For a turbine mounted on support structures with diameter between 6 and 25mm, C_p was found to increase with diameter. The effect appears to be related to the separation distance between blade swept area and support structure front face. C_p was found to decrease with increasing separation distance. This effect correlates with that observed in phase 2.

- The results of phases 2 and 3 appear to suggest the presence of three distinct regions in the area upstream of the support structure. Based on support structure diameter *d*, the region between 1.5*d* and 2.5*d* upstream of the front face appears to be an optimal performance region, within which turbulence is relatively low, and blade performance is maximal. In the region downstream of this (0*d* to 1.5*d*), turbulence is greater, and mean power coefficients are expected to be reduced to around 70% of those achieved in the optimal performance region. The third region (2.5*d* – 4*d*) experiences much greater turbulence and is expected to yield power coefficients around 40% of those in the optimal performance region.

6

Results – Multiple Turbines

6.1 – Experimental phases

As discussed in Section 5.2, four major experimental phases were conducted as part of this project. Initial wake experiments; the impact of blade position on turbine output; and the impact of support structure diameter on turbine torque output have all been discussed in Chapter 5. This chapter details the experiments conducted and results from further work building upon these results, incorporating multiple turbines. This work was defined as experimental phase 4.

6.1.1 – Phase 4: Impact of upstream turbine on downstream turbine performance

The aim of this phase of experimentation was to study the impact of placing a turbine in the wake of another turbine. This was achieved by conducting a series of experiments using a second turbine, installed at a range of positions upstream of the original turbine used during previous experimental phases, and monitoring the performance of the existing turbine. The results of this phase of experimentation are clearly critical to the development of arrays of tidal turbines, since nearly all devices in an array are likely to be positioned, to some degree, in the wake of other devices.

Experimental sub-sections

Within this phase, two sub-sections of experiments were conducted. The first involved the placement of an upstream turbine directly in front of the existing device (i.e. in the same cross-stream location and height above the channel base), at two streamwise separation distances, and two flow cases. The second involved offsetting the upstream device in the cross-stream direction, again under two upstream position conditions. In the second sub-section, a single flow condition case was used. These sub-sections are subsequently referred to as Phase 4a and 4b respectively. In each case, three diameters of downstream turbine support structure were also used (11mm (0.088D), 16mm (0.128D), and 20mm (0.16D)), while the upstream turbine support structure diameter remained constant in all cases, at 16mm. The central turbine mounting position was used in all cases, yielding downstream blade to support structure separation distances of between 30mm and 34.5mm, meaning that in all phase 4 cases, blades were located in the optimal performance region defined in Section 5.3.

Further details of the conditions used in each case are given in the relevant section, as well as figures illustrating the relative locations of upstream and downstream turbines (Figure 6-2 and Figure 6-37).

Flow conditions

As described above, two flow cases were used in this phase. These were as described in Chapter 5, and are summarised below for simplicity:

Variable	*Case 1*	*Case 2*
Turbine model scale (rotor diameter)	125mm	
Flow rate	30l/s	40l/s
Flow velocity	0.2m/s	0.3m/s
Water depth	300mm	

Blockage ratio	7%	
Reynolds number, Re	$2x10^5$	$3x10^5$
Froude number, Fr	0.046	0.062
Tip Speed Ratio, λ	3.5	3.1

Table 6-1 – Summary of two cases used during Phase 4a experimental work.

In both phase 4a and 4b, two turbines were used. In both cases, performance measurement was undertaken on the downstream turbine, with the upstream turbine operating as a scale model of a real turbine, but without the performance measurement equipment applied to the downstream device. The rotational speed and thus TSR of the upstream turbine was therefore not limited by the inherent friction caused by the measurement equipment as in the case of the downstream device. A simple control system was therefore applied in order to ensure that the upstream turbine would rotate at the correct rotational speed and therefore TSR defined in Table 6-1. This system allowed a grub screw perpendicular with the central shaft to be tightened or loosened as necessary in order to set the rotational speed, which was monitored by recording video footage of the rotating turbine using a digital camera at a known frame rate (25Hz), and measuring the number of frames required for the turbine to complete a full rotation. The two turbines as arranged for a test during phase 4a are illustrated in Figure 6-1. The downstream turbine driveshaft and measurement equipment can be observed in the background, as well as the upstream turbine offset mounting holes used during phase 4b in the foreground.

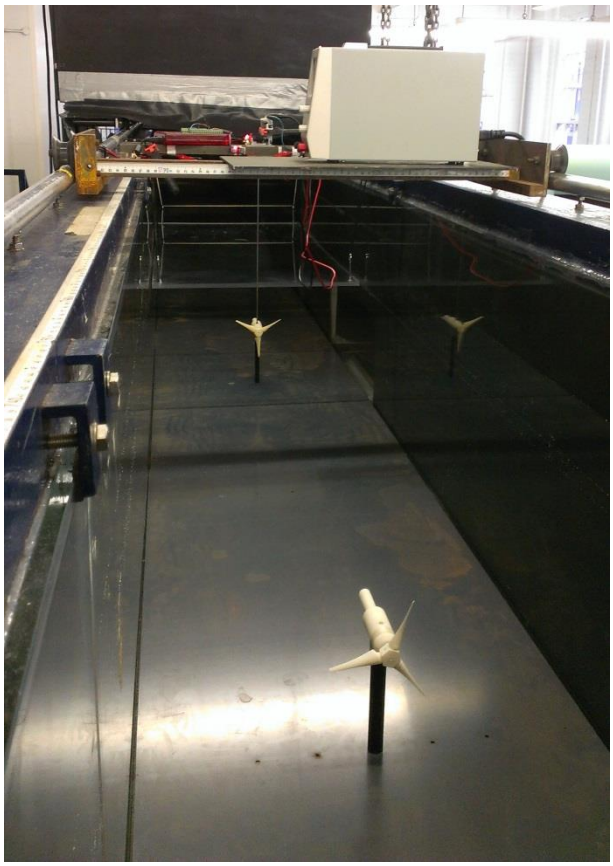

Figure 6-1 – Upstream and downstream turbines installed in water channel at "Far" spacing (10D) during Phase 4a testing.

6.2 - Results

6.2.1 – Phase 4a: Upstream turbine, streamwise separation

A total of fifteen experiments were undertaken during phase 4a. An image illustrating the cases studied during this phase is given in Figure 6-2.

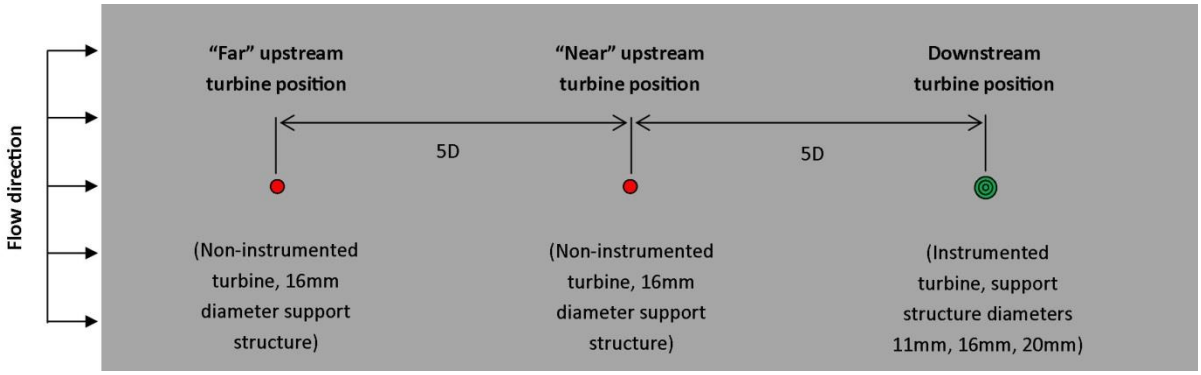

Figure 6-2 – Graphical representation of experiments carried out during phase 4a viewed from above (upstream turbine installation positions shown in red, downstream in green).

As illustrated in Figure 6-2, a second turbine was installed at streamwise positions of 5*D* (0.625m) and 10D (1.25m) upstream of the existing instrumented turbine, referred to as "Near" and "Far" respectively. An upstream support structure diameter of 16mm was used in all cases. These spacing distances are similar to those being considered for the first commercial tidal stream arrays, such as the MeyGen array discussed in Chapter 1. Experiments were conducted to measure the power coefficient of the downstream turbine, with both turbines rotating at the same TSR.

Rotational speeds of 10.5rad/s and 9rad/s were used to give λ values of 3.5 and 3.1 for both turbines under flow conditions 1 and 2, respectively. As has been discussed, the rotation of the upstream turbine was set at the start of each experiment, but the turbine rotation was not monitored, meaning that the relative rotational position of the two turbines was not known.

Potential errors

In addition to the near and far upstream turbine cases illustrated in Figure 6-2, results were also generated during phase 4a without an upstream turbine in place. These single turbine experiments were identical to those carried out during phase 3, and were thus used to compare results between the two phases in order to highlight any potential errors in the experimental arrangement or methods. Variation in C_p between identical experiments carried out during phase 3 and phase 4a for 11mm, 16mm and 20mm diameter support structures was 1.4%, 0.9% and 0.4% respectively.

The variation in C_p between these results shows that a shaft misalignment error, as discussed in Section 4.6, does not occur. However, the two other major sources of turbine measurement error (speed measurement and current measurement, with calculated maximum values of 0.4% and 1.5%) may be the cause of this variation.

A potentially erroneous result is observed in phase 4a data given in Figure 6-3, in which the 11mm diameter support structure case appears to generate a greater C_p with a far upstream turbine than with no upstream turbine. This result is believed to be erroneous since in all other cases the presence of an upstream turbine leads to a decrease in C_p. The difference between the results is 2%, and the variation between the far result and a predicted result based on the extrapolation of the 16mm and 20mm results is a further 4%, giving a total estimated error of 6%. This error is within the calculated range of turbine performance measurement errors described in Section 4.6 so is believed to be caused by either misalignment of the turbine drive shaft in the no upstream turbine case, or a speed or current measurement error in either case.

Performance data

Under flow case 2, downstream turbine power coefficients were measured with upstream turbines located in the near and far positions, as well as without an upstream turbine. The case without an upstream turbine represents the same configuration used in phase 2 and phase 3 experiments. In each upstream position case, three downstream turbine support structure diameters were used (11mm, 16mm and 20mm). Power coefficients measured during these experiments are given in Figure 6-3.

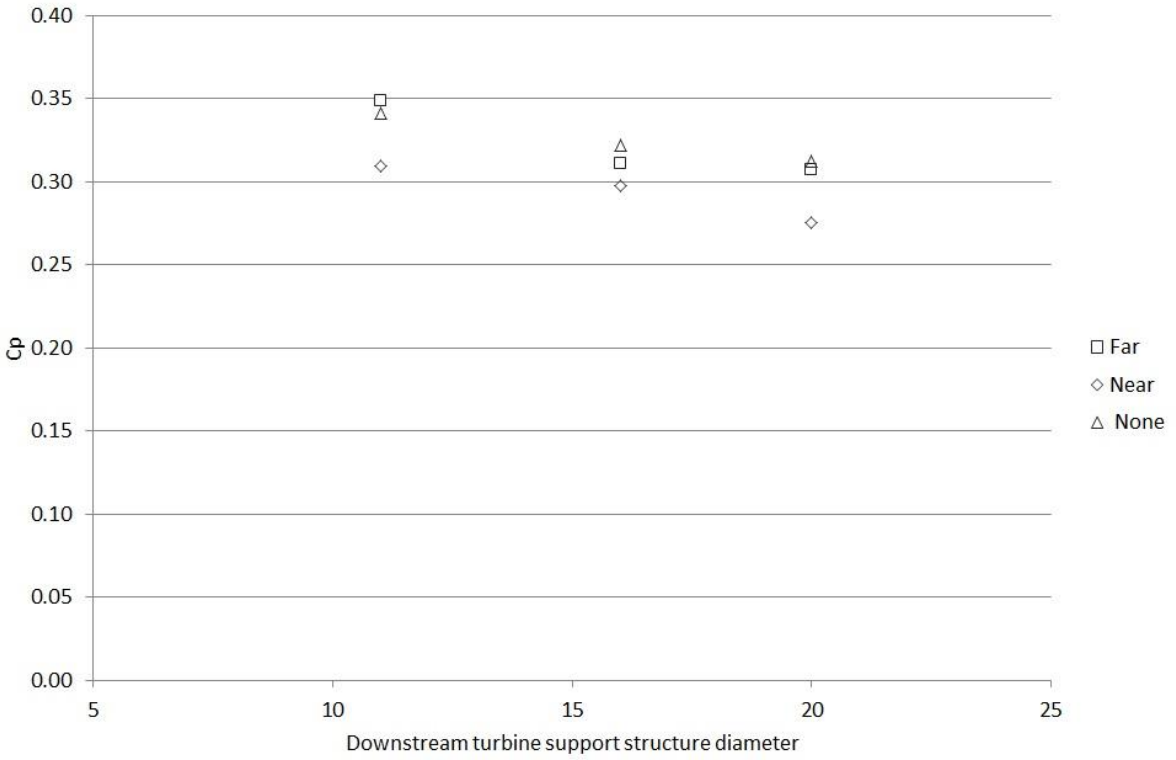

Figure 6-3 – C_p *for three downstream turbine support structure diameter cases in three upstream turbine cases (none, 5D, 10D) under flow case 2.*

These results indicate that the presence of an upstream turbine at 5*D* separation (near position) yields a reduction in C_p of between 8% and 12% compared to an identical case with no upstream turbine, and that the presence of an upstream turbine at 10D separation (far position) yields a reduction in C_p of between 2% and 4% in the 16mm and 20mm cases, but a slight increase (2%) in

the 11mm diameter case. As discussed above, the 11mm diameter support structure result with a far upstream turbine is believed to be erroneous, with an error of around 6%. It was considered possible that other such errors could be present, and could alter the data illustrated, but the trend observed in Figure 6-3 is consistent across all other data points and is greater in value than the error value, so this was not thought to be the case.

Further results from phase 4a at a second flow case were also conducted, and are illustrated in combination with those shown in Figure 6-3 in Figure 6-4 and Figure 6-5. These figures illustrate the same results, but are arranged to highlight two effects which appear to influence blade torque. Figure 6-4 primarily shows the influence of downstream device support structure diameter on C_p, also taking into account the flow case and upstream turbine position. Figure 6-5 focuses on the effect of the upstream turbine position, under two flow and three downstream support structure diameter cases.

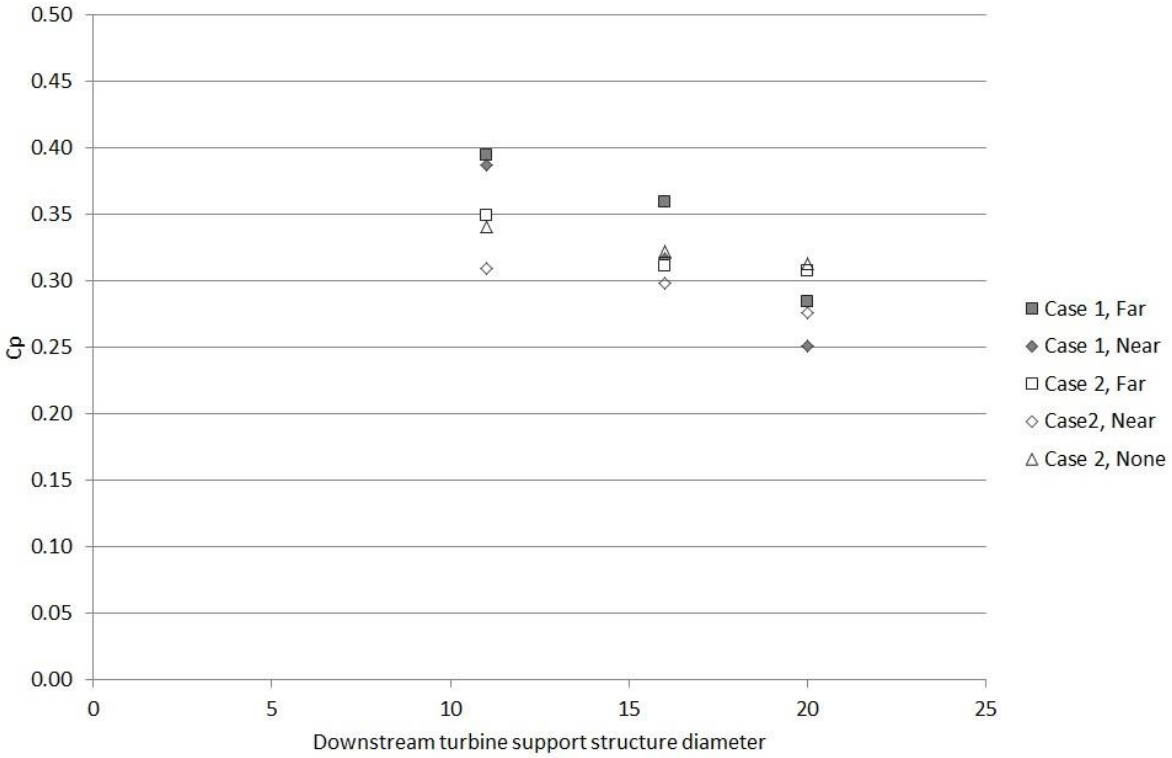

Figure 6-4 – Phase 4a results: Influence of downstream support structure diameter on torque output of downstream turbine.

These results initially appears to contradict those described in Section 5.2.3 (phase 3 results, as illustrated in Figure 5-48), which showed a trend for slightly increasing blade torque with increasing support structure diameter across the 6-25mm diameters tested. However, as detailed in Section 5.3, an optimal performance region of low turbulent kinetic energy was identified and was defined by a separation distance between the blades and support structure front face of between 25mm and 40mm. Separation distances within this region were used in all phase 4 tests.

Across the optimal performance region, a slight reduction in C_p with increasing support structure diameter was observed in phase 3 results (Figure 5-48), though C_p variation between the 11mm and 20mm cases was small (around 1%). Comparing the data shown in Figure 6-3 (no upstream turbine)

to that from phase 3 reveals a similar trend, though the variation in C_p this time is greater, at around 8%.

With upstream turbines in place, the trend for reducing C_p with reducing separation distance (i.e. increasing support structure diameter) remains, with a far upstream turbine yielding a variation between the 11mm and 20mm cases of 28% in flow case 1 and 12% in flow case 2, and a near upstream turbine yielding variations of 35% and 11% in the same cases. This suggests that the trend of decreasing torque with increasing support structure diameter is more dramatic under slower flow conditions.

Increased variation in the slower flow case is illustrated clearly in Figure 6-5, where wider ranges of C_p values can be seen in flow case 1 than flow case 2, in both near and far upstream turbine cases.

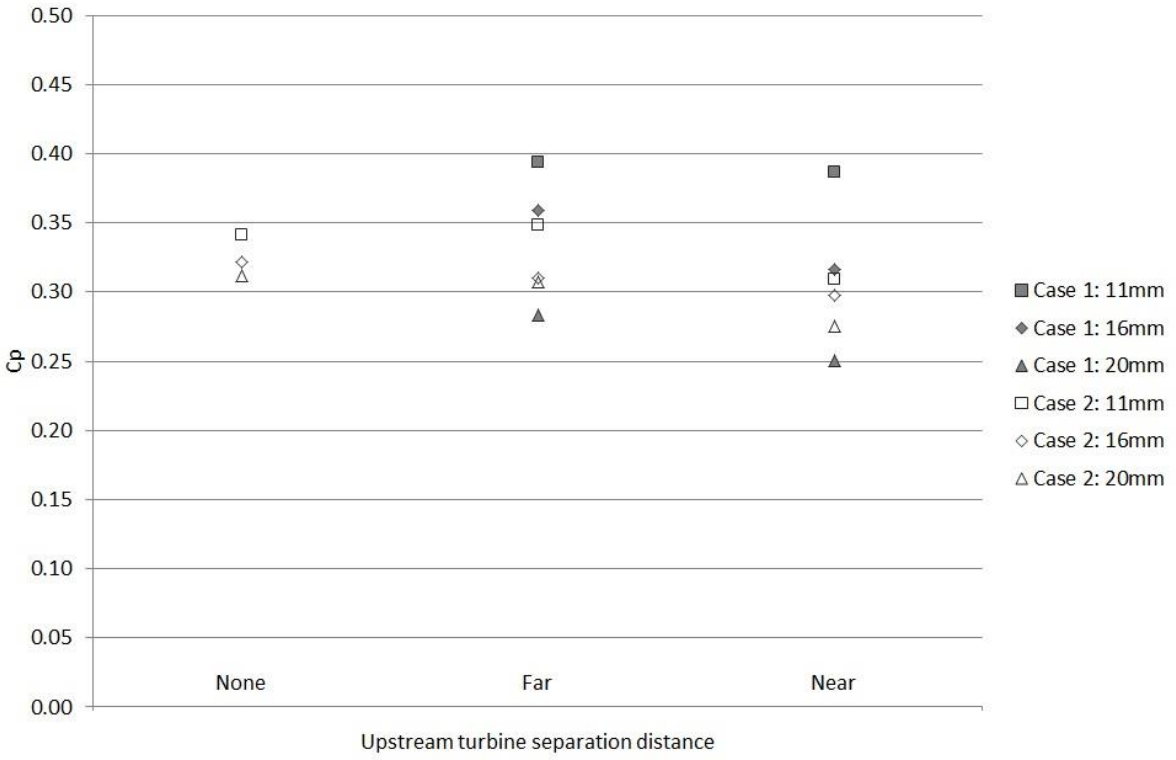

Figure 6-5 – Phase 4a results: Influence of upstream turbine position on torque output of downstream turbine.

Variation in C_p with support structure diameter has been attributed to variation in the separation distance between the turbine support structure front face and the blade swept region, and an optimal performance region was identified in Section 5.3, characterised by low horizontal plane turbulent kinetic energy. This region of relatively low k_{xy} is believed to be caused by the location of the primary and secondary horseshoe vortices in the region upstream of the support structure.

Phase 2 and 3 results also suggest that performance variation occurs within this region, with a greater diameter of structure producing a shorter separation distance, which places the blades in the inner range of the region, where relatively high turbulent kinetic energy is found. This leads to a reduction in C_p compared to blades located in the outer range of the region where k_{xy} is lower. This effect can also be observed in phase 4a results, as illustrated in Figure 6-5. Furthermore, the effect

appears to be amplified in flow case 1 in comparison to flow case 2, with a greater range of C_P variation between turbines mounted on the widest and narrowest support structures.

This result appears to suggest that a lower flow velocity allows the support structure upstream wake to have a greater influence on turbine performance. It is suggested that at lower flow velocity the horseshoe vortices observed upstream of the support structure are able to expand to a greater size, hence increasing their effect.

This is a significant conclusion, and suggests that the hypothesis generated by Chapter 5 results takes on another level of complexity when applied to a turbine in an array. However, these hypotheses cannot be fully confirmed with the limited number of test cases available in this study, and further investigation would be required in order to fully understand the observed effects. A summary of results from this phase is given at the end of the section, following analysis of PIV results. A combined discussion of phases 4a and 4b is also given in Section 6.3.

PIV Results

Generally, the results of this phase of work confirm that, as expected, the addition of an upstream turbine does lead to a reduction in the blade power generated and consequently C_p of a downstream turbine. In order to ascertain to what degree this effect is related to turbulence in the wake of the upstream device, PIV data for three cases (no upstream turbine; far upstream turbine; near upstream turbine) was studied, and is given in the following section.

Instantaneous velocity and horizontal plane vorticity frames generated by PIV analysis of a downstream turbine in the wake of an upstream turbine are given in the following figures. Results for flow case 2 at the three upstream turbine cases illustrated in Figure 6-5 are given. Results are first given as measured at the support structure mid height plane (66mm above the channel base), followed by results for the same cases at the turbine centre height plane (135mm above the channel base). The relative location and size of the turbine or support structure at each height is illustrated, and flow is from left to right in all cases.

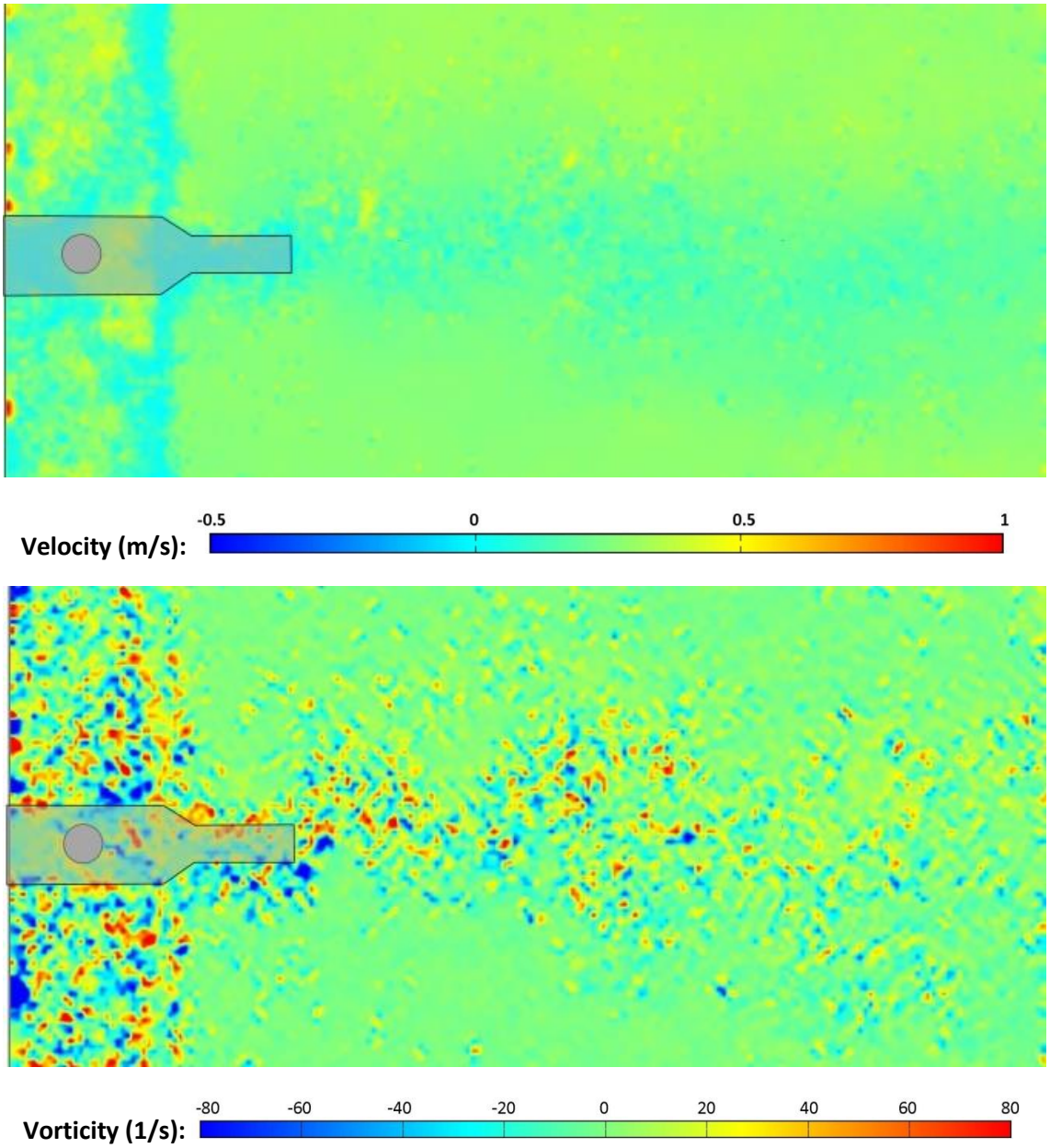

Figure 6-6 - Velocity (top) and horizontal plane vorticity (bottom) downstream of turbine on 16mm diameter support structure at 66mm measurement height. No upstream turbine.

Image scale: 0.36m x 0.27m (1.8D x 1.3D)

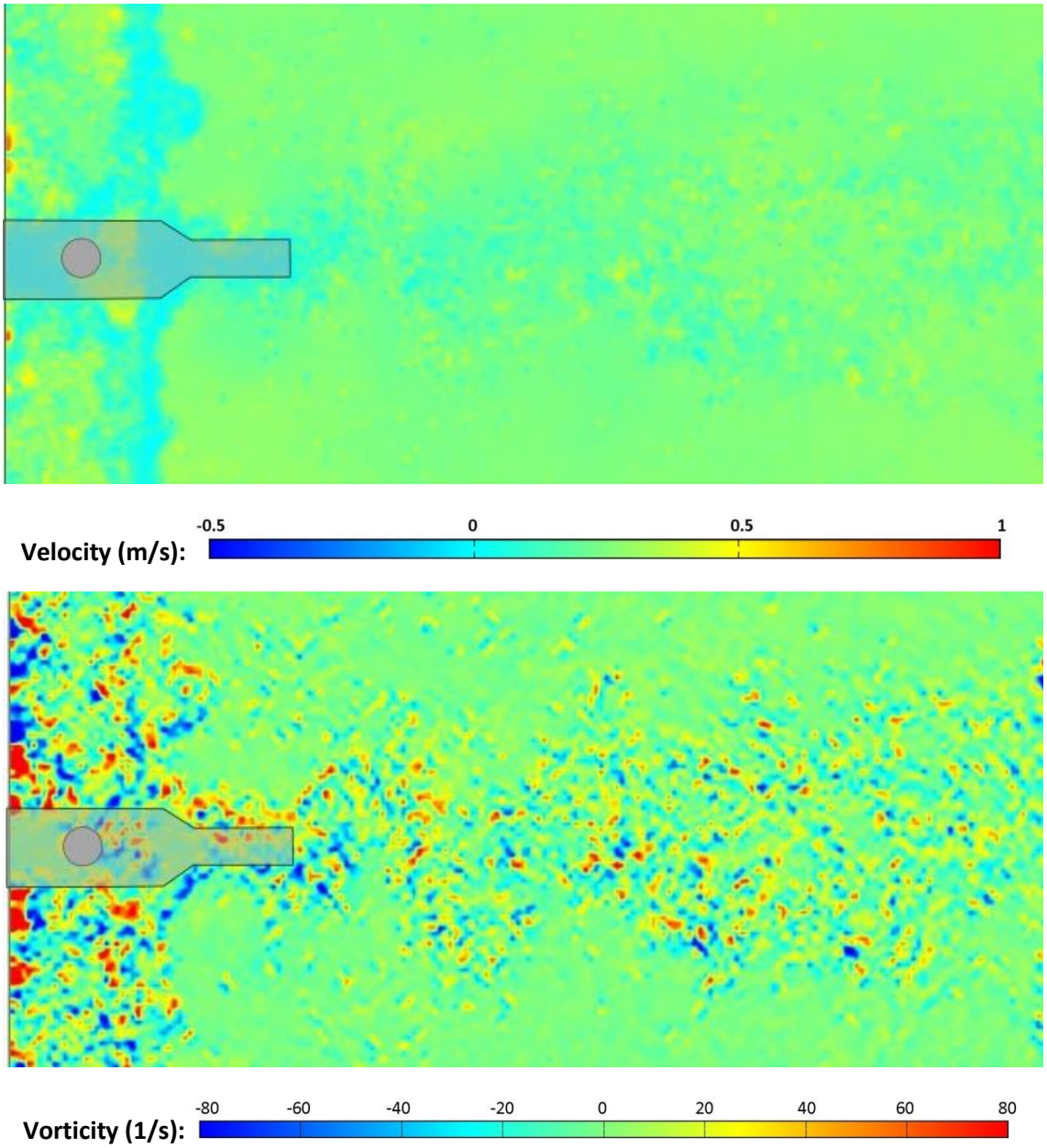

Figure 6-7 - Velocity (top) and horizontal plane vorticity (bottom) downstream of turbine on 16mm diameter support structure at 66mm measurement height. Upstream turbine in far location (10D).

Image scale: 0.36m x 0.27m (1.8D x 1.3D)

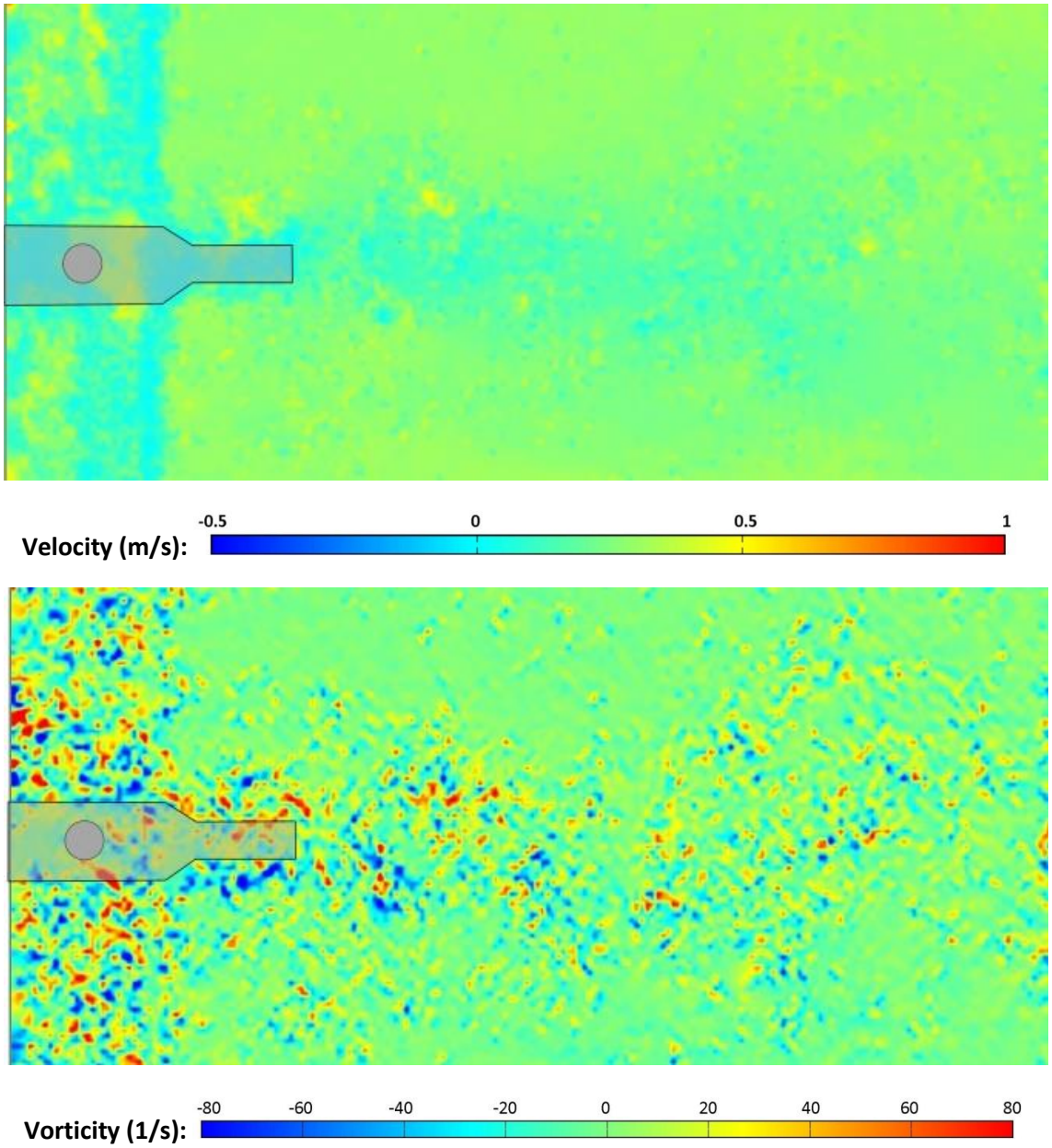

Figure 6-8 - Velocity (top) and horizontal plane vorticity (bottom) downstream of turbine on 16mm diameter support structure at 66mm measurement height. Upstream turbine in near location (5D).

Image scale: 0.36m x 0.27m (1.8D x 1.3D)

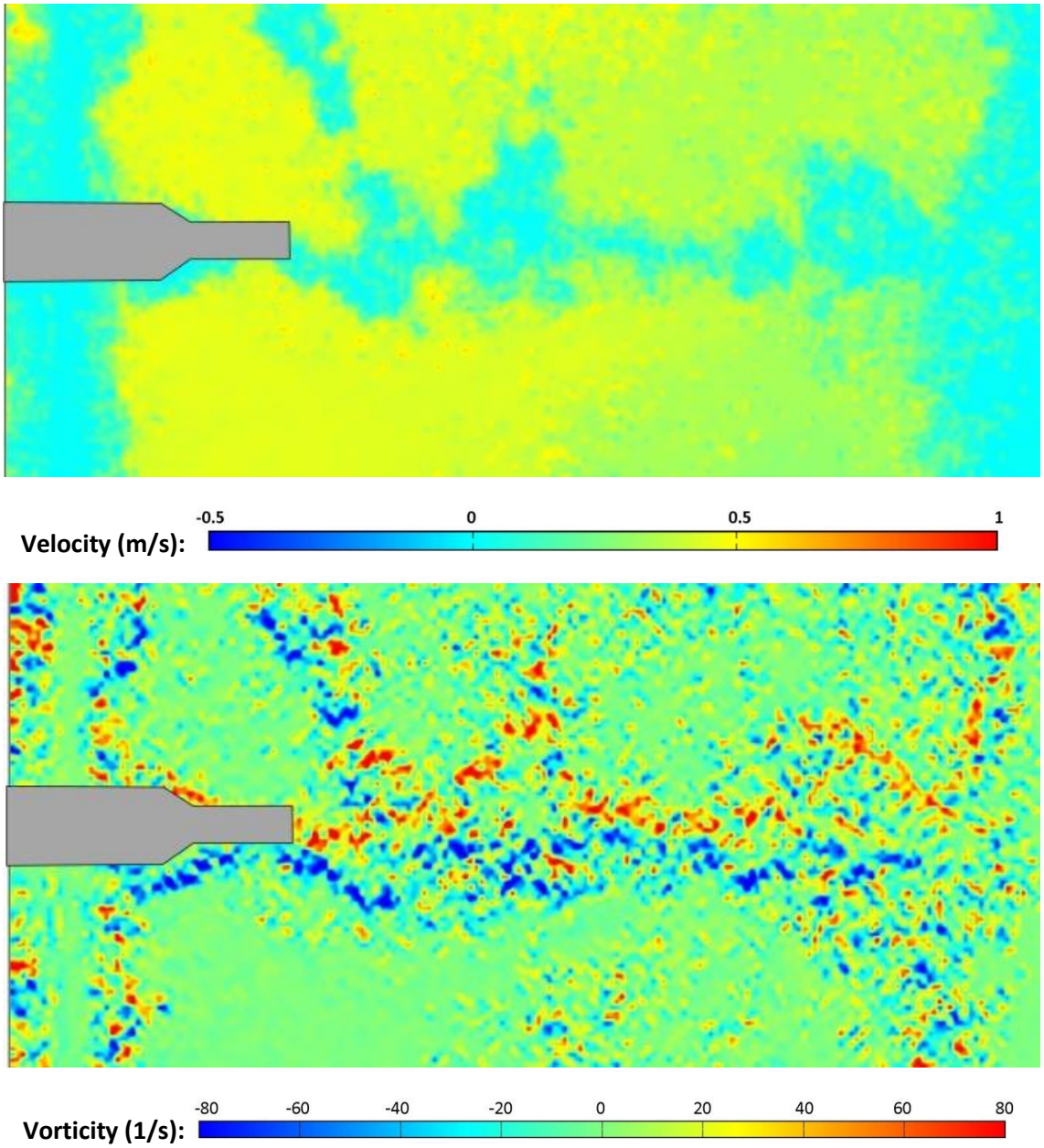

Figure 6-9 - Velocity (top) and horizontal plane vorticity (bottom) downstream of turbine on 16mm diameter support structure at 135mm measurement height. No upstream turbine.

Image scale: 0.36m x 0.27m (1.8D x 1.3D)

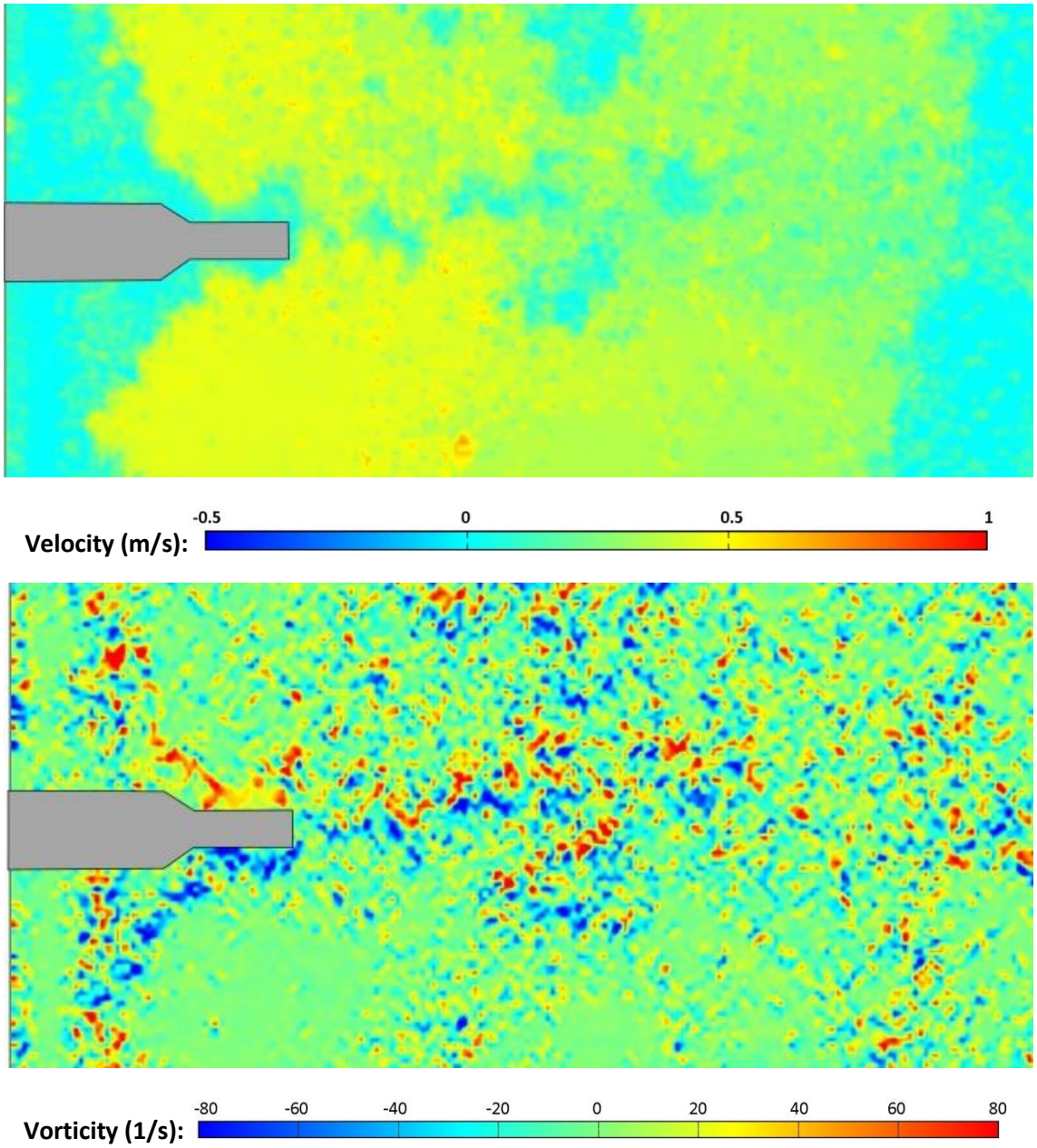

Figure 6-10 - Velocity (top) and horizontal plane vorticity (bottom) downstream of turbine on 16mm diameter support structure at 135mm measurement height. Upstream turbine in far location (10D).

Image scale: 0.36m x 0.27m (1.8D x 1.3D)

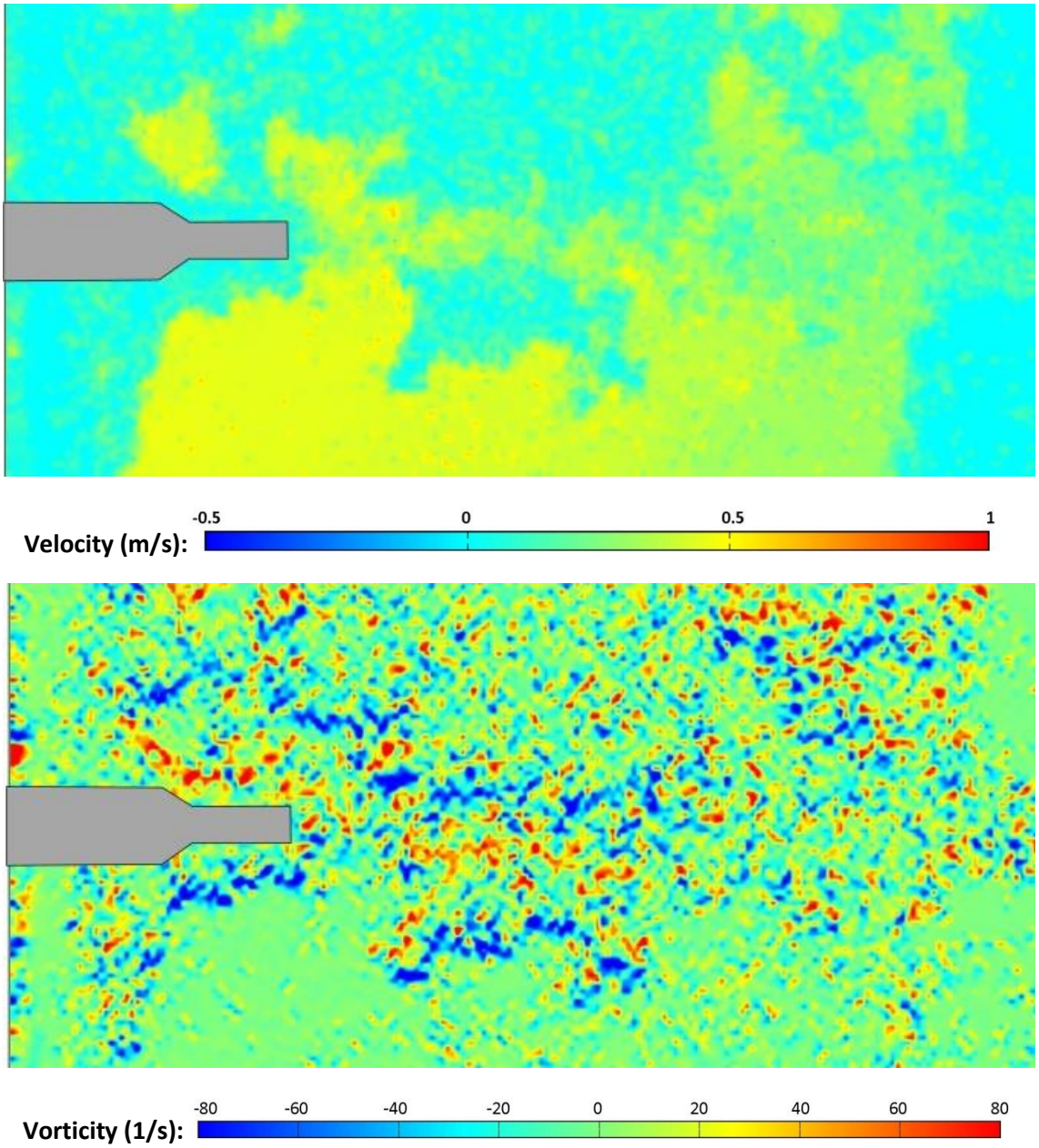

Figure 6-11 - Velocity (top) and horizontal plane vorticity (bottom) downstream of turbine on 16mm diameter support structure at 135mm measurement height. Upstream turbine in near location (5D).

Image scale: 0.36m x 0.27m (1.8D x 1.3D)

The PIV results illustrated in the above figures show a more disturbed flow pattern behind the downstream turbine when another turbine is placed upstream. In the cases with an upstream turbine, horizontal plane vorticity images illustrate a much larger region of disturbed flow behind the downstream turbine, illustrating that the influence of the upstream turbine extends into, and contributes to, the wake of the downstream turbine. It appears that the greater turbulence in the downstream turbine wake is caused by greater turbulence in the incoming flow due to the upstream turbine. This effect was quantified by studying the horizontal plane turbulent kinetic energy in each case, as described below.

It is also notable in the figures above that the turbulent region behind the downstream turbine appears to be biased in the positive cross-stream direction (i.e. towards the top of the image, or to the right if facing the oncoming flow). This effect is believed to be due to the rotation of the upstream turbine and the distortion of the flow field, and is discussed in detail following the illustration of further wake images, towards the end of this section.

Turbulent kinetic energy

Horizontal plane turbulent kinetic energy (k_{xy}) was calculated from PIV results of the cases illustrated in Figure 6-5, along the channel centreline at measurement heights of 66mm and 135mm above the channel base. TKE was then plotted for each of the upstream turbine cases to allow the direct comparison. Plots illustrating the 16mm diameter support structure case are given in Figure 6-12 and Figure 6-13, representing the 66mm and 135mm planes respectively. The relative size and position are again given by a diagram of the turbine and support structure. Note the difference in vertical axis scale between the two figures.

It should also be noted that numerical values recorded within 0.025m of the upper and lower limits of these figures are a result of potentially erroneous PIV results, which are themselves caused by insufficient illumination at the edges of the measurement region. These erroneous results can particularly be seen at the upper limit of Figure 6-12, and later at the lower limit of Figure 6-14.

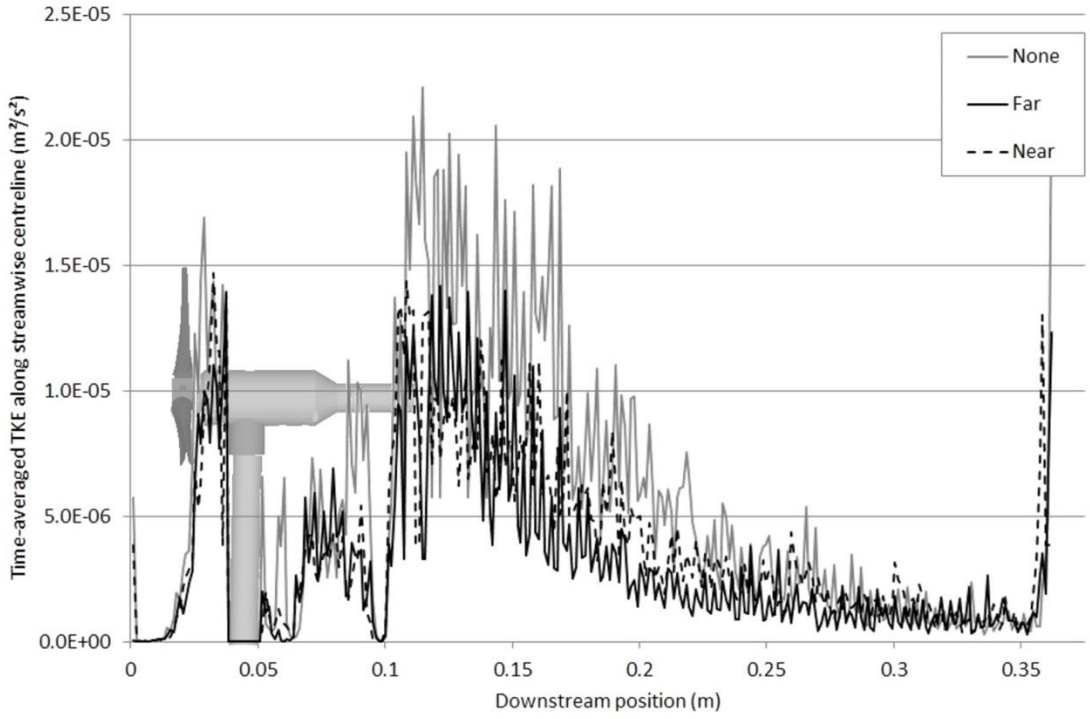

Figure 6-12 – Centreline streamwise k_{xy} *downstream of turbine mounted on 16mm support structure without upstream turbine and with upstream turbine at far (10D) and near (5D) upstream positions. Measurement at 66mm plane.*

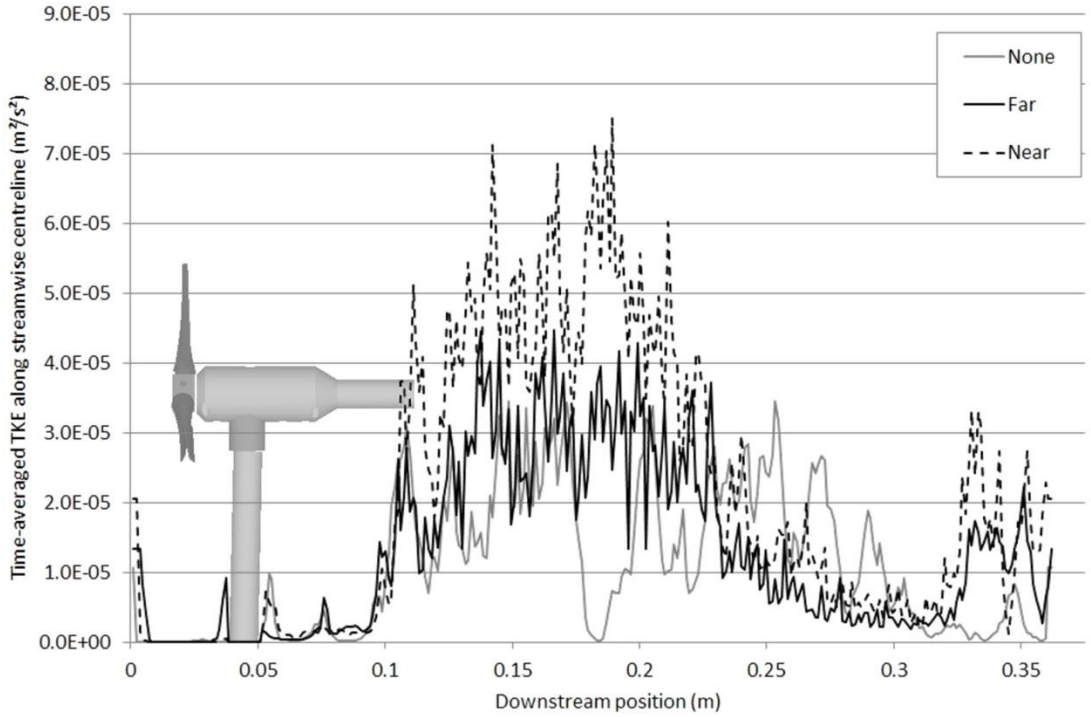

Figure 6-13 – Centreline streamwise k_{xy} *downstream of turbine mounted on 16mm support structure without upstream turbine and with upstream turbine at far (10D) and near (5D) upstream positions. Measurement at 135mm plane.*

Figure 6-12 illustrates the high incoming turbulent kinetic energy at support structure mid-height. At this measurement plane, the greatest TKE is observed in the case without an upstream turbine, and TKE values for the cases with near and far upstream turbines are similar (the variation in mean values between the two cases is 10%). However, despite initial variations, all three cases exhibit dissipation to k_{xy} = 1x10^{-6} m^2/s^2 by a downstream position of 0.35m, indicating that at this height, most (at least 90%) of wake TKE is dissipated within a distance of 2.5*D*.

A similar overall pattern is observed at the 135mm measurement plane, though at this height the greatest TKE values are generated in the near upstream turbine case, followed by the far upstream turbine case. At this measurement plane, the magnitude of TKE is around four times greater than at the 66mm measurement plane. Turbulent kinetic energy is observed to rise in the region downstream of the turbine body and peaks between 1*D* and 1.5*D* downstream of the turbine blades in all cases. TKE then appears to dissipate, reaching 10% of the mean peak level in all cases at a downstream distance of 2.2*D*. However, in the near and far upstream turbine cases TKE then rises again, whilst appearing to remain low in the case without an upstream turbine. This suggests that the wake behind an upstream device influences a device located downstream, and that the wake behind two inline devices has greater turbulent energy at a given point than downstream of a single device. At 2.6*D* downstream of the turbine blades, the case with a near upstream turbine shows k_{xy} of around 3x10^{-5} m^2/s^2. With a far upstream turbine, TKE is around 50% of this value, and without an upstream turbine the value is around 10%. This result shows a correlation with the generated C_p in each case illustrated in Figure 6-5, and appears to confirm that, as would be expected, increased turbulence in the wake of an upstream device leads to reduced power generation from a downstream device.

Cross-stream plots of horizontal turbulent kinetic energy were also generated at a distance of 1*D* (0.125m) downstream of the turbine blades (0.127m on the horizontal scale in Figure 6-12 and Figure 6-13) at both the 66mm and 135mm height planes. This data was plotted by generating a cross-stream line across the PIV result image at this location and calculating TKE for a series of 300 points across this line. Results for each frame were then combined to give time-averaged TKE plots at the 66mm and 135mm planes for the three upstream turbine cases illustrated previously. These cross-stream TKE plots are given in Figure 6-14 and Figure 6-15. Again the difference in vertical axis scales between the two measurement planes should be noted.

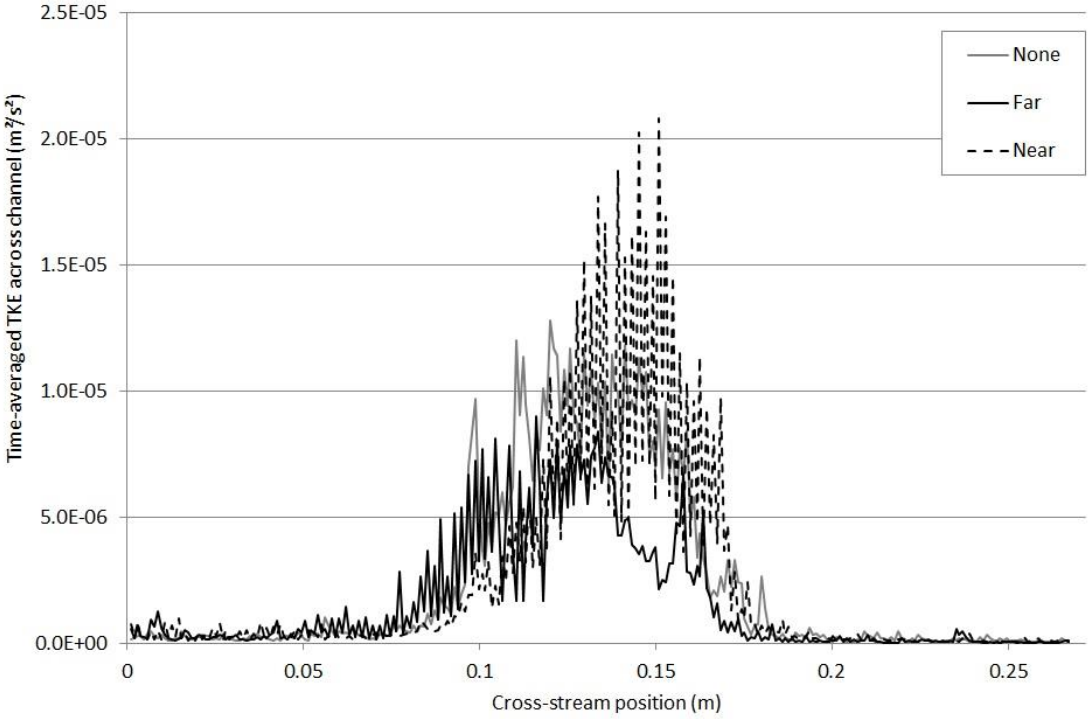

Figure 6-14 – Cross-stream k_{xy} *at 0.125m (1D) downstream of turbine mounted on 16mm support structure without upstream turbine and with upstream turbine at far (10D) and near (5D) upstream positions. Measurement at 66mm plane.*

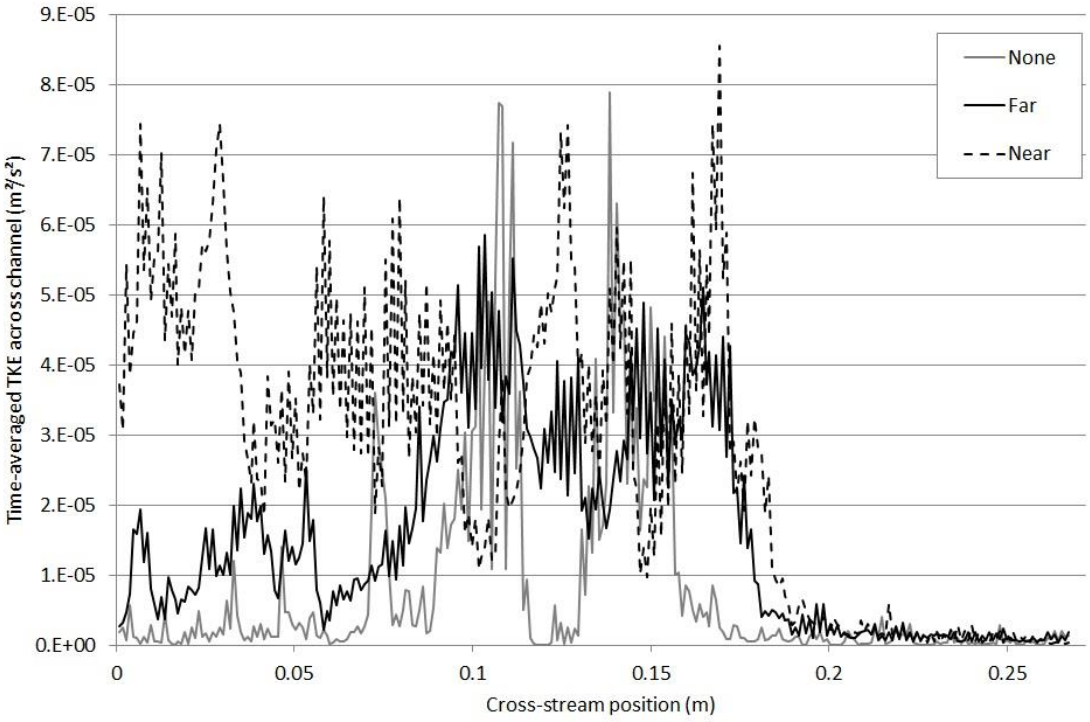

Figure 6-15 – Cross-stream k_{xy} *at 0.125m (1D) downstream of turbine mounted on 16mm support structure without upstream turbine and with upstream turbine at far (10D) and near (5D) upstream positions. Measurement at 135mm plane.*

These figures again show that greater TKE is observed behind a downstream turbine when an upstream turbine is in place. In all cases at blade height, TKE was found to be greater with the upstream turbine in the near position than in the case without a turbine or with a turbine in the far position. At blade height the second greatest TKE values are generated in the case with the far upstream turbine, followed by the lowest TKE values generated in the case without an upstream turbine. As illustrated in Figure 6-15, mean cross-stream TKE with a near upstream turbine was 2.4 times greater than in the far case, and 4 times greater than without an upstream turbine. This again correlates with the C_p values calculated previously, suggesting that lower TKE observed both in front of (as in phases 2 and 3) and behind the downstream turbine is associated with greater C_p.

However, it is interesting to note that at the 66mm plane, though the greatest TKE is still found in the case with a near upstream turbine, the second greatest TKE values were in some cases recorded in the case without a turbine, and the lowest recorded with a far upstream turbine. It appears in this case that the presence of an upstream turbine leads to the generation of a less turbulent wake at support structure height, though this does not appear to lead to greater blade torque. The reduced wake turbulence in this case may be due to the energy extraction by the upstream turbine and consequential reduction in downstream flow velocity, which results in a less energetic flow being experienced by the downstream turbine. This effect can be seen by comparing Figure 6-6 and Figure 6-7.

Wake drift

Figure 6-15 illustrates a pattern of TKE as may be expected in the near wake region of a rotating turbine, with a broad peak in the centre of the image illustrating the high TKE associated with the blade tip vortices and turbine wake structures. However, the figure also illustrates significantly greater TKE in the region to the left of this central peak than to the right. This region highlights the area in the positive cross-stream direction, i.e. to the right when facing towards the oncoming flow.

High TKE in this region can be observed to the greatest degree in the case of a near upstream turbine, in which case the TKE in this region is approximately equal to that directly downstream of the turbine. It can also be observed, to a lesser degree, in the far upstream turbine case (where TKE in the region to the left is approximately 25% of that directly downstream), and to a small degree (10% of the directly downstream value) in the case without an upstream turbine. High vorticity was also observed in this region in Figure 6-10and Figure 6-11, and a similar pattern is observed in the wake velocity plots in the following section, as well as in POD and dye injection results (Figure 6-16), all of which suggest that the wake downstream of a rotating turbine drifts around 0. 5*D* in the positive cross-stream direction within a downstream distance of 5*D*.

Figure 6-16 – Wake drift observed in dye injection results.

This effect is believed to be caused by the rotation of the turbine blades and the generation of a rotating wake. Turbine blade rotation in this study was anticlockwise in all cases. As described in Section 2.10, the wake downstream of a rotating turbine blade has three rotational elements: The blade tip vortex and core region wake rotate in the direction of turbine rotation, while the central region wake rotates in the opposite direction. The relative locations of these three elements are illustrated in Figure 6-17 (for clarity, only vortices generated by a single blade are illustrated).

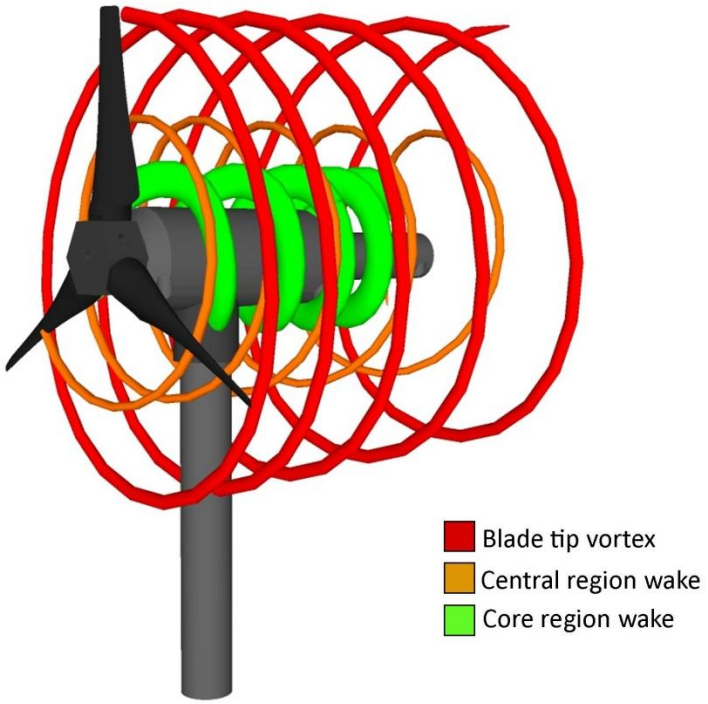

Figure 6-17 – Rotating blade wake elements

The existence of these rotating vortices within the blade wake appears to cause the wake to move in the direction observed. As highlighted above, the effect is seen in all cases with a rotating turbine, but occurs most noticeably when an upstream turbine is present at a relatively short separation distance. The fact that the effect is seen without an upstream turbine suggests that its existence is not a function of the upstream flow profile, though it would appear that the wake of an upstream device amplifies the effect.

The rotation of the blade tip vortex may cause the wake contained within it to move towards the positive cross-stream direction in the same way that an Archimedes screw moves a fluid or object. If one imagines holding one end of an Archimedes screw placed in fluid and rotating it, the design of the device would cause it to move to the right if rotated clockwise and to the left if rotated anti-clockwise. It is suggested that the same effect causes the wake of the turbine to move towards the positive cross-stream direction, leading to the increased TKE and reduced velocity observed in this region in phase 4a data. A similar result has been noted in some wind turbine studies [124]. Furthermore, the presence of a rotating upstream turbine leads to the generation of a low velocity wake, which it is believed will drift in the positive cross-stream direction. Consequently, a second turbine located downstream of the first would experience an incoming flow profile with lower velocity in the positive cross-stream direction, which would be further reduced by the rotational effect described above. In the case of a turbine located 5*D* upstream, less wake recovery would have occurred and velocity deficit would be greater than in the case of an upstream turbine at 10*D*, meaning that the resulting wake behind the second turbine would exhibit a greater deficit in the 5*D* case.

This effect is of interest when considering the layout of arrays of tidal turbines, and suggests that it may be sensible to consider an array incorporating devices rotating in opposite directions (as suggested by Mycek *et al* [62]).

Summary results – Phase 4a

- Turbulence kinetic energy is around four times greater in a horizontal plane at the level of the turbine drive shaft (135mm) than the support structure mid-height (66mm). At support structure level TKE appears to be is governed by downstream velocity, and is greater in cases with a higher upstream velocity. At turbine height TKE increases with the presence, and reducing separation distance, of an upstream turbine.

- The presence of an upstream device reduces the C_p of a downstream device. Compared to a single turbine case, the presence of an upstream device at 10D reduces downstream C_p by around 3%, and an upstream device at 5*D* reduces downstream C_p by around 10%.

- The reduction in C_p due to an upstream device is also influenced by downstream device support structure diameter, with a greater diameter yielding a lower C_p.

- The reduction in C_p due to these two effects is also amplified in cases of lower flow rate. It is suggested that in such cases the optimal performance region is allowed to expand further, and that turbulence is lower than in high speed cases.

- Wakes downstream of rotating turbines are observed to drift in the positive cross-stream direction, at a rate of around 0.5*D* per 5*D* downstream in the single turbine case. The effect is believed to be due to the blade tip vortices generated by the anticlockwise rotation of the turbines used in this study, and is most noticeable in the wake of a downstream turbine with a near upstream turbine.

6.2.2 – Phase 4a wake patterns

PIV data at both measurement planes (66mm and 135mm above the channel base) was used to generate plots of the velocity field behind downstream turbines mounted on 11mm, 16mm and 20mm support structures for three upstream configurations (no upstream turbine, far upstream turbine at 10D, near upstream turbine at 5*D*). These are illustrated in the following figures, and are arranged firstly by measurement location, then by support structure diameter.

Flow case 2 was used in all cases. Velocity scales of 0m/s to 0.5m/s and an image scale of 0.3m x 0.23m (2.4D x 1.8D) are used throughout, and flow is from left to right. The location and scale of the images relative to turbine position is illustrated in Figure 6-18. The example image is given at the 135mm measurement plane, but the same image size was also used at the 66mm measurement plane.

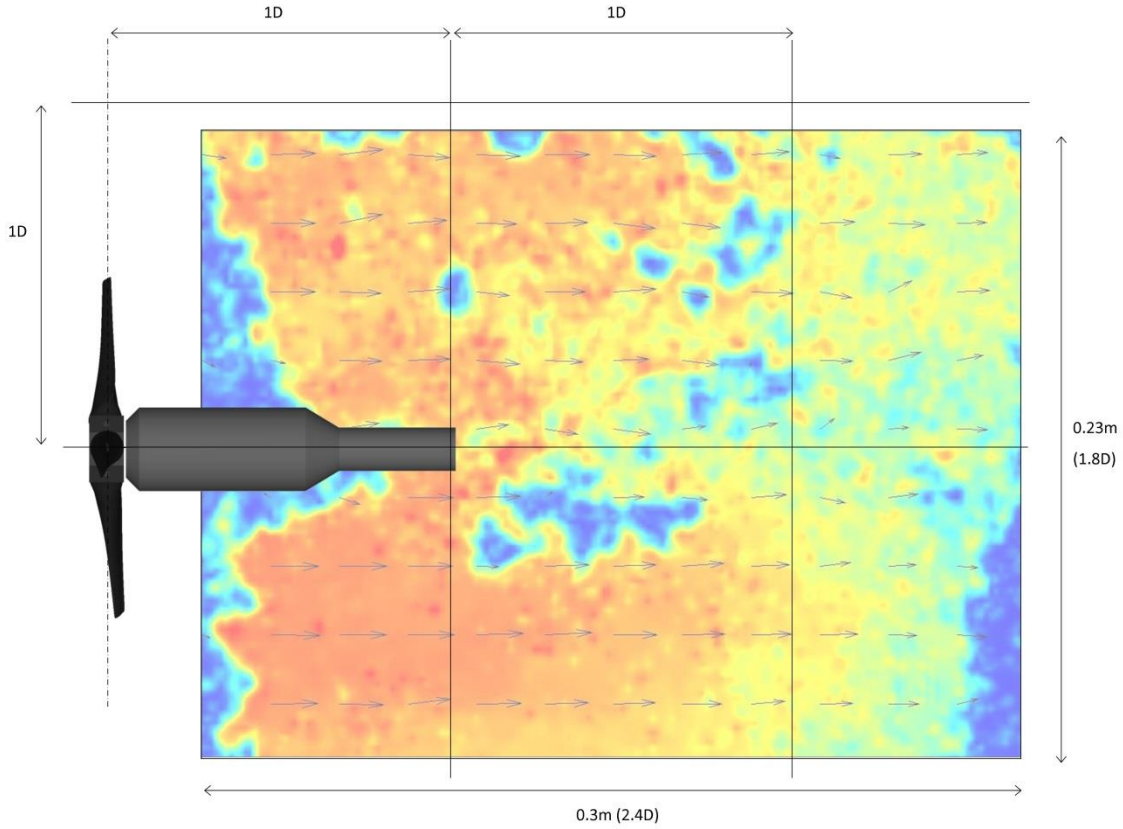

Figure 6-18 – Location and scale of wake images used in Sections 4a and 4b (sample velocity plot used for illustration).

11mm diameter support structure, 66mm plane: Instantaneous (l) and time-averaged (r) wakes

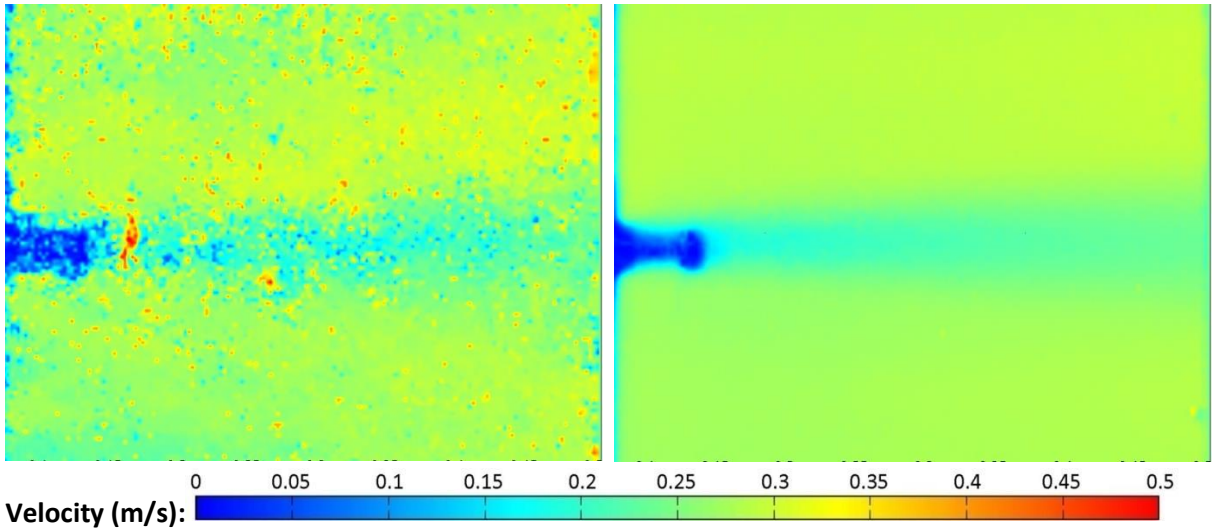

Figure 6-19 – 11mm diameter support structure, no upstream turbine.

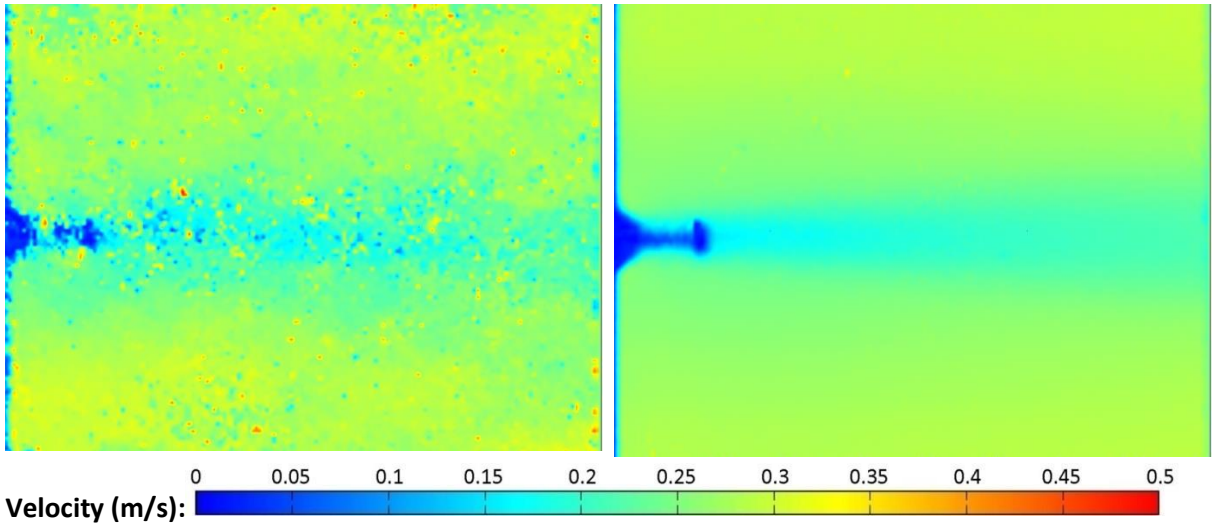

Figure 6-20 – 11mm diameter support structure, far upstream turbine.

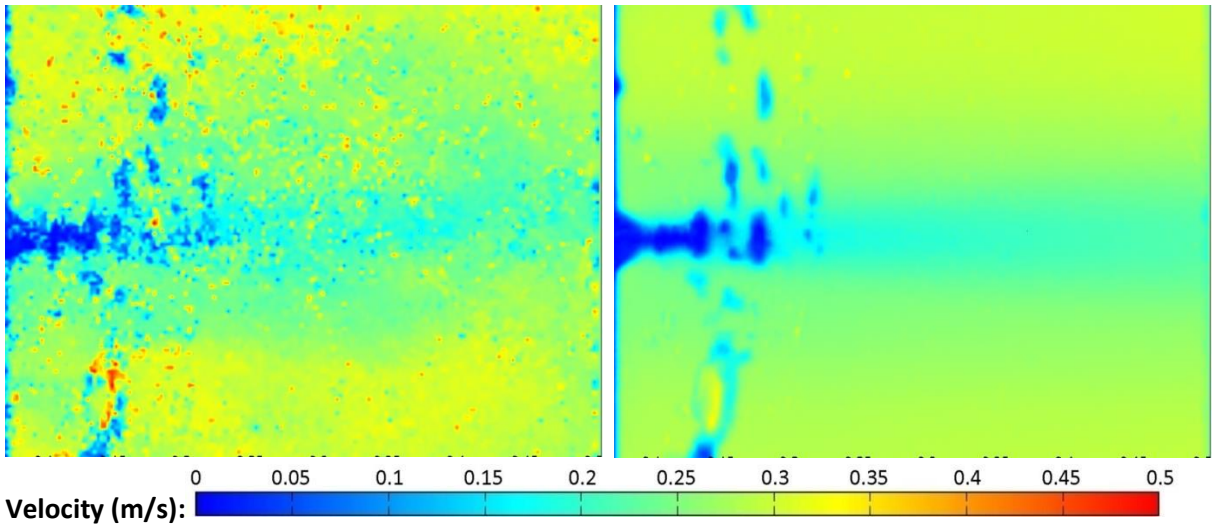

Figure 6-21 – 11mm diameter support structure, near upstream turbine.

16mm diameter support structure, 66mm plane: Instantaneous (l) and time-averaged (r) wakes

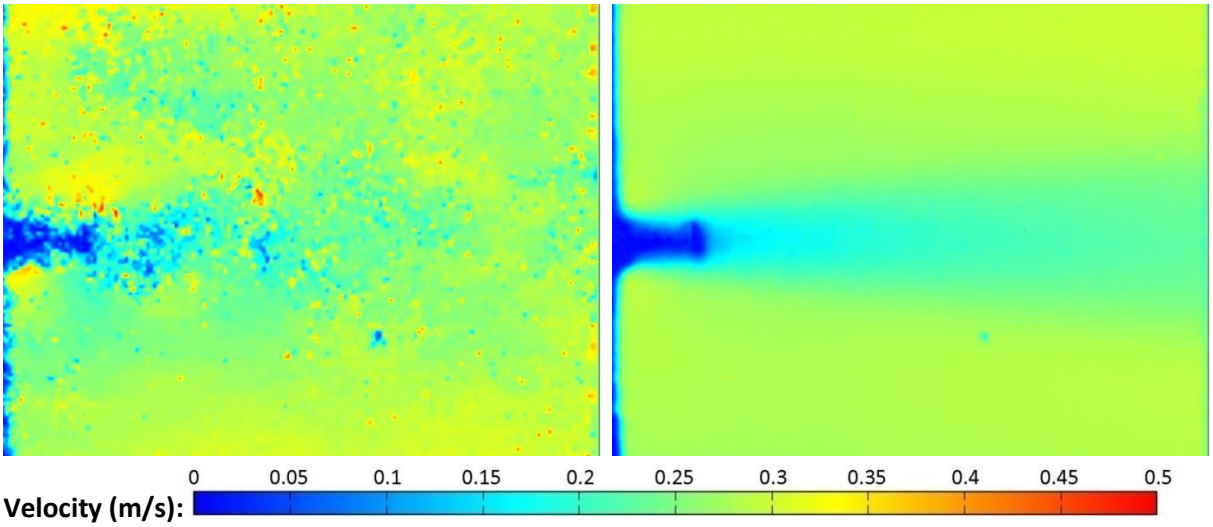

Figure 6-22 – 16mm diameter support structure, no upstream turbine.

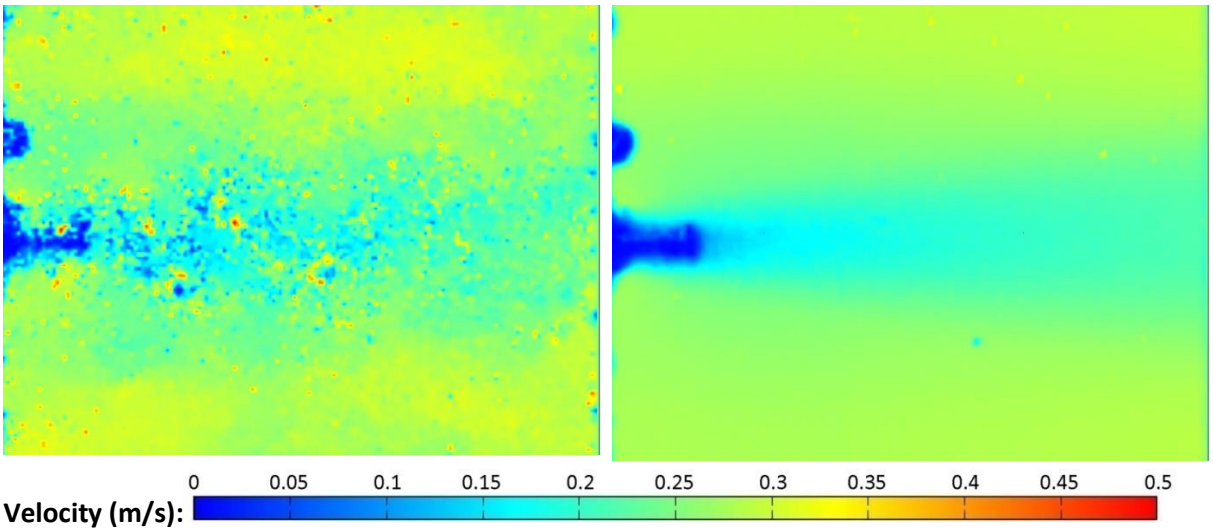

Figure 6-23 – 16mm diameter support structure, far upstream turbine.

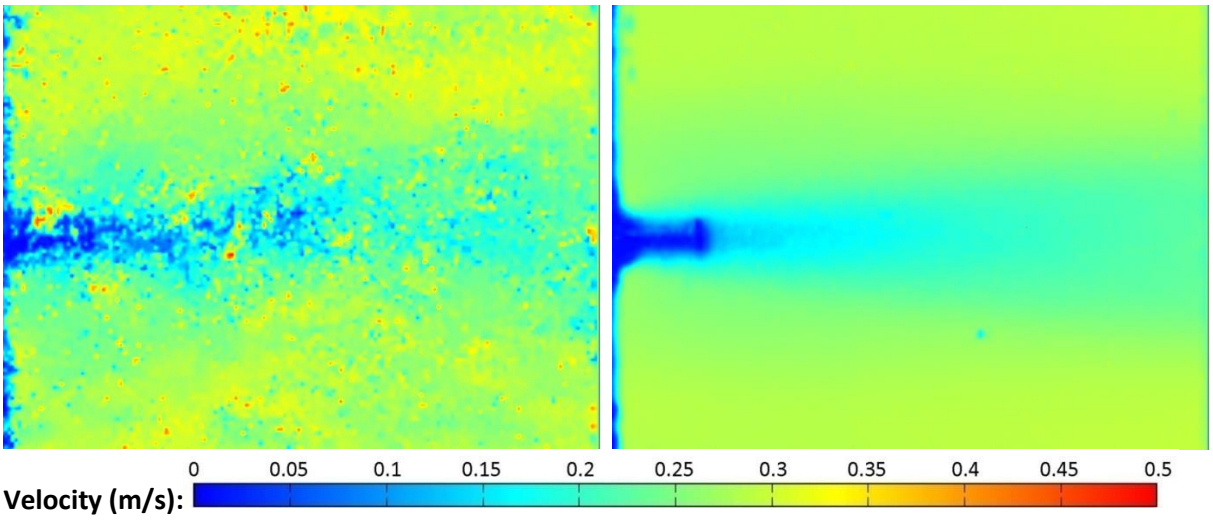

Figure 6-24 – 16mm diameter support structure, near upstream turbine.

20mm diameter support structure, 66mm plane: Instantaneous (l) and time-averaged (r) wakes

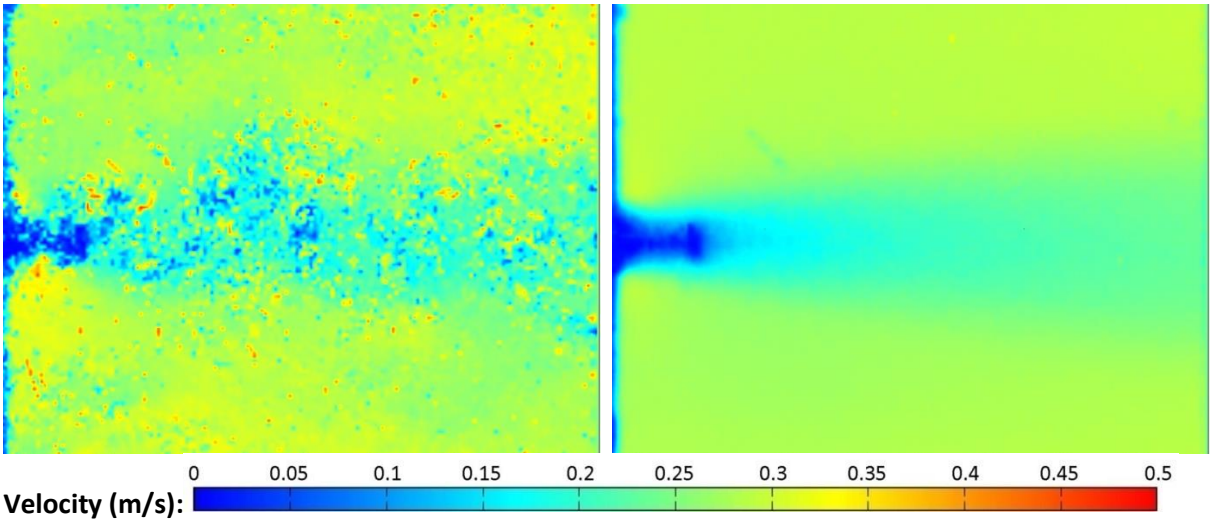

Figure 6-25 – 20mm diameter support structure, no upstream turbine.

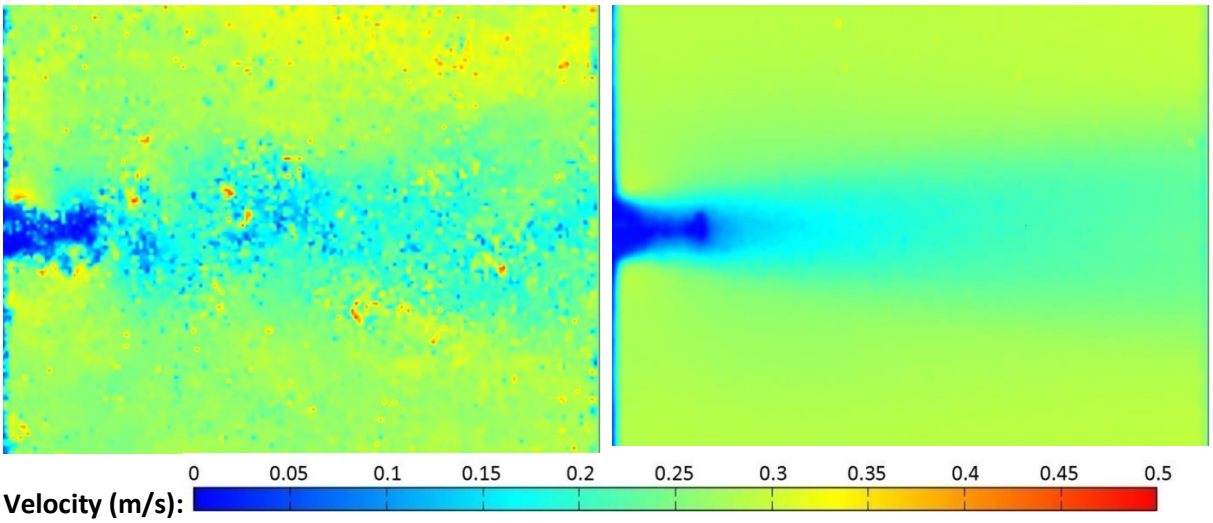

Figure 6-26 – 20mm diameter support structure, far upstream turbine.

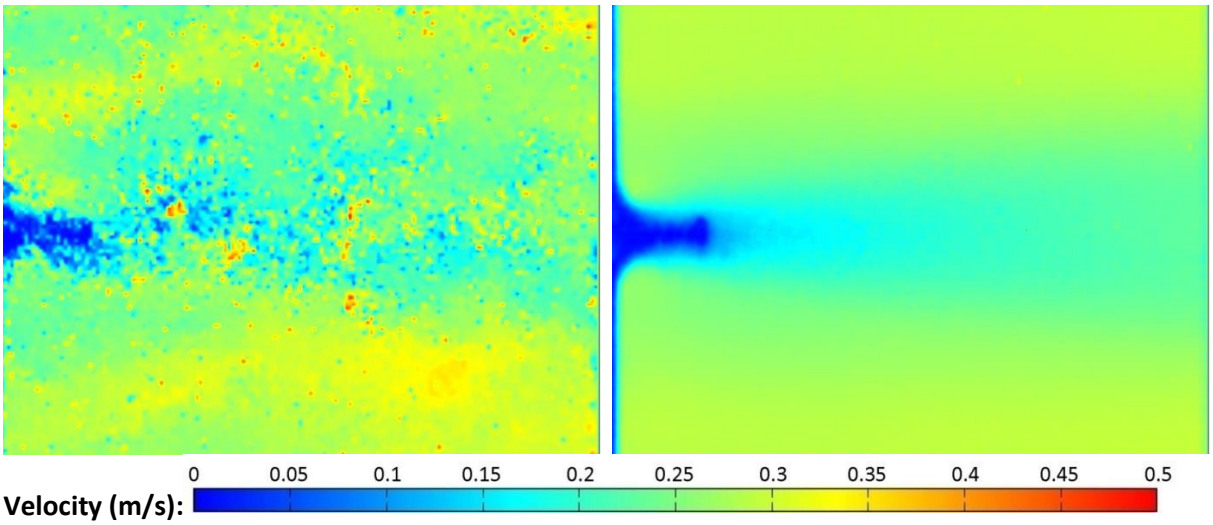

Figure 6-27 – 20mm diameter support structure, near upstream turbine.

The wake results illustrated in Figure 6-19 to Figure 6-27 appear to confirm that the downstream turbine wake is influenced by the incoming flow field caused by an upstream turbine. Increased velocity variation can particularly be noted in the cases with an upstream turbine located in the near position, leading to a reduction in the flow velocity and an increase in wake size compared to the cases with no upstream turbine, or an upstream turbine in the far position. This increased velocity variation suggests greater turbulence, as has been highlighted in previous results. Two major conclusions were drawn from this data:

- The downstream wake at support structure mid height increases in cross-stream size with increasing support structure diameter (Note, for example, the differing patterns between Figure 6-19, Figure 6-22, and Figure 6-25).

- The downstream wake at support structure mid height also increases in size with the presence of an upstream turbine, with a near turbine having the greatest effect (eg. Figure 6-19 - Figure 6-21).

By defining the wake region as a region with velocity below a given threshold, the influence of support structure diameter and upstream turbine position on the wake size can be defined. Using a velocity of 80% of free stream conditions at the 66mm plane as the wake boundary, the width of wakes at 2.4D downstream of the blades was calculated, and is given in Table 6-2. Free stream velocity at this height was 0.3m/s, giving a wake region edge velocity of 0.25m/s.

	Wake width at 2.4D downstream (D)		
Support structure diameter:	*11mm*	*16mm*	*20mm*
No upstream turbine	0.28	0.55	0.74
Far (10*D*) upstream turbine	0.37	0.64	0.81
Near (5*D*) upstream turbine	0.40	0.74	0.88

Table 6-2 – Influence of support structure diameter and upstream turbine location on cross-stream wake width at 2.4D downstream of turbine blades

This data quantifies the observed pattern of wake expansion with support structure diameter and upstream turbine, and also appears to illustrate a correlation between wake size and C_p, with increasing wake size indicating lower values of C_p. This also correlates with increased wake turbulence, with increasing turbulent kinetic energy correlating with both increasing structure diameter and reducing C_p.

The wakes illustrated in Figure 6-21 and Figure 6-23 show unexpected results. Figure 6-21 shows a low velocity region which extends in a broken line across the channel, approximately 1*D* downstream of the turbine blades. Figure 6-23 shows an area of low velocity approximately 0.5*D* from the centreline in the positive cross-stream direction, at the downstream limit of the image. C_p results for these cases do not appear to differ from the trends described, and no evidence of these effects was found in the corresponding 135mm wakes. These effects are therefore believed to be caused by experimental errors. In both cases the fact that the errors appear in all instantaneous images suggests that cause is an error at the PIV image capture stage rather than a calculation error.

It is suggested that these errors are both related to the surface smoothing plate placed on the water surface, as described in Section 3.4.5. In Figure 6-21, it appears that the plate may have become misaligned, leading to seeding particles becoming trapped underneath it, and causing the low velocities recorded in the image. The cause of the error in Figure 6-23 is believed to be the erroneous capture of reflections from the upstream edge of the plate by the PIV software.

Velocity wakes at the turbine centre height plane (135mm above channel base) are given in the following figures.

11mm diameter support structure, 135mm plane: Instantaneous (l) and time-averaged (r) wakes

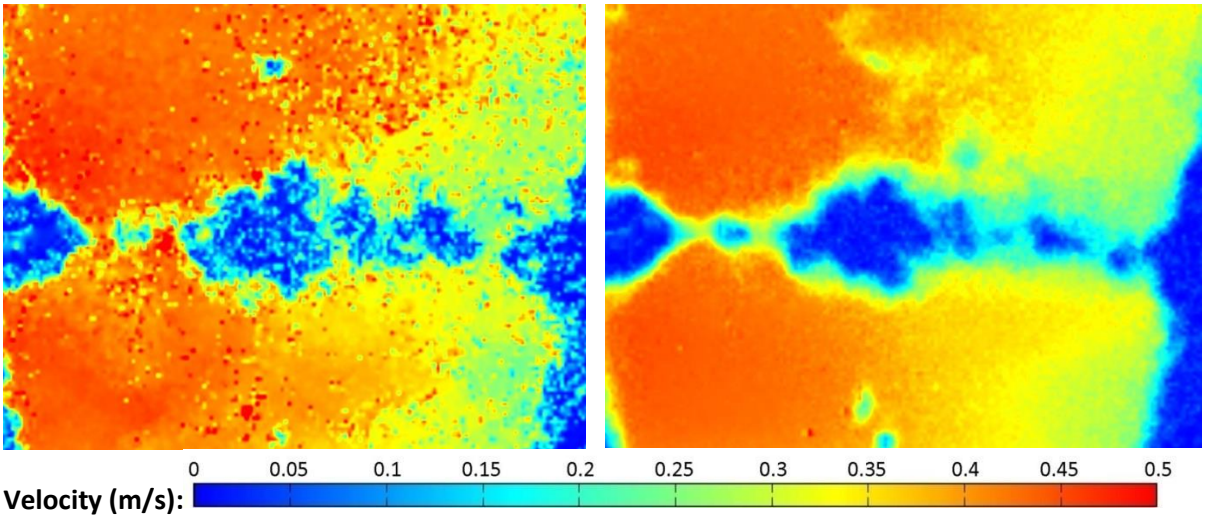

Figure 6-28 – 11mm diameter support structure, no upstream turbine.

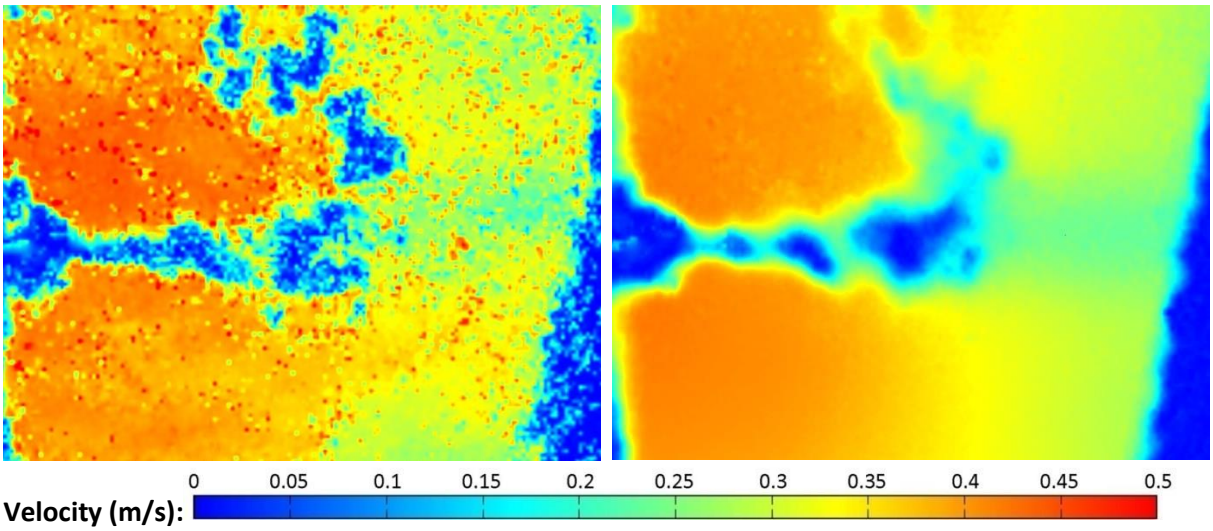

Figure 6-29 – 11mm diameter support structure, far upstream turbine.

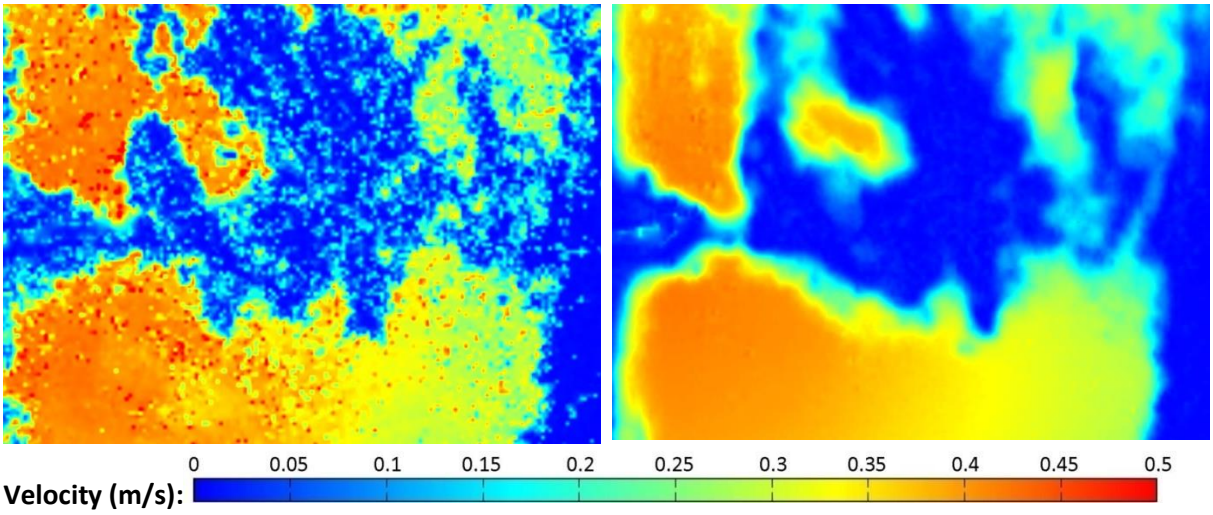

Figure 6-30 – 11mm diameter support structure, near upstream turbine.

16mm diameter support structure, 135mm plane: Instantaneous (l) and time-averaged (r) wakes

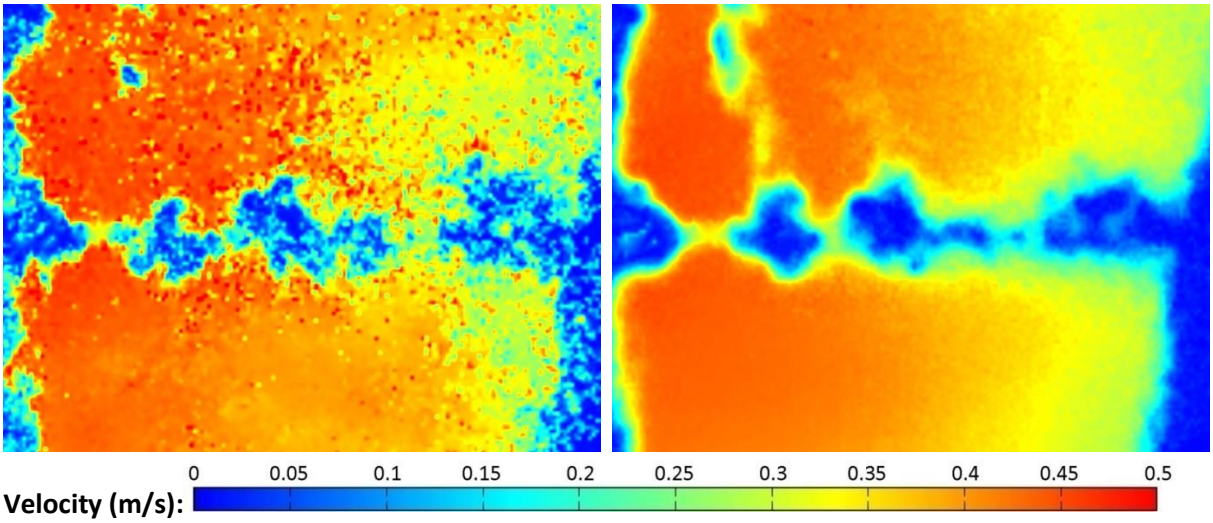

Figure 6-31 – 16mm diameter support structure, no upstream turbine.

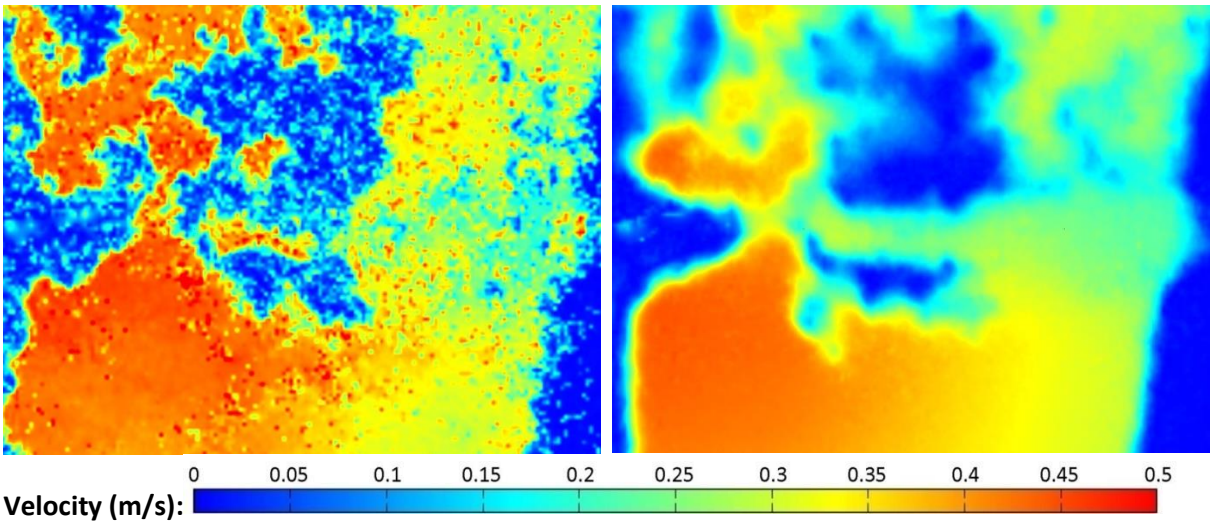

Figure 6-32 – 16mm diameter support structure, far upstream turbine.

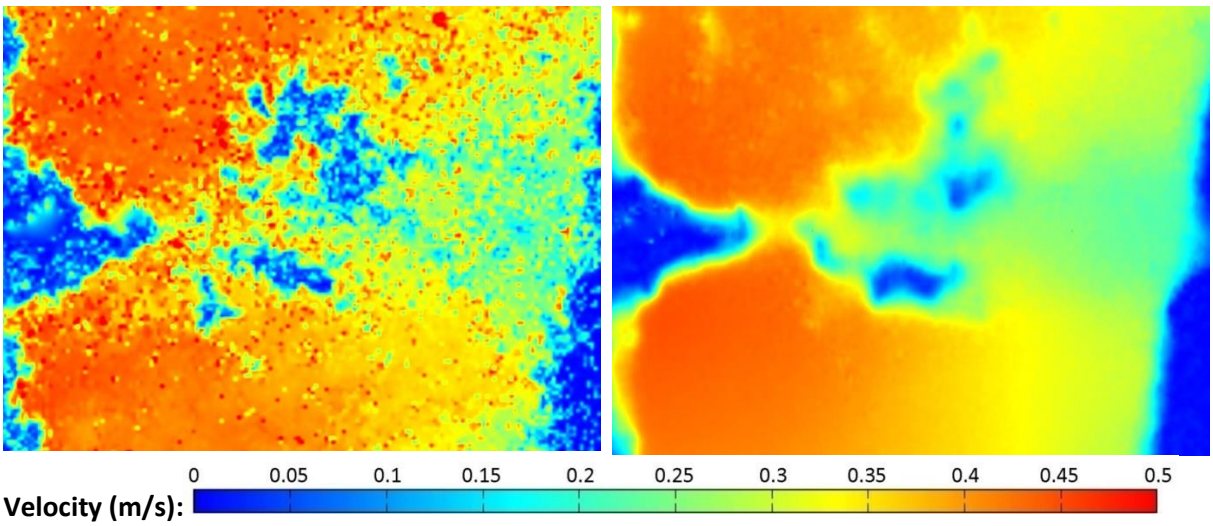

Figure 6-33 – 16mm diameter support structure, near upstream turbine.

20mm diameter support structure, 135mm plane: Instantaneous (l) and time-averaged (r) wakes

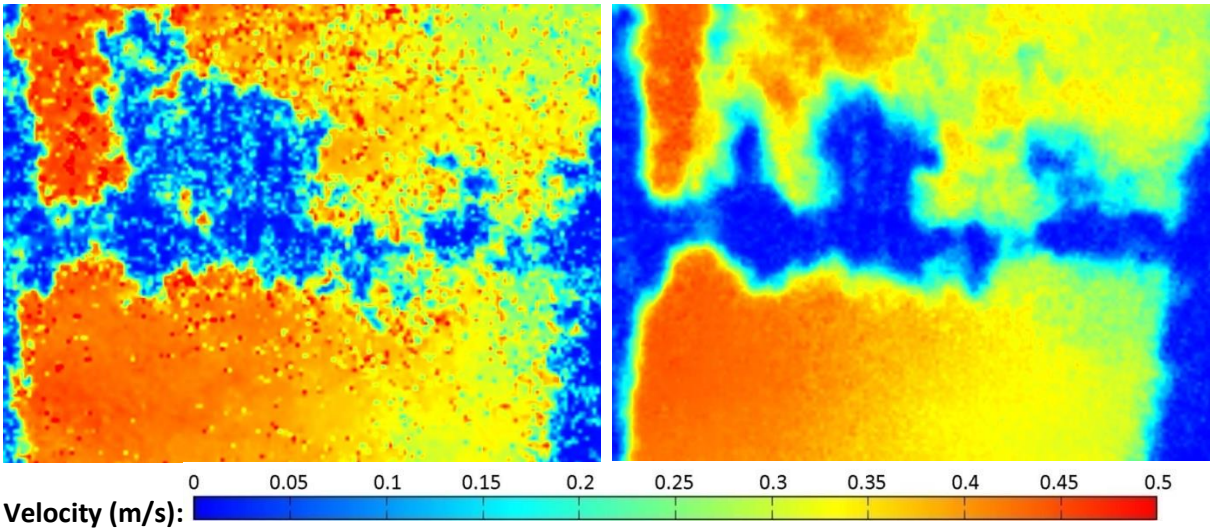

Figure 6-34 – 20mm diameter support structure, no upstream turbine.

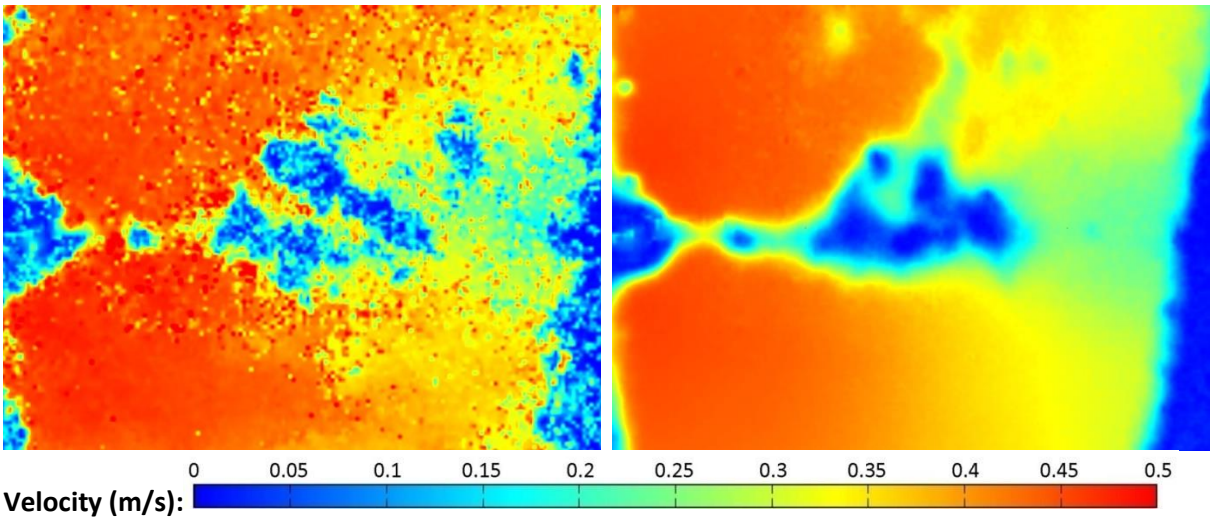

Figure 6-35 – 20mm diameter support structure, far upstream turbine.

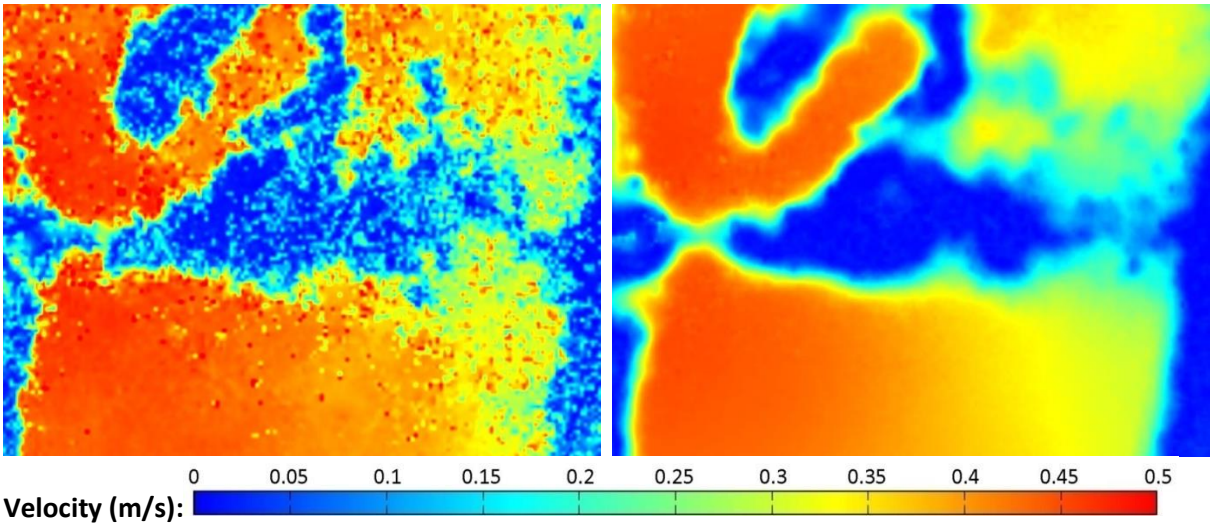

Figure 6-36 – 20mm diameter support structure, near upstream turbine.

As predicted by Figure 6-12 and Figure 6-13, greater turbulence is observed at the 135mm plane than at the 66mm plane illustrated previously. Greater flow velocity is also seen at this height than at the 66mm plane, as would be expected due to the velocity profile of the channel.

A number of further observations can be made from this data:

- The illustrated wake patterns support the vorticity plots generated previously (Figure 6-6 - Figure 6-11), suggesting that when an upstream turbine is present, the downstream turbine experiences greater incoming turbulence and consequently will produce a lower C_p. This effect increases with reducing separation distance between the turbines.

- At the 135mm plane height the wake size does not appear to grow uniformly with support structure diameter or upstream turbine location, as was found at the mid-height plane.

- A greater wake velocity variation between upstream turbine cases is observed in the case of a narrower diameter support structure (for example, the change in velocity from Figure 6-28 to Figure 6-30 is greater than from Figure 6-34 to Figure 6-36).

- Downstream turbine wakes are not symmetrical, and the lower velocity part of the wake appears to always occur to the left of the direction of flow. It is suggested that this is caused by the wake drift effect described in Section 6.2.1.

6.2.3 – Phase 4b: Upstream turbine, offset

Following multiple turbine in-line tests as described in the previous section, the final phase of this work aimed to understand the influence of an upstream turbine offset from the channel centreline. A turbine mounted on a 16mm diameter support structure was positioned at the same near (5*D*) and far (10*D*) upstream positions, at three cross-stream locations: 0*D* offset (centreline), Position 1 (0.5*D* cross-stream offset) and Position 2 (1*D* cross-stream offset). The downstream turbine was mounted on 11mm, 16mm and 20mm diameter support structures. Centreline position experiments were identical to those carried out during both phase 4a and phase 3. Offset positions were set to the right of the channel centreline when looking upstream from the turbine (the positive cross-stream direction), as illustrated in Figure 6-37.

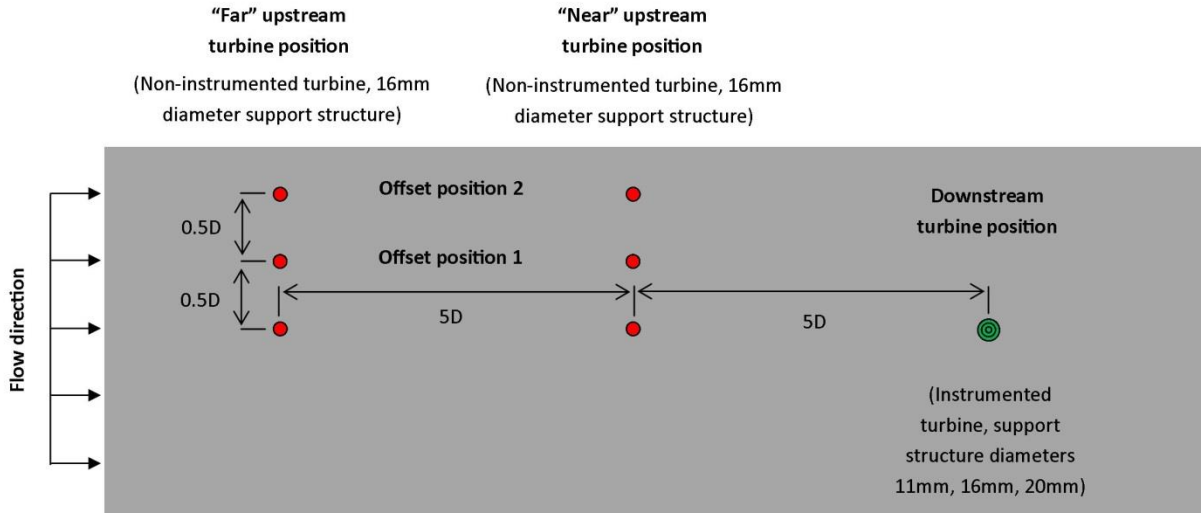

Figure 6-37 – Graphical representation of experiments carried out during phase 4b viewed from above (upstream turbine installation positions shown in red, downstream in green).

In all figures used in this section flow is from left to right, meaning that the upstream turbine offset positions are above the image centreline.

Actuator disk results from Section 5.2.1 suggest an upstream turbine at 5*D* streamwise separation and 0.5*D* offset will lead to a downstream turbine velocity deficit (below free stream conditions) of between 15% and 18%. With an upstream turbine at a streamwise separation of 5*D* and an offset of 1*D*, actuator disk results suggest that a deficit of between 4% and 7% should be observed. Single turbine actuator disk results also predicted full velocity recovery by 10*D* downstream in all cases, suggesting that the wake of an upstream turbine installed at 10*D* should have no effect on the incoming velocity profile of a downstream turbine, and that C_p should be comparable to that generated without an upstream turbine.

Performance measured in this phase demonstrates that the actuator disk results given in Section 5.2.1 do give a general prediction of the results which can be expected using full turbine models, but that they do not fully predict the turbine performance results observed.

Performance data

Power coefficients calculated for all phase 4b cases are given in Figure 6-38.

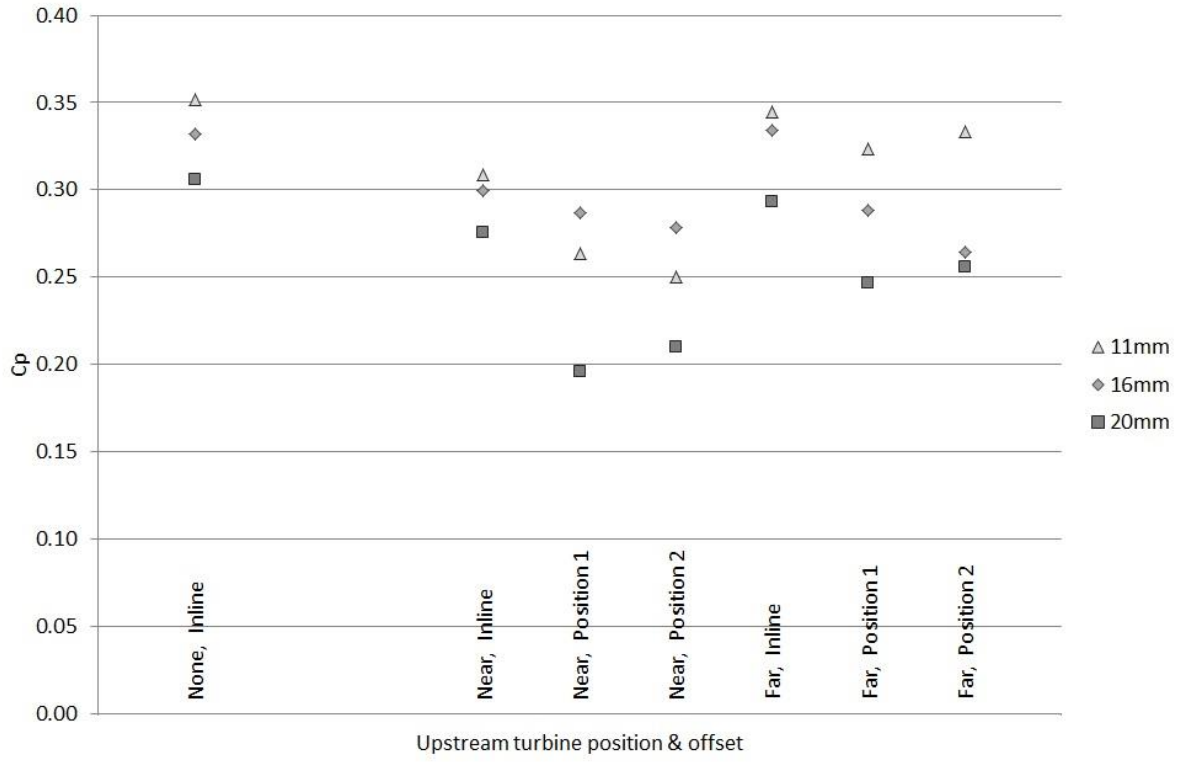

Figure 6-38 – Influence of upstream turbine streamwise and cross-stream position on C_p *of downstream turbine mounted on three diameters of support structure.*

In the majority of cases, these results illustrate that turbine C_p increases with decreasing support structure diameter, within the range studied. This result has also been shown in all preceding phases; subject to a separation distance between the blade swept area and the support structure front face which places the blades within the optimal performance region illustrated in Figure 5-64 (i.e. a separation distance of between 25mm and 40mm).

Nine of the results illustrated in Figure 6-38 are identical to experiments carried out in phase 4a. Results from tests with no upstream turbine, and with an inline upstream turbine at 5*D* and 10D streamwise separation, all with downstream support structures of 11mm, 16mm and 20mm were conducted independently in the two phases, and variation of between 1% and 8% between individual results was calculated. Results of these experiments conducted during phase 4b were as predicted by previous results:

- In the case of an upstream turbine at 5*D* streamwise separation, an inline arrangement of up- and downstream turbines produced a C_p around 12% lower than the single turbine case, and C_p was observed to reduce with increasing downstream support structure diameter.

- In the case of a far upstream turbine (10D streamwise separation), an inline arrangement of up- and downstream turbines produced a C_p around 2% lower than the single turbine case, and C_p was again observed to reduce with increasing downstream support structure diameter.

However, the introduction of cross-stream offset upstream turbines produces some variation from this expected result. In the near upstream turbine case with either a 0. 5*D* or 1*D* upstream offset, the

performance of the 11mm and 20mm diameter downstream turbines reduced dramatically in comparison to the inline case, while the 16mm diameter case did not exhibit such a reduction.

In the far upstream separation distance case, the trend for increasing C_p with reducing downstream support structure diameter (as observed in previous experimental phases) was again observed. In the far upstream case it was noted that the 11mm and 20mm downstream support structure diameter cases achieved greater C_p values with an upstream turbine at 1*D* offset than at 0. 5*D* offset. This effect was also recorded in the near upstream turbine case, though only for the 20mm diameter downstream support structure.

Due to the combined effects of upstream separation distance, upstream turbine offset and downstream diameter, a large volume of data is presented in Figure 6-38. In order to ascertain whether the observed trends stated above are genuine results, and to understand their causes, each one was approached independently, as described in the following subsections. Extracts from Figure 6-38 are given to help the explanation of each trend.

5D streamwise separation

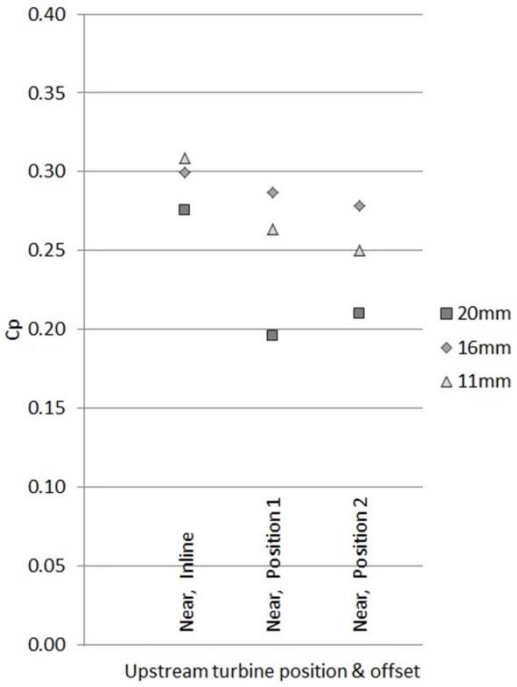

With an upstream turbine at 5*D*, increasing the cross-stream offset from 0*D* to 0.5*D* (Position 1) was found to have a much greater impact on the performance of a downstream device mounted on an 11mm or 20mm support structure (15% and 29% reduction in C_p respectively) than on a 16mm support structure (5% reduction in C_p).

A greater impact on the 11mm and 20mm diameter downstream support structures was again seen in the 1*D* (Position 2) offset case, relative to the inline case, with reductions in C_p of 18%, 10% and 24% for the 11mm, 16mm and 20mm cases respectively.

Furthermore, increasing the offset from 0.5*D* to 1*D* was observed to reduce C_p in the 11mm and 16mm diameter cases, and increase C_p in the 20mm case.

Figure 6-39 – Extract from Figure 6-38

Before attempting to explain these results, the potential for errors results was first considered. The inline results generated during this phase exhibited a maximum variation of 2% from those measured in the previous phase, and these results will have the same accuracy. However no previous results using cross-stream offsetting of the upstream turbines were conducted, so it was not possible to validate the position 1and position 2 results in the same way. As stated in Section 4.6, the calculated maximum error in the measurement of turbine performance results was 11%, which is largely attributed to shaft misalignment. An error of 11% in the 11mm or 16mm diameter results of the position 1 or position 2 offset cases could reverse the ranking of these results,

however given the lack of evidence for errors, it was decided to study the data further before making this conclusion. This analysis is described in Section 6.2.4.

10D streamwise separation

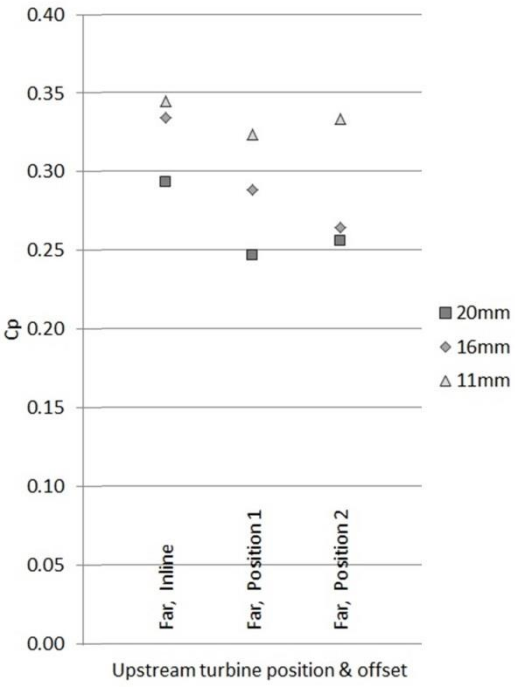

Figure 6-40 – Extract from Figure 6-38

The location of a turbine at the far upstream position (10*D* streamwise separation) was observed to result in the same ranking of downstream support structure diameters as observed in all previous phases, with C_p observed to increase with reducing support structure diameter *d*. With an upstream turbine at a cross-stream offset of 0.5*D* (Position 1) C_p was reduced in all cases, with increasing *d* leading to a greater reduction (6%, 14% and 17% respectively).

In the case of a 1*D* (Position 2) offset at the 10*D* upstream position, C_p was found to increase in the 11mm and 20mm downstream diameter cases, but to reduce in the 16mm downstream diameter case.

It was again deemed possible that the 16mm data point in the far upstream position 2 case was the result of experimental error, but given the lack of any specific evidence for this, further study of the data generated during these phases was carried out.

6.2.4 – Phase 4b wake patterns

Velocity wakes behind the downstream turbine are given in this section, at both the 66mm and 135mm height planes. In all cases, flow case 2 (flow rate=40l/s, TSR=3.1, Re=3x10^5) was used. Mean flow images are shown in all cases. Due to the closeness of the mean flow images and instantaneous frames illustrated in Section 6.2.2 (Figure 6-19 - Figure 6-36) this was deemed suitable for initial analysis, particularly as using mean flow images allowed the side-by-side comparison of results from the two offset positions. However, it was noted that the use of mean flow images could result in the loss of dynamic variations in the flow. In order to ensure important details were not lost, analysis of wake variation with time using instantaneous images was also carried out, and is described later in this section. Wake images illustrated in this section follow the same arrangement as described in Section 6.2.1 and illustrated in Figure 6-18, with velocity scales of 0m/s to 0.5m/s where applicable and an image scale of 0.3m x 0.23m (2.4D x 1.8D) in all cases.

When studying the wake patterns recorded during phase 4b, it appeared that the offsetting of upstream turbines had very little, if any, additional influence on the wakes observed behind the downstream turbine at the 66mm measurement plane. Due to the minor variation, it was difficult to distinguish differences in the wakes between cases using the wake images generated. However, it was found that by decreasing image saturation to zero (i.e. transforming the colour images to greyscale) and then changing the colour filter applied to the image to give a pure black and white image, an image could be produced illustrating the area bounded by a velocity of 0.25m/s, as

illustrated in Figure 6-41. 0.25m/s is 80% of the free stream velocity, as used as a wake boundary indicator in Section 6.2.2.

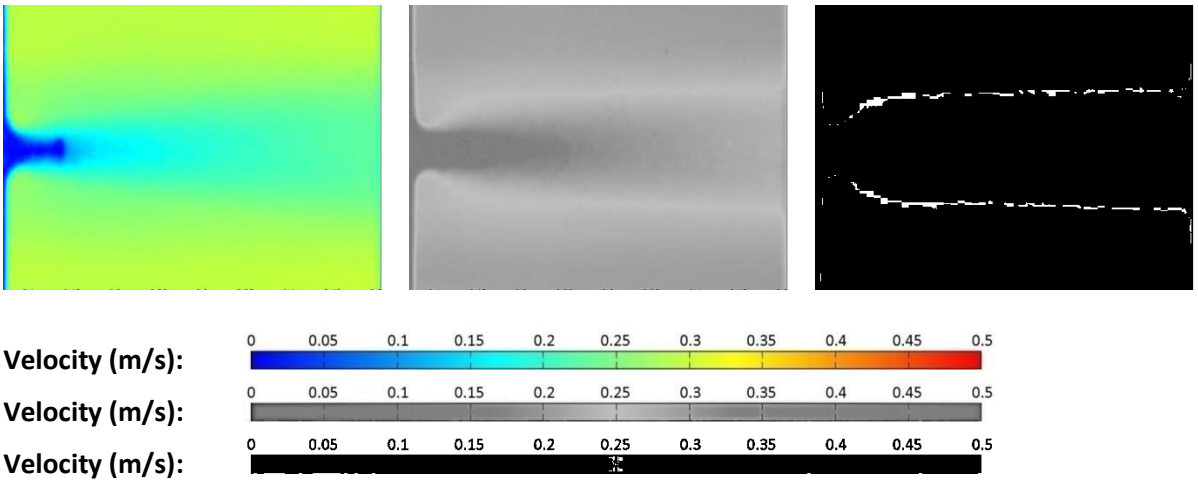

Figure 6-41 – Transformation of wake image from full colour (l) to 0% saturation grayscale image (middle) to black and white image illustrating 0.25m/s boundary.

This method is used to illustrate the boundaries of the 66mm plane wakes illustrated in this section. However, the method is not suitable for the visualisation of wakes at 135mm, since due to greater turbulence at this height the boundary of the wake cannot be defined correctly and flow velocity information is lost.

Using this method, the shape of wakes at 66mm plane height can be observed for three downstream turbine diameters in three offset cases, at both near and far upstream separation distances. These wakes are illustrated in Figure 6-43 and Figure 6-44. It can be seen that the wake shape differs with offset position, with wakes reaching a constant width within a shorter downstream distance in the inline case, and appearing to grow in width more slowly in the offset turbine cases.

In some cases, areas of low velocity flow can be observed towards the bottom of these images, as highlighted by the 0.25m/s threshold. One such area can be observed in the 0.5*D* offset upstream turbine and 16mm diameter downstream turbine case (the central image in Figure 6-42).These areas suggest that despite the offset turbine being in the positive cross-stream direction (upwards in these images); flow at the 66mm plane is faster on the negative cross-stream side of the turbine. Conservation of mass means that the restricted flow at turbine height causes the flow below it to accelerate in the streamwise direction in order that the overall mass transfer through the vertical plane where the turbine is located remains constant.

Far upstream turbine at 0*D*, 0.5*D* and 1*D* offset, 66mm plane: Time-averaged wakes.

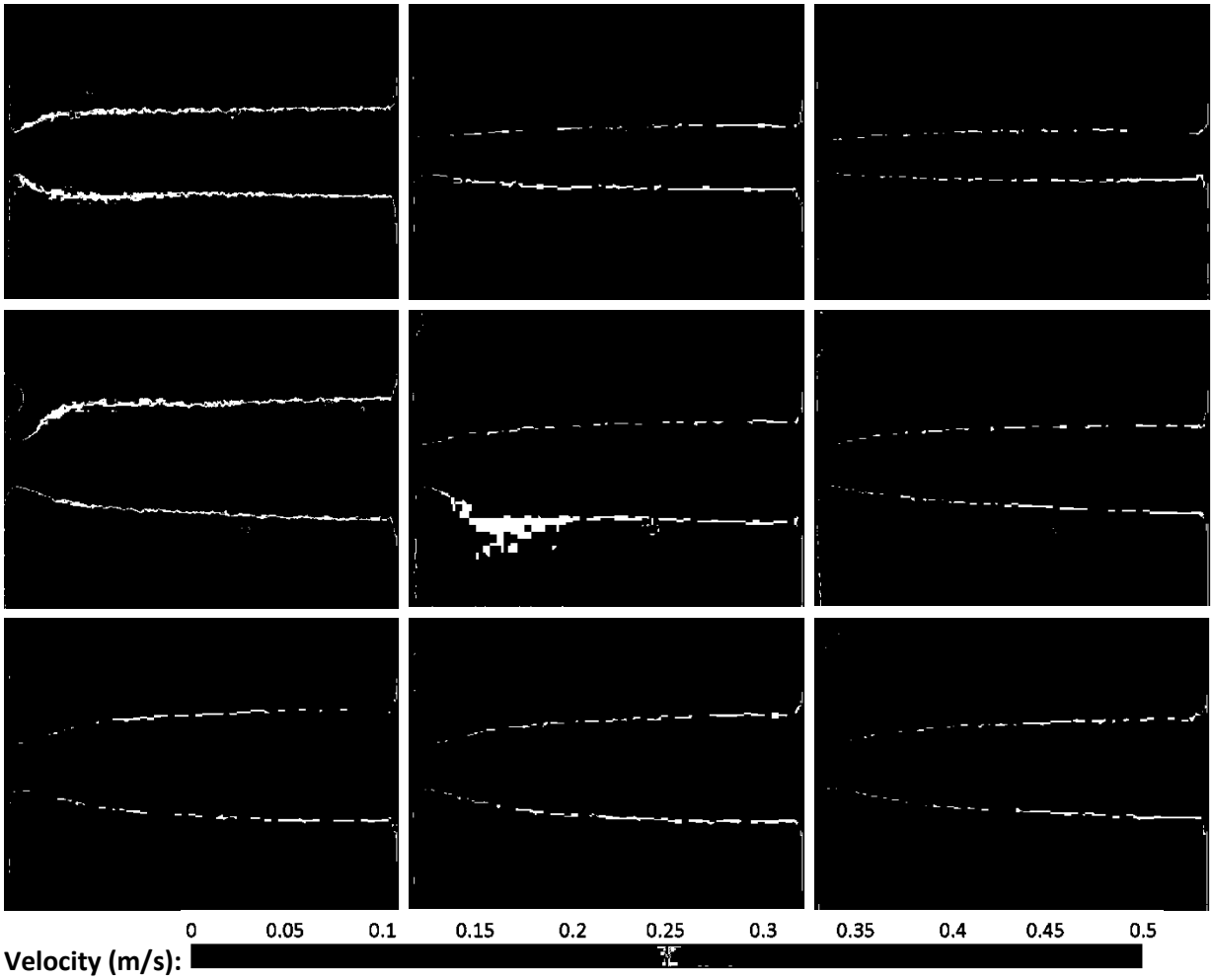

Figure 6-42 – Far (10D) upstream turbine, offset 0D (l), 0.5D (m) & 1D (r). Downstream turbine support structure diameter 11mm (top), 16mm (middle), 20mm (bottom).

Wake outline images at the 66mm measurement plane illustrate, as mentioned above, the differing wake shapes downstream of a turbine with an upstream turbine in the three offset positions. An upstream turbine in the inline (0*D* cross-stream) offset position appears to yield the widest wake, and a cross-stream width which grows relatively quickly downstream of the support structure, whereas the wake generated by an offset upstream offset turbine requires a longer downstream distance to widen. At 2.4*D* downstream of the downstream turbine, wakes generated in the case of a 0.5*D* offset upstream turbine are narrower than those generated by an inline turbine, and wakes generated by a 1*D* offset upstream turbine are narrower still.

Wake growth also appears to be a function of downstream support structure diameter, with a larger diameter support structure leading to a greater widening distance. This can be observed by comparing the shape of the wake shown in the top left of the image (no offset, 11mm diameter downstream support structure) with that in the bottom right, (1*D* offset, 20mm diameter downstream support structure), which illustrates the extremes of wake formation distance in this case. In the former case, a constant wake width is reached within less than 1*D*, whereas in the latter case this distance is greater than 2*D*, and could be said to be continuing to expand at the limit of the image (2.7*D* downstream of the blades).

It is proposed that this difference in wake formation distance is related to turbulence. It is suggested that the location of an upstream turbine in an offset position leads to greater turbulence in the incoming flow of the downstream turbine, and that a greater diameter of downstream support structure also leads to increased turbulence in its wake. An increase in turbulence in the wake of a greater diameter downstream turbine support structure was observed in single turbine results (phases 2 and 3), and can be observed in the results in Section 5.2.3. The suggested increase in turbulence in the downstream turbine incoming flow is investigated in Section 6.3.

Near upstream turbine at 0*D*, 0.5*D* and 1*D* offset, 66mm plane: Time-averaged wakes.

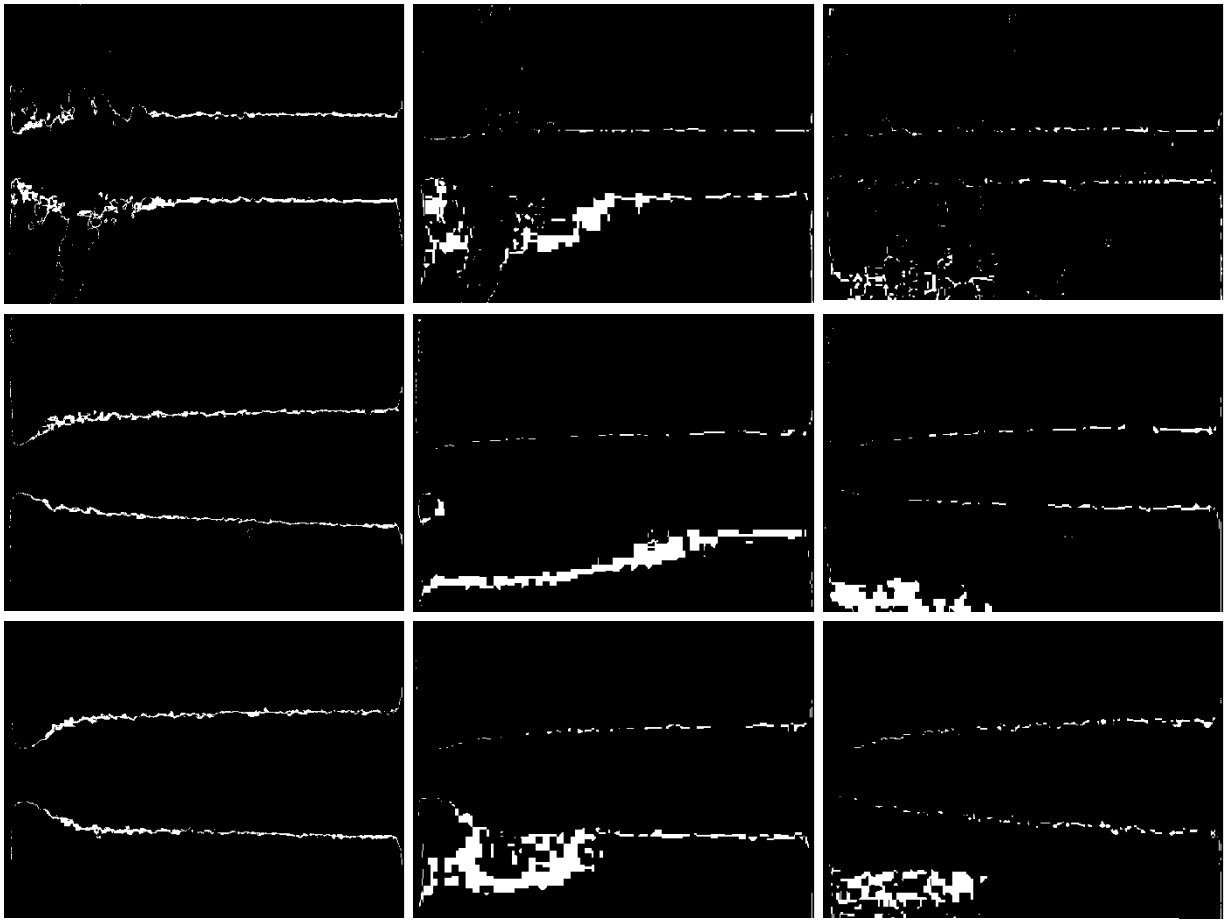

Figure 6-43 – Near (5D) upstream turbine, offset 0D (l) 0.5D (m) & 1D (r). Downstream turbine support structure diameter 11mm (top), 16mm (middle), 20mm (bottom).

Figure 6-43 illustrates a much greater proportion of wake images with areas of low flow speed outside the wake region than Figure 6-42, suggesting that on the whole flow velocities in the downstream turbine wake are lower with a near upstream turbine than with a far upstream turbine, for an otherwise identical case. This effect is expected, and it also appears that the offsetting of a near upstream turbine may further reduce the velocity in the wake of a downstream device, since all images illustrating a case with an upstream offset appear to show additional regions of low velocity flow. It is again believed that turbulence in the wake of the upstream turbine, and consequently in the incoming flow conditions at the downstream turbine, as will be discussed in Section 6.3, is the cause of this effect.

The 11mm diameter downstream support structure case (top) images in Figure 6-43 appear to illustrate errors in PIV image capture similar to that observed in Figure 6-21. In this case, as before, there appears to be a line of low velocity flow which extends across the channel at approximately 1*D* downstream of the turbine blades. The previous error was attributed to a slight vertical misalignment of the surface smoothing plate and resulting trapping of seeding particles, leading to a region of erroneous low velocity along the upstream edge of the plate. This is again believed to be the cause of the errors seen in Figure 6-43, which lead to distortion in the initial region of the wake. However, due to the static nature of these errors, the remainder of the image is believed to be unaffected and the effect of a narrowing wake with increased upstream turbine offset is consistent with that observed in other cases.

In both in Figure 6-42 and Figure 6-43, all wakes appeared to propagate directly downstream, and the wake drift effect observed previously at the 135mm measurement plane was not seen at this height. However, as discussed above, it appears that the area to the cross-stream negative side (the lower part of the wake images illustrated, or the left if facing the oncoming flow) of the support structure exhibits a lower velocity than the positive side. At the 66mm plane, velocity at -0.5*D* from the centreline in this direction was found to be between 2% and 9% lower than that on the opposite side (at +0.5*D*). This effect appears to suggest a reversal of the high and low velocity regions observed previously at the 135mm plane, which were attributed to the effect of wake drift due to the rotation of blade tip vortices. These previous results (as described in Section 6.2.2) were based on the location of upstream turbines in the inline position only, so further study of the wake observed at the 135mm plane was carried out, this time for results of offset turbines in the near and far streamwise separation distances.

Wake plots were produced at the turbine height plane (135mm above the channel base) for the same cases previously studied at the 66mm plane, though in this case wakes with an inline upstream turbine are not illustrated (these can be found in Figure 6-28 to Figure 6-36). The downstream turbine velocity wake is given in the case of upstream turbines at far (10D) or near (5*D*) streamwise separation distances, with position 1 (0.5*D*) or position 2 (1*D*) offset in the positive cross-stream direction (towards the top of the image).

Velocity wakes recorded at this plane are illustrated in Figure 6-44 and Figure 6-45. Flow case 2, velocity scales of 0m/s to 0.5m/s and image scale of 0.3m x 0.23m (2.4*D* x 1.8*D*) apply throughout, and flow is from left to right.

Far upstream turbine at 0.5*D* and 1*D* offset, 135mm plane: Time-averaged wakes.

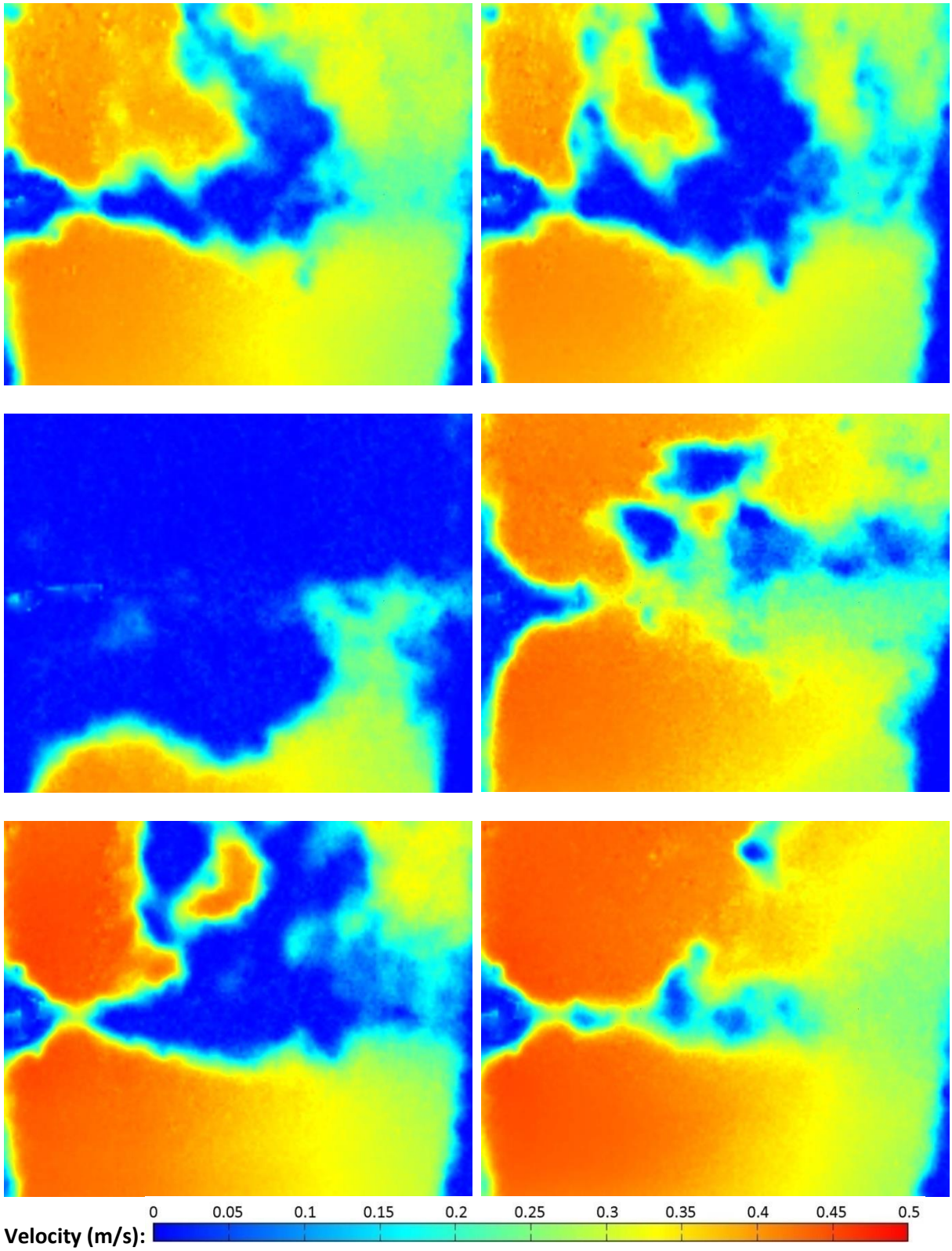

Figure 6-44 – Far (10D) upstream turbine, offset 0.5D (l) & 1D (r). Downstream turbine support structure diameter 11mm (top), 16mm (middle), 20mm (bottom).

Near upstream turbine at 0.5*D* and 1*D* offset, 135mm plane: Time-averaged wakes.

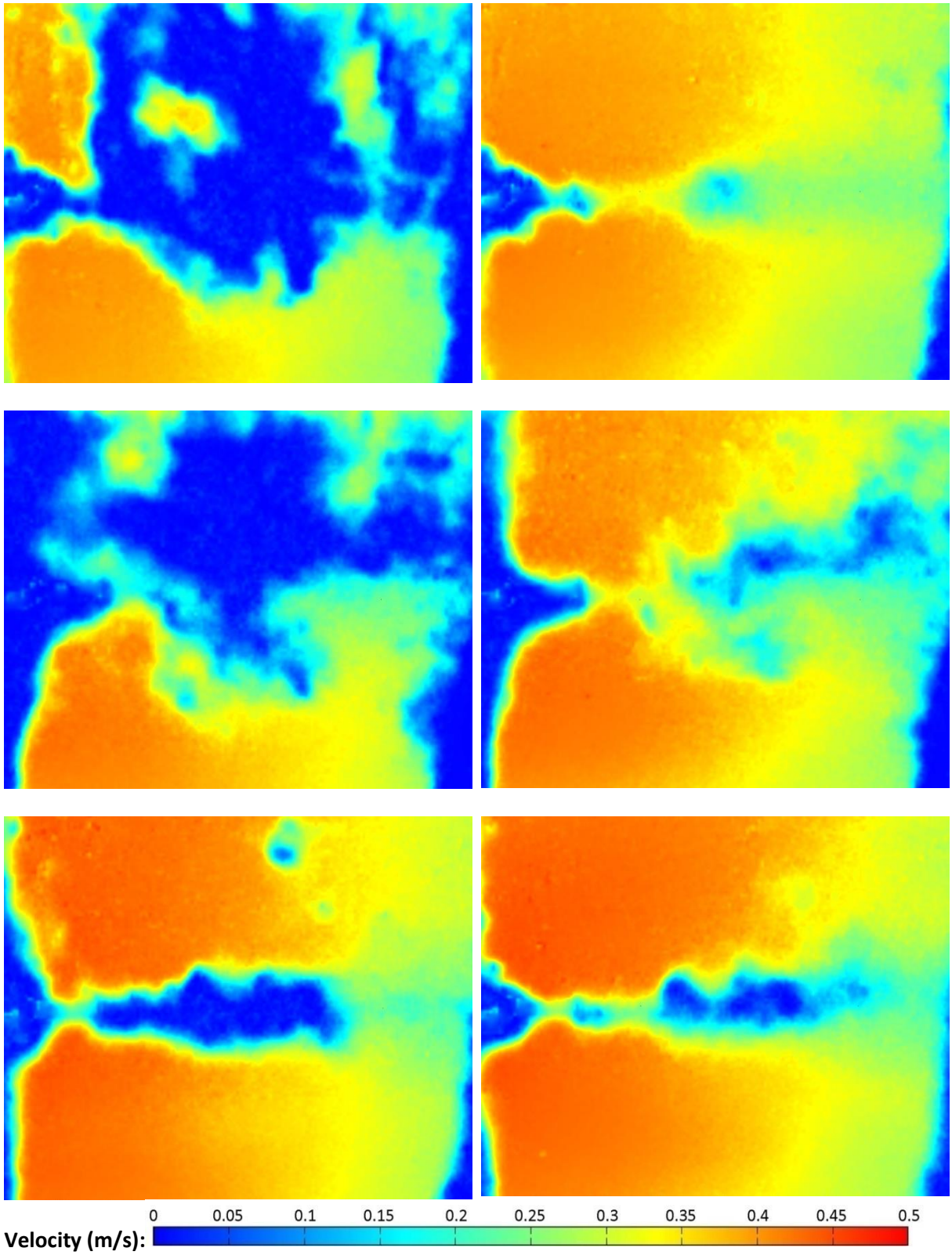

Figure 6-45 – Near (5D) upstream turbine, offset 0.5D (l) & 1D (r). Downstream turbine support structure diameter 11mm (top), 16mm (middle), 20mm (bottom).

With an upstream turbine at far separation distance, Figure 6-44 suggests that the greatest impact on the downstream wake is in the 0.5*D* offset case for 16mm and 20mm diameter support structures, and in the 1*D* offset case for an 11mm diameter downstream support structure (though the two wakes in this case are similar). In these cases, large areas of low velocity fluid are observed downstream of the turbine and in the positive cross-stream direction. The 16mm diameter downstream support structure case appears to exhibit particularly low velocity, with more than half of the area illustrated occupied by flow with a velocity below 0.05m/s. A video of PIV results for this (experiment 72) and other wake results can be viewed in an online video, the details of which are given in Appendix 2.

With a far upstream turbine at 1*D* offset, wake velocity in most cases appears to increase with support structure diameter. In all cases with an upstream turbine at far separation distance, the lowest velocity is seen in the positive cross-stream (upper) part of the image.

An upstream turbine at a near separation distance appears to have less impact on the downstream turbine than at far separation, particularly with an 1*D* offset, in which case flow fields are not dissimilar to those recorded without an upstream turbine (see Figure 6-28, Figure 6-31 and Figure 6-34). At 0.5*D* separation a greater impact is illustrated, though the 20mm downstream diameter case appears largely unaffected. A possible cause of this effect is described in Section 6.3.

Performance data

Returning to the C_p results discussed in Section 6.2.3, an explanation of findings in the far and near streamwise offset cases was sought from the wake images given in Figure 6-44 and Figure 6-45.

- C_p results appeared to show that in the far upstream case, changing the offset from 0*D* to 0.5*D* produced a reduction in C_p in all cases, but that increasing the offset further to 1*D* produced an increase in C_p in the 11mm and 20mm cases, but a reduction in the 16mm case. The wake images illustrated in Figure 6-44 may appear to support increased C_p in the case of the 11mm diameter downstream turbine since the velocity deficit increases between the 0.5*D* and 1*D* cases, but are inconclusive in the 20mm case, and appear to disagree with the C_p result in the 16mm case.

- In the near upstream case, C_p results appeared to show that the performance reduction of the 11mm and 20mm diameter support structure turbines was much greater than that of the 16mm diameter case, relative to inline results, when the turbine was offset either 0.5*D* or 1*D*. Studying the change from the images on the left of Figure 6-45 to those on the right, there does not appear to be any reason that the 11mm and 20mm results should exhibit a different pattern of performance change than the 16mm results. Videos of these results are again available (details are given in Appendix 2), and do not appear to illustrate any fundamental difference in the pattern of performance change between the three cases.

Consequently, it is suggested that the 16mm diameter support structure C_p results of 0.264 observed in the far upstream offset position 2 experiment, and the 0.286 and 0.278 results observed in the near offset position 1 and position 2 experiments are likely to be incorrect.

The remaining results and observed velocity wakes offer some agreement, but it is clear from these results that the wake recorded at the horizontal 135mm plane does not fully explain the measured turbine performance results. As has been highlighted throughout this project, the wake of a tidal stream turbine is highly complex and is made up of a number of interacting features, and it appears that further methods of study may be required in order to fully understand the complexities of the flow interaction in these cases. However, further conclusions can be drawn from the comparison of wakes in each support structure diameter case, and analysis is continued in Section 6.3. The primary observations of Section 6.2 are summarised below.

Summary results – Phase 4b

- At support structure height (66mm above channel base), larger diameter support structures were found to produce wider wakes and longer wake growth distances.

- At support structure height, increasing the cross-stream offset of an upstream turbine at either 5*D* or 10*D* streamwise separation was found to increase wake growth length, and to reduce wake diameter. This effect is believed to be caused by increased turbulence in the incoming flow.

- At support structure height, velocity in the positive cross-stream region (to the right when looking towards oncoming flow) was observed to be between 2% and 9% greater than in the negative region. At turbine height (135mm above channel base) the effect was reversed: Velocity in the positive cross-stream region was found, in most cases, to be between 5% and 25% lower than in the negative cross-stream region. The deficit observed at the 135mm plane suggests the effect of reduced incoming velocity in the wake of the upstream turbine.

- The correlation of turbine C_p results and recorded flow conditions in this phase has proved challenging, and it appears that the introduction of offset upstream turbines generates a flow field which must be studied in three dimensions to be fully understood.

6.3 – Discussion – Multiple Turbines

Comparison of phases 4a and 4b

As was discussed at the conclusion of the following section, it has not been possible to completely correlate the wake results captured in phase 4b data with turbine performance data. However, comparative study of these results and those from phase 4a does allow conclusions to be drawn, as will be discussed in this section.

Comparing the results of phase 4b to those of phase 4a, velocity contour images suggest that the downstream device wake appears to have a lower velocity when the upstream turbine is offset than when it is centrally-located. This effect is shown in Figure 6-46, which illustrates the wake of a downstream turbine mounted on an 11mm diameter support structure, with an upstream turbine at zero (left), 0.5*D* (middle) and 1*D* (right) cross-stream offset.

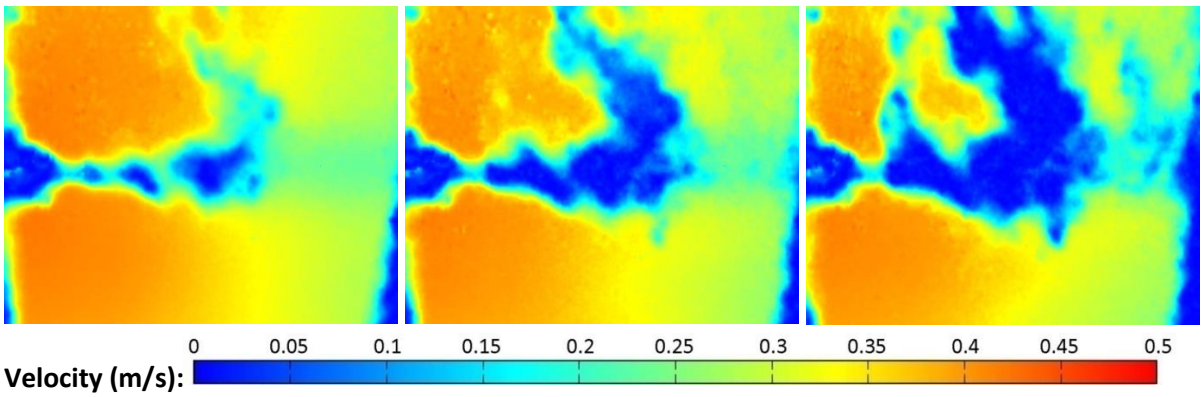

Figure 6-46 – Comparison of downstream turbine wake with a far upstream turbine located centrally (l) and at 0.5D (m) and 1D (r) offsets at 135mm measurement plane.

This result appears to be consistent at both measurement planes, and across all three support structure diameter cases. However, the variation in resultant downstream wake from the two offset positions is not consistent. Comparison of the wakes from offset turbines at near and far upstream locations led to the following conclusions:

- In cases with an upstream turbine in the far location, downstream turbine wakes appear similar whether the cross-stream offset between the two devices is 0.5*D* or 1*D*.

- In cases with an upstream turbine at the near location, downstream turbine wakes differ between the two cross-stream offset cases, with the 0.5*D* offset appearing to cause greater disturbance in the downstream device wake.

This observation led to the suggestion that when the upstream turbine is located in the far position at either 0.5*D* or 1*D* offset, the upstream device wake expands and causes a reduction in velocity at the blade swept region of the downstream turbine, leading to a reduction in performance. However, when located in the near position, the distance between the two turbines is shorter and results in a narrower wake reaching the downstream turbine. The cross-stream width of this wake is only sufficient to reach the downstream turbine when an offset distance of 0.5*D* is used. At an offset of

1*D*, the upstream turbine wake region will not have expanded sufficiently within 5*D* to influence the downstream turbine incoming velocity.

This theory was studied using previously-obtained turbine wake expansion data as described in the following section.

Wake expansion

Wake expansion at turbine level was estimated from POD analysis of dye injection results (as given in Section 5.2.1), which suggested that due to the interaction of the blade and support structure wake elements, the wake downstream of a turbine with support structure undergoes much less of a cross-stream expansion than the wake of a support structure alone. Images recorded during this phase are illustrated in Figure 6-47, and show wake diameters of 1.5*D* at 5*D* downstream, and 2.5*D* at 10*D* downstream.

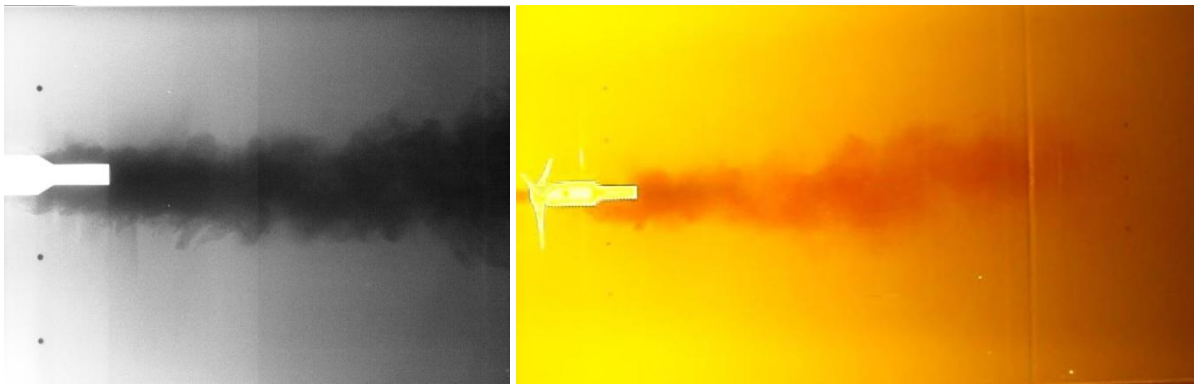

Figure 6-47a&b – Expansion of turbine and support structure wake as recorded during dye injection experiments (phase 1).

Using these wake expansion rates, the hypothesis proposed above was tested. Schematic images illustrating the relative position of upstream and downstream turbines and the wake of the upstream turbine (a conical expansion is illustrated for simplicity) are given in Figure 6-48 and Figure 6-49.

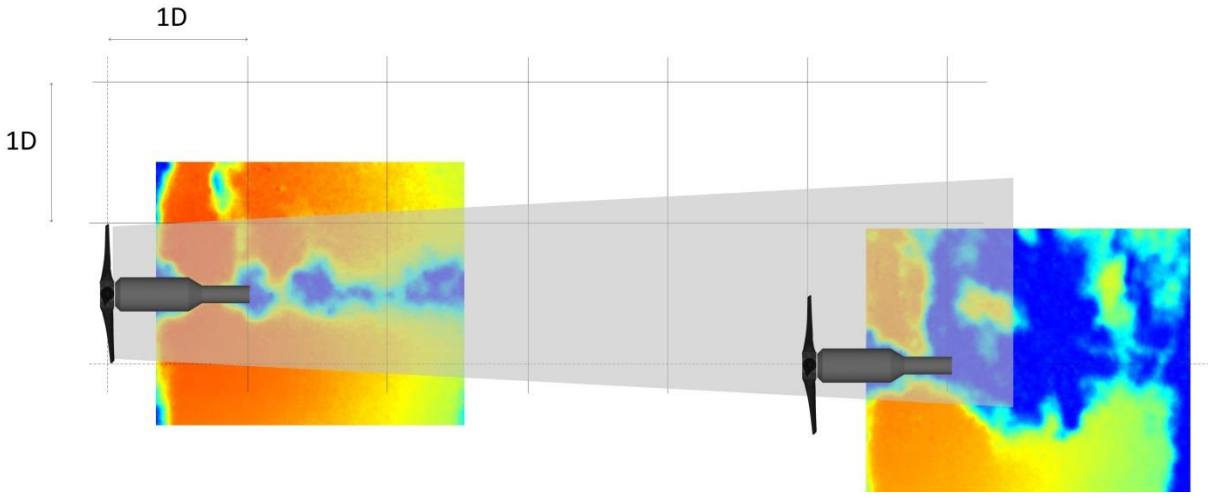

Figure 6-48 - Hypothesised wake behind a near upstream turbine at 0.5D cross-stream offset and its interaction with a downstream turbine.

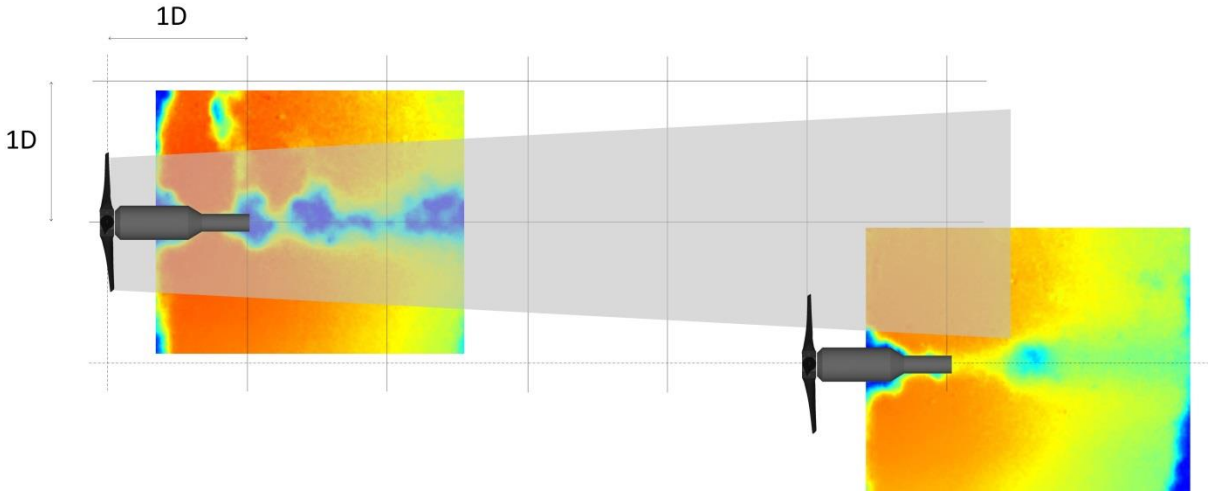

Figure 6-49 – Hypothesised wake behind a near upstream turbine 1D cross-stream offset and its interaction with a downstream turbine.

As illustrated in these figures, an upstream turbine with an offset of 0.5*D* would produce a wake region which would interact with a large portion of the swept area of the downstream turbine. At a cross-stream offset of 1*D*, the influence would reach only a small portion of the downstream turbine swept area.

However, whilst this theory appears to offer an explanation for the respective wake patterns of the downstream turbine in the two upstream offset cases, it would lead to the conclusion that the inline upstream turbine would yield the lowest incoming velocity at the downstream turbine, since the downstream turbine would be in the centre of the upstream turbine wake, where the maximum velocity deficit would be expected. This would suggest that this configuration would produce the lowest power output, but Figure 6-38 suggests that this is not the case. The inline configuration in fact yields the greatest C_p of the three offset positions, in all cases, though there is significant variation between cases.

Studying the POD data generated during phase 1, the turbulent energy of a turbine wake appears to be concentrated at the edges of the wake region. This would appear to agree with predictions from previous studies [53, 140, 172] as discussed in Chapter 2, which each identified distinct regions within the turbine blade wake. The three regions identified, as highlighted in Figure 2-44, are the blade tip vortex, which rotates in the direction of the turbine blades; the counter-rotating central region wake; and the core region wake, which again rotates in the blade direction. For the turbines in this study, the blade tip vortex will rotate anti-clockwise, the central region wake clockwise and the core region wake anti-clockwise.

In the POD analysis described in Section 5.2.1, excluding background flow which contained 13.4% of the total energy, the next two most energetic modes (modes 2 and 3) appeared to illustrate energetic structures in the region downstream of the upper and lower turbine blade edges, corresponding to the location of the blade tip vortices. These wake structures contain 12.5 % and 12.4% of the overall energy, meaning that excluding the background flow they make up 29% of the total wake energy, and are the most energetic individual elements. These structures are illustrated in the POD reconstruction given in Figure 6-50.

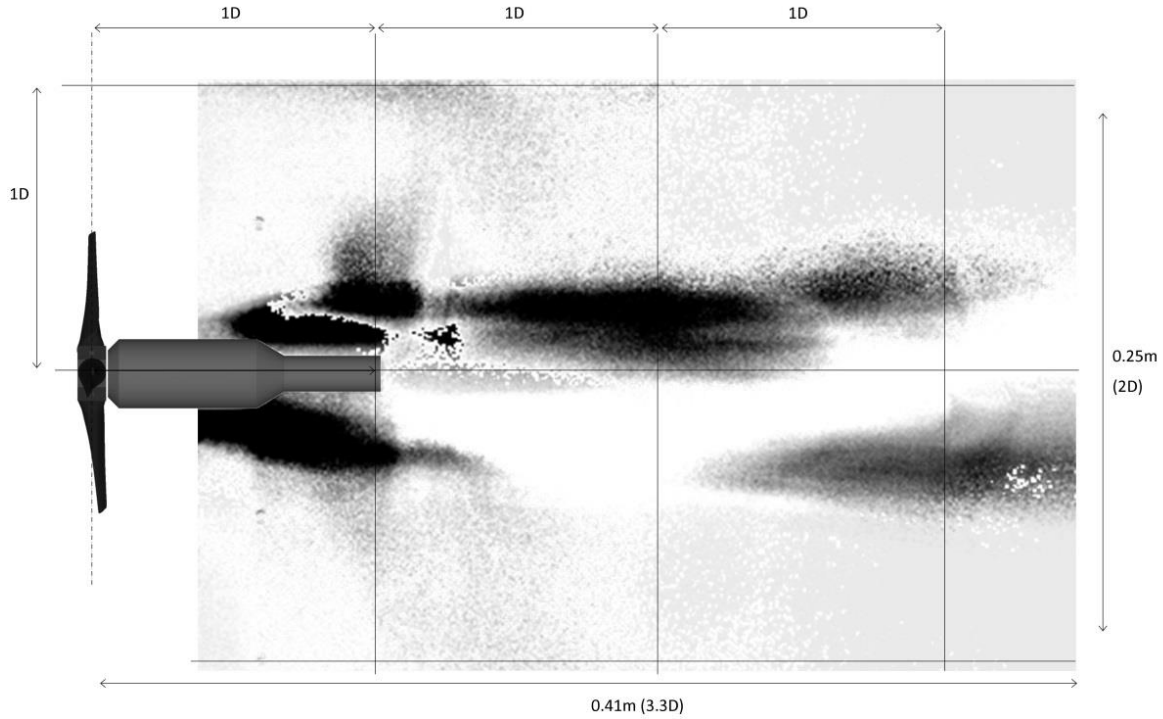

Figure 6-50 – Reconstruction of POD analysis modes 1 and 2 of wake behind a single turbine mounted on a 16mm diameter support structure in flow case 2 (high energy wake structures are indicated by dark colours).

Based on these observations, and supported by literature discussed in Section 2.7 suggesting minimal interaction blade hub and blade tip vortices [53], it was suggested that the most energetic parts of the turbine blade wake are those around the edge. It is believed that as the wake expands downstream in a conical fashion, this highly turbulent region will be wider than the swept area of an inline downstream turbine, meaning that the turbine does not experience the highest values of turbulent kinetic energy, and is consequently able to generate greater power than in an otherwise

identical case with an offset upstream turbine. This suggested wake expansion in the inline case is illustrated in Figure 6-51.

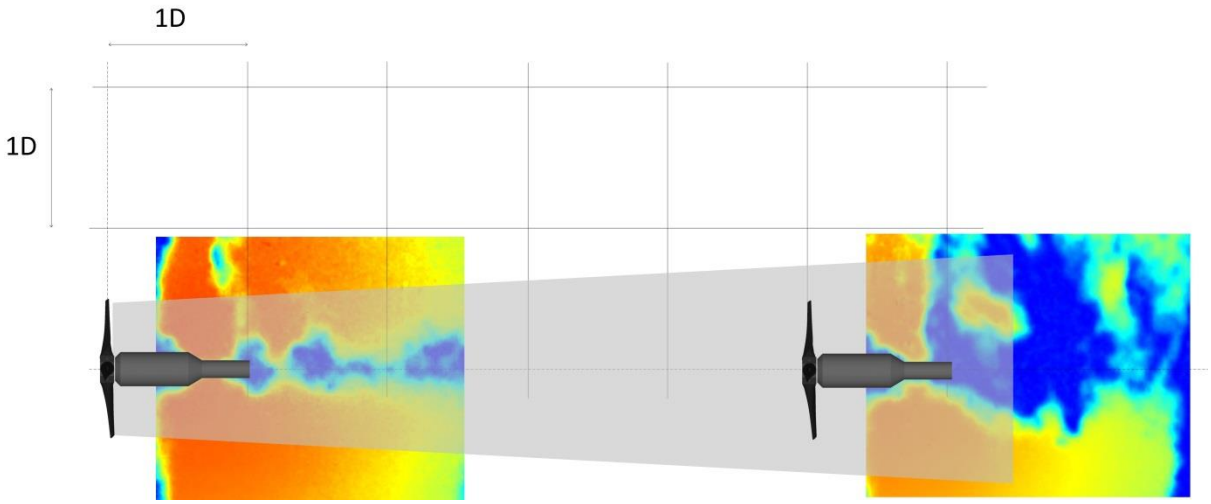

Figure 6-51 - Hypothesised wake behind an upstream turbine (no cross-stream offset) and its interaction with a downstream turbine.

Assuming as suggested that the edge of the wake region is the most energetic part of the wake, it follows that if an upstream turbine was positioned at a streamwise separation distance and offset such that this region of the wake interacted with a downstream turbine, it could be expected that the downstream turbine performance would be reduced due to the high turbulence expected in the incoming flow.

This hypothesis goes some way to explaining the differences in performance observed earlier in this section, for example the 11mm diameter support structure C_p results with an upstream turbine in the far position, which showed greater values of C_p with an inline or 1D offset than with an 0.5D offset. Again using the wake expansion rates calculated from POD and dye injection results, similar diagrams to those given previously were generated for the far upstream turbine case, as illustrated in Figure 6-52.

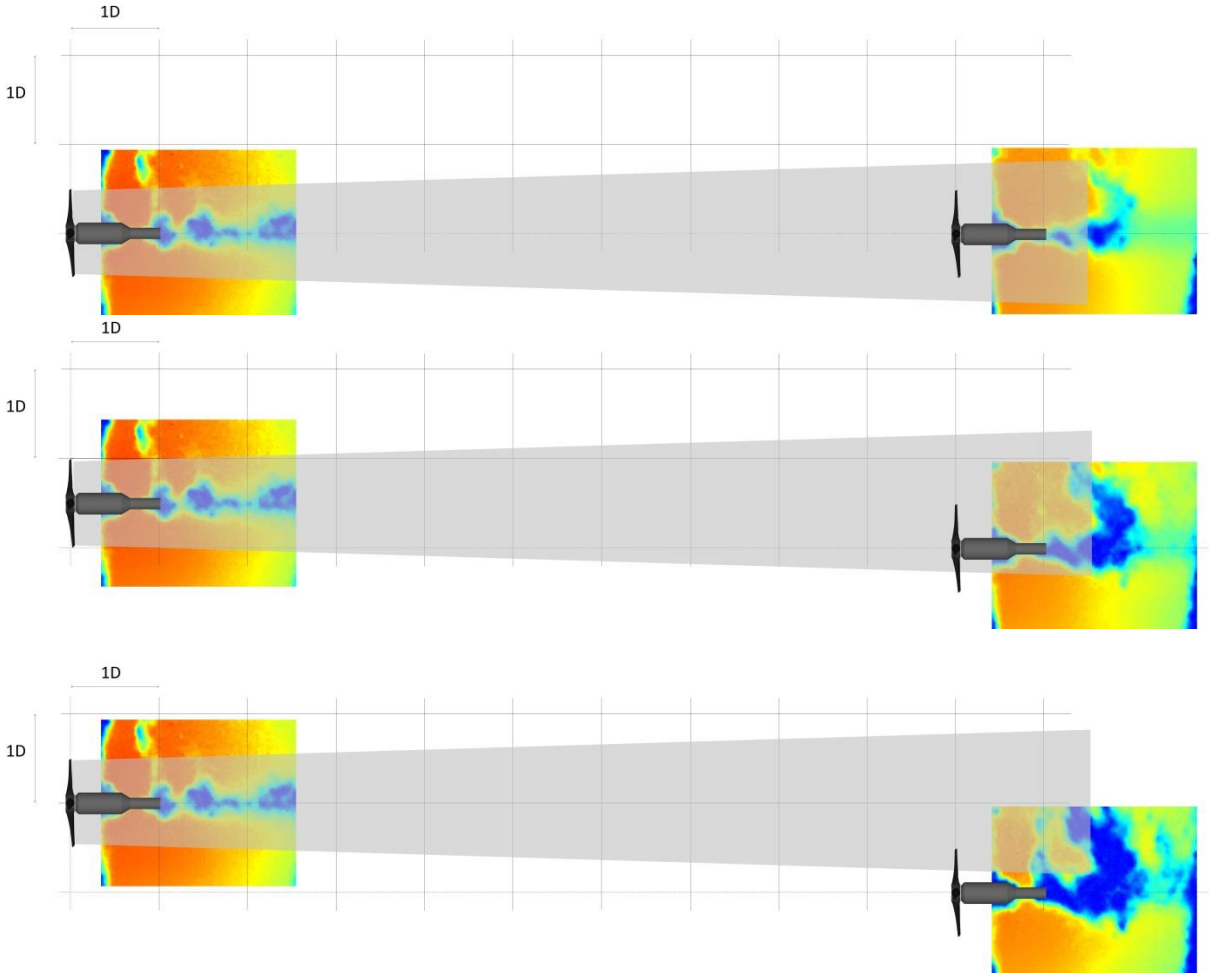

Figure 6-52 - Hypothesised wakes behind a far upstream turbine at 0D (top), 0.5D (middle) and 1D (bottom) offset and its interaction with a downstream turbine.

This image appears to illustrate that the hypothesised highly turbulent region at the edge of the upstream wake does lead to a reduction in turbine performance. Referring to the data in Figure 6-38 in the case of a far upstream turbine, after the removal of the erroneous 16mm results, the 11mm and 20mm support structure results generate the lowest C_p when the upstream turbine is offset at 0.5*D*. The data shown in Figure 6-52 suggests that the maximum interaction of the downstream turbine with the edge of the upstream turbine wake would occur in this case, which appears to support the proposed theory. It should also be noted that the wake drift observed in Section 6.2.1 would move the resultant wakes towards the top of the image by approximately 0.5*D*.

These results also highlight that although its C_p reduction effect is around 40% of that at 5*D* separation, the wake of an upstream turbine still has a significant effect on the performance of a downstream device, even at a separation distance of 10*D*.

7

Complex Support Structures

7.1 – Introduction

As was introduced in Section 2.5.2 and illustrated in Figure 2-24, the current range of tidal stream turbine designs comprise a number of different designs of support structure. The majority of designs use rigid base-mounted support structures broadly similar in concept to those tested in this project, though there is variation in the size and geometry of the major support element, as well as smaller supporting structures. Some designs also propose the use of alternative systems, such as cable mooring. All designs exhibit greater structural complexity than the single post design which has been tested in previous phases of this project, and each different design will influence the hydrodynamic interaction between the flow, the turbine, and the support structure itself.

During the final stages of this project, additional work was carried out to determine the relative effect of different complex support structure designs on turbine performance. This final phase of experimental work was based on the initial findings of this PhD project, and aimed to apply the findings described in chapters 5 and 6 to the study of complex support structure designs. It is hoped that this continuation will form the basis of a further project, which will be undertaken during the author's EPSRC-funded fellowship. Proposed further work is described in Section 8.3.

7.2 – The TEDSSWIP Project

This continuation phase, titled T.E.D.S.S.W.I.P. (Tidal Energy Device Support Structure: Wake Impact on Performance), was carried out at the University of Florence CRIACIV Wave-Current Flume during September 2014, and was funded by the EU FP7 MARINET [173] framework.

The aim of this phase was to generate experimental data on the relative performance of a tidal stream turbine mounted on four designs of support structure, based on those proposed by leading commercial device manufacturers. By using the same turbine design and flow conditions in each case, the work aimed to isolate the relative effect of each support structure design on the performance of the turbine. The CRIACIV water channel has a length of 40m, width of 0.8m and a maximum depth of 1m. Being significantly larger the University of Sheffield channel used during previous phases, this allowed the use of larger scale turbine models, and testing was carried out at Reynolds numbers of the order $Re = 3 \times 10^5$.

7.2.1 – Support Structure Models

Four support structure models were constructed and tested individually using a single turbine unit of blade diameter D = 250mm. With the turbine installed, the base to tip height of each support structure was 394mm, and a water depth of 600mm was used, giving a simple blockage ratio of B = 10.2%. The blade unit used was a simple two-blade design since the required result of this work was the recording of relative, rather than outright, turbine performance results. One support structure model with the turbine unit attached is illustrated in Figure 7-1.

Figure 7-1 – Complex tidal turbine support structure model with turbine unit attached.

As in previous phases, the turbine model used in these tests was driven and performance was measured using the same concept as described in Section 3.6, incorporating an optical encoder mounted on the turbine driveshaft to record rotational speed, a power supply, and a current measurement module to measure motor power. Both rotational speed and turbine supplied power were recorded at 50Hz using a LabJack data acquisition module.

In this project flow measurement was achieved using ultrasonic and acoustic Doppler velocimetry equipment (UDV and ADV, respectively). The UDV system was installed at 1*D* downstream of the turbine installation location, and was used to measure instantaneous velocity profiles over the full water depth. 75 profiles were captured over a 33 second recording period during each experiment. ADV data was recorded at the turbine blade-centre height at 10D downstream, and was recorded at a frequency of 25Hz over a time period of 90 seconds. Three ultrasonic depth gauges were also used to measure any changes in water level, and a magnetic flow gauge was used to measure the bulk flow rate through the water channel. The position of measurement equipment in the vicinity of the turbine installation location is illustrated in Figure 7-2. The magnetic flow measurement equipment and two of the ultrasonic depth gauges are not shown.

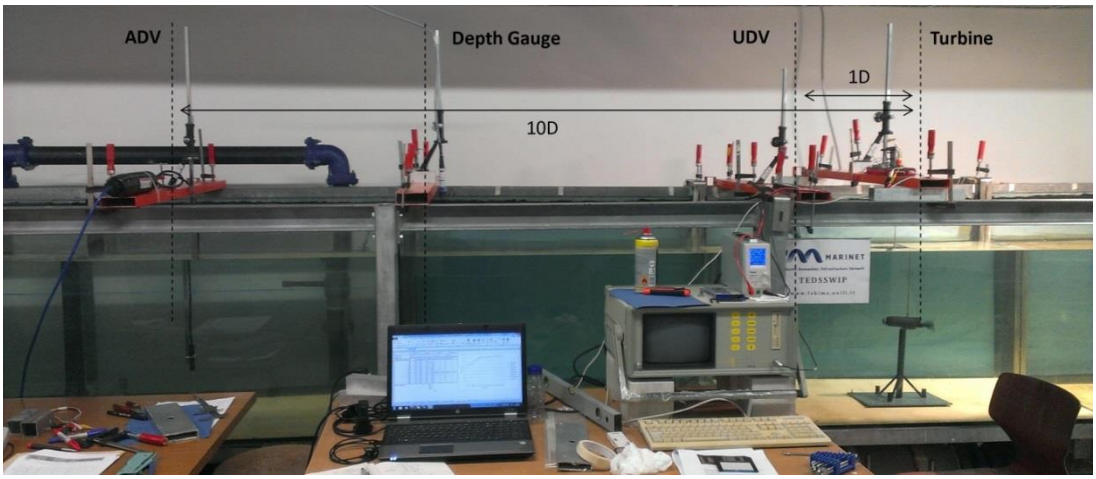

Figure 7-2 – Flow and turbine performance measurement equipment installed in the central area of the CRIACIV water channel during the TEDSSWIP project.

7.2.2 – Test cases

The four designs of support structure tested during this phase are illustrated in Figure 7-3.

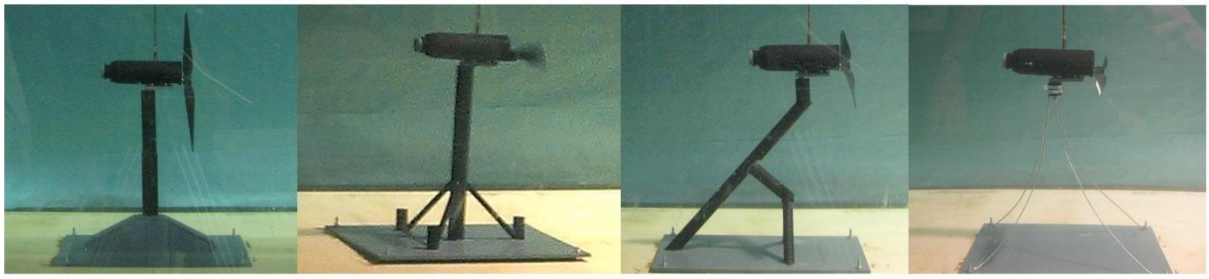

Figure 7-3 – Four complex tidal turbine support structure designs, as tested.

Tests were carried out for each support structure design at five values of Tip Speed Ratio, from $\lambda = 2$ to $\lambda = 6$. A constant flow rate of 74l/s was used in all cases, giving an approximate bulk flow velocity of 0.154m/s. TSR values were set by adjusting the turbine rotational speed to between 2.5 rad/s and 8.6 rad/s.

Turbine performance was measured by calculating the required drive power in each case, for otherwise identical experiments with and without turbine blades, using a method based on that described in Section 4.5.1. From measured power in each case, C_p was calculated, and eventually used to plot $C_p - \lambda$ graphs for each support structure case.

ADV and UDV profiles were also recorded for every experiment, and for a series of empty channel experiments both with and without flowing water, in order to gather data on the ambient velocity and turbulence characteristics of the channel. This data has not yet been analysed, but will be used during the major part of this project, which it is hoped will begin in December 2014.

7.2.3 – Results

To date, $C_p - \lambda$ graphs have been calculated for three of the four support structures. These results are given in Figure 7-4. C_p results are normalised by the maximum peak value. As illustrated in this figure, maximum C_p is generated in one structure case at $\lambda = 3$, and in two cases at $\lambda = 4$. Furthermore, of the two structures with peak C_p at $\lambda = 4$, one allows the turbine to generate a C_p of around 60% of maximum peak between $\lambda = 2$ and $\lambda = 3$, whereas the C_p of the second is much lower in this region. These differences underline the significant influence of the support structure on the performance of the turbine, as have been highlighted in the previous experimental work described in this thesis.

Further details of the work carried out to date on this project are available in a publication [174] (currently in press). The work described in this publication also considered the effect of the $C_p - \lambda$ data illustrated in Figure 7-4 on the performance of a device over a full tidal cycle for a sample installation site, and found that the device which achieved the greatest peak C_p did not necessarily deliver the most consistent power generation.

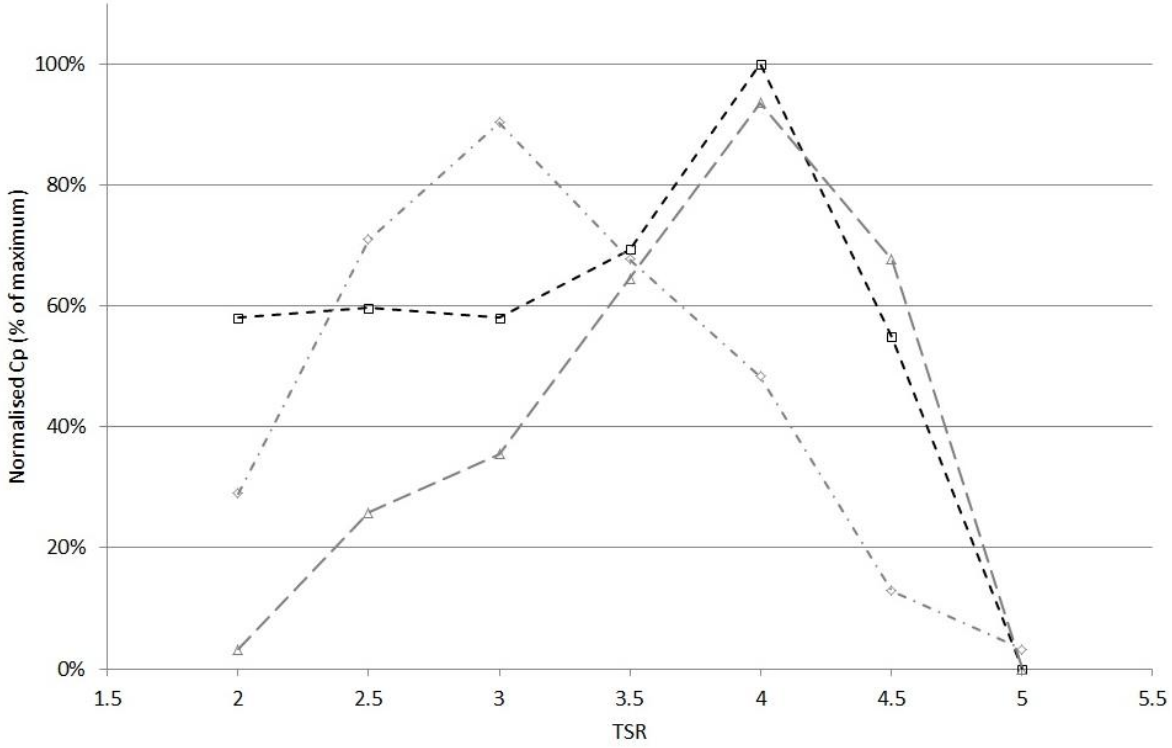

Figure 7-4 - C_p – λ *plot for three of four support structures tested during TEDSSWIP project.*

7.3 – Project continuation

It is hoped that further work on this project will involve the development of CFD models of the four support structures tested, which will be validated using the experimental results described previously. These numerical models will then allow the detailed analysis of the flow field in the region around the turbine and support structures. From results of this analysis and the application of results described in chapters 5 and 6, changes to the support structure designs will be proposed and tested, leading to the development of optimised designs. Following computational optimisation, it is hoped that further physical support structure models will be constructed and tested using the same experimental equipment and conditions as used in the initial testing. The final aim of the project is to understand which elements of each support structure lead to certain performance characteristics (for example peak C_p, or consistent C_p over a range of λ values), and to use this knowledge to design and test optimised support structures for given site characteristics.

The work described in Section 7.2 was funded by the Marine Renewables Infrastructure Network (MARINET, proposal number 271), and the proposed work described above will be carried out during a fellowship project funded by UK EPSRC (UK Engineering and Physical Sciences Research Council).

8

Conclusions and Further work

8.1 – Introduction

The final chapter of this thesis will describe the primary findings of the project, and their applications to real-scale tidal stream turbines. An assessment of the methodological contribution of the work is given, followed by the primary conclusions of the project, and finally by details of the potential for further work resulting from the conclusions of this study.

8.2 – Conclusions

The aim of this project, defined at the outset, was:

"the advancement of the understanding of hydrodynamic interactions between a tidal stream turbine and support structure, as well as the downstream interaction of multiple devices".

Following a literature review which revealed the lack of any significant body of work on the interaction of tidal stream turbine and support structure hydrodynamics, this was refined to give three specific technical aims, which were to investigate the impact on turbine performance of (a) changing the separation distance between the turbine blades and support structure, (b) changing the diameter of the support structure on which a turbine is mounted, and (c) the installation and relative positioning of an upstream turbine.

These aims have been achieved through the testing of scale model tidal stream turbines in a water channel, and a contribution has been made to the existing body of work on tidal turbine hydrodynamics, particularly on the effect of the wake of a tidal stream turbine support structure on the turbine performance. A contribution has also been made to the experimental techniques used in such work, by the development of an experimental method for the measurement of turbine blade-generated power and torque, which has subsequently been applied to a further study. Results of relevance to the development of tidal turbine design have been identified and are summarised in the following sections. The methods applied were not without limitations, and three primary limitations of the project are discussed in Section 8.2.3.

8.2.1 – Methodological Contribution

Turbine power measurement

The primary contribution of this study to the field of experimental turbine testing was the development of a method of power measurement. This method allowed the calculation of turbine blade-generated power through a calculation based on the results of two experiments. For a given flow case, each test was carried out twice: Once with the turbine blades in place and once without. The turbines used in this study were driven using a motor and gearbox system, meaning that the power applied was calculable from the current and voltage at to the motor. By subtracting the power applied to the drive motor in the case without blades from that with blades, the reduction in the power required to drive the turbine in the case with blades (which represents the power generated by the turbine blades) could be isolated.

The primary advantage of this method is that it does not require the calculation or estimation of any additional loads or losses within the turbine gearbox, drive system, motor, or power supply system,

since these effects are all applicable whether the blades are in place or not and are hence removed from the calculation when the subtraction takes place. The only additional effect which it was necessary to consider in the case of the blade test was the additional load on the turbine bearings. As discussed in Section 4.3.5, this additional load was calculated to be of the order of 0.002% of the blade-generated power, and was therefore deemed negligible.

This method of blade power measurement was successfully used in this project, with good agreement in C_p observed between sets of identical experiments conducted as part of different experimental phases (C_p variations of 1.4%, 0.9% and 0.4% between pairs of experiments carried out during phase 3 and phase 4a).The method has also subsequently been used in the TEDSSWIP project described in Section 7.3.2.

Furthermore, this project highlighted the difference between experimental results obtained using actuator disks and those obtained using scale turbine models. Actuator disks were found to over-predict wake length and velocity deficit, as well as being unable to replicate dynamic wake structures generated by rotating parts of the turbine. However, actuator disks can be useful in experimental cases where the use of turbine models is impractical due to scale or cost restrictions, but their limitations must be borne in mind.

8.2.2 – Technical conclusions

Hydrodynamic interactions between turbine and support structure

It was found that both the diameter of a turbine support structure and the separation distance between the plane of rotation of the turbine blades and support structure have a significant impact on the performance of the turbine. These effects are linked, since a larger diameter support structure places its front face closer to the blades, thus reducing the separation distance. A study of the relationship between separation distance and turbine performance resulted in the division of the region upstream of the support structure front face into three regions, characterised by different performance characteristics. The regions can be defined by their position upstream of the support structure front face, given in multiples of support structure diameter *d*.

- The first region (0*d* to 1.5*d* upstream from the support structure front face) allowed the turbine to achieve a mean coefficient of performance, C_p of 0.25.

- The second region was found to allow the turbine to generate a mean C_p of 0.3, decreasing from the downstream edge of the region at 1.5*d* ($C_p \approx 0.35$) to the upstream edge at 2.5*d* ($C_p \approx 0.25$). This region (1.5*d* to 2.5*d* upstream) was termed the region of optimal turbine performance.

- The final region (2.5*d* to 4*d* upstream) was found to cause the turbine to generate a significantly lower mean C_p of just 0.15.

The effect of turbine location relative to the support structure has great effect on the turbine.

The variation in turbulent kinetic energy of the flow in the region between the support structure and turbine blades is believed to cause the variation in turbine performance across the regions. A strong inverse correlation between the value of turbulent kinetic energy at blade location and the

performance of the turbine was measured. An increased turbulent kinetic energy is known to cause increased blade drag, which will reduce blade power generation and C_P. The primary and secondary horseshoe vortices generated by flow around the support structure appear to reduce turbulence levels in the optimal performance region.

Downstream interaction of multiple devices

Compared to a single turbine case, the installation of an upstream turbine reduces the performance of a downstream turbine. Based on turbine blade diameter *D*, the wake of an upstream turbine installed in line at 10*D* streamwise separation will reduce the C_p of the downstream device by around 4%, and an upstream device installed at 5*D* will reduce the C_p of the downstream device by around 10%. Offsetting the upstream turbine will further reduce the output of the downstream turbine, by between 5% and 25% for an offset between 0.5*D* and 1*D*. The performance reduction caused by an upstream turbine is exacerbated by downstream support structure diameter, with greater support structure diameter, *d*, leading to a still greater reduction in C_p.

A further effect of the upstream turbine relates to the expansion of its wake. This expansion is controlled by the upstream turbine support structure diameter and the highly energetic turbine blade tip vortices: If the edge of the upstream turbine wake reaches the area swept out by the downstream turbine blades, the downstream turbine C_p will be relatively low. If the centre of the upstream device wake reaches the downstream turbine, or the upstream wake misses the downstream device completely, C_p will be relatively high.

Wake drift occurs in all cases, with the blade region wake of a turbine observed to drift away from the centreline by a cross-stream distance of around 0.5*D* within a streamwise distance of 5*D*, downstream of a single turbine. Drift occurs in the direction of blade rotation at the top of the swept area. The presence of an upstream turbine exacerbates drift by reducing downstream velocity and increasing turbulent kinetic energy in the inflow conditions to the downstream turbine. The wake of the device support structure exhibits drift in the opposite direction to the blade region, the effect of which is again exacerbated by the presence of an upstream turbine. These two effects act in opposing directions combine to cause a rotation of wake structures downstream of the turbine.

Maximising turbine performance

Based on the conclusions of this study, it is suggested that the power generation of a downstream turbine, assuming that an identical upstream turbine is also present, can be maximised by:

- Installing both upstream and downstream turbine blades at a separation distance of 1.5*d* from the support structure face.
- Minimising the upstream support structure diameter.
- Maximising the streamwise separation distance between the two devices.
- Positioning the upstream device at such an offset that the edge of the wake region does not impact the downstream turbine swept area.

Turbine wakes

Through the use of PIV flow measurement, instantaneous and time-averaged flow field data was captured during each experimental phase. The initial downstream wake of a tidal stream turbine was found to comprise flow structures generated by both the support structure and turbine, and wake diameter was found to depend on the diameter of the support structure as well as the turbine. Turbine blade tip vortices were found to be a highly energetic wake element, and it is believed that these rotational structures contribute to the wake drift described previously.

PIV illustrated the increased complexity of the wake with the introduction of an upstream turbine, and a further increase in complexity if the upstream turbine was offset. The presence of an upstream turbine at *5D* was found to extend the wake width at support structure height by up to 42% from that of a single turbine, with a greater effect observed on a smaller diameter support structure.

Cases with an upstream offset turbine appeared to exhibit wakes with rotation about the streamwise, cross-stream and vertical axes, and in these cases it was not possible to fully correlate turbine performance data with the observed flow conditions. It is suggested that the use of 3D PIV methods may have allowed such complex structures to be accurately captured, potentially leading to a greater understanding of the performance characteristics.

8.2.3 – Applications

As was highlighted in Chapters 1 and 2, the tidal stream turbine industry is currently at a crucial juncture in the development of the technology. Single device designs have been successfully deployed and operated, and their performance characteristics are well understood. In order for tidal stream turbines to make a meaningful contribution to electrical generation on a national scale within the timescales identified for the reduction of greenhouse gas emissions, their installation in arrays must now begin. The installation of such devices in arrays presents hydrodynamic effects not previously considered, and it is to this stage of development that the results of this work aimed to contribute.

The work described herein demonstrates that the separation distance between the turbine blades and the turbine support structure are of critical importance to the performance of the turbine. This effect has been suggested by others [52] but was not found to have been studied to the level of detail included in this study, and was not considered in proposals for the optimisation of array layout [62, 115]. However, as discussed below, the simplistic design of support structures used in this study does have limitations and may not be entirely representative of the designs of support structure which will be used in future array installations, some examples of which can be seen in Figure 7-3. Nonetheless, the study of the interaction of support structure and blades, the identification of the optimal performance region and the underlying turbulent cause, and the contribution to knowledge on the effect of upstream device wakes all contribute to the growing body of work on tidal turbine hydrodynamics, which will be used to design the next generation of devices and arrays.

Limitations

Three primary limitations of this study in terms of applicability to full-scale tidal turbine applications have been identified, namely the geometry of the support structure design tested, the single scale at which the work has been undertaken, and the 2D nature of the flow measurement.

As has been illustrated throughout this work, though the turbine models employed in this study were accurate scale models of a commercial device design, the support structures tested were simple cylindrical posts. Real tidal turbine designs employ a range of support structure designs, as can be seen in Figure 2-24, some of which are broadly similar to cylindrical posts and some of which are entirely dissimilar. It is therefore true that the results described herein are only directly relevant to some support structure designs. However, the underlying principals identified are applicable to all designs of support structure, as are the experimental methods developed and used during this work.

A further phase of work based on the initial results of this study involved the testing of realistic support structures, as described in Chapter 7. In addition to base-mounted support structures; this phase also included the testing of a device mounting system which completely avoids the use of a traditional support structure, instead mooring the device using a system of catenary cables. Such "2nd generation" systems have been suggested by some as the likely future direction of tidal turbine support structure design.

A second limitation of this work is the single scale at which tests took place. During phases 1 – 4, turbine models of only one size were used, and though two flow cases were used, flow case 2 was used in the majority of results, meaning that only a single case of tip speed ratio was considered. In order for the validity of the results over a full range of operating conditions and at a full range of scales to be ascertained, it would be necessary to extend this project to test larger tidal stream turbine models.

The final limitation of this project became apparent during the study of the wake developed by a downstream turbine in the presence of an offset upstream turbine. In this case, due to the complex interaction of the upstream and downstream support structure and turbine wakes, rotational flow appears to occur around three axes. In this case it was not possible to fully correlate turbine performance with observed flow effects using two-dimensional measurement methods, and it is suggested that future work may wish to consider 3D flow measurement. Doing so would allow the calculated horizontal plane turbulent kinetic energy and vorticity values to be calculated over three dimensions, which may reveal additional flow structures.

8.3 – Further Work

8.3.1 – Opportunities for further work

At the culmination of this project, a number of opportunities for continuing work can be found. The project appears to have identified the underlying hydrodynamic effects which govern the performance of a tidal stream turbine in relation to its support structure and to an upstream turbine, and this knowledge can now be used to extend the project in a number of directions.

As identified in Section 8.2.3, the project suffers from three core limitations. The use of 3D flow measurement equipment is suggested as a solution to the final limitation, leaving the issues of support structure complexity and the single scale used. The latter limitation could be solved by the testing of support structure designs in different flow conditions and at different sizes, or by comprehensive study of complex support structure designs in a range of flow conditions it would be possible to address both limitations. The continuation of this work as described in Section 7.2 has begun this process, and the author hopes to continue this work as described in Section 7.3.

Other opportunities offered by the results of this project relate to the advancement of the research into array wakes, which could be undertaken using a larger number of turbine models to assess the impact of performance of multiple upstream turbines. As was concluded in Section 8.2.2, at this stage it would be necessary to consider the three-dimensional wake effects observed during the final stages of testing, and it is expected that 3D measurement equipment would be required in order to successfully correlate turbine performance with flow conditions.

Finally, though a multitude of other opportunities for further work exist, research could change direction and consider how the blades of a tidal turbine could be designed or operated in order to optimise their performance under the wide range of flow conditions identified. As was discussed in Section 3.5.5, pitch control was not incorporated into the models tested in the present work, and there may be opportunities for the development of control systems to enable the turbine to maximise its performance based on the incoming flow conditions.

References

1. Edenhofer, O., et al., *IPCC Special Report on Renewable Energy Sources and Climate Change Mitigation. Prepared by Working Group III of the Intergovernmental Panel on Climate Change*. 2011: Cambridge & New York. p. 1705.
2. Press, O.U., *The Greenhouse Effect*, in *Adobe Illustrator CS4*, F. 06.02.01, Editor. 2010, Kerboodle / Oxford University Press: Oxford. p. The Greenhouse Effect.
3. NAEI. *National Atmospheric Emissions Inventory*. 2014 July 2014 [cited 2014 26/08/2014]; National Atmospheric Emissions Data]. Available from: http://naei.defra.gov.uk/data/.
4. Petit, J.R., et al., *Climate and atmospheric history of the past 420,000 years from the Vostok ice core, Antarctica.* Nature, 1999. **399**(1): p. 429-436.
5. Huss, M., et al., *100-year mass changes in the Swiss Alps linked to the Atlantic Multidecadal Oscillation.* Geophysical Research Letters 2010. **37**.
6. *Human Development Report 2007/2008*, in *United Nations Development Programme*, K. Watkins, Editor. 2008.
7. Metz, B., et al., *Contribution of Working Group III to the Fourth Assessment Report of the Intergovernmental Panel on Climate Change*. 2007, IPCC: London.
8. Hickman, L. *Light goes out for incandescent bulbs*. [Online article] 2012 [cited 2014 15/10/2014]; Available from: http://www.theguardian.com/environment/2012/aug/31/lightbulbs-incandescent-europe.
9. *Key World Energy Statistics 2013*. 2013, International Energy Agency (IEA): Paris.
10. Sumanik-Leary, J., *Small Wind Turbines for Decentralised Rural Electrification: Case Studies in Peru, Nicaragua and Scotland.*, in *Mechanical Engineering*. 2013, Sheffield: Sheffield.
11. Sovacool, B., *Valuing the greenhouse gas emissions from nuclear power: A critical survey.* Energy Policy, 2008.
12. *What is our future?*, in *Human Universe*, N. Sharman, Editor. 2014.
13. E.On. *Electricity generation by source*. 2013 [cited 2014 08/11/2014]; UK electricity generation by source]. Available from: www.eonenergy.com/fuelmix.
14. *Drax Group - About our Business*. 9/12/2011]; Available from: http://www.draxgroup.plc.uk/aboutus/ourbusiness/.
15. Bleyl, F., *Record-Setting Power Plant*. 2011, Siemens. p. 96-98.
16. GoodEnergy, *Where does the UK's electricity come from?*, J. Davenport, Editor. 2014, Good Energy: Cheltnham.
17. Wood, I., *UK Continental Shelf: Maximising Recovery of Oil and Gas*, E. Davey, Editor. 2014, HM Government: London.
18. Hargreaves, B., *Still polarised as polling approaches*, in *Professional Engineering*. 2014, Institution of Mechanical Engineers: London. p. 88.
19. Younger, P.L., *Missing a trick in geothermal exploration.* Nature Geosci, 2014. **7**(7): p. 479-480.
20. Ekins, P., et al., *The UK energy system in 2050: Comparing Low-Carbon, Resilient Scenarios*. 2013, UKERC. p. 68.
21. DECC, *Summary of key findings: DECC Public Attitudes Tracker – Wave 8*, in *Public Attitudes Tracker*. 2014, Department of Energy & Climate Change: London.
22. Hardisty, J., *The Analysis of Tidal Stream Power*. 2009, Chichester: Wiley-Blackwell.
23. Newton, I., *Philosophiæ Naturalis Principia Mathematica*. 1687.
24. Morris, R.A.R.O., *Tidal Stream Atlas: Orkney and Shetland Islands*. 1986 (Reprinted 2009), Hydrographic Office: Taunton.
25. King, J. and T. Tryfonas, *Tidal Stream Power Technology – State of the Art.* IEEE, 2009.

26. Tswgb, *Luftbild des Gezeitenkraftwerks Rance*. 2007, Creative Commons License.
27. BBC, *Severn barrage tidal energy scheme scrapped by Huhne*, in *BBC News*. 2010.
28. de Laleu, V., *La Rance Tidal Power Plant: 40-year operation feedback - lessons learnt*, in *BHA Annual Conference*. 2009, BHA: Liverpool.
29. Renewables, S. *Whitelee Wind Farm*. 2013 [cited 2014 25/08/2014]; Available from: http://www.whiteleewindfarm.co.uk/about_windfarm?nav.
30. *Carbon Trust - Future Marine Energy*. 2006.
31. Davenport, J., *New tidal energy focus for Good Energy*. 2014.
32. Consense. *Tidal Lagoon Swansea Bay*. 2014 [cited 2014 14/10/2014]; Tidal Lagoon Swansea Bay: Project Overview]. Available from: http://www.tidallagoonswanseabay.com/default.aspx.
33. Mohr, P. and A. Lloyd, *LEVELISED COSTS OF POWER FROM TIDAL LAGOONS*. 2014, Pöyry: Helsinki. p. 38.
34. MacKay, D., *Sustainable Energy - Without the Hot Air*. 2008.
35. Hammons, T., *Tidal Power.* IEEE, 1993. **8**(3).
36. Ramsden, E., *Risk-based management of corrosion and biofouling of tidal stream energy converters*, in *Chemical and Biological Engineering*. 2013, University of Sheffield: Sheffield.
37. MeyGen. *The MeyGen Project*. 2013 [cited 2014 27/08/2014]; Description of the MeyGen project].
38. ScottishPowerRenewables, *Sound of Islay Non Technical Summary*. 2010, ScottishPower Renewables: Glasgow. p. 17.
39. E., D. and A. B., *Phase II UK Tidal Stream Energy Resource Assessment.* Carbon Trust, 2005.
40. *Accelerating marine energy*. 2011, Carbon Trust: London. p. 64.
41. Trust, C., *LCICG TINA Marine Energy Summary.*
42. DETINI, *Existing and confirmed ROC/MWh levels from 1 April 2013*. 2013, Department of Enterprise, Trade and Investment: London.
43. Osborne, G. and D. Alexander, *Investing in Britain's future*. 2013, HM Treasury: London.
44. Chatelain, E., *Alstom completes the acquisition of Tidal Generation Limited (TGL) from Rolls-Royce plc*. 2013, Alstom: Online.
45. Reynolds, O., *An investigation into the circumstances which determine whether the motion of water shall be direct or sinuous, and the law of resistance in parallel channels.* Philosophical Transactions of the Royal Society, 1883. **174**: p. 935 - 982.
46. Kundu, P.K. and I.M. Cohen, *Fluid Mechanics*. 4 ed. 2008, Oxford: Elsevier.
47. Chanson, H., *Development of the Bélanger Equation and Backwater Equation by Jean-Baptiste Bélanger (1828).* Journal of Hydraulic Engineering, 2009. **135**(3): p. 159-163.
48. Bornstein, A., *Laminar to turbulent transition visualisation*. 2011: Colorado.
49. Kolmogorov, A.N., *Dissipation of Energy in the Locally Isotropic Turbulence.* Proceedings: Mathematical and Physical Sciences, Turbulence and Stochastic Process: Kolmogorov's Ideas 50 Years On, 1941. **434**: p. 15-17.
50. Kolmogorov, A.N., *The local structure of turbulence in incompressible viscous fluid for very large Reynolds numbers.* Proceedings: Mathematical and Physical Sciences, Turbulence and Stochastic Process: Kolmogorov's Ideas 50 Years On, 1941. **434**(1890): p. 9-13.
51. Ross, I. and A. Altman, *Wind tunnel blockage corrections Reviewand application to Savonius vertical-axis wind turbines.* Journal of Wind Engineering and Industrial Aerodynamics, 2011. **99**: p. 523-538.
52. Bahaj, A. and L. Myers. *Near wake properties of horizontal axis marine current turbines*. in *Eighth European wave and tidal energy conference*. 2009. Uppsala, Sweden: EWTEC.
53. Troolin, D., L. Chamorro, and S.-J. Lee, *Volumetric Velocity Measurements on Underwater Turbines.* 16th International Symposium on Applications of Laser Techniques to Fluid Mechanics, 2012.

54. O'Doherty, T., et al., *Experimental and Computational Analysis of a Model Horizontal Axis Tidal Turbine.* Proceedings of the 8th European Wave and Tidal Energy Conference, Uppsala, Sweden, 2009.
55. Chen, T. and L. Liou, *Blockage corrections in wind tunnel tests of small horizontal-axis wind turbines.* Experimental Thermal and Fluid Science, 2011. **35**: p. 565-569.
56. Bahaj, A., et al., *Power and thrust measurements of marine current turbines under various hydrodynamic flow conditions in a cavitation tunnel and a towing tank.* Renewable Enegy, 2007. **32**(1): p. 407-426.
57. Vermeer, L.J., J.N. Sorensen, and A. Crespo, *Wind Turbine Wake Aerodynamics.* Progress in Aerospace Sciences, 2003. **39**.
58. Shen, H.-W., C.R. Johnson, and K.-L. Ma, *Visualizing vector fields using line integral convolution and dye advection*, in *Proceedings of the 1996 symposium on Volume visualization*. 1996, IEEE Press: San Francisco, California, USA. p. 63-ff.
59. Siebert, H. and K. Lehmann, *On the Use of Hot-Wire Anemometers for Turbulence Measurements in Clouds.* Journal of Atmospheric and Oceanic Technology, 2006. **24**(1): p. 980-994.
60. Lyon, V. and M. Wosnik, *Spatio-temporal resolution of different flow measurement techniques for marine energy applications*, in *2nd Marine Energy Technology Symposium*, METS2014, Editor. 2014: Seattle.
61. Rusello, P.J., et al., *Improvements in Acoustic Doppler Velocimetery*, in *The 7th International Conference on Hydroscience and Engineering (ICHE-2006)*. 2006: Philadelphia, USA.
62. Mycek, P., et al., *Numerical and experimental study of the interaction between two marine current turbines.* International Journal of Maine Energy, 2013. **1**: p. 70-83.
63. Hann, D. and C. Greated, *The measurement of flow velocity and acoustic particle velocity using PIV.* Institute of Physics: Measurement Science and Technology, 1997. **8**(1): p. 1517–1522.
64. Schimmels, S. *Forschungzentrum Küste*. 2014 [cited 2014 22/10/2014]; Available from: http://www.fzk.uni-hannover.de/.
65. Adrian, R., *Scattering particle characteristics and their effect on pulsed laser measurement of fluid flow.* Applied Optics, 1984. **23**(11): p. 1690-1691.
66. Raffel, M., et al., *Particle Image Velocimetry: A Practical Guide*. 2 ed. 2007, Berlin: Springer.
67. NewWaveResearch, *Solo PIV Nd:YAG Laser Users Manual*. 2002.
68. Adrian, R.J., *Twenty years of particle image velocimetry.* Experiments in Fluids, 2005. **39**(2): p. 159-169.
69. Pizer, S., et al., *Adaptive histogram equalization and its variations.* Computer Vision, Graphics, and Image Processing, 1987. **39**(3): p. 355-368.
70. Hummel, R., *Image enhancement by histogram transformation.* Computer Graphics and Image Processing, 1977. **6**(2): p. 184-195.
71. Shavit, U., R.J. Lowe, and J.V. Steinbuck, *Intensity Capping: a simple method to improve cross-correlation PIV results.* Experiments in Fluids, 2007. **42**: p. 225-240.
72. Bastiaans, R., *Cross-correlation PIV theory implementation and accuracy*. 2000, Eindhoven: CIP-DATA LIBRARY TECHNISCHE UNIVERSITEIT EINDHOVEN.
73. Pust, O., *PIV: Direct Cross-Correlation compared with FFT-based Cross-Correlation.*
74. Meyer, K.E., et al., *PIV in a model wind turbine rotor wake.* 10TH INTERNATIONAL SYMPOSIUM ON PARTICLE IMAGE VELOCIMETRY, 2013.
75. Thielicke, W. and E. Stamhuis, *PIVLab - Towards user-friendly, affordable and accurate digital particle image velocimetry in MatLab.* Journal of Open Research Software (In press), 2014. **2**(1).
76. Nogueira, J., A. Lecuona, and P. Rodriguez, *Data validation, false vectors correction and derived magnitudes calculation on piv data.* Institute of Physics: Measurement Science and Technology, 1997. **8**(1).

77. Westerweel, J., *Efficient detection of spurious vectors in particle image velocimetry data.* Experiments in Fluids, 1994. **16**(3-4): p. 236-247.
78. Hart, D., *PIV Error Correction.* Experiments in Fluids, 2000. **29**(1): p. 13 - 22.
79. Adrian, R., *Dynamic ranges of velocity and spatial resolution of particle image velocimetry.* Institute of Physics: Measurement Science and Technology, 1997. **8**(1): p. 1393-1398.
80. Thielicke, W., *The Flapping Flight of Birds - Analysis and Application*, in *Biology*. 2014, Rijksuniversiteit Groningen: Groningen.
81. Adrian, R.J., *Particle-Imaging Techniques For Experimental Fluid Mechanics.* Annual Reviews, 1991.
82. Betz, A., *Windmills in the light of modern research.* National Advisory Committee for Aeronautics, 1928. **XV**(46).
83. Burton, T., et al., *Wind Energy Handbook*. 2001, Chichester: John Wiley & Sons.
84. Foreman, K., B. Gilbert, and B. Oman, *Diffuser Augmentation of Wind Turbines.* Solar Energy, 1978. **20**(4): p. 305 - 311.
85. Vogel, C., R. Willden, and G.T. Houlsby, *The Power Potential of a Tidal Turbine Array with Turbine Power Capping*, in *2nd Asian Wave and Tidal Energy Conference*. 2014, AWTEC: Tokyo.
86. Finn, M., *Environment Description for the EMEC Tidal Test Site Fall of Warness, Orkney*. 2009.
87. Karsten, R., A. Swan, and J. Culina, *Assessment of arrays of in-stream tidal turbines in the Bay of Fundy.* Philosophical Transactions of the Royal Society A, 2013. **371**('New research in tidal current energy'): p. 15.
88. Dyer, K., *Current Velocity Profiles in a Tidal Channel.* Geophysics, Journal of the Royal Astronomical Society, 1970. **22**: p. 153-161.
89. O'Doherty, T., et al., *Considerations of a horizontal axis tidal turbine.* Proceedings of the Institution of Civil Engineers, 2010. **163**(EN3): p. 119-130.
90. De Chant, L., *The venerable 7th power law turbulent velocity profile.* Applied Mathematics and Computation, 2005. **161**: p. 463-474.
91. Brown, M., *Tidal streams and tidal stream energy device design*. 2009, Carbon Trust: London.
92. Okorie, P., A. Hossain, and P. Pollard, *Implications of using the Classical 7th Power Law in Modelling a Turbulent Environment (Poster)*. 2011.
93. von Karman, T., *Über den Mechanismus des Widerstandes, den ein bewegter Körper in einer Flüssigkeit erfährt (About the mechanism of resistance that a moving body undergoes in a liquid).* Nachrichten der K. Gesellschaft der Wissenschaften zu Göttingen, 1911: p. 509-517.
94. Mallock, A., *On the resistance of air.* Proceedings of the Royal Society A, 1907. **79**(1): p. 262-265.
95. Bernad, H., *Comptes rendus de l'Academie des Sciences.* 1908. **147**: p. 839-842, 970-972.
96. Williamson, C.H.K., *Vortex dynamics in the cylinder wake.* Annual Review of Fluid Mechanics, 1996. **28**: p. 477-539.
97. Kolar, V., *Vortex identification: New requirements and limitations.* International Journal of Heat and Fluid Flow, 2007. **28**(1): p. 638-652.
98. Hunt, J., A. Wray, and P. Moin. *Eddies, stream, and convergence zones in turbulent flows*. in *Proceedings of the Summer Program 1988*. 1988. Center for Turbulence Research: Stanford University.
99. Holmen, V., *Methods for Vortex Identification*. 2012. p. 46.
100. Ellison, J. *Blue Energy - Vertical Axis Hydro Turbine*. 2011 2011 [cited 2014 28/08/2014]; Description of Blue Energy Vertical Axis Hydro Turbine Concept]. Available from: http://www.bluenergy.com/vertical-axis-turbine/vaht/.
101. Ko, K.-W., et al., *A Study on Performance of Savonius Tidal Current Turbine.* Advanced Science Letters, 2013. **19**(6): p. 1709-1713.
102. Sagrillo, M. *The Myths & Mysticism of Vertical Axis Wind Turbines* Windletter, 2005. **24**.

103. Fraenkel, P., *Power from marine currents.* Proceedings of the Institution of Mechanical Engineers, Part A: Journal of Power and Energy, 2002. **216**.
104. Clarke, J., A. Grant, and C. Johnstone, *Output characteristics of tidal current power stations during spring and neap cycles*, in *WREC04*. 2004, University of Strathclyde, Glasgow: Denver. p. 5.
105. Kornfeld, M. and L. Suvorov, *On the Destructive Action of Cavitation.* Journal of Applied Physics, 1944. **15**.
106. Bahaj, A.S., *Generating electricity from the oceans.* Renewable and Sustainable Energy Reviews, 2011.
107. Winter, A.I., *Differences in Fundamental Design Drivers for Wind and Tidal Turbines.* IEEE, 2011.
108. Khan, M., et al., *Hydrokinetic energy conversion systems and assessment of horizontal and vertical axis turbines for river and tidal applications: A technology status review.* Applied Energy, 2009.
109. Hammerfest, *Renewable energy from tidal currents*. 2012: Hammerfest, Norway. p. 12.
110. *TGL DeepGen Brochure*. Tidal Generation Limited.
111. Smith, M. and T. Cornelius, *Presentation to Offshore Engineering Society Tidal Stream Energy - Atlantis Group.* 2009.
112. Cauwelaert, F.v., *EDF and OpenHydro Prepare to Install First Tidal Turbine in Brittany, France*. 2011.
113. Fraenkel, P., *Presentation - MCT's SeaGen Tidal Turbine*. 2011.
114. Hamilton, M., *Technology Update*. 2012, Scotrenewables: Orkney. p. 33.
115. Divett, T., R. Vennell, and C. Stevens, *Optimization of multiple turbine arrays in a channel with tidally reversing flow by numerical modelling with adaptive mesh.* Philosophical Transactions of the Royal Society A, 2013. **371**('New research in tidal current energy'): p. 13.
116. Walker, S., *Barriers to the Deployment of a 100MW Tidal Array in the UK.* International Journal of Energy Engineering, 2013. **3**(3): p. 80-92.
117. Fung, C., S. Walker, and R. Howell, *Effect of the velocity profile of incoming flow on the performance of a horizontal axis tidal stream turbine*, in *2nd Asian Wave and Tidal Energy Conference*. 2014, AWTEC: Tokyo.
118. Calvert, J. and R. Farrar, eds. *An Engineering Data Book*. 1999, Palgrave.
119. Crespo, A., et al., *Experimental Validation of the UPM Computer Code to Calculate Wind Turbine Wakes and Comparison with other models.* Journal of Wind Engineering and Industrial Aerodynamics, 1988. **27**(1): p. 77-88.
120. MacLeod, A.J., et al., *Wake effects in tidal current turbine farms.* IMarEST, 2002.
121. Kang, S., et al., *Numerical simulation of 3D flow past a real-life marine hydrokinetic turbine.* Advances in Water Resources, 2012.
122. VerdantPower, I. *The RITE Project*. 2014 [cited 2014 29/10/2014]; Available from: http://www.verdantpower.com/rite-project.html.
123. Smagorinsky, J., *General Circulation Experiments with the Primitive Equations: I. The Basic Experiment.* Monthly Weather Review, 1963. **91**(3): p. 99-164.
124. Churchfield, M.J., Y. Li, and P.J. Moriarty, *A Large-Eddy Simulation Study of Wake Propagation and Power Production in an Array of Tidal-Current Turbines.* 9th European Wave and Tidal Energy Conference 2011, 2011.
125. Sorensen, J.N. and W.Z. Shen, *Numerical modeling of wind turbine wakes.* Journal of Fluids Engineering, 2002. **124**(1): p. 393-399.
126. Pham, C. and V. Martin, *Tidal current turbine demonstration farm in Paimpol-Brehat.* 2009.
127. Hervouet, J.-M., *Hydrodynamics of Free Surface Flows. Modelling with the finite element method.* Wiley, 2007.
128. Leonard, A., *Vortex Methods for Flow Simulation.* Journal of Computational Physics, 1980. **37**(3): p. 289-335.

129. Pinon, G., et al., *Numerical simulation of the wake of marine current turbines with a particle method.* Renewable Enegy, 2012. **46**(1): p. 111-126.
130. Kirkil, G., S.G. Constantinescu, and R. Ettema, *Coherent Structures in the Flow Field around a Circular Cylinder with Scour Hole.* Journal of Hydraulic Research, 2008. **134**(5): p. 572 - 587.
131. Kirkil, G. and G. Contstantinescu, *A numerical study of the laminar necklace vortex system and its effect on the wake for a circular cylinder.* Physics of Fluids, 2012. **24**(1).
132. Yamada, H. and H. Osaka, *A Visualization Study on Necklace and Shedding Vortices Around a Three-Dimensional Protuberance*. Flow Visualisation VI. 1992.
133. Euler, T. and J. Herget, *Controls on local scour and deposition induced by obstacles in fluvial environments.* Catena, 2010.
134. White, F., ed. *Fluid Mechanics*. 2011, F. McGraw Hill Publishing.
135. Xu, G. and Y. Zhou, *Strouhaul numbers in the wake of two inline cylinders.* Experiments in Fluids, 2004. **37**: p. 248-256.
136. Nicolle, A. and I. Eames, *Numerical study of the flow through and around a circular array of cylinders.* Journal of Fluid Mechanics, 2011.
137. Simpson, R., *Junction Flows.* Annual Review of Fluid Mechanics, 2001. **33**(1): p. 415-443.
138. Unger, J. and W. Hager, *Down-flow and horseshoe vortex characteristics of sediment embedded bridge piers.* Experiments in Fluids, 2007. **42**(1): p. 1-19.
139. Myers, L. and A. Bahaj, *An experimental investigation simulating flow effects in first generation marine current energy converter arrays.* Renewable Energy, 2011. **37**.
140. Chamorro, L.P., et al., *On the interaction between a turbulent open channel flow and an axial-flow turbine.* Journal of Fluid Mechanics, 2013. **716**.
141. Stallard, T., et al., *Interactions between tidal turbine wakes: experimental study of a group of three-bladed rotors.* Philosophical Transactions of the Royal Society A, 2013. **371**.
142. Eames, I., C. Jonsson, and P.B. Johnson, *The growth of a cylinder wake in turbulent flow.* Journal of Turbulence,, 2011. **12**(N39).
143. Thomson, J., et al., *Measurements of Turbulence at Two Tidal Energy Sites in Puget Sound WA.* IEEE Journal of Oceanic Engineering, 2012. **37**(3): p. 363-374.
144. Taylor, G.I., *The Spectrum of Turbulence.* Proceedings of the Royal Society A, 1938. **164**: p. 476-490.
145. Pearson, K., *On Lines and Planes of Closest Fit to Systems of Points in Space.* Philosophical Magazine, 1901. **2**(11): p. 559-572.
146. Hotelling, H., *Analysis of a complex of statistical variables into principal components.* Journal of Educational Psychology, 1933. **24**(1): p. 417-441, 298-520.
147. Hotelling, H., *Relations between two sets of variates.* Biometrika, 1936. **27**: p. 321-377.
148. Brevis, W. and C.J. Keylock, *Lecture Slides: CIV4300 - Flow, Turbulence and Sediment Transport*, W. Brevis, Editor. 2012: Sheffield.
149. Jolliffe, I.T., *Principal Component Analysis, Second Edition*. 2002.
150. Adrian, R., K. Christensen, and Z.C. Liu, *Analysis and interpretation of instantaneous turbulent velocity fields.* Experiments in Fluids 2000. **29(3)**: p. 275–290.
151. *Engineering Turbulence Modelling and Measurements - 4*. in *4th International Symposium on Engineering Turbulence Modelling and Measurements*. 1999. Ajaccio, Corsica: Elsevier.
152. Brevis, W. and M. Garcia-Villalba, *Shallow-flow visualization analysis by proper orthogonal decomposition.* Journal of Hydraulic Research, 2011. **49**(5): p. 586 - 594.
153. Carmer, C., *Shallow turbulent wake flows: momentum and mass transfer due to large-scale coherent vortical structures*, in *Civil Engineering*. 2005, Universitat Karlsruhe: Karlsruhe.
154. Nicolleau, F.C.G.A. *Theory and application of turbulence*. 2011. 97 - 108.
155. Nortek, *Nortek Vectrino Lab Datasheet*. 2013.
156. MicroSphereTechnology, *Conductospheres M-18 Product Information Sheet*. 2009.
157. Plascoat, *Talisman 30 ES Data Sheet*. 2010.

158. Khodaparast, S., M. Milan, and N. Borhani, *Measurement Techniques: Digital Particle Imaging Velocimetry*. 2011.
159. Westerweel, J., C. Poelma, and K. Kiger, *Introduction to Particle Imaging Velocimetry*. 2010.
160. Neary, V., et al., *Near and far field flow disturbances induced by model hydrokinetic turbine ADV and ADP comparison.* Renewable Energy, 2013. **1**(6).
161. Giles, J., et al., *The downstream wake response of marine current energy converters operating in shallow tidal flows.* World Renewable Energy Conference, 2011.
162. Bahaj, A. and L. Myers, *Report - Experimental Tests - Array Project*. 2008, University of Southampton.
163. DirectPlastics, *Nylon 66 Data Sheet*. 2014.
164. MFA, *MFA / Como Drills Miniture motor specification sheet.* 2012.
165. Allegro, *ACS712 Current Sensing Module Data Sheet*. 2007, Allegto MicroSystems, Inc.: Worcester, Massachusetts, USA. p. 14.
166. Edwards, J., *The Influence of Aerodynamic Stall on the Performance of Vertical Axis Wind Turbines*, in *Mechanical Engineering*. 2012, Sheffield.
167. McNurty, P., *Length and time scales in turbulent flows*, in *Turbulence*. 2001: Utah. p. 5.
168. Jirka, G., *Large scale flow structures and mixing processes in shallow flows.* Journal of Hydraulic Research, 2001. **39**(6): p. 567-573.
169. Meyer, K.E., *Identify flow structures with Proper Orthogonal Decomposition*. 2008, Technical University of Denmark: DTU.
170. Blevins, R.D., *Flow-Induced Vibration*. 2nd ed. 2006, New York: Von Nostrand Reinhold Co. 377.
171. Blackmore, T., et al., *Influence of turbulence on the drag of solid discs and turbine simulators in a water current.* Experiments in Fluids, 2013. **55**(1): p. 1-10.
172. Kang, S., et al., *Numerical simulation of 3D flow past a real-life marine hydrokinetic turbine.* Advances in Water Resources, 2012. **39**: p. 33-43.
173. MARINET. *Marine Renewables Infrastructure Network for Emerging Energy Technologies*. 2014; Available from: www.fp7-marinet.eu/.
174. Walker, S., L. Cappietti, and R. Howell, *The effect of a tidal turbine support structure on device performance.* International Journal of Marine Energy, 2014. **(in press)**: p. 17.

A1

Appendix 1

The MatLab script used to conduct Proper Orthogonal Decomposition (POD) analysis of images captured of dye injection tests carried out during phase 1 is given below. Full details of the POD method and its application in this project are given in Section 2.9 and Section 4.4.2 respectively.

If the reader is unfamiliar with the MatLab programming language, the Mathworks website (*http://uk.mathworks.com/products/matlab/)* is suggested as an excellent starting point.

```
clc
clear

% Read in image for mean
meanIn = imread('meanimage.bmp');
meanOut = im2double(meanIn); % Convert to monochrome double
meanOut = meanOut(:,:,1); %extract just the first plane
meanOut = imresize(meanOut,[480 640]); %resize to 480 x 640

%access all bitmap files in folder
files = dir('*.jpg');
for k=1:(numel(files));
import=(files(k).name)

% Read in image
inIm = imread(import);
%extract filename parts for naming export
[pathstr, name, ext] = fileparts(import)

% Convert to monochrome double
size(inIm)
outIm = im2double(inIm);

%resize
outIm2 = imresize(outIm,[480 640]);
outIm2 = outIm2(:,:,1); %extract just the first plane

%deduct values from mean then invert
outIm3 = meanOut-outIm2;
outIm4 = 1-outIm3;

%write output double precision
outputname=['fluct', name, '.bmp'] %creates titles for the exports
imwrite(outIm4, outputname, 'bmp')

% Import files (as double precision bitmap)

files = dir('*.bmp');
for k=1:(numel(files));
import=(files(k).name);
Im = imread(import); % Read in the image
R = reshape(Im,[],1); % Each snapshot into a single long column
data8(:,k)=R; % Write into appropriate column of "data" matrix
data=im2double(data8); %convert data matrix from uint8 to double
end

% Do POD analysis
```

```
A=data'*data; % Autocovariance matrix
[eV,D]=eig(A); % solve: eV is eigenvectors, D is eigenvalues in
diagonal matrix

[L,I]=sort(diag(D)); % sort eigenvalues in ascending order - I is
sorted index vector
for i=1:length(D)
eValue(length(D)+1-i)=L(i); % Eigenvalues sorted in descending order
eVec(:,length(D)+1-i)=eV(:,I(i)); % Eigenvectors sorted in the same
order
end;

eValue(length(eValue))=0; % last eigenvalue should be zero
menergy=eValue/sum(eValue); % relative energy associated with mode m

% calculate the first 10 modes
for i=1:10
tmp=data*eVec(:,i); % find mode
phi(:,i)=tmp/norm(tmp); % normalize mode
end;

%individual modes
mode1=255*(phi(: , 1));
mode1=reshape(mode1,480,640);
mode1comp=imcomplement(mode1);
imwrite(mode1comp,'mode1.bmp')

mode2=255*(phi(: , 2));
mode2=reshape(mode2,480,640);
mode2comp=imcomplement(mode2);
imwrite(mode2comp,'mode2.bmp')

mode3=255*(phi(: , 3));
mode3=reshape(mode3,480,640);
mode3comp=imcomplement(mode3);
imwrite(mode3comp,'mode3.bmp')

mode4=255*(phi(: , 4));
mode4=reshape(mode4,480,640);
mode4comp=imcomplement(mode4);
imwrite(mode4comp,'mode4.bmp')

mode5=255*(phi(: , 5));
mode5=reshape(mode5,480,640);
mode5comp=imcomplement(mode5);
imwrite(mode5comp,'mode5.bmp')

mode6=255*(phi(: , 6));
mode6=reshape(mode6,480,640);
mode6comp=imcomplement(mode6);
imwrite(mode6comp,'mode6.bmp')

mode7=255*(phi(: , 7));
mode7=reshape(mode7,480,640);
mode7comp=imcomplement(mode7);
imwrite(mode7comp,'mode7.bmp')
```

```
mode8=255*(phi(: , 8));
mode8=reshape(mode8,480,640);
mode8comp=imcomplement(mode8);
imwrite(mode8comp,'mode8.bmp')

mode9=255*(phi(: , 9));
mode9=reshape(mode9,480,640);
mode9comp=imcomplement(mode9);
imwrite(mode9comp,'mode9.bmp')

mode10=255*(phi(: , 10));
mode10=reshape(mode10,480,640);
mode10comp=imcomplement(mode10);
imwrite(mode10comp,'mode10.bmp')

mode1energy=sum(sum(norm(mode1)));
mode2energy=sum(sum(norm(mode2)));
mode3energy=sum(sum(norm(mode3)));
mode4energy=sum(sum(norm(mode4)));
mode5energy=sum(sum(norm(mode5)));
mode6energy=sum(sum(norm(mode6)));
mode7energy=sum(sum(norm(mode7)));
mode8energy=sum(sum(norm(mode8)));
mode9energy=sum(sum(norm(mode9)));
mode10energy=sum(sum(norm(mode10)));
totalenergy=mode1energy+mode2energy+mode3energy+mode4energy+mode5ene
rgy+mode6energy+mode7energy+mode8energy+mode9energy+mode10energy;

modesenergy=[(mode1energy/totalenergy),(mode2energy/totalenergy),(mo
de3energy/totalenergy),(mode4energy/totalenergy),(mode5energy/totale
nergy),(mode6energy/totalenergy),(mode7energy/totalenergy),(mode8ene
rgy/totalenergy),(mode9energy/totalenergy),(mode10energy/totalenergy
)]
```

A2

Appendix 2

The table below gives details of a selection of animated sequences of instantaneous PIV results from experiments carried out in phase 3, 4a and 4b of the present project, which have been made available online. These sequences allow the reader to easily see the dynamic effects observed by the author and described in the text, which is not possible on paper. The videos detailed below can be accessed at via the following web address:

http://tidalsheffield.wordpress.com/piv-wake-videos/

All videos illustrate the wake downstream of the downstream turbine, without an upstream turbine and with an upstream turbine mounted on a 16mm diameter support structure located at far (10*D*) and near (5*D*) offset in the inline (0*D*), Position 1 () and Position 2 () cross-stream offset positions. Cross-stream offset is in all cases towards the top of the image, and flow is from left to right. The measurement plane is 135mm in all cases, and flow case 2 is used in all cases (Water depth = 300mm, Re = 3 x 10^5, Fr = 0.062, λ = 3.1, u_0 = 0.35m/s, B = 7%).

Real-time (15Hz) samples of 100 frames of recorded PIV data are given in each case.

Experiment number	*Phase*	*Downstream support structure diameter (mm)*	*Upstream turbine separation distance (D)*	*Upstream turbine offset distance (D)*
17	3	11	No upstream turbine	N/A
34	4a	11	10	0
46	4a	11	5	0
20	3	16	No upstream turbine	N/A
38	4a	16	10	0
50	4a	16	5	0
23	3	20	No upstream turbine	N/A
42	4a	20	10	0
54	4a	20	5	0
70	4b	11	10	0.5
71	4b	11	10	1
72	4b	16	10	0.5
73	4b	16	10	1
74	4b	20	10	0.5
75	4b	20	10	1
76	4b	11	5	0.5
77	4b	11	5	1
78	4b	16	5	0.5
79	4b	16	5	1
80	4b	20	5	0.5
81	4b	20	5	1